Exploring interactions between biological matter and dendritic nanoparticles through the application of fluorescence lifetime probes

Dissertation

zur Erlangung des Grades

Doctor rerum naturalium

(Dr. rer. nat.)

am Fachbereich Physik

der Freien Universität Berlin

vorgelegt von

Pierre Volz-Rakebrand

(geb. Volz)

Berlin 2020

Erstgutachterin: Prof. Dr. Ulrike Alexiev (Fachbereich Physik, Freie Universität Berlin)

Zweitgutachter: Prof. Dr. Karsten Heyne (Fachbereich Physik, Freie Universität Berlin)

Tag der Disputation: 16.07.2021

Abstract

Today's nanomedicine struggles with low success rates in clinical trials. Even though considerable efforts have been made, it is still not possible to exploit its full potential. One of the major problems is the clinical translations from pre-clinical *in-vitro* and *ex-vivo* studies to *in-vivo* applications. While this problem can be attributed to different reasons, such as the limited predictive power of biological test models, experimental methods, their analyses, and interpretations, the lack of information on the interactions between nanoparticles and the plethora of biomolecules poses the main challenge.

In order to shed some light on these interactions, this thesis presents the development and application of fluorescence lifetime spectroscopy and imaging approaches for dendritic nanoparticle systems. By applying fluorescence lifetime probes, the scope of fluorescence read-outs will be extended to monitor biological nanoparticle interactions. Identifying interactions between nanoparticles and target structures and elucidating whether loaded drugs reach their biological targets remain important problems to be solved. The thesis aims to identify nanoparticle locations, interaction states, and molecular environments in diverse *in-vitro* and *ex-vivo* test systems by TCSPC-based time-resolved fluorescence experiments and novel analysis approaches.

First, the sensitivity of fluorescence lifetime probes is characterized in model experiments on a molecular level. By means of a fluorescent molecular rotor (FMR) probe, molecular interactions between dendritic nanoparticles and biomolecules like *serum albumin* are investigated. They are responsible for the so-called protein corona formation, a crucial effect on the systemic application of nanomedicine as it alters further interactions of the nanoparticle during its transport through the body. Second, FMRs are applied to explore their potential for probing nanoparticles' molecular conformational changes and drug release mechanisms.

Moreover, I apply a cluster-based analysis tool for quantitative fluorescence lifetime imaging microscopy (FLIM) to living dermal cells interacting with cargo-loaded and FMR-equipped dendritic nanocarriers. Based on distinct changes in fluorescence lifetime parameters, I identify unknown cellular targets in primary human keratinocytes, quantify the binding affinity of a target surface receptor, visualize intracellular cargo release, and further endocytotic interactions. Thereby, the cellular uptake behavior and fate of the nanocarrier system was characterized in a time-resolved and non-invasive manner. In addition, I investigate the penetration behavior and identify target structures of dendritic nanocarriers after topical administration on different *in-vitro* and *ex-vivo* skin models by confocal FLIM. These experiments reveal specific interactions within the stratum corneal layers, the major interaction site of nanoparticles after topical application. Multiphoton excitation enables the live-tissue FLIM tomography of these interactions in reconstructed human tissue. This shows significant differences in the interaction modes of a dendritic nanocarrier with models of healthy skin and skin suffering from non-melanoma cancer.

Zusammenfassung

Seit ihrer Etablierung ist die Nanomedizin mit dem Problem geringer Erfolgsraten bei klinischen Studien konfrontiert. Trotz beträchtlicher Anstrengungen lässt sich ihr Potenzial immer noch nicht voll ausschöpfen. Das größte Problem stellt die Übertragung der Ergebnisse der Grundlagenforschung (*in-vitro* und *ex-vivo*) auf die klinische Anwendung dar. Die Gründe dafür sind vielfältig: Die prädiktive Kraft biologischer Testmodelle ist begrenzt, ebenso wie die der experimentellen Methoden, ihrer Analysen und Interpretationen. Die größte Herausforderung aber ist der Mangel an Informationen über die Wechselwirkungen zwischen Nanopartikeln und Biomolekülen. An diesem Punkt setzt diese Dissertation an. Sie stellt die Entwicklung und Anwendung von Fluoreszenzlebensdauerspektroskopie und fluoreszenzlebenszeitbasierten bildgebenden Verfahren für die Anwendung an dendritische *Nanocarrier*-Systemen vor. Durch die Anwendung von Fluoreszenzlebensdauersonden erweitere ich den Anwendungsbereich von Fluoreszenzanalysen, um biologische Nanopartikelwechselwirkungen experimentell überwachen zu können. Die Identifizierung von *Nanocarrier- Target*-Interaktionen und die Aufklärung, ob beladene Medikamente ihre biologischen Ziele erreichen, sind nach wie vor allgemeine Probleme, die es zu lösen gilt. In der Dissertation werden Nanopartikel, deren Wechselwirkungszustände und ihre molekulare Umgebung in mikroskopischen Bildern identifiziert. Dazu wurde verschiedene *In-vitro*- und *Ex-vivo*-Testsysteme durch zeitaufgelöste Fluoreszenzexperimente und neuartigen Analyseansätze analysiert.

Die Empfindlichkeit von Fluoreszenz-Lebensdauersonden wird in Modellexperimenten auf molekularer Ebene charakterisiert. Mit Hilfe einer fluoreszierenden molekularen Rotorsonde (FMR) werden molekulare Wechselwirkungen zwischen dendritischen Nanopartikeln und Biomolekülen wie *Serumalbumin* untersucht. Diese sind für die Bildung der so genannten Proteinkorona verantwortlich. Sie hat einen entscheidenden Einfluss auf die systemische Anwendung von Nanomedizin, weil sie weitere Wechselwirkungen des Nanopartikels während seines Transports durch den Körper modifiziert. Desweitern wurden das allgemeine Potenzial dieser FMR erforscht. Durch deren umgebungsabhängige Fluoreszenzlebenszeitsensitivität lässt sich auf intramolekulare Konformationsänderungen sowie Mechanismen der Wirkstofffreisetzung von Nanopartikeln schließen.

Darüber hinaus wende ich ein clusterbasiertes Analysewerkzeug für die quantitative Fluoreszenzlebensdauermikroskopie (FLIM) an, um die Interaktion zwischen lebende Hautzellen und beladenen dendritischen *Nanocarriern* zu untersuchen. Basierend auf signifikanten Veränderungen der Fluoreszenzlebensdauerparameter identifiziere ich unbekannte zelluläre Ziele innerhalb primären humanen Keratinozyten. Dabei quantifiziere ich die Bindungsaffinität eines identifizierten Zieloberflächenrezeptors und visualisiere die intrazelluläre endozytotische Interaktionen des *Nanocarriers* sowie die Freisetzung seiner Ladung. Dadurch wurde das zelluläre Aufnahmeverhalten und der zelluläre Verbleib des *Nanocarrier*-Systems auf nicht-invasive Weise charakterisiert.

Außerdem untersuche ich das Penetrationsverhalten und identifizierte Zielstrukturen von dendritischen *Nanocarriern* nach topischer Verabreichung an verschiedenen *In-vitro*- und *Ex-vivo*-Hautmodellen mittels konfokal-FLIM von Gewebeschnitten. Diese Experimente konnten spezifische Wechselwirkungen innerhalb des *Stratum corneums* nachweisen, dem Ort der Hauptwechselwirkung von Nanopartikeln nach topischer Applikation. Schließlich ermöglicht die Multiphotonenanregung eine FLIM-Tomographie dieser Interaktionen in lebendem, rekonstruiertem, menschlichem Gewebe. Diese zeigte signifikante Unterschiede in den Wechselwirkungsmodi eines dendritischen *Nanocarriers* zwischen Modellen gesunder Haut und Haut, die an nicht-melanotischem Hautkrebs leidet.

Table of content

Declaration of authorship / Selbstständigkeitserklärung

Name / Name: Volz-Rakebrand (geb. Volz)

First name / Vorname: Pierre

I declare to the Freie Universität Berlin that I have completed the submitted dissertation independently and without the use of sources and aids other than those indicated. The present thesis is free of plagiarism. I have marked as such all statements that are taken literally or in content from other writings. This dissertation has not been submitted in the same or similar form in any previous doctoral procedure.

I agree to have my thesis examined by a plagiarism examination software.

Ich erkläre gegenüber der Freien Universität Berlin, dass ich die vorliegende Dissertation selbstständig und ohne Benutzung anderer als der angegebenen Quellen und Hilfsmittel angefertigt habe. Die vorliegende Arbeit ist frei von Plagiaten. Alle Ausführungen, die wörtlich oder inhaltlich aus anderen Schriften entnommen sind, habe ich als solche kenntlich gemacht. Diese Dissertation wurde in gleicher oder ähnlicher Form noch in keinem früheren Promotionsverfahren eingereicht.

Mit einer Prüfung meiner Arbeit durch ein Plagiatsprüfungsprogramm erkläre ich mich einverstanden.

Date / Datum: _____ *Signature / Unterschrift:* _____

Pierre Volz-Rakebrand

Chapter 1: Motivation and thesis overview

1.1 Motivation

Nanotechnology is a term to describe the development, fabrication, and use of artificially created materials, structures, or devices with a characteristic size, ranging from 1 nm to 100 nm.[1-2] Due to this purely size-specific definition, the field of application is broad. Nanotechnology is found in semiconductor and surface physics, organic chemistry, molecular biology, and medicine, to name only but a few examples. In the case of nanomedicines, the functional properties of new nanomaterials in particular have led to a multitude of potential applications. Roughly speaking, these can be divided into the following areas: nanotherapeutics, nanodiagnostics and the hybrid form of nanotheranostics.[3] These applications bridge the gap between physical and biological sciences. They improve drug transport by enabling site-specific drug delivery and allow us to understand the underlying processes of nanoparticle transport, drug release and efficacy. The research of nanoparticulate drug delivery systems is a central area of nanomedical research.[1, 3-4]

In recent decades, considerable efforts have been made to exploit the potential of nanomedicine.[3, 5] However, there are still restrictions and limits to an efficient and effective translation of nanomedicines for human application.[6-8] For example, a recently published article on the efficacy of nanosized drug carriers in cancer therapy states that no significant clinical translation of cancer nanomedicine has taken place so far.[9] Designing novel nanotechnological platforms itself is not even the biggest obstacle. It is possible to design particles with precise physicochemical properties providing access to diverse biological systems and compartments. But it is rather the lack of control of when a nanoparticle interacts with multiple molecular structures within complex organisms that poses the problem.[9] The transition from *in vitro* to *in vivo* is the greatest challenge in the future study of nanomedicine. Mastering this challenge is essential to enable the effective use of nanotechnology in diagnosis and treatment of widespread medical conditions such as cancer, diabetes, cardiovascular and dermal diseases.[9-11]

In addition to the general problem of clinical translation, there are also shortcomings in the implementation of the nonclinical studies. Established experimental investigation methods and the use of current *in-vitro* and *ex-vivo* models are to be questioned. Recent studies show decisive differences between human cells grown on plastic surfaces and those within the humans organism.[12-13] Likewise the resemblance of animal models to the human body is questioned regularly.[14-15] Thus, some of the preclinical models used, human and animal based, need substantial improvements. For some diseases, the heterogeneity of patients requires the use of cells matching in age, sex, and body site.[12] One of the most promising approaches is culturing patient-derived cells in reconstructed 3D tissue models, either as organoids, or as multilayered tissues *in vitro* or as patient-derived xenografts in animals.[16-18]

Nonclinical studies on nanoparticulate drug delivery systems frequently aim to track the nanocarrier or cargo on their way to a potential target site. For this task, fluorescence labeling combined with fluorescence microscopy appears to be an easy, cheap, and fast method providing initial results on nanocarrier uptake in cells or their tissue localization. However, microscopic approaches like common fluorescence-based confocal laser scanning microscopy, highly depend on sample homogeneity, selection of the region of interest, and finally on the optical expertise of the performing researcher.[19] Although there are guidelines for standardized fluorescence measurements,[20] fluorescence probes used for labelling nanoparticles have to be fundamentally characterized with respect to their fluorescence properties both before and after their attachment or loading. In most cases, during the labeling procedure, a fluorophore is added in excess to ensure high labeling yields. Depending on nanoparticle and fluorophore, this might lead to complications when aiming for an assessment of local "concentrations" using a (semi-)quantitative evaluation. Here, a high labeling degree does not automatically result in higher photon emission due to intramolecular fluorescence quenching. Despite the fact of a high local fluorophore concentration, these effects reduce the detectability of the nanoparticle in fluorescence microscopic images. In addition, other influences on fluorescence emission intensities must be considered to a greater extent, such as intermolecular quenching/anti-quenching by the local environment or physicochemical factors such as pH, polarity, or viscosity.[19]

Advanced techniques such as time-resolved fluorescence lifetime spectroscopy or fluorescence lifetime imaging microscopy (FLIM) are suitable for improving fluorescence-based evaluations of nanomedicine in biological systems.[21-24] The fluorescence lifetime defines the characteristic decay time of the excited electronic state of a fluorophore. On the one hand, it can be considered a parameter independent of fluorophore concentration, fluorescence intensity and detection efficiency. On the other hand, fluorescence lifetimes can be sensitive to certain parameters of the physicochemical environment of a fluorophore, such as temperature, pH, viscosity, polarity, or specific molecular interactions.[25-28] This sensitivity of certain fluorophores makes time-resolved fluorescence experiments valuable tools in studying molecular interactions between nanoparticles and target molecules. This enables the probing of cellular and tissue-related interactions.

For such applications, it is essential to use fluorophores suitable for molecular probing. With the right fluorescent probes, FLIM can be applied to identify and visualize interactions of nano-sized drug delivery systems and loaded reporting drugs with spatial and temporal resolution.[29-31] For example, FLIM reveals different transport and activation mechanisms of the fluorescent chemotherapeutic drug doxorubicin by using changes in the fluorescence lifetime during its cellular uptake and target binding process. This is of special interest as doxorubicin in combination with a variety of nanocarrier systems (polymeric, gold, silica, iron oxide) overcomes the potentially high chemoresistance of several cancer types.[21, 24, 31-35]

However, quantitative FLIM analysis distinguishing different local fluorophore interactions is often hampered by the difficulty to acquire sufficient photon numbers in the fluorescence decay curves recorded in the individual pixels, that characterize the fluorescence lifetime. More than 10^4 photons are required to accurately fit a bi-exponential fluorescence decay.[36] Fast acquisition times, high magnification levels ((sub-)cellular resolution) and phototoxicity, all limit the detected photon number. Low photon counts increase the uncertainty of the pixel or area based decay fitting in the classical tau-plot FLIM analysis, leading to a potential distorted lifetime determination, in particular for multi-exponential fluorescence decays.[37-39] Advanced FLIM analysis techniques have been previously developed to deal with these problems, including rapid global fitting (FLIMfit)[39], Bayesian estimation,[37] pattern-matching using reference fluorescence lifetime signature s combined with additional spectral information,[40] or graphically based analyses, such as the phasor approach[37, 40-41]. Still, some major challenges for automated, fast, and reliable recognition and extraction of high-dimensional fluorescence decay patterns are not completely solved. One problem is the fitting-free parametrization and identification of high multidimensionality in fluorescence decay traces of different fluorescence species in an automated user independent process.

One of the most advanced approaches is the graphically based phasor plot. It yields fluorescence lifetimes for mono- and bi-exponential decays, and allows the identification of lifetime species by visual inspection of the phasor plot.[41] Another approach is FLIMfit, a fast analysis method for large data sets, but essentially also limited to resolving bi-exponential decays.[39] The same applies to the Baysian estimation approach.[42] Reference-based pattern matching approaches are not generally applicable to unknown fluorescence decay traces, unless one uses a reference pattern extraction. Making the user dependent on graphical interpretation like in the phasor approach.[43] In particular, the higher multi-dimensionality of complex FLIM data calls for new approaches reducing the data dimensionality, while retaining the essential information of the fluorescence lifetime characteristic. A possible solution to this problem is the Cluster-FLIM approach[44] developed in the group of Prof. Alexiev (Freie Universität Berlin, Germany). It is used and evaluated in this thesis for fluorescently labeled dendritic nanoparticles interacting with living dermal cells and human skin models *in vitro* and *ex vivo*.

These dendritic nanoparticles appear to be promising candidates for biomedical applications such as drug solubilization and transport as they are characterized by a high molecular density, a defined shape, a monodisperse nature and a large number of functional and tunable surface groups.[45] The name dendritic is derived from the Greek *dendron* ("tree-like") and is used here because the structures of these nanoparticles (2 – 20 nm) replicate the branching of trees.[46] Despite the advantages, dendritic nanoparticles, like most other nanoparticle systems, are rarely translated "from bench to bed and back"[47]. This work therefore tries to find new approaches to improve nonclinical studies on dendritic nanoparticles by time-resolved fluorescent spectroscopy and microscopy. For this purpose, I characterized fluorescent lifetime probes that monitor either biological environmental parameters

like pH values and levels of reactive oxygen species (ROS) or identify and visualize interactions of dendritic nanoparticles on molecular, cellular and tissue levels.

1.2 Thesis overview

This dissertation is divided into five chapters. Chapter 1 contains my motivation for the following investigations, resulting in this thesis. Chapter 2 introduces fundamental physical, technical and biological issues relevant to my investigations. I will start by giving background information on photophysical theory concerning the fluorescence phenomena. Then, I will discuss related quantities representing important parameters for fluorescence experiments. Subsequently, the technical and analytical aspects of time-resolved fluorescence spectroscopy and microscopy are presented and discussed. This is followed by an overview of how to use nanotechnology in medicine. After that, I will introduce various nanoparticles, particularly dendritic nanoparticles developed in the group of Prof. Haag (Freie Universität Berlin, Germany) and Prof. Romero (National University of Quilmes, Argentina). The second chapter ends with a description of skin anatomy and nanoparticle systems allowing transdermal transport.

Chapter 3 contains the experimental section and introduces the materials, methods and experimental setups used in my thesis. I present the preparation of biological and nanoparticulate samples obtained by diverse groups, the experimental conditions of the fluorescence probe characterization, and the experiments conducted. I provide an insight into the experimental procedures and analyses methods used in the individual fluorescence experiments.

Chapter 4 starts with the characterization of custom-built FLIM setups and analysis tools (Section 4.1).[44, 48-49] The time-resolved fluorescence imaging approaches used are, in part, new. I implemented a supercontinuum white light laser source for selective spectral excitation. Secondly, I established a multiphoton excitation FLIM setup for tomographic FLIM. Furthermore, Chapter 4 presents an evaluation of a novel, clustering based FLIM analysis tool[44] developed in the group of Prof. Alexiev (Freie Universität Berlin, Germany) and discusses its possibilities in biological imaging of fluorescence lifetime probes. These results are followed by time-resolved fluorescence characterization of fluorescence lifetime probes (Section 4.1). Section 4.2 and 4.3 show how to use the principles and capabilities of these fluorescence lifetime probes in order to monitor interactions between nanomaterials and biological systems on a molecular level. Section 4.4 demonstrates the possibilities of applying Cluster-FLIM-analysis using an interaction study of CMS nanocarriers (Haag group, Freie Universität Berlin, Germany) during their cellular uptake by keratinocytes, non-melanoma cancer, and dermal dendritic cells provided by various cooperating groups. These results, together with classical uptake inhibition experiments, reveal a receptor mediated uptake process of the dendritic nanoparticles in keratinocytes. Section 4.5 investigates localization and interaction of dendritic nanocarrier systems in skin tissue of different origin. Here, I studied normal and diseased human skin models, *in-* and *ex-vivo* and how they interacted with topical applied nanoparticle solutions. The used concepts of confocal and multiphoton FLIM together with an FMR probe allows new insights into the local penetration behavior of these drug transporters.

Finally, Chapter 5 contains a summary of the results presented in this thesis and a conclusion. Moreover, it gives an outlook on possible applications and questions which may be solved by future time-resolved fluorescence experiments.

Chapter 2: Fundamentals

This chapter presents the photophysical principles behind the fluorescence phenomenon first described by Sir John Herschel in 1845 for an acid quinine solution under "certain incidences of light"[50]. Starting with the fundamental mechanisms behind fluorescence, this chapter outlines important fluorescence properties, which constitute the basis of its high detection sensitivity and selectivity, leading to a plethora of fluorescence applications. This section is followed by an overview of time-resolved fluorescence detection techniques used in spectroscopic and microscopic fluorescence lifetime experiments. After focusing on theory and related technical aspects of fluorescence-based methods, I introduce dendritic nanoparticles and nanocarriers as central objects under investigation in this thesis. The introduction closes with information on nanoparticle interactions and the potential target tissues for polymeric nanomedicine: the human skin and its barrier function hindering effective transdermal drug transport.

2.1 Principles of fluorescence

2.1.1 Photophysical theory

The term fluorescence describes the phenomenon of spontaneous photon emission from an excited molecular entity induced by the transition from the first excited electronic state S_1 to the ground state S_0 after a previous photon absorption. The following section addresses the fundamental mechanisms behind fluorescence emission. Apart from processes like phosphorescence and delayed fluorescence, fluorescence belongs to the phenomena categorized as photoluminescence, a subcategory of the luminescent phenomena, that are, all types of spontaneous photon emission not resulting from heating (incandescence).

Photoluminescence can be observed in many substances, which can be classified in three major groups: substances/molecular entities containing organic compounds like aromatic hydrocarbons or polyenes, inorganic compounds like metal clusters, semiconductor crystals, or carbon nanotubes, and organometallic complexes like ruthenium, copper or porphyrin metal complexes.[51] For this thesis, I used and examined only small fluorescent organic molecules (here called fluorophores).

Perrin-Jablonski diagram

To illustrate processes involved in fluorescence emission of fluorescent organic molecules, the Perrin-Jablonski diagram (Figure 2.1.1) is frequently used. The diagram illustrates the energy levels of a fluorescent molecule. Electronic and vibrational states are drawn as black horizontal lines. The lowest energetic level is the electronic ground state S_0 (singlet). At room temperature, most of the molecules are located there. If stimulated by absorption of a photon from the ultra-violet or visible (UV-Vis) range, the molecule can be excited (Figure 2.1.1, black upward pointing arrows) into the vibrational levels of higher singlet states (S_1, S_2, S_3, …). Photon absorption and electronic transition take place on the femtosecond time scale, much faster ($>10^3\times$) than the following transitions.

From higher vibrational levels, the molecule de-excites back into the lowest energy level of the respective fundamental electronic state by vibrational relaxation, e.g., through transfer of vibrational energy through collisions with solvent molecules during the excited state. In solution, a second transition occurs, called internal conversion, a non-radiative transition between the vibrational levels of two electronic states with the same spin multiplicity, e.g., $S_2 \rightarrow S_1$ or $T_2 \rightarrow T_1$. Internal conversion is followed by vibrational relaxation transferring the molecule to the lowest energy level of the respective electronic state. Vibrational relaxation takes place in the picosecond time regime, resulting in a generally fast transition of the molecule into the lowest vibrational level of the first excited singlet state S_1. Due to the relatively long lifetime of the singlet state S_1, usually between 10^{-10} to 10^{-7} seconds, molecules will accumulate in this state. The transition from the lowest vibrational level of S_1 to the vibrational levels of S_0 may lead to the spontaneous emission of a photon. This process is termed fluorescence (green waved arrow). The effective emission of fluorescence photons occurs only in the lowest excited electronic state (Kasha's rule).[52] The energy of the emitted photon is usually lower than the one of the previously absorbed photon, as excited molecules transfer their vibrational energy typically to surrounding solvent molecules by vibrational relaxation. This phenomenon is called Stokes-shift and leads to a red-shift between absorption and fluorescence spectra (see absorption and fluorescence emission spectra). Tightly connected to the Stokes-shift and the vibrational relaxation in S_1 is Kasha-Vavilov's rule, stating that the probability of fluorescence is generally independent of the excitation wavelength.[53]

Beside the fluorescent transition, internal conversion from $S_1 \rightarrow S_0$ also occurs. However this transition has a relatively low probability, due to the large energy gap.[51] Another de-excitation route from S_1 is intersystem crossing to the triplet states T_i of different spin multiplicity. Following the classical selection rules of electronic transitions, intersystem crossing is forbidden. Yet, spin-orbit coupling between orbital and spin magnetic moment can facilitate the "forbidden" transition in some molecules, especially if the molecule contains heavy atoms.[51] If a molecule transits to the triplet states via intersystem crossing, vibrational relaxation and internal conversion leads to a de-excitation of the molecule into the lowest vibrational energy level of the T_1 state. From this state, the molecule can further de-excite to the S_0 ground state again via intersystem crossing and vibrational relaxation or via phosphorescence. According to the selection rules, transitions from $T_1 \rightarrow S_0$ are equally forbidden due to the change in spin multiplicity. However, spin-orbit coupling also can enable this transition. The low efficiency of $T_1 \rightarrow S_0$ results in long lifetimes of the excited T_1 state. The radiative transition, i.e., phosphorescence can be observed up to minutes after the excitation and is favored by low temperatures or by viscous solvents/environments due to the reduced likelihood of intersystem crossing and vibrational relaxation. Emitted photons via phosphorescence are red shifted compared to fluorescence photons due to the additional energy transfer via vibrational relaxation after intersystem crossing from $S_1 \rightarrow T_1$.

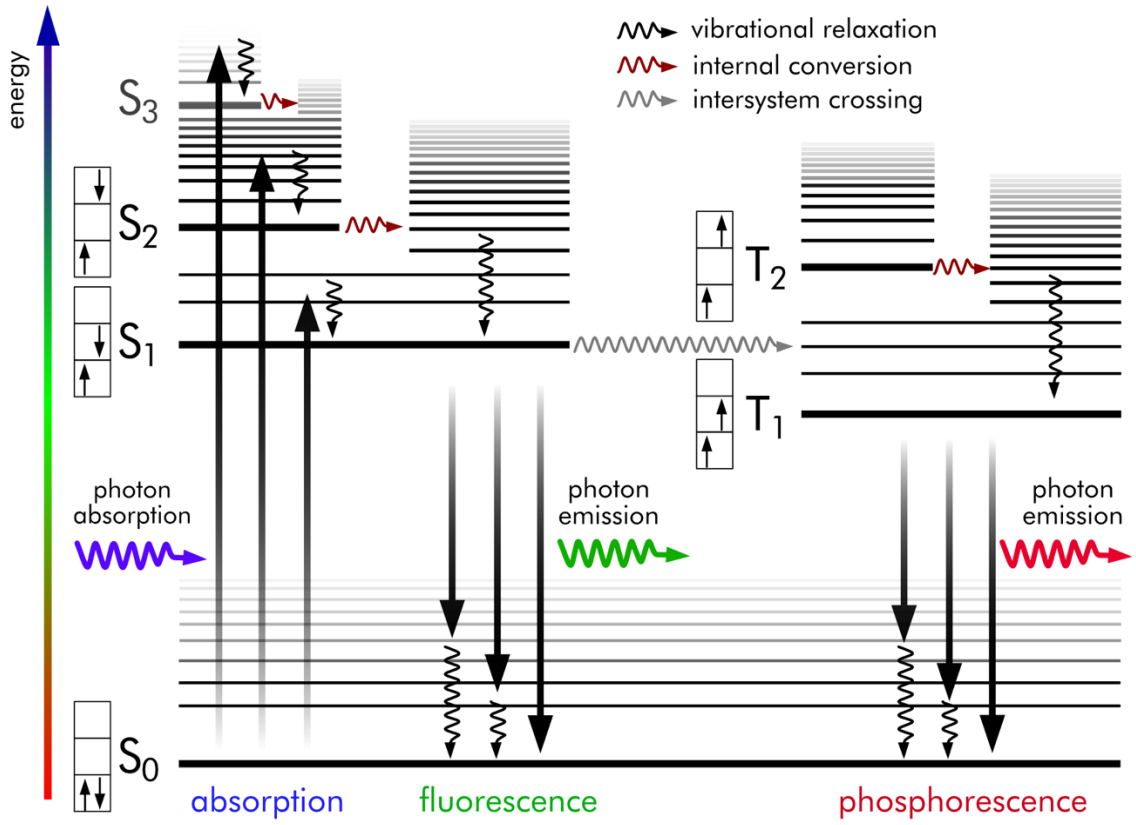

Figure 2.1.1: Perrin-Jablonski diagram. Photon absorption (blue waved arrow) of a molecular entity located in the electronic ground state S_0 results in an excitation to energetically higher singlet states (S_1,S_2,...). The vibrational levels of these singlet states are indicated by thinner lines. Relaxation from the upper vibrational levels into the lowest energy level of the respective electronic state, is indicated by black waved arrows. Transitions via internal conversion between overlapping vibrational levels of neighboring electronic states of the same spin multiplicity is illustrated brown waved arrows. The radiative transition $S_1 \rightarrow S_0$ via fluorescence is shown by a green waved arrow. Intersystem crossing between electronic singlet and triplet states via spin-orbit coupling is indicated by a gray waved arrow. The radiative transition $T_1 \rightarrow S_0$ via phosphorescence is demonstrated by a red waved arrow. Internal conversion between $S_1 \rightarrow S_0$ and $T_1 \rightarrow S_0$ is not indicated. The differences in spin orientation of singlet and triplet states are illustrated by black arrows shown in boxes next to the electronic states.

Photon absorption

In order to understand photon absorption processes in (fluorescent) organic molecules, it is advisable to consider the molecular orbital (MO) theory, a theory using quantum mechanics to describes the electronic structure and electronic transition of a molecule. MO theory defines electronic states resulting from different bonding types between atoms by approximating the MOs of electrons as linear combinations of their original atomic orbitals (LCAO).

The main categories of MOs are called bonding, non-bonding and anti-bonding orbitals. Bonding orbitals increase the electron density between two given atomic nuclei. Thus, they shield both nuclei charges from each other which reinforce the binding strength and minimizes the energy. Non-bonding orbitals do neither influence binding positively nor negatively. Electrons located in these orbitals have the same energy as in their isolated atomic orbitals. The electron density in anti-bonding orbitals is concentrated on the opposite side as for binding orbitals, i.e., the atomic nuclei are not shielded

anymore, and a repulsive force reduces the binding strength. Here, the energy is typically higher than the energy of the generating AO.

These supercategories of MOs are further subdivided into orbitals originating from the initial atomic orbitals. In Figure 2.1.2A,B, the construction principle of MOs from LCAOs is illustrated for the case of the simple homonuclear diatomic molecule difluorine (F_2). Electrons of the 1s- and 2s-orbitals of both fluorine atoms form a pair of a bonding and anti-bonding σ-orbital. The anti-bonding orbital is denoted by an asterisk. Also, the $2p_z$ orbitals have a collinear axis of symmetry forming a σ- and σ*-orbital. The remaining atomic 2p orbitals generate two pairs of π- and π*-orbitals. In order to establish a molecular bond, a bonding orbital has to have an empty matching anti-bonding orbital. Pairs of bonding and anti-bonding orbitals completely filled with electrons do not contribute to bonding. In the case of the F_2-molecule, only the σ_{2pz}-orbital has an empty matching orbital. So, only this orbital contains binding electrons and forms the bond between both atoms.

Bonds formed from σ- or π-orbitals are called σ- or π-bonds, respectively. The illustrated molecular orbital energy diagram in Figure 2.1.2B shows the electronic ground state configuration from where electrons can be excited into higher orbitals via photon absorption or other prosses. Two molecular orbitals are of special interest for electronic transitions: The highest occupied molecular orbital (HOMO) and the lowest unoccupied molecular orbital (LUMO), as the energy gap between both orbitals defines the minimal energy necessary to excite the molecule.

To take a closer look at different orbital/bonding types and their electronic transitions, the consideration of the methanal (formaldehyde) molecule (CH_2O) is more than helpful.[51] The CH_2O molecule contains localized σ- and π-bonds as well as non-bonding orbitals from the oxygen atom (Figure 2.1.2C). In the ground state configuration, the σ-orbitals between C-H and C-O and the π-orbital between C-O are fully occupied while the corresponding anti-bonding orbitals are empty (Figure 2.1.2D). This configuration results in the mentioned σ- and π-bonds between the respective atoms. Electrons located in n-orbitals are called lone pair electrons and do not contribute to any binding. LUMO of methanal are the n-orbitals, whereas HOMO is the π*-orbital which means that the electronic transition with the smallest transition energy is the n→π* transition. By this transition, the electron transits from the n-orbital of the oxygen to π*-orbital between C-H.

Other allowed transitions ranked in the ascending order of required energy are π→π*, n→π* and σ→σ*. In the case of methanal, only localized σ- and π-orbitals are present. The related energy gaps between these orbitals are relatively large, leading to electron transitions which can typically be excited by photons of the UV region.

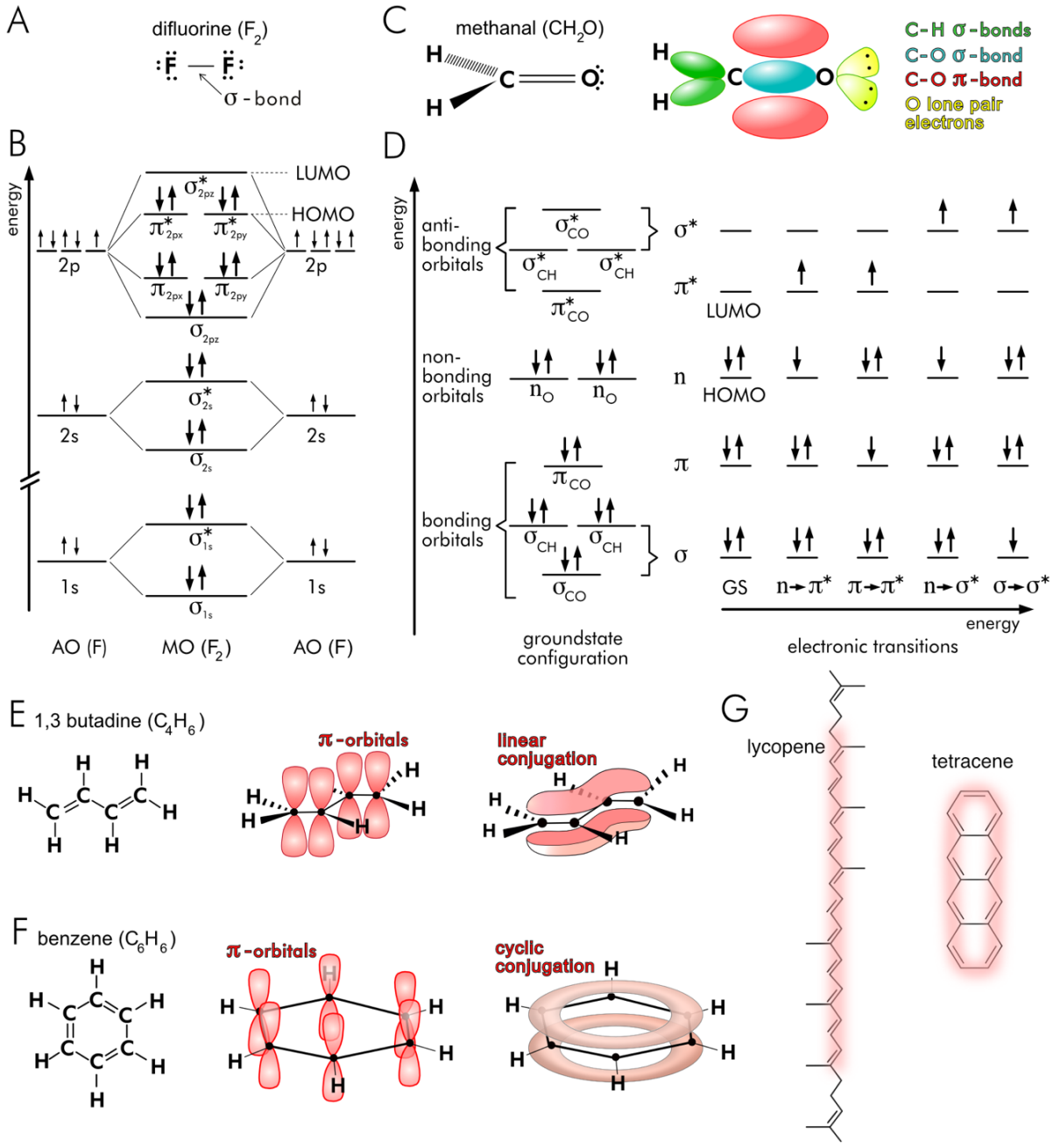

Figure 2.1.2: Molecule orbitals and electronic transitions. **A** Chemical structure of the homonuclear diatomic molecule difluorine F_2, the connecting σ-bond is indicated. **B** Atom orbitals (AO) and resulting molecule orbitals (MO) in F_2. Anti-bonding orbitals are denoted by an asterisk. The highest occupied molecular orbital (HOMO) in the ground state are the π_{2p}*-orbitals. The lowest unoccupied orbital is the σ_{2pz}*-orbital. Pairs of bonding and anti-bonding σ-orbitals formed by the 1s and 2s atom orbitals as well as the π and π*-orbitals formed by $2p_x$ and $2p_y$ are completely filled with electrons. Consequently, they do not contribute to the bonding interaction. Only electrons of the σ_{2pz}-orbital with its unfilled anti-bonding counterpart σ_{2pz}* form the σ-bond between both fluorine atoms. **C** Chemical structure of methanal (CH_2O), involved binding orbitals are drawn schematically. **D** Molecule orbitals, electron configuration and electronic transitions of CH_2O. The ground state (GS) configuration is shown on the left. Shown σ- and π- bonding orbitals have empty matching anti-bonding orbitals and thus contribute to the molecule bonds. Lone pair electrons of oxygen, i.e., electrons that are not forming either the C-O σ- or π-bond are located on the non-binding orbital n and are not involved in binding. On the right-hand side, possible electronic transitions from the GS into higher electronic states are illustrated. Ranked in the ascending order of required energy. **E** 1,3 butadine (C_4H_6): Chemical structure, illustration of π-orbitals and their linear conjugation. **F** Benzene (C_6H_6): Chemical structure, illustration of π-orbitals and their cyclic conjugation. **G** Lycopene and tetracene as representative for molecules with extended π-systems.

This behavior changes in the presence of so-called conjugated systems of delocalized π-orbitals. In conjugated systems, the absorbance shifts up to wavelengths of the visible and near-infrared region due to reduced energy gaps between the resulting conjugated π- and π*-orbitals. Conjugation occurs if a molecule has an alternating series of single and double carbon-carbon bonds (but can also include C-N-, C-O-, N-N-, N-O-bonds). In this case, the π-orbitals overlap across intervening not overlapping σ-orbitals and allow a complete delocalization of all involved electrons over the entire π-orbital system. One distinguishes between linear conjugated systems, like polyenes, e.g., 1,3-butadiene (Figure 2.1.2E) or lycopene (Figure 2.1.2G) and cyclic conjugated systems, like the aromatic molecules benzene (Figure 2.1.2F) or tetracene (Figure 2.1.2G). While 1,3-butadiene (λ_{max}=217 nm) and benzene (λ_{max}=255 nm) still absorb in the UV range, lycopene and tetracene absorb well above 400 nm due to their extensively conjugated π-systems.

In general, the larger the conjugated system is extended, the smaller the energy gaps for π→π* or n→π* transitions are. This means the absorption bands are moved to higher wavelengths. The four benzene rings of tetracene generate a cyclic conjugated system with an absorption maximum at λ_{max} = 480 nm, while the carotenoid lycopene containing a linear conjugated system of 11 carbon-carbon double bonds (Figure 2.1.2G) absorbs between 400 and 550 nm with a maximum at 470 nm. Lycopene solutions appear red-colored for the human eye under white light illumination due to the not absorbed but transmitted fraction of visible light. This relationship is called complementary color effect and can be used to estimate the color or absorbance regime, respectively.

In order to experimentally quantify and characterize the absorption probertites of a molecular entity, a wavelength λ dependent quantity called absorbance $A(\lambda)$ is used, defined by:

$$A(\lambda) = \log_{10}\left[\frac{I_{\mathrm{in}}(\lambda)}{I_{\mathrm{out}}(\lambda)}\right] \quad . \tag{1}$$

While $I_{\mathrm{in}}(\lambda)$ is the intensity of a light beam entering the absorbing medium, $I_{\mathrm{out}}(\lambda)$ is the fraction of not absorbed light transmitted by the medium. Consequently, an absorption/absorbance spectrum can be recorded by detecting both intensities while scanning the wavelength. The number of absorbed photons, i.e., the absorbance, is directly proportional to the concentration c and the path length l through the medium for broad concentration ranges of light absorbing molecules. The Lambert-Beer law describes this linear relationship by the following equation:

$$l \cdot c \cdot \varepsilon(\lambda) = \log_{10}\left[\frac{I_{\mathrm{in}}(\lambda)}{I_{\mathrm{out}}(\lambda)}\right] = A(\lambda) \quad , \tag{2}$$

where $\epsilon(\lambda)$ is the molar absorption coefficient which defines the ability of a molecular entity to absorb a photon of a given wavelength. Derivations from linearity are caused by low signal-to-noise ratios (SNRs) at low absorber concentrations and most notably inter-molecular interactions or aggregation at high concentrations. Typical molar absorption coefficients range between 100 and

100,000 $M^{-1}\,cm^{-1}$ depending on absorbing molecule and solvent. Considering the molecule as classical oscillating dipole, the integral of $\epsilon(\lambda)$ allows to define a further spectroscopic parameter, the oscillator strength f:

$$f = \frac{4\ \log(10)\,\epsilon_0 m_0\ c_0^2}{10\ \mathrm{N_A}\ n\ e^2} \int \lambda^{-2}\varepsilon(\lambda)\mathrm{d}\lambda \quad , \tag{3}$$

with ϵ_0 being the vacuum permittivity, m_0 the electron mass, e the electron charge, m_0 the mass of the molecule, c_0 the speed of light, $\mathrm{N_A}$ Avogadro's constant and n the reflection index. f can accept values between 0 and 1as it expresses the probability of photon absorption by the ratio of the molecular transition strength to the transition strength of a classical single-electron oscillator bound to the nuclear framework (semiclassical approximation).

In quantum mechanics, photon absorption is described by transition moments $\boldsymbol{m}_{if}$ between the electric dipole moments $\boldsymbol{\mu}_i$ and $\boldsymbol{\mu}_f$ of the absorbing molecule in the initial (i) and final state (f). Both states are characterized by wavefunctions (ψ_i and ψ_f). The transition moment is determined by

$$\boldsymbol{m}_{if} = \langle \psi_f | \boldsymbol{m} | \psi_i \rangle = \int \psi_f^* \, \boldsymbol{m} \, \psi_i \, \mathrm{d}\tau \quad , \tag{4}$$

with $\boldsymbol{m}$ being the dipole moment operator representing the interaction of the electric field $\boldsymbol{E}$ with the dipole resulting from the charge distribution in a given molecule. $\boldsymbol{m}_{if}$ is characterized by a spatial orientation and reflects the probability for a transition by the absolute square $\left|\boldsymbol{m}_{if}\ \boldsymbol{E}\right|^2$. Consequently, for large absorption transition moments one observes high absorption coefficients.

The direction of $\boldsymbol{m}_{if}$ is of importance if the incident light or the molecule orientation is anisotropic, e.g., for linearly polarized electric field vectors. Here, molecules preferentially absorb photons if their transition moments are parallel to the electric field vector. In the case of aromatic hydrocarbons absorption transition moments of the $\pi \rightarrow \pi^*$ transition are orientated within the molecular plane.[51] Figure 2.1.3A shows the directions of the absorption transition moments in the polycyclic aromatic hydrocarbon anthracene together with an illustrated absorption spectrum. For the $S_0 \rightarrow S_1$ transition $\boldsymbol{m}_{01}$ has an orientation along the short molecular axis while the absorption transition moment $\boldsymbol{m}_{02}$ ($S_0 \rightarrow S_2$) is oriented perpendicular in respect to $\boldsymbol{m}_{01}$.

In addition to 1-photon absorption, higher-order nonlinear optical processes also lead to electronic excitations by the simultaneous absorption of multiple photons. In 1932, Maria Göppert-Mayer developed the quantum mechanical theory of 2-photon absorption (2PA) by introducing virtual intermediate states in addition to the real molecular electronic states (eigenstates) of the photon absorption process (Figure 2.1.3B). Prerequisite for 2PA is the simultaneous absorption of two photons of half the energy or of twice the wavelength, leading to a transition between a lower and a higher (real) energy state. This process can be considered as a two-step event. In the first step, one photon

is absorbed which induces a transition from an initial lower (real) energy state into a virtual intermediate state. In the second step, a second photon is absorbed accompanied by a transition from the intermediate into the final (real) excited state. The virtual intermediate state has an "infinite" small lifetime (due to the uncertainty principle regarding the real occupied state)[54]. Consequently, the absorption of both photons has to occur simultaneously. 2PA has to be distinguished from the phenomenon of a cascaded two-photon absorption, called excited-state absorption. Here, the absorption of a first photon leads to an excitation into a real excited state with a finite lifetime. Then, the molecule absorbs a second photon inducing a transition into an even higher excited state.

The probability of one photon absorption has a linear dependence on the excitation intensity I, shown by the following equation[55]:

$$n^{1PA} = \sigma_1(\nu)\, N_{\text{ground}} \frac{I}{h\nu} \quad , \tag{5}$$

with n^{1PA} being the number of molecules excites by 1PA, $\sigma_1(\nu)$ is the one-photon cross section at frequency ν, N_{ground} is the density of molecules in the ground state and I is the excitation intensity. In contrast, 2PA is a non-linear optical process, where the probability of photon absorption is proportional to the square of the excitation intensity[55]:

$$n^{2PA} = \frac{1}{2}\sigma_2(\nu)\, N_{\text{ground}} \left(\frac{I}{h\nu}\right)^2 \quad , \tag{6}$$

where $\sigma_2(\nu)$ describes the molecular two-photon cross section at frequency ν. Other than in the case of 1PA where the molar (one photon) absorption coefficient is frequently used to describe the probability photon absorption, in the case of 2PA one chooses the two-photon cross section as a characteristic parameter. Typical values of $\sigma_2(\nu)$ for organic two-photon absorber molecules range from 10^{-51} to 10^{-46} cm^4s. As these values are very small, they are often expressed by informal Göppert-Mayer units ($1GM=10^{-50}cm^4s$). The non-linearity of multiphoton absorption can be expressed by the proportionality of the k-photon absorption probability to the k-*th* power of the local excitation intensity. For this reason, efficient 2PA and higher multi-photon absorption can only be achieved by using high local photon densities. To reach these photon densities for example pulsed femtosecond lasers combined with focusing optics are applied generating a spatially confined three-dimensional excitation volume of less than 100 attoliters. Such small excitation, detection, or manipulation volumes yield a broad application spectrum of multi-photon applications in laser scanning fluorescence microscopy, 3D data storage, microfabrication, up-converted lasing, photodynamic therapy, and for localized drug release of bio-active species.[55]

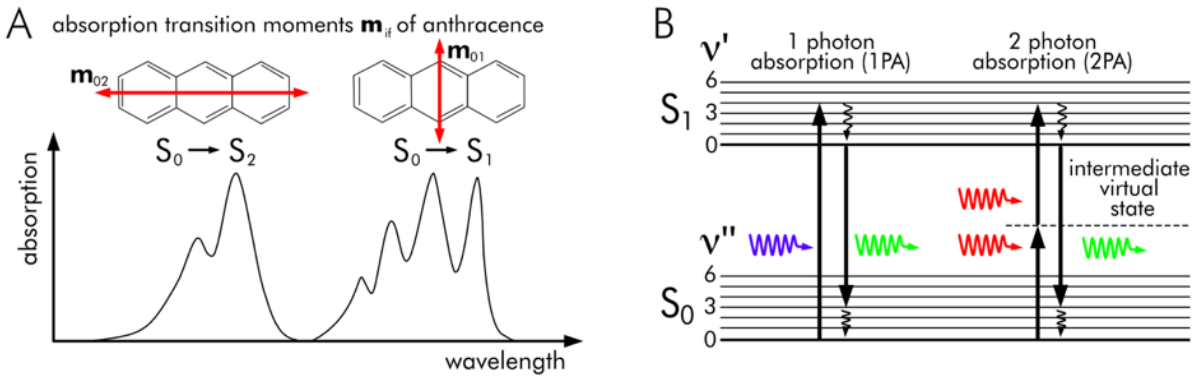

Figure 2.1.3: Transition moments and multiphoton absorption. **A** Direction (red arrows) of absorption transition moments $\boldsymbol{m}_{01}$ and $\boldsymbol{m}_{02}$ in polycyclic aromatic hydrocarbon anthracene for the $S_0 \rightarrow S_1$ and $S_0 \rightarrow S_1$ transition. Bottom: illustrated absorption spectrum of both transitions. **B** Comparison of one and two-photon absorption. Left: Absorption of one photon (blue waved arrow) leads to an $S_0 \rightarrow S_1$ transition. Right: Two photons of identical wavelength (red waved curve) are absorption via a virtual state leading to the $S_0 \rightarrow S_1$ transition. The molecule may deexcite $S_1 \rightarrow S_0$ via fluorescence (green waved arrow).

Absorption and fluorescence emission spectra

This section discusses the origin and theoretical background of steady-state energy/(wavelength) resolved absorption and fluorescence spectra. As described beforehand, the photon absorption probability of a molecular entity can be expressed via absorbance defined as the ratio of absorbed and transmitted light intensity at a certain wavelength (see Eq.1). Recording the absorbance while scanning the wavelength of the passing light yields a spectrum that indicates the amount of light absorbed by a sample as a function of photon wavelength (energy). To record a fluorescence emission spectrum, one must select a wavelength at which the fluorophore is excitable. While exciting the fluorophore by photons of this wavelength, the fluorescence spectrum can be recorded by detecting the emitted fluorescence intensities for varying wavelengths.

The absorption and emission spectrum of a fluorophore are tightly connected. Both spectra reflect energy and probability of vibronic transitions, i.e., simultaneous changes of the vibrational (ν) and electronic states (S, see Perrin-Jablonski diagram). The relationship between absorption and emission spectrum and the photophysical origin can be illustrated by the Franck-Condon principle. The principle expects that in the time span of vibronic transitions, the nuclear configuration experiences no significant alteration due to considerably different masses of electrons and atomic nuclei leading to other time scales of motion. This assumption, called Born-Oppenheimer approximation, describes the motion of atomic nuclei and electrons as separable processes. It permits for the separation of electronic and nuclear wavefunctions which simplifies their calculations and the prediction of possible transitions. The separation in Dirac notation can be easily expressed as

$$|\psi_{\mathrm{tot}}(R,r)\rangle = |\psi_{\mathrm{nuc}}(R)\rangle\,|\psi_{\mathrm{el}}(R,r)\rangle \quad , \tag{7}$$

with $|\psi_{\mathrm{tot}}(R,r)\rangle$ being the total (atomic or molecular), $|\psi_{\mathrm{nuc}}(r)\rangle$ the nuclear (or vibrational) and $|\psi_{el}(r)\rangle$ the electronic wavefunction, R represents nuclear and r electronic coordinates. The vibronic transition moment $\boldsymbol{m}_{if}$ is than given by

$$\begin{aligned}\boldsymbol{m}_{if} &= \langle\psi_{\mathrm{tot,f}}(R,r)|\boldsymbol{m}|\psi_{\mathrm{tot,i}}(R,r)\rangle = \langle\psi_{\mathrm{nuc},f}(R)\,|\langle\psi_{\mathrm{el},f}(R,r)|\boldsymbol{m}|\psi_{\mathrm{el},i}(R,r)\rangle|\psi_{\mathrm{nuc},i}(R)\rangle \qquad (8)\\ &= \langle\psi_{\mathrm{nuc},f}(R)|\psi_{\mathrm{nuc},i}(R)\rangle\,\langle\psi_{\mathrm{el},f}(R,r)|\boldsymbol{m}|\psi_{\mathrm{el},i}(R,r)\rangle\\ &\quad+\langle\psi_{el,f}(R)|\psi_{el,i}(R)\rangle\,\langle\psi_{\mathrm{nuc},f}(R,r)|\boldsymbol{m}|\psi_{\mathrm{nuc},i}(R,r)\rangle \quad .\end{aligned}$$

This expression can be simplified due to the orthogonality of the electronic wavefunction of different states to

$$\boldsymbol{m}_{if} = \langle\psi_{\mathrm{nuc},f}(R)|\psi_{\mathrm{nuc},i}(R)\rangle\langle\psi_{\mathrm{el},f}(R,r)|\boldsymbol{m}|\psi_{\mathrm{el},i}(R,r)\rangle \quad , \qquad (9)$$

by using the Condon approximation, that considers the electronic transition moments as independent of nuclear coordinates, Eq. 8 can be further simplified to

$$\boldsymbol{m}_{if} = \langle\psi_{\mathrm{nuc},f}(R)|\psi_{\mathrm{nuc},i}(R)\rangle\langle\psi_{\mathrm{el},f}(r)|\boldsymbol{m}|\psi_{\mathrm{el},i}(r)\rangle \quad , \qquad (10)$$

The remaining components defining the probability of a vibronic transition are the nuclear overlap integral or Franck-Condon integral $\langle\psi_{\mathrm{nuc},f}(R)|\psi_{\mathrm{nuc},i}(R)\rangle$, describing nuclear vibrations and the electronic transition moment $\langle\psi_{\mathrm{el},f}(r)|\boldsymbol{m}|\psi_{\mathrm{el},i}(r)\rangle$. The absolute square of the Franck-Condon integral is called Franck-Condon factor and modulates the vibronic transition intensities in dependence on the similarity of nuclear/vibrational wavefunctions at a certain nuclear coordinate. The electronic transition moment determines electronic transitions and thus the orbital selection rules.

Here, the Franck-Condon principle assumes that no nuclear vibrations occur on the time scale of vibronic transitions (10^{-15} s). So, the nuclear coordinates are constant. Consequently, the transitions between the vibrational levels of two electronic states are drawn as "vertical" transitions into an energy diagram. Figure 2.1.4A shows the electronic potential energy curves for a diatomic molecule assuming a Morse oscillator model (Morse potential) for the vibrational motion. At room temperature, most of the molecules are located in the electronic and vibrational ground state (S_0, ν_0), here the nuclear coordinate indicates the equilibrium distance (R_0) between both nuclei. After a transition to a vibrational level of a higher electronic state (e.g. S_1), the nuclear distance will change with some delay, in most cases to higher values compared to the ground state configuration. The transition probability, i.e., the intensity of a transition line or band in an absorption/emission spectrum is proportional to the absolute square of the overlap (Franck-Condon factor) of both vibrational wavefunctions in the original and final electronic state. In the example of Figure 2.1.4A, the transition probability from $S_0 \rightarrow S_1$ is the highest between the vibrational ground state and the second excited vibrational state ($2 \leftarrow 0$) due to a large overlap in the vibrational wavefunctions. This is indicated by the

thick blue vertical arrow, pointing to the respective vibrational level. The transitions probability is reflected by the high spectroscopic intensity in the absorption spectrum shown in Figure 2.1.4B. Other vibronic transitions from S_0 to S_1 occur with different probabilities due to other Franck-Condon factors. As already discussed for the Perrin-Jablonski diagram, vibrational relaxation leads to an accumulation of molecules in the vibrational ground state of S_1 with its relatively long lifetime. From this state, transitions back into the vibrational levels of S_0 occur which may lead to the emission of fluorescence photons. These $S_1 \rightarrow S_0$ transitions follow the same Franck-Condon principle, i.e., vertical transitions and probability dependence on the overlap of the involved vibrational wavefunctions.

Figure 2.1.4B connects transitions leading to photon absorption and (fluorescence) emission to the spectroscopic bands observed in absorption and fluorescence spectra. The fluorescence spectrum is typically red-shifted compared to the absorption spectrum (Stokes-shift, see also Figure 2.1.4C), except for the 0-0 vibronic transition. Here, the spectral bands of both spectra build a mirror axis. This phenomenon is termed mirror image rule and states that vibrational levels of the excited state resemble the vibrational levels of the ground state if the shape of the electronic potential energy curves of ground and excited state are similar or equal.

Figure 2.1.4B also displays the broadening of the spectral lines for a fluorophore in solution. In diluted gases, one can observe distinguishable spectral bands indicating the individual vibronic transitions (black dashed line, Figure 2.1.4B). The expected spectral lines are broadened by a finite lifetime of the participating states (natural line broadening). Typically, Lorentzian band profiles can be observed. For complex organic molecules in solution, the spectral band structures exhibit a much stronger broadening. Often the spectra seem almost structureless (gray continuous line, Figure 2.1.4B). This is caused by two separable effects. First, the presence of a continuous set of vibrational levels for each electronic state which lead to broader spectral lines. An effect that belongs to the class of homogenous broadening, because all molecules are affected in the same way. Superimposed, a second type of broadening occurs due to small differences in the solvation shell of each molecule. This inhomogeneous effect is based on collisions and electrostatic interactions between individual fluorophores and their respective surrounding solvent molecules.

At room temperature, absorption and fluorescence spectra show a partial spectral overlap in most cases (Figure 2.1.4C) indicating fluorescence is emitted partially at shorter wavelengths than the absorbed light. This phenomenon seems to be in contrast to the energy conservation law. However, it can be explained by a small fraction of molecules occupying higher vibrational levels of S_0 at room temperature, too.

In addition to a typical linear dependence between the absorbance strength and molecule concentration described by the Lambert-Beer law (Eq. 2), absorption spectra can be sensitive to the molecular environment of light absorbing molecules. The same holds true for fluorescence spectra which are often indicative for environmental changes, e.g., in pH, molecular interactions, or viscosity.

Changes in wavelengths (photon energies) are called hypsochromic or blue-shifts if they result in lower wavelengths. Wavelength changes in the opposite direction are called bathochromic or red-shifts (Figure 2.1.4D). If the spectral intensity is affected, one distinguishes between hyperchromic (increasing intensity) shifts and hypochromic (decreasing intensity) shifts (Figure 2.1.4E).

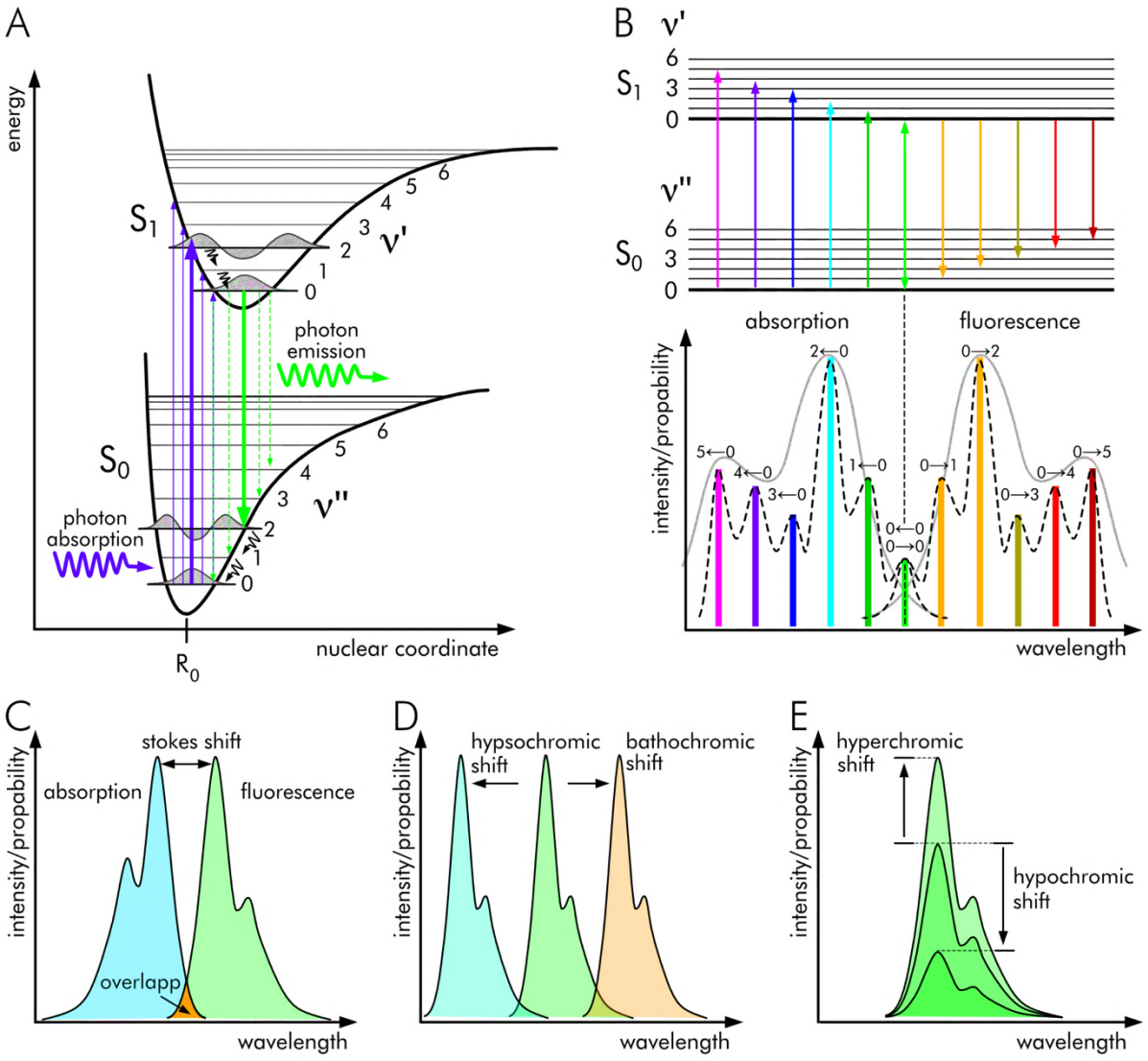

Figure 2.1.4: Absorption and fluorescence spectra. **A** Franc-Condon principle: Electronic potential energy curves for a diatomic molecule assuming a Morse oscillator model. Blue arrows indicate transitions after photon absorption from the electronic and vibrational ground state. **B** Mirror image rule of absorption and emission spectra. Line broadening for the individual transitions for diluted gases are shown as black dashed lines. The gray continued line shows the broad absorptions and emission bands observed for fluorophores in solution. **C** Stokes shift between absorption and fluorescence spectrum. **D** Bathochromic and hypsochromic shifts in emission spectra. **E** Hyperchromic and hypochromic shift in emission spectra.

2.1.2 Fluorescence properties

This section introduces fundamental fluorescence properties that give fluorescent probes versatile, sensitive, and quantitative capabilities utilized in numerous fluorescence-based investigations. I focus on the characteristics relevant for time-resolved fluorescence spectroscopy and imaging.

Fluorescence quantum yield, intensity, and brightness

The fraction of excited fluorophores that de-excites to the ground state S_0 by fluorescence is defined as the fluorescence quantum yield Φ_F. In other words, Φ_f describes the efficiency of a fluorophore to convert absorbed photons ($N_{ph,abs}$) into fluorescence photons ($N_{ph,f}$) and relates to the involved transition rate constants in the following way:

$$\Phi_f = \frac{N_{ph,f}}{N_{ph,abs}} = \frac{k_r}{k_{nr}+k_r} = \frac{1}{1+k_{nr}/k_r} \quad , \tag{11}$$

with k_r being the radiative emission rate constant (fluorescence) and k_{nr} being the non-radiative rate constate summarizing all other transitions (intersystem crossing, internal conversion, and intra- and intermolecular quenching) from S_1 to S_0. This means the existence of any other depopulation pathway from the S1 state after a previous photon absorption will reduce Φ_f.

The fluorescence quantum yield is connected to the fluorescence intensity I_f by

$$I_f = \Phi_f(I_{in} - I_{out}) \quad , \tag{12}$$

where $I_{in}(\lambda)$ is the intensity of an incident excitation light entering a solution of fluorophores, $I_{out}(\lambda)$ is the light fraction that is not absorbed. Applying Lambert-Beer law (Eq.2), this equation can be transformed to

$$I_f = \Phi_f I_{in}(1 - 10^{-c\cdot l\cdot \varepsilon}) \quad . \tag{13}$$

Using a Taylor series expansion this relationship can be expressed as

$$I_f = \Phi_f \; I_{in}\,(2.3\; c\; l\; \varepsilon - \tfrac{1}{2}(2.3\; c\; l\; \varepsilon)^2 + \tfrac{1}{6}(2.3\; c\; l\; \varepsilon)^3 - \ldots) \quad , \tag{14}$$

$$I_f \cong 2.3\; I_{in}\; \Phi_f\; c\; l\; \varepsilon = 2.3\; I_{in}\; \Phi_f\; A \;\; \text{(for low concentrations)}. \quad . \tag{15}$$

This equation shows that a quantitative concentration determination via fluorescence intensities is only valid for highly dilutes fluorophores, i.e., for low absorbances. The theoretical deviation from linearity at an absorbance of 0.1 already amounts to over 10 %, a substantial error making quantitative measurements, especially under unknown fluorophore concentrations, almost impossible. Additionally, high fluorophore concentrations can cause instrumental inner-filter effects during fluorescence excitation and emission. These effects are caused by inhomogeneous sample excitation due to a high absorption of excitation light before it passes to the observation center of a cuvette. Moreover, emitted fluorescence of the spectral overlap region between an absorption and emission spectrum (Figure 2.1.4C) can by re-absorbed. This radiative energy transfer distorts fluorescence

detection particularly due to wavelength dependent changes in the fluorescence intensity. Eq. 15 also indicates a theoretical linearity between fluorescence intensity and excitation intensity. Experimentally, this dependence only holds true for a certain range of excitation intensities as with rising photon densities the probability of photobleaching, that is, a photochemical change, reduction, or annihilate of a fluorophore's emission, increases.

The fluorescence quantum yield is often utilized to describe the capability of a fluorophore to fluoresce. However, Eq. 15 shows the molar absorption coefficient equally contributing to the total fluorescence intensity. So, fluorophores with a high Φ_f , but a low molar absorption coefficient show only marginal amounts of fluorescence. For this reason, a further quantity is introduced: the fluorescence brightness (fluorescence output per fluorophore). It is defined as the product of the molar absorption coefficient at the wavelength of maximal absorption and the respective quantum yield. A high brightness is of special interest in fluorescence based single molecules experiments or for labeling of lower-abundance targets by fluorescence probes.

Excited state/fluorescence lifetime

The average time a fluorophore remains in the excite state (S_1) before it de-excites back to the ground state via fluorescence is termed excited state, or more common, fluorescence lifetime (τ_f). Fluorescence lifetimes depend on a fluorophore's structure and environmental conditions. Most fluorophores show fluorescence lifetimes of pico- and nanoseconds. Equally to the fluorescence quantum yield, the fluorescence lifetime can be expressed by the radiative and non-radiative first order transition rate constants (k_r & k_{nr}):

$$\tau_f = \frac{1}{k_{nr}+k_r} = \frac{\Phi_f}{k_r} = \Phi_f \, \tau_r \quad . \tag{16}$$

This equation illustrates in a simple manner, that in the absences of non-radiative transitions the quantum yield must be unity and the excited state lifetime becomes equal to the pure radiative lifetime, also called natural fluorescence lifetime $\tau_r = 1/k_r$. Fluorescence lifetime experiments owe their environmental sensitivity to the general dependency of τ_f to non-radiative processes (Eq. 16), which are directly modulated by a fluorophore's molecular environments, conformations, or interactions. For example, specific alterations of fluorescence lifetimes can be observed upon changes in physicochemical parameters like temperature, viscosity, pH, electrostatics, polarity, or steric restrictions and various other excited-state processes. Other than that, the fluorescence lifetime is generally considered to be independent of the fluorophore concentration, a major benefit compared to sole intensity-based fluorescence experiments. To illustrate the meaning of the fluorescence lifetime, one could regard an ensemble of fluorophores upon excitation by an infinitely short light pulse. The initial number of excited molecules at time zero is given by $N(t = 0) = N_0$. The temporal progress of $N(t)$ can be expressed by the following differential equation:

$$\frac{d}{dt}N(t) = -N(t)\,(k_{nr} + k_r) = \; -N(t)\,1/\tau_f \,, \tag{17}$$

via integration and the proportionality of $N(t)$ and emitted fluorescence intensity $I_\mathrm{f}(t)$, one obtains:

$$N(t) = N_0 \exp\left(-\frac{t}{\tau_\mathrm{f}}\right) \quad ,$$

$$I_\mathrm{f}(t) = I_\mathrm{f}(0) \exp\left(-\frac{t}{\tau_\mathrm{f}}\right) \quad , \tag{18}$$

So, temporal depopulation of the excited state follows an exponential decay law with τ_f being the time constant. Thus, recording the temporal fluorescence intensity decay after a short excitation light pulse would allow the determination of τ_f (see Section 2.2.1) by fitting the decay with an exponential model function. Depending on environmental or structural factors such as those mentioned above, fluorophores in an ensemble, although being of the same kind, may exhibit several fluorescence decay components $\tau_{\mathrm{f},i}$ or fluorescence lifetime distributions. In order to reveal multiple decay components, from experimental fluorescence decay traces, multi-exponential fitting models can be applied:

$$I_\mathrm{f}(t) = I_\mathrm{f}(0) \sum_c^n \alpha_c \exp\left(-\frac{t}{\tau_{\mathrm{f,c}}}\right) \quad , \tag{19}$$

with n being the number of components c and α_c being the relative amplitudes. For multi-component decays one can calculate mean fluorescence lifetimes ($\tau_{\mathrm{m},\alpha}$ & $\tau_{\mathrm{m},\beta}$), either weighted on the relative amplitudes or weighted on the relative steady-state intensity contribution β_c (population of the fluorescence species).

$$\tau_{\mathrm{m},\alpha} = \sum_c^n \alpha_c \, \tau_{\mathrm{f,c}} \tag{20}$$

$$\tau_{\mathrm{m},\beta} = \sum_c^n \beta_c \, \tau_{\mathrm{f,c}} \quad \text{, with } \beta_i = \frac{\alpha_c \, \tau_{\mathrm{f,c}}}{\sum_c^n \alpha_c \, \tau_{\mathrm{f,c}}} \tag{21}$$

On the one hand, $\tau_{\mathrm{m},\beta}$ represents the average time a single fluorophore spends in its excited state. On the other hand, this parameter can be interpreted as the mean fluorescence lifetime of different fluorescence species in their excited states where the corresponding lifetime of each fluorescent species is weighted by its relative contribution to the total steady-state fluorescence intensity.[56] In contrast, $\tau_{\mathrm{m},\alpha}$ can be regarded as an equivalent for the lifetime that a fluorophore with mono-exponential decay behavior and the same stationary fluorescence intensity would have. Changes in the amplitude-weighted lifetime are proportional to the stationary intensity of a fluorophore or a mixture of different fluorescent species.[56] The use of both mean lifetimes types depend on the research question and the object of investigation and cannot be assigned in a generalized manner. For example, population-weighting of the fluorescence lifetime is often used for the analysis of dynamic quenching, whereas for fluorescence lifetime-based FRET applications only amplitude-weighting is applied.[57] More details to the fitting procedures of time-resolved fluorescence data is given in Section 2.2.1.

Fluorescence deactivation processes, quenching and photostability

A fluorophore in an excited state has large excess energy which can cause different inter- and intramolecular processes leading to fluorescence deactivation. Beside radiative (fluorescence) transitions (k_{r}), a variety of non-radiative de-excitation pathways (k_{nr}) are possible: Internal conversion (k_{IC}) is a de-excitation process where excess energy of the excited state is transferred to highly excited vibrational levels of the ground state (see Perrin-Jablonski diagram). IC is caused by collisions of excited fluorophores with surrounding solvent molecules and the subsequent emission of infrared radiation. A further fluorescence deactivation process is intersystem crossing (k_{ICS}) from S_1 to excited states of different spin multiplicity, for example from S_1 of T_1 (Figure 2.1.1). Photoreactive fluorophores can build photoproducts ($k_{\mathrm{ph,reac}}$) with respective molecules during their excited state and becoming non-fluorescent.

Excited-state energy can also be transferred to other molecules via non-radiative dipole-dipole coupling as observed for the Förster resonance energy transfer mechanism (k_{FRET}).[58] Here, an excited fluorophore (donor) transfers its energy to another fluorophore or non-fluorescent molecule, called acceptor, having a resonating transition dipole moment. Through FRET, the donor de-excites from its ground states LUMO (see Figure 2.1.2), while the acceptor is excited into its LUMO. k_{FRET} is highly dependent on the intramolecular distance of donor and acceptor ($\propto r^{-6}$), such that effective FRET occurs typically between 2 and 10 nm. A further non-radiative energy transfer mechanism is the exchange of an excited electron. This electron transfer, called Dexter electron transfer (k_{Dex}), is facilitated by overlapping orbitals between an excited fluorophore (donor) and an electron acceptor molecule in immediate vicinity ($r < 1$ nm). Similarly, charges (electrons or protons) can be transferred intramolecularly during the excited-state and result as well in fluorescence deactivation. Another intramolecular de-excitation pathway are conformational changes, like intramolecular rotations (k_{IMR}), i.e., a torsional motion of molecule subgroups while being in an excited state transferring excess energy into mechanical energy.

Such processes resulting in a deactivation of fluorescence, i.e., a decrease in fluorescence quantum yield or lifetime, are commonly known as fluorescence quenching. Molecules inducing non-radiative de-excitation are called fluorescence quenchers. Fluorescence quenching is often divided into static and dynamic quenching and is theoretically modelled by Stern-Volmer kinetics.[59] Static quenching describes quenching mechanisms with no alteration in the fluorescence lifetime but with changes in the steady-state fluorescence intensity. This behavior is frequently modelled by a spherical volume of effective quenching (Eq. 22) in the case of viscous solutions, or by assuming the formation of a non-fluorescent complex (or with different absorption probertites) while the fluorophore is in its ground state (Eq. 23).

$$\frac{I_{\mathrm{f}}^{0}}{I_{\mathrm{f}}\,([\mathrm{Q}])} = \exp(V_{\mathrm{eff}}\,\mathrm{N_A}\,[\mathrm{Q}]) \quad , \tag{22}$$

$$\frac{I_f^0}{I_f([Q])} = 1 + K_S[Q] \quad , \tag{23}$$

with $I_f([Q])$ and I_f^0 being fluorescence intensities in dependence of the quencher concentration and in absence of the quencher. N_A is Avogadro's constant, K_S is the Stern-Volmer's constant for static quenching and V_{eff} is the effective volume derived from Perrin's quenching sphere-of-action model.[60] For small quencher concentrations both models predict a linear increase of the intensity ratio.

In contrast, dynamic quenching affects the transition rate constants and so the fluorescence lifetime. This process is typically described by the following Stern-Volmer relation:

$$\frac{\tau_f^0}{\tau_f([Q])} = \frac{\Phi_f^0}{\Phi_f([Q])} = \frac{I_f^0}{I_f([Q])} = 1 + \tau_f^0 k_q[Q] = 1 + \tau_f^0 \frac{1}{[Q]}\left(\frac{1}{\tau_f([Q])} - \frac{1}{\tau_f^0}\right)[Q] = 1 + K_D[Q], \tag{24}$$

where $\Phi_f^0/\tau_f^0([Q])$ and Φ_f^0/τ_f^0 being fluorescence quantum yield/lifetime in dependence on the quencher concentration and in absence of the quencher. k_q is the bimolecular quenching constant and K_D is Stern-Volmer's constant for dynamic quenching. In the case of superimposed static and dynamic fluorescence quenching Eq. 23 and Eq. 24 can be combined to:

$$\frac{I_f^0}{I_f([Q])} = (1 + K_S[Q])(1 + K_D[Q]) \quad . \tag{25}$$

Absorption and emission of fluorophore can be considered as a repeated cycling process between ground and excited state propelled by the photonic interaction. The repetitive emission permits to detect fluorescence signals of a single fluorophore multiple times. This facilitates the fluorescence detection at low fluorophore concentrations and generates a high detection sensitivity per fluorophore. In reality, this cycling process may be disturbed after high intensity or prolonged excitation. This behavior is termed photobleaching and leads to a gradual reduction or loss in fluorescence intensity. The generation of non-fluorescent fluorophore species is a product of structural changes, like cleaving of covalent bonds or non-specific intermolecular reactions. Especially in time-lapse fluorescence microscopy of the same investigation site, photobleaching can alter the experimental outcome and complicates quantitate image analysis. The susceptibility to photobleaching strongly depends on the fluorophore. Some molecules can achieve thousands of absorption/emission circles while others degrade already after a few cycles.

Fluorescent molecular rotors

Fluorescent molecular rotors (FMR) are fluorophores capable of an intramolecular twisting motion, i.e., a torsional motion of molecule subgroups, while being in an excited state.[61] This isomerization process (k_{iso}) constitutes a competing de-excitation pathway and alters the fluorescence depending on the rotation efficiency. This makes fluorescence parameters sensitive to monitoring the intramolecular isomerization process, which in turn is related to local steric constraints and viscosities (η). The fluorescence deactivation in FMRs can be described by its first excited electronic state (S_1), the associated potential surface diagram and by the twisting coordinate (θ).[62] This consideration is used

in the twisted intramolecular charge transfer (TICT) model describing two excited states, a planar (0 °) locally exited (LE) state, as well as a 90 ° twisted state (TICT state) of lower energy.[63]

In the ground state (GS), the planar configuration is the dominant species due to a rotational barrier (Figure 2.1.5A). After photo excitation, FMRs experience an intramolecular charge transfer that increases the dipole moment, facilitated by the chemical composition of the molecule. Typically, FMR structures are built of three subunits: an electron donor and acceptor group, as well as a connecting spacer unit of alternating single and double bonds. A necessary electron-rich spacer, responsible for π-conjugation, minimizes the orbital overlap between donor and acceptor group and enables the electron transfer between them.[61] The probability of a transition between LE and TICT state, i.e., a rotation of the twisting coordinate around 90 °, is determined by a fluorophore's environment. It depends on viscosity and to some extent to the solvent polarity as this process is driven by electrostatic forces.[61] Figure 2.1.5B,C visualizes the underlying principle of two competing excited states as Perrin-Jablonski energy diagrams. While the LE state allows for a back-transition into the planar ground state via fluorescence, the relaxation mechanisms for the TICT state can be either non-radiative (Figure 2.1.5B) or radiative. However with changed emission wavelengths when compared to the LE fluorescence (Figure 2.1.5C).

If the de-excitation of the TICT state is non-radiative, due to a small energy gap to the twisted GS, one only observes a single fluorescence emission band generated by the LE→GS transition. The emission intensity (that means Φ_f, Figure 2.1.5D) as well as the fluorescence lifetime of this band changes with the probability of rotation/transition from LE to the TICT state. At high viscosity, a rotation is unlikely to occur and fluorescence emission from the LE state is the only depopulation pathway leading to hyperchromic shifts in the emission spectrum and prolonged fluorescence lifetimes. The lifetimes theoretically approach the pure radiative lifetime τ_r, if the rotation is totally prevented and no other non-radiative transitions occur (see Eq. 16). At lower viscosities a rotation in the excited state becomes more likely and the non-radiative relaxation from the TICT state competes with the fluorescence emission, leading to a reduction in fluorescence intensity and lifetime.

If the energy gap between TICT and twisted GS is large enough, a radiative transition is possible, generating a second red-shifted fluorescence band (Figure 2.1.5C). As the TICT state is highly sensitive towards solvent polarity due to its large dipole moment, the second (TICT) fluorescence band exhibits polarity dependent bathochromic shifts. This solvatochromism effect can be explained by the reorientation of solvent molecules. By the transition into the TICT state, molecules of the solvation shell are forced to align their dipole (dipolar relaxation) reducing the TICT state's energy. This change in energy leads to bathochromic shifts of TICT fluorescence depending on solvent polarity. Fluorescence intensities of both emission bands are determined by the probability of the LE→TICT transition and thus dependent on the local viscosity acting as transition barrier. The relative fraction of both bands is inversely proportional. So, one observes strong TICT and low LE emission for high transition rates (Figure 2.1.5E). The opposite can be observed in case of low transition rates. While dual band

emission, like the one of benzonitrile-based fluorophores, supports the simultaneous detection of viscosity and polarity, single band FMRs like stilbenes are more suited to detect viscosities as they are relatively insensitive towards solvent polarity.[61]

In 1971, Förster and Hoffmann theoretically described the viscosity dependent fluorescence quantum yield of crystal violet, a single band emitting FMR consisting of three rotating aniline groups.[64] Using a damped oscillator model for the rotation and the assumption of a Debye-Stokes-Einstein model for microfriction of the rotating aniline groups, a 2/3 power-law relationship were established that describes the experimental viscosity dependence of the fluorescence quantum yield for an intermediate viscosity range. This relationship is termed as Förster-Hoffmann equation for molecular rotors:

$$\Phi_f(\eta) = a \left(\frac{\eta}{\sigma}\right)^{2/3} \quad , \tag{26}$$

with a and σ being FMR specific constants which rely on mechanical and electrostatic rotor properties. For extremely low or high viscosities, the power-law dependence loses its validity. For the latter, no rotation takes place and one can assume that Φ_f approaches to the ratio of τ_f/τ_r. If no other non-radiative transitions participate this ratio becomes unity. In literature, the Förster-Hoffmann equation is commonly stated in an empirical form[65-66] as:

$$\Phi_f(\eta) = b\,\eta^x \quad , \tag{27}$$

in which b combines a and σ to a single constant and introducing x as a new parameter which may differ from the predicted value of 2/3 in the original Paper by Förster and Hoffmann. The deviation is caused by additional rotor or solvent specific influences. Bagchi et al. derived Eq. 27 by assuming a barrierless isomerization, described by a modified Smoluchowski model, and a Gaussian sink in the excited state potential energy surface defining the excited-state relaxation.[67] This model predicts a range of $0.5 \leq x \leq 0.8$ for the viscosity dependent coefficient, which itself is constant for an certain viscosity range. It should be mentioned that Loutfy et al. established a similar relationship by applying free volume theory.[68] By using Eq. 16, the power-law dependency can be expressed as a function of the fluorescence lifetime:

$$\tau_f(\eta) = \frac{b}{k_r}\,\eta^x = c\,\eta^x \quad . \tag{28}$$

The logarithmic form of this equation, typically likewise called Förster-Hoffmann equation, can be used to obtain FMR-specific parameters by linear regression of the experimentally determined fluorescence lifetime and viscosity values:

$$\mathrm{Log}(\tau_f) = \mathrm{Log}(c) + x\,\mathrm{Log}(\eta) \quad . \tag{29}$$

In addition, the generated linear fit function can serve as a simple fluorescence lifetime – viscosity calibration model, that permits to map a specific fluorescence lifetime value to the respective viscosity. Solvent viscosity depends naturally on temperature, and so does the fluorescence lifetime of an FMR. If temperature is additionally affecting the intramolecular rotation (isomerization) via changes in the excited state potential energy surface, the viscosity calibration model has to be extended using the following estimations: Firstly, the fluorescence lifetime can be generally expressed by radiative, isomerization and other non-radiative transition rates[69]:

$$\tau_{\mathrm{f}}(\eta, \mathrm{T}) = (k_r + k_{\mathrm{iso}}(\eta, \mathrm{T}) + k_{\mathrm{nr}})^{-1} \quad , \tag{30}$$

in which only the isomerization rate is dependent on viscosity and temperature. Secondly, by assuming that the temperature dependence is caused by the existence of an energy barrier expressed by the activation energy E_0 separable from pure viscosity effects, the isomerization rate via intramolecular rotation follows to Kramers-like theories an Arrhenius function[70-71]:

$$k_{\mathrm{iso}}(\eta, \mathrm{T}) = F(\eta) \exp\left(-\frac{E_0}{k_{\mathrm{B}} T}\right) \quad , \tag{31}$$

with E_0 being the isoviscous activation energy, k_B Boltzmann's constant, T the temperature, and $F(\eta)$ a universal function of solvent viscosity. If one now applies the free volume model of Doolittle[72], one receives a phenomenological fractional power law relationship of $F(\eta)$. This fits the experimental data obtained for fluorophores like 4,4'-dimethylstilbene[73] and can by applied for high viscosities[74]:

$$F(\eta) = \mathrm{d}\ \eta^{-y} \quad , \tag{32}$$

where y indicates the viscosity dependence and lies between 0.1 and 1.[73] To prevent the isomerization rate from becoming infinite at zero viscosity, a further parameter has to be introduced:

$$F(\eta) = \mathrm{d}\ (\eta + \mathrm{e})^{-y} \quad . \tag{33}$$

Here, e guarantees a finite isomerization time τ_{iso}^0 at zero viscosity. By combining Eq. 30, Eq. 31 and Eq. 33 a fluorescence lifetime-viscosity calibration model is obtained:

$$\tau_{\mathrm{f}}(\eta, \mathrm{T}) = \left(k_r + \mathrm{d}\ (\eta + \mathrm{e})^{-y}\ \exp\left(-\frac{E_0}{k_{\mathrm{B}} T}\right) + k_{\mathrm{nr}}\right)^{-1} \quad , \tag{34}$$

which considers a temperature dependent factor, defined by an energy barrier for the intramolecular rotation as well as a power law relationship between isomerization and viscosity. A global fit of experimental fluorescence lifetimes obtained by FMRs in reference solutions of known bulk viscosity and temperature to Eq. 34 generates isothermal calibration curves.

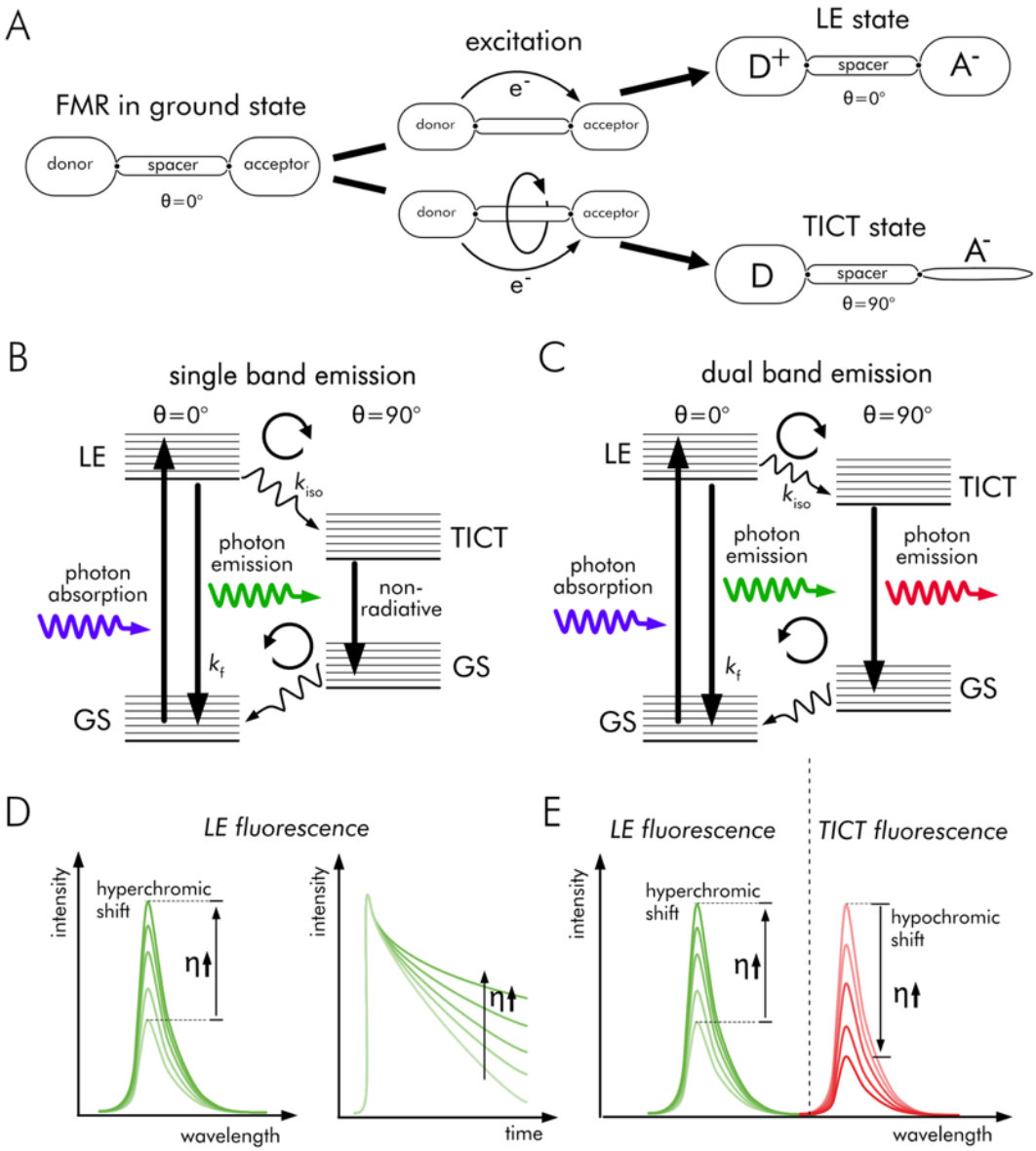

Figure 2.1.5: Fluorescent molecular rotors (FMR). **A** Subunits of FMRs: donor, spacer, and acceptor unit. In ground state (GS) configuration, no charge transfer between donor and acceptor unit is present and the FMR is in the planar conformation. Via photon excitation, a charge transfer occurs and a rotation around the twisting coordinate (θ) is possible. LE: planar locally excited state. TICT: twisted intramolecular charge transfer state. **B** Single band emission by the LE→GS transition, in case of a non-radiative TICT→GS transition. Photon absorption is indicated by a blue waved arrow, photon emission by a green waved arrow. **C** Dual band emission by LE→GS and TICT→GS transition. Photon absorption is indicated by a blue waved arrow, photon emission by green (LE→GS) and red (TICT→GS) waved arrows. **D** Influence of viscosity (η), tantamount to the rotation/transition probability from LE to TICT state, on the fluorescence characteristics of the LE→GS transition. **E** Influence of viscosity (η), on the fluorescence characteristics of the dual emission band.

2.1.3 Fluorescent probes

Polymethine carbocyanines: Indocarbocyanine & Indodicarbocyanine

Polymethine carbocyanines (PC) are organic fluorophores that belong to the class of fluorescent molecular rotors (FMRs). PCs exhibit structure-dependent absorption and fluorescence emission spectra between the UV and IR range and are characterized by relatively high fluorescence quantum yields, high absorption coefficients, photostability, and low binding rates to nucleic acids and

proteins.[75-76] Therefore, they are used as biological fluorescence markers, especially in FRET-based investigations of DNA, RNA, peptides, and proteins, but also as fluorescence labels in biomedical imaging.[77-78] Newer fields of application are interaction studies on macromolecules and environmental nanoviscosity detection.[79-80]

The backbone of PCs consists of two indole groups connected by a conjugated polymethine linker. There are different nomenclatures for PCs, for example the following nomenclature: "diIC$_m$(n)", where n defines the number of carbon atoms (C) in the polymethine linker and m the number of carbon atoms in the primary alkyl substituents attached to the nitrogen atoms of the indole group (I).[76] The symmetric sulfated PC derivatives used in this thesis, indocarbocyanine (ICC, Mivenion GmbH, Berlin) and indodicarbocyanine (IDCC, Prof. Haag's group, Freie Universität Berlin, Germany), belong to the groups of diIC$_2$(3) and diIC$_2$(5). These groups are commonly known as Cy3 and Cy5.

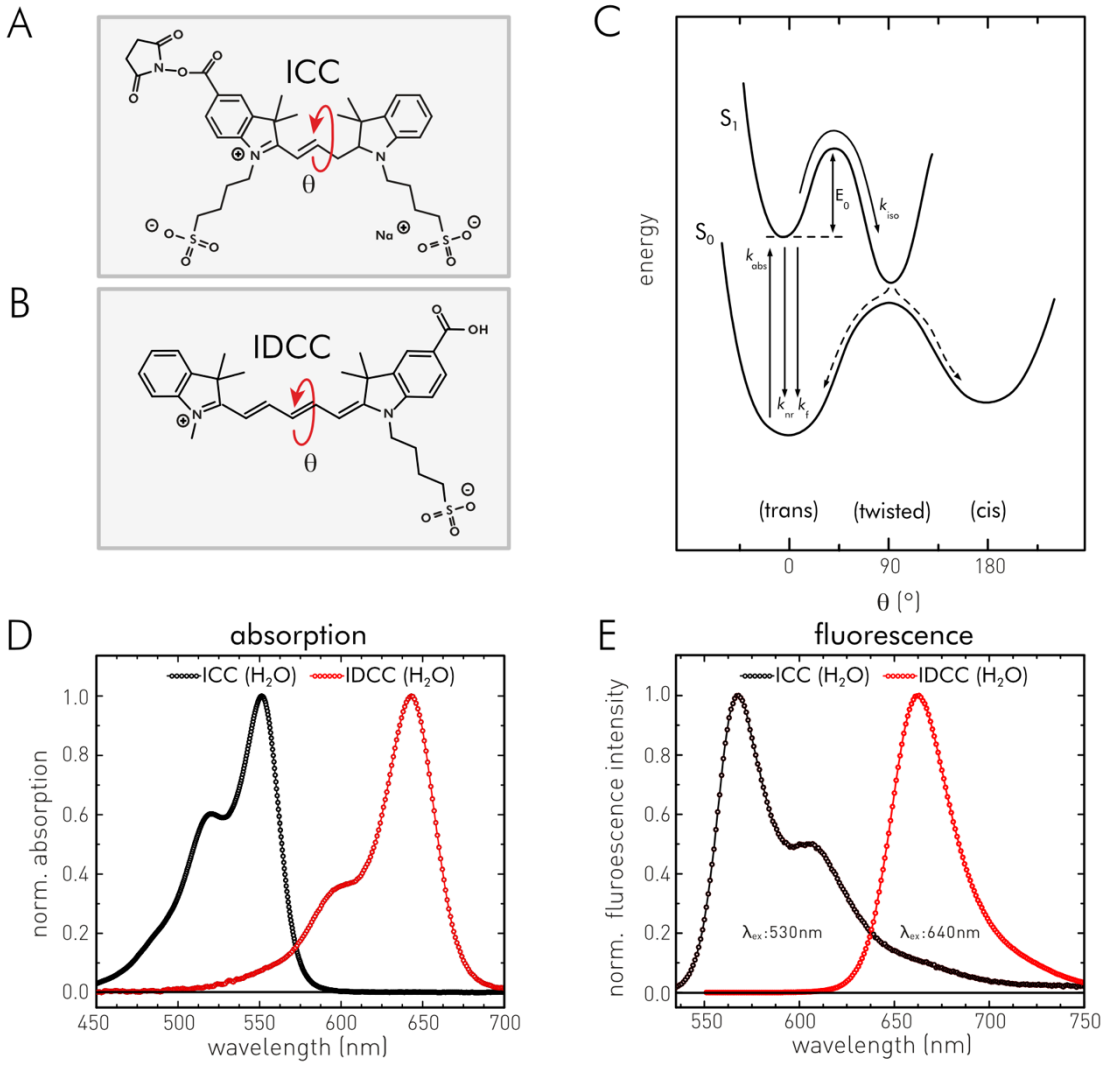

Figure 2.1.6: Chemical structures and spectral probertites of the applied polymethine carbocyanines. **A** Structure of ICC. **B** Structure of IDCC. **C** Illustration of the potential energy surface of S_1 and S_2. E_0 is the activation energy barrier of the photoisomerization and k_{iso} defines the isomerization transition rate. **D** Normalized absorption spectra of ICC and IDCC in H_2O. **E** Respective normalized fluorescence spectra of ICC and IDCC. Experimental conditions: λ_{ex} = 530 nm (ICC), 550 nm (IDCC); λ_{em}>545 nm (ICC), >650 nm (IDCC).

Since unmodified Cy3 and Cy5 molecules tend to aggregate in aqueous solution, sulfate moieties are attached regularly to their pyrrole groups to increase water solubility.[76] ICC and IDCC are such sulfated PCs. Their structure is shown in Figure 2.1.6A,B. ICC shows a strong absorption band around 551 nm (Figure 2.1.6D) and a carbocyanine-typical small stokes shift (~16nm), which generates a fluorescence emission spectrum with a maximum at 567 nm (see Figure 2.1.6E). The absorption band of IDCC is red-shifted compared to ICC (enlarged conjugated π-system, see Section 2.1.1). The spectral maximum locates at 643 nm (Figure 2.1.6D), a stokes shift of ~20nm generates a fluorescence emission spectrum with a main peak at 663 nm (see Figure 2.1.6E). The emission spectra of PCs are affected by the present solvent polarity, leading to bathochromic shifts in nm regime with degreasing polarity.[62]

ICC and IDCC belong to the group of single emitting FMRs (see Section 2.1.2). In FMRs, individual chemical groups undergo rotations, which can be described as molecule specific photoisomerization processes (Figure 2.1.6C). ICC/IDCC shows an intramolecular rotation around its C-C bounds in the polymethine linker, which are connected to a charge transfer between both indole groups. In the S_0 ground state ICC/IDCC adopts an all-trans conformation (0 °), the energetically lowest state. After photon absorption and transition into the higher singlet states, the molecules accumulate in the S_1 state. Here, ICC/IDCC can adopt a twisted (90 °) or cis conformation (180 °). The following depopulation from S_1 to the S_0 state are mainly established by two processes. In particular by fluorescence emission k_f, and by photoisomerization k_iso via rotation around a torsion angle θ defined by the axes of the central C-C bound in the polymethine linker (Figure 2.1.6C).[81] Both processes are competing, an increased rotation efficiency, i.e., a high k_iso value results in a reduced probability of photon emission, i.e., a low k_f. On the contrary, a small k_iso increase the probability of fluorescence emission. These changes in fluorescence emission, i.e., in the transition rate k_f, are directly reflected in the fluorescence lifetime as well.[82-84] In general, the efficiency of photoisomerization of an FMR depends on the solvent viscosity, but may additionally depend on temperature, activation energy, or steric rotational restrictions caused by neighboring substituents. These dependencies encourage the general use of ICC/IDCC, like other FMRs, as viscosity and interaction probes for a multitude of systems like aerosol particles, lipidic model vesicles, cell organelles, and living cells.[26, 79, 85-89]

Xanthenic fluorophores: Rhodamine, fluorescein and seminapthorhodafluors

Xanthenic dyes are one of the major fluorophore classes, used in a broad range of chemical and biological investigations. Fluorescein and rhodamine represent the two most widely distributed subclasses of the xanthenic group. Figure 2.1.7 shows the chemical structures of xanthene (A), fluorescein (B), rhodamine (B), and their derivatives fluorescein isothiocyanate (FITC, C) and Rhodamine B (RhoB, D), these derivatives are applied in this thesis. Both fluorophore families are characterized by relatively high molar absorption coefficients and quantum yields, narrow absorption and emission bands, and small Stoke shifts (see Ref. 90 & 91). Although depending on structure, chemical

substitutions and solvents, rhodamines provide commonly red-shifted excitation and emission bands compared to fluoresceins.[90-91] This phenomenon can be observed in the fluorescence spectra shown for FITC and RhoB in Figure 2.1.7G.

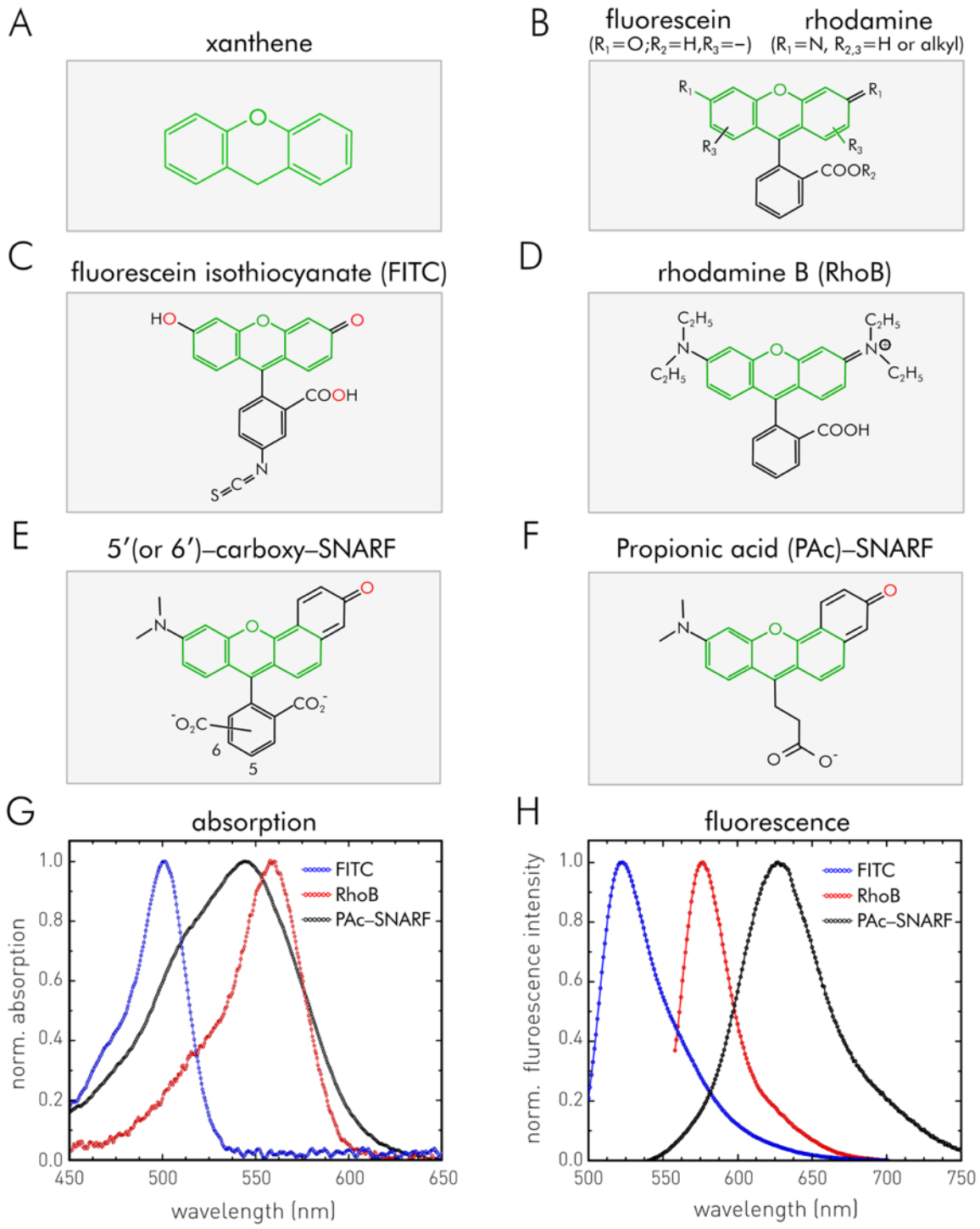

Figure 2.1.7: Chemical structures and spectral characteristics of xanthenic fluorophores. In this thesis the xanthenic fluorophores FITC, RhoB and PAc-SNARF were applied. **A** Structure of xanthene. **B** Structure of two xanthene-based fluorophore classes: Rhodamine and fluorescein; xanthenic backbone is indicated in green. **C** Fluorescein derivative fluorescein isothiocyanate (FITC); red-colored oxygens indicate protonatable sites. **D** Rhodamine derivative rhodamine B (RhoB). **E** 5′(or 6′)-carboxy-Seminapthorhodafluor (carboxy-SNARF). **F** Propionic acid Seminapthorhodafluor (PAc-SNARF). **G** Normalized absorption spectra of FITC, RhoB and PAc-SNARF in PBS pH 7.4. **H** Normalized fluorescence spectra of FITC, RhoB and PAc-SNARF. Experimental conditions: λ_{ex} = 495 nm (FITC), 526 nm (PAc-SNARF), 550 nm (RhoB); λ_{em}>500 nm (FITC), 530 nm (PAc-SNARF), 555 nm (RhoB).

Fluorescein derivatives are utilized extensively in fluorescence-based biomolecular sensing, tracing of analytes, in optical imaging, and as laser dyes. Absorption, fluorescence emission intensity, as well as the fluorescence lifetime of fluorescein exhibits a sensitivity to protonation between pH 1 to 8.[92] A dependency over such a large pH range is enabled by the existence of three protonatable groups of fluorescein: The neutral xanthene group, the carboxylic acid group, and the cationic xanthene group leading to four protonation states in aqueous solutions.[93] These states define the cationic, neutral, anionic, and dianionic forms of fluorescein with three pK_a-values (2.2, 4.4, 6.4) characterizing the transitions between them.[93]

Chemical substitutions in different fluorescein derivatives can change the pK_a and tune the spectral characteristics, but the general protonation dependency is maintained. For that reason, fluorescein homologous are frequently applied in pH sensing, even at high salt concentrations as their pK_a-values are almost insensitive to ionic strength.[92] For intracellular pH probing, special fluorescein derivatives were developed such as the fluorescein diacetate (FDA), 5(or 6)-carboxy-fluorescein diacetate (CFDA) and 2′,7′-bis(carboxyethyl)-5′(or 6′)-carboxy-fluorescein (BCECF). The cell-permeant FDA easily enters cells. Subsequently, hydrolysis generates fluorescein which monitors the intracellular pH via fluorescence. High emission intensities or long fluorescence lifetimes indicate basic (dianion, Φ_f=0.93, τ_f =4.06 ns) and lower intensities acidic pH (monoanion, Φ_f=0.37, τ_f =3.37 ns).[93] However, the generated fluorescein molecules are also cell-permeant and leak from the cell, a circumstance making quantitative pH determinations via an intensity-based pH calibration error prone.[94]

CFDA attempts to reduce this drawback by using a carboxy fluorescein derivative as pH probe. Carboxy-fluorescein is slightly more negatively charged which prevents high cell leaking rates. As the pK_a of carboxy-fluorescein is ~6.5 and thus sub-optimal for pH investigations in the cytosol (pH 6.8 – 7.4), a further fluorescein-based fluoroprobe was developed, BCECF. BCECF provides a pK_a shifted to a more physiological range of ~7 while further increasing the negative charge and so cell leakage.[95] In contrast to the absorbance bands, the shape of fluorescein's emission band does not alter significantly by protonation. Further pH probes were developed showing spectral changes on protonation and thus allowing for fluorescence intensity-based radiometric pH investigations less error-prone.

Seminapthorhodafluors (SNARF) are such a new family of pH sensitive fluorophores. SNARF homologues equally belong to the xanthene dyes as fluorescein and rhodamine and show two spectrally separated absorbance and fluorescence bands reflecting the absorption and emission from the protonated and deprotonated forms of SNARF. The absorbance band is relatively broad and also allows for selective or preferential excitation of one of both protonation states (Figure 2.1.7G). This circumstance is often utilized to enhance the comparatively weak emission band of the protonated SNARF form showing a generally reduced quantum yield compared to deprotonated SNARF. In acidic

environments an emission band around 580 nm is prominent, reflecting the protonated SNARF form while a second band at 630 nm reflecting the deprotonated form gains in intensity in basic environments. The ratio between both band intensities reflects the fluorophore's protonation statues, independently of the local fluorophore concentration. The pK_a of SNARF derivatives is commonly located in the physiological range. Although commercially available 5'(or 6')-carboxy-SNARF derivatives (Figure 2.1.7E) for intracellular pH probing has received a widespread distribution. Several disadvantages limit the application of the pH sensor. For one thing, synthesis of SNARF has low yield, making the production expensive. For the other thing, the unspecific position (5' or 6') of the second SNARF carboxy group makes the pH calibration difficult and error-prone as both isomers show a difference in pK_a of 0.15.[92] Such differences were also reported for the equivalent case of 5'(or 6')-carboxy-fluorescein.[94, 96] Finally, at higher pH, the dicarboxyphenyl ring causes a fraction of the SNARF to be in its lactonic form by hydrophobic interactions. This form is colorless and non-fluorescent. Consequently, the lactonic fraction of the SNARF probe is lost for pH probing.[92, 97] For that reason, a new SNARF derivative was devolved by exchanging the bulky dicarboxyphenyl ring which does itself not contribute to the xanthenic π-electron system of the fluorophore by a propionate group.[92] The propionic acid seminaphtharhodafluor (PAc-SNARF, Figure 2.1.7F) is applied in this work and was developed and synthesized by Dr. Celin Richter (Prof. Ernsting group, Humboldt Universität zu Berlin, Germany). PAc-SNARF shows a well-defined pK_a, is easily solvable in aqueous solutions and produces only a negligible fraction of its lactonic from at high pH values.

Difluoroboron-dipyrromethene (bodipy)

Boron-dipyrromethenes (bodipy) are one of the most versatile fluorophore classes, characterized by low photobleaching and high robustness against chemical degradation. Bodipy fluorophores have relatively narrow absorption and emission bands located in the visible to near infrared range, high molar absorption coefficients and fluorescent quantum yields between 40 – 90 %. These parameters make them suitable for many applications like protein labeling, lipid staining, bioimaging, pH-,viscosity-, or chemosensing.[98-102] Especially the simplicity of modifications, their good water solubility, their low tendency to self-aggregation, and their relatively long fluorescence lifetimes have attracted interest in the last decades leading to countless bodipy derivatives.[100]

In this thesis, the bodipy derivative 493/503 is used as hydrophobic cargo loaded non-covalently to a CMS-nanocarrier (Section 2.3.2). Bodipy™493/503 (here referred to as bodipy) has a molecular weight of 262 Da, a LogP value of 3.50 ±0.04,[102] and was previously applied as a staining agent for neutral lipid droplets (LDs).[102] LDs are dynamic lipid storage organelles found in all eukaryotic cells. They consist of triglyceride and other neutral lipids cores which has surrounding shells of phospholipids.[102-103] Bodipy stains LDs by two overlapping effects. Firstly by its lipophilicity (passive lipid targeting) and secondly by its increased fluorescence quantum yield in apolar environments compared to aqueous solutions. In MeOH, the molecular absorption coefficient amounts to

88,000 ± 6,000 M^{-1} cm^{-1} and the wavelength of maximal absorption amounts to 493 ± 3 nm.[104] The correspondent wavelength of maximal fluorescence emission is 504 ± 4 nm.[104]

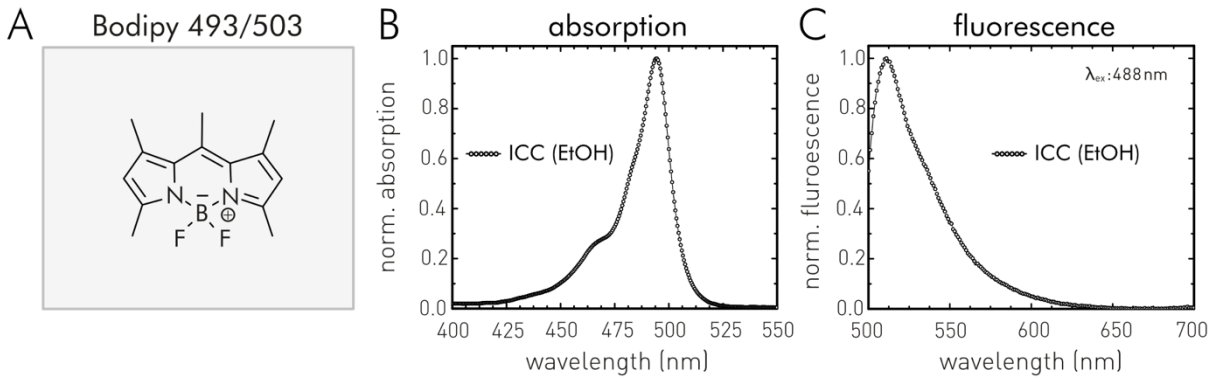

Figure 2.1.8: Chemical structure and spectral characteristics of bodipy 493/503. **A** Structure of bodipy 493/503. **B** Normalized absorption spectrum of Bodipy 493/503 in EtOH. **C** Normalized fluorescence spectrum of bodipy 493/503 in EtOH. Experimental conditions: λ_{ex} = 488 nm; λ_{em}>500 nm.

CellROX green reagent

Reactive molecules containing oxygen atoms such as hydrogen peroxide (H_2O_2), hydroxyl radical OH•), the superoxide anion radical ($O_2^{\bullet-}$) or singlet oxygen ($^1O_2$)) are summarized under the term reactive oxygen species, ROS for short.[105-106] These potentially green oxidants are formed during the normal endogenous metabolism. Low and intermediate ROS levels have positive effects by serving an organism as intra- and intercellular messengers (cell signaling) or by maintaining homeostasis.[49] At the same time, if present in high concentrations, ROS has negative effects, e.g., through unspecific damage to proteins, lipids and DNA by ROS' highly reactive nature.[107] Therefore, an organism tries to balance its ROS level. This is achieved by the cellular antioxidant activity, for example by catalase, superoxide dismutase and ascorbate-glutathione cycle enzymes.[108]

If ROS levels cannot be balanced, one speaks of oxidative stress. Unbalanced ROS levels are caused by an overproduction of ROS or by a strongly inhibited antioxidant defense.[109] Oxidative stress impairs normal cellular function and occurs in or triggers a number of pathologies including age-related cancer, cardiovascular, or neurodegenerative diseases.[107] Besides endogenous ROS producing factors there are also exogenous triggers of ROS formation like ultraviolet and ionizing radiation, heat exposure, or exogenous chemicals like H_2O_2.[110] A further potential exogenous source of ROS formation are nanomaterials.[111-112] For nanoparticles the high ratio between volume and surface causes a high chemical reactivity which leads to a potentially increased ROS production and related oxidative stress.[112] While some studies report on remarkable cellular ROS levels due to interactions with nanoparticles,[113-115] others show that ROS generation can also be controlled and modulated by special nanoparticle architectures.[116-117]

Cellular ROS generation can be quantified by several methods.[118] These include fluorescence-based methods using reactive fluorophores such as dichlorodihydrofluorescein (DCF) and

dihydroethidium. There are numerous other fluorescent probes for detection of specific ROS types in different applications.[119] Typical problems in fluorescence-based ROS detection have their origin in signal artefacts, for example in the case of DCF. Here, in a ROS-environments the fluorogenic substrate H_2DCF generates both the highly fluorescent DCF and other non-fluorescent products. Furthermore, the presence of locally high fluorophore concentrations or high excitation intensities may also alter the fluorescence read-out and its interpretations.[49] In addition, detection principles which do not discriminate single cells, such as plate readers, are often used in ROS detection. These methods are prone to detect fluorescence emission not only from a cellular origin, but also from activated fluorogenic substrate in the medium.

In order to avoid such effects, novel and more complex fluorogenic ROS reagents were developed such as the reactive fluorescent reagent CellROX Green.[120] This cell permeable reagent is designed for cellular applications and operates in a two-step reaction mode (see Figure 2.1.9A). After entering a cell in its initially reduced state, intracellular ROS oxidizes the reagent. After this activation step, the CellROX reagent becomes highly fluorescent and binds to double-stranded DNA (dsDNA). Thus, it accumulates at cellular sites containing dsDNA, like the nucleus or mitochondria. CellROX Green is a live-cell compatible reagent which allows a cellular incubation in complete medium. Its fluorescence excitation and emission spectrum after having bound to dsDNA is shown in Figure 2.1.9B. The wavelength of maximal absorption in this state amounts to 508 nm. The corresponding wavelength of maximal fluorescence emission is 525 nm.

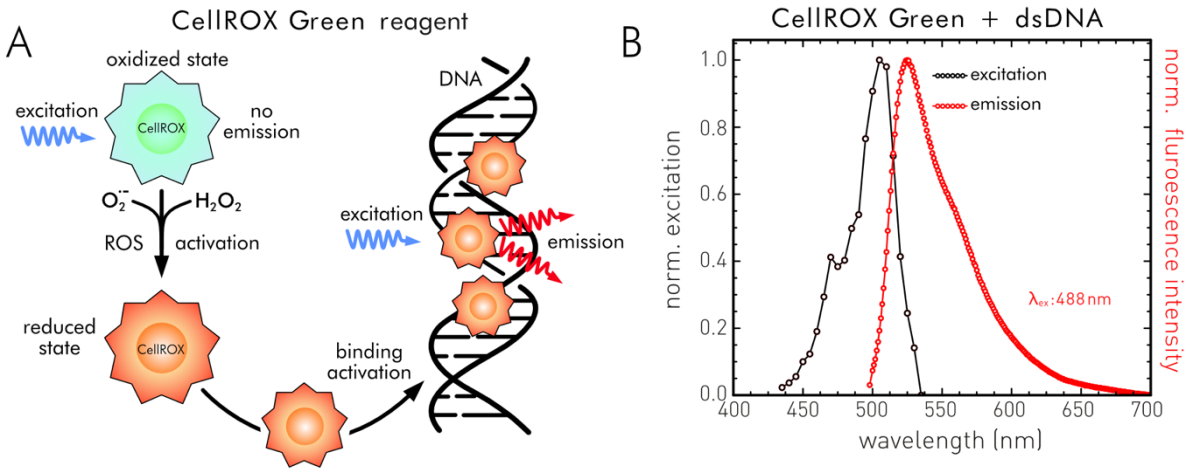

Figure 2.1.9: Working principle of the fluorescent CellROX Green oxidative stress reagents. **A** Working principle of CellROX reduction and DNA binding. **B** Normalized excitation and emission spectrum of CellROX green after binding to double-stranded DNA. Spectral data recorded by Jens Balke. Modified reprint from Balke et al. (2018, Ref. 49), Copyright 2020, with the kind permission of Small. Experimental conditions: λ_{ex} = 488 nm; λ_{em}>495 nm.

2.2 Time-resolved fluorescence spectroscopy and microscopy

2.2.1 Technical principles of time-resolved fluorescence detection

Excited state dynamics are significantly affected by the micro/nano environment, structure, or molecular interaction of a fluorophore (see Section 2.1.3). For this reason, the determination of the fluorescence lifetime (τ_f), which is directly related to the transition rates of electronically excited states via Eq. 16, is an essential observable in a broad spectrum of scientific disciplines ranging from physical chemistry to biophysics and applied medicine. During the last decades, several methods for time-resolved fluorescence detection have been developed and have become commercially available. The developed techniques can generally be divided into two main categories: time-domain recordings obtained by time-correlated single photon counting (TCSPC), fluorescence up-conversion spectroscopy (FLUPS), streak-cameras or time-gated imaging, and frequency-domain techniques such as phase modulation spectroscopy or methods based on phase-modulated image intensifiers. Each of these methods has its benefits and drawbacks leading to specific application fields. For detailed reviews see Ref.121-126. Here, the technical principles of time-resolved fluorescence detection based on phase modulation and TCSPC will be presented, as these are the most common detection schemes in the frequency and time domain.

Phase-modulation

Phase-modulation fluorescence spectroscopy, also termed phase-modulation fluorometry uses an intensity-modulated light source to excite a fluorescent sample (Figure 2.2.1A). The shape of the modulation follows a sinewave with the frequency f. f should be in the order of $1/(2\pi\tau_f)$. Thus, typical modulation frequencies are in the range of 10 MHz – 10 GHz, reflecting that fluorescence lifetimes are typically in the pico- and nanosecond regime. The resulting fluorescence signal is modulated in the same sinusoidal way as the excitation. In contrast to the frequency, however, the intensity signal is delayed in time and its peak amplitudes are reduced. This behavior is called harmonic response. Since the variations in the fluorescence signal are caused by the fluorescence lifetime, both the time delay, expressed as phase shift ϕ, and the demodulation, expressed as modulation ratio M can be independently used to determine the fluorescence lifetime (Figure 2.2.1B). While the ϕ can be directly obtained by the temporal offset between excitation and fluorescence response, M has to be calculated by the ratio of the modulation depth m_0 of the excitation and m of the response signal:

$$M = \frac{m}{m_0} = \left(\frac{2\, I_{\mathrm{Em,AC}}}{I_{\mathrm{Em,DC}}}\right) / \left(\frac{2\, I_{\mathrm{Ex,AC}}}{I_{\mathrm{Ex,DC}}}\right) \quad , \tag{35}$$

with $I_{\mathrm{Ex,AC}}$ and $I_{\mathrm{Em,AC}}$ being the amplitude of the excitation and emission modulation. The parameters $I_{\mathrm{Ex,DC}}$ and $I_{\mathrm{Em,DC}}$ reflect the average temporal intensities of the respective sinusoidal signals (see Figure 2.2.1B).

The phase shift ϕ and the modulation ratio M are related to the fluorescence lifetime by:

$$\phi = \tan^{-1}(\omega\,\tau_\phi) \tag{36}$$

$$M = \frac{1}{(1+\omega^2\tau_M^2)^{1/2}} \quad , \tag{37}$$

With τ_ϕ and τ_M being the phase and modulation lifetime, respectively, ω is the angular modulation frequency ($\omega = f/2\pi$). For mono-exponential fluorescence decays the fluorescence lifetime corresponds to τ_ϕ and τ_M. It applies:

$$\tau_\mathrm{f} = \tau_\phi = \tau_M \quad . \tag{38}$$

For complex decay characteristics like multi-exponentials, τ_ϕ and τ_M become divergent and reflect apparent lifetimes indicating a complex fractional weighting of the decay components ($\tau_{\mathrm{f,c}}$). In order to extract multiple decay components from phase-modulation fluorometry a multi-frequency analysis is necessary (Figure 2.2.1C). For this procedure one applies the sine (P) and cosine (Q) Fourier transforms of the multi-exponential fluorescence decays (Eq. 19) in the time domain. These transformations are functions of the angular frequency[127]:

$$Q(\omega) = \sum_c^n \frac{\beta_c}{1+\omega^2\tau_{\mathrm{f,c}}^2} \tag{39}$$

$$P(\omega) = \omega\sum_c^n \frac{\beta_c\,\tau_{\mathrm{f},c}}{1+\omega^2\tau_{\mathrm{f},c}^2} \quad , \tag{40}$$

where β_c are the relative steady-state intensity contributions of the individual decay components (see Eq. 21). $Q(\omega)$ and $P(\omega)$ and thus β_c and $\tau_{\mathrm{f},c}$ are linked to the experimental observables ϕ and the M via the following relations[51]:

$$\phi(\omega) = \tan^{-1}\left(\frac{P(\omega)}{Q(\omega)}\right) = \tan^{-1}\left(\frac{\omega\sum_c^n \frac{\beta_c\,\tau_{\mathrm{f},c}}{1+\omega^2\tau_{\mathrm{f},c}^2}}{\sum_c^n \frac{\beta_c}{1+\omega^2\tau_{\mathrm{f},c}^2}}\right) \tag{41}$$

$$M(\omega) = \sqrt{P^2(\omega)+Q^2(\omega)} = \sqrt{\left(\omega\sum_c^n \frac{\beta_c\,\tau_{\mathrm{f,c}}}{1+\omega^2\tau_{\mathrm{f,c}}^2}\right)^2 + \left(\sum_c^n \frac{\beta_c}{1+\omega^2\tau_{\mathrm{f,c}}^2}\right)^2} \quad . \tag{42}$$

Both equations become equal to Eq. 36 & 37 for a single decay component and allow independent extraction of multiple components via least-square fitting of the frequency dependent traces of ϕ and M. This procedure is simulated in Figure 2.2.1C as an example for a 1:1 mixture of two fluorophores individually exhibiting (mono-exponential) fluorescence lifetimes of 1 ns and 3 ns, respectively. The data points show the multi-frequency determination of ϕ and M over serval frequency decades. By fitting them to Eq. 41 & 42, displayed by the orange and blue continued lines, one can extract the amplitudes and decay times of the individual components. For comparison, dashed lines indicate the harmonic response of the individual fluorophores according to Eq. 36 & 37.

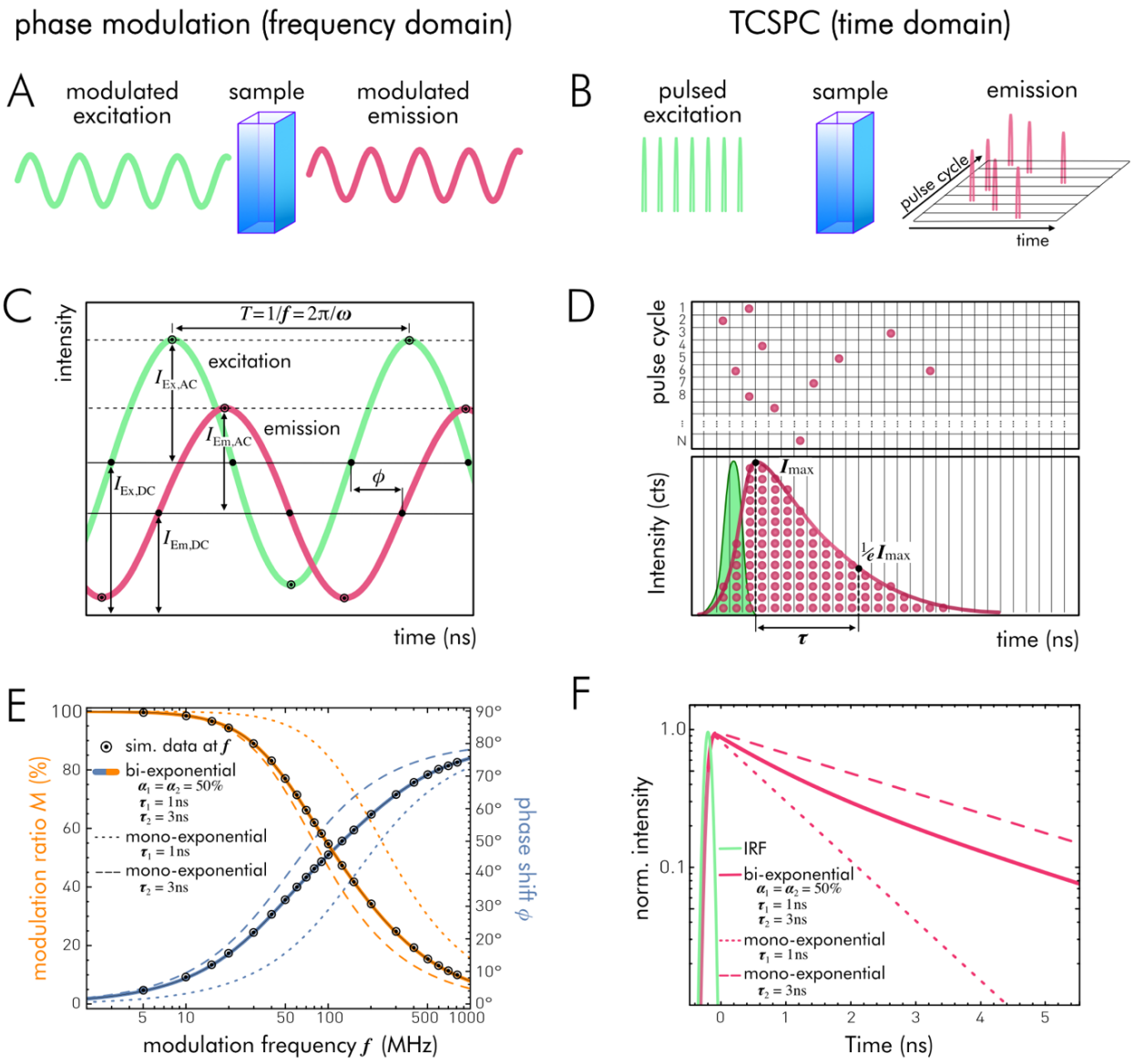

Figure 2.2.1: Time-resolved fluorescence detection in frequency and time domain. **A** Phase modulation principle, modulated excitation and fluorescence emission are shown. **B** TCSPC principle, pulsed excitation leads to single photon detection. **C** Characteristic quantities of phase modulation fluorometry. f is the modulation frequency, ω is the angular modulation frequency and T is the periodic time. $I_{\mathrm{Ex,AC}}$ and $I_{\mathrm{Em,AC}}$ represent amplitude of excitation and emission modulation. $I_{\mathrm{Ex,DC}}$ and $I_{\mathrm{Em,DC}}$ reflect the average temporal intensities of the respective sinusoidal signals. ϕ indicates the phase shift between excitation and emission modulation. **D** TCSPC: determined start-stop times of individual excitation pulse/detection cycles are sorted into a histogram, this reveals the fluorescence decay behavior $S(t)$ (red curve) of an investigated fluorescent sample. Additionally, the instrument response function ($I_{\mathrm{IRF}}(t)$) that is convoluted with the original fluorescence signal $I(t)$ is indicated (green curve). τ is the fluorescence lifetime time, e.g., the constant where the emission intensity is decreased to 1/e. **E** Complex decay characteristics in phase fluorometry: Simulated multi-frequency modulation and phase shift data points of a 1:1 fluorophore mixture ($\alpha_1 = \alpha_2$) individually exhibiting (mono-exponential) fluorescence lifetimes of 1 ns and 3 ns. Continues lines (yellow: modulation, blue: phase shift) show the theoretical curves described by Eq. 41 & 42 for these decay parameters. Additionally, modulation ratios and phase shifts for single fluorophore populations showing mono-exponential decays of 1 ns and 3 ns are indicated (long (3 ns) & short (1 ns) dashed lines). **F** Simulated TCPSC based fluorescence measurement of the same fluorophore mixture as in (E). The green curve indicates an instrument response function (IRF) with a FWHM of 118 ps. The thick red continues line shows the theoretical decay trace for two components with 1 ns and 3 ns and an amplitude ration of 50 % given by Eq.19 convoluted with the IRF. Additionally, single fluorophore populations showing mono-exponential decays of 1 ns and 3 ns are indicated (long (3 ns) & short (1 ns) dashed lines).

The correctness of the applied fit model, e.g., the right number of decay components can be judged by the reduced chi square (χ^2_{red}) parameter[51]:

$$\chi^2_{red} = \frac{1}{2N-p}\left(\sum_f^N \frac{\left(\phi(\omega_f)-\phi_{fit}(\omega_f)\right)^2}{\sigma_\phi^2} + \sum_f^N \frac{\left(M(\omega_f)-M_{fit}(\omega_f)\right)^2}{\sigma_M^2}\right) \quad , \tag{43}$$

with N being the number of measured frequencies ω_f, p the number of independent fit parameters, and M_{fit} /ϕ_{fit} the calculated fit value of modulation ratio and phase shift in the frequency bin f. $\sigma_\phi$and σ_M are the experimental uncertainties of the phase and modulation values.

Time correlated single photon counting (TCSPC)

Time correlated single photon counting combines short repetitive excitation light pulses and single photon counting (SPC) techniques to statistically reconstruct the temporal fluorescence decay in the time domain. A common way to establish TCSPC is the application of femto- and picosecond laser sources that excite a fluorescent sample repetitively on a MHz time scale. The applied excitation intensities are set to low magnitudes compared to steady state or phase-modulation fluorometry as the detection of the fluorescence emission takes place in the single photon detection/counting regime.[128] The high photon sensitivity and picosecond time-resolution are achieved by different technologies like photo multiplier tubes (PMTs), avalanche photo diodes (APD), hybrid photo detectors (APD+PMT), or micro-channel plates (MCP) and the utilization of fast signal processing electronics. Principally, the TCSPC concept can be compared to periodically occurring stopwatch measurements. After an excitation pulse the detector unit registers the first photon that arrives (Figure 2.2.1B). By calculating the difference between excitation time and photon arrival time at the detector, one obtains the fluorescence lifetime of a single excitation/photon detection cycle. Such a lifetime reflects the time between excitation and emission of a single fluorophore. To obtain the characteristic fluorescence lifetime parameter defining the underlying exponential decay law one has to analyze many fluorophores. Thus, sorting lifetimes of thousands to millions of excitation/photon detection cycles into a histogram reveals the statistical relationship. The resulting histogram reflects the temporal detection probability of a fluorescence photon relative to the excitation pulse (Figure 2.2.1C).

As fluorescence decay behaviors, i.e., the temporal depopulation of the excited state follows Poisson statistics, fitting the generated histogram by mono- or multi-exponential decay models (Eq. 19) allows to directly retrieve decay components. For multi-exponential decays these are defined by a relative amplitude and the respective fluorescence lifetime. Figure 2.2.1F exemplary shows a simulated decay of a bi-exponential fluorescence species. Both decay components have a relative amplitude of 50 %, the fluorescence lifetimes amount to 1 and 3 ns. In contrast to phase modulation fluorometry, time-resolved fluorescence signals $S(t)$ by TCSPC are convoluted with a finite excitation function, called instrument response function (IRF). This phenomenon is illustrated in Figure 2.2.1D. The convolution product is high during and immediately after excitation, resulting in an increasing fluorescence signal passing through a maximum before it begins to decay (Figure 2.2.1F). For later

points in times the convolution becomes negligible and the fluorescence decay can be considered identical to a decay of a hypothetical δ-pulse excitation. In this case "tail"-fitting of the decay histogram would be sufficient to resolve the fluorescence lifetime. In order to extract fast decay components, a deconvolution of the original fluorescence signal $I(t)$ and $I_{\mathrm{IRF}}(t)$ during the fitting process is necessary. The convolution can be described by

$$S(t) = I_{\mathrm{IRF}}(t) \otimes I(t) = \int I_{\mathrm{IRF}}(t')\, I(t-t')\, dt' \quad . \tag{44}$$

Width and shape of the IRF depend on the laser pulse width, detector response and the used electronics in the TCSPC system. For proper signal deconvolution it is crucial to get information about the $I_{\mathrm{IRF}}(t)$ (green curve, Figure 2.2.1D). Usually, IRFs are experimentally determined by measuring a reflecting non-fluorescent sample. Typical IRFs show full-width half-maxima (FHWM), ranging from a few up to hundreds of picoseconds.[128] Another approach is the assumption of a Gaussian IRF shape. Width and amplitude are then treated as further parameters during the fitting process. To retrieve the original fluorescence signal $I(t)$, $I_{\mathrm{IRF}}(t)$ and $S(t)$ are repeatedly deconvoluted and reconvoluted during non-linear least square fitting steps using a Levenberg-Marquardt algorithm. The reconvolution with the IRF is necessary to compare the current fit result with the experimental histogram entries. The quality of the applied fit model, e.g., the right number of decay components can be judged again by the reduced chi square (χ^2_{red}) parameter[51]:

$$\chi^2_{red} = \frac{1}{N-p}\left(\sum_j^N \frac{\left(S(t_j) - S_{fit}(t_j)\right)^2}{\sigma^2(t_j)}\right) \quad , \tag{45}$$

with N being the number of time bins t_j in the decay histogram, p the number of independent fit parameters. $S_{fit}(t_j)$ is the calculated fit value of the reconvoluted intensity in time bin t_j and σ the respective uncertainty. In the time domain, the uncertainty of the photon counts per time bin obeys a Poisson statistic. This defines σ as $\sqrt{S(t_j)}$. In addition to χ^2_{red}, graphical tests as the weighted residuals $R_w(t_j)$ are used to show the fit quality of TCSPC measurements:

$$R_w(t_j) = \frac{S(t_j) - S_{fit}(t_j)}{\sigma\,(t_j)} \quad , \tag{46}$$

In order to prevent TCSPC measurement artifacts, e.g., an increased population at shorter times of the decay histogram by detecting multiple photons per measurement cycle (pile-up effect), one reduces excitation intensities to levels in which a fluorescence photon is detected only once in 200 excitation cycles.[128-129] Figure 2.2.2A illustrates the electronic components and signal processing in a TCSPC setup. The electronic registration of excitation (sync) and photon detection signals, constitute the start and stop signal (or vice versa) of the individual time measurements. This is technically realized by two constant fraction discriminators (CFD). CFLS separate an electric pulse signal into two separate pulses. Afterwards it inverts and changes the amplitude of one pulse signal and delays the

other pulse signal (Figure 2.2.2B). By adding both modified signals a new signal is produced with a zero crossing (ZC) that is always constant in time and not altered by varying pulse heights. The resulting zero crossings of the start and stop signals trigger the individual measurement cycles. Time measurement is realized by a time to amplitude converter (TAC). The TAC utilizes a capacitor that charges after the ZC trigger of the start pulse and stops by the ZC trigger of the stop pulse (Figure 2.2.2C). The resulting charge is proportional to the passed time and is converted to a digital signal (Figure 2.2.2D) by an analog-digital converter (ADC). The digital signal amplitude corresponds to the time between a start-stop trigger pulse. Using a multi-channel analyzer (MCA), these time values are sorted into a histogram of equally distributed time bins (t_i).

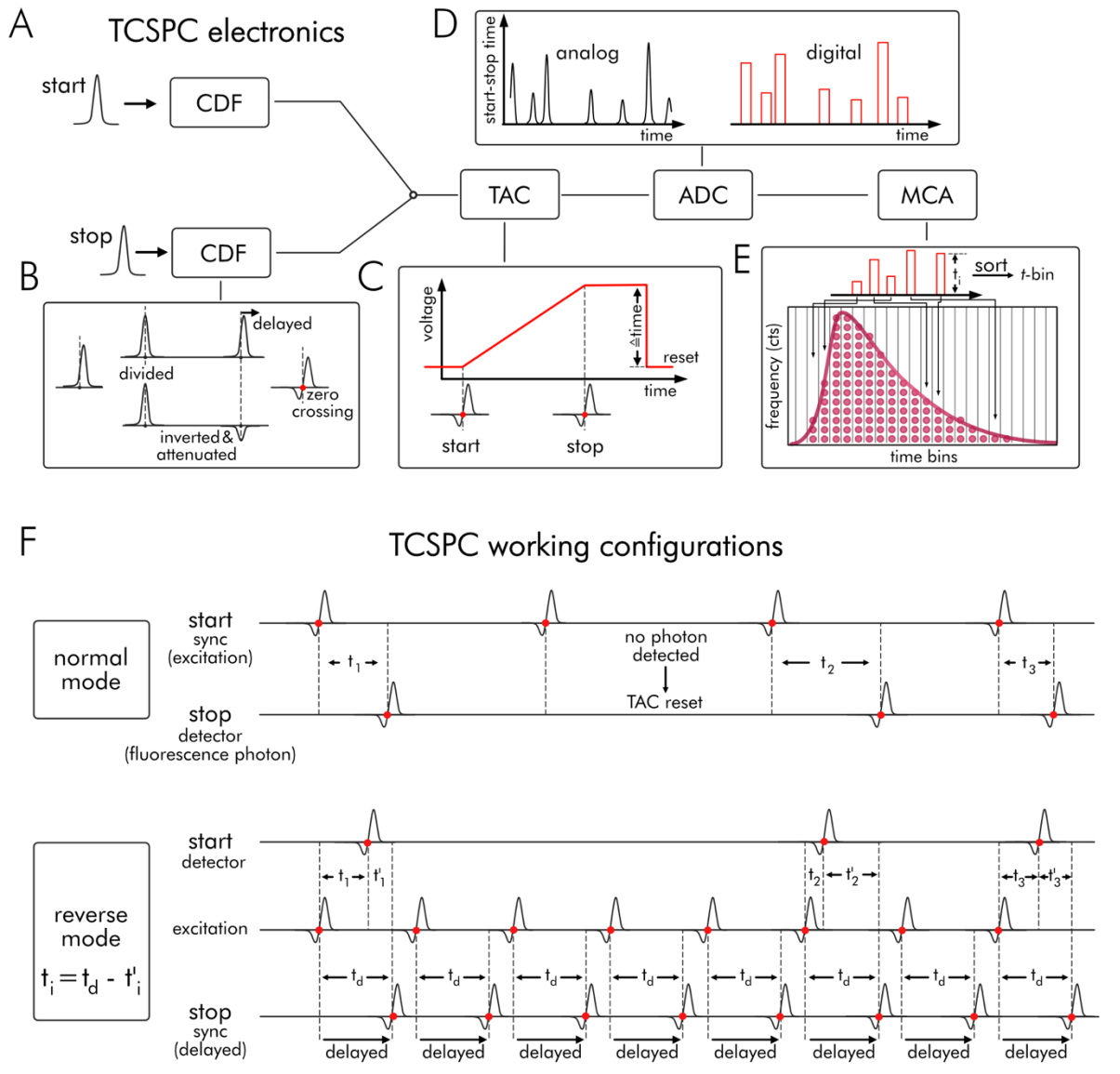

Figure 2.2.2: General working scheme of TCSPC. **A** Components of TCSPC system. **B** Two constant fraction discriminators (CFD) locate the temporal position of start and stop pulses by determining a zero crossing of the electric signals. **C** The CFD output is further processed by a time to amplitude converter (TAC) which ascertains the time interval between start and stop signal. **D** the analog TAC output, i.e., the electronic signal that's height is proportional to the start – stop time is converted into a digital signal by an analog to digital converter (ADC). **E** A multi-channel analyzer sorts the digital start – stop times into a histogram of equally distributed time bins. The histogram entries reflect the temporal fluorescence decay behavior. **F** Comparison of normal and reverse

TCPSPC working configurations. Top: Normal mode, typically used for low repetition rates. The sync trigger pulse of the excitation source acts as start signal for the time measurement which is stopped by the detector pulse signal after the first fluorescence photon is recognized. The next sync pulse starts the next measurement cycle. For that cycles, where no photon is recognized (which is most often the case to a void a "pile-up" effect) the TAC has to be reset for the following cycle. Bottom: Reverse Start-Stop mode, used for fast excitation repetition rates, where the TAC reset cannot be fast enough to guarantee a proper photon counting. Here, the start signal is triggered by the detection of a fluorescence photon and the stop signal is given by the sync signal. To measure the right time span between the photon detection and the respective excitation pulse responsible for the photon emission of this specific photon one uses a delay line to shift the temporal detection of sync signal.

As mentioned above, both, exaction and detection pulses can act as the start signal for a TCSPC measurement circle. In normal or classical operation modes, the sync pulse of the excitation source functions as a start trigger for the TAC. In order to avoid "pile-up" artifacts, the TAC has to be reset before the next measurement cycle starts, since most of the excitation pulses generate no detected fluorescence photon. At lower excitation repetition rates up to the lower MHz range this is no problem. However, due to the finite time of the TAC reset operation, the normal mode configuration is not advisable to use at high repetition rates like the typical ~80 MHz of a titanium-sapphire (Ti:Sa) laser system. For such repetition rates, in which a TAC reset is not fast enough to guarantee proper photon counting the reverse start-stop mode should be applied. Here, the start signal is triggered by the detection of a fluorescence photon and stopped by the sync signal. To ensure to measure the right time span (t_i) between the photon detection and the respective excitation pulse responsible for the photon emission of this detected photon, one uses a delay line to shift the temporal registration (t_d) of the sync signal. The major advantages of TCSPC based time-resolved fluorescence detection over phase modulation techniques are the higher detection sensitivity due to single photon counting, increased dynamic range and signal linearity, low excitation levels (photobleaching), direct visualization of fluorescence decays, and well-defined Poisson statistics.

2.2.2 TCSPC-based fluorescence spectroscopy

In this section, I explain the functional principles of a TCSPC L-shaped fluorometric setup for time-resolved fluorescence spectroscopy of fluorescent samples in solution (Figure 2.2.3). As TCSPC is dependent on pulsed excitation, serving as start or stop triggers for time resolution (see last paragraph), a variety of illumination sources is applicable. Early TCSPC setups utilized flash lamps as they can deliver nanosecond pulses with repetition rates up to the MHz regime. However these light sources are restricted to UV excitation wavelengths. For this reason, pulsed light-emitting diodes (LEDs) are becoming increasingly common in commercially available TCSPC systems. LEDs provide pulse widths of less than a nanosecond, a broad range of possible wavelengths ranging between the UV and the IR spectrum, and low operating and maintaining costs. Most commonly, laser systems like titanium-sapphire (Ti:Sa) or picosecond diode lasers are used in time-resolved fluorescence spectroscopy as they combine short laser pulses in the femtosecond and picosecond range with MHz repetitions rates. Both mentioned laser types provide their own advantages: While diode lasers are

in general less expensive, easy to use, and long-term stable, Ti:Sa systems are wavelength tunable with outstanding short pulse widths of down to some tens of femtoseconds.

The excitation light in TCSPC experiments is typically linearly polarized to guarantee proper decay histograms as time-dependent anisotropy effects of the fluorophore orientations due to rotational diffusion may disturb recorded fluorescence decay shapes (see below). Most laser systems have an intrinsic defined polarization axis. For LEDs and flash lamps, one has to apply polarizers (Figure 2.2.3B). The polarized excitation light passes the cuvette glass and enters the solution with an ensemble of fluorophores exhibiting an isotropic distribution of orientations. The molecular orientation can be defined by the absorption transition moment (see Section 2.1.2). Assuming excitation light of vertical linear polarization (parallel to the z-axis, Figure 2.2.3C) in respect to the plane of the instrument table (defining x- and y-axis), the probability of excitation is dependent on a proper orientation, that means a high parallelism of the absorption transition moment and excitation polarization axis. One can describe the molecular orientation in the excitation/absorption process using two angles θ and φ (Figure 2.2.3D). While θ defines the (azimuthal) angle between polarization axis (z-axis) and absorption transition moment ($\boldsymbol{m_a}$), φ is an (equatorial) angle within the x,y-plane defining the tilt between x-axis and $\boldsymbol{m_a}$. The probability to excite a fluorophore located in the origin of the coordinate system is proportional to the projection of its $\boldsymbol{m_a}$ to the polarization axis, i.e., to cosine square of θ:

$$p_{\mathrm{ex}}(\theta,\varphi) \propto \cos^2(\theta) \quad , \tag{47}$$

that means only molecules exhibiting a component of their transition moment along the polarization axis of the excitation can absorb photons.

When considering an ensemble of fluorophores, one is confronted with an ensemble of absorption transition moments of isotropic orientations. For this situation it is possible to assume that the transition moments are uniformly distributed on a sphere S, where the area fragment $dS = \sin\theta\, d\theta\, d\varphi$ is proportional to probability of finding a transition moment pointing in this direction. Using this proportionality together with Eq. 47 and assuming no molecular rotation during the excitation process, the probability of fluorophore excitation can be expressed by

$$p_{\mathrm{ex}}(\theta,\varphi)\, d\theta\, d\varphi = \frac{\cos^2(\theta)\ \sin(\theta)\, d\theta\, d\varphi}{\int_0^{2\pi} d\varphi \int_0^{\pi} \cos^2(\theta)\sin\theta\, d\theta} = \frac{3}{4\pi}\cos^2(\theta)\ \sin(\theta)\, d\theta\, d\varphi \quad , \tag{48}$$

this distribution is symmetrical around the z-axis. But in general, the orientation of the excited molecules is anisotropic and so is the emission. The anisotropy of the emission transition moments can be expressed by the emitted photon intensities parallel and perpendicular to the excitation polarization axis:

$$r = \frac{I_{\parallel}^{\mathrm{em}} - I_{\perp}^{\mathrm{em}}}{I_{\mathrm{tot}}^{\mathrm{em}}} = \frac{I_{\parallel}^{\mathrm{em}} - I_{\perp}^{\mathrm{em}}}{I_{\parallel}^{\mathrm{em}} + 2I_{\perp}^{\mathrm{em}}} \quad . \tag{49}$$

For the simple case of parallel absorption and emission transition moments ($\theta_a = \theta_e = \theta$), the relation to azimuthal angle θ can be obtained by assuming the following relations for the ensemble averages:

$$I_{\parallel}^{\mathrm{em}} \propto \langle \cos^2(\theta) \rangle \quad \& \quad I_{\perp}^{\mathrm{em}} \propto \langle \sin^2(\theta) \rangle \langle \sin^2(\varphi) \rangle \quad . \qquad (50)$$

$\langle \sin^2(\varphi) \rangle$ can be set to 0.5 due to the cylindrical symmetry around the z-axis:

$$\langle \sin^2(\varphi) \rangle = \frac{\int_0^{2\pi} \sin^2(\varphi) d\varphi}{\int_0^{2\pi} d\varphi} = 0.5 \quad , \qquad (51)$$

using this relation and the identity: $\langle \sin^2(\theta) \rangle = 1 - \langle \cos^2(\theta) \rangle$, the fluorescence anisotropy can be expressed by:

$$r(\theta) = \frac{\langle \cos^2(\theta) \rangle - 0.5 \langle \sin^2(\theta) \rangle}{\langle \cos^2(\theta) \rangle + \langle \sin^2(\theta) \rangle} = \frac{3\langle \cos^2(\theta) \rangle - 1}{2} \quad . \qquad (52)$$

The anisotropy of a non-rotating single fluorophore can theoretically range between -0.5 and 1.0. But in an ensemble, the value is determined by the ensemble average of $\langle \cos^2(\theta) \rangle$:

$$\langle \cos^2(\theta) \rangle = \frac{\int_0^{2\pi} \int_0^{\pi} \cos^2(\theta)\, p_{\mathrm{ex}}(\theta, \varphi)\, d\theta\, d\varphi}{\int_0^{2\pi} \int_0^{\pi} p_{\mathrm{ex}}(\theta, \varphi)\, d\theta\, d\varphi} = \frac{\int_0^{\pi} \cos^4(\theta)\, \sin(\theta)\, d\theta}{\int_0^{\pi} \cos^2(\theta)\, \sin(\theta)\, d\theta} = \frac{3}{5} \quad , \qquad (53)$$

giving a fundamental anisotropy of 0.4 for non-rotating fluorophore ensemble. In multi-photon absorption, the excitation probability changes, e.g., the two-photon absorption probability is proportional to $\cos^4(\theta)$ instead of $\cos^2(\theta)$ leading to a maximum anisotropy of 4/7≈0.57. In a more general scenario, absorption and emission transition moments ($\theta_a \neq \theta_e$) are not parallel. This non-parallelism can be described by a further angle κ which defines the tilt between both transition moments (Figure 2.2.3D). For this case, Eq. 52 can be adapted to

$$r(\kappa) = \frac{3\langle \cos^2(\theta_a) \rangle - 1}{2} \cdot \frac{3\cos^2(\kappa) - 1}{2} = \frac{3\cos^2(\kappa) - 1}{5} \quad . \qquad (54)$$

Thus, the anisotropy of non-rotating fluorophores depends on angle κ and ranges between -0.2 for $\kappa = 90$ ° and 0.4 for $\kappa = 0$ °. As fluorophores located in a medium are not fixed in space, rotation will occur during the excited state. This effect allows for time-resolved fluorescence depolarization experiments, however, it may also disturb time-resolved intensity measurements. In a L-Shape fluorometry setup, the fluorescence emission is detected under a 90 ° angle in respect to the propagation of excitation light. Although this vastly reduces the detection of excitation light, a fluorescence emission filter (long- or bandpass filter) is frequently necessary to remove residual scatted excitation light from the fluorescence signal (see Figure 2.2.3E).

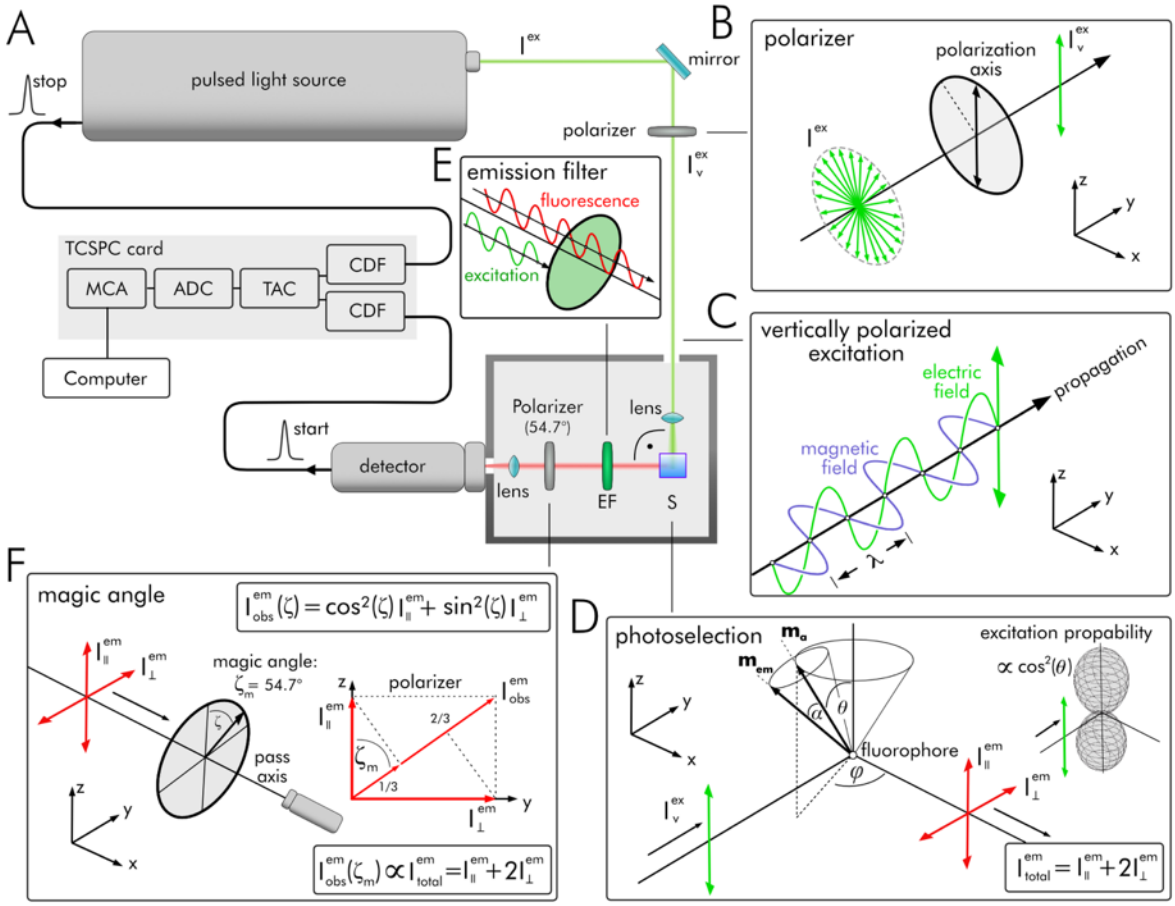

Figure 2.2.3: TCSPC based fluorescence spectroscopy. **A** Schematic diagram showing the major components of a single photon counting L-shape fluorimeter: A pulsed light source (laser or flashlamp + monochromator) + polarizer generates linear vertically polarized light pulses ($I_{\mathrm{v}}^{\mathrm{ex}}$), that excite a fluorescence sample in a glass cuvette. Emitted fluorescence (I^{em}), is detected under a 90 ° angle after passing an emission filter (EF) and a polarizer adjusted to the magic angle, where $I_{\mathrm{obs}}^{\mathrm{em}} \propto I_{\parallel}^{\mathrm{em}} + 2I_{\perp}^{\mathrm{em}}$. Single photon counting is implemented by TCSPC. **B** excitation light is vertically linear polarized. **C** Illustration of the excitation light as an electro-magnetic wave, i.e., synchronized oscillations of the electric and magnetic field along the propagation axis. **D** Photoselection by linear polarized excitation light. Fluorophores are excited in dependence of the orientation (θ) of their absorption transition diploe moments ($\mathbf{m_a}$). The excitation probability is proportional to $\cos^2(\theta)$) and is illustrated by distribution of excited fluorophores. The fluorescence emission is orientated along the emission dipole moment ($\mathbf{m_e}$) and is in general not parallel to $\mathbf{m_a}$. The rotation is indicated by α. **E** An emission filter separates scattered excitation light from the fluorescence. **F** Magic angle: Using a polarizer in the 90 ° pass axis of the fluorescence emission allows to adjust the detected intensity ($I_{\mathrm{obs}}^{\mathrm{em}}$) to be proportional to the total fluorescence emission $I_{\mathrm{total}}^{\mathrm{em}} = I_{\mathrm{z}}^{\mathrm{em}} + I_{\mathrm{y}}^{\mathrm{em}} + I_{\mathrm{x}}^{\mathrm{em}} = I_{\parallel}^{\mathrm{em}} + 2I_{\perp}^{\mathrm{em}}$ by using a detection angle of 54.7 °.

To avoid time-dependent anisotropy influences on the time-resolved fluorescence intensity signal, a polarizer is installed in optical emission path axis. As mentioned earlier, the total fluorescence emission intensity is equal to $I_{\mathrm{z}}^{\mathrm{em}} + I_{x}^{\mathrm{em}} + I_{\mathrm{y}}^{\mathrm{em}} = I_{\parallel}^{\mathrm{em}} + 2I_{\perp}^{\mathrm{em}}$. In an L-Shape fluorometer only $I_{\parallel}^{\mathrm{em}}$ and $I_{\perp}^{\mathrm{em}}$ is observed, the fraction along the propagation direction ($I_{\mathrm{y}}^{\mathrm{em}}$) is not detected. To compensate for that and simultaneously remove any dependency on the time-dependent anisotropy, a polarizer is applied. Adjusting the polarization angle (ζ) to the magic angle (ζ_{m}), that is, a 54.7 ° tilt in respect to the z-axis has two benefits: firstly, the complete loss of anisotropy as only emission of fluorophores can pass the polarizer which are isotropic as $r(\theta = \zeta = \zeta_{\mathrm{m}}) = 0$. Secondly, the detected fluorescence signal ($I_{\mathrm{obs}}^{\mathrm{em}}$) is directly proportional to the total intensity ($I_{\mathrm{tot}}^{\mathrm{em}}$) as:

$$I_{\mathrm{obs}}^{\mathrm{em}}(\zeta) = \cos^2(\zeta)\, I_{\parallel}^{\mathrm{em}} + \sin^2(\zeta)\, I_{\perp}^{\mathrm{em}} \tag{55}$$

$$I_{\mathrm{obs}}^{\mathrm{em}}(\zeta_{\mathrm{m}}) = \frac{1}{3}(I_{\parallel}^{\mathrm{em}} + 2I_{\perp}^{\mathrm{em}}) \propto I_{\mathrm{tot}}^{\mathrm{em}} = I_{\parallel}^{\mathrm{em}} + 2I_{\perp}^{\mathrm{em}} \quad . \tag{56}$$

Fluorescence detection is commonly realized using fast detectors with single photon sensitivity (see Section 2.2.1).

2.2.3 Fluorescence lifetime imaging

Combining time-resolved fluorescence detection with microscopic imaging opens new fields of application for the environmental sensitive fluorescence lifetime parameter. In general, both time and frequency domain technologies (see Section 2.2.1) can be adapted to microscopy. The resulting microscopic approaches are summarized by the term fluorescence lifetime imaging microscopy (FLIM). FLIM allows to determine of spatially resolved fluorescence lifetime maps on the submicrometer range, enabling a fluorescence lifetime-based investigation of micro- and nanostructures, their molecular environments, interactions and functions, for example within cells and tissues. FLIM techniques record either fluorescence decay histograms (time domain) or phase-modulation changes (frequency domain) for each image pixel of a microscopic image and thus enables the determination of the fluorescence lifetime information in a spatially resolved manner. Utilized imaging techniques are confocal and multiphoton laser scanning, or wide-field microscopy.

Wide-field microscopy

Wide-field microscopy illuminates a large section of a fluorescent sample all at once. This section defines the microscopic field of view (FOV). The emitted fluorescence is detected simultaneously by a position-sensitive detection unit like time-gated or modulated image intensifiers combined with CCD-cameras.[130] Recently, non-camera based TCPSC wide-field FLIM approaches were introduced using spatially resolved MCPs unit or SPAD arrays.[122] The general benefit of wide-field microscopy is the simultaneous fluorescence detection that permits fast time laps investigations. The possible acquisition speed is limited only by the fluorescence brightness of the sample, photon sensitivity and speed of the detection unit.

A simplified scheme of wide-field microscopy is shown in Figure 2.2.4A. An expanded illumination beam (green) is reflected at a dichroic mirror and directed into an infinity corrected objective. Here, the beam is focused onto the focal plane, where fluorophores preferably are excited (red). Besides this preferred excitation range, fluorophores also absorb photons along the z-direction to a certain extent. The objective collects the complete generated fluorescence and directs it, through the back focal plane, onto the dichroic mirror which is transmissive to fluorescence photons due to their higher wavelengths (see Stokes-shift). After passing the dichroic mirror, the fluorescence image is projected by a tube lens onto the microscope's image (camera) plane. Here, the magnified intermediate image is directly recorded by a camera. The tube lens is necessary as the infinity corrected objective places

the projection of the virtual image to infinity. Fluorescence emitted by fluorophores located at positions distant from the focal plane, along the z-axis (red dotted line) results in out-of-focus fluorescence detection. This effect can lead to blurred fluorescence images.

Laser scanning microscopy

In contrast to wide-field microscopy, scanning microscopy does not illuminate (excite) the entire sample simultaneously. This technique detects the fluorescence emission separated in time in small restricted areas (focal volume). The spatial fluorescence selection can either be achieved by a spatial pinhole (confocal) placed in the detection path or by a small absorption cross section (multiphoton excitation, see Section 2.1.1).

Confocal scanning microscopy usually uses a laser beam for sample illumination and is therefore called confocal laser scanning microscopy (CLSM). Figure 2.2.4B shows the working principle of a CSLM. A collimated laser beam for excitation (green) is reflected into the microscope objective by a dichroic mirror. The objective focuses the beam to a small point in the focal plane where it excites fluorophores within a double cone. Fluorescence emitted from this double cone is collected by the objective and directed to the dichroic mirror which is transmissive to the red-shifted fluorescence. A subsequent tube lens focuses the fluorescence emission onto a pinhole. Only photons that pass this pinhole are detected. Similar to the wide-field approach, fluorescence emitted (red, dashed lines) from distant z-layers within the double cone in respect to the focal plane (out-of-focus emission) is likewise directed to the detector. However, these photons cannot pass the pinhole as they are projected from different angles. By rejecting the out-of-focus fluorescence, the signal-to-noise ratio of the confocal fluorescence image is increased.

A similar approach is used for multiphoton LSM (mpLSM), where not the detection volume is reduced but the excitation volume in the focal plane. This is achieved by the generally small absorption cross section of the multiphoton absorption process (see section 2.1.1). Typically, in mpLSM pulsed fs-lasers are used. These lasers can produce the required illumination intensities after focusing the laser beam to a small volume by a microscope objective. In the center of this volume, the local photon density can be high enough to generate a minute multiphoton excitation volume ($\sim$1 femtoliter). This excitation principle inherently reduces out-of-focus emission drastically.

In order to archive spatial resolution in scanning microscopy, the point illumination is moved relative to the sample. This can be realized either by scanning mirrors which raster the excitation laser across the sample or by scanning the whole sample over a fixed excitation beam by an automated x-y sample stage. The emitted fluorescence of each scanned image pixel is serially directed to a detector unit. After collecting the fluorescence data, a complete image can be reconstructed. Due to the reduced detection of out-of-focus fluorescence, equivalent to a high z-resolution, confocal and multiphoton excitation are predestined for tomographic (3D) images. In order to scan in z-direction one changes the focal plane optically by moving the objective or the sample position relative to a

fixed focal plane using an adjustable x-y-z sample stage. The main advantage of scanning microscopy over wide-field microscopy is the suppression of out-of-focus detection, either by a spatial pinhole and the resulting suppression of higher or lower diffraction patterns in the fluorescence signal (confocal) or by the reduction of excitation volumes (multiphoton). The differences in illumination, excitation, and detection volume for the three microscopy techniques are visualized in Figure 2.2.4D.

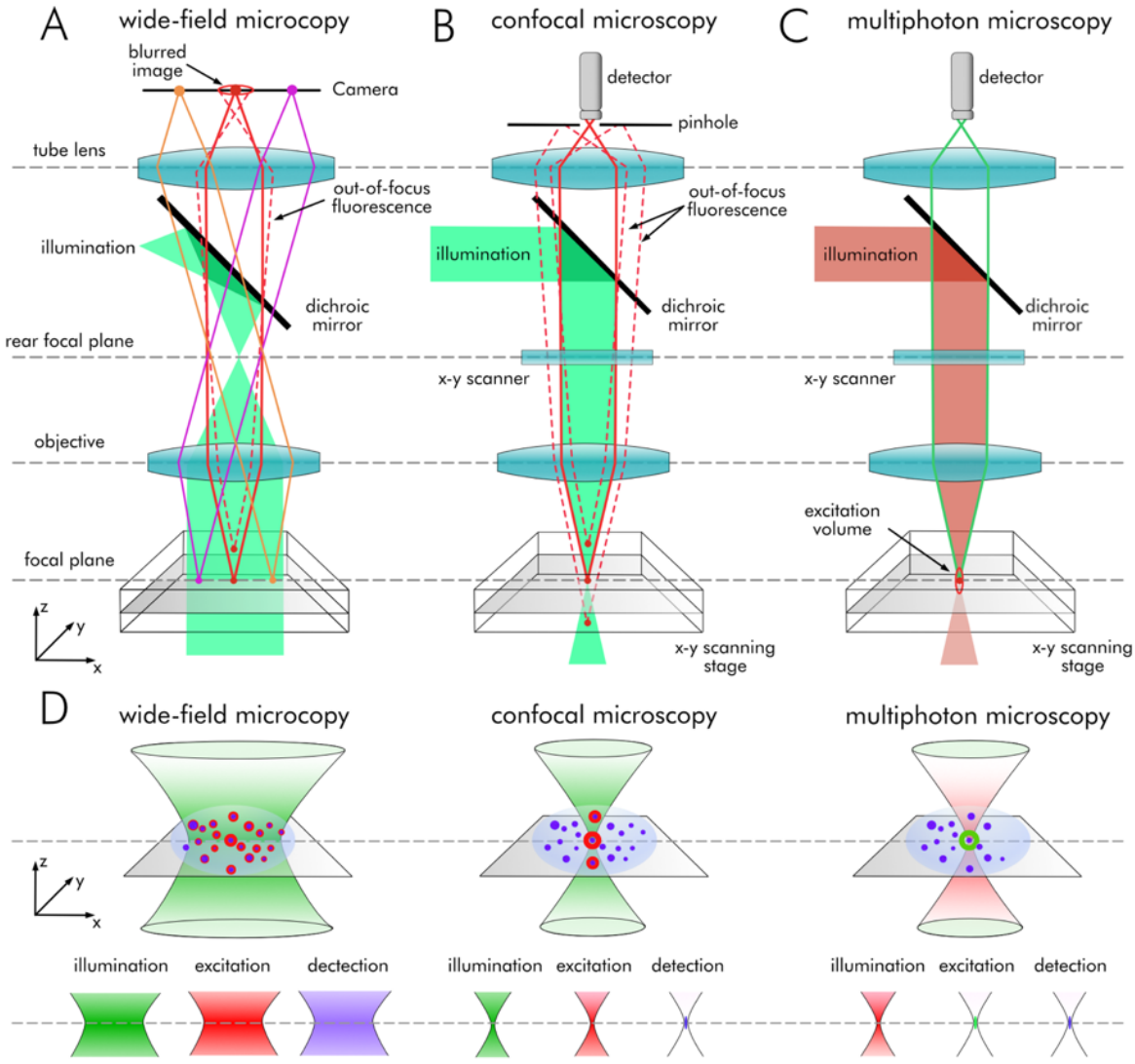

Figure 2.2.4: Differences in wide-field, confocal, and multiphoton fluorescence microscopy. **A** Wide-field fluorescence microscopy: After expansion an illumination beam (green) is reflected at a dichroic mirror into a microscope's objective. Here, the beam is focused onto the focal plane, where it illuminates the whole field of view simultaneously. Fluorophores are preferably excited in this plane. Emitted fluorescence (magenta, red, orange lines) from different x,y-locations is collected by the objective, passes a dichroic mirror and is projected by a tube lens onto the camera plane. Here, the magnified fluorescence image is recorded in a full-frame acquisition mode. Fluorophores located at some distance (z-direction) to focal plane generate to out-of-focus fluorescence (red dashed line). **B** confocal laser microscopy: A dichroic mirror reflects a collimated laser beam (green) into the microscope's objective. The objective generates a focused beam at the focal plane. Here, only a small diffraction limited spot (in x- & y-direction) is illuminated. Fluorophores located in this spot are excited, with the highest probability in the focal plane (red), but also at other positions along the z-axis. Emitted fluorescence is collected by the objective and directed to tube lens. The tube lens focuses the fluorescence onto a spatial pinhole. Only fluorescence originated from the focal plan can pass this pinhole an is detected. Out-of-focus fluorescence (dashed red lines) emitted by fluorophores distant to the focal plane is suppressed. **C** Multiphoton microscopy: A fs-pulsed laser beam (red) is focused to the focal plan. Due to the small multiphoton absorption cross section only fluorophores in a minute volume (~1 femtoliter) get excited. Thus, only a negligible amount of out-of-focus fluorescence is emitted. To get x-y resolution in

both scanning techniques, either a mirror scanner, or a x-y scanning sample stage has to be used. **D** comparison of illumination, excitation and detection volumes.

TCSPC-based confocal and multiphoton FLIM

The following paragraph introduces the basic working principles of TCSPC-based confocal and multiphoton fluorescence lifetime imaging microscopy (Figure 2.2.5). A pulsed laser source establishes fluorescence excitation by emitting light of the ultraviolet or visible spectrum (confocal) or in the infrared (multiphoton) with repetition rates typically in the MHz regime and excitation intensities in the µW (confocal) to mW (multiphoton) range. The illumination beam is initially reflected by a dichroic mirror and directed on two subsequently positioned mirror galvometers which scan the beam in x- and y- direction over the entire FOV by changing the deflection angle. The scanned beam is directed into the microscope, where it passes a special scanning lens. The scanning lens (F-Theta lens type) is necessary because without it or when using a standard lens, the laser beam will be focused on a spherical surface instead of a flat image plane. The f-theta lens guarantees a constant illumination spot size over the whole scan field. By knowing the deflection angles in x and y-directions, the image (temporal photon counts per pixel) can be reconstructed as these angles are directly proportional to a pixel position. As emitted fluorescence from the scanned FOV has to be focused onto a fixed spatial pinhole (see Figure 2.2.4B), one has to apply a de-scan loop in CLSM. Descanning is realized by directing the fluorescence beam back to the mirror galvometers which deflect the beam in such way that a spatially stationary fluorescence beam is directed onto the pinhole. Since the mpLSM works without any pinhole, fluorescence is detected in a non-de-scan mode. Before the fluorescence photons originating from the focal plane can hit the detector head, short-, long- or band-pass emission filters can be applied to select a fluorophore specific wavelength region.

The detection of a fluorescence photon triggers a TSCPC measurement cycle while the corresponding time-delayed excitation pulse stops the cycle. After millions of cycles, fluorescence decay histograms in every pixel of the FLIM image can be reconstructed. For this procedure, a scanning interface provides the spatial information by sending a scan clock signal containing the pixel clock, the frame, and line sync to a computer interface. Each measured excitation/detection time by TCPSC is addressed to the pixel from where the triggering photon originates (parameter-tagging). The computer memory stores a distribution of the photons over x, y, and t, resulting in an array of fluorescence decay histograms (FLIM image). The benefit of parameter-tagging (image frame, line and pixel) is that it is not necessary to reduce the scan speed such that each image pixel is serially measured until enough fluorescence photons for a high SNR are collected.

Instead, it is possible to record at the highest scan rate for serval subsequent image frames until the total number of photons are high enough to ensure a proper data analysis of the fluorescence decay histograms. Afterwards the frames are unified to a single image containing the pooled decay histograms. Supplementary, the parameter-tagged data can be used for time lapse FLIM investigations at the highest possible scanning speed, as the individually scanned image frames or lines can

separately analyzed or temporally re-binned to investigate potential kinetic variation. Modern FLIM systems can achieve pixel resolutions of 2048 x 2048 pixels with 256 sub-picosecond time bins per pixel.

Serval analysis procedures exist to reveal the fluorescence lifetime information from the photon distribution saved in the FLIM image. The general problems one faces during the data analysis of FLIM-images are the data-dimensionality, parameterization, and interpretation of the decay histograms in each image pixel. As it is not possible to visualize all decays histograms of the whole image reasonably, one has to choose parameters which can be visualized in an image for example by color-coding. The most common analysis methods are the tau-plot analysis and the phasor approach. For more information see Section: Materials and methods (Section 3.2.2).

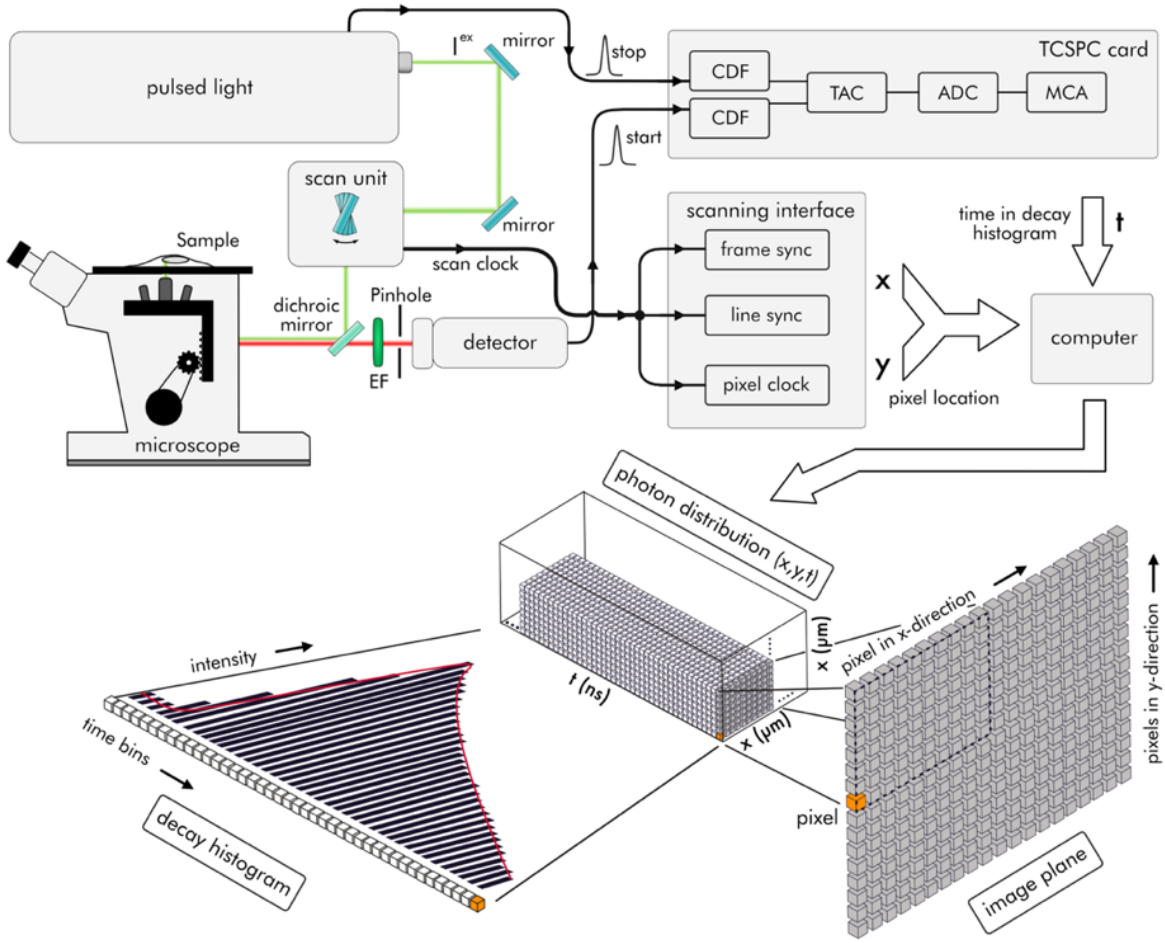

Figure 2.2.5: TCSPC based confocal laser scanning FLIM. **A** FLIM setup: A pulsed laser source emits an excitation beam (I^{ex}) which is reflected at a dichroic mirror and deflected by scanning unit consisting of two mirror galvometers which scan the laser beam in the x- and y-direction. Before the laser beam hits the sample, it passes a scan lens to achieve a flat imaging plane. The emitted Fluorescence is de-scanned and directed to a detector unit after passing the dichroic mirror and a stationary spatial pinhole. To obtain temporal resolution via TCPSC, fluorescence photon detection generates the plus signal to start a TCPSPC measurement cycle, while the repetitive pulse signal of the laser acts as stop trigger (see TCPSC, Section 2.2.1). The galvoscanner unit provides the spatial information by suppling the scan clock signal (frame sync, line sync and pixel clock) to a computer system. **B** The accumulated photon information is used to calculate the photon distribution by combining pixel localization in x- and y- direction and the TCSPC fluorescence decay histograms. The photon distribution contains the fluorescence decay histogram for each pixel in the image plane.

2.3 Dendritic nanoparticles and nanocarriers

2.3.1 Nanotechnology in medical diagnosis and therapy

Nanotechnology, or nanotech for short, describes artificially created materials with a characteristic size ranging from 1 nm to 100 nm.[1] Due to this purely size-specific definition, the field of application is broad. Nanotechnology is particularly important in semiconductor and surface physics, organic chemistry, molecular biology, and medicine, to name only but a few examples. In the case of nanomedicines, the functional properties of new nanomaterials in particular have led to a multitude of potential applications. Roughly speaking, these can be divided into the following areas: nanotherapeutics, nanodiagnostics and the mixed form of nanotheranositics.[3] Nanoparticles (NP) and their applications bridge the gap between physical and biological sciences. They improve drug transport by enabling site-specific drug delivery and allow us to understand the underlying processes of nanoparticle transport, drug release, and efficacy. The research of nanoparticulate drug delivery systems is a central area of nanomedical research.[1, 3-4]

NPs can be subdivided into organic and inorganic materials. The best-known inorganic NPs include metallic NPs, which consist of gold, silica or iron oxide, as well as non-metallic quantum dots and carbon nanotubes. The most common organic representatives are polymeric NPs, peptide and protein-based NPs, and lipidic NPs, such as liposomes or solid-lipid NPs.[1-2] NPs in biomedicine can also be classified according to their purpose, e.g., they can be active drugs themselves, be used as controlled drug delivery systems, called nanocarriers, for poorly soluble or absorbent drugs, or serve as diagnostic tools.[1-2] In this thesis, dendritic NPs are investigated, a subgroup of polymeric NP. Dendritic NPs consist of a variety of biocompatible or biodegradable monomers like polyglycerol, poly(amidoamine), polylactides, poly(methyl methacrylate), poly(alkyl cyanoacrylates), or poly(ethylene glycol).[131] The name dendritic is derived from the Greek *dendron* ("tree-like") and is used here because the structures of these nanoparticles (2 – 20 nm) replicate the branching of trees.[46]

Dendritic nanoparticles are characterized by a high density, defined shape, and provide a large number of functional surface groups.[45] The terminal groups define the pharmacokinetic behavior, biological distribution and target specificity.[132] Compared to their linear polymeric counterparts, they are characterized by low intrinsic viscosity, a low tendency to chain entanglement, a smaller hydrodynamic radius and good water solubility.[133] There are three basic types of dendritic nanoparticles: Dendrimers, dendrons, and hyperbranched polymers.[46] Furthermore, mixed forms such as dendrimer-like star or dendronized polymers are synthesized which combine dendritic structures with linear polymers.[133]

Dendrimers consist of a core surrounded by radial aligned symmetric shells, called generations which consist of covalently conjugated monomers. Their three-dimensional spherical structure is characterized by a perfectly regular shape with a 100 % degree of branching. Thus, they achieve a polydispersity index of 1, making them monodisperse NP architectures.[45] Dendrimers show no chain

entanglement, have many cavities to load potential cargo, and have the largest number of end groups among the dendritic NP.

Dendrimers were introduced by Vögtle et al.[134] in 1978 and are products of iterative polymerization procedures, where dendrons, regularly branched wedged-shaped structures, are connected to dendritic cores using their focal point (see Figure 2.3.1). The reactive focal point is a single functional group that determines the iterative dendritic growth and enables the controlled grafting of dendrons to surfaces, as well as the covalent attachment to polymeric structures or biomacromolecules. With their parent dendrimers, dendrons share properties like monodispersity and multiple terminal groups.[135] The major drawback of dendrimer and dendron architectures is the tedious and lengthy multi-step synthesis which requires several protection/deprotection steps which limits their availability and makes production costs often uneconomical.[46]

Randomly hyperbranched polymers represent a further dendritic architecture, the so-called hyperbranched polymeric NPs. These NP can be synthesized by a fast and easy to scale up one-pot synthesis (one-step polymerization reaction), and although they have an irregular topology with a polydispersity of molecular weight, they share many properties with perfect dendrimers.[46, 132, 136] Hyperbranched polymers (HMPs) show only weak chain entanglement, a low viscosity and high solubility. They have a spherical shape and are formed by a mixture of linear and branched units with functional end groups on their surface.[137] HMP-based nanocarrier architectures show a high biocompatibility and are able to transport chemotherapeutic agents, peptides, proteins and genes using either cavities in the hyperbranched structures for host-guest encapsulation or by linkage to the peripheral functional groups.[138] Various hyperbranched drug delivery systems exist which are often hybrid forms of polymer architectures. Typical systems are hypergrafted polymeric NPs, linear-hyperbranched hybrid copolymers, core-shell and core-multishell nanocarriers.[132] Some of these architectures provide controlled release mechanisms for their guest molecules triggered by environmental stimuli such as pH, temperature, magnetic field, salt concentration, light, reactive oxygen species, or enzymatic activity.[136, 138-139]

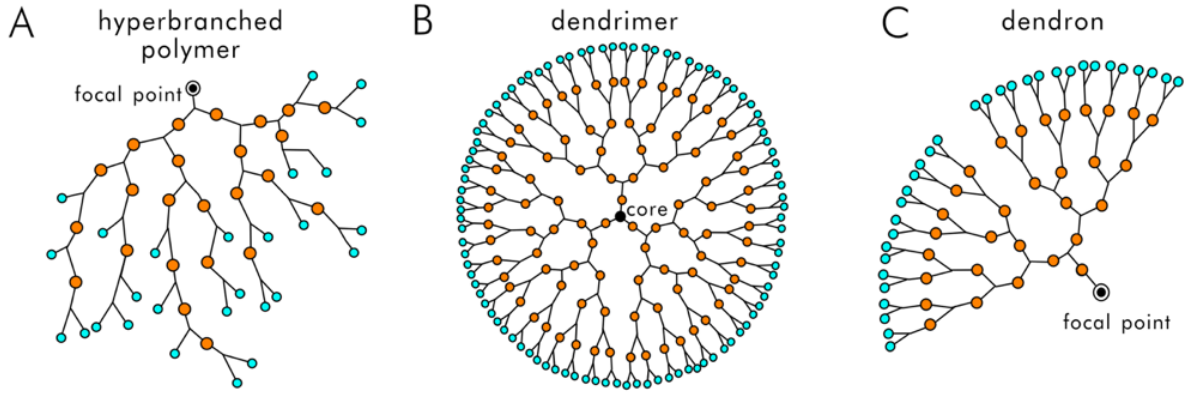

Figure 2.3.1: Schematic representations of dendritic architectures. **A** Randomly hyperbranched polymeric structure. **B** Dendrimer. **C** Dendron wedge. Orange dots indicate dendritic units, cyan dots terminal units, black dots surrounded by an empty circle focal points, and the black dot shows the dendritic core of the dendrimer.

2.3.2 Investigated dendritic nanoparticles

Dendritic polyglycerol sulfate

Dendritic polyglycerol sulfate (dPGS) is a nanoparticle (~4 – 6 nm) synthesized by sulfation of hyperbranched polyglycerol (dPG), first performed in the lab of Prof. Haag (Freie Universität Berlin, Germany).[140] dPG is a synthetic nanomaterial, first developed in the 1960s and is characterized by a high biocompatibility, a compact, well defined and stable structure, similar to the respective perfect dendrimers.[141-143] dPG consists of an aliphatic polyether backbone, has a defined molecular weight and a narrow molecular polydispersity. Due to several functional end groups, dPG has the additional advantage of a defined mono- and multifunctionalization compared to perfect dendrimers.[144] The sulfation of hydroxy groups on the dPG surface by sulfur trioxide-pyridine complex yields the polyanionic dPGS. Functionalization of dPGS is achieved prior to this sulfation step by chemical conjugation of azide or amine groups by mesylation followed by a partial azidation of some surface hydroxy groups.[142] The surface (ζ) potential of dPGS amounts to -13.6 ± 3.1 mV.[145] Like dPG, the resulting dPGS nanoparticles (Figure 2.3.2A) have a high biocompatibility and their use as anti-inflammatory drugs due to a high anti-complementary activity is often discussed in literature.[142, 146-147] Likewise, dPGS shows a virus-inhibiting function and its use as a drug delivery system by a corresponding functionalization is very promising. dPGS shows a complex structure-activity relationship in its interaction with biological matter in which multivalent binding mechanisms, particle size and structural flexibility of the polymer play a decisive role.[144-146] Interactions with biological systems such as complementary system proteins, serum albumins or tumor cells are described in Section 2.3.3.

Hyperbranched polyglycerol-based dendritic core-multishell nanocarriers

Dendritic nanoparticles with a core-shell (CS) architecture are constructed from a core and one or more sounding shells (referred to as core multishell (CMS) architecture) wherein at least one component is a dendritic polymer. CS-nanoparticles are suitable as nano-sized carrier systems for poorly soluble drugs by encapsulation of the active agents.[148] This is promising because it allows to increase the concentration of water-insoluble hydrophobic drugs, for example in the blood, during systemic applications. Additionally, CS-nanoparticles can increase blood circulation times and thereby improve pharmacokinetic properties of the transported drugs. Combined with other benefits of nanosized drug-delivery such as the tendency towards passive drug targeting of cancer cells through the so-called enhanced permeability and retention (EPR) effect[148] which describes the passive accumulation of macromolecules (20 – 200 kDa) in tumor tissue, CS-nanocarriers seem to be an auspicious approach. Depending on the realized architecture, unimolecular CS-nanocarriers can encapsulate hydrophobic and/or hydrophilic guest molecules at different sites: In the core, in their shell(s) or at the interface of core/shell or shell/shell.[149] Additionally, a supramolecular loading mechanism was observed were serval unimolecular units encapsulate guest molecules by formation/self-organization of supramolecular aggregates.[150]

While CS-nanoparticles mimic the structure of a lipid micelle, CMS-systems imitate the polarity gradient of a liposome. The first dendritic CMS-architecture was introduced by Radowski et al.[150] in 2007. These nanoparticles consisted of hyperbranched poly(ethyleneimine) (PEI) core, a dicarboxylic acid-based inner shell, and monomethylpoly (ethylene) glycol (mPEG) outer shell. The PEI-CMS-nanoparticles were successfully used as nanocarrier systems for hydrophilic and hydrophobic guests. Later, CMS-architectures exchanged the PEI core to a hyperbranched polyglycerol (hPG) core due to toxicity concerns.[151-153]

The dendritic CMS-nanocarriers investigated in this work were developed in Prof. Haag's group (Freie Universität Berlin, Germany) and belong to this second generation and thus consist of a hPG core, octadecanoic acid, mPEG (Figure 2.3.2B). They can be described by the formula: $PG_{10000}(-NH_2)_{0.7}(C_{18}mPEG_6)_{1.0}$) and consists of a dendritic 10 kDa hPG core which is surrounded by two polymer shells.[150] The inner shell consists of octadecanoic diacid chains with 18 carbon atoms (c18) and the outer shell is composed of mPEG with 6 repeating units of glycol. The nanoparticle size differs due to aggregation effects depending on the loaded cargo. In the case of unimolecular CMS-nanoparticles, diameters between 7 – 16 nm were determined, whereas CMS aggregates can reach dimensions up to 160 nm. Typical molecular weights of a unimolecular CMS-nanoparticle range between 40 and 80 kDa, with a mean weight of 60 kDa. The CMS-nanoparticles were successfully used as nanocarriers for a wide range of hydrophobic and hydrophilic compounds, like cell-penetrating peptides, drugs, and fluorescent dye surrogates.[4, 150]

In addition to completely passive CMS nanocarrier systems, various modifications have been developed to introduce controlled drug release mechanisms via specific sensitivities to environmental stimuli. For example, different biodegradable ester-based CMS systems were developed which (partially) disintegrate via enzymatic reactions, e.g., by lipase activity.[154-156] Another CMS-nanocarrier system applies a pH dependent degradation via an introduced imine linker.[157]

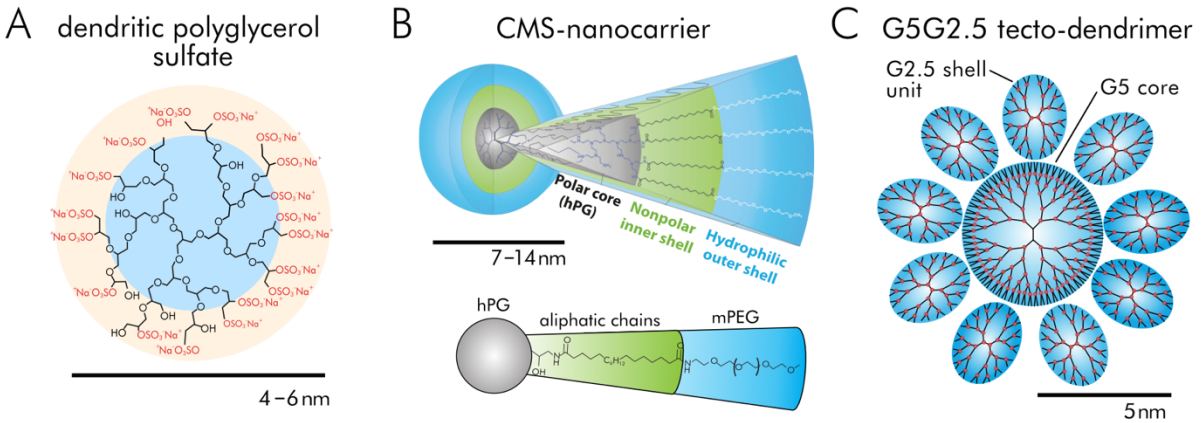

Figure 2.3.2: Schematic representations of investigated dendritic nanoparticles. **A** Dendritic polyglycerol sulfates (dPGS). **B** Dendritic core-multishell nanocarrier (CMS-NC). **C** G2.5G5 core-shell tecto-dendrimer (G5G2.5-GM).

G5G2.5 core-shell tecto-dendrimers

G5G2.5 core-shell tecto-dendrimers are megamers (MG), i.e., clusters of reactive dendrimers which serve as nanoscale modules, called tectons. They were developed by the group of Prof. Romero (National University of Quilmes, Argentina) and characterized in terms of their biological effects in the group of Prof. Schäfer-Korting (Freie Universität Berlin). The covalent conjugation of these tectons is forming a new class of higher ordered macromolecular complexity[158] which is used to create new nanocarrier platforms with many cavities for drug loading.[159] The striking advantage of the megamer architecture over perfect dendrimers of the same loading capacity is the avoidance of many synthesis steps. This allows for a rapid construction, especially when compared to the synthesis of higher-generation dendrimers. For example, the production of a generation 9 poly(amidoamine) PAMAM dendrimer requires 18 individual reaction steps.[160] However, depending on the application, these larger dendrimers are extremely desirable, as they can load more cargo molecules than smaller dendrimers, due to a higher number of intramolecular cavities. The strategy of clustering several small dendrimers units is therefore an attractive alternative, as it also avoids the construction problem of larger perfect dendrimers due to the de Gennes dense packing phenomenon.[160]

The G5G2.5 core-shell tecto-dendrimers (G5G2.5-MG) investigated in this Thesis was synthesized by Dr. Priscilla Schilrreff (Romero group, National University of Quilmes, Argentina) consist of an amine-terminated polyamidoamine (PAMAM) core of generation 5 (G5) and a saturated shell of 9 – 11 carboxyl-terminated PAMAM G2.5 dendrimers (Figure 2.3.2C). If assuming that each G5G2.5-MG consists of a single G5 core dendrimer, the saturation level of the G2.5 shell amounts to 60 % – 67 %.[159] The molecular weight of the nanoparticles amounts to ~87 kDa, with a weight distribution ranging between 75 and 96 kDa.[161] The hydrodynamic diameter of G5G2.5-MG is about 11 nm and the ζ-potential is slightly negative (-4 – -9 mV) in Hank's balanced salt solution.[161] G5G2.5-MG was successfully loaded with the cancer drugs methotrexate and zoledronic acid.[162] Interactions with biological systems such are described in Section 2.3.3.

2.3.3 Interactions of dendritic nanoparticles with biological systems

Dendritic polyglycerol sulfate

dPGS was originally synthesized as an analogue of glycosaminoglycan heparin, an anticoagulant that is used as a drug for heart attacks and unstable angina.[140] It also acts as an inhibitor for complement activation in the immune response, tumor growth, viral activity and angiogenesis.[142] Compared to Heparin, dPGS shows a much higher efficiency in compliment inhibition than it promotes anticoagulant activation.[147] In the case of an application as an inflammatory drug this would lead to a reduced risk of blood thinning. The anti-inflammatory effect is attributed to the interactions of dPGS and endothelial P- and leukocytic L-selectin. This interaction is moderated by multivalent selectin binding of the polyanionic nanoparticle to the positively charged ligand binding pockets of selectin via electrostatic forces. Investigations of this process suggest a complex structure-activity

relationship.[147] Heparin, which also binds to these binding pockets, shows a weaker binding affinity, which would argue for the substitution by dPGS. Likewise, dPGS interactions with factors C1q, C3a, and C5a of the complement system were demonstrated and indicate an inhibitory binding mode of dPGS to the complement factors in the nanomolar concentration range.[25, 147, 163] Together, selectin and compliment factor interactions of dPGS may lead to a general decreased inflammatory response.

Several articles have investigated the interaction of dPGS with different cell types and revealed an efficient uptake of the nanoparticles in tumor cells.[142] Macroscopically, dPGS appears to accumulate in tumor tissue.[164] Both observations suggest that the hyperbranched nanoparticle is suitable as a carrier system for cancer drugs. Different dPGS-based carrier systems were loaded with anticancer drugs like doxorubicin (DOX) and paclitaxel (PTX) and provide efficient drug delivery for example by pH trigger release mechanisms.[164-165]

Hyperbranched polyglycerol-based dendritic core-multishell nanocarriers

The special amphiphilic character of CMS-nanocarriers renders them excellent drug delivery system for the topical treatment of skin.[166] Equipped with flexible hydrophilic as well as hydrophobic shell units, it is assumed that they can adapt to the barrier located in the SC, which is formed by a lipidic matrix surrounding protein-rich corneocytes (Section 2.4). This assumption is motivated by the ability of CMS-nanocarriers to change their arrangement once exposed to a non-polar solvent. Here, they partially fold their hydrophilic shell groups inwards while pointing their hydrophobic chain groups of the inner shell towards the surface.[167] This behavior changed the picture of the stationary arrangement of the "core-multishell model" observed in aqueous solutions. The used amphiphilic site chains provide saturated carbon chains which have been previously suggested as an perfect chemical structure that allows skin penetration enhancement.[168]

The topical application of CMS-nanocarriers on healthy skin leads to an accumulation in the layers of the SC, in hair follicles, and skin furrows.[169] Penetration into deeper skin layers of the viable epidermis (VE) was observed only at individual sites and not in a systemic way. So far, no conclusive mechanism for the nanoparticle accumulation in SC has been postulated, a behavior which could be associated with specific interactions and related modification in the extracellular lipid matrix. However, several studies on reconstructed skin using Franz diffusion cells show that a SC-barrier-disruptions can generate high penetration rates of CMS-nanocarrier into VE.[170-171]

CMS-nanocarriers can significantly enhance the notoriously low skin penetration of many topically applied drugs and (fluorescent) drug mimetics in native skin, and different animal and reconstructed human skin models.[166, 172-173] An important feature that may reduce severe adverse effects in the systemic treatment of skin diseases.[4] Furthermore, animal models of chronic inflammatory skin diseases like murine psoriatic or atopic dermatitis skin showed full biocompatibility.[166, 172] These observations were further supported by *in-vitro* assays on keratinocytes (HaCaT) and Langerhans-like

dermal immune cells (XS52).[166, 174] These studies revealed neither cytotoxicity of CMS, increased oxidative stress levels, a reduction in cell viability, induction of apoptosis, nor an immunological response.

Finally, pH-triggered doxorubicin-loaded CMS-nanocarrier were able to release the fluorescent chemotherapeutic agent doxorubicin efficiently within acidic intracellular compartments leading to higher cytotoxicity in comparison to the stable CMS nanocarrier.[157]

G5G2.5 core-shell tecto-dendrimers

The G5G2.5 core-shell tecto-dendrimers (G5G2.5-MG) were originally developed to overcome the limited tolerability of dendritic cationic polyamidoamine (PAMAM) nanocarriers and to increase the transport capabilities by a higher number of drug cavities.[19, 159] It was also shown that the megamer nanocarrier can act as active drug against certain cancer cells. This behavior was observed in a recent *in-vitro* study on G5G2.5-MG interactions with melanoma cells (SK-Mel-28) and human keratinocytes (HaCaT). The tecto-dendrimer showed a specifically cytotoxic effect on the melanoma cells which can be related to a rapid depletion of intracellular levels of Glutathione (GSH) and increased levels of oxidative stress (ROS).[159]

A subsequent study observed that the cytotoxic effects were further increased by loading the anticancer drugs methotrexate (MTX) and zoledronic acid (ZOL) to the G5G2.5-MG nanocarrier system. Especially the MTX-loaded nanocarriers were promising candidates for future *in-vivo* studies as they seem harmless to keratinocytes while cytotoxic to SK-Mel-28 cells.[162] In contrast, G5G2.5-MG/ZOL increases the cytotoxicity in both cell types, compared to the free drug ZOL. Furthermore, the authors observed different uptake mechanisms for both cell types. In HaCaT cells they observed a dependency of G5G2.5 uptake on the dynamics of the actin cytoskeleton and the microtubular assembly. While macropinocytosis mediated uptake was excluded for the HaCaT cell line, they assumed a uptake mechanism compatible with macropinocytosis in SK-Mel-28.[162]

Another recently published study showed that G5G2.5-MG can be actively internalized by primary glial cells of the central nervous system in a time- and dose-dependent manner.[161] After the uptake the authors observed a incorporation of the nano-scaled carrier systems in lysosomal compartments. In corresponding *in-vitro* experiments, a selective uptake of the nanocarriers could be established, since other investigated cell types of the nervous system did not show any internalization. In addition, oxygen-glucose deprivation, lipopolysaccharide exposure and brain ischemia *in vivo* increase glial G5G2.5-MG uptake. These properties of the dendrimer-based platforms indicate a potential for a targeted glial-cell based therapy.[161]

2.4 The human skin: A potential target for nanomedicine

2.4.1 Skin anatomy

The human skin forms the outermost barrier of the human organism. It is a highly structured tissue, that protects against pathogens and other harmful materials and maintains homeostasis. Besides these protective and regulatory functions, it is a sensory organ, that is sensitive to heat, pain and pressure. Although the skin is the largest human organ with a mass of up to four kilograms and an area of about two square meters, it is also a highly flexible and elastic structure. In general, skin tissue is divided into two main layers: the dermis and the epidermis (Figure 2.3.3A).[175-176]

The dermis is located below the epidermis and connects the viable epidermis with the subcutaneous tissue.[177] The main functions of the dermis are to provide stability and elasticity to the skin through collagen and elastin structures and to supply the non-vascular epidermis with nutrients through a basal membrane. The dermis consists of connective tissue and is divided into two layers: the *stratum reticulare* and the *stratum papillae*. The *stratum reticulare* is the deepest layer of skin. It contains dense and branched protein fiber networks of collagen and elastin as well as blood vessels. In addition, this layer houses epithelially derived structures such as sweat and oil glands or hair follicles. Cellular components of the *stratum reticulare* are fibroblasts and immunocompetent cells such as macrophages, mast cells and dendritic cells.[178] The *stratum papillae*, also known as the papillary layer, which lies directly above, has a thinner diameter. It consists of looser and less organized collagen fiber networks which are predominantly composed of type I and type III collagen. The *stratum papillae* is attached to the epidermis by *dermal papillae* which extend into areas between the epidermal crests. This increases the interface between the two layers, resulting in efficient nutrition and gas transport through dermal blood vessels.[176]

The epidermis fulfils the important barrier function of the skin. Depending on the body site the epidermis shows different diameters, typically between 50 and 100 µm.[179] Figure 2.3.3B illustrates the structure of the epidermis. The most common cell type within the epidermis are keratinocytes with a cytoskeleton based on keratin. The keratin filaments can be classified as intermediate filaments due to their diameter of 10 nm. They are built by α-helical polypeptides and protect the skin from shear forces. Keratinocytes undergo a 28-day differentiation process, whereby they migrate through various epidermal layers. The starting point of the differentiation process is the *stratum basale*. This layer is connected to the basal membrane via hemidesmosomes. The basement membrane represents a thin interface between the dermis and the epidermis, which regulates the transport of cells and nutrients into the non-vascular epidermis.[180-181] The *stratum basale* contains epidermal stem cells and keratinocytes with a high mitosis rate. The cells within the stratum *basale* have a cubic to cylindrical shape and are oriented perpendicular to the basal membrane.

The next differentiation process of keratinocytes takes place in the adjacent *stratum spinosum*, where keratinocytes are characterized by a cubic shape with slightly flattened ends and a central nucleus. The *stratum spinosum* ensures the mechanical stability of the entire epidermis by its particularly high desmosome and keratin filament density. In the next higher epidermal layer, called *stratum granulosum* (SG), the most extensive chemical and morphological changes of the keratinocytes take place. At the end of this process, they will be transformed into non-metabolic corneocytes. The keratinocytes of the *stratum granulosum* have a flattened and polygonal shape. Individual cells in the second SG layer are connected by a tight junction network which achieves homeostasis and is integral part of the epidermal barrier by preventing the penetration of solutes through the intercellular space (Figure 2.3.3A).[182-183] At this stage, two defining structures develop: membraneless keratohyalin granules containing keratin filaments and histidine-rich profilaggrin, and lamellar granules, filled with lipids and proteins, also known as Odland bodies.[184] In the interface between stratum granulosum and corneum, the last epidermal layer, the final differentiation steps are initiated. The lamellar granules, which have their origin in the Golgi apparatus, have a diameter of 0.1 to 0.3 µm. Typical lipids within the lamellar granules are phospholipids, cholesterol and glycosylceramides. These lipids are essential for the formation of the further barrier function. First, the content of the lamellar granules is released into the extracellular space. Here, a conversion process takes place in which acid hydrolysis splits the phospholipids into free fatty acids and the glycosylceramides are converted into ceramides. In addition, the profilaggrin within the keratinocytes is transformed into highly reactive filaggrin leading to irreversible connections between individual keratin filaments by means of disulfide bridges. Further processes enable the dissolution of the cell nucleus, further cell flattening and the interruption of cell metabolism.[176]

The end product of the epidermal differentiation process is the skin's important physical barrier, located in the stratum corneum (SC). The barrier is composed of flat, non-metabolic corneocytes integrated in a lipidic matrix of ceramides, cholesterol and free fatty acids (Figure 2.3.3B). Human SC typically consists of 15 to 20 cell layers, resulting in a total SC thickness of 15 to 20 µm. A basic model illustrating the SC structure is the so-called "brick and mortar" model.[185] Here, the corneocytes are thought of as bricks. They offer mechanical stability through their keratin-filament network, while the intercellular lipid matrix is the mortar that seals the skin to the outside and thus protects against harmful pathogens and minimizes transdermal water loss.

In detail, the lipid matrix consists of a highly ordered multilamellar system of lipid double layers. In single cells, the lipid matrix consists of a highly ordered, multilamellar system of lipid bilayers. While phospholipids, an essential component of most biological lipid membranes, are not abundant in SC, other lipid components such as ceramides (50 %), cholesterol (25 %) and free fatty acids (15 %) are found.[186] The membrane-forming function in SC is taken over by ceramides. Together with cholesterol and free fatty acids they form stable bilayers. Although they have no charged head groups, they ensure the stability of the bilayers. Ceramides are divided into nine subgroups;

ceramides with linoleic acid esterified ω hydroxy fatty acids (O) in their sphingosine (S) or phytosphingosine (P) skeleton play a key role. Examples are ceramide 1 (EOS), a kineolic acid linked to a very long acyl, and ceramide 9 (EOP), a phytosphine-based acylcermide (see Figure 2.3.3B).[187] Both are also called molecular "rivets" or "nails" because their linoleic acids have the ability to pass through the polar region and separate two adjacent bilayers into the next bilayer. This behavior generates bilayer stacks of high stacking capacity.

Further structuring factors are the high cholesterol content of 25 %, which forces adjacent fatty acid chains into regular arrangements, and the most hydrophilic ceramide 6 (AP), which with its four OH groups can stabilize the hairpin structures by forming water bonds.[188] These stabilization mechanisms force even long ceramides like EOS or EOP into bilayers with a typical thickness of 4.5 to 6.0 nm.[188]

2.4.2 Topical nanoparticulate drug delivery

The goals of topical drug administration can be divided into two groups. One is the sustained drug delivery to the vascular bloodstream via percutaneous/dermal absorption, which is divided into the following steps: (1) Penetration of the skin barrier, (2) further diffusion of the drug through the epidermal and dermal layers, and (3) uptake of the drug into the vascular system.[189] The second group is the local and sustained administration of an active substance to sites of diseased skin.[4]

Penetration routes within the SC can be divided into three major pathways (Figure 2.3.3C). The first one is the intercellular route. Molecules penetrating on this route stay only within the lipid matrix. The second pathway is the intracellular route. Here, molecules have to penetrate through both corneocytes and lipid matrix. The third pathway is the follicular route. This pathway is especially important for larger molecules. Hair follicles pass through several layers of skin. The follicular route starts at the skin surface, goes through the physical penetration barrier of the SC and ends in the dermis. Thus, the latter is a potential route for administering large drugs to the dermis. However, effective penetration within the follicle is often hindered by the passage of sebum.

While larger molecules, especially macromolecules like nanoparticles with molecular weights of several thousand Daltons, may pass the SC only under special circumstances,[177, 190] small molecules up to 500 Da pass the SC skin barrier in most cases (500 Da rule).[191] But the molecular weight/size is not the only determinant for the penetration ability of a molecule. Due to the hydrophobic nature of the barrier structure (lipid matrix), hydrophilic substances can only sparsely penetrate the SC barrier. Other than that, hydrophobic substances penetrate the SC (water content: 13 %) more easily for the same reason, but may remain stored there, since the viable VE layers are more hydrophilic (water content: 70 %).[189] This polarity dependence often hinders an efficient delivery of drugs even with low molecular weight. Therefore, various chemical and physical methods have been developed to improve the penetration, such as chemical penetration enhancers (like azone or ethyl acetate),

iontophoresis, electroporation or microneedles. These methods alter the state of the SC barrier and thereby increase the penetration rates of the drugs. In addition to purely physical penetration limiting effects, other environmental induced changes of the drug lead to a reduction in the general efficiency of transdermal drug delivery. The acidic environment of the skin and metabolic enzymes in the viable epidermis and dermis play a major role in reducing the effectiveness of the penetrating drug by neutralization or degradation.[181]

Nanoparticulate drug delivery systems have been developed in order to reduce these effects. They provide an alternative to conventional medicine by protecting their loaded drugs from environmental influences. Nanocarrier systems aim at controlled skin penetration of their loaded cargo, a high specificity for dermal target sites, sustain cargo release, and reduced adverse effects by smaller applied drug concentrations.[3-5, 136, 139] Nanoparticular drug delivery systems for dermal applications are based, among others, on polymeric (dendritic) architectures, liposomes, solid lipid nanoparticles, nanogels, and nanoemulsions.[4, 177, 192]

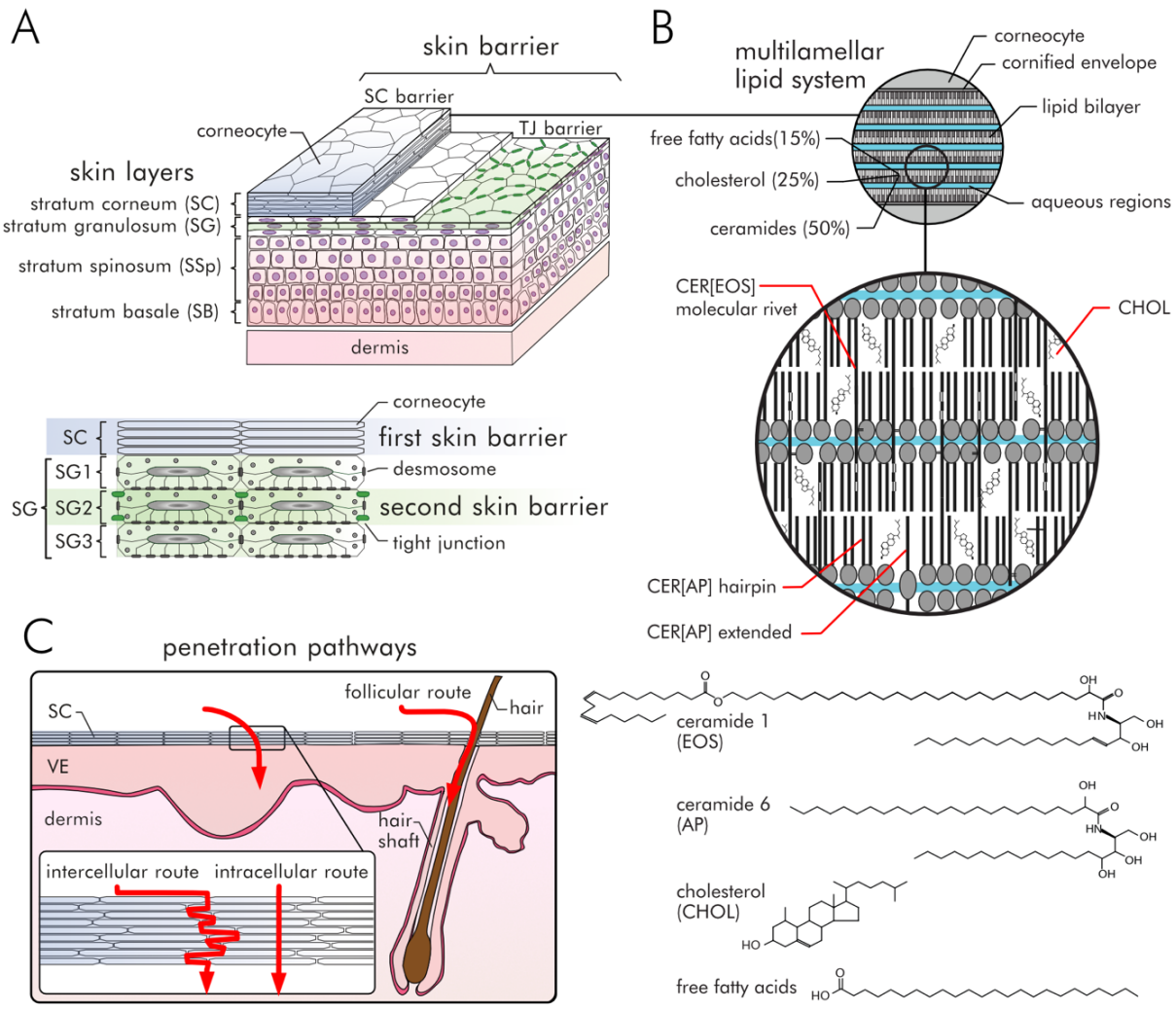

Figure 2.3.3: Schematic of human skin and barrier localizations. **A** skin layers of the viable epidermis: *Stratum corneum* (SC), *stratum granulosum* (SG), *stratum spinosum* (SSp), and s*tratum basale*. Skin barrier: the SC constitutes a first mechanical/physical barrier for penetrating substances. A second barrier is built up by tight junctions in the second layer of the SG. **B** multilamellar lipid

system connecting the corneocytes in the stratum corneum. molecular structure of ceramide 1: Esterified ω-hydroxy fatty acid sphingosine (EOS), ceramide 6: α-hydroxy fatty acid phytoshingonisine (AP), free fatty acid, and cholesterol (CHOL). **C** Transdermal penetration pathways.

While non-crosslinked particles such as liposomes, which consist of small units, disintegrate because of their interaction with the SC barrier, polymeric and inorganic nanocarriers usually penetrate the SC barrier intactly where they release their cargo. A deeper penetration of nanomaterials was observed mainly via the follicular route (Figure 2.3.3C). This penetration process is itself dependent on the size of the nanocarriers. Vogt et al. observed an increased follicular penetration of nanoparticles with a diameter of 40 nm compared to larger diameters of 750 and 1,500 nm.[193] Another study postulated a "ratchet" effect on larger nanoparticles with a size of approximately 600 nm.[194] Nanoparticles of this size seem to have a high chance of entering the hair follicle's *infundibulum*.[195]

Chapter 3: Experimental section

3.1 Materials

3.1.1 Fluorescence lifetime probes

Indocarbocyanine and Indodicarbocyanine

The NHS ester of indocarbocyanine ($\varepsilon_{550\mathrm{nm}}$ ≈120,000 $M^{-1}\cdot cm^{-1}$ in H_2O) was obtained by Mivenion (Berlin, Germany). Indodicarbocyanine (IDCC, $\varepsilon_{640\,\mathrm{nm}}$ ≈120,000 $M^{-1}\cdot cm^{-1}$ in H_2O) was synthesized by Dr. Virginia Wycisk (Haag group, FU Berlin, Berlin, Germany).

Propionic acid seminapthorhodafluorine

Propionic acid seminapthorhodafluorine (PAc-SNARF) was synthesized by Dr. Celin Richter in Prof. Ernsting's group (Humboldt Universität zu Berlin, Germany) according to Ref. 92. The molar absorption coefficient of PAc-SNARF in its deprotonated form is 47,100 ± 500 $M^{-1}\,cm^{-1}$ and the fluorescence quantum yield amounts to 0.35.[92] Tris-base, Tris-HCL, sodium citrate dihydrate, and citric acid for the preparation of the Tris-citrate pH calibration buffer were obtained from Sigma Aldrich (München, Germany).

CellROX green reagent

CellROX green reagent (CellROX) was purchased from Thermo Fisher Scientific (Waltham, USA).

FITC

Fluorescein isothiocyanate (FITC) was obtained from Thermo Fisher Scientific (Waltham, MA).

FluNa

Fluorescein sodium salt (FluNa) was obtained from Merck (Darmstadt, Germany).

3.1.2 Molecular interaction experiments

Bovine *serum albumin* (BSA) and fucoidan were purchased from Sigma Aldrich (München, Germany). Human serum was obtained from Prof. Dr. Jens Dernedde (Charité – Universitätsmedizin Berlin, Germany). The triple-helical peptide MSR-1 was synthesized by the Peptide Specialty Laboratories (Heidelberg, Germany) according to the sequence described by Anachi et al (Ref. 303). DMPC was purchased from Anatrace (Maumee, USA) and DPPC from Avanti Polar Lipids (Alabaster, USA).

3.1.3 Live-Cell experiments

Bodipy™493/503 (4,4-difluoro-1,3,5,7,8-pentamethyl-4-bora-3a,4a-diaza-s-indacene, bodipy), LysoTracker™ Deep Red (LysoTracker), Cholera Toxin Subunit B-Alexa Fluor™647 Conjugate (CTB-A647), CellMask™ Deep Red Plasma Membrane Stain (CellMask), and Glutamax were purchased

from Thermo Fisher Scientific (Waltham, USA). 4',6-diamidin-2-phenylindol (DAPI) was obtained from Dianova (Hamburg, Germany). Methyl-β-cyclodextrin (MβCD), genistein, wortmannin, fucoidan, polyionosinic acid (Poly I), and polycytidylic acid (Poly C) were obtained from Sigma Aldrich (München, Germany). Indocarbocyanine (ICC) was obtained from Mivenion (Berlin, Germany). A Caveolin-1-Alexa Fluor™488 (Cav-1-A488) conjugated antibody (reactivity: human, Clone# 7C8, Catalog# IC5736G) were obtained from R&D Systems (Minneapolis, Minnesota, USA). 35 mm glass bottom cell culture dishes were purchased from Greiner Bio-One (Frickenhausen, Germany). Cell media and supplements were purchased from Sigma Aldrich, München, Germany. Penicillin, streptomycin and fetal calf serum (FCS) superior were obtained from Biochrom (Berlin, Germany). Granulocyte-macrophage colony-stimulating factor (GM-CSF), recombinant mouse, was obtained from Miltenyi Biotec (Bergisch Gladbach, Germany). Methyl-b-Cyclodextrin, dynasore hydrate, phorbol myristate acetate (PMA), LY294002 hydro-chloride, Bafilomycin A1 (BMA1), Chloroquine diphosphate, lipopolysaccharide (LPS) were purchased from Sigma-Aldrich (Schnelldorf, Germany). Bovine *serum albumin* (BSA), sodium dodecyl sulfate (SDS) and hydrogen peroxide were purchased from Carl Roth (Karlsruhe, Germany). All other chemicals were of the highest purity available.

3.1.4 Tissue experiments

Collagen I was obtained from Biochrom (Berlin, Germany), cell culture inserts (0.4 µm pore size) were from Corning (Corning, U.S.A.). Keratinocyte growth medium (KGM) was purchased from Lonza (Basel, Switzerland) and construct culture medium from CELLnTEC Advanced Cell Systems (CNT-PR-3D; Bern, Switzerland). Cell proliferation ELISA, BrdU (colorimetric) was purchased from Roche Diagnostics (Rotkreuz, Switzerland) and the senescence cells histochemical staining kit from Sigma Aldrich (München, Germany). Antibodies were from Cloud-Clone Corp. (Houston, TX, USA: b-gal; cat no. PAA196Hu01; 1:250) and from Cell Signaling Technology (Cambridge, UK, b-actin; cat no. 6883; 1:1000). Pierce bicinchoninic acid protein assay kit was obtained from Thermo Fisher Scientific (Waltham, USA) and nonfat dry milk powder sucofin from TSI (Zeven, Germany). Protein marker Western-C precision and protein marker (biotinylated, HRP-conjugated) were purchased from Bio-Rad (München, Germany), ammonium persulfate, polyvinylidene fluoride membrane Immobilon P, and Rotiphorese Gel 40 from Carl Roth (Karlsruhe, Germany). ECL reagent SignalFire was obtained from Cell Signaling Technology (Danvers, MA, USA). Mice were purchased from Charles River (Sulzfeld, Germany). Hair removal cream was obtained from Veet (Heidelberg, Germany). Imiquimod (Aldara 5 % cream) was purchased from Meda AB (Solna, Sweden) and oxazolone (OX) from Sigma Aldrich (München, Germany). Mouse anti-human CD1a antibody was purchased from Agilent Dako (Santa Clara, USA). Fluorescein isothiocyanate (FITC)-labelled horse anti-mouse secondary antibody was obtained from Vector Labs (Burlingame, U.S.A.). The anti-body against claudin-1 (1C5-D9, cat-no. H00009076-M01) was purchased from Novus Biologicals (Cambridge, UK), and the Alexa 594-labeled secondary antibody was from Dianova (Hamburg,

Germany). All other chemicals were of the highest purity available and bought from Sigma Aldrich (München, Germany).

3.2 Methods

3.2.1 Syntheses and other preparations

CMS-NC synthesis and indocarbocyanine tagging

The indocarbocyanine (ICC)-labeled core-multishell nanocarrier (CMS-ICC) was prepared as described in Ref. 170 by Dr. Michael Unbehauen in the lab of Prof. Haag (Freie Universität Berlin, Germany). In short, hyperbranched polyglycerol amine (hPG-NH_2) with a molecular weight of 10 kDa and a degree of functionalization of amines of 70 % was reacted with approximately one molecule of an NHS-ester of the ICC dye. Afterwards, the residual amines were reacted with the amphiphilic double shell, resulting in the empirical formula $(PG_{10000}\ (NH_2)_{0.7}(C_{18}mPEG_{7.2})_{0.98}(ICC_{0.02})$. The indocarbocyanine-labeled CMS-nanocarrier was characterized by dynamic light scattering (DLS) and gel permeation chromatography (GPC). The results were in accordance with previously studies on the CMS-ICC nanocarrier.[174] DLS size determination was performed using a Malvern Zetasizer Nano ZS (λ = 633 nm; Malvern Instruments Ltd, Malvern, UK).

The cargo bodipy has a logP value of 3.50 ± 0.04 (octanol/water)[102] and is thus able to serve as a lipophilic fluorescent drug mimetic. It was encapsulated into the nanocarriers via a variation of the so-called film uptake method.[170] 1.2 mg of bodipy was dissolved in ethanol, added into a vial and the solvent evaporated, leaving a film of the dye. The aqueous nanocarrier solution (1.5 ml, 5 g/l) was then added and the suspension stirred for 22 h at 1,200 rpm and filtrated (regenerated cellulose, 450 nm pore size). The amount of encapsulated bodipy was determined to 0.0027 % (0.7 molecule bodipy per molecule CMS-ICC nanocarrier) by absorption spectroscopy after lyophilization and redissolution of an aliquot in methanol using the extinction coefficient of bodipy of 91,000 M^{-1} cm^{-1} at 493 nm.

dPGS synthesis and fluorescence tagging

Dendritic polyglycerol sulfate (dPGS) nanoparticles with a molecular weight of approximately 12,000 g/mol were synthesized and fluorescently labeled with indocarbocyanine (ICC) by Mivenion (Berlin, Germany) according to published protocols.[25, 147, 196] In short, dPGS with a molecular weight of approximately 12,000 g/mol was synthesized via an anionic multi-branching ring-opening polymerization of glycidol and a sulfation using a sulfurtrioxide-pyridinium complex.[147] The hydrodynamic diameter of dPGS was determined to be 6.0 ± 1.5 nm by dynamic light scattering, and the ζ-potential of the nanoparticle amounts to -13.6 ± 3.1 mV.[145]

A detailed protocol of the ICC dye conjugation with dPGS is shown in Ref. 197. Briefly, an azido-linker (linker 11-azido-1-undecanyltosylate) was conjugated to the polyglycerol scaffold at a molar

ratio of approximately one linker per polymer before sulfation. After sulfation, the azido-containing polymer was conjugated with a propargyl derivative of ICC by copper-catalyzed 1,3-dipolar cycloaddition (click conjugation) in a water/ethanol mixture. The molecular weight of the dPGS-ICC conjugate was approximately 14,000 g/mol. The hydrodynamic radius was determined to be 4.4 ± 0.3 nm by time-resolved fluorescence anisotropy experiments.[198] After synthesis, the dPGS-ICC was lyophilized. All experiments were conducted with freshly dissolved dPGS-ICC from the lyophilizate of the same batch.

Cleavable dPGS-ICC/(-SS-IDCC) nanoparticle conjugates were synthesized by Dr. Nadine Rades in the lab of Prof. Haag (Freie Universität Berlin, Germany). The fluorophore indodicarbocyanine (IDCC) was modified and synthesized by Dr. Virginia Wycisk (Prof. Haag's group) with the aim to serve as fluorescent drug mimetic with similar lipophilicity as the antineoplastic agent monomethyl auristatin E. The respective protocols are described in Ref. 199. dPGS, with a dPG core of 10 kDa, was fluorescently double tagged by propargyl-ICC and propargyl-SS-IDCC (SS: disulfide linker) using an alkyne-azide cycloaddition as described above. The applied reductively cleavable disulfide linkage is described in Ref. 200. The dye-to-polymer ratios were determined by UV/Vis spectrosopy to be 0.18 ICC molecules and 0.16 IDCC molecules per dPGS nanoparticle.

G5G2.5 core-shell tecto-dendrimer synthesis and FITC labeling

G5G2.5 core-shell tecto-dendrimers (megamers, MG) were synthesized and purified by Dr. Priscila Schilrreff in the groups of Prof. Romero (National University of Quilmes, Argentina) and Prof. Schäfer-Korting (Freie Universität Berlin, Germany) as previously described in Schilrreff et al..[159] Fluorescein isothiocyanate (FITC, 5 mg/mL) was dissolved in acetone and slowly added to a G5G2.5-MG solutions in phosphate-buffered saline (PBS, pH 7.4) at different molar ratios (G5G2.5-MG : FITC) with increasing excess of FITC. Subsequently, this solution was incubated at 4 °C for 24 h in the dark to allow the amino groups of the G5 core to react with the FITC. The FITC-labeled tecto-dendrimers (G5G2.5-MG-FITC) were then separated from free FITC by size-exclusion chromatography on a Sephadex-G25 fine column (GE Healthcare, Chicago, IL). Elution of G5G2.5-MG-FITC was facilitated by centrifugation (1000 × g) of the loaded column for 1-min runs to obtain the individual fractions.

G5G2.5-MG and G5G2.5-MG-FITC were analyzed by polyacrylamide gel electrophoresis (SDS-PAGE; 15 % acrylamide, 0.375 M Tris-HCl (pH 8.9), and 0.1 % (w/v) SDS). G5G2.5-MGs of unknown concentrations and reference G5G2.5-MGs with known concentrations were solubilized in PBS (pH 7.4) and 17 % glycerol. Electrophoresis was performed using a running buffer of 25 mM Tris-HCl (pH 8.8) and 1 % (w/v) SDS at a constant voltage of 200 V. After electrophoresis, gels were stained with Coomassie Brilliant Blue R-250 (AppliChem, Darmstadt, Germany) in 20 % methanol and 10 % acetic acid. Images of the de-stained gels were taken and band intensities quantified using ImageJ (National Institute of Health). The reference bands of the G5G2.5-MGs with known particle

concentration were used to generate a calibration curve (band intensity versus concentration) by a linear regression.[159] Using that calibration curve, the concentration (in mol/L) of the G5G2.5-MG-FITC sample was determined from the respective band intensities.

Molar concentrations of attached FITC molecules were determined by UV-Vis spectroscopy using the Lambert-Beer law. The absorbance of FITC at 488 nm (PBS, pH 7.4) and the corresponding extinction coefficient of 65,000 $M^{-1}\,cm^{-1}$ was used. Reference measurements were performed at alkaline pH with a fully deprotonated fluorescein and an extinction coefficient of 78,000 ± 7,000 $M^{-1}\,cm^{-1}$ (50 mM potassium phosphate buffer at pH 9),[201] and the corresponding maximum absorbance of the pH-sensitive absorption band was determined. The molar labeling ratio of G5G2.5-MG-FITC was then determined as the molar ratio FITC : G5G2.5-MG.

Formation of unilamellar vesicles

For preparation of giant unilamellar vesicles (GUV), DMPC (1,2-dimyristoyl-sn-glycero-3-phosphocholine) was dissolved in chloroform to a final concentration of 2.9 mM and was applied to the electrodes of a home-built GUV electroformation chamber.[198] The chamber was dried in a vacuum desiccator for 120 min. A cleaned cover slip free of solvent residues was assembled together with the chamber and placed into the specimen holder of the FLIM-setup. The chamber was filled with H_2O and heated to 40 °C, after that a voltage of 3 V at 10 Hz was applied for 90 minutes. After termination of the vesicle formation, CMS-ICC (10 µg/ml) was added and FLIM measurements were conducted in the electroformation chamber. For the preparation of SM/Chol/DOPC GUVs[202], sphingomyelin (SM), cholesterol (Chol), and 1,2-dioleoyl-sn-glycero-3-phosphocholine (DOPC) were dissolved in chloroform at a molar ratio of 1:1:1 yielding a lipid solution with a final concentration of 6 mM, which was applied to the electroformation chamber. The following electroformation procedure was the same as for DMPC GUVs.

For preparation of small unilamellar vesicles (SUV, diameter ~20 nm),[88] I used DMPC (Anatrace, Maumee, USA) and DPPC (Avanti Polar Lipids, Alabaster, Alabama, USA) with a molecular weight of 677.9 and 734.0 g/mol. For this purpose, 13.6 mg of DMPC or 14.7 mg DPPC was dissolved in 5 mL buffer solution (30 mM sodium phosphate buffer, pH 7, 150 mM KCl). The resulting solution were sonified for 30 min at 20 °C for SUV generation. This stock solution contains 4 mM DMPC or DPPC, respectively, and was stored at 4 °C before use.

The preparation of multilamellar vesicles (MLVs) using DMPC was performed using a thin-layer method.[203] 1 mg DMPC was dissolved in 1 mL chloroform to obtain a 1.5 mM stock solution. A thin lipid film was formed by the evaporation of chloroform. The DMPC film was hydrated with 5 mL H_2O-MQ. The resulting solution was first heated to 90 °C for 30 minutes, then incubated at 65 °C over 8 hours and stored at 4 °C before use. To characterize the vesicle size distribution, I generated fluorescence intensity linescans of 400 dPGS-ICC stained MLVs. The diameters measured have sizes between 0.2 µm and 2.1 µm and were sorted into a histogram which was fitted by a log-normal

distribution (due to the random fragmentation of the MLV particles) resulting in a mean diameter of 0.66 ± 0.01 µm and a distribution width of 0.3 ± 0.1 µm.

Preparation of FluNa-agarose blocks

For the preparation of FluNa-agarose blocks, fluorescein sodium salt (FluNa) was dissolved in 10 mM Tris-buffer (pH 8) to concentrations of 6 µM (1x stock) and 60 µM (10x stock). To both solutions (10 mL), 1.5% agarose (NuSieve™ 3:1, Lonza, Cologne, Germany) was added with stirring. After 15 minutes, the solutions were heated in a microwave oven at medium power for 120 seconds. In a second heating step, the solutions were heated for another 60 seconds at high power. After the second heating step, the solutions were poured into sterilized 35mm cell culture dishes (Greiner Bio-One, Frickenhausen, Germany). After gelling, both FluNa-agarose samples were subjected to the mpFLIM setup for reference measurements.

3.2.2 Fluorophore and nanoparticle characterization

Apparent binding constants K_{50}

The apparent binding constant K_{50} of a molecule, e.g., a protein binding to an indocarbocyanine labeled nanocarrier, is determined using changes in the mean fluorescence lifetime upon binding. For this purpose, I recorded fluorescence decay traces of the ICC tagged nanoparticles in dependence of different concentrations of the binding partners ([BP]) and calculated the fractional saturation of the binding process in % by

$$fractional\ saturation\ ([\mathrm{BP}]) = \left(\frac{\tau_m([\mathrm{BP}]) - \tau_{m,0}}{\tau_{m,max} - \tau_{m,0}}\right) \cdot 100 \quad , \qquad (57)$$

where $\tau_{m,\beta}$ is the mean fluorescence lifetime weighted on the relative steady-state intensity contribution, calculated by equation (Eq. 21) at a certain concentration of the binding partner (BP), $\tau_{m,0}$ the mean fluorescence lifetime in the absence of the BP, and $\tau_{m,max}$ the mean fluorescence lifetime at the maximum concentration of BP.[25] The resulting values of the fractional saturation were plotted against the BP concentration and fitted to a Hill-model:

$$fractional\ saturation\ ([\mathrm{BP}]) = \frac{S \cdot [\mathrm{BP}]^g}{({K_{50}}^g + [\mathrm{BP}]^g)} \quad , \qquad (58)$$

where S is the saturation of the binding process, [BP] the BP concentration, K_{50} the half-maximum binding constant (apparent binding affinity), and g the Hill-coefficient (cooperativity factor).

PAc-SNARF

10 mM Tris-citrate buffer was supplemented with 190 mM NaCl and 5 % DMSO and subsequently titrated to pH 10. The sodium salt of PAc-SNARF, synthesized in the lab of Prof. Ernsting (Humboldt

Universität zu Berlin, Germany), was first dissolved in this Tris-citrate buffer to a concentration of 2.5 µM. Afterwards, the generated solution was subjected to UV-Vis absorption, steady-state fluorescence, and time-resolved fluorescence spectroscopy. Subsequent titration steps by addition of NaOH down to pH 5 resulted in absorption and emission spectra with clear isosbestic points. The respective pH was supervised by a glass pH electrode.[92]

The pK_a of the protonation equilibrium can be determined by the Henderson-Hasselbalch (HH) equation in the following representation:

$$x_{\mathrm{depro}} = \frac{10^{-\mathrm{pK_a}}}{10^{-\mathrm{pK_a}}+10^{-\mathrm{pH}}} \text{ and } x_{\mathrm{pro}} = 1 - x_{\mathrm{depro}} \quad , \qquad (59)$$

x_{pro} and x_{depro} are the relative mole fractions of the protonated and deprotonated form of PAc-SNARF which are assumed to be in pH-depended equilibrium. The molar fractions at a certain pH values are either expressed directly by the relative decay amplitudes of two fluorescence decay components that can be assigned to the protonated and deprotonated form of PAc-SNARF, or indirectly using separated spectral regions in the absorbance and fluorescence emission spectra, respectively. In the latter case a modified HH-model is applied:

$$x'_{\mathrm{depro}} = \mathrm{A_{max}} \frac{10^{-\mathrm{pK_a}}}{10^{-\mathrm{pK_a}}+10^{-\mathrm{pH}}} + B_{\mathrm{off}} \text{ and } x'_{\mathrm{pro}} = \mathrm{A_{max}} - x'_{\mathrm{depro}} \quad , \qquad (60)$$

with $\mathrm{A_{max}}$ and B_{off} being two constants which ensure the adaption of the HH model to data sets, that are not scaled between 0 and 1.

Indocarbocyanine

Molar concentrations of ICC were determined by UV-visible (UV-Vis) spectroscopy using the Lambert-Beer law. For the calculation I used the absorbance of ICC at 550 nm (PBS, pH 7.4) and the corresponding extinction coefficient of 120,000 M^{-1} cm^{-1}. The final ICC concentration investigated is indicated in the respective Figures.

dPGS-ICC and CMS-ICC

Molar concentrations of dPGS-ICC and CMS-ICC were determined by UV-visible (UV-Vis) spectroscopy using the Lambert-Beer law. For the calculation I used the absorbance of free ICC at 550 nm (PBS, pH 7.4) and the corresponding extinction coefficient of 120,000 M^{-1} cm^{-1}. The final dPGS-ICC and CMS-ICC concentration investigated is indicated in the respective Figures.

G5G2.5-MG-FITC

G5G2.5-MG-FITC was characterized as described in Ref.[19]. Molar concentrations of attached FITC molecules were determined by ultraviolet-visible (UV-Vis) spectroscopy using the Lambert-Beer law. The absorbance of FITC at 488 nm (PBS, pH 7.4) and the corresponding extinction coefficient of

65,000 M^{-1} cm^{-1} was used. Reference measurements were performed at alkaline pH with fully deprotonated fluorescein and an extinction coefficient of 78,000 ± 7000 M^{-1} cm^{-1} (50 mM potassium phosphate buffer at pH 9), and the corresponding maximum absorbance of the pH-sensitive absorption band was determined. The molar labeling ratio of G5G2.5-MG-FITC was then determined as the molar ratio FITC/G5G2.5-MG.

Absorption spectra of FITC and G5G2.5-MG-FITC were measured either in a 3 × 3 mm quartz cuvette with a UV2450 (Shimadzu, Kyoto, Japan) or using a NanoDrop One (Thermo Fisher Scientific) UV-Vis spectrophotometer. The absorbance was recorded between 300 and 600 nm with a spectral resolution of 0.5 nm. Fluorescence emission spectra of FITC and G5G2.5-MG-FITC were recorded with a Fluoromax-3 (Horiba Jobin Yvon, Kyoto, Japan) using a 3 × 3 mm quartz cuvette. The temperature was set to 20 °C, and all samples were excited at 488 nm. The fluorescence emission was recorded between 500 and 700 nm with a spectral resolution of 1 nm. Experimental conditions of the time-resolved fluorescence are described in the Figure legends.

CellROX

The stock solution of CellROX Green (2.5×10^{-3} M) was prepared by Jens Balke (Prof. Alexiev's group, Freie Universität Berlin, Germany). The CellROX stock was stabilized in dimethyl sulfoxide and diluted in PBS at pH 7.4 to a concentration of 5×10^{-6} M. Diluted samples were stored in the dark at 4 °C prior to all experiments.

3.2.3 Live-cell FLIM experiments

NHDF cell culture

Normal human dermal fibroblasts (NHDF) were obtained from Prof. Schäfer-Korting's group (Freie Universität Berlin, Germany). NHDFs were isolated from juvenile foreskin of medically indicated circumcisions of boys younger than 9 years old (ethical approval EA1/081/13, ethics vote from the – Universitätsmedizin Berlin, Germany). 2.5×10^5 cells were seeded per compartment of glass bottom cell culture dishes and cultured at 37 °C in Fibroblast growth medium (FGM, Lonza, Köln, Germany) 750 µL for 2 days in a humidified atmosphere containing 5 % CO_2; medium was changed once on the 2nd day.

NHK cell culture

Normal human keratinocytes (NHK) were obtained from Prof. Schäfer-Korting's group (Freie Universität Berlin, Germany). NHKs were isolated from juvenile foreskin of medically indicated circumcisions of patients younger than 9 years old (ethical approval EA1/081/13, ethics vote from the – Universitätsmedizin Berlin, Germany). 2.5×10^5 cells were seeded per compartment of glass bottom cell culture dishes and cultivated at 37 °C in 750 µL keratinocyte growth medium (KGM, Lonza, Köln,

Germany) for 2 days in a humidified atmosphere containing 5 % CO_2; media was changed once on the 2nd day.

SCC-12/SCC-25 cell culture

The human squamous cell carcinoma (SCC) cell lines SCC-12 (cutaneous) and SCC-25 (tongue), passage 98 – 100 were obtained as a kind gift from Howard Green (Dana-Farber Cancer Institute, Boston, MA, USA) and were authenticated by single nucleotide polymorphism profiling (Multiplexion, Heidelberg, Germany). SCC cell lines were cultivated in Prof. Schäfer-Korting's lab (Freie Universität Berlin, Germany) at 37 °C in DMEM/F2, supplemented with 100 U/mL Penicillin, 100 µg/mL Streptomycin (Sigma Aldrich) and 2 mM L-Glutamine) in a humidified atmosphere containing 5 % CO_2; media was changed once on the 2nd day.

XS52 cell culture

The long-term immature Langerhans cell-like dendritic cell (DC) line XS52 was a kind gift from G. Müller (Mainz, Germany). The XS52 cells were cultivated in Prof. Kleuser's lab (Universität Potsdam/Freie Universität Berlin, Germany) as described in Ref. 174, 204-205. In short, XS52 cells were cultured in Iscove's modified Dulbecco's medium (IMDM) with GlutaMAX® with supplements (100 U/mL penicillin, 100 mg/mL streptomycin, 50 U/mL GM-CSF, 10 % NS47 fibroblast supernatant and 10 % FCS superior) at 37 °C, in a humidified atmosphere containing 5 % CO_2. The NS47 fibroblast supernatant was generated using NS47 cells. For this purpose, NS47 cells were cultivated in IMDM with GlutaMAX® with supplements (100 U/mL penicillin, 100mg/mL streptomycin and 10 % FCS superior) at 37 °C, in a humidified atmosphere containing 5 % CO_2. After the cells reached a confluence grade of 90 %, the supernatants were collected and added to the culture medium of the XS52 cells. The fibroblastic stromal NS47 cell line was kindly provided by A. Takashima (University Toledo, OH, USA).

PAc-SNARF based pH determination in NHK

PAc-SNARF dissolved in 10 mM Tris-citrate buffer was mixed 1:1 (Vol:Vol) with KGM resulting in a concentration of 1.25 µM. NHK cells were incubated for 18 minutes at 37 °C and 5 % CO_2 and subjected to FLIM.

Isolation and CD1a staining of human epidermal cells

Isolation and CD1a staining of human epidermal cells were performed by Dr. Janna Frombach in the lab of Prof. Vogt (Charité – Universitätsmedizin Berlin, Germany). CMS-ICC or PBS (control experiments) was topically applied on an area of 2 cm^2 of excised full-thickness human skin for 16 h with permission and informed consent of the donor. After the incubation, epidermal cells were isolated from this tissue block by the following procedure. First, the skin was cut into squares of 1 mm^2 and digested with dispase (2.4 U/ml dispase I, Roche, Germany) for 2.5 h at 37 °C. Following

digestion, epidermis and dermis were separated mechanically. Cell suspensions were generated by incubation of epidermal sheets with 0.025 % trypsin and 1.5 mM $CaCl_2$ in PBS (pH 7.4) for 15 min at 37 °C). The suspensions were filtered (70 µm Cell Strainer, BD Falcon, Germany) and the cells were collected by centrifugation (10 min, 216× g). Cells were fixed in 2 % paraformaldehyde and placed into sterilized 35 mm CELLVIEW® cell culture dishes with 4 compartments and a glass bottom of 175 ± 15 µm thickness (Greiner Bio-One, Germany) for FLIM investigation. In order to identify $CD1a^+$ cells and correlate them with CMS-ICC uptake, a fraction of the isolated cells was immunolabeled with a human anti-CD1a antibody (mouse allophycocyanine (APC) anti-human CD1a, BD Bioscience, Germany).

CMS-ICC uptake kinetics in NHK and SCC-25

NHK cells (2.5×10^5 cells per compartment) obtained from Prof. Schäfer-Korting's lab were incubated for 15, 45, 90, 180, and 270 minutes at 37 °C and 5 % CO_2 with CMS-ICC/bodipy at a concentration of 10 µg/ml in KGM. Immediately before the FLIM, cells were washed twice and KGM was exchanged with PBS (pH 7.4). Subsequently, the cells were stained with DAPI (28 µM) and CellMask (0.5 µg/ml) for 5 – 10 minutes. FLIM experiments were performed four times. For each experiment, and at each time point, two different images (usually full image and zoom) were measured.

SCC-25 cells were incubated in the respective growth medium (see above) for 15, 180, 270, 370 min. Cell uptake of CMS-ICC was directly investigated by FLIM after two washing steps and medium exchange to PBS (pH 7.4).

CMS-ICC uptake and release kinetics in XS52

XS52 cells were seeded (2×10^5 cells per chamber) two days prior to the FLIM measurements into sterilized 35mm 4-chamber cell culture dishes with a glass bottom by Dr. Alexander Edlich in Prof. Kleuser's lab (Universität Potsdam/Freie Universität Berlin, Germany). For the uptake experiments, XS52 cells were incubated with 50 g/L of CMS-ICC in whole-cell medium for the indicated time intervals at 37 °C, in a humidified atmosphere containing 5 % CO_2. Before subjected to FLIM, cells were washed four times with PBS (pH 7.4).

For investigating the release kinetics of the CMS nanocarrier, XS52 cells were incubated with 50 mg/mL of CMS-ICC (CMS-ICC) at 37 °C for 5 h. Then, the cells were washed and further incubated in a CMS-ICC-free medium for the indicated time intervals at 37 °C. At selected points in time after the incubation cells were washed four times with PBS (pH 7.4) and subjected to FLIM.

Inhibition studies of cellular uptake of CMS-ICC towards NHK

NHK uptake inhibition and receptor blocking experiments were performed by a 30- to 60-minute pre-incubation with the respective inhibitor and a subsequent co-incubation with CMS-ICC/bodipy without any washing or changing of KGM at 37 °C. For adenosine triphosphate (ATP) inhibition,

NHK cells were incubated with azide (3 mg/ml). Cholesterol depletion experiments were performed by incubation with methyl-β-cyclodextrin (5 mg/ml). Phosphoinositide 3-kinase activity was inhibited by wortmannin (150 ng/ml). Clathrin-mediated endocytosis was inhibited by chlorpromazine (10 µg/ml). Caveolae-mediated cell uptake was blocked by genistein (27 µg/ml). Scavenger Receptor (SR) binding was blocked by polyionosinic acid (50 µg/ml) or fucoidan (100 µg/ml). As a positive control, NHK cells were incubated with policytidylic acid, not a ligand of SR. Low temperature experiments were performed at 4 °C. For investigating binding of unlabeled CMS to SR, NHK cells were incubated at 4 °C with CMS at a concentration of 1000 µg/ml. Subsequently, NHK cells were incubated for at least 180 minutes with CMS-ICC/bodipy at a concentration of 10 µg/ml in KGM.

Co-localization studies of CMS-ICC with cholera toxin subunit B, Caveolin-1 and LysoTracker

For co-localization with cholera toxin subunit B uptake pathways, NHK cells were incubated for 15 min with CMS-ICC/bodipy (10 µg/ml) and CTB-A647 (5 µg/ml) at 37 °C and 5 % CO_2 in KGM. For co-localization with caveolae, NHK cells were incubated for 90 min with CMS-ICC (10 µg/ml) and a Cav-1-A488 antibody at a 1:20 dilution. For lysosomal co-localization studies, NHK were incubated for 600 min with CMS-ICC/bodipy (10 µg/ml) and during the last 45 minutes, LysoTracker was co-incubated at a concentration of 50 nM. FLIM measurements were conducted without any washing or exchanging of KGM.

For lysosomal co-localization studies with CMS-ICC in the XS52 LC-like cell line, lysosomes were stained by incubating XS52 cells with 500nM LysoTracker for 30 min at 37 °C after a 3 h pre-incubation with CMS-ICC (50 µg/ml). The cells were washed four times with PBS (pH 7.4) and subjected to FLIM.

Co-localization of CMS-ICC and cholera toxin subunit B, Caveolin-1 and LysoTracker was quantified by Manders' co-localization coefficients M_1 and M_2, after an automatic threshold search as described in Ref. 206. M_1 and M_2, representing the overlapping fraction of two spectral channels A and B with respect to the other, i.e., M_1 is the overlap of spectral channel A with spectral B and M_2 is the overlap of spectral channel B with spectral A. Manders' co-localization coefficients can take values between 0 (no co-localization) and 1 (co-localization). To obtain the coefficients, I used the Coloc2 plugin integrated in the image-processing package FIJI.[207]

Concentration-dependent CMS-ICC uptake in NHK and displacement of CMS-ICC from NHK plasma membranes by CMS.

To investigate the concentration dependence of the CMS-ICC uptake, NHK were incubated with CMS-ICC for 270 min at concentrations ranging from 0 to 25 µM in KGM at 37 °C. The uptake behavior was analyzed by intracellular fluorescence intensities I at the different CMS-ICC

concentrations. The observed non-linear uptake behavior was fitted by a Michaelis-Menten-like equation[208] (corresponds Eq. 58 with g=1):

$$I = I_{max} \frac{[\mathrm{CMS}]}{K_{50} + [\mathrm{CMS}]} \quad , \tag{61}$$

with I_{max} being the saturation fluorescence intensity, [CMS] the concentration of CMS-ICC and K_{50} the half-maximum uptake concentration.

To study CMS-ICC displacement from the NHK plasma membrane by unlabeled CMS, NHK were incubated with CMS-ICC (0.5 µM) in KGM at 4 °C for 1 h. Afterwards, unlabeled CMS was added in concentrations ranging from 10 to 10,000 nM at 4 °C. The displacement of CMS-ICC from the plasma membrane was analyzed by the area of the CMS-ICC occupied plasma membrane. The decrease of occupied membrane areas with increasing CMS concentrations was fitted by a modified Hill-function:

$$A = A_{max} + \frac{(A_{min} - A_{max})\,[\mathrm{CMS}]^g}{{K_{50}}^g + [\mathrm{CMS}]^g} \quad , \tag{62}$$

where A_{max}, A_{min} are the maximal and minimal area of CMS-ICC membrane occupation, [CMS] the CMS concentration, K_{50} the half-maximum binding constant (apparent binding affinity), and g the Hill-coefficient (cooperativity factor).

Spatiotemporal development of the FLIM-Clusters in NHK and kinetic model of CMS-ICC internalization and transport.

For analyzing the spatiotemporal development of the FLIM clusters in NHK cells, I performed kinetic modelling using the relative cluster concentrations. The relative cluster concentrations were expressed as the fraction of the total CMS-ICC intensity. The time-dependence of the concentration of the three FLIM-clusters (cyan (c), yellow (y), red (r)) in the plasma membrane (pm) and in the cytoplasm (cp) was fitted to a simple kinetic reaction model:

$$[\mathrm{NC\text{-}R}]_{pm,c} \rightleftharpoons [\mathrm{NC\text{-}R\text{-}C}]_{pm,y} \rightarrow [\mathrm{NC\text{-}R\text{-}C}]_{cp,y} \rightarrow [\mathrm{NC^*}]_{cp,r} \quad , \tag{63}$$

with $[\mathrm{NC\text{-}R}]_{pm,c}$ being the CMS-ICC nanocarrier bound to the SR receptor on the plasma membrane (cyan cluster). $[\mathrm{NC\text{-}R}]_{pm,y}$ describes the CMS-ICC nanocarrier bound to the SR receptor in lipid raft/caveolae containing areas of the plasma membrane (yellow cluster). $[\mathrm{NC\text{-}R\text{-}C}]_{cp,y}$ is the fraction of CMS-ICC bound to the SR receptor in caveolar vesicles in the cytoplasm (yellow cluster), while $\mathrm{NC^*}_{cp,r}$ describes CMS-ICC in lysosomal compartments (red cluster). I assume first order reactions and describe the kinetic model of CMS-ICC internalization and transport by the following set of differential equations:

$$\frac{d[\mathrm{NC-R}]_{\mathrm{pm,c}}}{dt} = \frac{1}{\tau_{-1}}[\mathrm{NC-R-C}]_{\mathrm{pm,y}} - \frac{1}{\tau_1}[\mathrm{NC-R}]_{\mathrm{pm,c}} \quad (64)$$

$$\frac{d[\mathrm{NC-R-C}]_{\mathrm{pm,y}}}{dt} = \frac{1}{\tau_1}[\mathrm{NC-R}]_{\mathrm{pm,c}} - \frac{1}{\tau_2}[\mathrm{NC-R-C}]_{\mathrm{pm,y}} \quad (65)$$

$$\frac{d[\mathrm{NC-R-C}]_{\mathrm{cp,y}}}{dt} = \frac{1}{\tau_2}[\mathrm{NC-R-C}]_{\mathrm{pm,y}} - \frac{1}{\tau_3}[\mathrm{NC-R-C}]_{\mathrm{cp,y}} \quad (66)$$

$$\frac{d[\mathrm{NC^*}]}{dt} = \frac{1}{\tau_3}[\mathrm{NC-R-C}]_{\mathrm{cp,y}} \quad , \quad (67)$$

where τ_1 is the time constant of the transition of receptor bound CMS-ICC in the plasma membrane to lipid raft/caveolae containing membrane areas τ_{-1} describes the time constant of the correspondent back transition. τ_2 is the time constant of the dissociation of CMS-ICC loaded caveolar vesicles from the plasma membrane into the cytoplasm and τ_3 describes the time constant of the transport into lysosomes. The fitting procedure with differential equations (Eq. 63 – 67) was conducted in Mathematica 11.0 (Wolfram Research, Champaign, USA).

3.2.4 Tissue experiments

Human skin explants (*ex-vivo* human skin)

Human skin explants for the characterization experiments of the mpFLIM setup were obtained from Prof. Dr. Martina Meinke's group (Charité – Universitätsmedizin Berlin, Germany) from plastic surgeries. Volunteers had signed an informed consent form approved by the Institutional Ethics Committee of the Medical Faculty of the Charité – Universitätsmedizin Berlin, Germany (approval EA1/135/06). After surgery, the skin was handled according to standardized procedures to avoid surface contamination with subcutaneous lipids. The skin explants were incubated in a FluNa solution (60 µM, 10 mM Tris buffer pH 8) for at least 12 h. After the incubation, the skin sample was subjected to mpFLIM.

Human skin explants for the investigation of G5G2.5-MG-FITC and G5G2.5-MG/RhoB penetration *ex vivo* were prepared by Dr. Christian Zoschke in Prof. Schäfer-Korting's lab (Freie Universität Berlin, Germany) according to Ref. 19. Human, abdominal skin with no visible damages, stretch marks or scars was obtained from plastic surgeries with permission and informed consent from male donors (age: 40 – 60 years, ethical approval EA4/091/10). After surgery, the skin was handled according to standardized procedures to avoid surface contamination with subcutaneous lipids. Cryo-conserved and thawed human skin was dermatomized to 500 µm and punched for a surface area of 2 cm². For skin penetration studies, 30 µL/cm² of 50 µM G5G2.5-MG-FITC and G5G2.5-MG/RhoB in PBS pH 7.4 were applied onto the tissue model's surface and incubated at 37 °C and 5 % CO_2

for 6 h. Subsequent to the removal of excess formulation, the skin samples were embedded in cryo medium, snap frozen and cryo-sectioned into 6 µm slices (Leica CM 1510S, Wetzlar, Germany), which were placed on cleaned precision coverslides (170 ± 5 µm, No. 1.5H, Marienfeld, Germany) and subjected to confocal FLIM.

Human skin explants for the investigation of CMS-ICC penetration *ex vivo* were prepared by Dr. Janna Frombach in the lab of Prof. Vogt (Charité – Universitätsmedizin Berlin, Germany). according to Ref. 169. Briefly, intact excised human skin was obtained within 6 h after surgical excision from healthy Caucasian volunteers undergoing plastic surgery and handled according to Declaration of Helsinki Principles. Volunteers had signed an informed consent form approved by the Institutional Ethics Committee of the Medical Faculty of the Charité – Universitätsmedizin Berlin, Germany (approval EA1/135/06). Damaged tissue areas were identified macroscopically and microscopically and excluded from experiments. Indocarbocyanine-labelled CMS-NC (CMS-ICC) and untreated controls (phosphate-buffered saline (PBS, pH 7.4)) were topically applied on slightly stretched and fixed skin. 200 µg CMS-ICC per cm^2 within 20 µL solution were applied onto skin leading to total concentration of 10 g/L; for reference (untreated control) 20 µL PBS per cm^2 were used. To avoid undesirable interaction between different treated areas on the same tissue block, adequate distance was left in each direction of any sample. After incubation in a humidified chamber at 37 °C, 5 % CO_2, 100 % humidity for 16 h, remaining solvents were removed. The samples were embedded in cryo medium, snap frozen and cryo-sectioned into 5 µm slices (Leica CM 1510S, Wetzlar, Germany), placed on cleaned precision coverslides (170 ± 5 µm, No. 1.5H, Marienfeld, Germany) and subjected to confocal FLIM.

Animal model skin

The murine psoriasis and atopic dermatitis models for the investigation of CMS-ICC penetration in diseased skin under *in-vivo* conditions were prepared by Hanna Pischon and Moritz Radbruch in Prof. Gruber's lab (Freie Universität Berlin, Germany) according to Ref. 172 and 166. In short, six- to eight-week-old, male BALB/c mice (Charles River, Sulzfeld, Germany, n = 3 per group) for the psoriasis model and hairless male SKH-1 mice (Charles River, Sulzfeld, Germany, n = 3 per group) for the atopic dermatitis model were used. Experiments were performed according to national guidelines for animal studies and humane care and approved by the State Office of Health and Social Affairs, Berlin, Germany (LaGeSo; G 0126/13). All measurements and topical applications were conducted under isoflurane anesthesia, while the mice lay on a heating mat. To facilitate dermal application and measurements, the right flank was clipped on an area of 2.0 × 2.0 cm and chemically depilated two days prior to the start of experiments with Veet hair removal cream (Mannheim, Germany) for 4 min.

Psoriasis-like dermatitis was induced on a 1.5 × 1.5 cm area of the depilated right flank by imiquimod (62.5 mg, Aldara 5 % cream, Meda AB, Solna, Sweden) application for seven subsequent

days (from day -3 to 4).[209] Atopic-like dermatitis was induced on a 1.5 × 1.5 cm area of the depilated right flank via repeated topical hapten challenges with oxazolone (OX, Sigma-Aldrich, St. Louis, USA) as described in Ref. 210 with minor modifications. On day -26 the mice were treated with 5 % OX dissolved in EtOH and from day -19 on every other day up to day 3, 12× daily with 0.1 % OX EtOH solutions.

CMS-ICC solutions (5 g/L) and 0.9 % sodium chloride (NaCl) reference solutions (negative controls) were topically applied twice daily for five days (from days 0 to 4, see Figure 4.5.6A) on the right flank (44.5 µL) using a nylon mesh for even distribution of aqueous solutions. On day 0 to 4, mice with psoriasis-like dermatitis received their imiquimod treatment approximately 4 h after the second application of CMS-ICC or references solution. Following a 3-min massage, the test substance was allowed to dry and seep in for 1 h. Approximately 24 h after the last treatment, animals were euthanized by isoflurane overdose. Vertical paraffin sections of formalin-fixed, paraffin-embedded murine skin were counterstained with DAPI and measured through a precision coverslide (thickness: 170 ± 10 µm, Thermo Scientific) by FLIM.

Reconstructed human epidermis

3D multicellular reconstructed human epidermis models were produced by Dr. Lilian Löwenau in Prof. Schäfer-Korting's lab (Freie Universität Berlin, Germany) as described previously.[211] 3 × 10^5 keratinocytes were cultivated per construct for two weeks according to the CELLnTEC Advanced Cell Systems protocol. Irradiated keratinocytes were used for UVB-stressed constructs (UVB-RHE); non-irradiated cells from the corresponding donor were used for normal reconstructed human epidermis (RHE). In brief, keratinocytes were seeded onto the insert membranes and cultivated submerged in the culture medium. 24 h after seeding, the keratinocytes were exposed to the air-liquid interface and cultivated for a total cultivation period of 14 days. The constructs were cultivated in an incubator at 37 °C and 5 % CO_2. The culture medium was changed three times a week. Penetration of CMS-ICC into UVB-RHE was studied by adapting the previously published in vitro protocols.[170, 212]

In short, 80 µL/ cm^2 of an aqueous CMS-ICC nanocarrier solution (5 g/L) were applied onto the constructs, then kept at 37 °C, 5 % CO^2 for six hours. For reference (untreated control group) 20 µL PBS per cm^2 were used. After incubation, constructs were embedded in cryo medium (Leica; Wetzlar, Germany), snap frozen in liquid nitrogen, sectioned into 10 µm slices (Leica CM 1510S; Wetzlar, Germany), placed on cleaned precision coverslides (170 ± 5 µm, No. 1.5H, Marienfeld, Germany) and subjected to confocal FLIM.

Reconstructed human skin

3D multicellular reconstructed human skin models were produced by Christopher Wolff and Dr. Christian Zoschke in Prof. Schäfer-Korting's lab (Freie Universität Berlin, Germany) as described previously.[48, 213] Briefly, reconstructed human skin (RHS) models of normal (healthy) skin and non-

melanoma skin cancer (NMSC) of the type of cutaneous squamous-cell carcinoma (cSCC) were cultivated for 3 weeks using 0.6 × 10^6 normal human dermal fibroblasts and 3.0 × 10^6 NHKs per model. Primary NHKs and NHDF (passage 3, pooled from three donors) were from therapeutically indicated circumcisions (ethical approval EA1/081/13) after parents have signed a written consent form. For the NMSC models investigated, 0.3 – 2.0 × 10^6 SCC-12 cells (passage 98 – 100, a generous gift from Howard Green, Dana-Farber Cancer Institute; Boston, MA, USA) were added additionally to the tissue constructs during their growing process.[213] Cell culture was performed according to standard operating procedures and referred to good cell culture practice.

Briefly, 30 µL per cm^2 of an aqueous CMS-ICC/bodipy solution (5 g/L) were applied onto the constructs, then kept at 37 °C, 5 % CO^2 for 6 and 24 hours in a humidified chamber. For reference (untreated control group) 30 µL PBS per cm^2 were used. The remaining solvents were removed after incubation and the constructs were placed upside down in 35 mm glass bottom cell culture dishes. In this condition, the samples were subjected to the FLIM.

Immunostaining of skin sections

Immunofluorescence staining for claudin-1 detection was performed by Christopher Wolff in Prof. Schäfer-Korting's lab (Freie Universität Berlin, Germany) according to standard protocols. Briefly, tissue cryosections were fixed using ice-cold acetone and washed with PBS containing 0.1 % *bovine serum albumin* (BSA) and 0.1 % Tween 20 (PBS-BSA-Tween). Subsequently, skin sections were incubated with goat serum (5 % in PBS-BSA-Tween) to block unspecific antibody binding. Next, the primary anti-claudin-1 antibody was applied to the tissue sections and incubated overnight at 4 °C. To avoid any spectral overlap with the absorbance and emission of FITC and G5G2.5-MG-FITC, a secondary antibody labeled with Alexa Fluor 594 was selected. After washing, the secondary antibody was incubated for 1 h at room temperature. The slices were finally washed and subjected to FLIM.

Immunohistochemical staining of CD1a positive-cells within human skin cryo-cross sections was performed by Dr. Janna Frombach in the lab of Prof. Vogt (Charité – Universitätsmedizin Berlin, Germany) according to established procedures.[193] For the immunohistochemical staining of CD1a, a mouse anti-human CD1a antibody (1:50, Agilent Dako, USA) was used as primary anti-body. In order to identify the sites of CD1a positive cells using fluorescence microscopy, a horse anti-mouse-FITC (1:50, Vector Labs, USA) secondary antibody was applied.

3.3 Experimental setups

3.3.1 UV-Vis absorption spectrometry

Steady-state absorption spectroscopy were performed using a UV-2450-PC dual-beam UV-VIS scanning spectrometer (Shimadzu, Kyto, Japan). Sample absorbance were recorded in a 3 x 3 mm quartz cuvette (Hellma Analytics, Müllheim, Germany) between 250 and 750 nm, using a slit width of 2.0 nm, increment intervals of 0.5 nm, and a medium scan speed, unless otherwise stated.

3.3.2 Steady-state spectro-fluorometry

Steady-state fluorescence spectra were recorded with a SPEX Fluoromax-3 spectrofluorometer (HORIBA Jobin Yvon, Kyoto, Japan) in L-shape configuration using the DataMax Software Version 2.20 (HORIBA). Fluorescence excitation and emission spectra were recorded in 3x3 mm quartz cuvettes (Hellma Analytics, Müllheim, Germany) at 20 °C, unless otherwise stated. An installed Peltier element allows for temperature scans. Increment intervals, integration times, excitation and emission wavelengths, as well as respective slit configuration are indicated in the results section. The uncertainty of the measured fluorescence intensities is caused by sample handling, pipetting, and instrumental noise of the spectrofluorometer. The largest influence originates from the pipetting process. I estimate the experimental uncertainty to 5 % of the determined fluorescence intensities.

3.3.3 Time-resolved fluorescence spectroscopy

Time-resolved fluorescence spectrometry of dissolved fluorescent samples are performed in a home-build cuvette-based setup of Prof. Alexiev's lab.[129] Figure 3.3.1 illustrates the beam path and the involved components. Fluorescence excitation is generated either by a ps-pulsed titanium:sapphire (Ti:Sa) laser or a supercontinuum white light (SWL) laser. The system consists of a diode pumped solid-state laser (DPSSL, Millenia Vs, Spectra Physics, Santa Clara, California, U.S.A.), that optically pumps a Ti:Sa laser system (Tsunami, model #3950, Spectra Physics) by 5 W at 532 nm. The mode-locked Ti:Sa laser emits laser pulses of 1.5 – 2.0 ps, with a repetition rate of 82 MHz at a tunable wavelengths ranging between 710 nm and 1000 nm. A down-streamed pulse selector/ frequency doubler unit (model #3980, Spectra Physics) reduces the repetition rate to 4.05 MHz, this corresponds to 1 excitation pulse every 250 ns, much longer as the fluorescence lifetimes investigated in this thesis. This ensures that the time span between two subsequent pluses is long enough to avoid wrongly assigned photon detections in subsequent TCPSC measuring cycles. The frequency doubler generates the second harmonic of the fundamental laser line, i.e., it reduces the wavelength to values ranging from 355 nm and 500 nm.

In order to guarantee that no residual fraction of the fundamental disturbs the experiment, a short-pass filter is installed, removing wavelengths above 640 nm. The laser beam has an intrinsic linear

polarization axis with a horizontal orientation in respect to the laboratory axis. For this reason, an achromatic double Fresnel rhomb is used to change the plane of orientation by rotating the polarization axis by 90 °= λ/2 to a vertical linear polarization. The second excitation source is a picosecond-pulsed SWL laser system (400 – 2400 nm, 6 ps (FWHM), SuperK Extreme EXU-3, NKT Photonics, Birkerød, Denmark), with a tunable repetition rate, adjusted to 19.5 MHz and a linear polarization axis. After fiber coupling (FD7, NKT Photonics) into an acousto optical tunable filter (AOTF, SELECT UV-VIS, NKT Photonics, Denmark) the SWL beam is spectrally filtered for a selective fluorescence excitation. In order to obtain a clean excitation beam, a quad-notch laser filter (ZET 405/488/532 /642, Chroma, U.S.A.) is installed removing residual light passing the AOTF at the target excitation wavelengths (± 5nm): 405 nm, 488 nm, 530 nm, and 640 nm. The filtered excitation beam leaves the AOTF via a second optical fiber (FD7). The fiber outlet is rotated so that the polarization axis is aligned to vertical linear polarization.

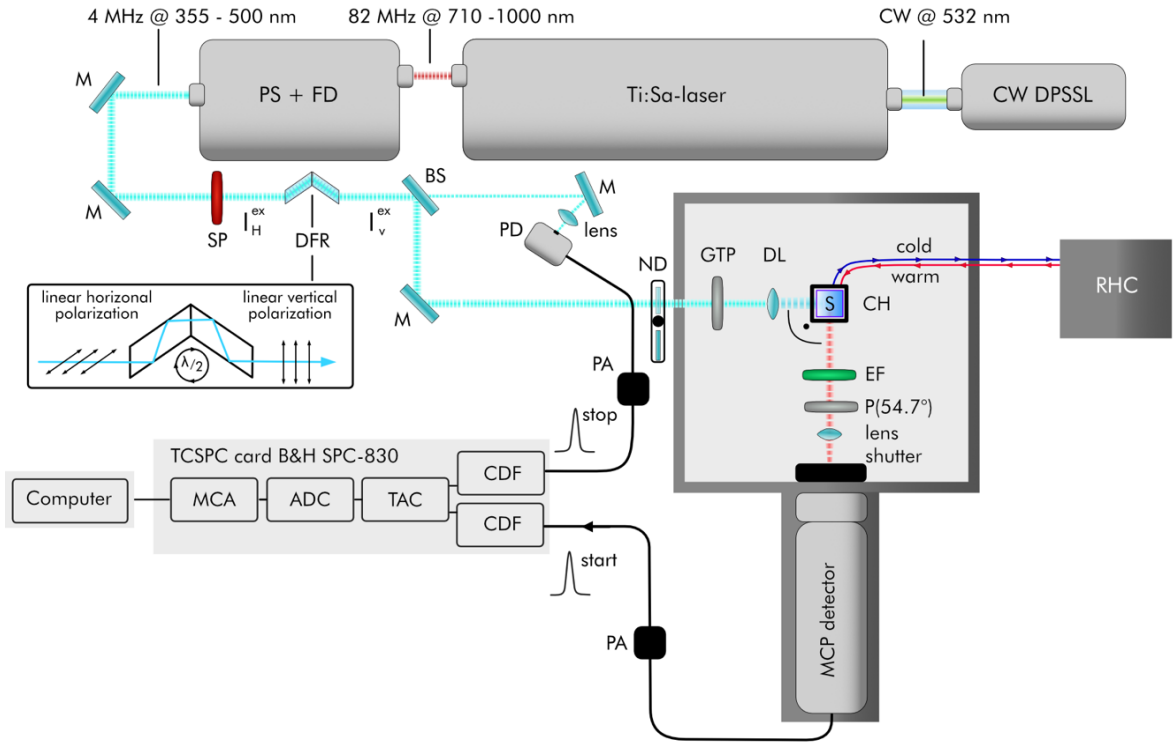

Figure 3.3.1: Schematic of the used cuvette-based TCSPC setup for time-resolved fluorescence spectrometry of dissolved fluorescent samples. A diode pumped solid-state laser (DPSSL) optically pumps a titanium:sapphire (Ti:Sa) crystal with 5 W at 532 nm. The resulting mode-locked Ti:Sa emission has a repetition rate of 82 MHz, and a tunable wavelength between 710 nm and 1000 nm. A down-streamed pulse selector changes the repetition rate to 4.05 MHz and a frequency doubler reduces the wavelength by a factor of two. The resulting excitation beam is optically cleaned by short-pass filter (SP, 640 nm) and the original horizontal linear polarization is changed by a double Fresnel rhomb (DFR) rotating the polarization axis by 90 °= λ/2 to vertical linear polarization. A beam splitter (BS) separates a small fraction of the excitation beam and direct this fraction to a photo diode (PD). The PD temporally recognizes the laser pulse and provides the TCSPC excitation references (stop) signal. The intensity of the excitation can be adapted by neutral density (ND) filters. After passing the sample enclosure, the excitation beam is directed through a Glan-Thompson polarizer (GTP), and a dispersing lens (DL) to the sample. The dissolved sample (S) is situated in a quartz cuvette standing in a temperature adjustable cuvette holder (CH). Temperatures are regulated by a refrigerated/heating circulator (RHC). Emitted fluorescence is detected under L-shape geometry after passing an emission filter (EF), a polarizer (p) set to the magic angle configuration and a focusing lens by a micro-channel plate (MCP) detector. Signals from MCP and PD are preamplifier (PA) and processed by a SPC-830 TCSPC module. A shutter unit protects the MCP unit from ambient light while samples are exchanged.

The Ti:Sa excitation beam is reflected on a beam splitter which transmits a small amount of the excitation beam. The transmitting fraction is directed onto to a nanosecond-photo diode (DET210, Thorlabs). The generated electronic signal is amplified by a 1 GHz preamplifier (#9369, Ortec, Oak Ridge, Tennessee, U.S.A.) and serves as the excitation reference (stop) signal for the TCPSC measurements (see Section 2.2.1). The supercontinuum laser has a trigger/NIM output. This signal serves directly as a reference for the TCPSC cycles. The fraction of the excitation laser beam reflected on the beam splitter is adjusted in intensity by a set of neutral density filters installed in a dual filter wheel to final excitation intensities in the µW range. This low intensity prevents "pile-up" effects in the fluorescence decay histograms as the ratio between start and stop signals does not exceed the critical number for single photon counting of 1:200. After passing the sample enclosure, a Glan-Thompson polarizer (GTP) orientated to the vertical axis, filters a potentially residual fraction of non-vertically polarized photons from the excitation beam before a disperse lens expands the beam for a homogeneous sample excitation.

Fluorescent samples in solution are placed into a 3 x 3 mm quartz-cuvette (Helma), that is inserted into a temperature-controlled cuvette holder. A refrigerating/heating circulator (F25-MU, Julabo, Seelenbach, Germany) adjusts the temperature which is supervised by a reference thermometer. Fluorescence detection takes place under a L-shape geometry, that is, a 90 ° angle between excitation and detected emission. Along the detection path axis, the fluorescence is filtered from residual scattering excitation photons by an emission filter (see Table 3.1). A subsequently installed sheet polarizer rotated to 54.7 °, in respect to vertical axis (magic angle configurations) avoids polarization effects (see Figure 2.2.3). A lens focuses the fluorescence emission to a micro-channel plate detector (MCP, R3809U, Hamamatsu, Hamamatsu, Japan) installed into a thermoelectric cooled housing in order to establish the necessary working temperatures for a minimal dark count level. A 1.6 GHz preamplifier (HFAC-26, Becker & Hickl) amplifies the generated detector signal, which is fed into a TCSPC module (SPC-830, Becker & Hickl) in addition to the signal from the reference photo diode. The SPC-830 module is operated in first-in-first-out (FIFO) mode. This measurement configuration prevents the after-pulsing behavior of the R3809U-MCP detector.[214] The SPC-830 collects the photon into 1024 time bins with a bin width of either 9.98 ps or 19.97 ps. Light scattering experiments using a colloidal silica solution (LUDOX, Grace, Columbia, Maryland, U.S.A.) allowed to determine the instrument response function (IRF) of the system to be less than 40 ps (FWHM) using Ti:Sa excitation.

3.3.4 Confocal fluorescence lifetime imaging microscopy

Confocal TCSPC-based fluorescence lifetime imaging microscopy (FLIM) was performed in a custom-built FLIM setup of Prof. Alexiev's lab.[19, 48, 130] The setup utilizes an inverted microscope body (IX71, Olympus, Tokio, Japan) equipped with 4 objectives: A 60x water objective (NA=1.2, UPLSAPO60XW, Olympus, Japan) resulting in a total field of view (FOV) of 300 µm side length for highly resolved images of cells and tissue, and three air objectives with a 4x, 20x, and 40x

(NA=0.1/0.4/0.65, Olympus) magnification used for topographic images. Fluorescence was excited by one of two installed laser systems depending on the target wavelength.

On the one hand, a picosecond-pulsed supercontinuum white light laser (SWL) source (400 – 2400 nm, 6 ps (FWHM), SuperK Extreme EXU-3, NKT Photonics, Birkerød, Denmark), with a tunable repetition rate was used, typically adjusted to 19.5 MHz. The generated white-light was spectrally filtered by an acousto-optical tunable filter (AOTF, SELECT UV-VIS, NKT Photonics, Denmark) for selective fluorescence excitation. In order to obtain a spectral clean excitation beam, a quad-notch laser filter (ZET 405/488/532/642, Chroma, U.S.A.) is installed removing residual light passing the AOTF at the target excitation wavelengths: 405 nm, 488 nm, 530 nm, and 640 nm. On the other hand, a ps-pulsed laser diode (BDL-405-SMT, Becker & Hickl, Berlin, Germany) served as excitation source emitting photons at 405 nm. The laser diode has a pulse width of less than 100 ps and a repetition rate of 20 MHz. Laser scanning, optical coupling of excitation light to the microscope, and confocal detection was implemented by using a scanning unit (DCS120, Becker & Hickl).

The DCS120 contains two mirror galvometers, spatial pinholes, a main excitation/emission dichroic (mirror) beam splitter, a scanning lens, a secondary dichroic allowing for the beam-splitting between two accessible detection channels, and emission filter holders for spectrally resolved fluorescence detection. Emission filters were selected in dependence on the investigated fluorophore and are summarized in Table 3.1. Gallium arsenide phosphide (GaAsP) hybrid PMTs (HPM-100-40, Becker & Hickl) detect fluorescence photons. The generated signals are processed by a time-correlated single photon counting (TCSPC) module (SPC-160, Becker & Hickl). FLIM-images were recorded by the SPCM software (Becker & Hickl) with a spatial pixel number of 512x512 pixels and temporal resolution of 1024 time bins with a bin width of 19.97 ps. The instrument response function (IRF) of the FLIM system was determined to be less than 130 ps (FWHM) by light scattering experiments using a colloidal silica solution (LUDOX, Grace, Columbia, Maryland, U.S.A.). For temperature dependent investigations, a temperature-controlled specimen holder was installed. Please see Section 4.1 for a more detailed description of the newly established and configured FLIM setup. A scheme of the TCPSC-FLIM setup is shown in Figure 4.1.1.

3.3.5 Multiphoton fluorescence lifetime imaging microscopy

Multiphoton FLIM (mpFLIM) was conducted in a custom-built setup. A mode-locked pulsed femtosecond titan:sapphire laser (Mira 900, Coherent, USA) is pumped by a diode-pumped solid state laser (Verdi V5, Coherent, USA) generating laser pulses shorter than 200 fs with a repetition rate of 76 MHz at a wavelength of 800 nm (FLIM-ROX) or 845 nm (CMS-ICC/bodipy). An objective (NA=1.2, 60x water, UPSLAPO60XW, Olympus, Japan) focused and a scanning unit (DCS-120, Becker & Hickl, Germany) scanned the excitation laser beam over the sample placed on an inverted microscope (IX-73, Olympus, Japan). Fluorescence emission was separated from excitation by a dichroic beam splitter with an edge wavelength of 705 nm (705 nm edge BrightLine multiphoton

single-edge, Semrock, USA) for the CMS-ICC/bodipy experiments, or an edge wavelength of 643 nm (H 643 LPXR superflat, AHF, Germany) for the FLIM-ROX experiments and in both cases with a fixed protection short-pass filter (700 nm, O-FSP-700-22MM, Becker & Hickl, Germany) to remove residual excitation photons. For FLIM-ROX, only a single detection channel was used with a spectral window between 500 and 550 nm using a 525/50 bandpass filter. CMS-ICC fluorescence was separated from bodipy fluorescence and other fluorescent species by a dichroic beam splitter with an edge wavelength of 532 nm and a combination of a long-pass filter (>575 nm, Chroma, Rockingham, USA) and a short-pass filter (<600 nm, Coherent, Santa Clara, USA) generating a spectral detection window between 575 and 600 nm for CMS-ICC. The second detector channel uses a 480/40 nm band pass filter to selectively determine bodipy fluorescence. Fluorescence photons were collected in non-de-scanned detection mode by hybrid detectors (HPM-100-40, B&H, Germany). The IRF of the system was below 130 ps (FWHM). Collected photons were sorted into 1024-time channels (width 9.7 ps) by a TCSPC module (SPC-160, Becker & Hickl, Germany). A scheme of the setup is shown in Figure 4.1.3. Please see also Section 4.1.2 for a more detailed description of the newly established mpFLIM setup.

3.3.6 Dichroic beam splitters and fluorescence emission filters

Table 3.1: Fluorescence emission filters. Applied filters are indicated by short names in the respective Figure legends.

short name	manufacturer	product name	filter type	λ (nm)
452/45	Semrock	BrightLine 452/45 HC	band-pass	430 - 475
480/40BP	Chroma	ET480/40m	band-pass	460 - 500
525/50BP	Chroma	ET525/50m	band-pass	500 - 550
G515LP	Schott	OG515	long-pass	> 515
H515LP	Semrock	BrightLine 515/LP HC	long-pass	> 515
545LP	Chroma	HQ545LP	long-pass	> 545
575LP	Chroma	AT575LP	long-pass	> 575
580BP	Edmund	47139 THGC	band-pass	575-585
600SP	Coherent	35-5388	short-pass	< 600
630BP	Edmund	EO65706	band-pass	630-635
665LP	Chroma	ET665LP	long-pass	> 665
715LP	Schott	OG715	long-pass	> 715
745SP	Semrock	SP745 BrightLine HC	short-pass	< 745
Quad-Notch filter	Semrock	405/488/532/635nm StopLine quad-notch	notch filter	411-480 496-523 541-629 629-646
DM-BS 532	AHF	Z 532 RDC	beam splitter	532
DM-BS 643	AHF	H 643 LPXR superflat	beam splitter	643
DM-BS 705	Semrock	705 nm edge BrightLine multiphoton single-edge	beam splitter	705

3.4 Analysis of time-resolved fluorescence data

3.4.1 Time-resolved ensemble fluorescence spectroscopy

Fluorescence decay traces are analyzed using the software package Globals Unlimited V2.2 (Laboratory for Fluorescence Dynamics, Irvine, California, U.S.A.). Globals Unlimited fit the fluorescence time traces by an iterative non-linear least square analysis (see Section 2.2.1) using sums of exponentials (Eq. 19). The exact fit parameters f_i are indicated in the respective Figures and Tables of Chapter 4: results and discussion. The quality of the fit and selected decay model was verified by the χ^2_{red} parameter and weighted residuals $R_{\mathrm{w}}(t_j)$, according to Eq. 45 and Eq. 46. A fit of an exemplary fluorescence decay traces is shown in Figure 3.4.1A.

Uncertainties of the individual fit parameters (Figure 3.4.1B,C) can be estimated using a confidence interval analysis according to Ref. 215. For this purpose, the fluorescence decay traces are first subjected to a non-linear least square analysis, i.e., minimization of the χ^2_{red} parameter using all fit parameters f_i. Subsequently, the confidence interval of each parameter f_i is analyzed separately in an exhaustive error analysis approach. To this end, equidistant values $f_{\mathrm{fix},i,j}$ are defined in an interval around the f_i to be analyzed. For each of these $f_{\mathrm{fix},i,j}$, a new χ^2_{red} minimization is performed, but only the other fit parameters are set free and are varied. The investigated $f_{\mathrm{fix},i,j}$ is kept constant during this minimization. Through this process, the examined $f_{\mathrm{fix},i,j}$ can be plotted against the obtained χ^2_{red} values (see Figure 3.4.1D-F). The resulting plots can be fitted to a polynomial function, which allows to determine the value of f_i that generates the minimal χ^2_{red} value ($\chi^2_{\mathrm{red,min}}$).

In a next step, a confidence level $\chi^2_{\mathrm{red,conf}}$ is calculated, which is defined as:

$$\chi^2_{\mathrm{red,conf}} = \chi^2_{\mathrm{red,min}} + \frac{\Delta\chi^2_{\mathrm{red}}\,(p,\nu)}{N} \qquad , \tag{68}$$

with N being the number of time bins and $\Delta\chi^2_{\mathrm{red}}\,(p,\nu)$ being a parameter defining the boundary of the confidence interval. The probability distribution of the determined fit parameters is generally not normally distributed. However, it is assumed that the confidence level is the value of χ^2_{red}, where the percentage p to find a certain value in the probability distribution is 68.3% (uncertainty of 1 σ). The number of parameters of interest ν is one since the confidence interval analyses are performed for each f_i separately. For these values of p and ν the boundary parameter $\Delta\chi^2_{\mathrm{red}}\,(1\sigma,1)$ amounts to 1.00 according to Ref. 216. After calculating $\chi^2_{\mathrm{red,conf}}$, the intersections between this level and the polynomial function determined before can be located (see Figure 4.3.1D). These intersection points define the confidence interval for the investigated f_i. The obtained values are rounded up to a single significant digit and are used as uncertainty measure of the fluorescence decay fitting analysis (Figure 4.3.1B,C). Uncertainties of mean fluorescence lifetimes (Eq. 20 & 21) and relative steady-state fluorescence populations (β_c) are calculated by Gaussian uncertainty propagation.

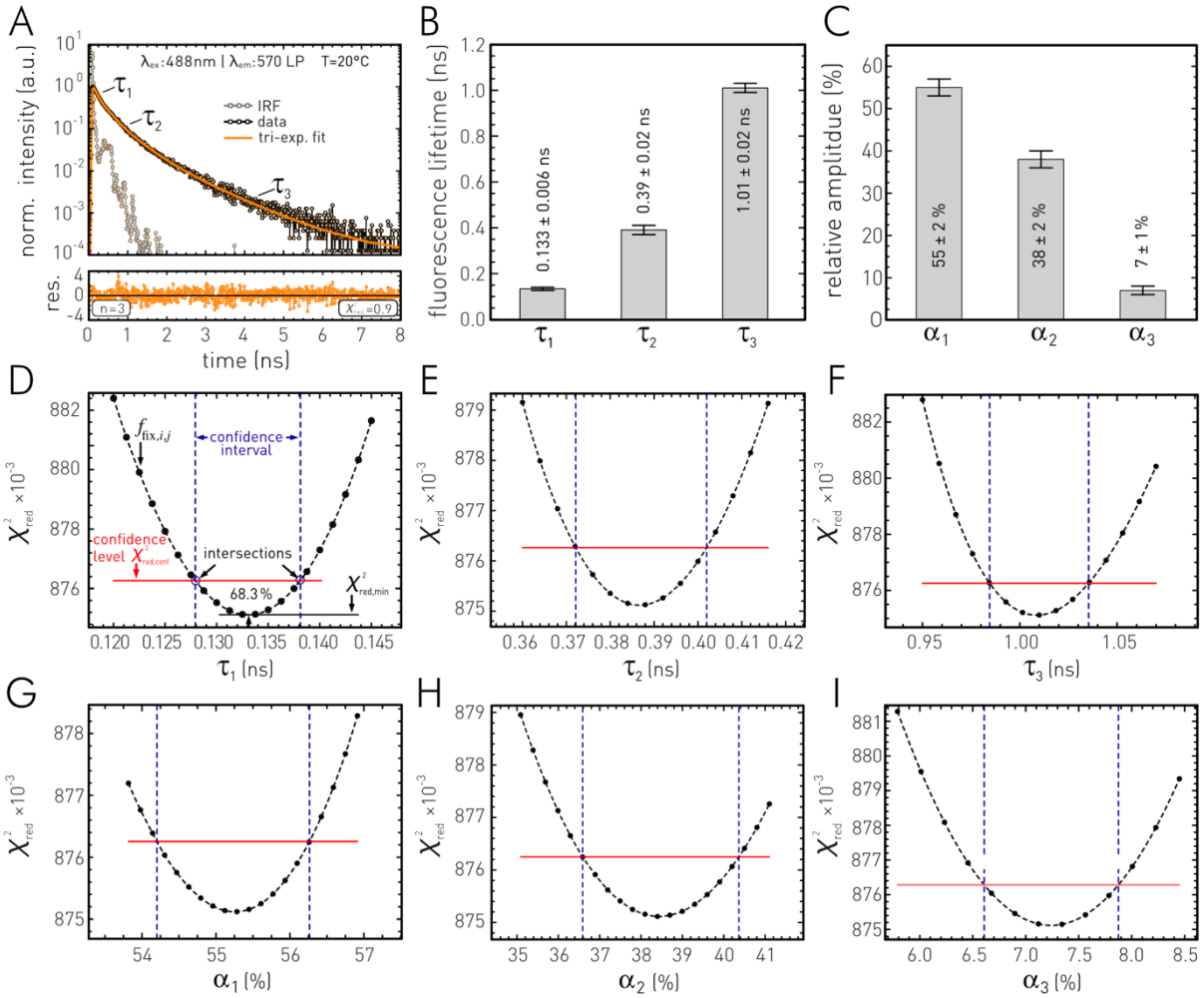

Figure 3.4.1: Estimation of fit parameter uncertainties in the applied iterative non-linear least square fitting analysis of fluorescence decay curves. **A** Exemplary fluorescence decay trace of dPGS-ICC, experimental conditions as indicated. The orange line indicates a three-exponential decay fit (n = 3). Instrument response function (IRF) is shown in gray. The correspondent weighted residuals (res.) are shown below. **B** Resulting fluorescence decay components of the fitting procedure and correspondent uncertainties determined by a confidence interval analysis. **C** Relative amplitudes of the three decay components and their uncertainties. **D-I** Determination of the confidence intervals of the individual fit-parameters. The calculated confidence level is indicated by a red continuous line. The minimal χ^2_{red} is illustrated by a black continues line. The confidence interval is indicated by two blue dashed lines. It is determined by the crossing points of the confidence level and the dashed black line (polynomial fit) connecting the points $(f_{\mathrm{fix},i}, \chi^2_{\mathrm{red}}(f_{\mathrm{fix},i}))$.

3.4.2 FLIM analysis

Raw TCSPC FLIM data typically contains the information of thousands of fluorescence decay histograms originating from every pixel of a microscopic image. The pixel-based decay histograms may originate from a multitude of fluorescing molecules and/or varying fluorescence decays of the same fluorophore, depending on the local environment at a certain location. The data structure can be represented as an array $\mathrm{X} = [t_1, \ldots, t_i \ldots t_b]$ of b image pixels i, where t_i depicts the individual fluorescence decay histograms $t_i = (t_{i,1}, \ldots, t_{i,j}, \ldots t_{i,N})^T$ which themselves consist of N time bins indexed by j. The width of a time bin is given by δ_{t}.

To visualize the fluorescence decay information of the FLIM data in false color images, the pixel-based decay histograms must be parameterized. This parameterization can be done by different methods. The limiting experimental factor for a good parameterization is the number of photons counted per image pixel. The number of photons is often limited due to fast acquisition times, high magnification levels, phototoxicity and photobleaching. Methods such as the tau-plot analysis, which uses classical decay fitting, utilizes local pixel binning to increase the number of photons up to a sufficient level to provide a reliable fit result. It is important to note that about 10,000 photons are needed to fit a bi-exponential decay with low uncertainty.[36] Of course, this approach is at the expense of spatial resolution, but is particularly necessary when multi-exponential decays are present. Advanced FLIM analysis procedures select other parameterizations.[37-39] These methods include the fast global fitting procedure (FLIMfit)[39], the Bayesian estimation analysis[37], pattern matching[40] with reference fluorescence decays and spectral information, graphically based parameterization such as the phasor approach[41, 217], or pattern recognition methods like the Cluster-FLIM analysis.[44]

Tau-plot analysis

The direct way to analyze TCPSC based FLIM data is the tau-plot method. The approach transforms fluorescence intensity images like in Figure 3.4.2A into false-color FLIM images representing fluorescence lifetime parameters continuously. Figure 3.4.2A displays four different fluorophore solutions: ICC, RhoB, FluNa and a 1:1:1 mixture of all three fluorophores. The exemplary false tau-plot analysis shown in Figure 3.4.2C directly visualizes the mean lifetime of each solution directly by the overlaid coloring. The underlining process sequence of the tau-plot analysis is illustrated in Figure 3.4.2B.

The analysis starts with pixel-based curve fitting (1&2, Figure 3.4.2B) of all decay histograms by mono- or multi-exponential model functions (Eq. 19) revealing a set of fluorescent decay parameters (3, Figure 3.4.2B). As described in Section 2.2.1, this procedure needs a frequently repeated deconvolution and reconvolution of the fluorescence decay signal and the IRF during the non-linear least square fitting steps. The number of pre-selected fluorescence decay components is judged by χ^2_{red} and $R_w(t_j)$ according to Eq. 45 & 46. The decay parameter can be visualized in a frequency distribution histogram, showing how many pixels have a certain parameter value. The histogram can be further analyzed by a (multi-)Gaussian fit analysis. These analyses were performed in Origin 2019 (OriginLab, Northampton, Massachusetts, U.S.A.). In a next step, one assigns a distinct color to a specific decay parameter (4, Figure 3.4.2B). This false-color code is then applied to the FLIM image, where pixels obtain a parameter specific color, typically overplayed with the total intensity in the pixel (5, Figure 3.4.2B). By default, one selects the mean fluorescence lifetime (Eq. 20 or 21) to color-code the FLIM image as it reflects the average fluorescence lifetime present in each image pixel. However, some applications require individual decay components, their respective amplitudes, or ratios, in this case these parameters are color-coded accordingly.

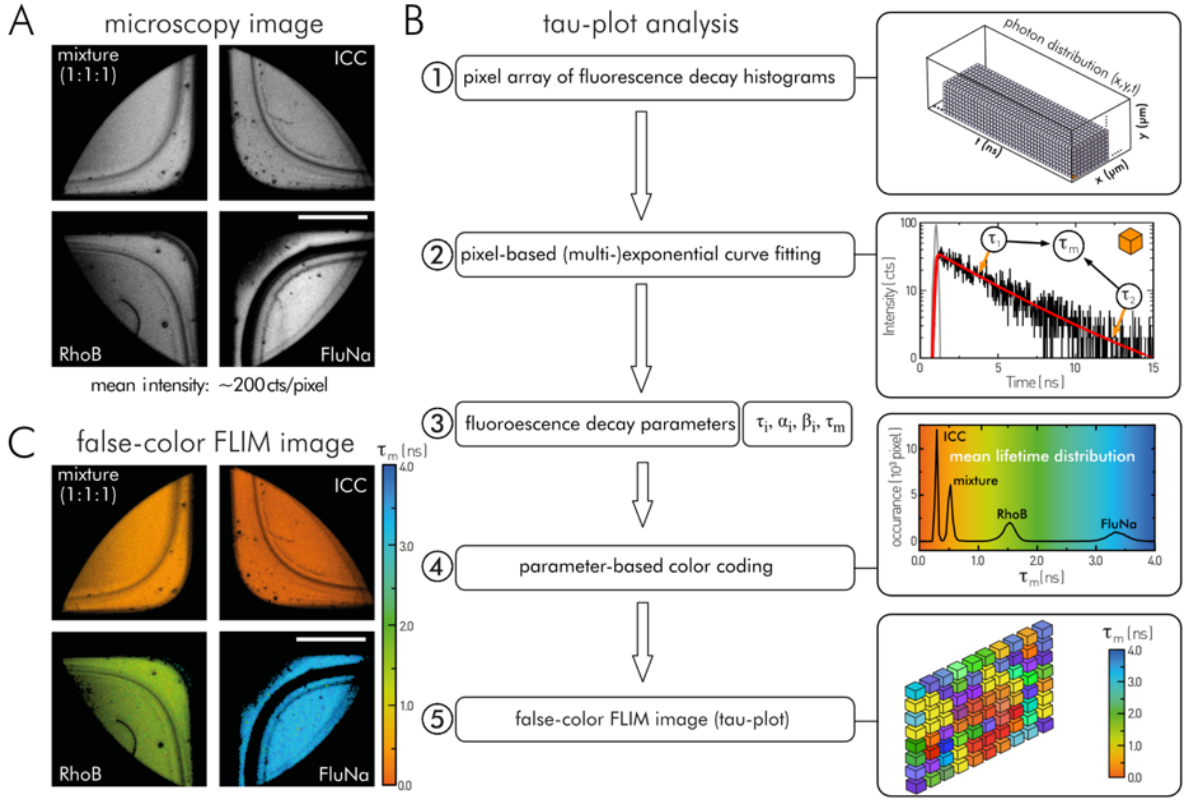

Figure 3.4.2: Process sequence in a tau-plot FLIM analysis. **A** Intensity-based microscopic images of ICC, RhoB, FluNa and a 1:1:1 mixture of all three fluorophores in PBS, pH 7.4. The average total intensity per pixel amounts to 200 cts. The fluorophore solutions were placed into a in 4-well glass bottom dish and recorded simultaneously using the confocal FLIM setup (see Section 3.3.4) and a 4x air objective. Scalebar represents 700 µm. **B** Process sequence of a tau-plot FLIM analysis: False-color FLIM images are generated by pixel or pixel-area based (multi-)exponential decay fitting and parameter-based color coding. **C** Tau-plot analysis: false-color FLIM images of the fluorophore solutions shown in A in accordance to the mean fluorescence lifetime.

The benefit of tau-plot analyses is the possibility of continuous color-coding of image pixels, which reflect continuous distributions of decay parameters occurring in many FLIM images of biological samples. The major drawback of the method is the need for high photons counts per image pixel if the FLIM data has to be fitted to multi-exponentials.[36] In some experimental scenarios one can improve the photon statistics by long acquisition times or high excitation intensities, which, however, may lead to artefacts through fluorescence bleaching or other dynamic long-term effects. In many FLIM experiments, the amount of photon counts per pixel is immanently limited. Here, spatial re-binning of pixels is an option. Re-binning is achieved by merging decay histograms of several locally neighboring pixels in order to increase the photon statistics and validity of the fit at the expense of spatial resolution. Another general drawback of tau-plot analyses is the reduction of fluorescence decays to a single parameter. In the case of complex decay traces, this parameter can be ambiguous, because different multi-exponential decay traces can lead to the same parameter, e. g., when choosing the mean fluorescence lifetime or selecting the ratios of decay components. An effect which is aggravated with an increasing number of decay components (multi-exponentials). This problem was observed in a previous study where the phenomenon led to false positive identifications of a fluorescent probe in an autofluorescent background.[198] The authors conclude that their tau-plot based

ratiometric approach loses its sensitivity if more than two decay components are required. Also, the constant number of decay components during the analysis of a tau-plot FLIM image can lead to artifacts since FLIM images can contain fluorescent species, whose number of decay components varies significantly. In order to determine a reasonable FLIM parametrization providing the identification and discrimination of different complex decay traces at lower photon counts and full image resolution, other non-fitting-based analysis approaches have emerged in the last years.[19, 37, 40-43, 218]

Phasor-plot analysis

The phasor-plot analysis for FLIM is based on Fourier transformations first described by Weber for fluorescence lifetime data.[217] In the case of phase-modulation FLIM, one can directly transform the frequency dependent modulation ratio M_i and phase-shift ϕ_i of each image pixel i to polar (phasor) coordinates, short phasors (P_i ,Q_i) by:

$$Q_i(\omega) = M_i(\omega)\sin(\phi_i(\omega)) \tag{69}$$

$$P_i(\omega) = M_i(\omega)\cos(\phi_i(\omega)) \quad , \tag{70}$$

This is equivalent to consider a vector of length M_i, that form an angle with the Q-axis given by ϕ_i (see Figure 3.4.3A). For TCSPC data, a decay histogram t_i can be Fourier transformed to phasors by

$$Q_i(\omega) = \frac{\sum_{j=1}^{N} t_{i,j}(t)\cos(\omega\, j\, \delta_t)}{\sum_{j=1}^{N} t_{i,j}(t)} \tag{71}$$

$$P_i(\omega) = \frac{\sum_{j=1}^{N} t_{i,j}(t)\sin(\omega\, j\, \delta_t)}{\sum_{j=1}^{N} t_{i,j}(t)} \quad . \tag{72}$$

Jameson et al. introduced a geometrical representation for systems of heterogenous lifetimes, called phasor-plot (P_i vs. Q_i), that is, a polar-plot that visualizes a set of fluorescence lifetime measurements like the individual pixels i of a FLIM image.[219] For mono-exponential fluorescence decays, one can make use of Eq. 36 – 38 to obtain a simple relationship between M_i and ϕ_i:

$$M_i(\omega) = \cos(\phi_i(\omega)) \quad . \tag{73}$$

A consequence of this relationship, together with Eq. 69 & 70 is that all mono-exponential fluorescence decays are located on a universal semicircle (Figure 3.4.3A) with a diameter of one, that centers on the Q-axis at the coordinate (0.5,0). In other words:

$$(Q_i - 0.5)^2 + {P_i}^2 = 0.25 \quad . \tag{74}$$

Multi-exponential decays can be considered as being linear combinations of individual mono-exponential decays and thus located within the semicircle (see Figure 3.4.3B). Bi-exponential decays can be found on a line connecting the generating mono-exponential decays. The respective distances

between these mono-exponential decays reflect the weighting and corresponds to the relative amplitudes (Figure 3.4.3B). The same concept applies to tri-exponential and higher multi-exponential decays which are located in a connecting triangle or higher dimensional polygons of the generating decays. If a fluorescence decay is found outside the semicircle, the reason can be background noise or reactions during the excited state, like dipole interactions (FRET) or excimer formations.[220]

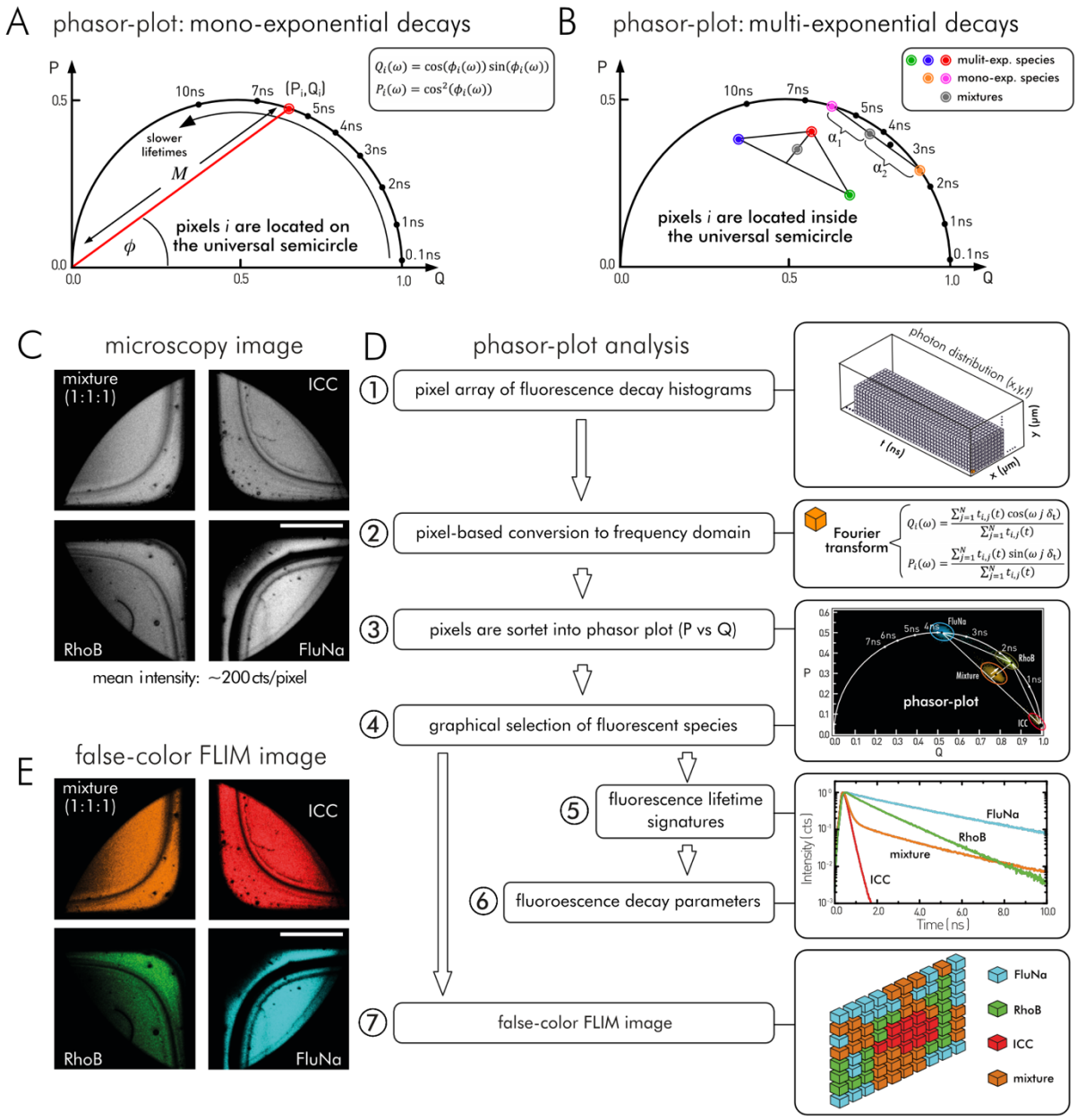

Figure 3.4.3: Process sequence in a phasor based FLIM analysis. **A** Phasor-plot interpretation: phasors (P_i ,Q_i) containing mono-exponential decays are located on the universal cycle. **B** Phasors containing multi-exponential decays are located inside the universal cycle. Mixtures of two exponential species locates on a connecting line between them. Pixels containing mixtures of three species locates in the connecting triangle. **C** Intensity-based microscopic images of ICC, RhoB, FluNa and a 1:1:1 mixture of all three fluorophores in PBS, pH 7.4. The average total intensity per pixel amounts to 200 cts. The fluorophore solutions were placed into a in 4-well glass bottom dish and recorded simultaneously using the confocal FLIM setup (see Section 3.4.4) and a 4x air objective. Scalebar represents 700 µm. **D** Process sequence of a phasor based FLIM analysis for time domain data: Decay histograms in each image pixel i can be transformed to the Fourier space (P_i ,Q_i) using Eq. 71 & 72. Afterwards all pixels are sorted into a phasor plot (P vs. Q). Separated fluorescent species can be graphically selected. By accumulation of all decay histograms of a found species

generates a species characteristic fluorescence lifetime signature (FLS). Finally, a false-color FLIM image is produced by coloring all image pixel belonging to the same fluorescent species with the same color. **E** False-color FLIM image of the fluorophore solutions shown in C in accordance to the revealed fluorescent species. The phasor-based identification for this example works accurately as each fluorophore solution has a discrete color.

The application of the phasor approach in FLIM allows for a graphical separation and identification of fluorescent species or, more exactly, pixels containing these species, based on a geometrical separation of the lifetime information in the phasor-plot.[41] In the case of TCSPC FLIM data, the pixel-based fluorescence decay histograms are converted into phasor coordinates by Eq. 71 & 72 (2, Figure 3.4.3D).[217] The phasor coordinates are then plotted in a 2D phasor-plot. Pixels containing similar fluorescence decay patterns, i.e., phasor coordinates, will scatter around accumulation points (3, Figure 3.4.3D). These aggregations of image pixels enable a graphical selection of fluorescent species (4, Figure 3.4.3D), which can also be used for the identification of certain fluorescent species in different FLIM images. The false-color coding of the image pixels is accomplished by assigning a discrete color to the identified species (7, Figure 3.4.3D).

For TCSPC FLIM data, one can generate fluorescence lifetime signatures (FLSs) of identified species by accumulating the single time bins of all decay histograms assigned to a species. This results in a species characteristic decay histogram (5, Figure 3.4.3D). Supplemental curve-fitting of such an FLS reveals underlying decay parameters (6, Figure 3.4.3D). Beside the intuitive graphical interpretation of FLIM data, the phasor-plot has additional benefits: it prevents systemic errors and provides fast computation times by avoiding complex and thereby time-consuming curve-fitting. Finally, the phasor-plot can be applied to quantify FRET data using the FRET trajectory approach.[220]

As an example, four different fluorophore solutions: ICC, RhoB, FluNa and a 1:1:1 mixture of all three fluorophores are subjected to FLIM and subsequently analyzed by a phasor analysis. Figure 3.4.3C displays microscopic fluorescence intensity images of the recorded fluorophore solutions. After transformation into phasor coordinates (Eq. 71 & 72), the image pixels are visualized in a phasor-plot (4, Figure 3.4.3D), showing four separated groups of pixels representing the four solutions. ICC, RhoB, and FluNa feature accumulation points on the universal semicircle and thus exhibit mono-exponential decays. As expected, the 1:1:1 mixture is located within the semicircle. More precisely, one observes the accumulation point in the connecting triangle of the three pure fluorophore solutions. As shown by the false-color coded FLIM image in Figure 3.4.3E, identification by the phasor-plot worked out (3, Figure 3.4.2D): Each fluorophore solution has a discrete color.

Cluster-FLIM analysis

The Cluster-FLIM method was developed by Robert Brodwolf and Prof. Alexiev at the Freie Universität Berlin.[44] The automated multivariate clustering method groups pixel-based (multi-)exponential fluorescence decay curves in accordance to their feature similarity into clusters without any *a priori* information and extracts a fluorescence lifetime signature (FLS) for each found group (cluster, fluorescent species) which represents the characteristic fluorescence decay curve of the respective group. Cluster-FLIM uses no pixel-based decay fitting algorithm and is cable to distinguish different and multi-exponential fluorescence decay curves in a single FLIM-image or a set of FLIM-images by parametrizing and clustering decay characteristics (Figure 3.4.4). The method can preserve the full resolution of the FLIM image as it typically avoids combining neighboring pixels, necessary in pixel-based decay fitting at low photon counts per pixel.

The common multi-exponential fluorescence decay characteristics and the Poisson distributed signal noise in FLIM-images restrict the extraction of the underlying fluorescence decay parameters.[40] The general problem of determining the intrinsic unknown structure of the fluorescence decay data, when no information other than the recorded FLIM data is available, can be solved by grouping similar patterns (fluorescence decays) into clusters. The members of these clusters are to be more similar to each other than to members of other clusters according to some similarity/dissimilarity measure used by a cluster algorithm, e.g., the Euclidian distance in *k*-means.[221] No *a priori* knowledge of patterns (i.e. FLS) that belong to certain groups is necessary for this type of clustering. The raw FLIM data described by a set of patterns $\mathrm{X} = [t_1, \dots, t_i \dots t_b]$, where t_i represents the fluorescence decay histogram $t_i = (t_{i,1}, \dots, t_{i,j}, \dots t_{i,N})^T$ in a single image pixels i of a FLIM-image built-up by b pixels. A d dimensional feature space $\mathbb{R}^{\mathrm{d}}$, with the individual features $x'_{i,j}$ is generated and the Euclidian distance D_{ij} for each cluster member x'_i to a respective cluster center x'_c is calculated by

$$D_{ij} = \left(\sum_{l=1}^{d} \left| x'_{i,l} - x'_c \right|^2 \right)^{1/2} \tag{75}$$

and serves as a similarity/dissimilarity measure in the clustering. Using the distances D_{ij} the fluorescence decay patterns of the individual pixels were partitioned into meaningful groups (i.e. clusters) by applying the *k*-means algorithm.[221] A fluorescence decay trace is assigned to a certain cluster if its position lies within 2 σ of the cluster-center. Two clusters are regarded as dissimilar if their cluster centers are more than 1 σ apart. Assigning a distinct color to all pixels containing a fluorescence decay trace that belonged to a certain cluster generates false-color images. Figure 4.2.1 and 4.2.2 show an evaluation of the method.

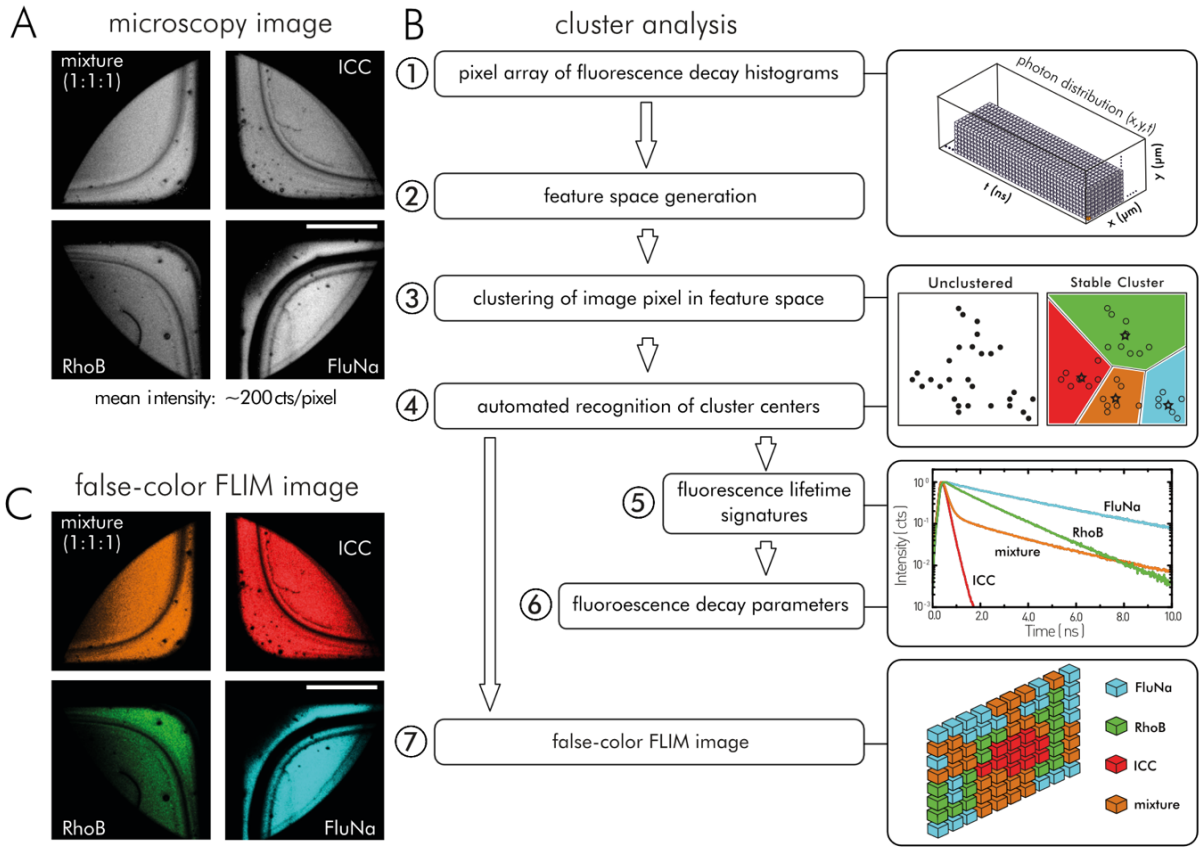

Figure 3.4.4: Process sequence in a cluster-FLIM analysis developed by Robert Brodwolf in the group of Prof. Alexiev (Freie Universität Berlin, Germany). **A** Intensity-based microscopic images of ICC, RhoB, FluNa and a 1:1:1 mixture of all three fluorophores in PBS, pH 7.4. The average total intensity per pixel amounts to 200 cts. The fluorophore solutions were placed into a in 4-well glass bottom dish and recorded simultaneously using the confocal FLIM setup (see Section 3.3.4) and a 4x air objective. Scalebar represents 700 µm. **B** Process sequence of a cluster-FLIM analysis: Decay histograms in each image pixel *i* are transformed to a low dimensional feature space. A clustering algorithm groups pixels with similar decay characteristics (pixels containing the same fluorescent species) to clusters and determines the cluster centers (3, black stars). Cluster characteristic fluorescent lifetime signatures (FLSs) are generated by accumulation of all decay histograms in all pixels assigned to a cluster. The FLS can be used to investigate underlying decay parameters. Finally, a false-color FLIM image is produced by coloring all image pixel belonging to FLIM cluster with the same color. **C** False-color FLIM images of the fluorophore solutions shown in A in accordance to the four identified FLIM clusters. The clustering for this example works accurately as each fluorophore solution has a discrete color.

Chapter 4: Results and discussion

4.1 Characterization of custom-build FLIM setups and analysis tools

4.1.1 Supercontinuum white light lasers in fluorescence lifetime imaging microscopy

Typically, simultaneous fluorescence imaging of several fluorophores with distinguishable excitation bands requires more than one excitation source. Therefore, these imaging technologies often use several laser systems or laser sources with several laser lines to enable selective fluorescence excitation. TCSPC-based FLIM, as applied in this thesis, additionally requires picosecond pulsed excitation with repetition rates in the MHz range. Laser diode heads or titanium:sapphire (Ti:Sa) lasers offer such repetition rates and emit narrow excitation bands that allow specific fluorophore excitation and thus a fluorophore specific selection in the FLIM image. Using such laser systems has drawbacks like fixed wavelengths (diode heads) or the high costs of wavelength adjustable Ti:Sa systems. A restricted number of excitation wavelengths limits the choice of fluorophores. Another problem is that switching between individual laser units, laser lines, or wavelengths, for example by using an optical parametric oscillator, can lead to optical misalignments in the excitation and detection beam path and often results in optical artifacts.

To overcome these limitations, supercontinuum white light laser systems (SWL) are applied, emitting a broad wavelength range. Some spectroscopic and microscopic studies use a broadband laser excitation generated by photonic crystal fibers (PCFs) which simultaneously excite fluorescence over a large energy spectrum.[222-228] With regard to time-resolved fluorescence, some studies have used light emitted by PCFs directly in order to excite different fluorophores simultaneously. Such experiments were previously described for a spectroscopic experiment,[228] or combined with optical filters to allow for selective excitation.[224, 227] For a long time, the self-assembly of a fiber lasers has limited the application of SWL in fluorescence studies. In recent years, however, commercial SWL lasers have become available, that offer picosecond laser pulses with a repetition rate in the kHz and MHz regime and a broad emission spectrum from UV to IR. These features make them suitable laser systems for FLIM applications. The SWL generated by the SuperK EXTREME EXU-3 (NKT, NKT Photonics, Birkerød, Denmark) ranges between 400 and 2400 nm. This laser system uses a polarization-maintaining single-mode PCF which is pumped by a seed laser at a wavelength of 1064 nm.[229]

In this section, I describe and characterize this SWL laser (SuperK EXTREME EXU-3) in combination with a continuous acousto optical filter (AOTF) as an alternative excitation source for fluorophore selective FLIM experiments. The SWL/AOTF-based excitation allows the simultaneous selection of one or multiple narrow spectral bands of the SWL spectrum as well as their relative intensities. This permits simultaneous selective excitation in multi-color FLIM experiments and thus overcomes some limitations of conventional single wavelength emitting lasers systems. The data shown below was first

published in Z. Phys. Chem. (Volz et al., Ref. 48). Hence, the next paragraph relies on the description I have given in this paper.

Equipping a confocal TSCPC-FLIM setup with a SWL/AOTF excitation source

In the context of my doctoral thesis, I have implemented the following TCSPC-FLIM setup that uses a SWL-laser/AOTF combination to generate multiple spectral excitation bands. Together with fast hybrid detectors, TCPSC cards and galvano scanners, the setup provides a picosecond time resolution that resolves the fluorescence decay within each pixel of a microscopic image (Figure 4.1.1). The used supercontinuum white light laser (SuperK Extreme EXU-3, NKT Photonics) emits a broad spectrum from 400 to 2400 nm with a maximum output power of 0.95 mW/nm. The seed laser for supercontinuum generation has a wavelength of 1064 ± 2 nm and a pulse width of ~5 ps. Its repetition rate is adjustable between 152 kHz to 80 MHz (Figure 4.1.1-1). With an AOTF (UV-VIS Select, NKT Photonics), up to eight narrow spectral bands (full width half maximum (FWHM): 1.8 – 8.5 nm) can be cut out of the UV-VIS range of the white light spectrum (400 – 650 nm, Figure 4.1.1-2), with individual band intensities continuously selectable. The number of simultaneous excitation wavelengths can be extended by 8 excitation bands in the IR range when using the second AOTF (Figure 4.1.1-2).

Before the spectrally selected photons are coupled into a broadband fiber (FD7, NKT Photonics), a quad-band clean-up filter (ZET 405/488/532/642, Chroma, U.S.A.) removes residual photons of other wavelengths. The broadband fiber is mechanically coupled into the first laser input of the scanner unit (DCS 120, Becker & Hickl, Berlin, Germany) for confocal laser scanning (Figure 4.1.1-3). The selected excitation photons pass the main beam splitter (z405/473, Becker & Hickl) and are directed onto the galvanometer scanning mirror. From here, the laser beam is directed into the inverted microscope (IX7, Olympus, Tokyo, Japan) through the scan lens (Figure 4.1.1-4). The objective focuses the beam onto a small volume centered in the focal plane. Within this excitation volume, fluorophores get excited (see Section 2.2.3). The scanning mirror is driven by a galvano controller (GVD120, Becker & Hickl), moving the laser beam over the specimen placed into a temperature-controlled specimen holder. A refrigerating/heating circulator (F25-MU, Julabo, Seelenbach, Germany) adjusts the temperature which is supervised by a reference thermometer. The size of the scanned field of view (FOV) depends on the objective. By using a 60× objective (UPLSAPO60XW, Olympus), a maximal FOV of 300 × 300 µm is accessible. The FOV can be resolved in up to 2048 × 2048 pixels. By applying finer scanning steps, the physical size of the FOV can be scaled down gradually up to a minimum of 30 × 30 µm while preserving the same pixel raster. The excitation beam scans in a repetitive mode leading to rather low pixel dwell times (typically 5 µs/frame) and reduces photobleaching. The acquisition time depends on the fluorescence intensity and varies typically between 1 and 15 min for tissue sections. Within this time range, a sufficient signal-to-noise ratio (SNR) of the TCSPC decay histograms can be obtained.

The emitted photons of the specimen are collected by the objective and directed back to the scan lens. Then, the emission light is de-scanned by the scanning mirror and the emitted photons pass the main beam splitter (z405/473) and the secondary beam splitter (options: 100 % detector 1, 100 % detector 2, polarizing beam splitter, 515 DCLP, 565 DCR). Here, photons can be directed on detector 1 and/or detector 2 (Figure 4.1.1-5). Before the photons hit the detector heads, they pass a pinhole and emission filter. The pinhole suppresses out-of-focus photons (Section 2.2.3) and the pinhole diameter (given in Airy units) can be adjusted for varying fluorescence intensities and for the required resolution. In addition to emission filters for selecting the desired emission range, a quad notch filter (see Section 3.3.6) suppresses the remaining photons from the excitation beam. Hybrid PMT detectors (HPM-100-40, Becker & Hickl) with an instrument response function (IRF) of about 120 ps FWHM and a quantum efficiency of 45 % (at 500 nm) collected the passing fluorescence photons. The installed GaAsP hybrid PMT tube (R10467-40, Hamamatsu) in the detector module guarantees time resolution in the picosecond range, clean IRFs and a negligible after-pulsing probability.[230] The signals of the single detected photons are fed into the signal port of the TCSPC modules (SPC-160, Becker & Hickl) and trigger the individual TSCPC start-signals. The corresponding stop-signals are generated via the sync pulse from the EXU-3 through the nuclear instrumentation module (NIM) port (Figure 4.1.1-1/6). The TCSPC modules sort the detected photons into 1024 time bins with a bin width of 19.97 ps.

For the fluorophores and fluorescence probes applied in this thesis, excitation wavelengths in the UV-VIS range are required. The applied SWL laser/AOTF1 combination generates photons for the fluorescence excitation in a wavelength range between 400 and 700 nm (Figure 4.1.2A). The maximum photon intensity of 333 µW was obtained when the AOTF selects a laser emission band at 590 nm (~6 nm FWHM). The intensity generally decreases towards the edges of the SLW spectrum, at 400 and 700 nm. This drop is particularly steep between 410 and 400 nm and 675 and 700 nm. Typically, an excitation intensity between 75 and 150 µW is selected for FLIM investigations on living cells or tissue sections, depending on the fluorophore concentrations and fluorophore stability in the investigated samples. Such low intensities can significantly minimize photobleaching effects. Higher intensities are only needed at very low fluorophore concentrations and only are beneficial if the fluorophore under investigation has a certain photostability.

To ensure selective fluorophore excitation and high temporal detection resolution, the spectral and temporal width of the excitation pulses must meet certain requirements. On the one hand, the number and width of the spectrally selected excitation pulses determine how precisely and how many different fluorophores can be excited with the laser system. On the other hand, the temporal pulse width determines the temporal resolution and the quality of the decay fit analyses. The temporal width of the excitation pulse is particularly important to correctly deconvolute and analysis of the fluorescence decay data since it defines the width of the instrument response function (IRF) and thus significantly determines the resolution limits for fast decay components.[129] For example, a TCSPC

system based on a Ti:Sa laser with a typical pulse width of 1.5 ps and a spectral width below 1 nm (FWHM), a MCP detector (see above), and the TCSPC module SPC-830 (Becker & Hick) generates IRFs of ~30 – 40 ps (FWHM). These temporal widths are typically constant over the entire accessible wavelength range (350 – 500 nm) of the tunable Ti:Sa laser system and allow a proper deconvolution that resolves fluorescence decay components up to a two-digit picosecond range.[129, 231] Fast decay components in this time scale can be observed especially when a strong fluorescence quenching occurs, often caused by strong molecular interactions.[232-233]

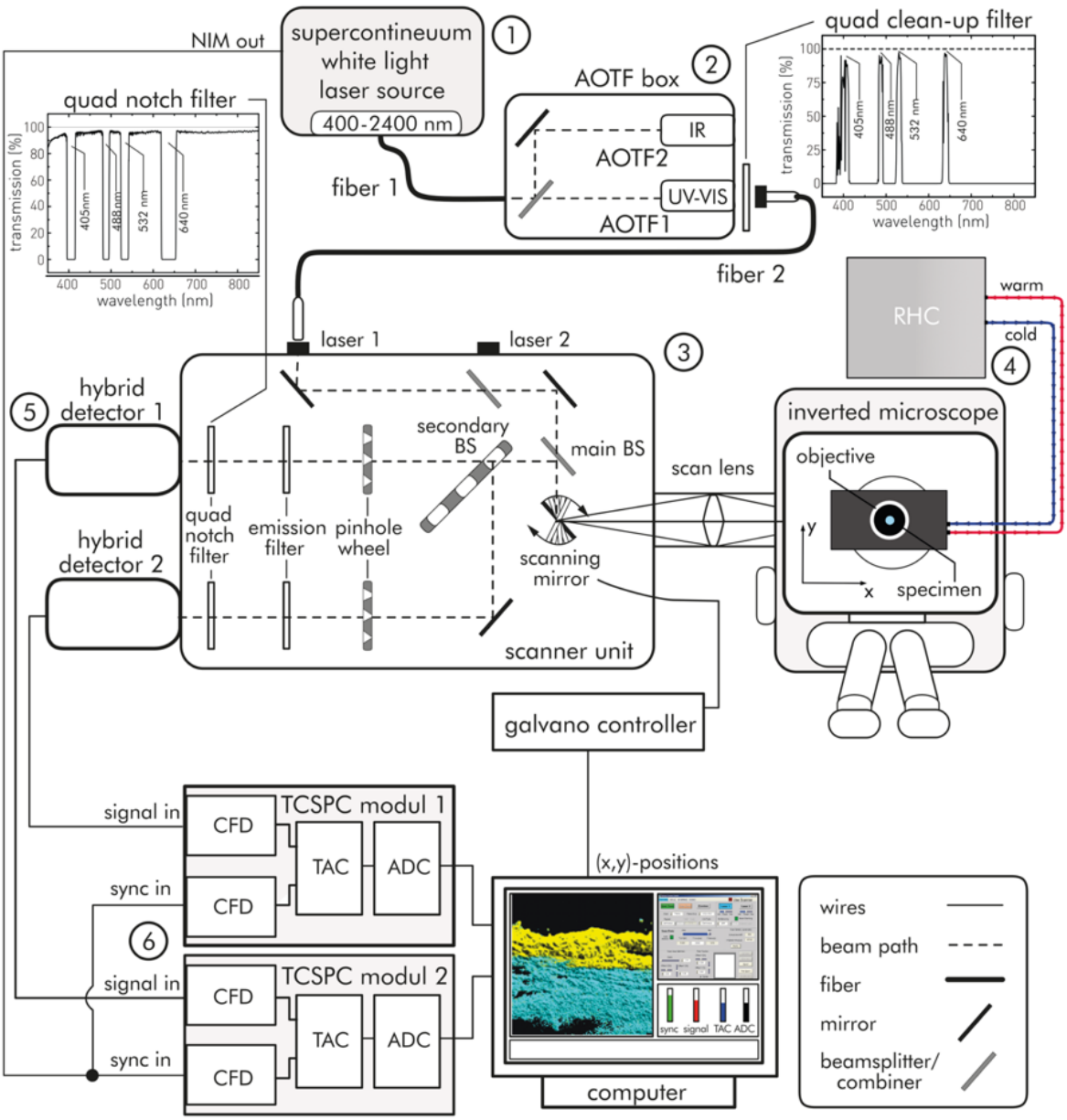

Figure 4.1.1: Scheme of confocal TCSPC-FLIM setup. Reprinted from Volz et al.[48], Copyright 2020, with the kind permission of the Z. Phys. Chem.. Abbreviations: NIM – nuclear instrumentation module; BS – beam splitter; AOTF – acousto optical tunable filter; IR – infrared; UV – ultraviolet. CFD – constant fraction discriminator; TAC – time to amplitude converter; ADC – analog to digital converter; RHC – refrigerated/heating circulator.

Characterization of the SWL/AOTF fluorescence excitation

The spectral excitation bands selected from the EXU-3 SWL spectrum via AOTF1 shows wavelength-dependent spectral widths, that become broader with increasing wavelengths. The FWHM ranges between 2.4 and 7.0 nm (Table 4.1.1, Figure 4.1.2B), with an approximately linear increase over the selectable wavelength range (Figure 4.1.2C). In comparison to the typical spectral widths of a picosecond Ti:Sa laser system of about one nm, this spectral broadening of the excitation pulses has to be taken into account. This is especially true when narrow excitation profiles in the red wavelength range are required. However, most fluorophores used in FLIM experiments have broad excitation bands. For these cases, the specified spectral widths of the SWL/AOTF excitation bands are sufficient.

Besides the differences in the spectral properties of the excitation bands, the time course of the excitation pulses has an elementary influence on the quality of TCSPC-based fluorescence lifetime experiments. Therefore, the influence of different selected excitation wavelengths on the IRFs will be investigated next. Due to the faster detector response of MCPs compared to Hybrid HPM detectors, these experiments were performed on the cuvette based TCPSC setup (Section 3.3.3) using colloidal silica solution (LUDOX, Grace, Columbia, Maryland, U.S.A.) as scattering martial to record the IRFs. The experiments reveal that depending on the wavelength, the IRFs in the TCSPC decay histogram shift in time due to the different propagation times of the emitted photons in the light guide material. Red-shifted photons of the generated SLW leave the fiber earlier than their counterparts from the UV range. If one now considers a TCSPC excitation/detection cycle (see Section 2.2.1), excitation photons from the red wavelength spectrum reach and excite the sample earlier, which means that the fluorescence photons generated by them also hit the detector head earlier. Since the TCSPC sync signal is triggered by the SWL seed pulse, the wavelength-dependent photon velocities within the PCF result in a time shift of the IRF and fluorescence decay traces within the decay histogram. The absolute time axis is not altered by this effect. Figure 4.1.2D,G illustrates the shifting behavior of the individual IRFs for the selected emission band 405, 488, 530 and 640 nm. The total absolute difference in the time shift between photons of 405 nm and 640 nm amounts to 1.4 ns.

The temporal width of the IRFs decreases from ~83 ps (FWHM) at 405 nm to ~52 ps (FWHM) at 640 nm (Table 4.1.1, Figure 4.1.2E,F). In contrast to the IRF of a titanium-sapphire laser system, the rising pulse edge is broader with a blue-shift of the excitation wavelengths (Table 4.1.1, Figure 4.1.2E). At 488 nm, the rising edge is pronounced to a plateau (arrow, 10 % max intensity, Figure 4.1.2E). This effect limits a reliable extraction of fluorescence decay components to a certain degree, especially in the lower picosecond range. A concrete photonic origin of the shoulder is not known. However, testing of several SLW laser types showed that all lasers produced such slowly rising IRF flanks with varying relative intensities and time periods. Since even SWL systems of identical construction types differ in the characteristics of the plateau, it is probable that the origin of these phenomena lies in the production process of the white light generating PCF.

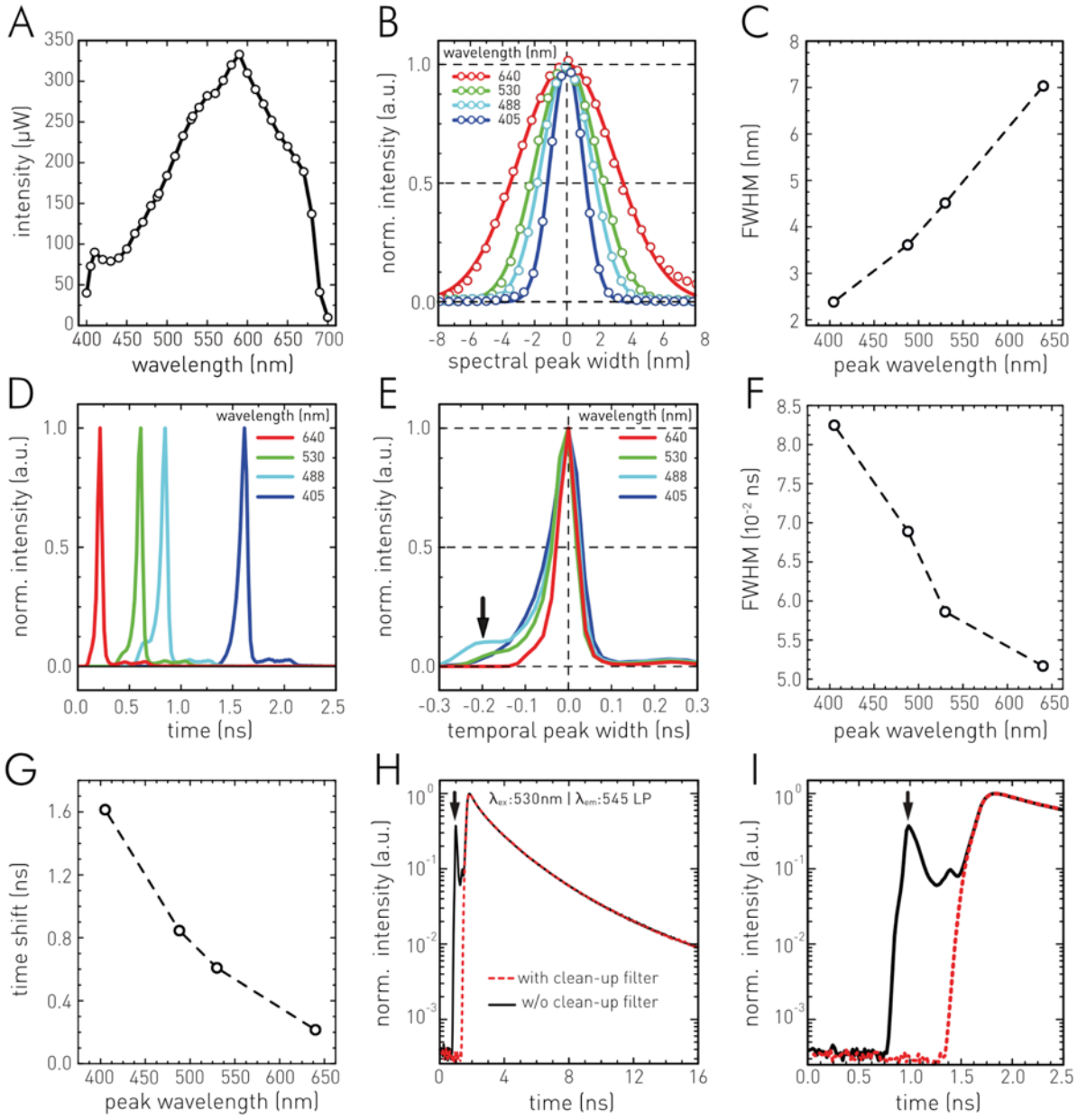

Figure 4.1.2: Characterization of the supercontinuum white light laser (SWL). **A** Laser intensity of EUX-3 after AOTF and fiber. **B** Spectral widths of single AOTF-selected emission wavelengths (405, 488, 530, 640 nm). **C** Spectral FWHM of the selected emission wavelengths in B versus the central wavelength. **D** Excitation pulses of the SWL laser recorded as instrument response functions (IRF) in the TCSPC-cuvette setup for selected wavelengths showing the real temporal sequence (E). **E** IRFs shown in D, with the temporal peak position located at the point of origin. **F** Temporal FWHM as function of selected wavelength (AOTF). **G** IRF time shift as function of selected wavelength (AOTF). **H/I** Implementation of a laser clean-up filter in the excitation path of the FLIM setup to avoid reflection artefacts in the optical pathway. **H** Fluorescence decay traces of human skin autofluorescence obtained by SLW laser excitation at 530 nm, and detection >545 nm with (red dotted) and without (black-straight-line) an installed clean-up filter. **I** Close-up to the temporal region of the pre-peak artefact.

If the SWL/AOTF-excitation in the FLIM setup is operated without any clean-up filter in the emission beam path, the recorded TCSPC decay histograms show photon detection artifacts. Figure 4.1.2H,I shows the fluorescence decay trace of autofluorescence in human skin tissue. The skin sample is excited at a wavelength of λ_{ex} = 530 nm, while the generated fluorescence emission is detected with an installed 545 nm long-pass filter and without a clean-up filter for the 530 nm excitation. The

black colored decay trace shows the effect of residual photons from unselected wavelengths, that were not suppressed entirely by AOTF1. The plot suggests that these photons may be reflected on the sample glass slide and find their way to the detector head. These incorrectly detected photons lead to a substantial pre-peak in the fluorescence decay trace (marked by the arrow in 4.1.2I) which directly indicates that the AOTF alone is not sufficient to remove all unselected photons from the entire SWL spectrum. The photons responsible for the pre-peak are red shifted compared to the selected excitation band because they emerge earlier in the TCSPC histogram. For that reason, they can easily pass through the installed emission filters and generate the pre-peak in the fluorescence decay histogram. Fitting a fluorescence decay trace with such an artificial pre-peak produces less accurate fluorescence decay data and circumvents a proper analysis due to incorrected deconvolution with the IRF.

To avoid the detection of such photons, a clean-up filter can be installed as shown by the red-colored decay trace in Figure 4.1.2H,I. In order to maintain the AOTF multi-color functionality, the use of a multi-band-clean-up or notch filter should be considered. In this FLIM setup a quad-band clean-up filter (ZET 405/488/532/642, Chroma, USA) is placed in front of the fiber coupling. Additionally, a matching quad-band notch filter (see Section 3.3.6) is installed into one of both emission filter holders of the DCS-120 (Figure 4.1.1). This allows to automatically change the excitation wavelength bands between the four wavelengths without changing the installed clean-up or notch filter mechanically. Another way to increase the efficiency of the AOTF and suppress red-shifted photons would be to loop the filtered light through the AOTF again. However, this process leads to losses in excitation intensity. In summary, it can be stated that SWL excitation in combination with AOTFs allows targeted fluorescence excitation in TCSPC-FLIM. The use of SWL-lasers allows to investigate several spectrally separated fluorophores within the same sample, thus reducing the acquisition time per sample. Thus, the simultaneous and selective imaging of several fluorophores in living cells or tissue sections can be achieved in a simple and efficient way.

Table 4.1.1: Characterization of excitation pulse widths for the application of the SLW laser system in TCSPC-FLIM. For characteristic excitation wavelengths selected by AOTF1, spectral width of the laser pulse and the generated Instrument response function (IRF) of the TCSPC system are given. Reproduction from Volz et al. (2018, Ref. 48), Copyright 2020, with the kind permission of the Z. Phys. Chem.. FWHM uncertainty corresponds to the selected spectral resolution. IRF uncertainty corresponds to a half temporal bin width.

selected wavelength (nm)	wavelength ± SD (nm)	spectral band width [FWHM] (nm)	IRF width (ps)
405	406 ± 1	2.4 ± 0.5	83 ± 5
488	489 ± 2	3.6 ± 0.5	68 ± 5
530	530 ± 2	4.5 ± 0.5	57 ± 5
640	640 ± 3	7.0 ± 0.5	52 ± 5

4.1.2 Establishing a multiphoton fluorescence lifetime imaging microscope

Multiphoton laser scanning microscopy (mpLSM) enables the non-invasive tomographic examination of microscopic structures hidden deep inside living organisms and tissue.[234] In contrast to traditional fluorescence microscopy, mpLSM excites fluorescence via nonlinear light absorption which can only be triggered by more than one photon (see section 2.1.1). Since cross sections of multiphoton absorption are extremely small, it is unlikely that these processes occur randomly within a photon field.[235] For this purpose, high photon densities are necessary, as they occur, for instance, in the focal volume of a focused femtosecond (fs) pulsed laser beam.[236] mpLSM typically uses near infrared (NIR) fs laser beams with high pulse intensities.[236] Since biological tissue offers low single photon absorption and scattering probabilities at this wavelength range, high penetration depths of up to several millimeters into biological material can be achieved. Simultaneously, such laser systems provide a sufficient yield to ensure efficient multiphoton fluorescence excitation (mpFE). In addition, the NIR range offers further advantages such as lower phototoxicity and a reduction in photobleaching.[234, 237]

Since only in the focal plane of the microscope's objective photon intensities are sufficient to generate mpFE, mpLSM technologies provide an inherent optical depth sectioning, applicable to optical tomography with high depth resolution. For technical aspects of mpLSM, please see Section 2.2.3. mpFE-based tomography allows a non-perturbative investigation of living systems on their surface but also in deeper layers. In parallel to the high depth resolution, i.e., in the z-direction, mpLSM also provides a high x-y-resolution within the plane of the individual optical sections, high enough to allow subcellular investigations like in CLSM.[238] In comparison to CLSM, mpLSM has the advantage of higher x-y resolution and signal intensities in deeper tissue layers with the consequence of images less blurry. This is enabled by a photon detection scheme collecting all detectable fluorescence photons, even if they are multiply scattered (non-de-scanned detection). This is possible because the smaller excitation volume allows to precisely know the spatial location of the excitation which defines the origin of the emitted fluorescence photons.[237] In contrast, CLSM needs an de-scan loop for directing fluorescence photons through the confocal pinhole.

The field of mpLSM applications in biological and biomedical investigations has expanded rapidly since its first successful implementation[239] in 1990 by Denk et al. and continues to expand. These days, mpLSM is applied to detect tumor growth and metastases,[240-241] to perform *in-vivo* studies on brain cancer[242] and neuronal networks[243] as well as on the cerebral metabolism,[244] to name but a few. However, the organ that is most often examined using mpLSM is the skin which is predisposed for *in-vivo* studies due to its location, dimensions, and morphology. All features meet the physical limits of mpFE-based deep tissue investigations. mpLSM has been used successfully in a large number of publications on dermal diseases.[245-246] For example, mpLSM enabled scientists to study the biochemical state of inflamed skin,[238] to follow the development of basal cell carcinomas,[247] and to non-invasively image the metabolic progression of melanoma.[248]

Like CLSM, mpLSM benefits from a combination with FLIM techniques (mpFLIM) through the advantages of fluorescence lifetime sensitivity to the state of a fluorophore and to its biochemical environment (see section 2.1.2). These advantages can also be exploited in mpFLIM studies on nanoparticles – tissue interactions. This is accomplished in many ways, for example via the fluorescence lifetime signature of the autofluorescent intracellular coenzyme nicotinamide adenine dinucleotides (NADH) which can provide information on the metabolic effects of cellular nanoparticle interactions.[244, 249] Moreover, fluorescently labelled or fluorescent nanoparticles can be distinguished from autofluorescent tissue by means of the fluorescence lifetime.[250] For this reason, I set up and characterized an mpFLIM system with the aim to investigate nanoparticular interaction in intact skin layers of the viable epidermis. In the following section, I present the components used, their configuration and test measurements on detection depth and fluorescence lifetime detectability in human skin.

Establishing a multiphoton fluorescence lifetime imaging microscopy setup

The established custom-built multiphoton TCSPC-FLIM setup uses multiphoton fluorescence excitation generated by a near-infrared emitting femtosecond pulsed Ti:Sa laser system. The newly implemented FLIM system has similar time-resolved detection properties as the confocal FLIM system described above. The selected combination of galvano scanner, hybrid PMT detectors, and TCSPC modules enables the spatiotemporal resolution of fluorescence decay traces within each pixel of a microscopic image with a temporal resolution in the picosecond range (see Figure 2.2.5 and Figure 4.1.2).

The Ti:Sa system used for mpFE consists of a diode pumped solid state laser (DPSSL, Verdi V5, Coherent, USA) which pumps a mode-locked femtosecond Ti:Sa laser (Mira 900, Coherent, USA). The generated fs-laser pulses have a temporal width of less than 200 fs at a repetition rate of 76 MHz. The emitting wavelength is adjustable to a range between 700 and 980 nm. In the experiments conducted for this thesis, the laser system was adjusted either to a wavelength of 800 nm (FLIM-ROX) or 845 nm (CMS-ICC/bodipy). The initially emitted laser intensity amounts to approximately 800 mW directly after leaving the laser housing (Figure 4.1.3A-1). Neutral density (ND) filters placed into a filter holder wheel attenuate this intensity to 120 – 200 mW. Subsequently, the passing photons are projected from a 1-inch mirror mounted in a 3-axis precision kinematic mount (KS1, Thorlabs, USA) onto a first of two adjustable pinholes (PHs), installed for beam alignment purposes only. When the FLIM setup is in operation, both PHs are completely open and do not interfere with the laser beam. After passing the first PH, the beam is reflected by two further subsequent 1-inch mirrors installed in 3-axis mounts and passes the second adjustable PH (see Figure 4.1.3A-2). This mirror array is used for coupling the laser beam into the laser scanning unit (modified DCS 120, Becker & Hickl, Germany) at optimal solid angles. The PHs are used for daily monitoring and realignment of the beam axis.

After entering the scanning unit, the intensity of the laser beam can be finely adjusted by a continuous ND wheel. For *ex-vivo* FLIM investigations on skin tissues explants, the final excitation intensity at the specimen was selected to be below 20 mW, depending on the fluorophore concentration and the fluorophore stability in the investigated samples. Within the scanning unit, the attenuated laser beam is guided by two scanning mirrors via a scanning lens into an inverted microscope (IX73, Olympus, Japan, see Figure 4.1.3-3). The scanning mirrors are controlled by a galvano controller (GVD120, Becker & Hickl, Germany) and enable the scanning of the excitation laser beam over the sample in x- and y-direction (Figure 4.1.3-4). In the microscope, a further mirror reflects the excitation laser beam in a 45 ° angle onto the main (dichroic) beam splitter, mounted in the microscope's fluorescence mirror turret. Depending on the experimental conditions, a main BS with either an edge wavelength at 705 nm (705 nm Edge BrightLine multiphoton single-edge, Semrock, USA), or at 643 nm (H 643 LPXR superflat, AHF, Germany) was installed (Figure 4.1.3B).

The laser beam passes the beam splitter at a relative angle of 45 ° and is focused by the microscope's objective onto a femtoliter volume centered in the focal plane (see Figure 4.1.3B). By placing a specimen in this excitation volume, fluorophores present therein can be excited (see Section 2.2.3). To achieve this, the sample is placed in a temperature-controlled holder, that is fixed on the microscope stage. A connect cooling/heating circulator (F25-MU, Julabo, Seelenbach, Germany) sets the temperature, which is monitored by a reference thermometer. The z-position of the objective, i.e., the focal plane can be adjusted and controlled by a piezo-based objective nanopositioner (PIFOC P-725.2CD, Pi-Systems, Germany) allowing an objective travel range between 0 – 250 µm, with a precision of 0.75 nm. In order to generate tomographic FLIM images, the individual depth-planes (in z-direction) are scanned with this nanopositioner. This was conducted by the following sequence: Starting at the sample surface a FLIM image is recorded in x-y-direction using the galvano scanners, then the z-plane is changed by the nanopositioner to the next deeper layer typically by a 0.5 – 2.0 µm step. Here, the next z-plane is recorded followed by a further change of the z-position and so on. This procedure allows finally a tomographic reconstruction of a 3D fluorescence image.

Using a 60× water objective (NA=1.2, UPLSAPO60XW, Olympus, Japan), the galvano scanning produces a maximum field of view (FOV) within the z-plane of 300 × 300 µm resolved in up to 2048 × 2048 pixel. The FOV can be scaled down gradually down to a minimum of 30 × 30 µm by applying finer scanning steps while preserving the same pixel raster. The galvano mirrors scan the excitation volume in a repetitive imaging mode within the z-plane, which results in low pixel dwell times (typically 5 µs/image). Low pixel dwell times are needed as they reduce the general photobleaching probability but also photo toxicity. This is especially important for mpLSM as the high local excitation intensities can locally heat up and damage the biological sample.

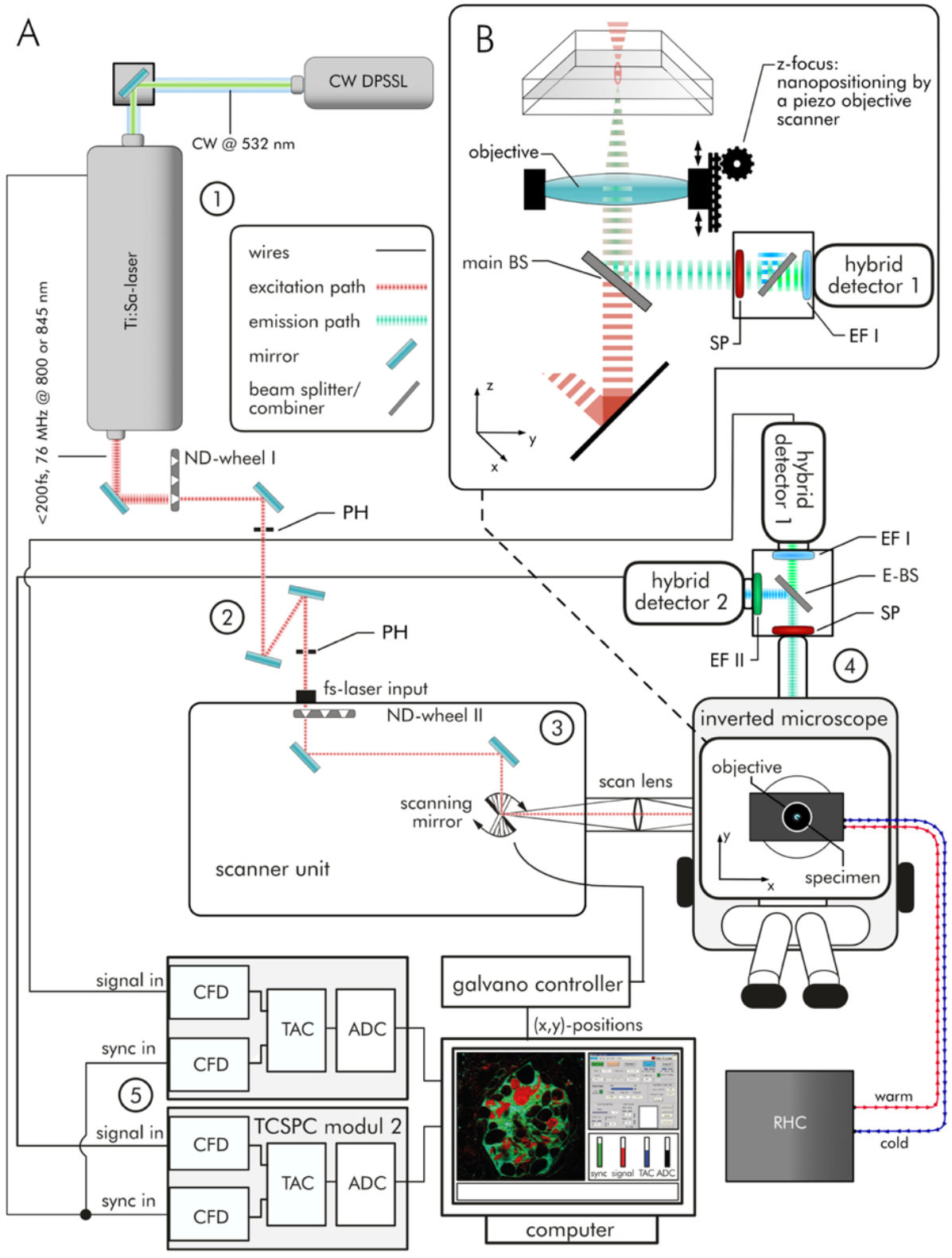

Figure 4.1.3: A Scheme of the TCSPC-mpFLIM setup. **B** excitation/emission path within the microscope. Abbreviations: CW – continues wave; DPSSL – diode-pumped solid state laser; Ti:Sa – titan-sapphire; fs – femtosecond; ND – neutral density; PH – (adjustment) pinhole; EF – emission filter; SP – short-pass filter; E-BS – emission beam splitter; BS – beam splitter; CFD – constant fraction discriminator; TAC – time to amplitude converter; ADC – analog to digital converter; RHC – refrigerated/heating circulator.

The generated fluorescence from the excitation volume is collected in a non-de-scanned manner. This means that all photons which are blue-shifted in respect to the multiphoton excitation wavelength are directed onto the detectors without using a de-scan procedure like in the confocal FLIM setup (Section 4.1.1). The main BS performs the necessary filtering by directing the blue-shifted fluorescence photons to the emission filter/detector unit at an angle of 90 ° to the propagation direction while the excitation photons reflected from the sample pass through the main BS (see Figure 4.1.3B). Before the fluorescence photons are detected, emission filters select the desired emission range (see Section 3.3.6) and suppress remaining photons from the excitation beam reflected by the main BS. More precisely, a fixed protection short-pass filter (edge wavelength: 700 nm, O-FSP-700-22MM, Becker & Hickl, Germany) is installed in the emission beam path as well as variable short- and long-pass emission filters and a secondary BS for dual color detection mode in the emission filter/detector unit (see Figure 4.1.3B).

Depending on the detection mode (single or dual color detection), one or two hybrid PMT detectors (HPM-100-40, Becker & Hickl, Germany) are used. They have an instrument response function (IRF) of about 120 ps FWHM and a quantum efficiency of 45 % (at 500 nm). The installed GaAsP hybrid PMT tube (R10467-40, Hamamatsu, Japan) in the detector module guarantees time resolution in the picosecond range, clean IRFs and a negligible after-pulsing probability.[230] The signals of the single detected photons are fed into the signal port of the TCSPC modules (SPC-160, Becker & Hickl, Germany) and trigger the individual TSCPC start-signals. The corresponding stop-signals are received via the sync pulse from the Ti:Sa laser system (Figure 4.1.3-1/5). The TCSPC modules sort the detected photons into 1024 time bins with an individual bin width of 9.7 ps. The respective instrument response function (IRF) of the mpFLIM system was determined to be less than 130 ps (FWHM) by light scattering experiments using a colloidal silica solution (LUDOX, Grace, Columbia, Maryland, U.S.A.). The FLIM-images are recorded by the SPCM software (Becker & Hickl). The selected acquisition times depend on the fluorescence intensity of the investigated specimen and varies typically between 1 and 5 minutes for each z-plane. Within this time range, a sufficient signal-to-noise ratio (SNR) of the TCSPC decay histograms could be achieved for further FLIM analyses.

mpFLIM setup applied in tomographic tissue imaging of the skin

First, I would like to start with the results on the general laser penetration and fluorescence detection depths of the established mpFLIM system. For this purpose, reference measurements were performed on fluorescein-containing agarose blocks at different depths ranging from 0 to 250 µm. Since emitted fluorescence photons from deeper sample layers could be reabsorbed on their way through the agarose blocks by fluorescein molecules (internal filter effect), I investigated two fluorescein concentrations. The concentrations amount to 6 µM (1-fold) and 60 µM (10-fold). By comparing the detected fluorescence intensities at different sample depths for both concentrations, I estimate a possible depth-dependent sensitivity loss and the magnitude of re-absorption.

Figure 4.1.4A shows fluorescence intensities accumulated from each pixel of the recorded z-planes at scanned depths between 0 and 250 µm. The total reduction in detected photons for the low concentration sample amounts to 11 % between the surface of the agarose block and the maximum depth of 250 µm. For the high concentrated sample, I observed a decrease of 26 %. The depth dependent intensities profile (Figure 4.1.4A) of both concentrations shows that the fluorescence intensity at surface of the highly concentrated sample (10-fold) has an 8.3-fold increased intensity compared to the 1-fold concertation, while this ratio decreases to 6.9-fold at deeper sample layers. Thus, it must be assumed that fluorophore concentration-dependent internal filter effects occur, probably overlaid with a scattering related contribution to the intensity reduction caused by the agarose media. However, the extent of these effects seems relatively small for the investigated case, so that a high sensitivity of the mpFLIM apparatus by purely optical aspects is given even in deeper layers of up to 250 µm.

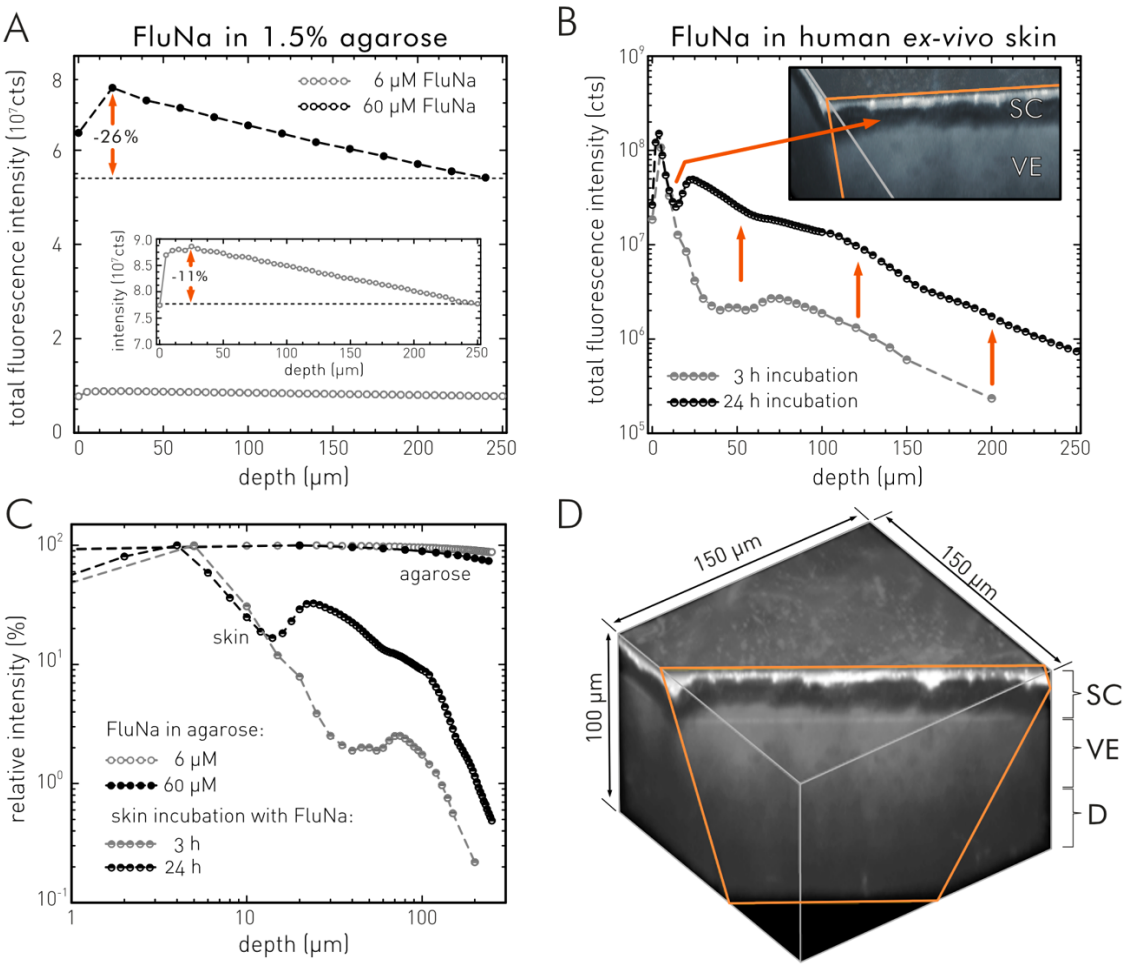

Figure 4.1.4: Depth dependence of detected fluorescence intensities in the mpFLIM setup. **A** Depth-dependent total fluorescence intensity of indicated concentrations of fluorescein sodium salt (FluNa) homogenously distributed within an 1.5 %-agarose block. **B** Depth-dependent total fluorescence intensities of human skin explants (*ex-vivo*) incubated with 60 µM FluNa in PBS, pH 7.4 for 3 h and 24 h. Plotted intensities are determined by accumulating all photons detected in a microscopic image plane; (A) and (B) are visualized as Lin-Log plots. **C** Comparison of (A) and (B) by normalizing all plots to their maximum, data is shown as Log-Log plot. **D** Tomographic visualization of the recorded fluorescence intensity of *ex-vivo* skin with topical applied fluorescein, after the 24h-incubation (see B). Experimental conditions: λ_{ex} = 845 nm, main beam splitter edge wavelength at 705 nm, single detector mode: λ_{em} = 500 – 550 nm (525/50BP). Abbreviations: SC: *stratum corneum*; VE: viable epidermis; D: Dermis.

In a next step, I would like to verify the suitability of the mpFLIM system for fluorescence detection in different tissue depths. Since the microscope will later be used for fluorescence lifetime-based investigations of nanoparticular interactions after topical application on skin models, the basic characterization was performed on excised human *ex-vivo* skin. Thus, the sample-related scattering and absorption behavior in relation to emitted fluorescence photon is well reflected to the later investigated scenarios. Since this section is intended to demonstrate the setup, its optical limitations and the realization of deep tissue measurements in skin, the well-established fluorescence tracer fluorescein sodium salt[251] dissolved in PBS was applied to stain the skin tissue blocks. Although the fluorescein molecules are relatively small (m_w = 376 Da), it takes some time for them to penetrate into deeper skin layers and to accumulate there in high concentrations. For this reason, two skin blocks were subjected to mpFLIM-based deep scans treated with a short and a long incubation period (3 and 24 h).

Figure 4.1.4B compares the absolute detected fluorescence intensity obtained after both incubation times at different depths up to a surface distance of 250 µm in a half logarithmic representation. The displayed profiles indicate several effects. As expected, a longer incubation time leads to a considerable accumulation of fluorescein in deeper skin layers (Figure 4.1.4B, orange arrow). The increase of the fluorescence intensity due to the longer incubation time in the viable epidermis (VE, at 25 µm) amounts to a factor of ~11, while in the dermis (100 µm) a ~7-fold increase can be observed at the longer incubation. Another observation is the strong accumulation and fluorescence emission of fluorescein in the *stratum corneum* (SC). The fluorescence level between the two incubation times is approximately the same, but even in the 24h incubation the fluorescence intensity of SC exceeds that of the VE by a factor of five. On the one hand this shows that the fluorophore accumulates in the SC, but on the other hand cannot penetrate the SC barrier undisturbed.

Interestingly enough, the transition region between SC and VE shows an intensity drop (see also Figure 4.1.4D), independent of the short or long incubation time. Whether this reduction in fluorescence intensity is associated with a local low residence probability of the fluorescein molecules or an altered fluorescence emission, i.e., non-visibility due to environmental influences on absorption or emission behavior (like pH or polarity) was not conclusively clarified. But it is quite conceivable that the latter phenomenon occurs since the absorption and emission properties of fluorescein are highly sensitive to pH-fluctuations due to several protonatable groups of this fluorophore (see Section 2.1.3). The SC in particular has a steep pH gradient, ranging from pH values below 5 on the surface to over 7 at lower SC layers.[252-253] Especially the lower pH values lead to a reduction in the absorption and fluorescence emission probability of fluorescein.[254] Moreover, a similar phenomenon was observed recently for dexamethasone molecules.[255] Dexamethasone has a similar size to fluorescein, but is more hydrophilic. The authors observed a drop in the concentration of dexamethasone at the interface of SC and VE. By modeling the interplay of diffusivity and free energy profiles, they

attributed this penetration behavior to a low diffusivity in the SC and a slight increase in free energy with higher SC depths.

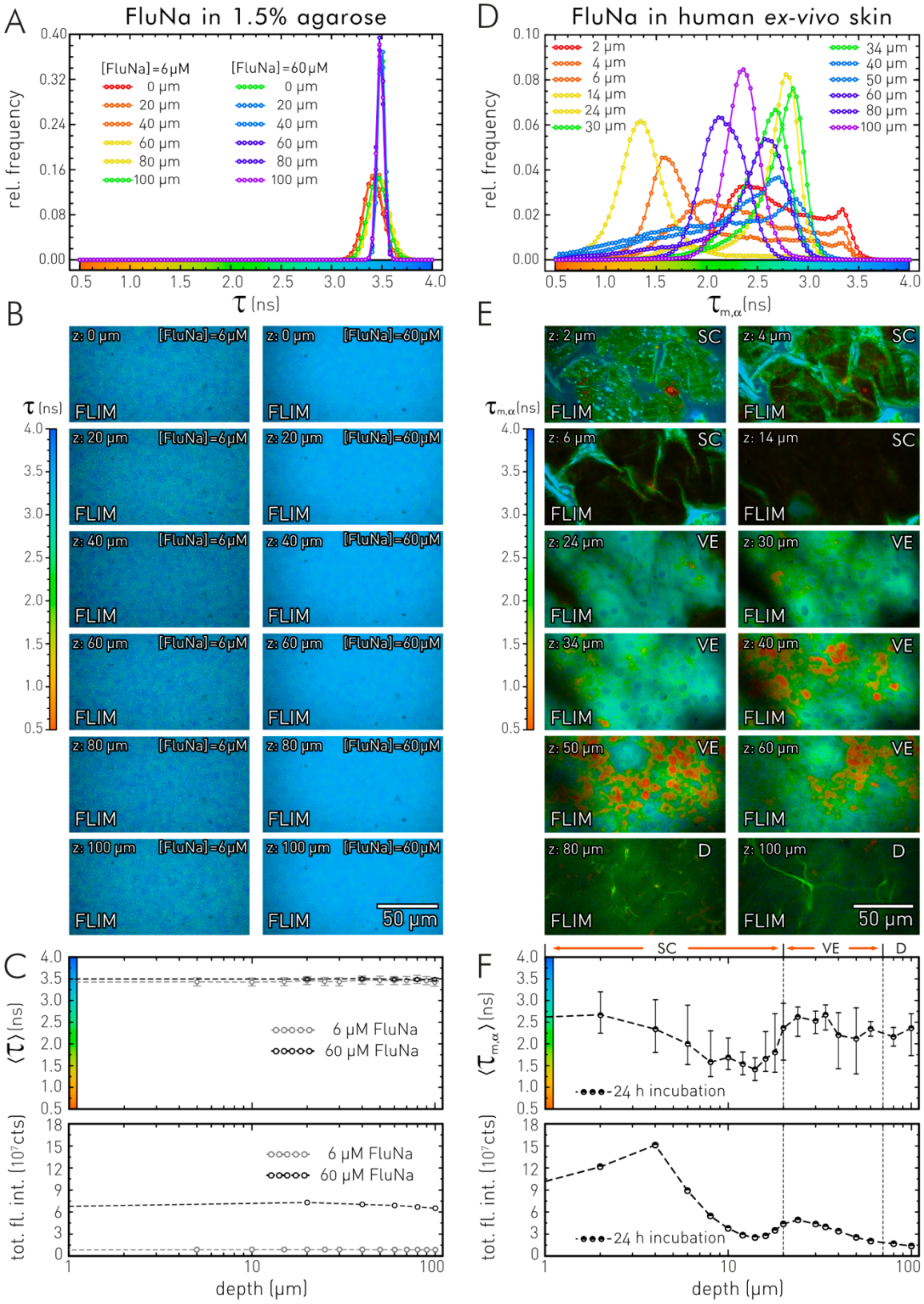

Figure 4.1.5: mpFLIM: Time-resolved fluorescence detection of fluorescein (FluNa) homogenously distributed in agarose blocks and penetrated into human skin. **A** Fluorescence lifetime distributions of fluorescein in agarose (1.5 %, pH 8) at different depths at two FluNa concentrations (6 and 60 µM). **B** FLIM images of fluorescein in agarose based on the fluorescence lifetime (tau-plot approach) at selected depths. **C** Respective depth-dependent fluorescence lifetime (mean values ⟨τ⟩ of the fluorescence lifetime distributions

shown in A, error bars: distribution width: $\pm 1\sigma$) and fluorescence intensity profiles in the agarose blocks. **D** Fluorescence lifetime distributions of fluorescein in human skin after 24h incubation (60 µM) at different depths. **E** FLIM images of fluorescein in human skin based on the mean fluorescence lifetime (tau-plot approach). **F** Respective depth-dependent fluorescence lifetime (mean values $\langle \tau_{m,\alpha} \rangle$ of the mean fluorescence lifetime distributions shown in D, error bars: distribution width: $\pm 1\sigma$) and fluorescence intensity profiles in the human skin. Experimental conditions: λ_{ex} = 845 nm, main beam splitter edge wavelength at 705 nm, single detector mode: λ_{em} = 500 – 550 nm (525/50BP). Abbreviations: SC: *stratum corneum*; VE: viable epidermis; D: Dermis.

Comparing the examined agarose blocks to the tissue samples (Figure 4.1.4C), it can be observed, that in particular the inhomogeneity of fluorophore distribution, scattering, and re-absorption probability within the examined tissue defines the detection capability in deeper tissue layers. In general, it can be stated that the established mpFLIM setup can reliably detect photon intensities emitted by fluorophores located in skin tissue over two orders of magnitude. Thus, the mpFLIM setup seems sensitive enough to allow fluorescence-based investigations of fluorescently labeled nanoparticles penetrated into deeper skin layers. But to what extent does the generated FLIM data allow the determination of fluorescence lifetimes based on the recorded time-resolved fluorescence decays? This will be examined more closely in the following on the basis of the fluorescein-containing agarose and skin tissue blocks already introduced.

I will start with the mpFLIM data of the fluorescein-containing agarose blocks. The recorded FLIM-images at different depths were analyzed by tau-plot analyses. In these analyses the time-resolved fluorescence decay traces in the FLIM-images were fitted to a mono-exponential model function (Eq. 19, $n = 1$). Figure 4.1.5A shows the corresponding fluorescence lifetime distributions for some of the investigated sample depths. The center of these distributions is further used as the mean fluorescence lifetime value at a certain depth and the distributions width ($\pm 1\sigma$) is applied to describe the respective scattering of the fluorescence lifetimes in the distributions. Both FluNa concentrations investigated (6 and 60 µM) produced similar results. The determined mean fluorescence lifetimes fluctuate around the value of ~3.5 ns. The reduced fluorescence intensities in the case of the low FluNa concentration lead to a broadening of the fluorescence lifetime distribution compared to the 10-fold higher concentrated sample. This phenomenon can be attributed to a reduced fit accuracy due to a lower photon statistic (see also Appendix, Figure 1A). The broadened fluorescence lifetime distribution is expressed in the tau-plots of Figure 4.1.5B. They show a larger variation range of the applied color scale for the lower FluNa concentration. For both concentrations, however, the center of the determined fluorescence lifetime distributions is independent of the observation depth. The small and depth-independent width of the fluorescence lifetime distributions ($\sigma < 0.1$ ns) over a depth of 100 µm (see Figure 4.1.5A/C) is also worth mentioning.

The fluorescein-incubated skin blocks show a completely different picture. In the tau-plot FLIM analysis of the corresponding mpFLIM images, the pixel-based fluorescence decay traces in the individual FLIM images of the z-stack could not be fitted via a mono- but only via a tri-exponential model function (Eq. 19, $n = 3$). The mean fluorescence lifetime calculated from the individual decay components shows broad distributions within the individual z-planes (see Figure 4.1.5D) which also change with skin depth. At the skin surface (depth: 2 – 6 µm), the fluorescence lifetime distributions

still show a side peak at ~3.3 ns which resembles the depth-constant Gaussian-shaped fluorescence lifetime distribution of fluorescein in the agarose blocks. With deeper skin layers, the penetrated fluorescein displays strong changes in its fluorescence lifetime distributions. Figure 4.1.5E visualities the mpFLIM data as the tau-plots for the investigated skin layers at different depths. Here, the transition from SC to VE is clearly visible. In the upper SC layers, fluorescein is present in two states. One state is defined by a mean fluorescence lifetime of around 2 ns (tau-plot: green color). This lifetime signature can be observed in the lipid matrix between the corneocytes. The other state has a slower fluorescence lifetime (> 3.5 ns), similar to the fluorescein-containing agarose blocks. This signature is present in larger furrow-like structures that cross the surface of the SC. Fluorescein molecules located there, probably have not yet interacted with the lipid matrix and are still in their initial aqueous state.

In the deeper SC (12 – 20 µm), the fluorescence signal vanishes. Here, fluorescein either emits less fluorescence photons or it has a reduced probability of being present in these layers (see also Figure 4.1.5F). In the VE (20 – 70 µm) the fluorescence intensity increases again. Here, an inhomogeneous spatial fluorescence lifetime distribution within the living keratinocytes is noticeable (Figure 4.1.5E). While the cytoplasm is characterized by shorter fluorescence lifetimes (colored red – green; 1 – 3 ns), the tau-plots show slower lifetimes in the cell nuclei (colored blue; > 3.5 ns). Fluorescein penetrated into the dermis exhibits similar mean fluorescence lifetime values as in VE. However, in this skin layer, heterogeneity is much less pronounced.

Figure 4.1.6 shows tomographic FLIM images generated from the individual FLIM images of the acquired z-stack. For the generation of these images, the mpFLIM data was first false color-coded using the tau-plot approach (see Figure 4.1.5). The resulting images were transformed into tomographic 3D images using the 3D Volume viewer plug-in of the image processing and analysis application ImageJ/FIJI.[207] Figure 4.1.6A and B illustrate the advantages of the additional fluorescence lifetime information (B) compared to simple fluorescence intensity-based tomography (A). The applied fluorescence lifetime-based false coloring significantly increases the contrast and can provide specific information depending on the given lifetime sensitivity. The generated tomographic images show that the established mpFLIM setup provides the necessary resolution to resolve structures on a subcellular level. This is particularly evident in Figure 4.1.6E,F where cytoplasm and nucleus of a keratinocyte can be clearly resolved by different intracellular fluorescence lifetimes. Furthermore, Figure 4.1.6C,D shows the fluorescein-filled furrows in the SC (see also Figure 4.1.5E) which extend a few micrometers deep into the skin surface. But also, in deep skin layers (>70 µm) such as the dermis, the mpFLIM setup makes it possible to resolve and visualize dermal structures such as collagen fibers.

Finally, the multi-color compatibility of the mpFLIM setup is investigated. The mpFLIM setup allows the parallel time-resolved fluorescence detection of two spectrally distinguishable fluorophores by the installation of two HPM detectors and corresponding spectral filters and beam splitters in the

detection unit. This feature will be exploited in the experiments shown in Chapter 4, in which a core-multishell nanocarrier labeled with indocarbocyanine (ICC) as well as its cargo, the fluorescent drug mimetic (bodipy), are to be spatially localized by their spectral properties. In the following, I present the discrimination capability of the mpFLIM setup in relation to both fluorophores.

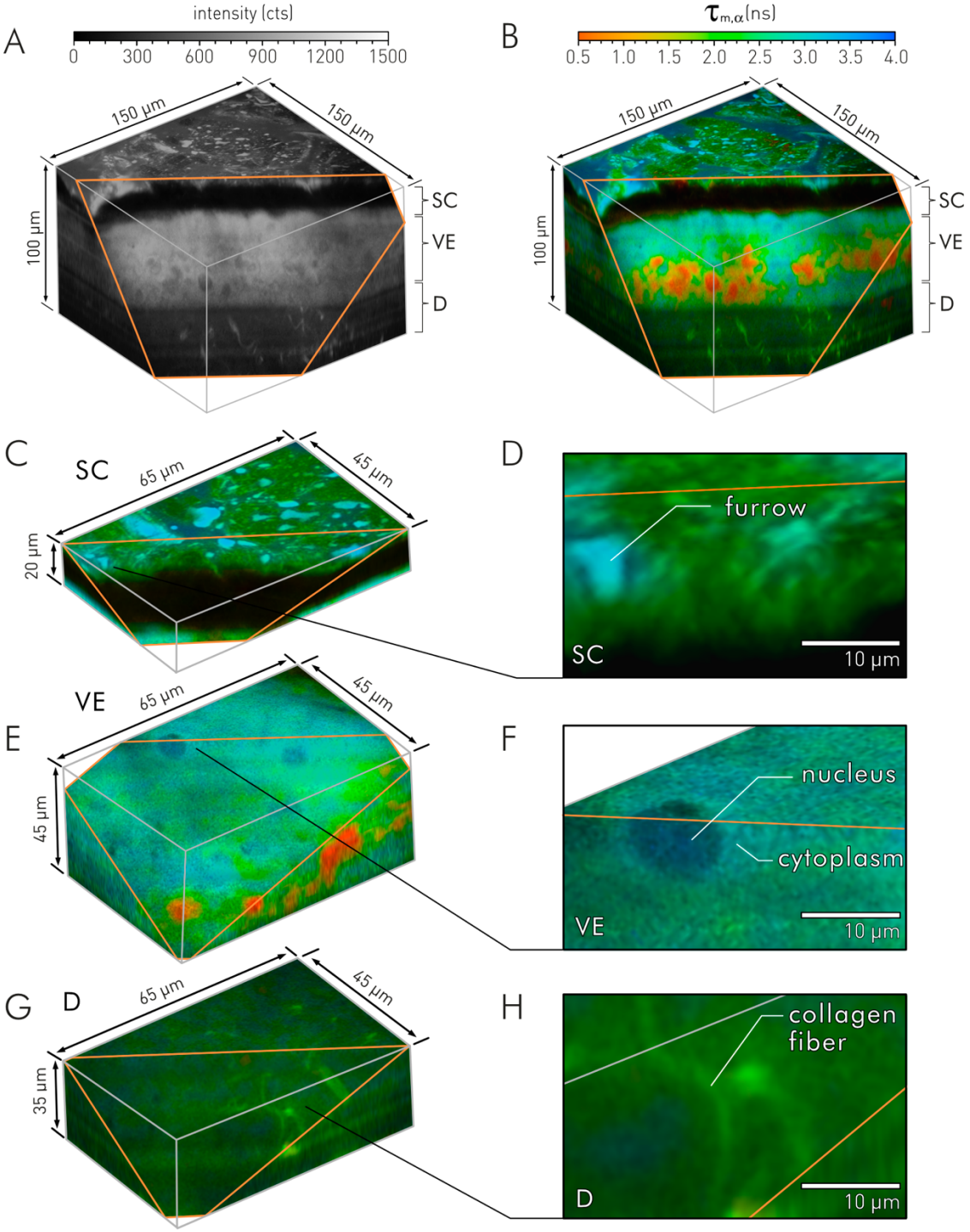

Figure 4.1.6: Tomographic visualization of mpFLIM data from *ex-vivo* skin with topical applied fluorescein (24h-incubation time). **A** Fluorescence intensity-based tomographic image, main dermal layers are indicated. **B** Fluorescence lifetime-based tomographic image using the tau-plot analysis shown in Figure 4.1.5. **C** Detail visualization of the SC. **D** Image section of C showing fluorescein in a skin furrow. **E** Detail visualization of the VE. **F** Image section of E showing nucleus and cytoplasm of a keratinocyte. **G** Detail visualization of the D. **H** Image section of G showing a collagen fiber in the dermis. Experimental conditions: λ_{ex} = 845 nm, main beam splitter edge wavelength at 705 nm, single detector mode: λ_{em} = 500 – 550 nm (525/50BP). Abbreviations: SC: *stratum corneum*; VE: viable epidermis; D: Dermis.

Figure 4.1.7A shows the detection scheme for the CMS-ICC/bodipy experiments. In order to spatially separate ICC and bodipy, the mpFLIM setup has to be operated in a dual-color channel detection mode. The two detection channels use the following spectral windows: photons between 575 and 600 nm are collected in the ICC channel. The bodipy channel, however, detects photons between 460 and 500 nm. How these spectral windows are generated will be briefly described in the following. Before the total fluorescence emission of the sample is directed to the HPM detectors, it is filtered by two subsequent short-pass filters (the fixed protection short-pass (700 nm) + 600SP) removing photons above 600 nm from the emission beam. This ensures that no excitation photons remaining in the emission beam hit the detector and damage it. Also, the sensitivity to ICC fluorescence is sharpened against higher wavelengths by focusing the detection on its emission peak (Figure 4.1.7B). To collect the emission photons efficiently, a second BS (z 532 RDC, AHF, Germany) is installed. This splitter roughly sorts the emitted photons into the two spectral channels according to their wavelength. It transmits photons with a wavelength above 532 nm and reflects photons with a shorter wavelength at an angle of 90 °. The transmitted photons fall on the HPM detector for the ICC channel. Before that happens, however, a further emission filter is used which limits the ICC detection window to smaller wavelengths below 575 nm (575LP). This completes the spectral focusing of the ICC detection channel to a spectral window of 575 – 600 nm. The photons reflected by the BS are filtered by a band-pass filter (480/400BP), which defines the spectral window of 460 – 500 nm of the bodipy channel.

To estimate the detection sensitivity and selectivity as well as spectral bleed-through effects, three samples were measured under identical conditions. The samples are dissolved ICC, bodipy and CMS-ICC loaded with bodipy. Figure 4.1.7B,E,H show the resulting microscopic intensity images of both detection channels. The correspondent intensity ratio between the ICC and the bodipy channel is ~213 (CMS-ICC), ~0.28 (bodipy) and ~27 (CMS-ICC/bodipy) (Figure 4.1.7C,F,I). The resulting decay curves are shown in Figure 4.1.7D,G,J. These results indicate that false-positive detection of ICC in the bodipy channel is not significant due to a minimal emission probability of ICC in the spectral range between 460 and 500 nm (compare Figure 4.1.7A). However, it is possible to detect bodipy in the ICC channel. Here, the ratio is ~0.28, this means a spectral bleed-trough of almost 30 %, i.e., almost every third emitted photons by bodipy is collected in the ICC channel. However, due to the time-resolved fluorescence detection and the large difference between the fluorescence lifetimes of both fluorophores (Figure 4.1.7J), it is still possible to separate them even within a single detection channel by means of the lifetime information.

These demonstration experiment shows that the established mpFLIM setup is capable of detecting time-resolved fluorescence behavior even in greater tissue depths. Depth-related disturbances of fluorescence lifetime detection due to optical conditions of the mpFLIM setup can be largely excluded by the FluNa-agarose experiments that show no variations in the fluorescence lifetime of fluorescein in the homogenous agarose environment. The exemplary skin reference experiments with penetrated

fluorescein indicate that the mpFLIM setup can be applied for fluorescence lifetime-based deep tissue investigations in the VE of human skin. For this purpose, the tested detection depth of up to 100 µm is sufficient from a tissue morphological point of view. The achieved spatial resolution of fluorescence lifetime in all three spatial dimensions allows subcellular investigations in tomographic images. This capability is necessary to deepen the understanding of nanoparticle interaction mechanisms and therapeutic responses in a complex tissue environment. The established mpFLIM-setup meets the requirements to study fluorescently labeled nanoparticles on a single cell level deep within skin tissue and is applied in tissue investigations presented in Chapter 4.

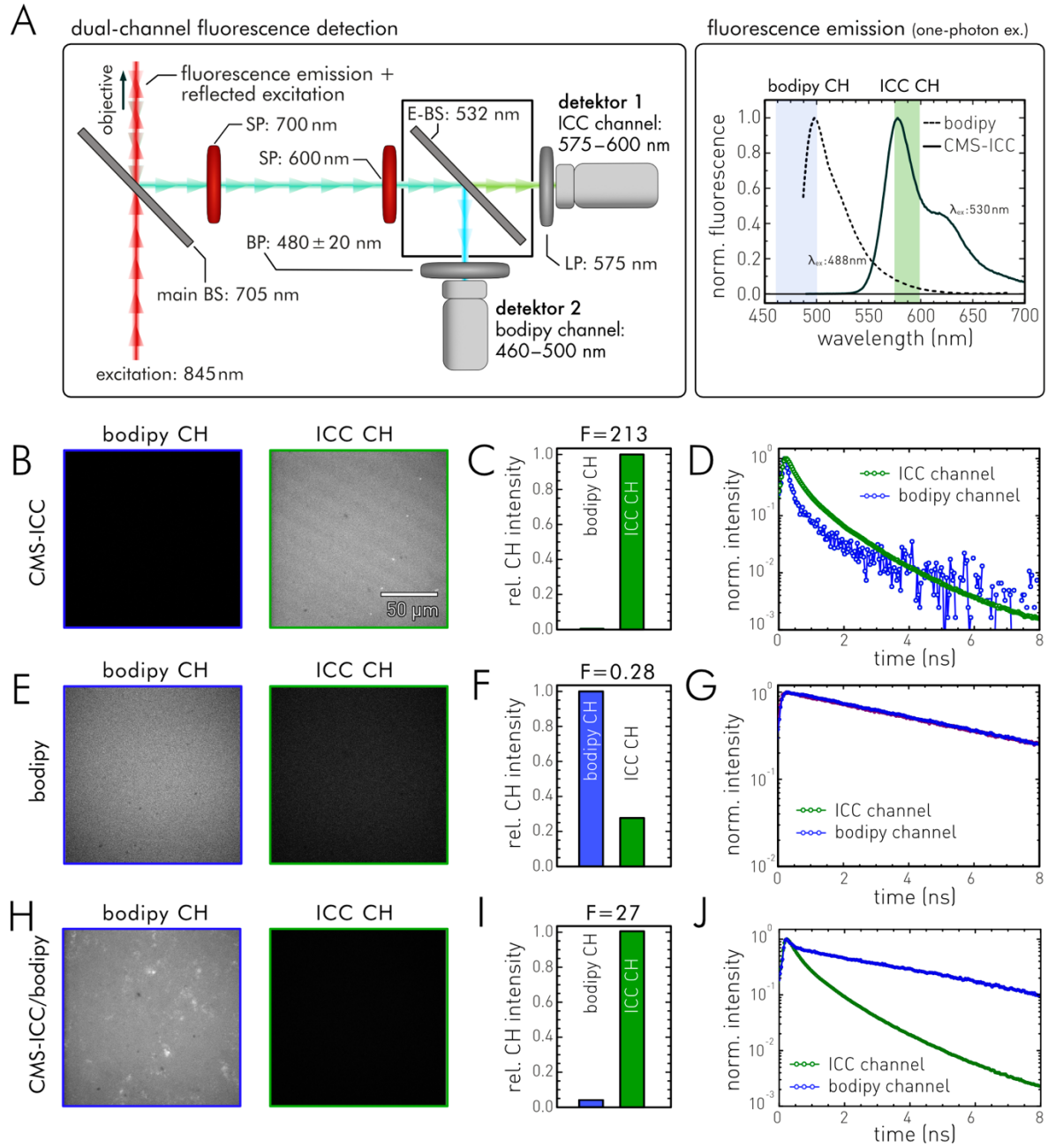

Figure 4.1.7: Dual detection scheme of the mpFLIM setup. **A** Left: Detection scheme for ICC and bodipy detection. Right: spectral properties of the (one-photon) fluorescence emission of ICC and bodipy. The spectral windows of both detection channels are indicated. The following filters are applied: DM-BS 705 (main BS), 700SP (fixed), 600SP, DM-BS 532 (E-BS), 575LP, 480/40BP. Fluorescence excitation at 845 nm. To quantify the detection bleed-trough, the following samples are compared: CMS-ICC, bodipy,

and CMS-ICC/bodipy (in 10 mM sodium phosphate buffer, pH 7). **B** Comparison of the image channels of bodipy (blue) and ICC (green) when measuring a CMS-ICC solution. **C** Comparison of the relative fluorescence intensities in both channels (bodipy (blue) and ICC (green)) when measuring a CMS-ICC solution. **D** Comparison of the recorded fluorescence decay traces in the bodipy (blue) and ICC (green) channel when measuring a CMS-ICC solution. **E** Comparison of the image channels of bodipy (blue) and ICC (green) when measuring a bodipy solution (containing 30 % EtOH). **F** Comparison of the relative fluorescence intensities in both channels (bodipy (blue) and ICC (green)) when measuring a bodipy solution (containing 30 % EtOH). **G** Comparison of the recorded fluorescence decay traces in the bodipy (blue) and ICC (green) channel when measuring a bodipy solution (containing 30 % EtOH). **H** Comparison of the image channels of bodipy (blue) and ICC (green) when measuring a CMS-ICC/bodipy solution. **I** Comparison of the relative fluorescence intensities in both channels (bodipy (blue) and ICC (green)) when measuring a CMS-ICC/bodipy solution. **J** Comparison of the recorded fluorescence decay traces in the bodipy (blue) and ICC (green) channel when measuring a CMS-ICC/bodipy solution. F indicates the factor between ICC and bodipy channel. Abbreviations: BS: beam splitter; ICC: indocarbocyanine; LP: long-pass filter; SP: short-pass filter; E: emission; CH: channel.

4.1.3 Validation of a Cluster-FLIM analysis approach

Quantitative FLIM image analysis must distinguish and parameterize thousands of fluorescence decay histograms recorded in each image pixel. This process is especially difficult at high noise levels in which insufficient photon counts per decay histogram occur (low photon statistics). As described in Section 3.4.2, serval methods were developed to solve the problem in FLIM data parametrization, like the decay fitting-based tau-plot analysis or the graphical phasor-plot approach. In this section, the automated multivariate Cluster-FLIM analysis (Section 3.4.2, Cluster-FLIM) is validated by simulated and experimental FLIM data. Cluster-FLIM groups the (multi-)exponential fluorescence decay curves recorded of single image pixels in accordance to their feature similarity into clusters without using any *a priori* information. The algorithm extracts for each recognized group (cluster, fluorescent species) a fluorescence lifetime signature (FLS). The FLSs represent the characteristic fluorescence decay curves of the recognized fluorescence species. The Cluster-FLIM algorithm requires neither decay fitting nor the use of reference fluorescence decay curves as pattern matching methods. The extraction capability of multiple unknown fluorescent species characterized by their specific FLS is the major advance over other FLIM parametrization techniques. The approach allows a visualization of the molecule of interest (MOI), its interactions, or environmental changes in space and time without knowing the intrinsic unknown structure of the respective fluorescence decays *a priory*. To demonstrate that Cluster-FLIM is capable of distinguishing multiple (multi-)exponential fluorescence decay curves in the pixels of a FLIM image or globally in a set of FLIM images, the following two example files are analyzed.

Cluster-FLIM of synthetic FLIM data

The first example is the validation of a synthetic FLIM image showing different fluorescence lifetime signatures (Figure 4.1.8). The Cluster-FLIM software tool was developed by Robert Brodwolf (Prof. Alexiev's group, Freie Universität Berlin, Germany). The data set consists of seven image regions containing pixels with different (multi-)exponential decays, i.e., there are seven different types of (multi-)exponential decays in total. Three of them have the same mean lifetime, so a conventional tau-plot based on the mean lifetime could not resolve them. Figure 4.1.8A shows the generation of

synthetic FLIM data with a FLIM simulation tool developed by Robert Brodwolf. The FLIM simulation consists of three individual pixel layers named *R*, *G*, and *B* (512 x 512 pixels). In each pixel layer, a mono-exponential fluorescence decay of the same fluorescence lifetime is simulated, the respective photon counts are sorted into pixel-based decay histograms. Please note that only in pixels of the areas (circle segments) indicated in 4.1.7A decays are simulated. The simulated lifetimes in the single layers are $\tau_1 = 1$ns (*B*), $\tau_2 = 2$ ns (*G*) and $\tau_3 = 3$ ns (*R*). The pixel-based decay histograms have a total intensity of 500 counts, a Poisson distributed background noise and are convoluted with an IRF. After simulating the mono-exponential fluorescence decays, the generated decay histograms in the three layers are superimposed on a pixel basis with equi-fractional contributions. This leads to a synthetic FLIM image (Figure 4.1.8B), that shows seven regions (indicated by the numbers 1 – 7 in Figure 4.1.8B) with mono-, bi-, and tri-exponential decays (Figure 4.1.8C).

Figure 4.1.8D displays the false-color image generated by the Cluster-FLIM analysis. The color-coding allows an easy discrimination between the seven simulated fluorescence decay regions. That means, that the Cluster-FLIM algorithm identifies the characteristic decay structures, and separated and color-coded the pixels, respectively. The respective extracted FLSs are plotted in Figure 4.1.8F. In addition to the FLIM image, Figure 4.1.8D also shows seven enlargements to individual image sections of region 1 – 7. The magnification is selected so that individual pixels can be seen. The images show that although the seven regions in the Cluster-FLIM image look well separated, the algorithm has not identified 100 % of the ~260,000 pixels correctly. Some pixels are assigned to the wrong group, especially in region number 6 and 7. For both regions, the similarity in the fluorescence decay is particularly high (Figure 4.1.8C, magenta and gray colored decay). The quality of the assignment is shown in Figure 4.1.8E. The bar graph shows the percentage of correctly assigned pixels within the seven regions. For region 1 – 5 and 7, over 85 % of the pixels are assigned to the right cluster. For the region number 6 with the lowest assignment rate, more than 62 % are still correctly assigned. Figure 4.1.8G shows a comparison of the theoretical mean fluorescence lifetimes ($\tau_{\mathrm{m,sim}}$) of the simulation and the calculated values ($\tau_{\mathrm{m,Cluster-FLIM}}$) using the fit parameters of a subsequent decay fitting of the extracted FLSs. The values generally deviate by less than 2.5 %.

Figure 4.1.8G shows that the mean fluorescence lifetime of regions 2, 6, and 7 are equal. This makes it impossible to identify the difference by a tau-plot analysis using the standard mean-lifetime parameterization. In a tau-plot like this, all three regions would have the same color. The analysis of the synthetic FLIM image using the phasor analysis approach could separate region 2 and 6, due to the mono- and bi-exponential nature of these decays. However, the method would fail to separate regions 6 and 7, since tri-exponential decays cannot be distinguished from bi-exponential decays due to the geometric limitation in the two-dimensional approach.

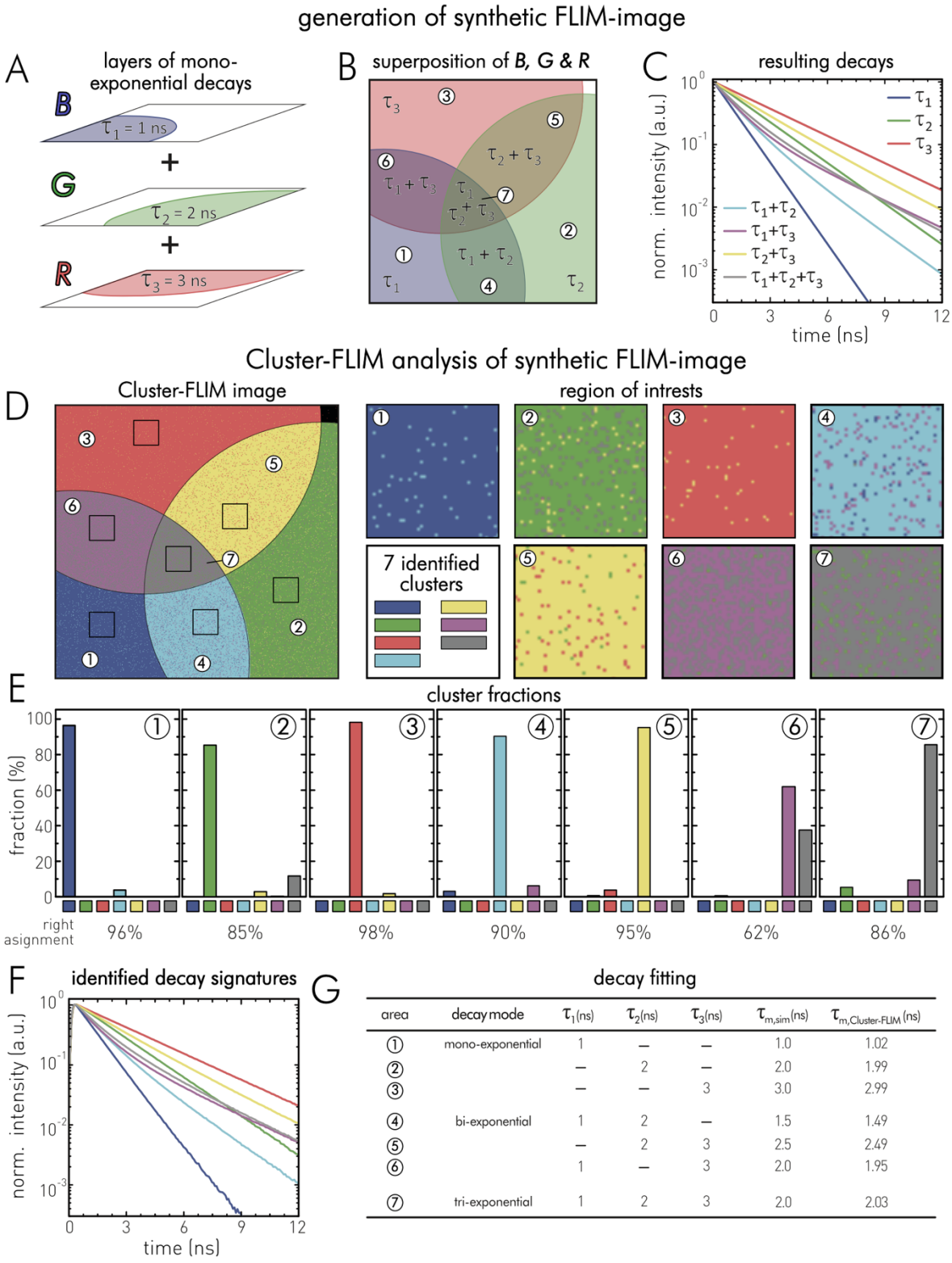

area	decay mode	τ_1(ns)	τ_2(ns)	τ_3(ns)	$\tau_{m,sim}$(ns)	$\tau_{m,Cluster\text{-}FLIM}$ (ns)
①	mono-exponential	1	–	–	1.0	1.02
②		–	2	–	2.0	1.99
③		–	–	3	3.0	2.99
④	bi-exponential	1	2	–	1.5	1.49
⑤		–	2	3	2.5	2.49
⑥		1	–	3	2.0	1.95
⑦	tri-exponential	1	2	3	2.0	2.03

Figure 4.1.8: Validation of Cluster-FLIM using synthetic FLIM data. Generation of synthetic FLIM-data and the application of a Cluster-FLIM analysis to this data set. **A** Individual layers of a simulated FLIM-image (512 x 512 pixel). In each pixel of the three circles mono-exponential fluorescence decay traces are simulated with fluorescence lifetimes of τ_1=1ns (*B*), τ_2=2 ns (*G*) and τ_3=3 ns (*R*) with an average pixel intensity of 500 counts (cts) and Poisson distributed background noise. Simulation was performed by a Software tool written by Robert Brodwolf. As in a real experiment the theoretical fluorescence decay curve is convoluted with an IRF (here FWHM ~170 ps). **B** Synthetic FLIM image constructed of three circle segments (*R,G,B*). In areas of overlapping circles the fluorescence decays traces are super-positions of the individual decays of *R,G,B* with equi-fractional contributions. This leads to seven areas (indicated by number 1-7) of different fluorescence lifetime signatures (FLS). **C** Theoretical plot of the seven occurring fluorescence decays signatures (including multi-exponential decay curves). **D** Cluster-FLIM image (left) after analyzing the simulated

FLIM-image, false-color coding according to FLS shown in C. Close ups to the seven regions of interest (ROIS) indicated by black squares on the Cluster-FLIM image. **E** Pixel assignments to the respective cluster (FLS) within the areas 1-7, expressed as relative fractions. Percentage of the right cluster assignments is indicated below the individual plots. **F** Identified FLS by the cluster analysis (color code according to D). **G** Initial decay components of the simulation and the corresponding theoretical mean fluorescence lifetimes are summarized and compared to the result of the cluster analysis.

Cluster-FLIM of experimental FLIM data

In a second example the specificity of the Cluster-FLIM analysis is validated using experimental FLIM data. For this purpose, four solutions of the fluorophore ICC were recorded using TCSPC-FLIM. Each sample consists of ICC in a different microenvironment. The fluorescence lifetime of this fluorescent molecular rotor is very sensitive to its local environment. Thus, the environmental dependency also affects the recorded fluorescence decay curves. Differences in this decay behavior are to be detected by cluster FLIM. The four chosen environments are H_2O, 69 % sucrose (%w/w), ICC attached covalently to the surface of dPGS, and attached covalently to the core of a CMS-NR.

A global Cluster-FLIM analysis of the FLIM data (Figure 4.1.9), measuring ICC in its four environments was performed at four different intensity regimes (35, 90 ,120, and 170 cts/px). Figure 4.1.9A shows the global Cluster-FLIM analysis of FLIM images with the lowest photon detection intensity, i.e., the lowest signal-to-noise detection ratio. Cluster-FLIM algorithm identified four different clusters by their FLS which can be attributed to the four different fluorophore environments. The false color FLIM images generated by the Cluster-FLIM algorithm have the following color code: Red-colored pixels indicate the identified characteristic fluorescent species of ICC in H_2O, cyan-colored pixels ICC in 69 % sucrose, magenta-colored pixels dPGS-ICC and green-colored pixels CMS-ICC. The inlay in the upper right-hand corner shows a magnification that allows individual pixels to be recognized and thus to see the pixel-cluster assignment by the eye. Additionally, bar plots visualize the quality of the assignment next to the respective FLIM-image. The plots present the relative fractions of the identified clusters. Finally, on the left hand-side, the reference FLS of the individual ICC solutions are compared with the FLS obtained by the Cluster-FLIM analysis.

At 35 cts/px CMS-ICC shows the lowest assignment rate. Around 21 % pixels are wrongly assigned. The mean value over all misassignments within the four FLIM images is 14 ± 5 %. As expected, the comparison of the individual intensity regimes (Figure 4.1.9A-D) shows a continuous decrease of cluster misassignment with increased photon statistics. The only significant deviation between the identified FLSs and the respective reference curves occurs at the lowest detection intensity (Figure 4.1.9A, left plot). In the case of ICC, the difference in H_2O is caused by a mismatch of pixels to the dPGS-ICC cluster, resulting in a slower decay of the FLS (Figure 4.1.9A, arrow). In return, the FLS of dPGS-ICC decays faster. At higher detection intensities, the mismatch of pixels to the right cluster becomes neglectable (<1 %, Figure 4.1.9E).

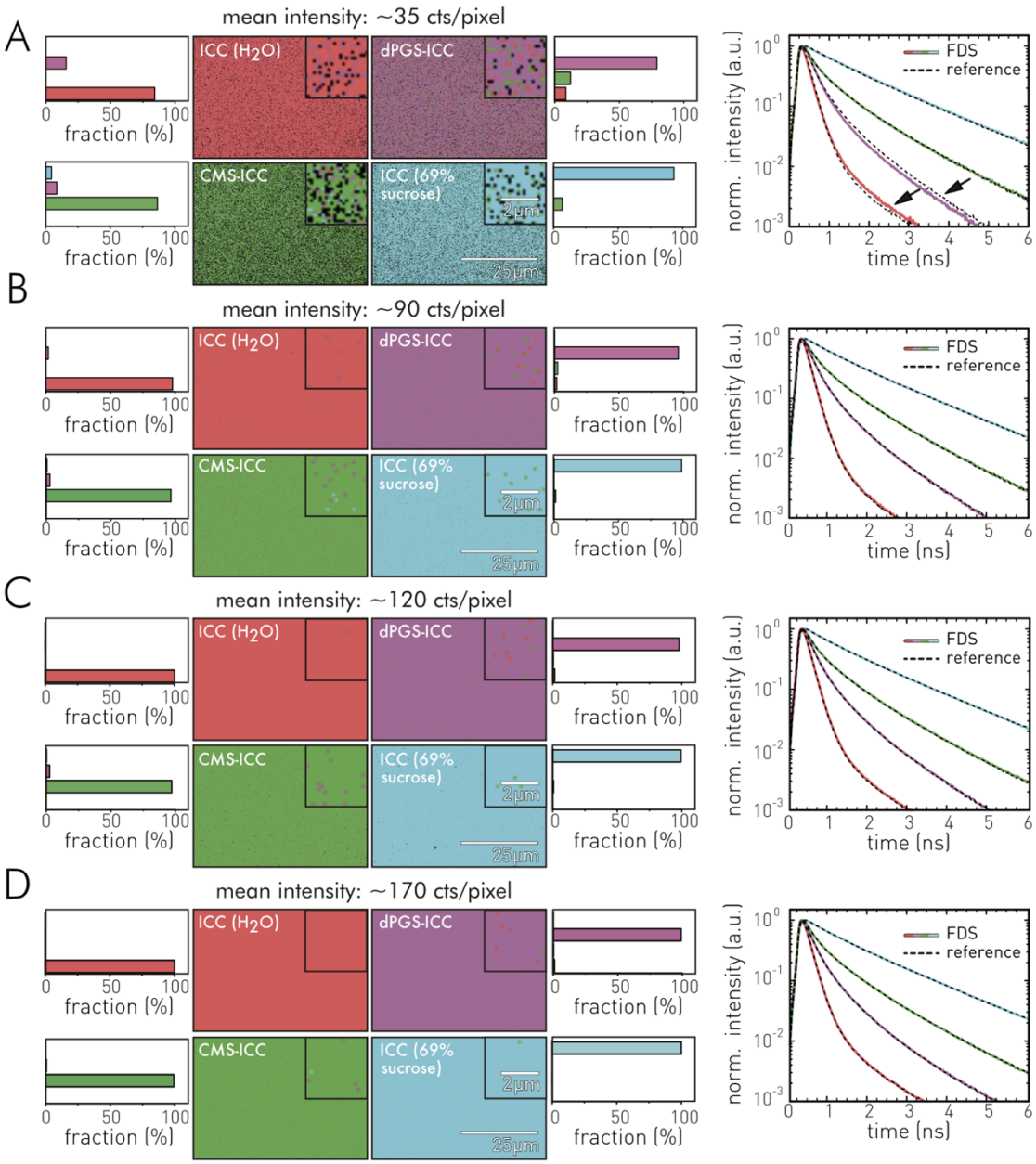

E

percentage of misassignments

mean intensity	ICC (H_2O)	dPGS-ICC	CMS-ICC	ICC (69% sucrose)	Mean ± SD
35 cts/pixel	16 %	21 %	13 %	6.8 %	(14 ± 5) %
90 cts/pixel	1.9 %	4.2 %	3.4 %	1.2 %	(2.7 ± 1.2) %
120 cts/pixel	0.21%	2.0 %	2.9 %	0.64 %	(1.4 ± 1.1) %
170 cts/pixel	0.17%	0.99 %	0.71 %	0.05 %	(0.44 ± 0.42) %

Figure 4.1.9: Validation of Cluster-FLIM using experimental FLIM data of ICC in varying environments and at different photon intestines: Cluster-FLIM analysis of the same fluorophore in four different environments identifies four multi-exponential fluorescence lifetime signatures. The decays show mean lifetimes of 0.25 ns, 0.47 ns, 0.80 ns, and 1.46 ns. **A-D** Global Cluster-FLIM analyses of FLIM-images from homogeneous solutions of ICC in H_2O (red), in a 69 % (w/w) sucrose (cyan), and attached to dPGS (magenta) and CMS (green) for different mean pixel intensities of 35 counts/pixel (A), 90 cts/px (B), 120 cts/px (C), and 170 cts/px (D). The recorded image area and all other experimental conditions are identical within the clustering analysis, i.e., a global analysis of four recordings of ICC in the different environments at the same pixel intensity. A bar plot next to the respective FLIM-image area shows the relative fraction of cluster assignments. On the right, extracted FLSs are compared to reference fluorescence decays (input raw data) generated by integrating the decay histograms over the respective FLIM-image area. Cluster assignment errors may lead to a deviation of the FLS from the reference decay as shown in (A) and indicated by arrows. **E** Error analysis: Assignment errors (in %) of Cluster-FLIM for the four different ICC environments as a function of collected photons.

4.2 Characterization of fluorescent lifetime probes

4.2.1 Indocarbocyanine a fluorescence lifetime sensor for environmental changes

Indocarbocyanine (ICC) belongs to the group of fluorescent molecular rotors (FMR, see Section 2.1.2 and Section 2.1.3). ICC's fluorescence lifetime and quantum yield depend on its intramolecular rotation. This behavior can be attributed to an additional depopulation path of ICC's first excited molecular state besides radiative transitions responsible for the fluorescence emission. In detail, FMRs undergo intramolecular rotations while being in their excited state. These molecule-specific photoisomerization processes deexcite the FMR. This leads to a dependency between rotation efficiencies and the probability of radiative transitions. In case of increased rotation efficiencies, the fluorescence lifetime decreases.[82-84] This effect encourages the general use of FMRs as probes for dynamic and spatially resolved nanoviscosities of a multitude of systems like aerosol particles, lipidic model vesicles, cell organelles, and living cells.[79, 85-89] Here, the term nanoviscosity describes the apparent viscosity a small molecule of nano size experiences in a complex liquid.[256-257] In general, the efficiency of photoisomerization of an FMR can also be dependent on temperature, activation energy, or steric rotational restrictions caused by neighboring substituents. These multiple interdependencies motivated me to use ICC as a probe for molecular interaction monitoring between ICC-labeled nanoparticles and various molecular biological targets and living systems such as cells and tissues.

The fluorescence lifetime of ICC observed in aqueous solution is relatively short, typically between 0.14 – 0.18 ns. However, it can also adopt values of several nanoseconds after binding ICC to macromolecules, or if ICC is dissolved in solvents of high viscosity.[25, 198, 232] The short lifetimes in aqueous solution are caused by an efficient rotation around the C-C bond of ICC's methine linker (see Figure 4.2.1A), leading to a high non-radiative isomerization transition rate k_{iso}.[62] If this process is hindered, either by friction with solvent molecules (viscosity) or other steric restrictions leading to higher activation energies, the radiative transition path gets more occupied increasing the fluorescence lifetime according to Eq. 16. In the following, the influence of the viscosity- and temperature-dependent photoisomerization properties of the ICC FMR on the fluorescence lifetime is systematically characterized as well as influences of local environmental changes after attaching the ICC probe to nanoparticles.

Fluorescence emission of ICC in different environments

First, I would like to demonstrate the general influence of different molecular environments on the fluorescence properties of the ICC probe. For this purpose, I used different exemplary solvents and nanomaterials to investigate the changes on ICC's fluorescence properties: H_2O as a polar solvent, EtOH as solvent providing both polar and apolar properties, and glycerol as a highly viscous solvent. Furthermore, changes after the attachment of ICC to dendritic nanomaterials are shown by the

covalent attachment to dendritic polyglycerol sulfate (dPGS) nanoparticles and core-multishell (CMS) nanocarriers with an hyperbranched polyglycerol core (Figure 4.2.1B,C).

First, the environmental effects on the spectral fluorescence emission are demonstrated. ICC's fluorescence is typically excited between 475 nm and 575 nm (see Sec. 2.1.3). In the following experiment the excitation was set to 530 nm. Figure 4.2.1D compares the resulting emission spectra of ICC dissolved in H_2O (blue), EtOH (red), glycerol (black), and covalently attached to the dPGS-NP surface (magenta), and to the polyglycerol core of a CMS-NP (green), respectively.

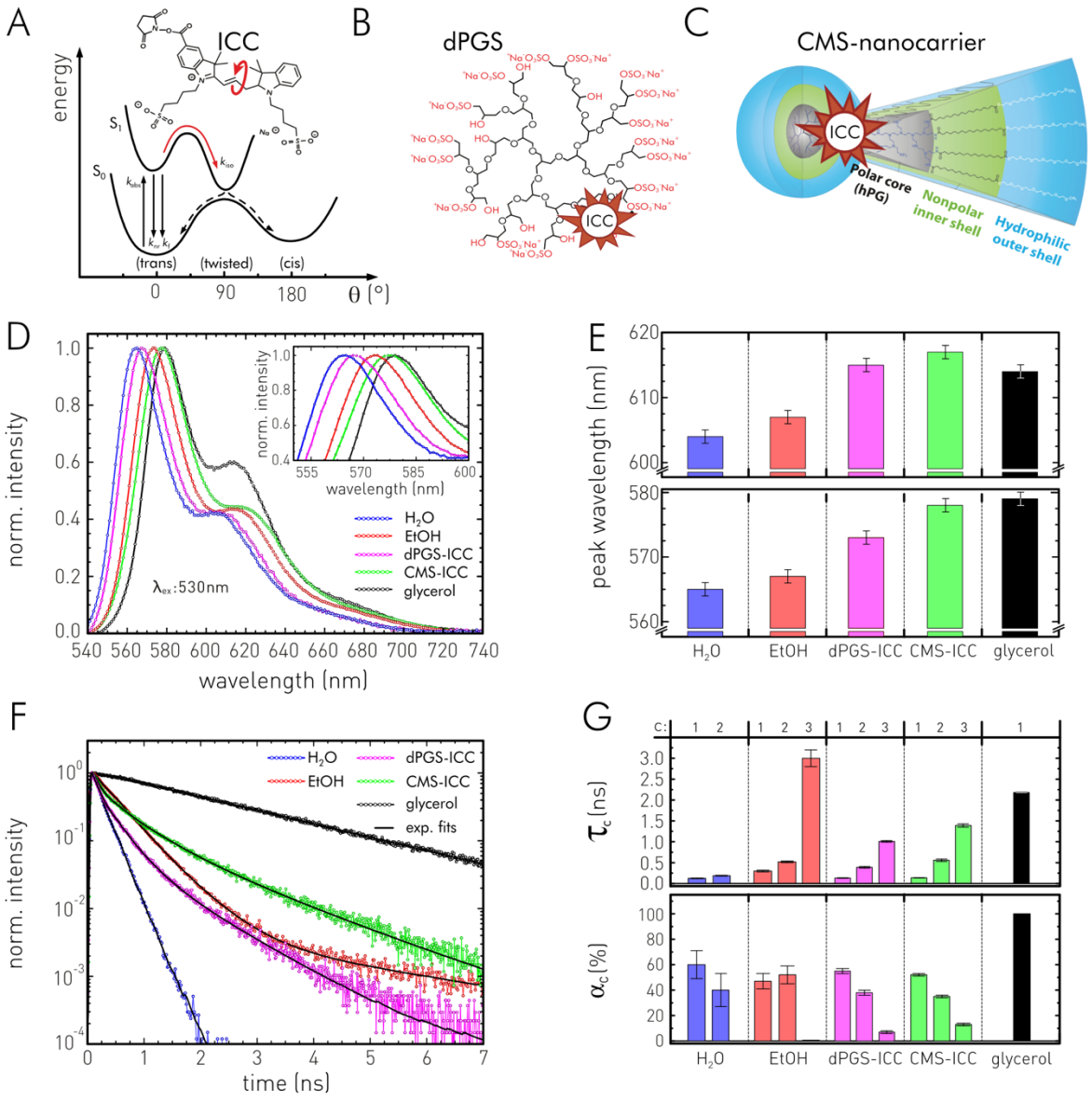

Figure 4.2.1: ICC in different molecular environments. **A** Chemical structure of ICC and illustration of the potential surface. **B** Scheme of ICC covalently attached to the surface of dPGS. **C** Scheme of ICC covalently attached to the dendritic core of a CMS-nanocarrier. **D** Fluorescence emission spectra of ICC in H_2O (blue), EtOH (red), glycerol (black), and attached to dPGS (magenta) and CMS-nanocarrier (green), **E** Peak wavelengths of the observable fluorescence bands in the emission spectra shown in D. Indicated uncertainties correspond to the selected spectral bin-width Δλ. Experimental conditions: λ_{ex} = 530 nm, λ_{em} > 550 nm, Δλ = 1 nm, Δt = 1 s. **F** Fluorescence decays and (multi-)exponential model fits (Eq. 19) of ICC in the environments shown in D. **G** Fit

results of (multi-)exponential decay analysis (See also Table A1). Indicated uncertainties are based on confidence interval analyses (Section 3.4.1). Experimental parameters are given in in Figure 4.2.2.

The emission spectrum of ICC generally shows two broad bands characterized by a main and a bathochromic shifted side peak. The intensity ratio between both peaks has its maximum for H_2O and dPGS-ICC, while ICC dissolved in glycerol shows the smallest ratio. The spectral positions of both peaks are visualized in Figure 4.2.1. The main peak position shifts from 565 ± 1 nm for ICC in H_2O to 579 ± 1 nm in glycerol. In literature, such bathochromic shifts (see section 2.1.2) are reported frequently for indocarbocyanine-based FMRs, typically in connection with decreasing solvent polarity.[76] This certainly applies to the shift between H_2O and EtOH. The polarity of glycerol, however, lies between both solvents and still shows the largest bathochromic shift. This suggests that viscosity and polarity affect the peak position simultaneously. Spectral changes can be generally attributed to fluctuations in the energy level of the excited state of a fluorophore. Such changes may also alter the activation energy barrier and shape of the potential energy surface (Figure 4.2.1A) defining the photoisomerization probability.[62]

When ICC is covalently bound to CMS-NP or dPGS-NP, the emission spectrum of ICC receives a red-shift. This was also observed in earlier studies on ICC nanoparticle conjugates.[198, 258] In this case, it can be assumed that the attachment site causes overlapping effects by polarity changes and steric restrictions on the photoisomerization. This is especially expected for CMS-ICC, as the ICC probe is bound to the hyperbranched polyglycerol core. Therefore, there is a high probability that ICC is found in the nonpolar inner spherical shell, which consists of octadecanoic acid. At this site, steric restrictions on the intramolecular rotation are very likely. At the same time, the inner shell has a much lower polarity than a aqueous solution allowing for the transport of lipophilic compounds.[4, 132] A similar picture emerges for dPGS-ICC where the ICC probe is attached near the anionic sulfate groups on the surface of the dendritic nanoparticle. As with CMS-NPs, this position simultaneously leads to steric restrictions of the intramolecular rotation by nanoparticle substituents and to polarity changes due to the charge distributions on the sulfated dPGS surface.

Besides the influence on the spectral emission properties of ICC, the general molecular environment is also a crucial factor on ICC's fluorescence lifetime and thus determines the shape of its time-resolved fluorescence decays. Figure 4.2.1F shows ICC's fluroescence decay traces recorded for the solvents and nanomaterials mentioned above. The color code corresponds to the respective emission spectra. The fast fluorescence decay of ICC in aqueous solution (blue line) shows the aforementioned efficient intramolecular rotation of ICC leading to a non-radiative transition from S_1 to S_0 via photoisomerization. Changing the solvent from H_2O to EtOH results in a significant slow down of the fluorescence decay. This effect is caused by an altered activation energy barrier for the intramolecular rotation around ICC's methine-linker. The activation energy seems to be increased by the solvent change leading to a less efficient rotation. A significant viscosity effect on the rotation can be excluded *per se* as the difference in solvent viscosity between H_2O and EtOH at 20 °C is

minimal (1.00 cP versus 1.19 cP).[259] An even stronger increase in the fluorescence lifetime is observed for glycerol. ICC disolved in this trihydric alcohol shows the slowest decay investigated. It can be assumed that restrictions of ICC's intramolecular rotation due to friction with glycerol molecules leads to this increase in fluorescence lifetime. The viscosity of the glycerol solution amounts 1,412 cP at 20 °C, a dramtic increase compared to the viscoscity level of ~1 cP in H_2O at the same temperature. However, it cannot be excluded that changes in the activation energy may have contributed. Fluorescence decays of the ICC probe attached to both nanoparticles show highly multi-exponenital decays with a fast component similar to ICC in H_2O next to slower components that may originate from changed activation energies by steric resticitions or polarity changes after the attachment to the nanoparticle.

In order to further characterize the individual fluorescence decay traces, I performed decay anaylses (see Section 3.4.1) by fitting the fluorescence decays to (multi-)exponential decay models (Appendix, Table A1). Figure 4.2.1G displays the determined decay components τ_c and relative decay amplitudes α_c. The fitting analyses reveal fast fluorescence decay components between 0.127 ± 0.008 ns (in H_2O) and 0.30 ± 0.02 ns (in EtOH). With the exception of glycerol, which has only a single decay component of 2.180 ± 0.003 ns. The fast fluorescence decay component τ_1 is characteristic of the efficient isomerization of the methine linker, which is not present in the highly viscous glycerol. The fast decay dominates for ICC also when conjugated to nanoparticles, expressed by high relative amplitudes of τ_1. This points to an efficient isomerization even after the attachment. That means the intramolecular rotation of ICC is only marginally hindered by surrounding polyglycerol branches and surface sulfation of dPGS or in the case of CMS by the inner octadecanoic diacid shell. Additionally, steric restrictions or other changes to the rotational activation energy barrier upon ICC conjugation generate a second and third decay component with values around 0.4 – 0.6 ns and 1.0 – 1.4 ns. These values are comparable to fluorescence lifetimes previously reported for indocarbocyanines after covalent binding to polymers.[198, 258] The simultaneous occurrence of several decay components indicates that different fluorescence species are superimposed. Some of the emitting ICC molecules appear to rotate freely, others are sterically restricted by substituents, or show reduced isomerization due to solvent friction (viscosity). All processes are additionally overlaid by local variations in the activation energy barrier which itself can depend on serval factors like the local environmental polarity.

A valid decay analysis is essential to understand the underlying processes of fluorescence lifetime changes. For this reason, I would like to present the decision-making process for the appropriate number of decay components selected in the fitting analysis next. As described in section 3.4.1, the quality of the fit and the selected decay model was verified by the χ^2_{red} parameter and weighted residuals $R_w(t_j)$. Therefore, the fluorescence decays of the examined ICC samples were fitted with mono-, bi- or tri-exponential model functions (Eq. 19, n =1,2,3) and their quality was subsequently compared and reviewed. The recorded fluorescence decay traces, IRFs, fit curves and residuals for

ICC dissolved in H_2O, MeOH, EtOH, glycerol and attached to dPGS-NP and CMS-NP are shown in Figure 4.2.2. The respective fit parameters are summarized in Table A1 (Appendix). The number of decay components n were considered as sufficient, which produced randomly distributed residuals, χ^2_{red} values of ~1, and for which the next higher n did not yield a significant improvement. In particular, the decay traces of ICC in H_2O can be fitted by two decay components just like ICC in MeOH. In pure EtOH, three components are necessary, however, with an amplitude of the third component α_3 of under 1 %. For ICC dissolved in the high viscous glycerol, the use of one decay component is sufficient. If the FMR probe is bound to dPGS and CMS, three decay components are generally necessary to fit the fluorescence decay trace appropriately to an exponential model. An identical number of fluorescence decay components was observed in previous investigations of similar dPGS-ICC and CMS-ICC nanoparticles.[198, 258] The presented selection of the decay components is also used for the further evaluation of ICC fluorescence decays in the next sections. For binary solvent mixtures, the number of decay components is adjusted if necessary. The corresponding quality control of these fits is then indicated by the χ^2_{red} parameter in respective tables (see Appendix).

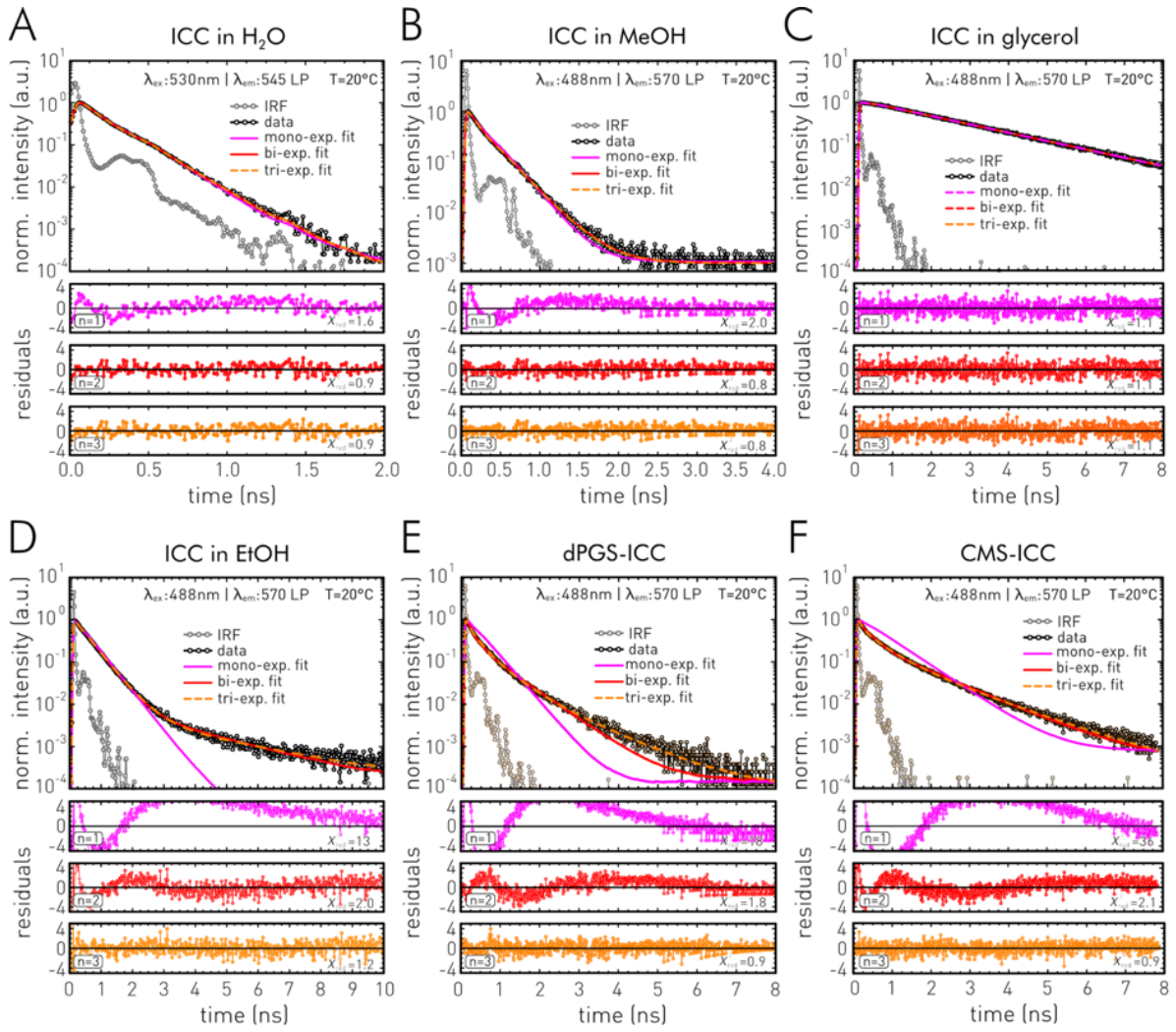

Figure 4.2.2: Assessing an appropriate number of decay components in multi-exponential decay fitting of ICC fluorescence decay traces in different environments. The goodness of fit for varying numbers of decay components (n = 1–3) are examined by weighted residuals (R_w, Eq. 46) and reduced chi squares (χ^2_{red}, Eq. 45). **A** ICC dissolved in water. **B** ICC dissolved in MeOH. **C** ICC dissolved

glycerol. **D** ICC dissolved in EtOH. **E** ICC covalently attached to surface of dPGS. **F** ICC covalently attached to the polyglycerol core of a CMS-nanocarrier. Normalized original TCSPC decay traces (data) are indicated in black connected open dots. The instrumental response function is shown in connected gray dots. Solid lines display exponential fits using magenta for mono-exponential (n=1), red for bi-exponential and orange for tri-exponential fits. Experimental conditions: TCSPC-cuvette setup (Section 3.3.3), spectral parameters and temperatures are indicated in the individual plots. Fit parameters and uncertainties according to a confidence interval analyses of the fit parameters are given in Table A1 (see Appendix).

Fluorescence lifetime – photoisomerization dependency of ICC

After having considered the fluorescence decay behavior of ICC in different solvents and attached to dendritic nanoparticles, I would like to focus on a more systematic characterization of the photoisomerization process and its consequences on ICC's fluorescence lifetime. ICC is an FMR with a single emission band (see section 2.1.2). Thus, viscosity and steric restrictions directly influence the fluorescence transition, reflected in the fluorescence emission intensity. For cyanines like ICC, the *trans-cis* isomerization is the main non-radiative transition that competing with the radiative fluorescence depopulation path.[77] The respective isomerization rate constant k_{iso} depends on the local viscosity and activation energy barrier E_0.[62, 70]

To investigate these dependencies in a simple experimental configuration and over a wide viscosity range, I dissolved ICC in glycerol, whose viscosity can be easily adjusted between 31.5 cP and 6,647 cP by the present temperature (80 °C – 5 °C). The use of a single solvent has the advantage over binary solvent mixtures, that a potential activation energy barrier E_0 is probably not influenced by pure temperature changes (see Eq. 42) and thus remains constant for the individual set viscosity values. Binary solutions are more likely to affect E_0 because two different solvent molecules with different physicochemical properties are used, which could affect E_0 differently for each solvent ratio.

Figure 4.2.3A shows the effect of temperature-dependent viscosity changes of glycerol on the spectrally resolved fluorescence emission bands of ICC. Independent of temperature, excitation at 530 nm results in fluorescence emission ranging from 550 nm to 750 nm, with a maximum at 576 ± 1 nm. The spectra display that the fluorescence emission intensity increases with increasing viscosity induced by decreasing solvent temperatures (rainbow color code). The underlying principle describing this behavior is defined by Eq. 27. In this equation, an activation energy barrier is not considered. The fluorescence quantum yield and thus the observed fluorescence intensity is treated only as a function of the local viscosity. The observed relative intensity increase is not constant over the whole emission spectrum. Figure 4.2.3B shows the emission spectra of Figure 4.2.3A normalized to their maximum. In this representation, the smaller second peak at 613 ± 1 nm increases relatively to the main peak with reduced viscosity/increased temperature, accompanied with a small bathochromic shift of the main peak at 576 ± 1 nm. The total fluorescence intensity of ICC, here, the integral over the entire recorded emission spectrum, is a function of the present glycerol viscosity. As the solvent viscosity is directly dependent on the temperature, I visualized the fluorescence intensity – viscosity – temperature relationship as a two-dimensional plot in Figure 4.2.3.C as well as a three-

dimensional plot in Figure 4.2.3D. Both Figures are realized as linear – log plots (T vs. η) and show an almost linear behavior in the range between 50 and 1,000 cP.

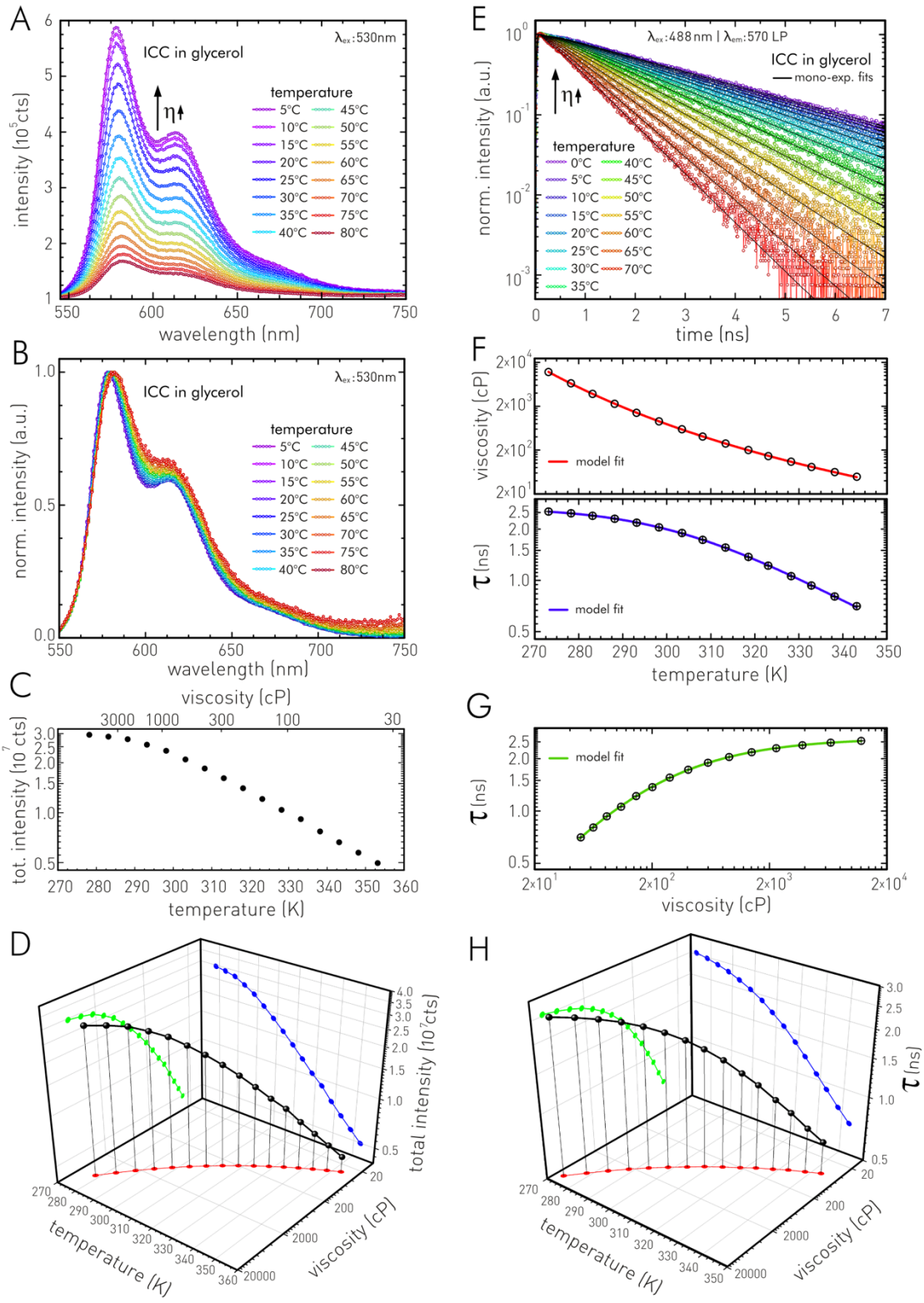

Figure 4.2.3: Fluorescence emission spectra and decay traces of 0.1 µM ICC dissolved in glycerol solutions of different viscosities as function of temperature. **A** Fluorescence emission spectra of ICC dissolved in glycerol as function of temperature. **B** Normalized spectra shown in A. **C** Total fluorescence emission intensity of ICC as function of absolute temperature. **D** 3D visualization of total fluorescence intensity versus absolute temperature and corresponding viscosity of glycerol. Experimental conditions: λ_{ex} = 530 nm, λ_{em} > 550 nm, Δλ =1nm, Δt=1 s. **E** fluorescence decay traces of ICC dissolved in glycerol at indicated temperatures

(rainbow colors), black solid lines display mono-exponential fits. **F** Top: Glycerol viscosity as function of absolute temperature (see Ref. 260). Red solid line indicates theoretical behavior of viscosity to temperature according to $\eta(T) = A \exp\left(\frac{B}{C-T}\right)$ model. Bottom: ICC's fluorescence lifetimes in glycerol obtained by mono-exponential decay analysis (E) as function of absolute temperature. Blue solid line shows fit of data points to Eq. 34. **G** ICC's fluorescence lifetimes (Table A2) in glycerol as function of glycerol viscosity. green solid line shows fit of data points to Eq. 34. **H** 3D visualization of fluorescence lifetime as function of absolute temperature and corresponding viscosity of glycerol. Experimental conditions: TCSPC-cuvette setup (Section 3.3.3), λ_{ex}=488 nm, λ_{em} > 570 nm. Indicated uncertainties are based on confidence interval analyses (Section 3.4.1), values are given in Table A2.

The dependency between viscosity and fluorescence intensity of an FMR is a valuable relationship, that may allow the determination of viscosities by a suitable calibration.[61] However, as soon as a defined FMR concentration is no longer available, misinterpretations occur. In this case, it is not possible to distinguish whether an increase in intensity is caused by an increase in viscosity or only by an increase in concentration. The same problem occurs when additional fluorescence quenching effects not related to the isomerization occurs. Since the concentration of an FMR often cannot be kept constant during an experiment, especially in microscopic approaches, the use of fluorescence lifetimes as an alternative measure of viscosity becomes interesting.[61, 66, 69, 261] This has the additional benefit that some quenching induced fluorescence lifetime changes can be directly recognized. According to Eq. 28, the fluorescence lifetime of an FMRs can be expressed also as a function of the local viscosity. However, unlike the fluorescence intensity, this parameter is independent of FMR concentrations. For this reason, I will now focus further on the effects of viscosity on the fluorescence decay behavior of ICC. Figure 4.2.3E displays the fluorescence decay traces of ICC dissolved in glycerol. Again, I adjusted the viscosity by the solvent temperature (70 – 0 °C), this time between 49.4 cP and 12,100 cP. Here, too, as with the fluorescence intensity, a change can be observed. The fluorescence decays become steadily slower and slower with higher viscosities. This fluorescence lifetime effect leads to totally increasing fluorescence intensities, since the area under the fluorescence decay curves is proportional to the observable steady-state intensity.

The fluorescence decay behavior of ICC is further investigated by a decay analysis (see Sec. 3.4.1). For this purpose, I fitted the time-resolved fluorescence traces to a mono-exponential decay model (Appendix, Table A2). The decay analysis of the glycerol experiments reveals a minimal fluorescence lifetime of 0.71 ns at 49.4 cP (70 °C) and a maximum lifetime of 2.54 ns at 12,100 cP (0 °C). The determined fluorescence lifetimes at the respective glycerol viscosities are visualized as a function of the glycerol temperature in Figure 4.2.3F. In the upper penal, an additional fit curve of a viscosity – temperature dependency model is plotted in red (see legend). The lower panel visualizes the dependence between fluorescence lifetime and temperature. The resulting dependency of ICC's fluorescence lifetimes on the glycerol viscosity is shown in Figure 4.2.3F, realized as a double logarithmic Förster-Hoffmann plot. As one can easily see, the data points deviate from a straight line according to the Förster-Hoffmann equation (Eq. 28 & 29). Only the lower viscosity range shows a linear dependence. In the higher viscosity range, however, the curve becomes increasingly saturated. For this reason, the temperature-dependent viscosity – fluorescence lifetime model function according to

Eq. 34 is now applied. The saturating behavior is caused by a present energy barrier for the photoisomerization which leads to increased rotation efficiencies at higher temperatures and thus to a flattening of the fluorescence lifetime increase. The fluorescence lifetime data were fitted to Eq. 34 using the respective temperature information. The obtained fits are plotted in Figure 4.2.3F (green) and Figure 4.2.3G (blue). The latter describes the fluorescence lifetime – viscosity dependence of ICC and can be used as a calibration curve for a lifetime-based viscosity determination. Additionally, the fluorescence lifetime – viscosity – temperature relationship is visualized in Figure 4.3.3H as a three-dimensional plot. The fit to the model (Eq. 34) yields the activation energy E_0, required for intramolecular rotation of ICC in glycerol, as well as the FMR specific parameter y that describes the sensitivity of the fluorescence lifetime to the present viscosity. The activation energy was determined to ~20 kJ/mol, the rotor-specific viscosity exponent to 0.4.

According to Eq. 34, the rate constant k_{iso} determining the isomerization process between the *trans* – *cis* configuration in S_1 can be expressed as a product of two terms: an activation energy dependent term and a term describing the interaction between FMR and the solvent, which is caused by microfriction and can be related to the solvent viscosity.[62] According to Kramer's theory, the activation activity, i.e., the height of the potential barrier between *trans* and *cis* configuration as well as the shape of the one-dimensional potential energy surface should classically be independent of physical solvent properties and only dependent on the FMR structure. However, it must be assumed that solvent properties such as the dielectric constant, viscosity, pressure, or temperature, may affect E_0, making functional descriptions difficult.[62, 70] The value of E_0 determined here is comparable to previous works which used the fluorescence quantum yield to investigate Cy3-based FMRs in different alcohols[70] and a sulfonated Cy3 in Tris-buffer[262]. A further study applied hybrid quantum mechanics/molecular mechanics approaches to simulate the potential energy surfaces in the excited state of a non-sulfated Cy3 in MeOH. They determined a theoretical activation energy value of 7 kJ/mol.[81] By simulating the attachment of Cy3 to single-stranded DNA, this energy is increased to 18 kJ/mol. Experimental data of Cy3 bound to DNA revealed an increase in activation energies from 19 to 25 – 33 kJ/mol.[262] In this bound configuration, the structure of the FMR is most rigid, i.e., the intramolecular rotation senses the highest steric restriction due to an FMR – DNA stacking interaction. This leads to an increase in the activation energy barrier, which in turn makes relaxation via fluorescence more efficient than relaxation via the *cis* – *trans* isomerization in S_1 and a subsequent non-radiative transition to S_0.

In most studies, FMRs and their fluorescence lifetime – viscosity dependencies are characterized by binary mixtures of a low and a high viscous solvent. This procedure expands the respective viscosity interval from a few to several thousand centipoises, by just using different molecular ratios between both solvents. Subsequently, this characterization can serve as a lifetime – viscosity calibration (Förster-Hoffmann plot) to determine nanoviscosity, for example in living cells.[12, 15, 80, 94] In addition, the general viscosity – temperature dependence allows to further increase the viscosity range

by using temperature series. However, this procedure may change the activation energy of FMR isomerization for each applied solvent ratio, with the potentially consequence of saturating calibration curves that cannot adequately described by Eq. 34 which assume a constant E_0 and a saturation only caused by changing temperatures. Additionally, a fluorescence lifetime plateau, leads to an inaccurate viscosity assignment due to the reduced sensitivity for higher viscosities. Since the dielectric constant (ε) is a parameter that can affect E_0, typically solvents of similar ε are used to prevent strong polarity effects disturbing the calibration.

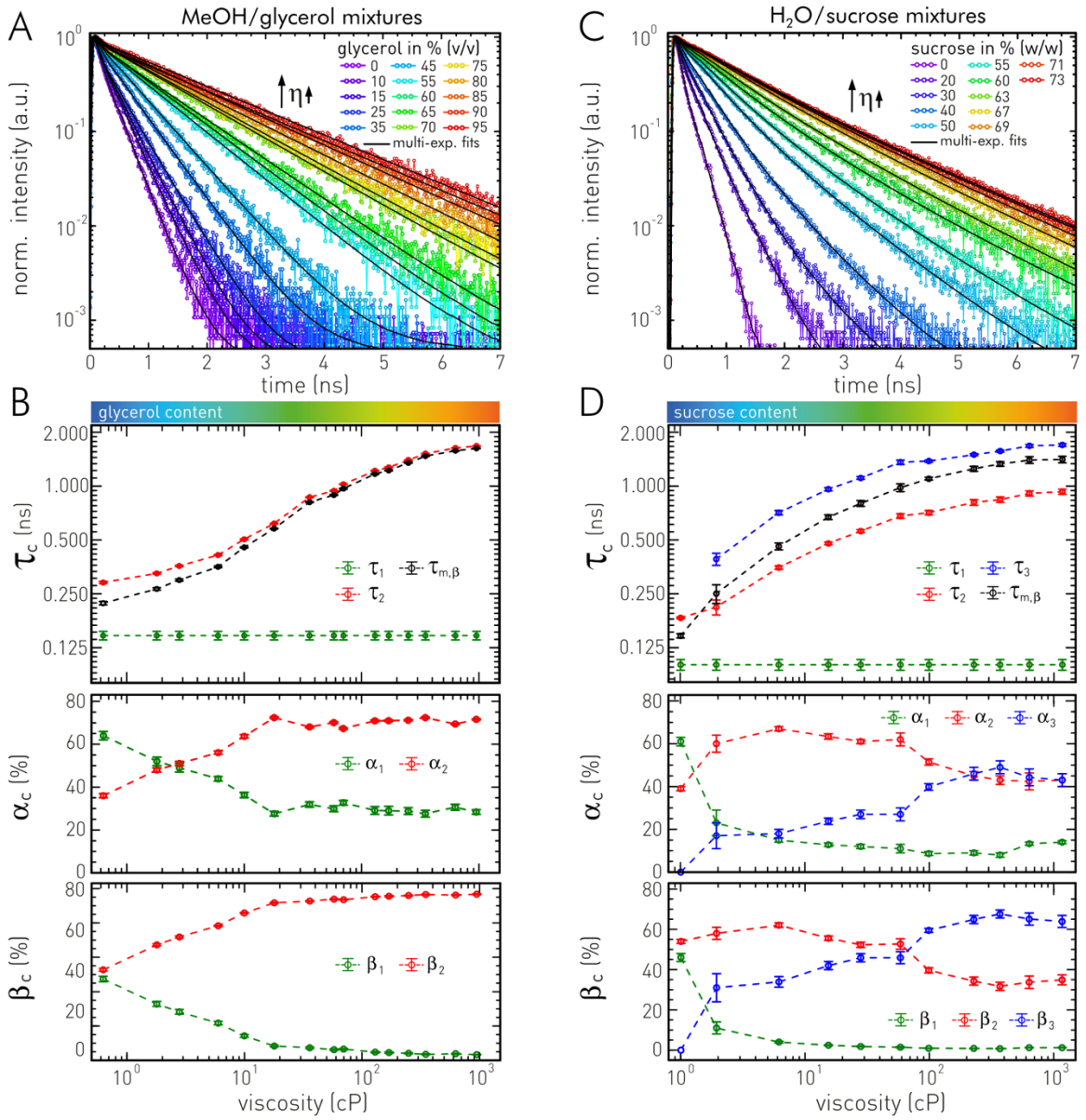

Figure 4.2.4: Fluorescence decay characteristics of 0.1 µM ICC at different viscosities generated by MeOH/glycerol and H_2O/Sucrose mixtures of varied molecular ratios. **A** Fluorescence decay traces of ICC dissolved in MeOH/glycerol mixtures of different ratios (rainbow colors), i.e., different viscosities at 25 °C. Black solid lines display multi-exponential fits (see Table A3). **B** Top: Förster-Hoffmann plot of ICC's decay components and mean fluorescence lifetime versus the respective viscosity. Center: Relative decay amplitudes versus viscosity. Bottom: Relative steady-state fluorescence contributions β_c versus viscosity. **C** Fluorescence decay traces of ICC dissolved in H_2O/sucrose mixtures of different ratios (rainbow colors), i.e., different viscosities at T=20 °C. Black solid lines display multi-exponential fits (see Table A4). **B** Fit results. Top: Förster-Hoffmann plot of ICC's decay components and mean fluorescence lifetime versus the respective viscosity. Center: Relative decay amplitudes versus viscosity (log scale). Bottom: Relative

steady-state fluorescence contributions β_c versus viscosity (log scale) Experimental conditions: TCSPC-cuvette setup (Section 3.3.3), spectral parameters for both series in A and C: λ_{ex} = 488 nm, λ_{em} > 570 nm. Indicated uncertainties are based on confidence interval analyses (Section 3.4.1).

To test the fluorescence lifetime behavior of ICC in binary solution mixtures, I examined ICC in two solvent mixtures at a low and at a higher polarity range. First, I dissolved ICC in MeOH/glycerol mixtures and recorded the resulting fluorescence decay traces at 25 °C. The dielectric constant of both solvent at this temperature is 33 for MeOH and 42 for glycerol. Figure 4.2.4A shows fluorescence decay traces of 0.1 µM ICC in MeOH/glycerol mixtures of different ratios. The respective viscosities vary between 0.6 cP and 950 cP. Like in the glycerol experiments, the fluorescence decay traces clearly show that ICC's fluorescence decays slow down with increasing viscosity. This again reflects the reduced efficiency of intramolecular rotation (photoisomerization) at higher viscosities, which is associated with a reduced non-radiative depopulation of the S_1 state and is thus reflected in the fluorescence lifetime. The increased depopulation via fluorescence results in longer fluorescence lifetimes and thus in slower fluorescence decays.

The fluorescence decay behavior of ICC is further investigated using a decay analysis (see section 3.4.1) by fitting the time-resolved fluorescence traces of Figure 4.2.4A to a bi-exponential decay model (Table A3). Figure 4.2.4B shows in its upper segment the determined decay components τ_c as a function of solvent viscosity realized as a Förster-Hoffmann plot (Log-Log). While the fastest decay component (τ_1 = 0.147 ± 0.008 ns) remains constant over the viscosity interval, the second decay component increases from 0.291 ± 0.004 ns to 1.686± 0.004 ns. The corresponding relative decay amplitudes (α_c) shown in the middle segment of Figure 4.2.4B change accordingly as follows: the amplitude α_1 decreases with higher viscosities from 64 ± 2 % to 28 ± 1 %. The second amplitude α_2 increase from 36 ± 1 % to 71.6 ± 0.3 %. To study the relative population of the individual fluorescence species, the relative-steady state contributions β_c were calculated. The results are shown in the lower segment of Figure 4.2.4B. This graph clearly shows that the contribution of the fast decay component τ_1 decreases with increasing viscosity drastically (47 ± 2 % to 3.3 ± 0.2 %). In contrast, the population of the second component increases from 52.7 ± 0.8 % to 96.7 ± 0.3 %. A classical linear dependence of the fluorescence lifetime ($\tau_{m,\beta}$) as would be expected according to Förster-Hoffmann (Eq. 28 & 29) can only be detected in the lower viscosity range (<10 cP). At higher viscosities, the linearity is increasingly undercut. If one looks at Eq. 34 and considers the temperature constant, a change in the activation energy is probably responsible for this deviation, resulting from different solvent ratios and the resulting physical properties in the local environment of the ICC molecules.

The second solvent mixture examined is an aqueous sucrose solution. The dielectric constant of H_2O at 20 °C is 80.4, for a 60 % (w/w) sucrose solution ε declines to 61.8. Figure 4.2.4C shows fluorescence decay traces of 0.1 µM ICC in H_2O/sucrose mixtures at different ratios. The solvent mixtures investigated have viscosities between 1.01 cP and 1,170 cP. The fluorescence decay traces

show, likewise to the MeOH/glycerol mixtures and the glycerol solution, that the fluorescence lifetime of ICC slows down with increasing viscosity. Once again, higher viscosities lead to increased depopulation by fluorescence, which results in a longer fluorescence lifetime and thus slower fluorescence decay.

The fluorescence decay behavior (Figure 4.2.4C) of ICC is to be further investigated in a decay analysis (see section 3.4.1). Here, the time-resolved fluorescence traces were fitted to a tri-exponential decay model (Table A4). Figure 4.2.4D shows in its upper segment the determined decay components τ_c as a function of the solvent viscosity, which was realized as a Förster-Hoffmann plot (Log-Log). While the fastest decay component ($\tau_1 = 0.100 \pm 0.007$ ns) remains constant over the entire viscosity interval, the second and third decay component rises from 0.183 ± 0.002 ns to 0.93 ± 0.03 ns, and from 0 ns to 1.70 ± 0.003 ns, respectively. The corresponding relative decay amplitudes (α_c), which are shown in the middle segment of Figure 4.2.4D, change accordingly as follows: The amplitude α_1 decreases at higher viscosities from 61 ± 2 % to 14.0 ± 0.7 %. The second amplitude α_2 increases slightly from 39 ± 1 % to 43.0 ± 0.7 %, while α_3 increases from 0 % to 43.0 ± 0.7 %. The relative steady state contributions β_c were calculated again to investigate the relative population of the individual fluorescence species. The results are shown in the lower segment of Figure 4.2.4D. This plot shows that the contribution of the fast decay component τ_1 decreases by more than 97 % (46 ± 2 % to 1.2 ± 0.1 %) while the population of the second component decreases only from 54 ± 1 % to 35 ± 3 %, between 0 and 1,170 cP. In contrast, the third component increases simultaneously from 0 % to 64 ± 3 %. Again, there is no classical linear dependence of the fluorescence lifetime, here represented by $\tau_{m,\beta}$, as it would be expected according to the Förster-Hoffmann equation (Eq. 28 & 29). At higher viscosities, the linearity becomes increasingly flattened, even more so than with MeOH/glycerol. Here, too, it must be assumed that due to the different ratios of sucrose and H_2O, changes occur in the activation energy.

Since polarity can have a strong effect on the activation energy barrier of an FMR,[263] I investigated the effect of binary solvent mixtures with similar viscosity but different dielectric constants on ICC's fluorescence behavior. For this purpose, I chose EtOH/H_2O mixtures of varying ratios. While, the viscosity of these solvents only differ marginally (1.18 cP vs. 1.01 cP)[259], their dielectric constant ranges from 25.1 for EtOH to 80.4 for H_2O.[264] The effect of the H_2O/EtOH mixtures on the spectrally resolved fluorescence emission of ICC is displayed in Figure 4.2.5A,B. The individual spectra show a bathochromic shift with increasing EtOH concentrations (rainbow color code), i.e., with a decreasing dielectric constant. The wavelength shift of the emission peak as a function of dielectric constant is visualized in Figure 4.2.5C and takes place between 565 ± 1 nm and 574 ± 1 nm. The strongest increase is observed between a dielectric constant of 80 and 60, thereafter the slope flattens out, before it increases again starting from $\varepsilon = 30$.

If one considers the effects of the same mixtures on the fluorescence decay characteristic of ICC, one observes a similar dependency. With increasing EtOH content, i.e., decreasing dielectric

constant, a slowdown of the fluorescence decay can be observed. A decay analysis by fitting the fluorescence traces (Figure 4.2.5D) to bi-/tri-exponential model functions (see Section 3.4.1) yields the following picture: While the fastest decay component (τ_1 = 0.13 ± 0.02ns) remains constant for all mixing ratios, the second component increases from 0.202 ± 0.002 ns to 0.91 ± 0.03 ns. A third component occurs at an EtOH fraction of 33.3 % (w/w) with a value of 0.74 ± 0.02 ns which increases to 2.7 ± 0.2 ns in 100 % EtOH.

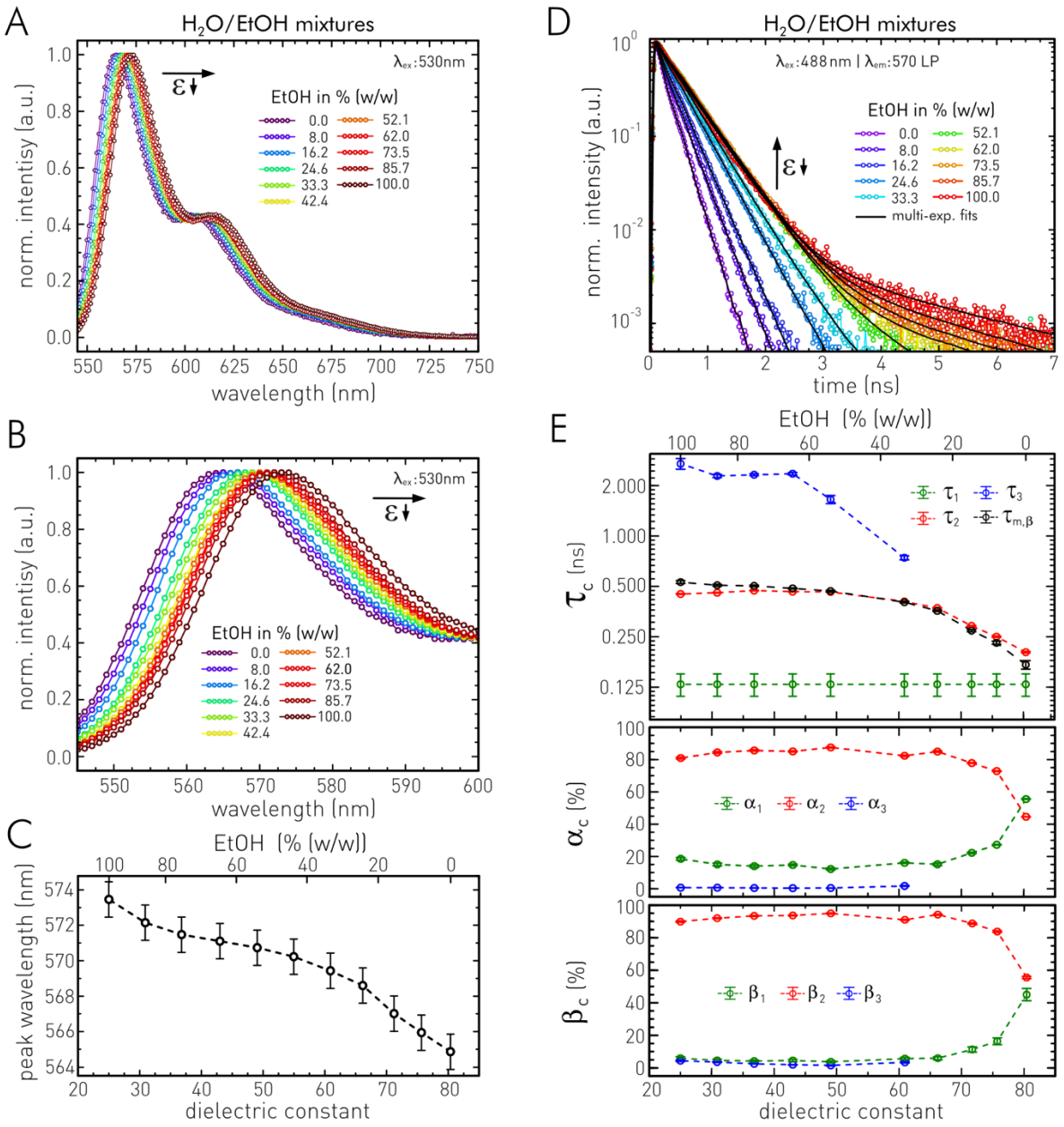

Figure 4.2.5: Influence of polarity to ICC's fluorescence characteristics. 0.1 µM ICC is dissolved in H_2O/EtOH mixtures with different molecular ratios. **A** Fluorescence emission spectra of ICC dissolved in H_2O/EtOH mixtures with different molecular ratios at 20 °C. **B** Normalized spectra shown in A. **C** shift of emission peak wavelength as function of the respective dielectric constant (ε). Indicated uncertainties correspond to the selected spectral bin-width Δλ. Experimental conditions: λ_{ex} = 530 nm, λ_{em} > 550 nm, Δλ = 1 nm, Δt=1 s. **D** Fluorescence decay traces of ICC dissolved in H_2O/EtOH mixtures of different molecular ratios (rainbow colors), black solid lines display multi-exponential fits. **E** Fit results (see Table A5). Top: ICC's decay components and mean fluorescence lifetime versus the respective dielectric constant. Center: Relative decay amplitudes versus dielectric constant. Bottom: Relative steady-state fluorescence contributions β_c versus dielectric constant. Experimental conditions: TCSPC-cuvette setup (Section 3.3.3), Spectral parameters are indicated in D. Indicated uncertainties are based on confidence interval analyses (Section 3.4.1).

All results are summarized in Table A5 (Appendix) and Figure 4.2.5E. The relative decay amplitudes (α_c) are shown there in the middle segment as follows: the amplitudes α_1 decreases with higher EtOH fractions from 55.5 ± 0.7 % to 18.5 ± 0.8 %. On the contrary, the second amplitude α_2 increase from 44.5 ± 0.1 % to 80.9 ± 0.6 %. The third component has only a negligible fraction with about 0 % – 1.7 ± 0.2 %. To study the relative population of the individual fluorescence species, the relative-steady state contributions β_c were calculated. The results are shown in the lower segment of Figure 4.2.5D. This Figure shows that the initial relevance of the first component decreases more and more with increasing EtOH content, and finally levels off at around 5 – 6 %. The second component, on the other hand, becomes more and more dominant with increasing EtOH content and reaches a level of almost 90 %. The complete transition process takes place between an EtOH fraction of 0 and 33.3 % (w/w). This corresponds to a shift in ε from 80 to 60.

The transition directly correlates with the previously described change in the spectrally resolved stead-state fluorescence emission. If one compares the maximum value of $\tau_{m,\beta}$ (0.53 ± 0.01 ns) in 100 % EtOH with the values plotted in the Förster-Hoffmann plot of both binary solvent mixtures in Figure 4.2.4B/D, one observes that this value corresponds to a viscosity around 10 cP. This suggests that the typically used calibrations for Cy3 derivatives are prone to errors at low viscosities, where polarity effects in the investigated sample may interfere with the calibration of the reference bulk solution mixtures. However, it can generally be assumed that the more viscosity-dependent sensitivity of the fluorescence lifetime predominates, especially at higher viscosities.

In summary, the results of this section confirm that ICC is a suitable fluorescence lifetime probe for nanoparticle systems, allowing to study interactions with their molecular nanoenvironment. ICC, like most water-soluble sulfocyanines, exhibits reduced aggregation and low non-specific binding to cellular components, while its brightness is high compared to its non-sulfonated counterparts and other red-emitting fluorophores.[265-266] The relatively high excitation wavelength of 530 – 570 nm additionally allows excitations in deeper positions of a tissue sample. The high excitation and emission wavelengths have the further advantage of a reduced phototoxicity in living cells.[267] ICC's fluorescence lifetime shows a high sensitivity to the local viscosity of its environment caused by microfriction and to steric restrictions to its intramolecular rotation by structures of the nanoparticle itself. The strength of this restriction and the associated change in ICC's activation energy for the intramolecular rotation may be altered by interactions of the nanoparticle with its environment. This has a direct effect on the fluorescence behavior and changes the time constant of the radiative transition process, i.e., the fluorescence lifetime (Figure 4.2.6A).

ICC's fluorescence lifetime also showed a sensitivity to the ambient polarity. However, this influence is much weaker than for the two effects mentioned above. The general monitoring of nanoparticle interactions by means of the ICC probe is not restricted by this. Only when attempting a viscosity determination, falsifications may occur, since the viscosity – fluorescence lifetime calibration takes place in reference bulk solutions. Binary solvent mixtures are often used for this purpose. Here, care

is taken to ensure that they have a similar polarity range. The chemical structures of the solvents used here are shown in Figure 4.2.6C. The two solvent mixtures, MeOH/glycerol and H_2O/Sucrose lead to a Förster-Hoffmann plot with a non-linear dependence between τ and η, at constant temperature. This means that the different mixing ratios resulting in the desired reference viscosities have an influence on the activation energy due to solvent dependent physicochemical variations. For this reason, potential calibrations only allow limited conclusions to be drawn about the viscosity in an unknown environment.

Consequently, it should be ensured that only the linear part of the Förster-Hoffmann plot is used. This is a general problem when using FMRs in viscosity determination and can only be avoided by new FMR designs that have a largely environment independent or relatively small E_0. All determined Förster-Hoffmann plots of ICC are compared in Figure 4.2.6B. The polarity effect on ICC's fluorescence lifetime as mentioned above can be seen for the H_2O/EtOH mixtures. Although the viscosity changes only slightly, from about 1 cP for pure EtOH and pure H_2O up to 2.7 cP for a 1:1 (w/w) mixture, the observed fluorescence lifetimes differ significantly, 0.17 ± 0.01 ns versus 0.53 ± 0.01 ns. However, if one considers the different measurement series and leaves out the strong polarity differences of EtOH and H_2O (ε =25 vs. 80), a corridor is obtained in which the fluorescence lifetimes follow a Förster-Hoffmann plot.

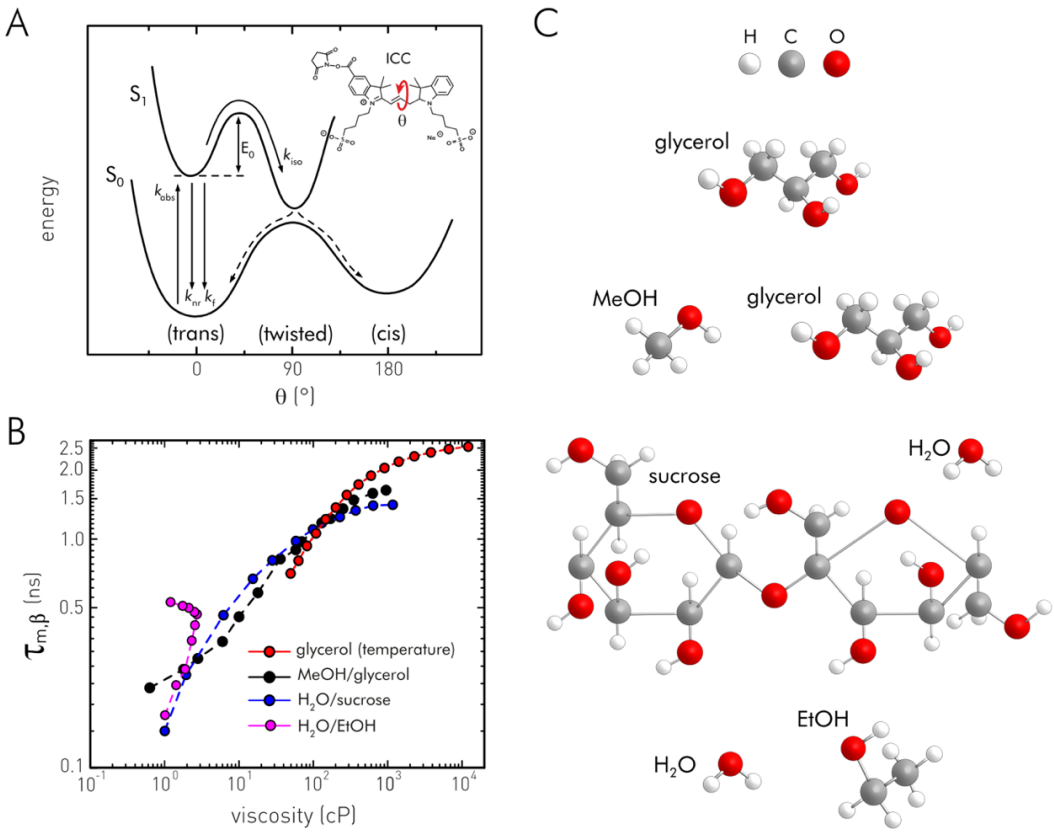

Figure 4.2.6: Summary of ICC characterization in reference solutions from different components. **A** Illustration of the potential energy surface of S_1 and S_2. E_0 is the activation energy barrier of the photoisomerization, k_{iso} defines the transition rate by isomerization. **B** Comparison of all mean fluorescence lifetimes in the different solvent mixtures as a function of the bulk viscosity. **C** Chemical structure of solvent molecules. Viscosity values of H2O/EtOH mixtures are estimated from Ref. 259.

4.2.2 PAc-SNARF a pH-responsive fluorescence lifetime probe

This section presents the time-resolved fluorescence characterization of a novel pH reactive propionic acid seminapthorhodafluorine probe (PAc-SNARF). The PAc-SNARF design and synthesis was developed by Dr. Celin Richter (Prof. Ernsting's group, Humboldt Universität zu Berlin, Germany) to remove several drawbacks of the frequently used 5'(or 6')-carboxy-SNARF derivatives (see Section 2.1.3, xanthenic dyes). Steady-state absorption and fluorescence emission of the dual-band fluoroprobe were already described by a spectral decomposition of absorbance and emission bands in the protonated and deprotonated state of PAc-SNARF using log-normal model functions.[92] The focus of my investigations is set on the time-resolved fluorescence properties and possible applications of PAc-SNARF as a pH responsive fluorescence lifetime probe.

The general concept underlying the time-resolved fluorescence characterization of the pH probe is to first determine changes in fluorescence lifetime parameters of PAc-SNARF in different pH environments. Since live-cell experiments represent a major field of application of a pH probe, my thesis then takes a closer look at the intracellular pH sensitivity. Cellular pH monitoring also has a certain importance in relation to the uptake of nanocarriers and their release mechanisms. In theory, pH titration of PAc-SNARF changes its protonation state, this process should be reflected in PAc-SNARF's absorption and steady-state/time-resolved fluorescence emission. According to the Henderson-Hasselbalch model (Eq. 59), such protonation-dependent changes follow a simple two-state transition, defined by the pK_a being the equilibrium constant of the protonation. It is investigated if this model holds true in the case of PAc-SNARF in the next paragraphs. The following results have been partially published in PCCP (Richter et al., 2015, see Ref. 92)

Stationary absorption and fluorescence characterization

First, I performed a spectral characterization of the PAc-SNARF pH probe in different pH environments by stationary absorption and fluorescence spectroscopy. This initial experiment aims at a general investigation of the spectral behavior as a function of the protonation state. It also ensures that the fluorophore is soluble and not aggregated at the pH values investigated. In order to illustrate the existence of two separated spectral absorbance and emission bands originating from the protonated and deprotonated SNARF forms, I performed fluorescence excitation/emission scans at pH 5.1, 7.0, and 9.4 (Figure 4.2.7A-C). At these pH values, PAc-SNARF is either in a purely protonated, in an intermediate protonated, or in a totally deprotonated state.

Figure 4.2.7A shows an excitation/emission map of the protonated PAc-SNARF form (pH 5.1) visualized as a contour-plot. The excitation/emission maximum of the protonate form locates at ($\lambda_{ex,max}$, $\lambda_{em,max}$) = (541 ± 1 nm/576 ± 1 nm). On the contrary, the maximum of the deprotonated form (pH 9.4) shifts to (569 ± 1 nm/624 ± 1 nm) as indicated in Figure 4.2.7C by white lines. At pH 7.0, a mixture of both protonation states is present, reflected by the excitation/emission map shown in Figure 4.2.7B. The visualization clearly shows that the excitation and emission in this

intermediate protonation state is composed of two fluorescent species, which can be identified by the purely protonated and deprotonated PAc-SNARF form. The excitation/emission maximum at pH 7.0 remains near to the position of the deprotonated form (see white lines, Figure 4.2.7B). This is attributable to both a much higher molar absorption coefficient and a higher quantum yield of PAc-SNARF in its deprotonated state.[92]

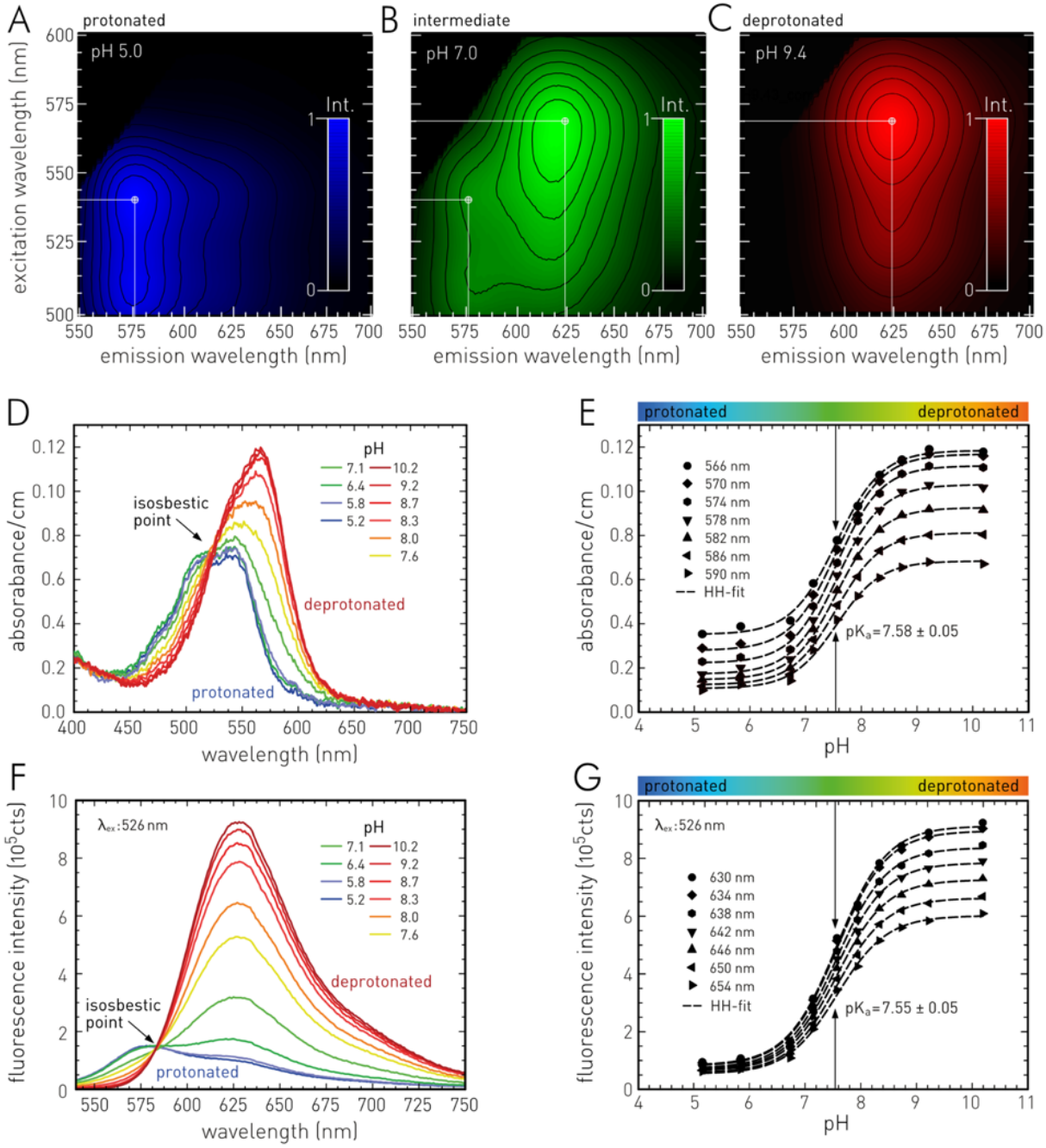

Figure 4.2.7: UV-VIS spectroscopy and steady-state fluorometry of 2.5 µM PAc-SNARF in 10 mM Tris-citrate buffer, 190 mM NaCl, and 5 % DMSO at various pH values (blue: protonated, red: deprotonated). **A-C** fluorescence excitation-emission plots of PAc-SNARF at pH 5.0 (protonated), pH 7, and at pH 9.4 (deprotonated). **D** Absorbance spectra of PAc-SNARF at indicated pH; isosbestic point: 526 nm. **E** pH dependent changes in absorbance at a set of selected wavelengths in the spectral range where the deprotonated form of PAc-SNARF is dominant (566 – 590 nm, $\Delta\lambda$ =4 nm). **F** Fluorescence spectra of PAc-SNARF at indicated pH; isosbestic point: 584 nm. Spectral conditions: λ_{ex}=526 nm, λ_{em}>545 nm. **G** pH dependent changes in fluorescence emission at a set of selected wavelengths in the spectral range where the deprotonated form of PAc-SNARF is prominent (630 – 654 nm, $\Delta\lambda$ =4 nm).

Shown pK_a-values are determined using global fits to a modified Henderson-Hasselbalch (HH) model (Eq. 60). Absorbance and emission spectra shown in D and F were recorded by Constantin Schneider (Prof. Alexiev's group, Freie Universität Berlin, Germany). Uncertainty of pH values is estimated to be ± 0.1

Before PAc-SNARF samples in different pH environments were investigated by time-resolved fluorescence spectroscopy, each sample was characterized individually by steady-state absorption and fluorescence spectroscopy. For this propose, a 2.5 µM stock was prepared by dissolving the sodium salt of PAc-SNARF in 10 mM Tris-citrate buffer at pH 10 supplemented with 190 mM NaCl (see Methods section). For the sake of obtaining clear isosbestic points and maintaining a constant fluorophore concentration, the stock solution was divided into aliquots and individually titrated to each investigated pH value by adding highly concentrated NaOH or HCl. Constantin Schneider recorded the stationary spectra shown in Figure 4.2.7D,E.

Figure 4.2.7D shows the absorption spectra of PAc-SNARF at various pH values between pH 5.1 (fully protonated) and 10.1 (fully deprotonated). At 526 ± 1 nm, the spectra show an isosbestic point, i.e., a wavelength where the absorbance remains constant, independent of the current pH. A simple approach to monitor the transition between the protonated and deprotonated state of PAc-SNARF is to analyze the changes in the deprotonated absorbance band as a function of the pH. Please note that a complete decomposition of the absorbance spectra into the "protonated" and "deprotonated" absorbance bands is shown in Ref. 92. To avoid a contribution of the protonated form in the simple model applied here, it is advisable to study the absorption spectra above 565 nm. The correspondent absorbance change at seven wavelengths (566 – 590 nm) is visualized in Figure 4.2.7E. A clear transition between two absorbance levels are present for all selected wavelengths. Using a global fit (shared pK_a parameter) of the data to a modified Henderson-Hasselbalch model according to Eq. 60 revealed a protonation equilibrium at 7.58 ± 0.05.

Fluorescence emission spectra (Figure 4.2.7F) were excited at the isosbestic point pf absorbance ensuring an equal excitation probability of the deprotonated and protonated PAc-SNARF species. Fluorescence mission was collected between 545 and 750 nm. The fluorescence emission spectra reflect the pH dependency of the absorbance spectra and show an isosbestic point (for the 526 nm-excitation) at 585 ± 1 nm. A reduced quantum yield of PAc-SNARF in its protonated form becomes obvious by comparing the peak intensity of the "protonated" emission band at 576 ± 1 nm at pH 5.1 ± 0.1 to the intensity of the "deprotonated" emission band at 626 ± 1 nm at pH 10.1 ± 0.1. While the disparity in peak absorbance of both states can be quantified by a factor of ~2, it is even higher for the fluorescence emission by a factor of ~6. However, the fluorescence emission equally allows to monitor the transition to the protonation state. Again, spectral regions assigned to the deprotonated state are subjecting to the same simple approach of analyzing the pH dependent transition as for the absorbance spectra. Figure 4.2.7G shows the pH-dependent fluorescence intensity changes for a set of seven wavelengths between 630 – 654 nm. This time, a global fit to the modified HH model yields a pK_a of 7.55 ± 0.05.

Time-resolved fluorescence characterization

In the next step, I characterized the time-resolved properties of the PAc-SNARF probe. Figure 4.2.8 summarizes the time-resolved spectroscopic fluorescence characterization of PAc-SNARF in Tris-citrate buffer at varying pH. Again, an excitation at 526 nm representing the isosbestic point of absorbance ensures an equal excitation probability of both SNARF's protonation states. The induced fluorescence emission of both fluorescent PAc-SNARF species was detected collectively above 545 nm. Figure 4.2.8A displays the fluorescence decay traces of PAc-SNARF as a function of pH. A distinct change in the decay behavior between an acidic (protonated) and a basic environment (deprotonated) can be identified. While the fluorescence decay of the deprotonated SNARF species follows a distinct mono-exponential decay, the protonated fluorophore shows a multi-exponential decay with a major decay component, much faster than the one observed for the deprotonated state.

Analogous to the stationary emission spectra where the emission of the intermediate protonation states can be decomposed into two distinct fluorophore fractions[92], PAc-SNARF in its protonated and deprotonated state, one can assume that both species have a specific fluorescence lifetime. According to this consideration, the fluorescence decays observed at intermediate pH levels can be treated as superpositions of both fluorescent species. Under this assumption, the extraction of the relative decay amplitudes by bi-exponential curve-fitting would allow probing the present protonation state. To verify this assumption, I globally fitted the fluorescence decays shown in Figure 4.2.8A to a bi-exponential decay model (Eq. 19, c=2). Table A6 (Appendix) displays the revealed decay parameters. At pH 10, the deprotonated form of PAC-SNARF can be detected as a pure fluorescent species with a lifetime of 2.214 ± 0.002 ns. Whereas the protonated form at pH 5.1 shows two components: a main component (97.2 %) with a lifetime 0.49 ± 0.07 ns and a slow component of 3.99 ± 0.03 ns. To address this circumstance of a varying slow decay component, only the fast decay component of ~ 0.49 ns was shared during the global fitting process. Figure 4.2.8B visualizes the pH dependent behavior of both decay components. One recognizes a general shift of the second decay component to slower fluorescence lifetimes for more acidic environments. This effect sets in when the pH falls below the pK_a.

Additionally, a phasor-plot illustrates this phenomenon (Figure 4.2.8C, see Section 3.4.2). Plotting the correspondent relative amplitudes that reflect the molar fractions of both protonation states as a function of pH, shows a clear transition process (Figure 4.2.8B). A global fit of the pH course of these amplitudes to a HH model yield a pK_a of 7.54 ± 0.05. An identical equilibrium constant of 7.55 ± 0.05 was obtained using the calculated amplitude-weighted mean fluorescence lifetimes as shown in the middle panel of Figure 4.2.8B.

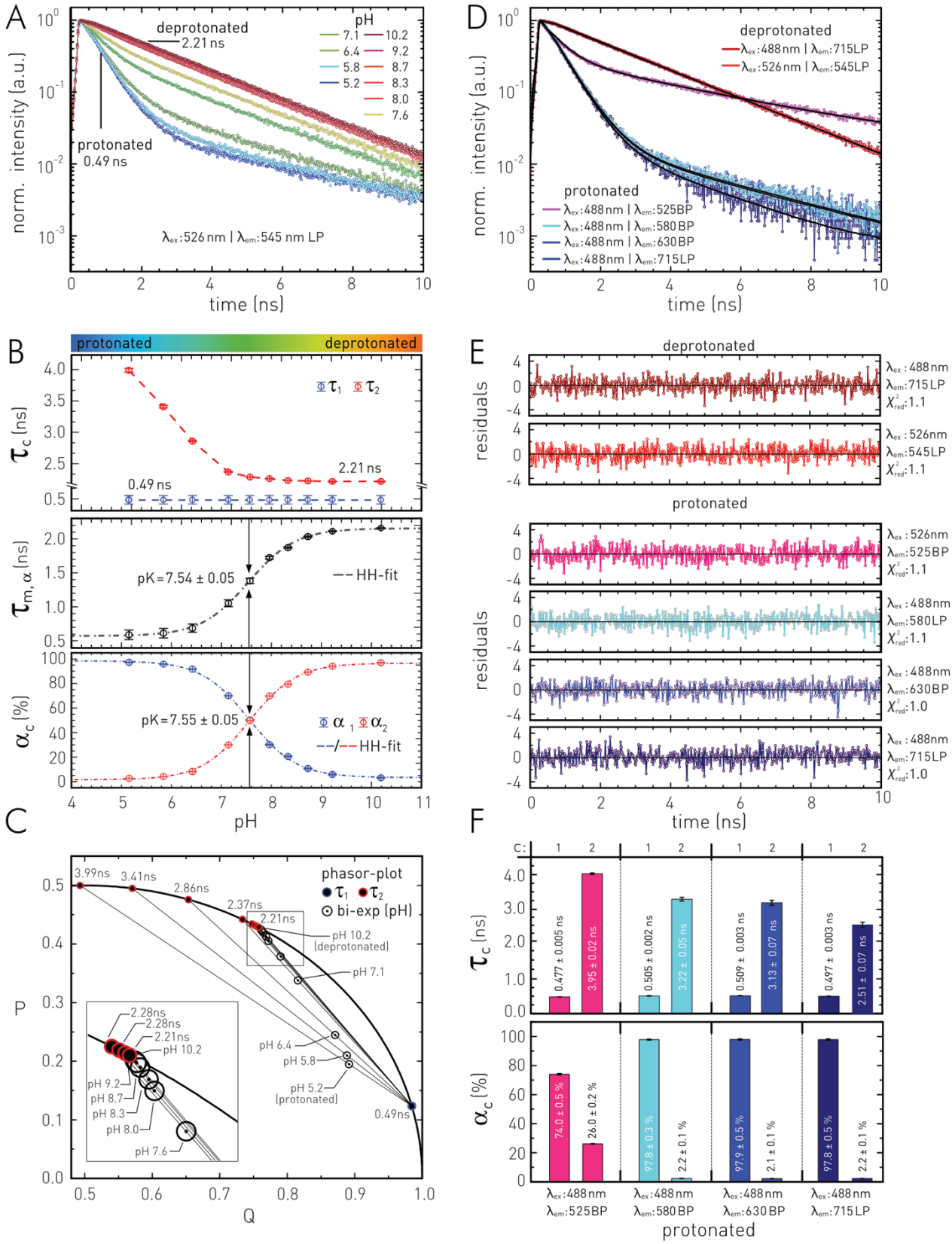

Figure 4.2.8: Time-resolved fluorescence spectroscopy of PAc-SNARF as a function of pH. **A** Fluorescence decay traces of 2.5 µM PAc-SNARF in 10 mM Tris-citrate buffer, 190 mM NaCl, and 5 % DMSO at various pH values (blue: protonated, red: deprotonated). Characteristic fluorescence lifetimes of the protonated (0.49 ns) and deprotonated (2.21 ns) fluorescence species are indicated. Spectral conditions: λ_{ex}=526 nm, λ_{em}>545 nm. **B** pH-dependence of revealed decay components, relative amplitudes and amplitude-weighted mean lifetime. The latter data set was fitted using a Henderson-Hasselbalch equation (Eq. 60, HH), revealing a pK_a of 7.54 ± 0.05. Fitting of the relative amplitudes versus pH gives a pK_a of 7.55 ± 0.05. Fit parameters of the decay fitting are

shown in Table A6 (Appendix). **C** Visualization of the fitting parameters in a phasor-plot. pH values are indicated next to each phasor. **D** fluorescence decay traces and bi-exponential fits (black) of protonated and deprotonated forms of PAc-SNARF at different excitation and emission wavelengths. **E** Residuals (R_w) and χ^2_{red} of decay fitting shown in D. (BP: band-pass; LP: long-pass emission filter). **F** Dependence between the observed fluorescence decay components of protonated PAc-SNARF and spectral detection window. A,B,D & E are modified reprints from Richter et al.[92] Copyright 2015, with the kind permission of Phys. Chem. Chem. Phys.. Uncertainty of indicated pH values is estimated to be ± 0.1. Shown uncertainties of decay components and relative amplitudes are based on confidence interval analyses (Section 3.4.1).

Next, I investigated the dependence of PAc-SNARF's fluorescence decay components on excitation and emission wavelengths. The deprotonated species at pH 10.2 seems to have a constant fluorescence lifetime of ~2.2 ns even when excited in the spectral region of the "protonated" absorbance band (λ_{ex}=488 nm) and simultaneous fluorescence collection above 715 nm using a long-pass filter (Figure 4.2.8D). Independent of the selected spectral regions one observes two decay components for the protonated SNARF species. The fluorescence decay (τ_1) of 0.49 ± 0.07 ns is obviously the main component in the spectral detection windows above 545 nm with relative amplitudes between 96 – 97 %, regardless of whether the fluorophore has been excited at the isosbestic point or at 488 nm (Table A6, Figure 4.2.8F). Only if detecting the emission between 500 and 550 nm, the second component (τ_2) becomes more pronounced (α_2 = 26.0 ± 0.2 %). τ_2 varies in the different spectral windows: When detecting the fluorescence in the spectral regions around the maximum of the "protonated" emission band at 580 nm or around the maximum of the "deprotonated" band at 630 nm, one observes lifetimes of 3.22 ± 0.05 ns and 3.13 ± 0.07 ns. Shifting the detection window above 715 nm leads to a shorter lifetime of 2.51 ± 0.07 ns. Whereas collecting fluorescence emission between 500 and 550 nm or collectively over the entire wavelength region above 545 nm generates higher values of τ_2 around 3.96 – 3.99 ns.

PAc-SNARF for pH probing in FLIM

After characterizing PAc-SNARF's stationery and time-resolved fluorescence properties, I focus on the applicability of the fluorophore as a pH probe in fluorescence lifetime imaging microscopy. The general idea behind the usage of PAc-SNARF for FLIM-based pH-detection is that a simple pH – lifetime calibration, like the fit function of the pH-dependent changes in PAc-SNARF's mean fluorescence lifetimes (HH-model, Figure 4.2.8B), can be utilized to determine the local pH in every image pixel. This would avoid the need of different spectral detection regimes necessary in established fluorescence intensity-based ratio-metric approaches.[268]

In a first step, I conducted a proof-of-principle experiment using two drops of PAc-SNARF solution with different pH values (6.5 ± 0.1 and 7.8 ± 0.1) and placed them on a cover slip. Both drops were recorded simultaneously by FLIM using a 4× objective. Figure 4.2.9A shows a false-color coded FLIM image of both drops according to the amplitude-weighted mean fluorescence lifetime. At a first glance, one recognizes an unequal coloring, i.e., a difference in the fluorescence lifetimes between both drops. To illustrate the distinction of the occurring fluorescence decay traces, I accumulated the pixel-based fluorescence decay traces in two ROIs located at the respective centers of the drops

(Figure 4.2.9B). Bi-exponential curve fitting revealed decay components similar to the ones in the ensemble experiments. After calculating the amplitude-weighted mean lifetimes in both ROIs, an assignment to the pH becomes possible using the HH-fit to the ensemble data (Figure 4.2.8B) as a calibration curve (Figure 4.2.9C). The resulting pH values match the target pH determined by a glass electrode within the limits of uncertainty. Please note that the pH calibration follows a sigmoidal function. One can roughly regard the transformation as linear around the pK_a, in the case of PAc-SNARF approximately in region between pH 6.2 and 8.8. The general non-linearity of pH – fluorescence lifetime conversion is reflected in the scales of the x-axis in Figure 4.2.9D. In order to avoid calibration errors, it is advisable to use only the linear region around the pK_a where the lifetime reacts very sensitively to pH-changes. Since the fluorescence lifetime is calibrated directly to the pH, it does not matter whether the calibration was conducted in a cuvette-based ensemble or microscopic setup, as long as the excitation and emission wavelengths are comparable. Figure 4.2.9D displays the frequency distribution of the amplitude-weighted mean fluorescence lifetimes calculated in the individual image pixels. The distribution shows two distinct accumulations reflecting both drops. Fitting the distribution by two Gaussians reveals their centers and distribution widths which can be directly converted into pH values using the same calibration as before (Figure 4.2.9D).

To further illustrate the capabilities of FLIM-based pH determination using the PAc-SNARF probe, FLIM images of a set of seven PAc-SNARF solutions with varying pH-environments (Figure 4.2.9E) were recorded using a higher magnification level (60× objective + increased scanning zoom) resulting in a pixel size of 0.3 µm near the Abbe's diffraction limit. In the following paragraph, I compare tau-plot analysis applied beforehand using exponential decay fitting (The Figure 4.2.9E) to the graphical phasor approach (The Figure 4.2.9F).

The tau-plot FLIM images were generated using a bi-exponential model (Figure 4.2.9E). The applied false color code maps the determined amplitude-weighted mean fluorescence lifetime values ranging between 0.5 and 2.25 ns to a rainbow color gradient, starting from blue over green to red. Next to the tau-plot FLIM images, Figure 4.2.9E displays the corresponded fluorescence lifetime distributions for each solution. One clearly observes a shift in the distribution center from lower to higher lifetimes by rising the pH-level. Assuming that the probability of finding a certain mean lifetime is normally distributed in a homogenous pH-environment, I applied single Gaussian fits to reveal mean and width of the lifetime distributions. The resulting fluorescence lifetimes are converted into pH values, if they locate in the pH – lifetime calibration area (Figure 4.2.9C). Once again, the lifetime determined pH matches the target pH-values determined by a glass electrode within the limits of uncertainty.

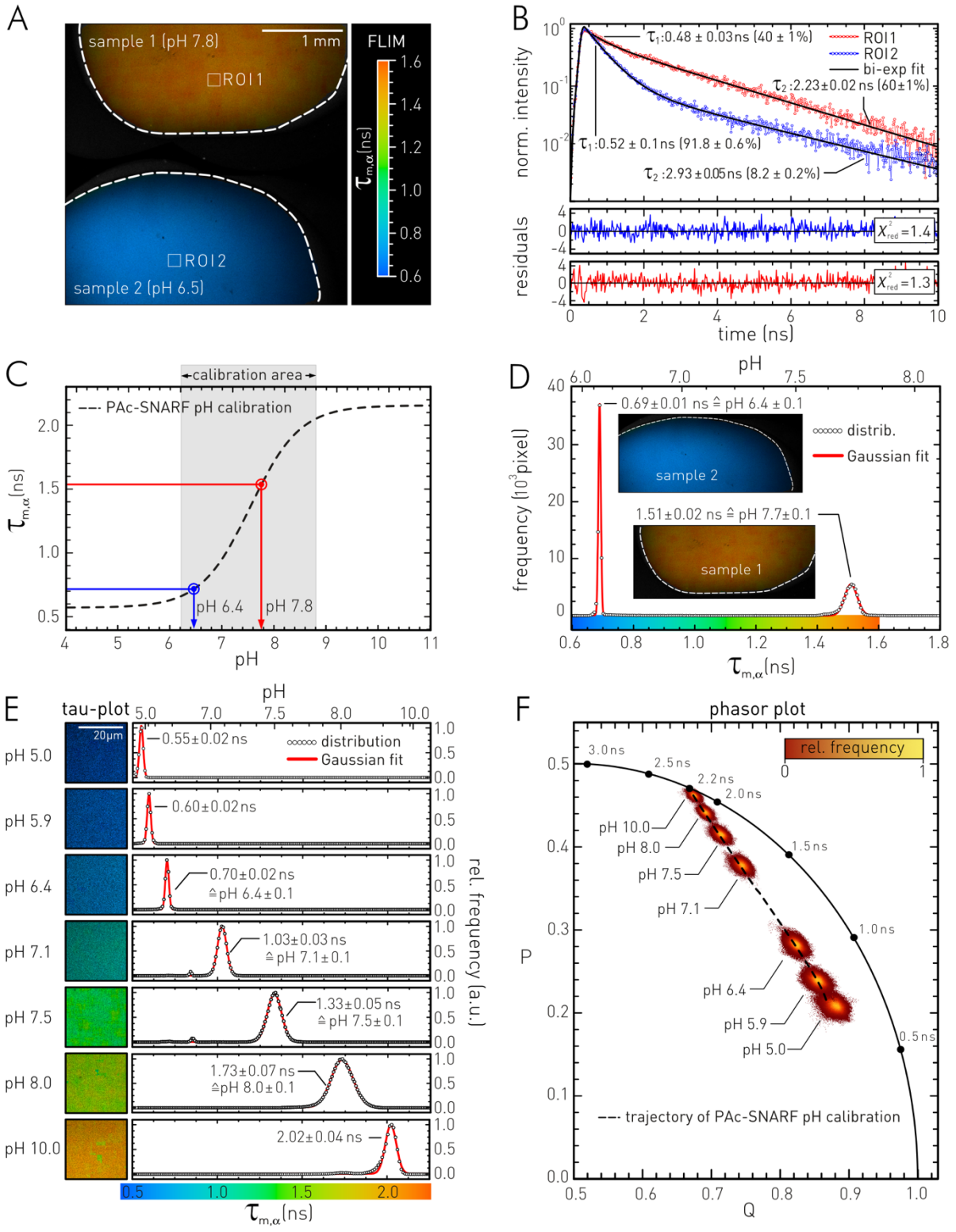

Figure 4.2.9: FLIM of PAc-SNARF solutions of different pH environments. **A** FLIM image showing two drops of two PAc-SNARF solutions (2.5 µM,10 mM Tris-citrate buffer, 190 mM NaCl, and 5 % DMSO). Solution 1 has a pH value of 7.8 (top). Solution 2 has a pH value of 6.5 (bottom). False-color code according to the amplitude-weighted mean fluorescence lifetime calculated after bi-exponential fitting (see color bar). Experimental conditions: 4X objective, λ_{ex} = 526 nm, λ_{em} > 545 nm. **B** Fluorescence decay traces and bi-exponential fits (black) of ROI 1 (blue, solution1) and ROI 2 (red, solution 2) indicated by white squares in in A. Decay components and relative amplitudes determined by decay fitting are directly indicated. Residuals (R_w) and χ^2_{red} are shown below. **C** Assignment of the determined amplitude-weighted mean lifetimes in both ROIs to the local pH using the HH-fit to the ensemble data (Figure 4.2.8D) as calibration. **D** Pixel frequency distribution and assignment of the pixel-based mean fluorescence lifetimes to the calibration according to HH-fit of Figure 4.2.8B. The fluorescence lifetime distributions are fitted to a Gaussian function, means

and SDs are indicated. **E** FLIM of PAc-SNARF solutions of different pH environments. False-color code according to the amplitude-weighted mean fluorescence lifetime calculated after bi-exponential fitting (see color bar). Relative frequency distribution, Gaussian fitting and pH assignment are shown. Experimental conditions: 60× objective, λ_{ex} = 526 nm, λ_{em} > 545 nm. **F** Phasor-plot of the FLIM images shown in E. pH values are indicated at each phasor distribution. Color code: indicates pixel frequency in the phasor plot. A is a modified reprint from Richter et al.[92] Copyright 2015, with the kind permission of Phys. Chem. Chem. Phys.. Abbreviations: SD: standard deviation; HH: Henderson-Hasselbalch; ROI: Region of interest. Uncertainty of indicated pH values is estimated to be ± 0.1. Shown uncertainties of decay components and relative amplitudes are based on confidence interval analyses (Section 3.4.1).

Next, the FLIM data was subjected to a phasor-plot analysis for a direct comparison of both analysis methods. For that purpose, the pixel-based decay traces are converted into phasors (2D phasor coordinates) using Eq. 71 and Eq. 72. Figure 4.2.9F displays the calculated phasors of all seven PAc-SNARF solutions in a single a phasor-plot. To address the relative frequency of the phasors (pixels) in a certain area of the plot, I plotted the phasors as density histograms with a color code ranging from red to yellow indicating low and high frequencies in phasor plot. The different PAc-SNARF solutions appear in the phasor-plot as recognizable groups, that are aligned along a trajectory (dashed line) calculated using the fitting data of the ensemble experiments. When applying the phasor approach for pH determinations, this trajectory can be used as a phasor – pH calibration. Thereby one avoids the fitting process of the FLIM data which reduces potential fitting errors as in the case of Tau-Plot analyses and additional saves computational time. Additionally, a graphical selection of the separated phasor distributions allows for a discrete false color-coding in the FLIM image as the assigned group of each phasor can be mapped to its image pixel.

Intracellular pH-probing using PAc-SNARF and FLIM

To further expand the scope of FLIM-based PAc-SNARF pH-probing to a real biological scenario, I applied PAc-SNARF to living cells. The cytoplasmic pH is a strictly controlled parameter due to its importance to numerous enzyme activities like in the synthesis of DNA and proteins.[269] A defined pH value is also essential for the conductivity of ion channels. Furthermore, intracellular pH-oscillations seem to be important to control the cell cycle and the proliferative capacity of a cell.[269] It is therefore not surprising that abnormal intracellular pH values are characteristic of many diseases such as Alzheimer's, stroke and cancer.[270]

In order to investigate PAc-SNARF's potential to detect intracellular live-cell pH, human normal keratinocytes (NHK) were incubated in a 1.25 µM PAc-SNARF solution for 18 minutes and subjected to FLIM. After this time span, the fluorophore accumulates intracellularly as indicated by confocal intensity images (Figure 4.2.10F, left), showing that the intracellular fluorescence clearly exceeds the extracellular fluorescence of PAc-SNARF solution. Furthermore, the intensity image reveals an inhomogeneous intracellular distribution of the fluoroprobe with the highest intensities present in the NHK nuclei. On average, these intensities are twice as high as in the surrounding cytoplasm.

A first, FLIM analysis based on decay fitting shows significant differences in fluorescence lifetimes within different intracellular regions (Figure 4.2.10A, right). The experience from the solution-based

ensemble measurements suggests that different cellular pH environments are likely to be present and reflected in the fluorescence lifetime. However, the bi-exponential fit model sufficient for the ensemble data had to be extended by another decay component to achieve a sufficient fit quality. The scale of the determined amplitude-based mean fluorescence lifetimes (Eq. 20), calculated by the decay components of the tri-exponential fits, is shown in Figure 4.2.10A and ranges from 0.75 to 1.5 ns. In contrast to PAc-SNARF in solution, the intracellular localization shows a fast third decay component of about ~0.18 ns. This is probably due to intracellular interactions of the PAc-SNARF leading to a quenching process, which in turn is another non-radiative depopulation of the S1 state. Interestingly enough, the other two components, here further called τ_1 and τ_2, with values around ~0.5 ns and ~3.0 – 3.5 ns, are comparable to the ensemble experiments.

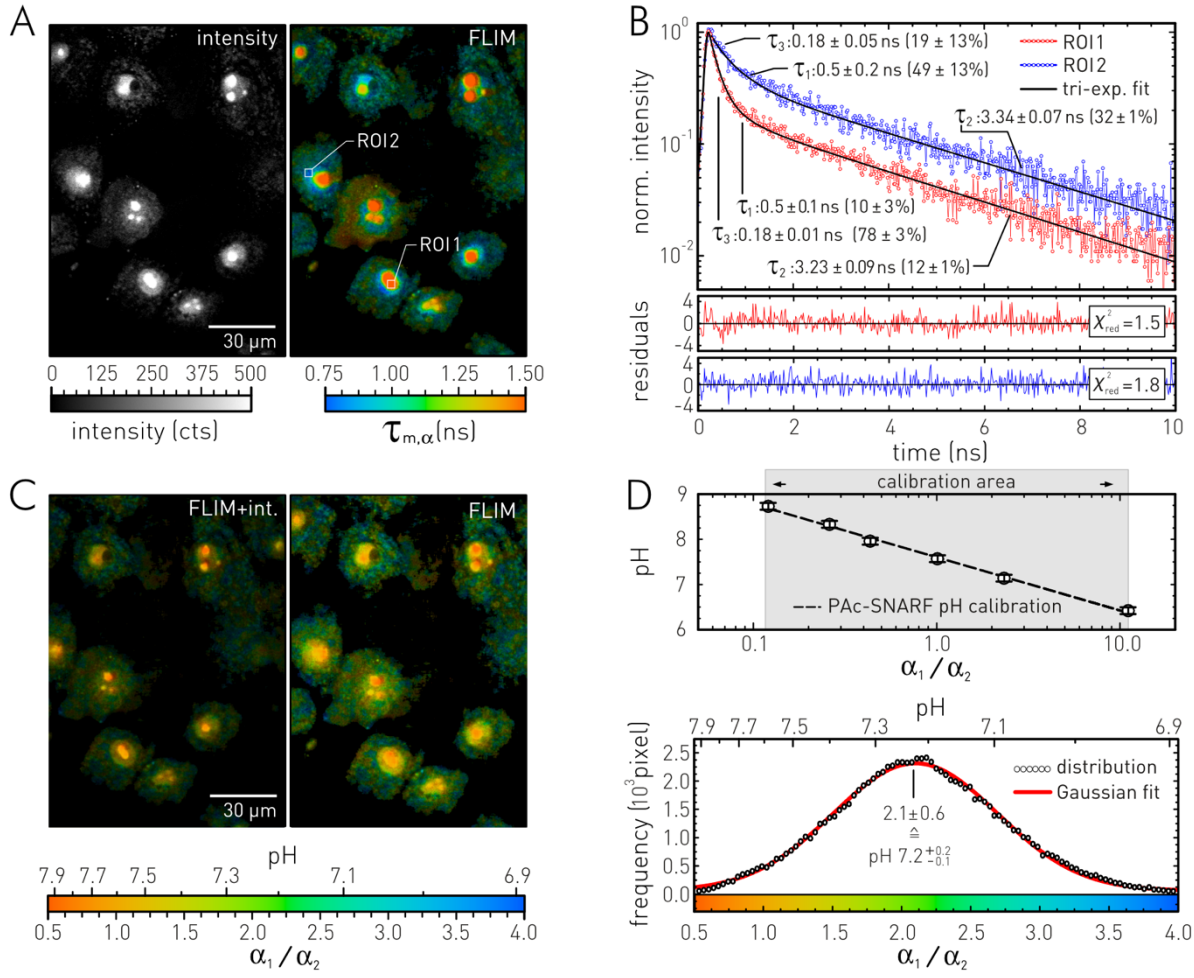

Figure 4.2.10: PAc-SNARF used as a cellular pH-probe for fluorescence lifetime imaging. **A** Confocal fluorescence intensity and FLIM image of NHK cells after incubation with 1.25 µM PAc-SNARF in KGM (pH 7.5) for 18 min at 37 °C, 5 % CO_2. Color code according to the amplitude-weighted mean fluorescence lifetime calculated after tri-exponential fitting (see color bar). Experimental conditions: 60× objective, λ_{ex} = 530 nm, λ_{em} > 545 nm, 37 °C. **B** Fluorescence decay traces and tri-exponential fits (black) of ROI 1 (red) and ROI 2 (blue) indicated by white squares in A. Decay components and relative amplitudes determined by decay fitting are directly indicated. Shown uncertainties of decay components and relative amplitudes are based on confidence interval analyses (Section 3.4.1). The given digits of α_c are chosen so that the individual values add up to 100 %. The respective uncertainties are indicated by the same number of digits. Residuals (R_w) and χ^2_{red} are shown below. **C** FLIM images (intensity overlay and pure) based on the amplitude ratio α_1/α_2 of τ_1 and τ_2. **D** Calibration of α_1/α_2 to pH values based on the ensemble data (Figure 4.2.8D). Linear regression of ratios between 0.1 and 10 serving as pH calibration curve. Bottom: Pixel frequency histogram of α_1/α_2

(amplitude ratio distribution), respective pH values are shown. A Gaussian fit gives distribution mean and SD. Abbreviations: KGM: Keratinocyte growth medium, SD: Standard deviation, ROI; Region of interest.

The relative amplitudes of the third component vary strongly within individual regions of the NHK cells. A major difference exists between cytoplasm and nucleus. In the latter, the third decay component has an amplitude of up to 80 %. To illustrate this, two ROIs are selected from Figure 4.2.10A, which are representative of the decay curves in the cytoplasm and the nucleus. Figure 4.2.10B shows the fluorescence decay curves that appear here, together with the values of the individual decay components. Due to the newly occurring third component, the previously applied pH – fluorescence lifetime calibration cannot be used directly. To be able to continue using the original calibration, the third component must not be taken into account. This is achieved by using only the ratio of the first two components as the basis for the pH calibration. This is possible because the two decay components are intracellularly unchanged. Therefore it can be assumed that the ratio between both continues to indicate protonation (see Figure 4.2.8B for comparison). The new calibration function is based on the ratio α_1/α_2 of the ensemble calibration experiments (Figure 4.2.10D, top). Here, the pH is plotted against ratio in a Lin – Log scale. The resulting curve has a linear course approximately between pH 6.3 and 9.0.

Applying this pH calibration to the FLIM data of NHK cells generates the pH images in Figure 4.2.10C. The PAc-SNARF probe within the cells show α_1/α_2 ratios between $\sim$0.5 and 4 (see the amplitude ratio distribution in Figure 4.2.10D), reflecting pH values between 6.9 and 7.9. The respective pH distribution is likewise visualized in Figure 4.2.10D, showing a mean cellular pH value of 7.2. The largest pH differences within the cells occur between the cytoplasm and the nucleus. This is clearly shown in the detailed image in Figure 4.2.11A. It can be seen that the pH within the nucleus is significantly increased compared to the surrounding cytoplasm. This behavior is even more evident in the contour plot in Figure 4.2.11B. For this reason, pH scans were performed inside the NHK cells (Figure 4.2.11C,D). These scans visualize and quantify the increase in pH within the nucleus. The range of the determined intracellular pH values, separated for cytoplasm and nucleus, is shown in Figure 4.2.11C,D. For all NHK cells studied ($n = 8$), an increased intranuclear pH value was found, which is 7.48 ± 0.05 on average. In contrast, the cytoplasm shows an ensemble averaged pH value of 7.21 ± 0.02.

Elevated intranuclear pH in relation to the cytoplasm have also been observed in other cell types such as macrophages (7.55 vs. 7.24) or fibroblasts (7.77 vs. 7.49).[271] The origin of the high pH values could be the better efficiency of DNA replication by DNA polymerases at higher pH. [269] The local differences within the cytoplasmic pH range from pH 6.9 up to pH 7.9. Within the cytoplasm, cluster-like structures are prominent with a pH around $\sim$7 (Figure 4.2.11B, dark blue), that cross the cytosol These pH-values could indicate PAc-SNARF located in the Golgi apparatus.[272] A slightly higher pH between 7.1 and 7.2 (Figure 4.2.11B, cyan) is characteristic for the endoplasmic curriculum. Occasionally, cytoplasmic pH values of almost 8 (Figure 4.2.11B, yellow) were observed in

small circular structures, which could indicate a mitochondrial origin.[272] Lower pH-values between 5.5 and 6.9 could not be detected by the PAc-SNARF probe. These values would be characteristic for endosomal and lysosomal compartments.[272] It is difficult to reveal this lower pH range by the time-resolved method as the calibration below 6.9 becomes insensitive (Figure 4.2.9C). Furthermore, although using a confocal approach, the FLIM experiment collects the fluorescence emission from different cell depths. Thus, there is a good chance that the PAc-SNARF emission from acidic compartments may be overlaid with more basic regions from different depths. Since deprotonated PAc-SNARF species has a greater impact on the pH-conversion even at the same fluorophore concentration due to a higher absorption coefficient and quantum yield, it is difficult to study these acidic intracellular environments.

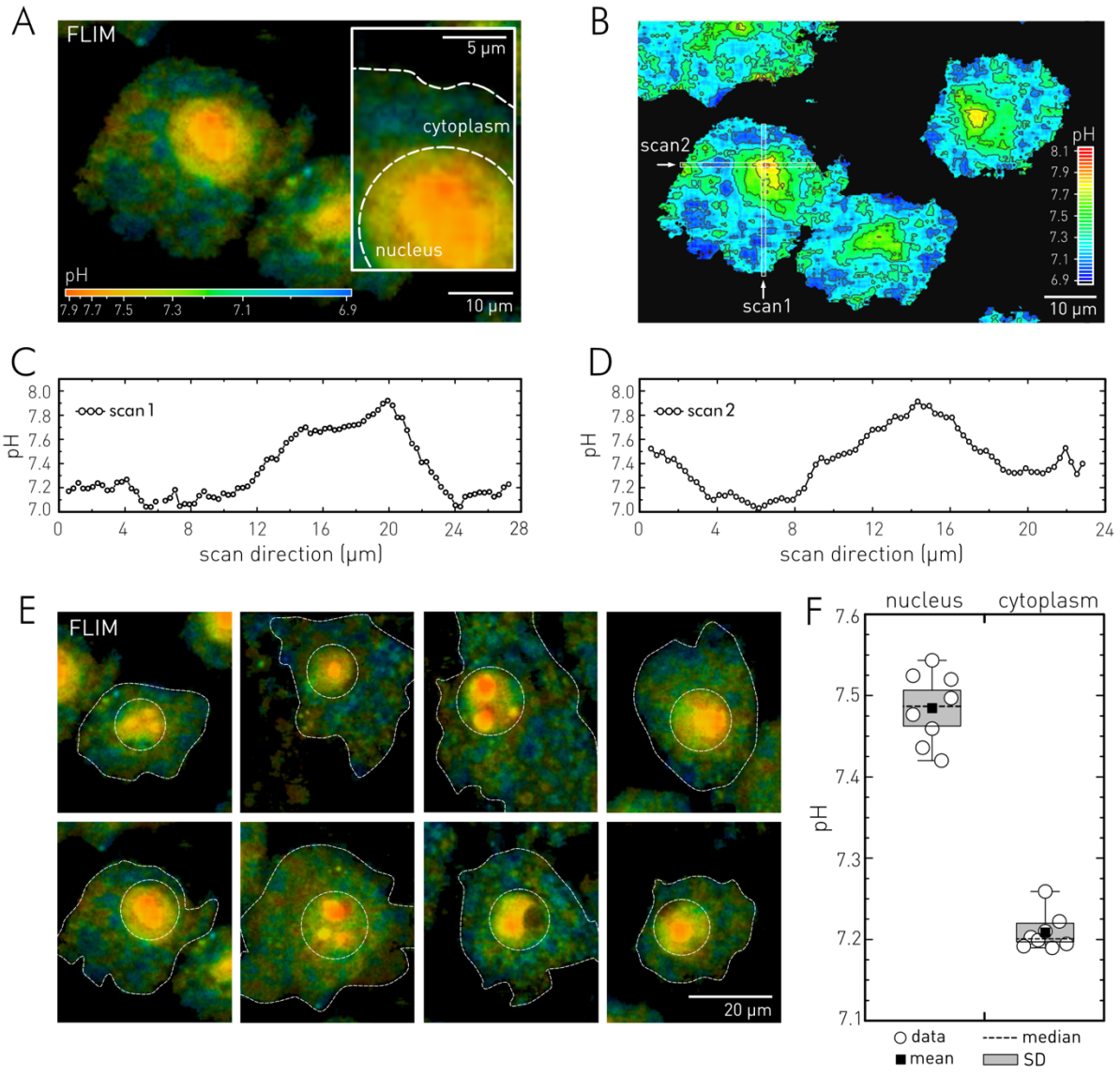

Figure 4.2.11: Intracellular pH determination in NHK cells using PAc-SNARF and FLIM. **A** Magnified FLIM image of NHK cells after incubation with of NHK cells after incubation with 1.25 µM PAc-SNARF in KGM (pH 7.5) for 18 min at 37 °C (see Figure 4.2.10). Colorbar displays false-color code according to local pH (calibration, see Figure 4.2.10D). Inlay shows a magnified field of view into the intracellular space: White dashed lines indicate borders between nucleus and cytoplasm and cytoplasm and extra cellular space. **B** Contour plot of the NHK cells in dependence on the pH level. White lines show positions of two pH bar-scans through the

cell shown in A. **C/D** pH scans along the indicated bars. **E** pH maps in different NHK cells, cytoplasm and nuclei are indicated. **F** pH distribution of cells shown in E. Single cell analysis reveals significant differences between nucleus and cytoplasm.

The PAc-SNARF probe presented here together with the fluorescence lifetime-based pH-calibration, has several benefits compared to other fluorescent pH-probes with intensity-based pH-calibration modes. First, pH-determination using the novel approach presented here is completely unaffected by concentration effects, photobleaching, and probe leakage from the cells. Classical pH-sensitive fluorophores, such as FDA, CFDA, or BECEF (see section 2.1.3) are susceptible to these effects as they react to pH changes by changing their fluorescence emission intensities. This means that the generated fluorescence read-out cannot be interpreted correctly in the case of different intracellular concentration distributions of the pH probe. This severely restricts intracellular pH resolution. Furthermore, the approach presented here also has advantages over the more advanced ratiometric fluorescence intensity approaches, which are equally resistant to the above-mentioned effects. The FLIM-based PAc-SNARF approach requires only a single excitation (isosbestic point) and a single fluorescence detection window. There have been other studies that applied time-resolved fluorescence methods and corresponding analyses tools like the phasor approach for pH determination. However, the intracellular resolution achieved here within NHK cells after application of the PAc-SNARF probe is higher in direct comparison.[97, 273-274] To the best of my knowledge, this is the first time that the intracellular pH of primary keratinocytes *in vivo* has been determined in such detail. In the future, an application of the Pac-SNARF pH probe is conceivable in which it is attached to nanoparticles. Thereby intracellular localizations of these nanoparticles could be observed via FLIM-based intracellular imaging. The lifetime information could be used to determine the locally pH. Also, for nanoparticles that selectively be transported into endosomes and lysosomes, a determination of the low pH-values prevalent there, should be possible, as interference signals from other areas would be avoided. Such experiments are of special interest to nanocarrier architectures using pH responsive stimuli targeting these acidic cellular compartments.[157, 275-276]

4.2.3 CellROX based ROS detection in living cells

Side effects of nanoparticles and nanoparticulate drug delivery are gaining more and more attention in the field of nanomedicine. Currently, studies report on cytotoxic and genotoxic effects of nanoparticles summarized under the term nanotoxicity.[277] But the underlying molecular mechanisms of these toxic effects are often poorly understood. Among others, one important mechanism in nanotoxicity seems to be the increased formation of ROS and the related oxidative stress (see Section 2.1.3).

This increase in ROS can also occur on a subcytotoxic level, which nevertheless has a nanotoxic effect on the cellular homeostasis and thus eventually on human health.[49] In an article I previously co-published, a novel fluorescence lifetime-based approach, called FLIM-ROX, was introduced that applies the commercially available fluorogenic reagent CellROX Green (CellROX, see Section 2.1.3) to quantify reliably and reproducibly the ROS generation in cells upon nanoparticle interaction by

means of the fluorescence lifetime (Balke et al. 2018, Small, Ref.[49]). Jens Balke (Prof. Alexiev's group, Freie Universität Berlin) first observed and described the lifetime sensitivity of CellROX, which changes its fluorescence decay behavior after activation and DNA binding. The FLIM-ROX approach introduced by Jens Balke uses the Cluster-FLIM algorithm to detect cellular ROS levels by identifying and analyzing the activated CellROX Green species within the single cell nuclei. The ROS calibration was established by externally applied H_2O_2 as well as by menadione, a naphthoquinone generating intracellular superoxide.

In this section, I would like to take a closer look at the general time-resolved fluorescence behavior of CellROX Green after cellular uptake and show another approach to determined cellular ROS level from live-cell FLIM data, based on classical decay-fitting (tau-plot analysis), since this method is the standard evaluation tool used in most laboratories applying FLIM. Furthermore, a bi-exponential decay fit is sufficient to describe CellROX's fluorescence decays. Hence, this approach is not inclined to produce wrong parameterizations (see Section 3.4.1). The CellROX reagent operates in two step reaction mode. After entering a cell in its initially reduced state, intracellular ROS oxidizes the reagent. After this activation step, the CellROX reagent becomes highly fluorescent and binds to double-stranded DNA (dsDNA). The binding process to DNA leads to an inhomogeneous distribution of the activated probe within the incubated cells. In the typical stationary fluorescence approaches, cellular ROS levels are calibrated to the total cellular CellROX fluorescence intensities after addition of cellular ROS stimuli, like H_2O_2. CellROX's time-resolved fluorescence emission changes with DNA binding, this information can be exploited to reduce experimental uncertainties by separating cellular autofluorescence and avoiding probe concentration-based intensity biases.[49]

Time-resolved fluorescence characterization of CellROX Green

To compare both approaches, I incubated in cooperation with Jens Balke (Prof. Alexiev's group, Freie Universität Berlin, Germany) living HeLa cells with the CellROX probe and subjected the cells to intensity based CLSM and FLIM. The general behavior and localization of CellROX after an uptake in HeLa cells without any exogenous cellular ROS trigger is shown in the confocal live-cell intensity image of Figure 4.2.12A (left). Accordingly, these fluorescence intensities represent the basal activation level of CellROX. The corresponding intracellular intensity distribution is characterized by high intensity levels in the cytoplasm and low intensities in the intranuclear regions. By adding the external cell stressor H_2O_2 in a high concentration of 0.1 %, the distribution switches and almost all fluorescence emission originates from the cell nuclei. The respective confocal intensity-based image in Figure 4.2.12F (left) shows increased fluorescence intensities in the nuclei which appear highly structured in the fluorescence image.

In addition to this pure increase in intensity, the CellROX fluorescence emission also changes in its time-resolved properties. In order to quantify these changes, I conducted a first fluorescence decay analysis using a bi-exponential fit. The resulting mean-fluorescence lifetimes range from 1.3 to

5.0 ns. Using this lifetime range, I generate the tau-plot FLIM images in Figure 4.2.12A and F. Here, one recognizes a distinct difference in the fluorescence lifetime in cytoplasmic and nuclear regions. In order to illustrate this change in more detail, two representative ROIs are selected from Figure 4.2.12A and F, characteristic of the decay traces in the cytoplasm and the nucleus. Figure 4.2.12B and G show the fluorescence decay traces that appear there together with the values of the individual determined decay components. The major difference between both fluorescence decay traces is the occurrents of a fast decay component τ_1 of ~0.5 ns in the cytoplasm which vanishes completely when CellROX binds to DNA. This 0.5 ns species must have its origin in cytoplasmic interactions upon the ROS oxidation process leading to a dynamic fluorescence quenching process, i.e., a secondary non-radiative depopulation of the S_1 state. Once CellROX binds to DNA, this process is inhibited, leading to slower decay components. A mechanistic explanation for this effect on the time-resolved fluorescence behavior could be that CellROX performs DNA intercalation, which limits its structural flexibility and polarization properties. Similar effects are observed with fluorophores used in nucleic acid staining. For example, the fluorescent DNA dye 4′,6-diamidino-2-phenylindole (DAPI) undergoes a change in its photon absorption and fluorescence behavior after it specifically binds into the minor groove of DNA as quantum mechanical modelling and spectroscopic investigations have shown.[278]

Besides a fast decay component τ_1 of ~0.5 ns, the cytoplasmic CellROX shows also a slower component τ_2 of 3.5 – 4.0 ns ($\alpha_2 = 25 – 35$ %, Figure 4.2.12B). The slower fluorescence decay traces observed in the nuclei is determined by a fast decay component τ_1 of ~3.2 ns and a τ_2 of 5.5 – 6.0 ns ($\alpha_2 = 50 – 60$ %). Interestingly enough, the effect of higher ROS values shows no significant change in the fluorescence decay traces of the cytoplasmic and nuclear regions and the respective decay components (Figure 4.2.12F). Only the frequency between both decay patterns changes. So, the higher the ROS levels, the more prominent the nuclear species become in the microscopic fluorescent image. This is reflected by the higher nuclear intensities (Figure 4.2.12A vs. Figure 4.2.12F), but also in the mean fluorescence lifetime distribution indicated by the higher amount of cyan colored pixels in Figure 4.2.12F. The frequency distribution histogram of the mean fluorescence lifetime indicates an increase of the slower decay pattern for the elevated ROS levels compared to the basal level (Figure 4.2.12H). The histogram also shows that in addition to the slow decay pattern present in the cell nucleus, an additional slower pattern (>4 ns) develops in the cytoplasm.

A good overview of the occurring fast (τ_1) and slow (τ_2) decay components characterizing both CellROX FLS can be seen in the frequency distribution histograms of Figure 4.1.12D/I. For basal ROS levels, τ_1 is dominated by the 0.5 ns-component appearing in the cytoplasm (Figure 4.1.12D). The nuclear 3 ns-component is only weakly pronounced. Additionally, the frequency histogram for τ_1 shows a previously unmentioned fluorescence lifetime species of about 1.7 ns, which also occurs in the cytoplasm, but its frequency is only half as high. τ_2 at a basal ROS level is dominated by a 3.5 – 4.0 ns species, which originates from the cytoplasm, while the slower nuclear CellROX species (5.5

– 6.0 ns) is only weakly pronounced. The whole picture changes with increased ROS values, as described above. The fast fluorescence species of τ_1 originating from the cytoplasm, are now drastically reduced in favor of the nuclear 3.0 ns-species (Figure 4.2.12I). The same is true for τ_2, in which the 3.5 – 4.0 ns specie almost completely disappears, and the 5.5 – 6.0 ns species dominates.

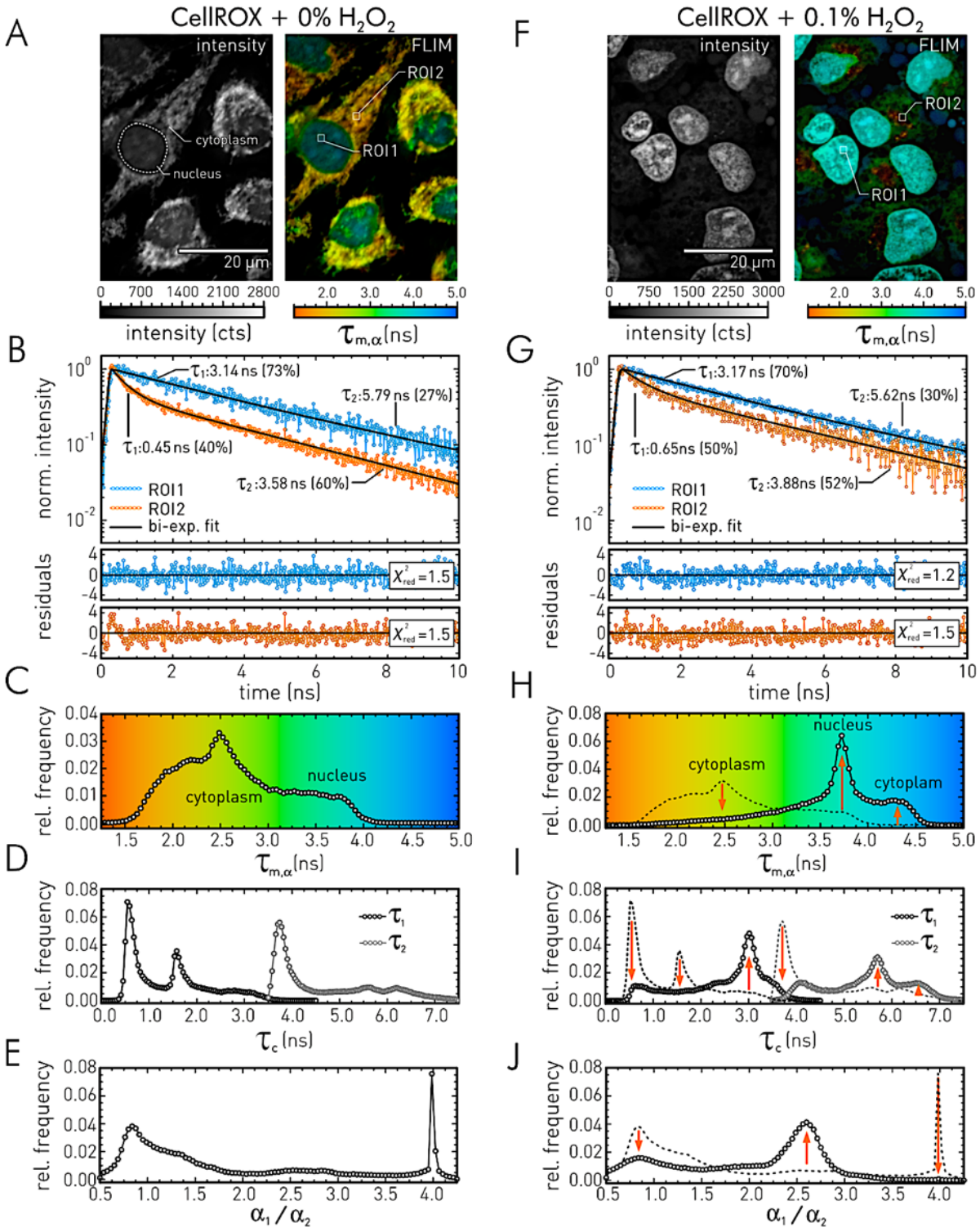

Figure 4.2.12: Characterization of CellROX Green's fluorescence lifetime properties in HeLa cells. **A** HeLa cells after incubation with CellROX green (basal ROS level). Left: Intensity CLSM image; right: FLIM image based on a mean fluorescence lifetime (tau-plot) of the same site. **B** Fluorescence decay traces and respective bi-exponential fits for both ROIs indicated in A. **C** Frequency distribution of the mean fluorescence lifetime (1.3 – 5.0 ns) according to tau-plot analyses in A. **D** Frequency distribution of fast and slow decay components according to the tau-plot analyses in A. **E** Frequency distribution of the respective (D) decay amplitudes ratio α_1 and

α_2. **F** HeLa cells after incubation with 0.1 % H_2O_2 and CellROX green (elevated ROS level). Left: Intensity CLSM image; right: FLIM image based on a mean fluorescence lifetime (tau-plot) of the same site. **G** Fluorescence decay traces and respective bi-exponential fits for both ROIs indicated in F. **H** Frequency distribution of the mean fluorescence lifetime (1.3 – 5.0 ns) of the tau-plot analyses in F, dashed lines indicate distribution shown in C. **I** Frequency distribution of fast and slow decay components according to tau-plot analyses in F, dashed lines indicate distribution shown in D. **J** Frequency distribution of the respective (I) decay amplitudes ratio α_1 and α_2. Abbreviations: ROI: region of interest. Experimental conditions: CellROX excitation at λ_{ex} = 488 nm; λ_{em} = 500 – 550 nm; objective: 60×.

Scatterplot approach for lifetime-based ROS detection

In the following, I would like to use the observed properties of both CellROX patterns of fluorescence decay traces after their activation in the cytoplasm and after having bound to the DNA in the nucleus. Additionally, I show the corresponding decay components in order to establish a novel calibration approach for ROS detection based on tau-plot FLIM analyses. This approach is different from the FLIM-ROX approach used in Balke et al. which is based on Cluster-FLIM and the pattern recognition of activated CellROX.[49]

In typical intensity based CellROX assays, like in plate readers, FACS or microscopic approaches, the cellular fluorescence intensity of activated CellROX is used as read-out for the present cellular ROS level. Using solely the fluorescence intensity information, different CellROX concentrations in the individual cells will be a significant source of error. A reduction of these errors can be achieved by microscopically examining the cells, identifying the nuclei and correlating the nuclear with the cytoplasmic fluorescence intensity. This allows for an inherent normalization, which is independent of the CellROX concentration. However, this procedure requires a high manually effort since the automation of cell nucleus recognition is often problematic, especially at low ROS levels, in which high cytoplasmic fluorescence levels are present and the nuclei are hardly visible.

This is where the idea of using the fluorescence lifetime information for the detection of cytoplasmic and nuclear CellROX species comes into play. In the last section, I showed that both regions can be identified by their characteristic fluorescence decay patterns and the correspondent fluorescence decay components obtained by the decay-fitting in the tau-plot analysis. The easiest way to visualize both decay components is to apply a scatterplot that sorts both decay components of each image pixel in a two-dimensional point plot (τ_1, τ_2). Exemplary scatterplots for CellROX green in HeLa cells at basal and elevated (0.1 % H_2O_2) ROS levels are shown in Figure 4.2.13A and B. Here, the color parametrization of the tau-plot analysis is indicated by coloring each scatterplot by its color within the FLIM image. This shows that the scatterplot can be divided into several regions. For the further ROS-calibration, two quadrants are of importance here. One is the lower left quadrant (τ_1: 0.0 – 2.5 ns, τ_2: 3.5 – 5.0 ns), which is characteristic for the cytoplasmic CellROX species and the quadrant defined by τ_1 = 2.5 – 3.5 ns and τ_2 = 5.0 – 6.0 ns, indicating the nuclear species. A next step is to calibrate the information of the scatterplots to the ROS levels. For this purpose, a H_2O_2 concertation series was performed with living HeLa cells incubated first with a specific H_2O_2 concentration (0.0 – 0.1 %) and then with CellROX. Figure 4.2.13C and D show live-cell FLIM images of

this calibration series. In Figure 4.2.13D, the nuclei are indicated by a white dashed line. The FLIM images show the continuous increase in intensity of the blue-colored CellROX areas. This increase can also be seen in the frequency distribution diagram of the mean fluorescence lifetime in Figure 4.2.13E.

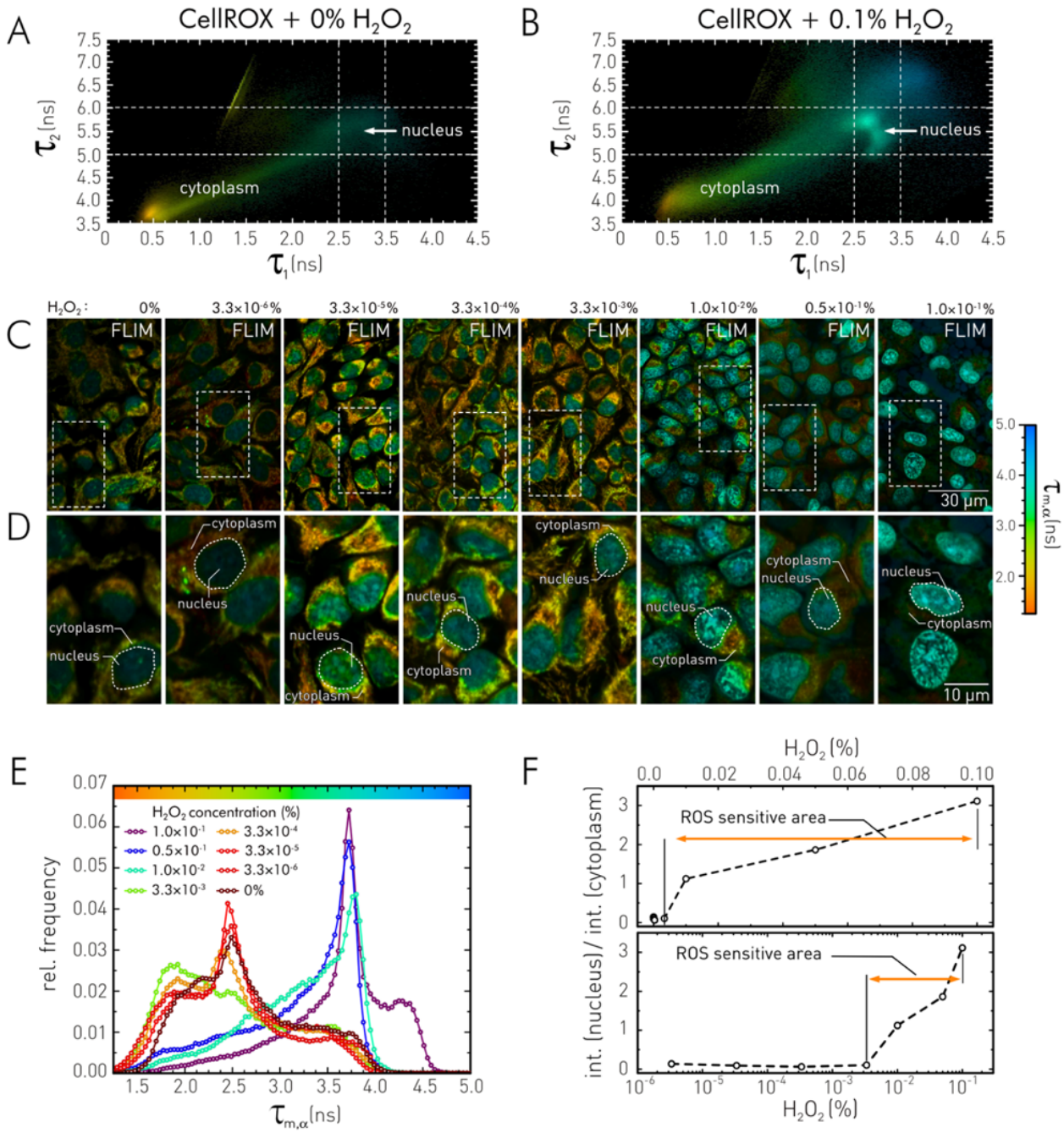

Figure 4.2.13: Scatterplot approach for FLIM-ROX lifetime-based ROS detection. **A** (τ_1, τ_2)-Scatterplot after bi-exponential Tau-plot analysis of HeLa cells incubated only with CellROX. **B** (τ_1, τ_2)-Scatterplot after bi-exponential Tau-plot analysis of HeLa cells incubated with 0.1 % H_2O_2 and CellROX. Color indicates the mean fluorescence lifetime parameterization of the tau-plot analysis. **C** Tau-plot FLIM images of HeLa cells after incubation with indicated H_2O_2 concentrations and CellROX. **D** Image details of C, dashed line indicates nuclei. **E** Frequency distribution of the mean fluorescence lifetime (1.3 – 5.0 ns) according to tau-plot analyses in C. **F** Fluorescence lifetime – ROS calibration curves defined by the intensities of the "cytoplasmic" and "nucellar" quadrants in the scatterplots. Abbreviations: ROI: region of interest. Experimental conditions: CellROX excitation at λ_{ex} = 488 nm; λ_{em} = 500 – 550 nm; objective: 60x.

In my scatterplot approach for a fluorescence lifetime – ROS calibration, I use the intensity ratio of both defined quadrants within the scatterplots. This results in a calibration that is inherently independent of the cellular CellROX concentration and at the same time does not require a structural identification of cytoplasm and nucleus. This is possible by replacing the morphological with a fluorescence lifetime-based identification of both compartments. The resulting calibration curves are shown in Figure 4.2.13F indicating a ROS sensitivity of 0.002 % – 0.1% H_2O_2 -equivalents in HeLa cells.

4.3 Monitoring molecular interactions of dendritic nanoparticles

4.3.1 Dendritic polyglycerol sulfate

Fluorescence decay behavior of dPGS-ICC

The fluorescence decay behavior of dPGS-ICC was first investigated in detail by Boreham et al. in 2014.[198] The authors found changes in ICC's fluorescence lifetime after the conjugation to the dendritic nanoparticle. The corresponding fluorescence decay curves were described as characteristic "fluorescence lifetime signatures" for the local ICC environment which differ when dPGS-ICC is exposed to different solvents. The dPGS-ICC examined by the authors showed a characteristic fluorescence decay behavior in aqueous solutions, which was best described by three fluorescence decay components (τ_i (α_i), Eq. 19) of 0.16 ns (69 %), 0.4 ns (26 %), and 0.9 ns (5 %).[198] All following experiments on dPGS-ICC fluorescence decay characteristics were performed on the same lyophilized dPGS-ICC stock as in Ref.[198]. It was freshly suspended for each experiment.

To estimate the experimental precision of the determined fluorescence decay components and to compare my results to the earlier experiments mentioned above, I visualized the decay parameters obtained from dPGS-ICC samples over a period of 4 years (Figure 4.3.1). All samples showed a fluorescence decay characteristic best fitted by tri-exponential model function (Eq.19, compare Figure 4.2.1/4.2.2). The values obtained are compatible with the results from Ref.[198] (see table 4.3.1). The relative precision of the individual experiments ranges between 9 % for the slow (τ_3) and 14 % for the fast (τ_1) decay component. The corresponding decay amplitudes fluctuate between 8 % (α_1) and 17 % (α_3). A similar picture emerges for the calculated relative steady state fluorescence contributions and mean fluorescence lifetime. These variations may have their origin in the general sample handling, the suspension process of the lyophilized dPGS-NP stock, the measurement uncertainties, and the corresponding uncertainty of the decay analysis.

Table 4.3.1: Precision and fit accuracy in time-resolved fluorescence experiments of dPGS-ICC. Tri-exponential decay fitting of seven independent time-resolved fluorescence experiments result in the indicated mean values of the individually determined fit parameters. The respective standard deviation is used as a measure of the general experimental precision (see Figure 4.3.1). Mean and standard deviation of the absolute and relative fit accuracy are determined by seven single confidence interval analyses of the fluorescence decay traces from seven individual experiments.

fit parameter	**mean**	**precision**		**fit accuracy**	
		absolute	*relative*	*absolute*	*relative**
τ_1	0.14 ns	0.02 ns	14 %	0.004 ± 0.001ns	2.9 ± 0.7 %
τ_2	0.40 ns	0.05 ns	13 %	0.016 ± 0.007 ns	4 ± 2 %
τ_3	1.1 ns	0.1 ns	9 %	0.026 ± 0.007 ns	2.4 ± 0.6 %
α_1	61 %	5 %	8 %	2.6 ± 0.8 %	4 ± 1 %
α_2	33 %	4 %	12 %	2.4 ± 0.9 %	7 ± 3 %
α_3	6 %	1 %	17 %	0.5 ± 0.2 %	8 ± 3 %

* relative values refer to the given mean.

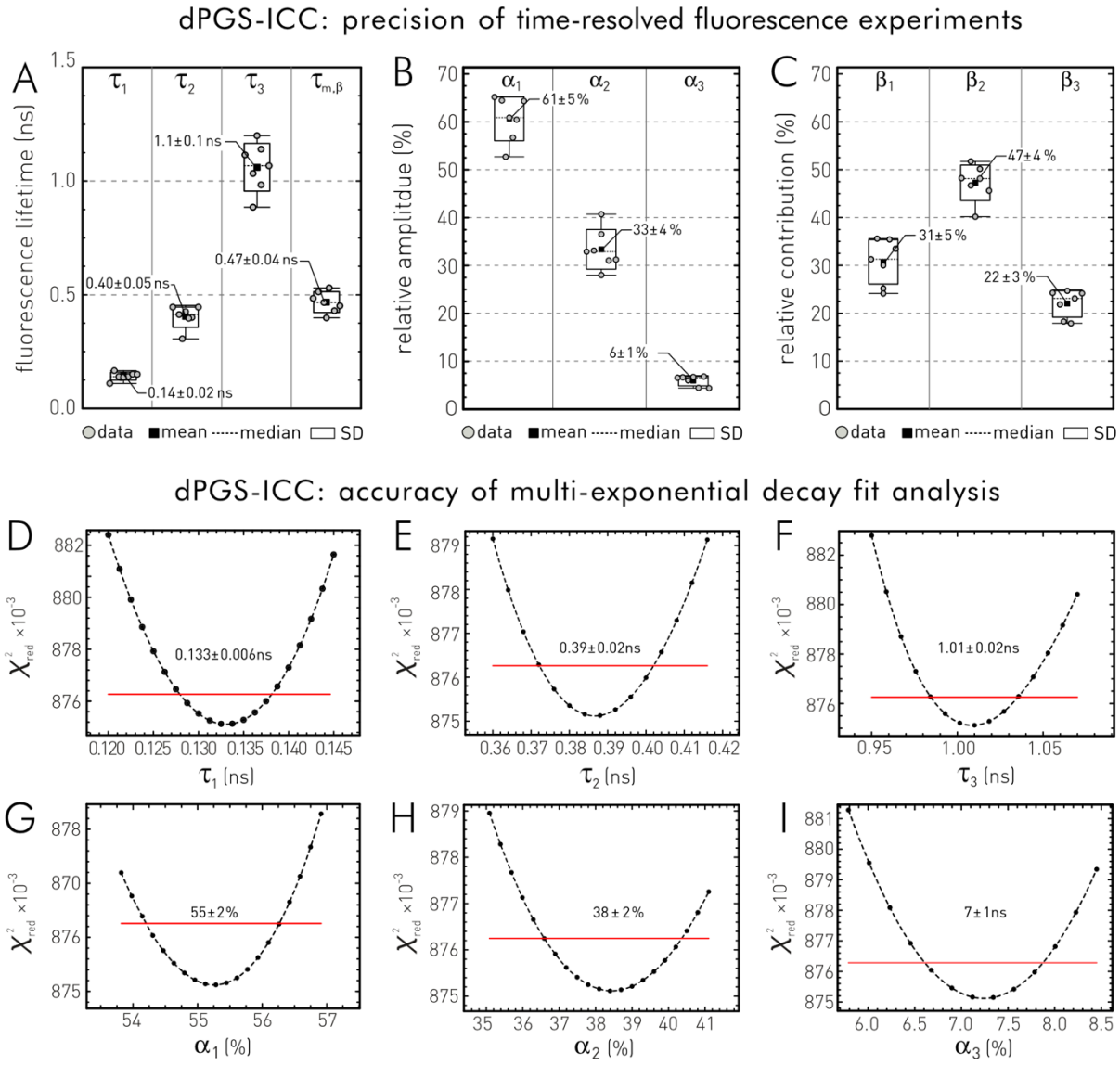

Figure 4.3.1: Precision and fit accuracy in the fluorescence decays measurements of dPGS-ICC. Tri-exponential decay fitting of seven different TCSPC experiments on dPGS-ICC in aqueous solutions originating from the same polymer syntheses are compared. The experiments were conducted over a period of 4 years. **A** Fluorescence decay components and mean fluorescence lifetime. **B** Relative decay amplitudes. **C** Relative steady-state fluorescence contributions. Box plots show the individual fitting parameters as gray dots. Black squares indicate the respective mean and the dashed black lines the median. The box visualizes the standard deviation (SD). Whiskers show minimal and maximal values. **D-I** Exemplary determination of the accuracy of fit-parameters obtained by a confidence interval analysis according to Section 3.4.1. Red lines indicate confidence level. Experimental conditions: TCSPC-cuvette setup (Section 3.3.3), T=20 °C, λ_{ex} = 488 nm, λ_{em} > 570 nm.

The uncertainties of the decay fit analyses were estimated by confidence interval analyses of the individual fit parameters according to Section 3.4.1. Table 4.3.1 shows mean and standard deviation of these fit uncertainties by applying the approach to the data files of the seven dPGS-ICC experiments. The displayed values shall serve as a general measure for the accuracy of the decay fit analysis of dPGS-ICC's time-resolved fluorescence behavior. The relative accuracy ranges between 2.4 ± 0.6 % for the slow (τ_3) and 4 ± 2 % for the fast (τ_1) decay component. The respective decay amplitudes vary between 4 ± 1 % (α_1) and 8 ± 3 % (α_3). Similar relative accuracies were determined previously in fluorescence decay analyses of fluorescein-labeled ChR2 proteins, recorded with

the same fluorescence spectroscopic setup and using the same decay fitting approach.[279] Since the general precision of the time-resolved fluorescence experiments is significantly lower than the accuracy of the fit analyses, the relative precision is used in the following as a measure for the experimental uncertainty of the individual fluorescence decay analyses.

dPGS-ICC interactions with model proteins and receptors

If synthetic materials like dendritic nanoparticles enter an organism, protein absorption may occur on their surfaces. This effect is summarized by the term protein corona formation.[280-281] The protein corona largely determines further interactions in the organism. Absorbed proteins may determine whether certain cells recognize the nanoparticle or whether it remains invisible to them (stealth effect).[281-282] Often, the protein corona alters the physicochemical functions and biological activity of a nanoparticle, so that *in vitro* experiments cannot be reproduced *in vivo*.[283] The best-known example of protein corona formation occurs during the systemic administration of nanoparticles.[284] In blood serum, a particular interaction with the protein *serum albumin* occurs, the most common serum protein.[285-286] Serum albumins maintain oncotic pressure, buffer blood pH, and have been shown to contribute to the transport, distribution, and metabolism of many endogenous and exogenous ligands.[144, 287-288] In the human organism, human *serum albumin* (HSA) regulates the antioxidative capacity and has several binding pockets for ligands such as fatty acids, amino acids and toxins.[141] Many of these ligands would not be soluble in serum by themselves and dependent on HSA for systemic distribution. The binding pockets of the 65 kDa protein also attract nanomaterials. The interactions with them mostly take place via electrostatic interactions with target structures on the nanoparticle's surface.[144] As for non-synthetic ligands, the equilibrium and kinetic parameters of these protein-ligand interactions are typically investigated by methods like size exclusion chromatography, gel filtration, surface plasmon resonance, centrifugation-based pull-down assays, or isothermal titration calorimetry.[280]

In the following section, I investigate the interactions of dPGS with human serum (HS) and *bovine serum albumin* (BSA) by changes in the fluorescence lifetime of the FMR probe ICC covalently attached to the hyperbranched polyglycerol nanoparticle. Thereby, I extend the possibilities of fluorescence lifetime-based interaction monitoring of dPGS-ICC compared to previous studies. Some of the results have already been published in Molecules (Boreham et al., Ref. 25). Hence, the next paragraph relies partly on my contributions to this paper. The publication investigates the nanoparticle – protein interaction of dPGS-ICC with L-selectin and the complement protein C1q as well as the general dPGS – HS interaction based on the fluorescence lifetime changes of ICC. With the serum experiment, my contribution to the paper, I would like to start this section. I investigate the protein binding of dPGS-ICC in HS (protein content: 71 mg/mL)[289] via changes in its fluorescence decays. Figure 4.3.2A shows the fluorescence decay traces of 0.1 µM dPGS-ICC dissolved in differently diluted HS solutions. The plot clearly shows how the fluorescence decay of dPGS-ICC slows down with

increasing HS concentration, i.e., with higher probability of molecular interaction between dPGS-ICC and serum proteins. Higher interaction rates gradually increase the steric restrictions of the FMR probe so that an effective de-population of ICC's S_1 state via this non-radiative path decreases. Conversely, an increased depopulation via fluorescence occurs, resulting in longer observed fluorescence lifetimes. This process saturates for high serum concentrations because the majority of dPGS-ICC is then interacting with serum proteins.

To investigate this behavior in detail, I performed fluorescence decay analyses (see Sec. 3.4.1) by fitting the fluorescence decays (Figure 4.3.2A) to a tri-exponential decay model (see Appendix, Table A7). Figure 4.3.2B shows in its upper segment the determined decay components τ_c as a function of CMS concentration. While the fastest decay component (τ_1 = 0.16 ± 0.02 ns) remains constant over the entire HS concentration range, the second and third decay component increases from 0.46 ± 0.06 ns to 0.9 ± 0.1 ns and from 1.2 ± 0.1 ns to 2.3 ± 0.1 ns , respectively. The corresponding decay amplitudes (α_c) shown in the middle segment of Figure 4.3.2B change accordingly as follows: While α_1 decreases with higher serum concentrations from 60 ± 5 % to 26± 2 %, the amplitude α_3 increases from 5.9 ± 0.7 % to 39 ± 5 %. The amplitude of the second component changes only marginally between 34 ± 4 % and 39 ± 5 %. To study the relative population of the individual fluorescence species, the relative-steady state contributions β_c of the three decay components were calculated. The results are shown in the lower segment of Figure 4.3.2B. The graph clearly shows that while the largest increase occurs in the third component, with over 240 % (22 ± 3 % to 74 ± 5 %), the population of the second component decreases sparsely (48 ± 5 % to 24 ± 4 %) at high HS concentrations. The population of the first component falls below 3 %.

Next, a simple model is applied (fractional saturation method), which indirectly considers the fluorescence lifetime information as a measure of binding affinity. It is assumed that the calculated mean fluorescence lifetime $\tau_{m,\beta}$, or more precisely the change in mean fluorescence lifetime due to the binding interaction, is directly proportional to the HS concentration and the occurring protein binding (Figure 4.3.2C). For reasons of simplicity, it is assumed that dPGS-ICC exists in only two states, the bound and the free state. It is further assumed that both states have their own distinguishable characteristic fluorescence lifetime and the difference in $\tau_{m,\beta}$ at 70 % HS and 0 % HS constitutes the value of maximum saturation of the binding reactions. To determine the binding affinity, a fractional saturation value in % was calculated via Eq. 57 (differences in $\tau_{m,\beta}$), plotted versus the HS concentration and subsequently fitted to a Hill function (Eq. 58). The fit revealed an apparent binding affinity K_{50} of 0.41 ± 0.05 % HS (Figure 4.3.2C). Furthermore, the fit yielded a cooperation factor of 0.66 ± 0.05, which corresponds to a binding stoichiometry of less than one. This means that once a dPGS molecule bounds to a serum protein, its affinity for other proteins decreases.

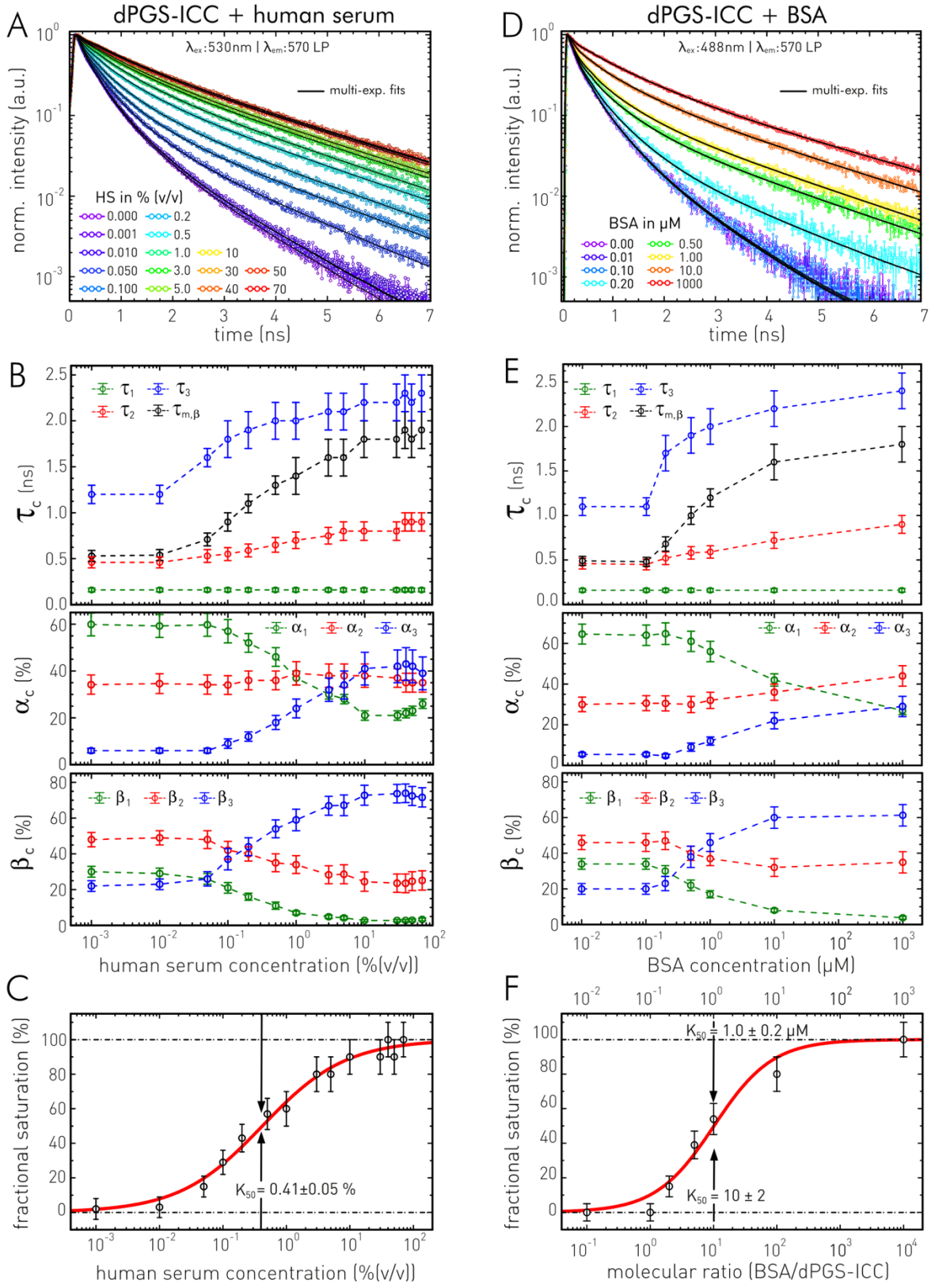

Figure 4.3.2: dPGS-ICC interaction with human serum (HS) and bovine *serum albumin* (BSA). **A** fluorescence decay traces of 0.1 µM dPGS-ICC in solutions of varying HS concentration (rainbow colors), black solid lines display multi-exponential fits. T = 20 °C. **B** Fit results (see Table A7). Top: dPGS-ICC's decay components and mean fluorescence lifetime versus HS concentration (in log scale). Center: Relative decay amplitudes versus HS concentration (in log scale). Bottom: Relative steady-state fluorescence contributions β_c versus HS concentration (in log scale). **C** Fractional saturation (Eq. 57) of the binding of dPGS-ICC to HS constituents and fit to a Hill model (Eq. 58). K_{50} amounts to 0.41 ± 0.05 %, g = 0.66 ± 0.05. **D** fluorescence decay traces of 0.1 µM dPGS-ICC in solutions of varying BSA concentration (rainbow colors), black solid lines display multi-exponential fits. T = 20 °C. **E** Fit results (see Table A8). Top: dPGS-ICC's decay components and mean fluorescence lifetime versus BSA concentration (in log scale). Center:

Relative decay amplitudes versus BSA concentration (in log scale). Bottom: Relative steady-state fluorescence contributions β_c versus BSA concentration (in log scale). **F** Fractional saturation (Eq. 57) of the binding of dPGS-ICC to BSA molecules and fit to a Hill model (Eq. 58). K_{50} amounts to 1.0 ± 0.2 µM (≙ 10 ± 2 BSA/dPGS-ICC molecules), g = 0.9 ± 0.2. Experimental conditions: TCSPC-cuvette setup (Section 3.3.3), spectral parameters are indicated in A and D. Indicated uncertainties are based on relative precision, see Table 3.4.1.

In the following experiment, the interaction between dPGS-NP and serum constituents will be examined in more detail. Therefore, the interaction of dPGS with the main protein of the serum, the serum *albumin* (35 – 55 mg/ml)[290], will be investigated. I use BSA as a model for HSA, firstly because of its complementary structural similarity to HSA.[287] Secondly, BSA is a widely used reference protein to study the corona formation of newly developed nanoparticles and allows for a better comparison.[144, 291-292]

I investigate the binding affinity of dPGS-ICC to BSA again based on changes in the fluorescence decays behavior of ICC. Figure 4.3.2D shows the respective fluorescence decay traces of 0.1 µM dPGS-ICC interacting with BSA at different concentrations. The decay traces indicate that the fluorescence decay of dPGS-ICC slows down with increasing BSA concentration, i.e., with higher probability of molecular interaction between both interaction partners. This process saturates for high BSA concentrations. The fluorescence decays of the BSA series (Figure 4.3.2) behave qualitatively similar to the decays of the HS series. Conversely, this indicates that the majority of interactions in serum take place between dPGS and HSA.

To compare the time-resolved fluorescence behavior more quantitively, I applied a decay analysis (see Sec. 3.4.1) to the fluorescence decay traces of Figure 4.3.2D again, using a tri-exponential decay model (see Appendix, Table A8). Figure 4.3.2E shows in its upper segment the determined decay components τ_c as a function of BSA concentration. While the fastest decay component (τ_1 = 0.16 ± 0.02 ns) remains constant over the entire concentration range of BSA, the second and third decay component increases from 0.46 ± 0.06 ns to 0.9 ± 0.1 ns and from 1.1 ± 0.1 ns to 2.4 ± 0.2ns, respectively. The corresponding decay amplitudes (α_c) shown in the middle segment of Figure 4.3.2E change accordingly as follows: While α_1 decreases with higher BSA concentrations from 65 ± 5 % to 27 ± 5 %, the amplitude α_3 increases from 5.4 ± 0.7 % to 29 ± 4 %. The amplitude of the second component changes only marginally between 30 ± 4 % and 44 ± 5 %. To study the relative population of the individual fluorescence species, the relative-steady state contributions β_c of the three decay components were calculated. The results are shown in the lower segment of Figure 4.3.2E. The graph indicates that while the largest increase occurs in the third component, with over 215 % (20 ± 3 % to 61 ± 5 %), the population of the second component decreases only sparsely (46 ± 4 % to 35 ± 5 %) at high HS concentrations and the population of the first component declines below 4 %.

These results are similar to the previous investigation of dPGS in HS. The similarity in the fluorescence decay behavior suggests that the main interaction taking place in the serum occurs with HSA. The most frequently occurring protein there. By applying the same fractional saturation method and

using a fit to a Hill function (Eq. 58), I determined apparent binding affinity K_{50} of 1.0 ± 0.2 µM BSA (Figure 4.3.2F). Furthermore, the fit yields a cooperation factor of 0.9 ± 0.2 indicating a non-cooperative binding mode. This means that if a dPGS molecule binds to a BSA protein, the affinity for other dPGS – protein interactions is not altered. The binding constant determined in the human serum experiments can be converted to its proportion of HSA. The result is an apparent binding affinity of 2.1 – 3.3 µM HSA. Comparing these values to the K_{50} value of BSA, confirms the assumption that the protein interaction of dPGS-NP in serum occurs to a large extent with HSA. Interactions of different dPG-NP were previously studied by tryptophan fluorescence quenching.[144] This method yielded strong interactions of BSA with dPG-amines. dPGS, however, showed only a weak effect on the BSA's tryptophan fluorescence. This suggests that the FMR-based fluorescence lifetime method presented here is a sensitive alternative, able to detect and resolve even weaker binding interactions. A second paper investigated the thermodynamics behind the interaction of dPGS and HSA using isothermal titration calorimetry. It compared is results to coarse-grained computer simulation assuming dPGS as sulfated polyglycerol dendrimers. The authors found a formation of a 1:1 complex between the 2 kD dPGS and HSA, corresponding to a G2-dendrimer in their simulations. For larger dPGS-NP, like these investigated here (~10 – 12 kD), several HSA molecules bound to a single dendritic polyglycerol. This behavior is reflected in the data shown here as several *serum albumins* bind to a single dPGS-ICC molecule (Figure 4.3.2F, see molecular ratios). Since corona proteins significantly determine the specific cellular uptake via cell surface receptors[293], the study of corona formation of proteins is fundamental for the future understanding of NP-cell interactions.

After studying the serum interaction, I set out to investigate the interaction of dPGS with a model receptor. Possible protein corona influences on this interaction will not be considered in this thesis. I did, however, investigate the general possibility of monitoring the binding of polyanionic dPGS to a receptor solely by fluorescence lifetime changes. The model receptor under investigation is a scavenger receptor (SR). These cell surface receptors are characterized by their ability to bind to the modified low-density lipoprotein (LDL).[294] In contrast to the vast majority of membrane receptors, the SRs which belong to the receptors for the recognition of surface patterns, bind and transport not only a specific, but a broad spectrum of endogenous and microbial ligands.[295] They are characterized by a high affinity to different polyanionic or macromolecular molecules. The exact parameters that determine the binding capacity have not yet been conclusively identified.[296-297] Among the ligands of SRs are also a large number of NPs. Different studies show the internalization and transport within the cytosol. The interaction with SRs has been studied for various NP-systems such as silica, silver, polystyrene, and polyvalent oligonucleotide-functionalized gold NPs.[298-302]

In a first experiment, I investigated the binding affinity of dPGS-ICC to a triple-helical peptide model (MSR-1) mimicking the macrophage scavenger receptor (MSR). The applied model consist of a 30-mer peptide: $(POG)_3PKGQKGEKG\text{-}(POG)_4$ and was first synthesized and investigated by Anachi et al. in 1995.[303] MSR-1 contains a lysine-rich 9 residue sequence from the collagen-like domain of

MSR and adopts a stable triple-helical conformation at physiological pH and temperatures below 30 °C. The 9-residue peptide sequence is critical for the ligand binding in MSR.[303] The MSR-1 peptide is water soluble and was directly incubated with dPGS-ICC at different peptide concentrations.

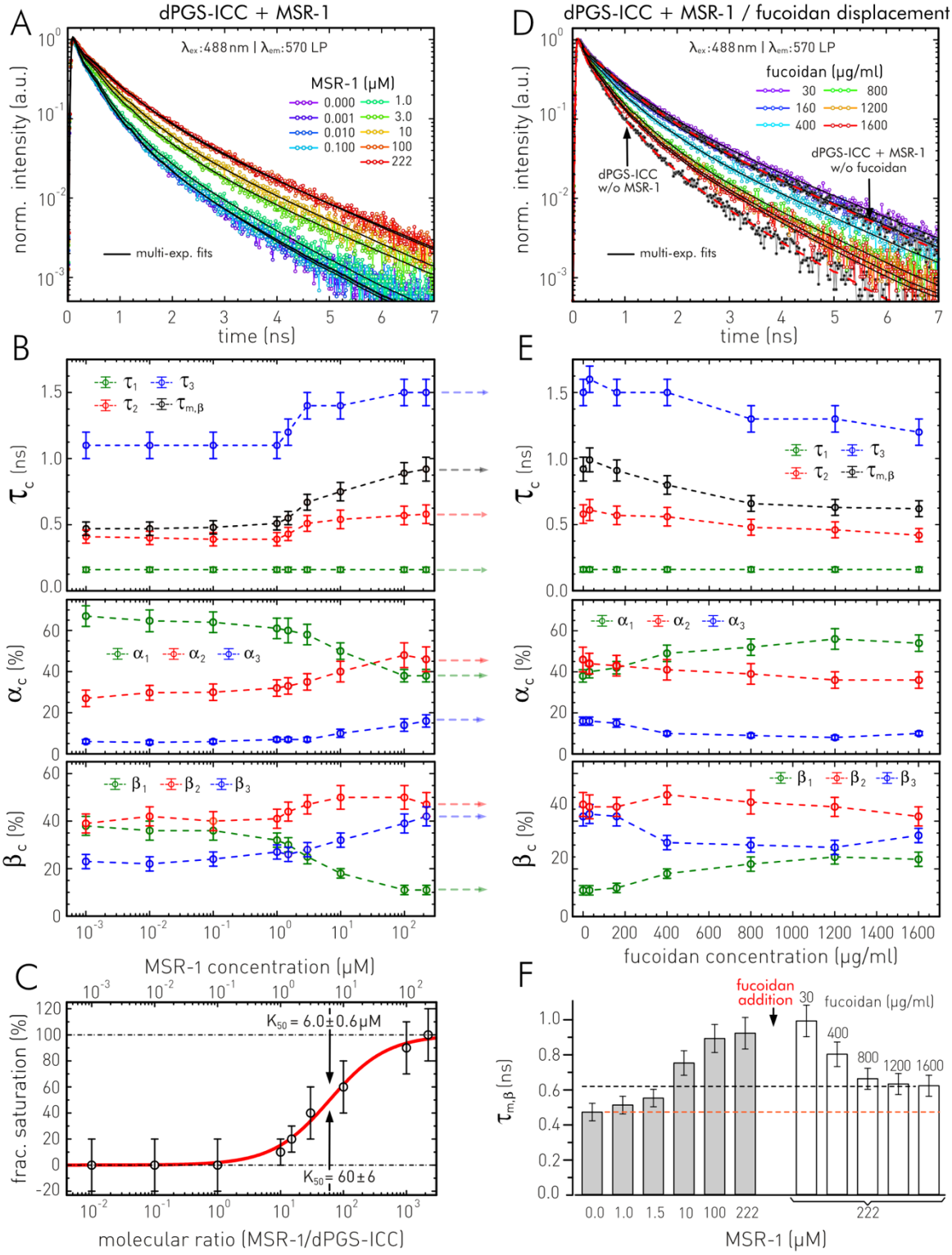

Figure 4.3.3: dPGS-ICC interaction with a triple helical model peptide (MSR-1) mimicking the macrophage scavenger receptor. **A** fluorescence decay traces of 0.1 μM dPGS-ICC in solutions of varying MSR-1 concentration (rainbow colors), black solid lines display multi-exponential fits. T = 20 °C. **B** Fit results (see Appendix, Table A9). Top: dPGS-ICC's decay components and mean fluorescence lifetime versus MSR-1 concentration (in log scale). Center: Relative decay amplitudes versus MSR-1 concentration (in log scale). Bottom: Relative steady-state fluorescence contributions β_c versus MSR-1 concentration (in log scale). **C** Fractional saturation

(Eq. 57) of the binding of dPGS-ICC to MSR-1 peptide and fit to a Hill model (Eq. 58). K_{50} amounts to 6.0 ± 0.6 µM (≙ 60 ± 6 MSR-1/dPGS-ICC molecules, g=0.95 ± 0.08. **D** fluorescence decay traces of 0.1 µM dPGS-ICC in solutions containing 222 µM MSR-1 and varying fucoidan concentration (rainbow colors), black solid lines display multi-exponential fits. T = 20 °C. **E** Fit results (see Table A9). Top: dPGS-ICC's decay components and mean fluorescence lifetime versus fucoidan concentration. Center: Relative decay amplitudes versus fucoidan concentration. Bottom: Relative steady-state fluorescence contributions β_c versus fucoidan concentration. **F** Comparison of dPGS-ICC's mean fluorescence lifetime upon addition of MSR-1 and fucoidan. Experimental conditions: TCSPC-cuvette setup (Section 3.3.3), spectral parameters are indicated in A and D. Indicated uncertainties are based on relative precision, see Table 3.4.1.

Figure 4.3.3A shows the obtained fluorescence decay traces of 0.1 µM dPGS-ICC interacting with different concentrations of MSR-1. The fluorescence decay traces clearly show how dPGS-ICC's fluorescence decay slows down with rising MSR-1 concentrations. This indicates a correlation between nanoparticle – peptide binding and fluorescence lifetime. This can be explained by a higher interaction rate inducing steric restrictions to ICC's intramolecular rotation which is gradually increased so that an effective depopulation of the S_1 state via this non-radiative path decreases. Conversely, an increased depopulation via fluorescence occurs, resulting in a longer observed fluorescence lifetime. This process saturates for high MSR-1 concentrations.

Compared to the dPGS-ICC – BSA interaction, the observed effect on the fluorescence decay is less pronounced, but well detectable. To investigate this behavior in detail, I performed a fluorescence decay analysis (see Sec. 3.4.1) by fitting the fluorescence decays (Figure 4.3.3A) to a tri-exponential decay model (see Appendix, Table A9). Figure 4.3.3B shows in its upper segment the determined decay components τ_c as a function of MSR-1 concentration. While the fastest decay component (τ_1 = 0.16 ± 0.02 ns) remains constant over the entire concentration range of the MSR-1 peptide, the second and third decay component increases from 0.41 ± 0.05 ns to 0.58 ± 0.07 ns and from 1.1 ± 0.1 ns to 1.5 ± 0.1 ns, respectively. The corresponding decay amplitudes (α_c) shown in the middle segment of Figure 4.3.3B change accordingly as follows: While α_1 decreases with higher MSR-1 concentrations from 67 ± 6 % to 38 ± 6 %, the amplitudes α_2 and α_3 increase from 27 ± 3 % to 46 ± 6 % and from 6.1 ± 0.7 % to 16 ± 2 %, respectively. To study the relative population of the individual fluorescence species, the relative-steady state contributions β_c of the three decay components were calculated. The results are shown in the lower segment of Figure 4.3.3B. This diagram shows that the changes in the individual components are not as pronounced as with the BSA interaction. The strongest influence upon receptor binding was observed for the first component with a reduction of 71% (38 ± 4 % to 11 ± 2 %). The populations of the second component increase sparsely (39 ± 4 % to 47 ± 5 %), while the third component increases with MSR-1 interaction by a factor of ~1.8 (23 ± 3 % to 42 ± 4 %).

Next, I apply the fractional saturation model again, which considers the fluorescence lifetime information as a measure of binding affinity. As for the BSA interaction, I assume that the observed changes in mean fluorescence lifetime $\tau_{m,\beta}$ is directly proportional to the concentration of MSR-1 peptide. The calculated fractional saturation values in percent (Eq. 57) are plotted against the MSR-1 concentration. This plot is subsequently fitted to a Hill function (Eq. 58). The model fit showed an

apparent binding affinity K_{50} of 6.0 ± 0.6 µM MSR-1 (Figure 4.3.3C). This corresponds to a K_{50} value of 60 ± 6 MSR-1 peptide per dPGS-ICC molecule (C = 0.1 µM, Figure 4.3.3C). Thus, compared to BSA, the binding affinity is reduced by a factor of 5. Furthermore, the fit yielded a cooperation factor of 0.95 ± 0.08, which corresponds to noncooperative binding. This means that the binding affinity of dPGS-NP to an MSR-1 peptide is not dependent on whether or not other MSR-1 has bound to dPGS-NP.

Having established the monitoring of the binding interaction between dPGS-ICC and the receptor model MSR-1 via fluorescence lifetime characteristics of the applied FMR probe, I am now going a step further to investigate a possible detachment process of MSR-1 bound dPGS-ICC by a further SR ligand. For that purpose, I use fucoidan, a classical inhibitor for scavenger receptor mediated endocytosis.[304] The idea behind this experiment is that the dPGS-ICC binding to MSR-1 is established by electrostatic forces so that the NP can be replaced by a competitive ligand in a displacement assay. Fucoidan is a naturally occurring sulfated polysaccharide originating from brown algae, that shows a strong binding affinity to MSR.[305-307]

In the displacement assay, fucoidan was added to a dPGS-ICC – MSR-1 solution (0.1 µM + 222 µM) at varying concentrations. Figure 4.3.3D shows the fluorescence decay traces of dPGS-ICC – receptor mixture at varying fucoidan concentration. After an initial further slowdown of the fluorescence decay of dPGS-ICC at the lowest added fucoidan concentration, the fluorescence decay gets continuously faster at higher fucoidan concentrations. This means the fluorescence lifetimes approach the values of free dPGS-ICC again, suggesting a detachment from the receptor by competitive fucoidan molecules. A fluorescence decay analysis (Figure 4.3.3E) by fitting the fluorescence decays to a tri-exponential decay model (Table A9) points into the same direction. The determined fluorescence decay components almost approach the original values of the free dPGS-ICC for high fucoidan concentrations. Only the third component is slightly slower (1.1 ± 0.1 ns vs. 1.2 ± 0.1 ns) in the highest investigated fucoidan concertation (1,600 µg/ml). The corresponding decay amplitudes (α_c), which are shown in the middle segment of Figure 4.3.3E, do not achieve the initial state. Especially the second and third components do not reach the original values.

These numbers could indicate that some dPGS-ICC molecules still interact with the MSR-1 receptor even at the high fucoidan concentrations of 1,600 µg/ml. If one assumes, that only a small number of dPGS-ICC molecules is still interacting with MSR-1 at these ligand concentrations, one could argue that the altered fluorescence decay characteristics could originate from a preferred conformation of dPGS-NP after the detachment process. This configuration could promote a changed amplitude ratio between the first and second decay component. Although this behavior cannot be resolved, it is remarkable that this experiment was successful and the fluorescence lifetime of the FMR ICC reversible indicates the interaction mode of the dPGS-NP with a receptor. To my knowledge, it is the first time that an interaction state between an NP and a receptor was monitored by the fluorescence lifetime.

dPGS-ICC interactions with lipidic model systems

This section focuses on the interaction between dendritic polyglycerol sulfate (dPGS) and lipid membranes. Previous publications have reported a strong interaction indicated by a high affinity between dPGS-ICC nanoparticles and lipid bilayers in form of giant 1,2-dimyristoyl-sn-glycero-3-phosphocholine (DMPC) unilamellar vesicles (DMPC GUVs).[25, 198] The following results were partially published in Langmuir (Ober et al., Ref. 88). The paper describes a systematic characterization of the viscosity and temperature dependent photo and isomerization properties of the molecular rotor probe ICC attached to the dPGS surface (dPGS-ICC) by different fluorescence-based experiments. These results support the potential use of dPGS-ICC as a nanoviscosity-sensitive nanoparticle for lamellar lipidic systems like small unilamellar vesicles (SUVs) or multilamellar vesicles (MLVs). The following section shows my contribution to the characterization of dPGS-ICC as a nanoparticle-based sensor system.

Molecular interactions between dPGS-ICC and lipidic systems has only been detected using fluorescence intensity and fluorescence lifetime information obtained by FLIM experiments (see Sec. 2.2.3) so far.[198] To verify these results by a second approach, I applied a spectroscopic method, that uses polarity dependent changes in the ICC fluorescence emission spectrum characteristic for environments of different polarities. Bathochromic shifts (see Sec. 2.1.2) are commonly observed for serval cyanines like ICC when the polarity of solvents is decreasing, an effect easily detectable in a spectrofluorometer.[76]

Figure 4.3.4A compares fluorescence emission spectra of ICC in different EtOH/H_2O mixtures with dPGS-ICC in aqueous solutions containing and not containing DMPC-based SUVs. As expected, the inset in the Figure shows, that the emission spectrum of ICC shifts bathochromicaly with increasing EtOH concentrations (0 – 100 %) from 565 ± 1 nm to 573 ± 1 nm. The corresponding change in polarity expressed by the dielectric constant ranges between 80 and 25.[264] If one compares the emission spectrum of ICC in aqueous solution with the spectrum of dPGS-ICC in H_2O (Figure 4.3.4A) now, a spectral red-shift becomes evident, caused by the covalent attachment of ICC to the surface of the sulfated nanoparticle. This indicates an environment of reduced polarity compared to H_2O.

Figure 4.3.4B shows the calibration of dPGS-ICC's fluorescence peak position directly to a dielectric constant using the peaks of ICC's emission spectra (EtOH/H_2O, Figure 4.3.4A). Using this assignment, the environment of anionic sulfate groups at the surface of the nanoparticle would correspond to a value of $\epsilon = 68$. By adding DMPC SUVs (see Sec. 3.2.1) to the aqueous solution this value is reduced further to $\epsilon = 48$. This clear indication of a molecular interaction between dPGS-ICC and the added lipid vesicles supports the previously observed enrichment of the nanoparticle in the lamellar lipid bilayer of DMPC-based GUVs.[198]

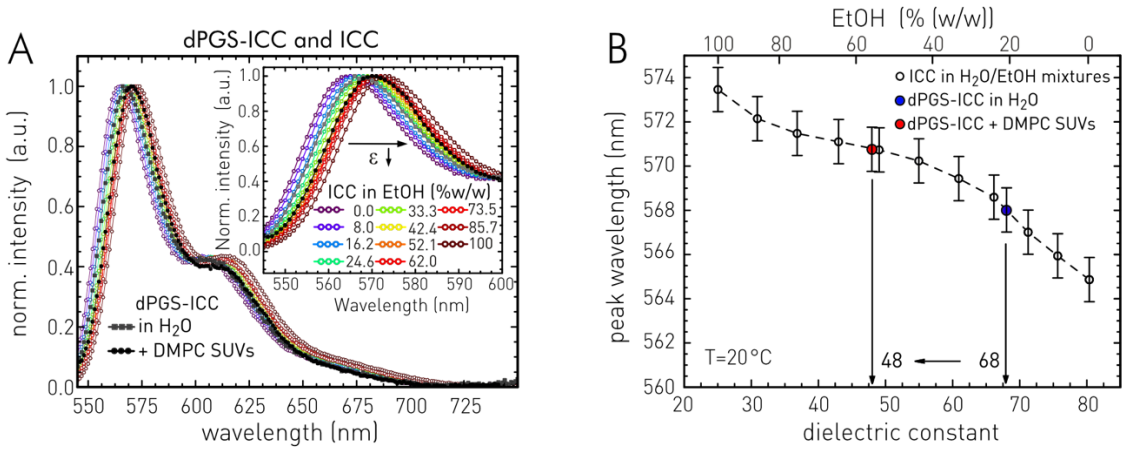

Figure 4.3.4: Effect of lipid interaction on dPGS-ICC's fluorescence emission spectra. **A** Emission spectra of dPGS-ICC in H_2O (black, connected solid circles) and in a sodium phosphate buffer (pH 7) containing DMPC SUVs (gray, connected solid squares). For comparison ICC emission spectra (rainbow-colored connected open circles) obtained in EtOH/H_2O mixtures are shown. Inset shows magnification to the wavelength region between 545 nm to 600 nm. **B** Shift of ICC's emission peak wavelength (black, open circles) as a function of the dielectric constant. Location of dPGS-ICC in H_2O (blue, solid circle) and in the DMPC vesicle solution (red, solid circle) indicates polarity shifts. Dielectric constants taken from Ref. 264.

The further characterization of the lipid – nanoparticle interaction is carried out by time-resolved fluorescence spectroscopy (see Section 3.3.3). In a first experiment, I investigated the binding affinity of dPGS-ICC to DMPC SUVs via changes in its fluorescence decays. As investigations by Katja Ober (Prof. Alexiev's Group, Freie Universität Berlin, Germany) indicate that the strength of this interaction depends on the temperature and lamellar lipid phase, I performed two experimental series.[88] The first series was recorded at 5 °C, well below the known main phase transition and pre-transition temperatures of DMPC which are located at 24 °C, and 14 °C, respectively.[308-309] Figure 4.3.5A shows the fluorescence decay traces of 0.1 µM dPGS-ICC interacting with different concentrations of DMPC SUVs. Please note, the concentration in the plots is expressed in µM DMPC, i.e., as the concentration of single lipid molecules. The fluorescence decay traces clearly show how dPGS-ICC's fluorescence decay slows down with increasing DMPC SUV concentration. This indicates a correlation between nanoparticle – lipid interaction and fluorescence lifetime. This can be explained with a higher interaction rate which induces steric restrictions to ICC's intramolecular rotation which is gradually increased so that an effective depopulation of the S_1 state via this non-radiative path decreases. Conversely, an increased depopulation via fluorescence occurs, resulting in a longer observed fluorescence lifetime. This process saturates for high DMPC SUV concentrations.

The fluorescence decay behavior of dPGS-ICC is further investigated using a decay analysis (see Sec. 3.4.1) by fitting the traces of Figure 4.3.5A to a tri-exponential decay model (see Appendix, Table A10). Figure 4.3.5B shows in its upper segment the determined decay components τ_c as a function of DMPC concentration. While the fastest decay component (τ_1 = 0.19 ± 0.03 ns) remains constant over the entire concentration range of DMPC, the second and third decay component increases from 0.62 ± 0.08 ns to 0.9 ± 0.1 ns and from 1.6 ± 0.1 ns to 1.9 ± 0.2 ns, respectively. The corresponding relative decay amplitudes (α_c) shown in the middle segment of Figure 4.3.5B

change accordingly as follows: the amplitudes α_1 and α_2 decreases with higher DMPC concentrations from 49 ± 4 % to 8.5 ± 0.7 %, and from 42 ± 5 % to 35 ± 4 %, respectively. The third amplitude α_3 increases from 9 ± 1 % to 57 ± 7 %. To study the relative population of the individual fluorescence species, relative-steady state contributions β_c were calculated. The results are shown in the lower segment of Figure 4.3.5B. This graph clearly shows that the largest increase occurs in the third component, with an increase of over 162 % (29 ± 3 % to 76 ± 5 %). In contrast, the population of the second component decreases (52 ± 4 % to 22 ± 5 %), while the first component vanishes almost completely at high DMPC concentrations (19 ± 3 % to 1.2 ± 0.3 %).

Next, a simple model is applied which indirectly considers the fluorescence lifetime information as a measure of binding affinity. It is assumed that the calculated mean fluorescence lifetime $\tau_{m,\beta}$, or more precisely the change in mean fluorescence lifetime due to the binding interaction, is directly proportional to the concentration of DMPC molecules present as SUVs (Figure 4.3.5C). For reasons of simplicity, it is assumed that dPGS-ICC exists in only two states, the bound and the free state. It is further assumed that both states have their own distinguishable characteristic fluorescence lifetime and the difference in $\tau_{m,\beta}$ at 4 µM DMPC to 0 µM DMPC constitutes the value of maximum saturation of the binding reaction. In order to determine the binding affinity, fractional saturation values in percent are calculated via Eq. 57 (differences in $\tau_{m,\beta}$) and plotted against the concentration of the DMPC molecules. This plot is subsequently fitted to a Hill function (Eq. 58). The model fit showed an apparent binding affinity K_{50} of 110 ± 10 µM DMPC molecules (Figure 4.3.5C). This corresponds to a K_{50} value of 1100 ± 100 lipid molecules per dPGS-ICC molecule (C = 0.1 µM, Figure 4.3.5C). Assuming SUV molecules of 20 nm diameter[88] and a head group area of 0.60 nm^2 of DMPC[310] this K_{50} value would correspond to ~0.2 SUVs per dPGS-ICC.[311] Furthermore, the fit yielded a cooperation factor of 0.95 ± 0.05 corresponding to noncooperative binding. This means the binding affinity of dPGS-NP to the DMPC SUVs is not dependent on whether or not other DMPC SUVs have bound to dPGS-NP.

A second experimental series performed at 20 °C focuses on the binding interaction of dPGS-ICC to DMPC SUVs between pre- and main phase transition of DMPC. At this temperature, the fluorescence decay traces show only a marginal change with increasing DMPC SUV concentrations (Figure 4.3.5D). This shows that, compared to measurements at 5 °C, no significantly increased probability of interaction between both molecules is observed with increasing DMPC concentration. The respective multi-component decay analysis of the time-resolved fluorescence traces show a similar picture. The fit results (see Appendix, Table A10) of the applied tri-exponential decay model are visualized in the three segments of Figure 4.3.5E. These concentration-dependent plots of the decay components (τ_c), relative amplitudes (α_c), and relative fluorescence contributions β_c give a uniform picture: The decay characteristic remains constant over the largest range of DMPC concentrations investigated. Only at the highest DMPC concentrations a small effect on the fluorescence lifetime of dPGS-ICC is observed. This effect is shown by an increase of τ_2 and τ_3. This indicates that a slight

restriction in the intramolecular rotation of the ICC probe occurs and the polarity of the ICC environment is slightly changed.

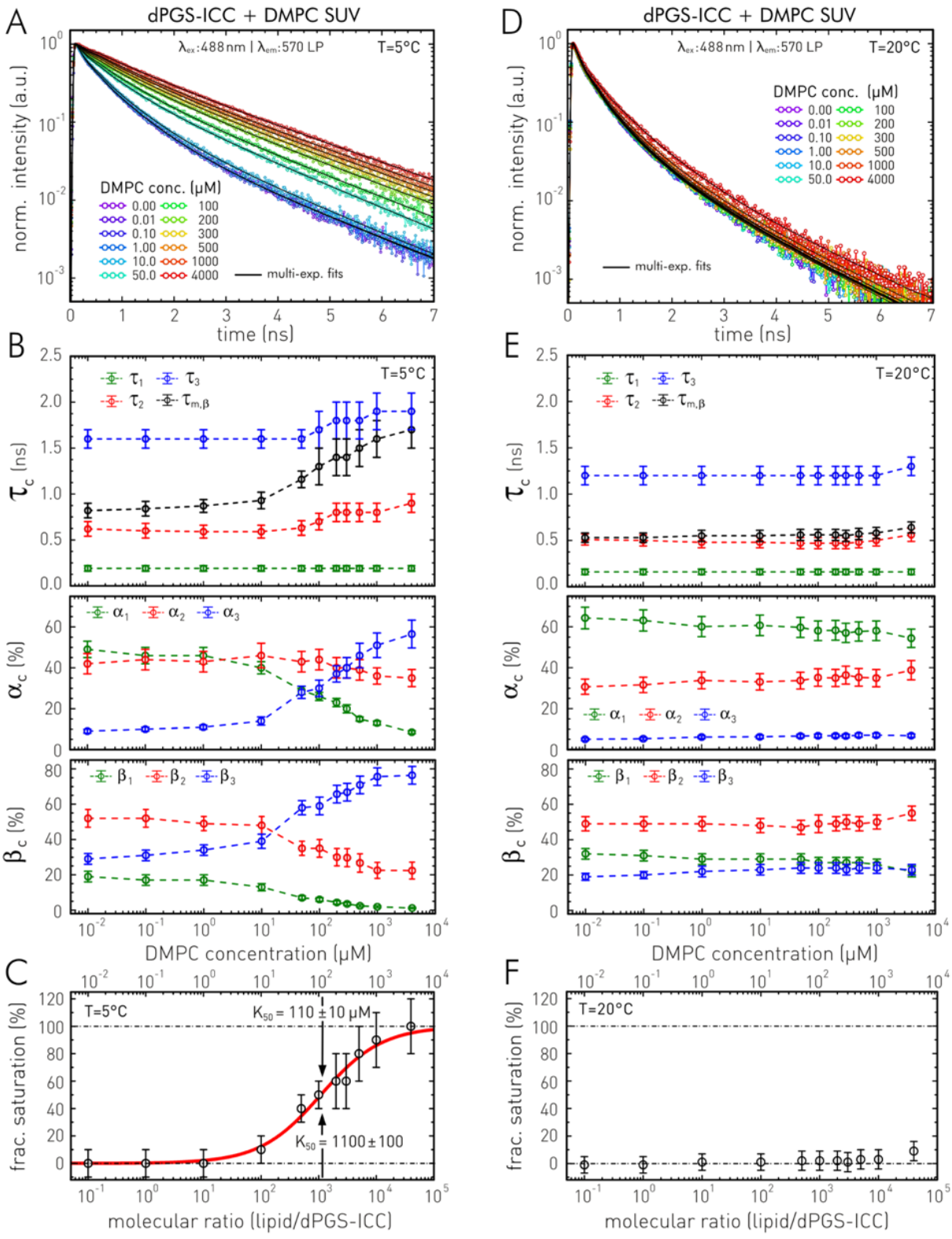

Figure 4.3.5: dPGS-ICC interaction with DMPC SUVs dissolved in sodium phosphate buffer (pH 7) at 5 °C and 20 °C. **A** fluorescence decay traces of 0.1 μM dPGS-ICC in solutions of varying DMPC SUV concentrations (rainbow colors), black solid lines display multi-exponential fits. T = 5 °C. **B** Fit results (see Appendix, Table A10). Top: dPGS-ICC's decay components and mean fluorescence lifetime versus DMPC SUV concentration (in log scale). Center: Relative decay amplitudes versus DMPC SUV concentration (in log scale). Bottom: Relative steady-state fluorescence contributions β_c versus DMPC SUV concentration (in log scale). **C** Fractional

saturation (Eq. 57) of the binding process of dPGS-ICC to DMPC vesicles and fit to a Hill model (Eq. 58) at T = 5 °C. K_{50} amounts to 104.4 ± 6.6µM (≙ 1044 ± 66 DMPC lipids/dPGS-ICC molecules), g=0.95 ± 0.05. **D** fluorescence decay traces of 0.1 µM dPGS-ICC in solutions of varying DMPC SUV concentration (rainbow colors), black solid lines display multi-exponential fits. T = 20 °C. **E** Fit results (see Table A10). Top: dPGS-ICC's decay components and mean fluorescence lifetime versus DMPC SUV concentration (in log scale). Center: Relative decay amplitudes versus DMPC SUV concentration (in log scale). Bottom: Relative steady-state fluorescence contributions β_c versus DMPC SUV concentration (in log scale). **F** Fractional saturation of the binding process between dPGS-ICC and DMPC SUVs at T = 20 °C scaled to the maximum of the interaction at 5 °C. Experimental conditions: TCSPC-cuvette setup (Section 3.3.3), spectral parameters are indicated in A and D. Indicated uncertainties are based on relative precision, see Table 3.4.1.

To illustrate this observation of a strongly reduced interaction affinity at 20 °C (Figure 4.3.5A-C), I calibrated the respective fractional saturation to the saturation level of the 5 °C series. Figure 4.3.5E shows these values, which are far from reaching the fractional saturation of the 5 °C series. Above all, no binding saturation can be observed and the highest value (at 4000 µM DMPC) of the 20 °C series reaches at most the level that is already observed at 10 µM DMPC in the 5 °C series. The strong binding interaction below 14 °C indicates an affinity of dPGS-ICC to DMPC in its gel phase.[309] By reaching the pre-transition temperature, a chain melting of lipid bilayers sets in, accompanied by a lateral expansion leading to the formation of periodic ripples in the membrane, known as ripple phase.[312] A similar sensitivity to a specific lipidic phase was previously reported for other fluorescent molecular rotor-based probes like Bodipy. [89] Therefore, further experiments were conducted to compare the interaction of dPGS-ICC with vesicles consisting of similar phosphatidylcholines: DMPC or DPPC (1,2- ipalmitoyl-sn-glycero-3-phosphocholine). Both lipids are neutral, have the same head group, but differ in their tails and consequently in their pre- and main phase transition temperature. Both transition temperatures are generally higher for DPPC than for DMPC. DPPC's pre-transition temperature is located at 33.5 °C and its main phase transition temperature at 41 °C.[89, 312]

Figure 4.3.6A and B compare the fluorescence decay traces of 0.1 µM dPGS-ICC interacting with 4 mM DMPC (A) and 4 mM DPPC (B) at 5 °C, 20 °C, 30 °C, and 45 °C. Lipids in this experiment are again present as SUVs. In order to achieve a sufficient interaction rate, e.g., most of the dPGS-ICC molecules are interacting with the SUVs, a high molecular ratio between nanoparticle and lipid of 1:40,000 (dPGS-ICC : lipid) was selected. Please note the concentration in the plots is expressed in µM DMPC, i.e., as the concentration of single lipid molecules. Before the nanoparticle – lipid interaction is considered, the focus is set on the temperature-related differences in the fluorescence lifetime of free, non-interacting dPGS-ICC in aqueous solution. As Figure 4.3.6A/B shows, the fluorescence decays become faster with increasing temperatures. This means that more energy is accessible for the intramolecular rotation process of the ICC probe, making depopulation of the S_1 state via this non-radiative transition more likely. With higher temperature, there is a higher probability of exceeding the isoviscous (rotational) activation energy (see Sec. 2.1.2). A possible temperature-induced change in the dPGS-ICC conformation affecting the fluorescence lifetime cannot be excluded *per se*, but an influence of the external viscosity can be ruled out due to the minimal viscosity change of an aqueous solution for such temperatures.

In the next step I investigate the question: How does the fluorescence lifetime of dPGS-ICC changes when it interacts with the different lipid types at different temperatures? At 5 °C, the lowest temperature studied, both lipids induce a pronounced slowdown in dPGS-ICC's fluorescence decay (Figure 4.3.6A/B). This indicates a molecular interaction between nanoparticles and lipid vesicles. The corresponding fluorescence decay traces show a comparable course, regardless of whether dPGS-ICC interacts with DMPC or DPPC SUVs. The fluorescence decay traces (Figure 4.3.6A/B) at the next higher temperature of 20 °C show a different picture. Here, the fluorescence of dPGS-ICC decays significantly faster when interacting with DMPC SUVs compared to those of DPPC. The major difference at a temperature of 20 °C is that DMPC already left its gel phase to the ripple phase while DPPC is still in the gel phase. The fluorescence decay traces of dPGS-ICC at the higher investigated temperatures show no difference for both lipid types.

For further analysis, I subjected the time-resolved fluorescence traces (Figure 4.3.6A/B) to a multi-component analysis. Figure 4.3.6C-F shows the fit results (see Appendix, Table A11) applying a tri-exponential decay model. The Figure visualizes the following decay parameters: decay component (τ_c), relative amplitude (α_c), mean fluorescence lifetime ($\tau_{m,\beta}$), and relative fluorescence contribution β_c as a function of temperature. If one considers the decay components, one observes that for at all investigated temperatures, the fastest component τ_1 is equivalent for free dPGS-ICC in aqueous solution (black dots) and dPGS-ICC interacting with DMPC (blue dots) or with DPPC (red dots). The second decay component τ_2 shows comparable values for lipid-interacting dPGS- ICC, which, however differ from free dPGS-ICC. Only the slowest decay component τ_3 varies in all three samples independently of the present temperature. In the case of free dPGS-ICC in solution (black dots), I observed an approximately linear temperature course for all other parameters (Figure 4.3.6D-F). A linear behavior is not observed for lipid-interacting dPGS-ICC. At 5 °C, the relative fluorescence contributions β_3 indicative of the strength of molecular interaction show, that the dPGS-ICC interaction with both phosphatidylcholines is similar, but strongly different from free dPGS-ICC. This behavior changes at a temperature of 20 °C. Here, one still observes a large difference between free and DPPC-interacting dPGS-ICC, while β_3 of the DMPC sample adapts to the value of free dPGS-ICC. For even higher temperatures (30 °C and 45 °C) only minimal differences between the lipid-interacting and free dPGS-ICC could be observed in respect to the parameter shown in Figure 4.3.6D-F. These results indicate at first glance, that the affinity of dPGS-ICC to the SUVs decreases strongly at temperatures above the pre-transition temperature, i.e., for phosphatidylcholines that are left their gel phases. This effect leads to more non-interacting dPGS-ICC molecules in solution, characterized by a faster fluorescence decay.

The high affinity of dPGS-ICC to lamellar lipid bilayers, the general ability of the ICC molecular rotor probe to measure nanoviscosities, together with the position of ICC on the dPGS surface suggests the idea of using dPGS-ICC as a nano-viscosity sensor for lipid membranes. For this reason, the last section focuses on this ability of the conjugated dPGS-ICC molecule. The objective of the

following investigation is to establish dPGS-ICC as an analytical nanoparticle. Not only for small structures like SUVs below the diffraction limit, but rather for larger structures like cells, that can be resolved microscopically.

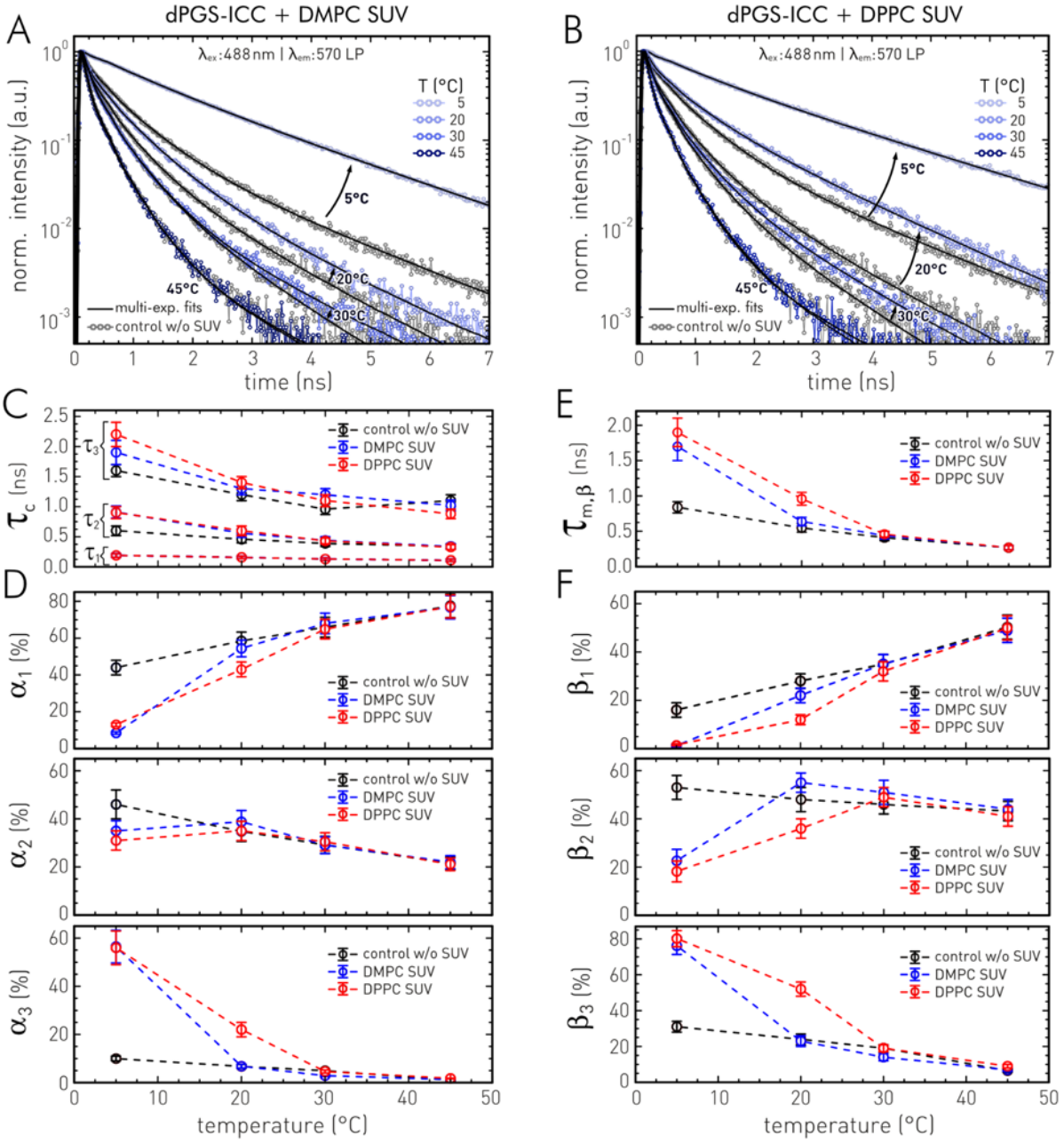

Figure 4.3.6: Differences in fluorescence decay characteristics of dPGS-ICC interacting with DMPC and DPPC lipids. **A/B:** Fluorescence decay traces of 0.1 µM dPGS-ICC interacting with DMPC (A) and DPPC (B) SUVs dissolved in sodium phosphate buffer (pH 7) at 5, 20, 30, and 40 °C. Lipid concentration amounts to 4 mM. Multi-exponential fits are shown as black solid line. Gray connected dots indicated dPGS-ICC fluorescence decay traces without interaction. **C** Temperature dependent fluorescence decay components of dPGS-ICC (black), and dPGS-ICC interacting with DMPC SUVs (blue) or DPPC SUVs (red). **D** Relative decay amplitudes of dPGS-ICC (black), and dPGS-ICC interacting with DMPC SUVs (blue) or DPPC SUVs (red) as function of temperature. **E** Respective mean fluorescence lifetime as function of temperature. **F** Relative steady-state fluorescence contributions β_c of dPGS-ICC (black), and dPGS-ICC interacting with DMPC SUVs (blue) or DPPC SUVs (red) as function of temperature. Experimental conditions: TCSPC-cuvette setup (Section 3.3.3), spectral parameters are indicated in A and D. Indicated uncertainties are based on relative precision, see Table 3.4.1.

But first I will stay with the dPGS-ICC – SUVs interaction. There are two important prerequisites for a robust assignment of the fluorescence lifetime of a molecular rotor probe to the viscosity of its environment. First, it must be ensured that all rotors measure the same environment. Therefore, the ratio of dPGS-ICC to lipid must be in the saturation range of the binding process. This ensures that only few dPGS-ICC molecules are free in the solution and report the viscosity of the surrounding water. The second prerequisite is a fluorescence lifetime – viscosity calibration. I apply a temperature-resolved calibration using different sucrose/water mixtures of a defined viscosity. This calibration function was determined by Katja Ober (Prof. Alexiev's group, Freie Universität Berlin, Germany).[88] Figure 4.3.7A shows the correspondent viscosity dependent behavior of the mean dPGS-ICC fluorescence lifetime and a global fit of all data points to Eq. 34. The extracted temperature-resolved calibration curves are additionally displayed in Figure 4.3.7B.

To establish dPGS-ICC as analytical nanoparticles in spatially resolved FLIM experiments, I exemplarily investigate DMPC-based multilamellar vesicles (MLVs) with a size of about 1 µm (Figure 4.3.7C). The general advantage of fluorescence microscopic investigations over pure fluorescence ensemble spectroscopy is that the background fluorescence of unbound dPGS-ICC (if present) can be spatially distinguished form dPGS-ICC interacting with the MLV structures using the spatial fluorescence lifetime information. This discrimination is well illustrated in Ref. 88.

In a next step, I will demonstrate how temperature affects the nano-viscosities of DMPC MLVs. For this purpose, I, in cooperation with Johannes Stellmacher (Prof. Alexiev's group, Freie Universität Berlin, Germany), recorded a temperature series (5 – 45 °C) of dPGS-ICC interacting with DMPC MLVs using confocal FLIM (see Sec. 3.2.1). The fluorescence lifetime information was extracted from FLIM images to determine the DMPC membrane viscosity using the temperature-resolved viscosity calibration curves (Figure 4.3.7B). This method yields an apparent viscosity between 40 and 1,000 cP for membrane-interacting dPGS-ICC. The obtained course of the temperature-viscosity dependence is presented as an Arrhenius plot in Figure 4.3.7D. For temperatures above the main phase transition (24 °C), a linear dependence of the apparent membrane viscosity is observed. In contrast to this homogeneous distribution, there was a great heterogeneity in membrane viscosities below 24 °C, which fluctuated strongly over the entire measuring range. Using the calibration (Figure 4.3.7B), apparent viscosity values between 40 and 92 cP were determined in the liquid disordered lipid phase and values up to 1000 cP (5 °C) in the gel phase (Table 4.3.2). These values are in good agreement with recent FLIM-based bodipy molecular rotor experiments.[313]

The FLIM-based viscosity data are also well comparable with a high viscosity regime determined with trans-stilbene. These experiments reveled apparent viscosity values of 250 cP above and 1700 cP below the phase transition.[314] The authors describe that the fraction of the high viscosity environment decreases rapidly until the main phase transition temperature is reached and then takes on an almost constant value.[314] A co-existence of different viscous nanoenvironments within the lipid bilayer membranes could lead to the observed large variations in DMPC MLV viscosities below the

phase transition (Figure 4.3.7D) and can be interpreted as membrane heterogeneities. The constantly low fraction of the highly viscous environment above the phase transition also agrees well with the perfect linear dependence one observes in this temperature range (Figure 4.3.7D). Table 4.3.2 compares the apparent DMPC viscosity values for MLVs observed here with literature values from fluorescence lifetime measurements with the molecular rotors bodipy[313] and trans-stilbene[314].

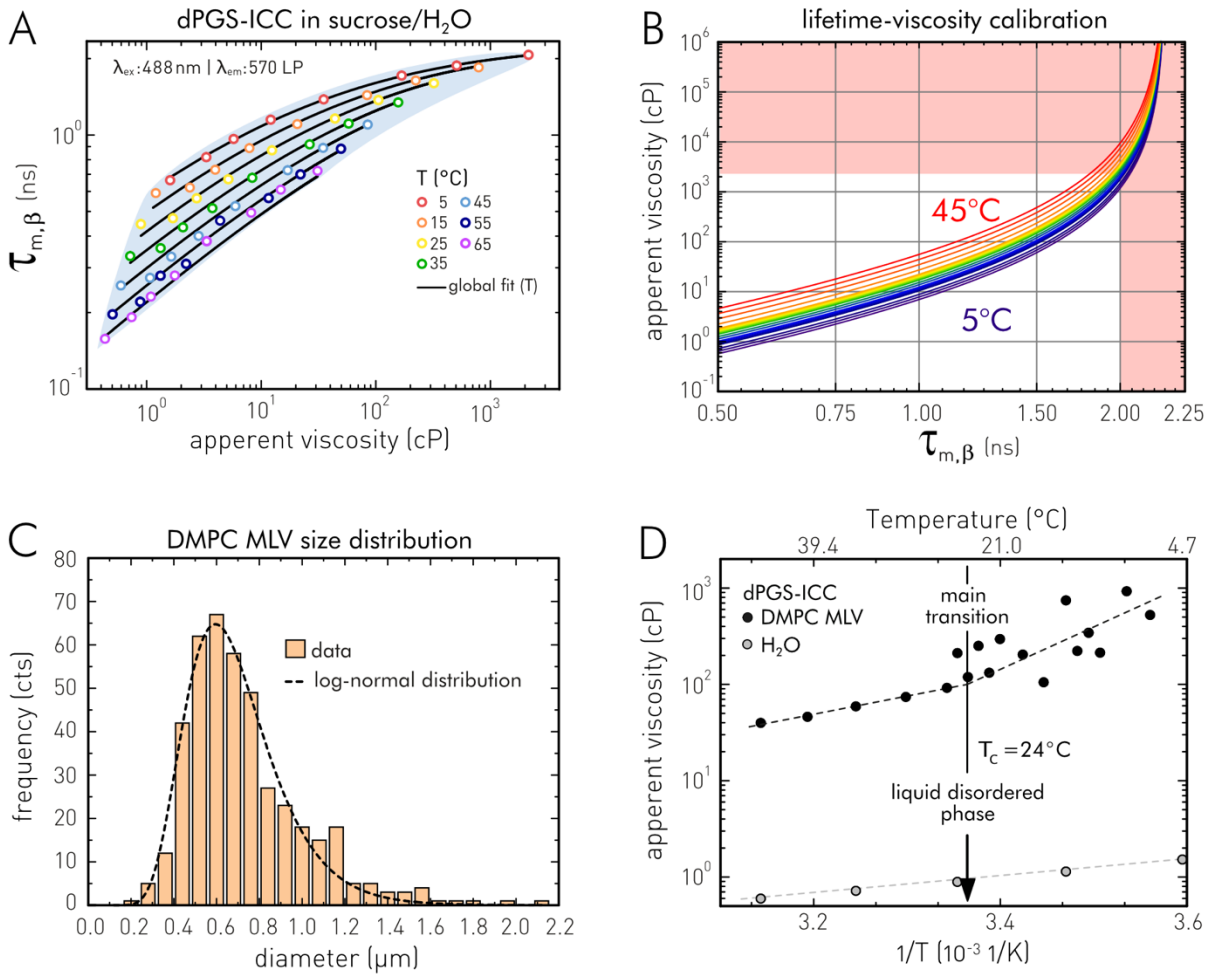

Figure 4.3.7: FLIM investigation of dPGS-ICC interacting with DMPC based multilamellar vesicles (MLV). Data shown were recorded and analyzed in cooperation with Johannes Stellmacher and Katja Ober (both from Prof. Alexiev's group, Freie Universität Berlin, Germany). **A** Förster–Hoffmann plots of dPGS-ICC as a function of viscosity obtained by different sucrose/H_2O mixtures and temperatures changes (data originating from Ref. 88, recorded and analyzed by Katja Ober). **B** Viscosity calibration based on temperature-resolved global fit of data shown in A to Eq. 34, red areas (> 2 ns, > 2000 cP) indicating extrapolated data. **C** Size distribution of the investigated DMPC MLVs. **D** Arrhenius plot of apparent DMPC membrane viscosity (solid black circles) calculated (B, calibration) from the mean fluorescence lifetime of dPGS-ICC interacting with the MLV lipids (green-colored areas in C). The main phase transition (T_c = 24 °C) of the liquid disordered phase is indicated. Viscosities of dPGS-ICC in aqueous solution are displayed for comparison by gray solid circles. Figures shown are reprints from Ober et al.[92], Copyright 2019, with the kind permission of Langmuir.

Table 4.3.2: Membrane viscosities in the gel phase and the liquid-disordered phase of DMPC vesicles determined using the fluorescence lifetime of the molecular rotor dPGS-ICC. For Comparison viscosity values determined by fluorescence lifetime experiments with a molecular rotor of the bodipy group[313] and trans-stilbene[314] are given. Table is a reprint from Ref. 88.

	dPGS-ICC		**bodipy rotor**		**trans-stilbene**	
lipid phase	*viscosity (cP)*	*temp. (°C)*	*viscosity (cP)*	*temp. (°C)*	*viscosity (cP)*	*temp. (°C)*
gel	92 – 1,000	24 – 5	230 – 280*	24 – 21	10 – 57 (fast) & 800 – 1700 (slow)	24 – 9
liquid-disordered	40 – 92	45 – 24	25 – 230*	71 – 24	1 – 10 (fast) & 250 – 800 (slow)	51 – 24

* values are estimated from data points and fit curve in Figure 4 from Ref. 313.

dPGS-ICC interactions with another dendritic nanoparticle

After having shown dPGS-ICC's strong interaction with lipidic systems in a temperature below the lipidic phase transition temperature, this section will investigate the interaction with artificial liposome mimicking dendritic nanoparticle of a core-multishell (CMS) type. Like the lipidic vesicle systems of the last section, CMS-NPs represent a macromolecular system that undergoes a temperature-dependent phase transition. The investigated dendritic polymer consists of a hyperbranched polyglycerol core surrounded by double-layered shells with a hydrophobic (octadecanoic diacid) and a hydrophilic monomethyl polyethylene glycol layer. This CMS architecture mimics the structure of a liposome with a diameter of 7 – 15 nm and shows a phase transition at 31– 32 °C.[258] The data shown below were first published in Langmuir (Ober et al., Ref. 88). Hence, the next paragraph relies on my contributions to this paper.

In a first experiment, I investigated the binding affinity of dPGS-ICC to CMS-NP via changes in the fluorescence decays. Figure 4.3.8A shows the fluorescence decay traces of 0.1 µM dPGS-ICC interacting with CMS-NP at different concentrations. The plot clearly shows how the fluorescence decay of dPGS-ICC slows down with increasing concentration, i.e., with higher probability of molecular interaction between the two nanoparticles. With a higher interaction rate, the steric restrictions of the fluorescent molecular rotor probe ICC are gradually increased so that an effective depopulation of the S_1 state via this non-radiative path decreases. Conversely, an increased depopulation via fluorescence occurs, resulting in a longer observed fluorescence lifetime. This process saturates for high CMS-NP concentrations.

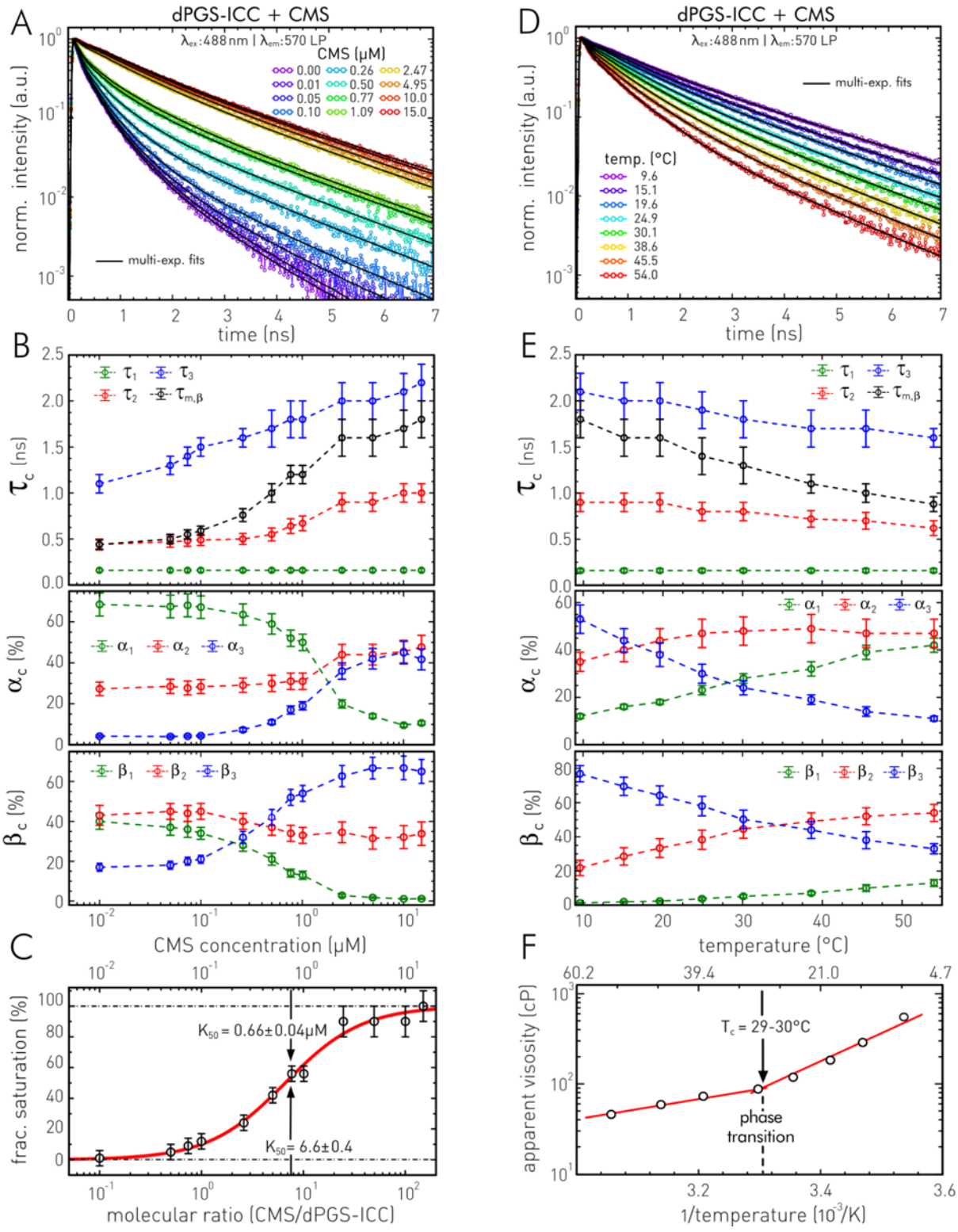

Figure 4.3.8: dPGS-ICC interaction with CMS nanoparticles (CMS-NP). **A** fluorescence decay traces of 0.1 μM dPGS-ICC in solutions of varying CMS-NP concentration (rainbow colors), black solid lines display multi-exponential fits. T = 20 °C. **B** Fit results (see Table A12). Top: dPGS-ICC's decay components and mean fluorescence lifetime. Center: Relative decay amplitudes. Bottom: Relative steady-state fluorescence contributions β_c versus CMS-NP concentration. **C** Fractional saturation (Eq. 57) of dPGS-ICC – CMS-NP binding and fit to a Hill model (Eq. 58). K_{50} amounts to 0.66 ± 0.04 μM (≙ 6.6 ± 4 CMS/dPGS-ICC molecules), g = 1.2±0.1. **D** fluorescence decay traces of 0.1 μM dPGS-ICC in a solution of 2.5 μM CMS-NP as function of temperature (rainbow colors), black solid lines display multi-exponential fits. **E** Fit results (see Table A13). Top: dPGS-ICC's decay components and mean fluorescence lifetime. Center: Relative decay amplitudes. Bottom: Relative steady-state fluorescence contributions β_c versus temperature. **F** Arrhenius plot of apparent viscosities calculated by the fluorescence lifetimes – viscosity calibration from Figure 4.3.7B and the mean

fluorescence lifetime values of E. Experimental conditions: TCSPC-cuvette setup (Section 3.3.3), spectral parameters are indicated in A and D. Indicated uncertainties are based on relative precision, see Table 3.4.1.

To investigate this behavior in detail, I performed a fluorescence decay analysis (see Sec. 3.4.1) by fitting the fluorescence decays (Figure 4.3.8A) to a tri-exponential decay model (see Appendix, Table A12). Figure 4.3.8B shows in its upper segment the determined decay components τ_c as a function of CMS concentration. While the fastest decay component (τ_1 = 0.16 ± 0.02 ns) remains constant over the entire concentration range of CMS-NP, the second and third decay component increases from 0.44 ± 0.06 ns to 1.0 ± 0.1 ns and from 1.1 ± 0.1 ns to 2.2 ± 0.2 ns, respectively. The corresponding decay amplitudes (α_c) shown in the middle segment of Figure 4.3.8B change accordingly as follows: While α_1 decreases with higher CMS concentrations from 69 ± 6% to 10.6 ± 0.9 %, the amplitudes α_2 and α_3 increase from 27 ± 3% to 48 ± 6 % and from 4.2 ± 0.2 % to 42 ± 5 %, respectively. To study the relative population of the individual fluorescence species, the relative-steady state contributions β_c of the three decay components were calculated. The results are shown in the lower segment of Figure 4.3.8B. This graph clearly shows that the largest increase occurs in the third component, with a plus of over 380 % (17 ± 2 % to 65 ± 6 %). In contrast, the population of the second component decreases only sparsely (43 ± 5 % to 34± 6 %), while the first component vanishes almost completely at high CMS-NP concentrations (40 ± 4 % to 1.2 ± 0.3 %).

If the fastest component represents the dPGS-attached ICC molecules with minimum steric restriction, the course of β_1 can be interpreted as an indicator of the reduction of rotational freedom with higher CMS interaction probability. This behavior is mirrored by β_3, which represents the increase in steric restriction. Here, however, two effects overlap: The percental increase in the number of sterically restricted ICC molecules is accompanied by slower fluorescence lifetimes of ICC due to the stronger steric restriction. Second, the intermediate decay component τ_2 may represents changes in the polarity of the ICC probe upon dPGS-ICC – CMS-NP interaction. The corresponding parameter β_2 displays only small changes over the concentration range of CMS-NP. This shows that the strongest effects originate from the steric restriction to the intramolecular rotation.

Next, a simple model is applied, which indirectly considers the fluorescence lifetime information as a measure of binding affinity. It is assumed that the calculated mean fluorescence lifetime $\tau_{m,\beta}$, or more precisely the change in mean fluorescence lifetime due to the binding interaction is directly proportional to the concentration of CMS molecules (Figure 4.3.8C). For simplicity, it is assumed that dPGS-ICC exists in only two states, the binding and the free state. It is further assumed that both states have their own distinguishable characteristic fluorescence lifetime and the difference in $\tau_{m,\beta}$ at 15 µM CMS-NP to 0 µM CMS-NP constitutes the value of maximum saturation of the binding reaction. In order to determine the binding affinity, a fractional saturation value in percent calculated via Eq. 57 (differences in $\tau_{m,\beta}$) are plotted against the concentration of the CMS molecules and subsequently fitted to a Hill function (Eq. 58). The model fit showed an apparent binding affinity K_{50} of

0.66 ± 0.04 µM of CMS molecules (Figure 4.3.8C). This corresponds to a K_{50} value of 6.6 ± 0.4 CMS molecules per dPGS-ICC molecule (C = 0.1 µM, Figure 4.3.8C). Furthermore, the fit yielded a cooperation factor of 1.2 ± 0.1, which corresponds to noncooperative binding. This means that the binding affinity of dPGS-NP to the CMS-NP is not dependent on whether or not other CMS-NP have bound to dPGS-NP.

After observing a high affinity between dPGS and CMS-NP, I performed a second experiment on a previously observed[258] phase transition of the CMS-NP caused by its polymeric branch flexibility. For this purpose, dPGS-ICC was added to a CMS nanoparticle solution with a concentration of 2.5 µM, well above the observed K_{50} value. Figure 4.3.8D shows the fluorescence decay traces of a nanoparticle mixture at varying temperatures, starting well below the phase transition temperature around 31 – 32 °C.[258] The plot indicates that the fluorescence decay of dPGS-ICC interacting with CMS-NP becomes faster with higher temperatures. This indicates that the steric restrictions of the fluorescent molecular rotor probe ICC increase due to temperature-dependent changes in the CMS structure. These effects on the fluorescence decays are much stronger than the temperature dependent changes observed for dPGS-ICC alone (compare Figure 4.3.8F) and must be addressed to changes in the dPGS-ICC – CMS-NP interaction.

A subsequently performed fluorescence decay analysis (Figure 4.3.8E) by fitting the fluorescence decays to a tri-exponential decay model (see Appendix, Table A13) indicates in which way the individual decay components are responsible for the reduction in the fluorescence lifetime with increasing temperatures. While the fastest decay component (τ_1 = 0.16 ± 0.02 ns) remains constant over the entire temperature range, the second and third decay components decrease from 0.9 ± 0.1 ns to 0.62 ± 0.02 ns and from 2.1 ± 0.2 ns to 1.6 ± 0.01 ns, respectively. The corresponding decay amplitudes (α_c) shown in the middle segment of Figure 4.3.8E change accordingly as follows: While α_1 and α_2 increase with higher temperature from 12 ± 1 % to 42 ± 3 % and from 35 ± 4 % to 47 ± 6 %, respectively, α_3 decreases from 53 ± 6 % to 11 ± 1 %. To study the relative population of the individual fluorescence species, the relative-steady state contributions β_c of the three decay components are calculated and presented in the lower segment of Figure 4.3.8D. The main contributors to the observed fluorescence lifetime reduction with increasing temperature are τ_2 and . While the population of the second component β_2 rises by a factor of 2.5 from 21 ± 5 % to 54 ± 5 %, β_3 is reduced by a factor of 2.3 from 77 ± 5 % to 33 ± 3 %. These numbers indicate a change in the ICC environment due to a changed CMS-NP state before and after the phase transition. This modified environment seems to be more polar, causing less restrictions to ICC's molecular rotation. The population of the first component increases only up to 13 ± 2 % with for temperatures above the phase transition temperature. This indicates that despite higher temperature and CMS phase transition, dPGS-ICC does not separate from the CMS-NP.

In a next step, I used the fluorescence lifetime – viscosity calibration of Figure 4.3.7B to determine the apparent nanoviscosity of the CMS-NP solution using the mean fluorescence lifetimes according

to Ref. 88. The respective nanoviscosities range between 45 and 550 cP, depending on temperature. Figure 4.3.9F displays the calculated viscosity values in the form of an Arrhenius plot. The sudden change in the temperature-induced viscosity gradient (red lines) indicates a molecular phase transition temperature of CMS-NP between 29 – 30 °C. These results are well in agreement with the previously published values determined by fluorescence anisotropy experiments.[258] To my knowledge, it is the first time that nanoviscosities of a CMS–NC were determined.

dPGS-ICC/IDCC cleavage

Finally, I investigated a modified dPGS nanoparticle, which is converted into a nanocarrier by conjugating a disulfide linker system to its surface. This cleavable linker can be used to attach different potential drugs or drug mimetics to the nanoparticle. The dPGS nanocarrier system was developed and synthesized by Nadine Rades (Haag group, Freie Universität Berlin, Germany).[200]

Here, I investigate a variant fluorescently labeled with two different FMR sensors. The first one, ICC, is attached covalently to the dPGS surface like in the previous experiments. The second one, IDCC, is attached via the disulfide linker. The probe design is intended to allow fluorescence microscopic observations of potential cell uptake and fate of the dPGS nanocarrier and at the same time to locate the cellular sites where IDCC, acting as a drug mimetic, is released. The resulting nanocarrier conjugate is termed dPGS-ICC/(-SS-IDCC). A scheme of its structure is shown in Figure 4.3.9A.

The spectral differences in the excitation and emission bands of both cyanines allow the use of the nanocarrier test system in fluorescence microscopic approaches like cellular co-localization studies. Figure 4.3.9B shows that with suitable excitation bands and fluorescence emission filters, both fluorophores can be easily spectrally separated.

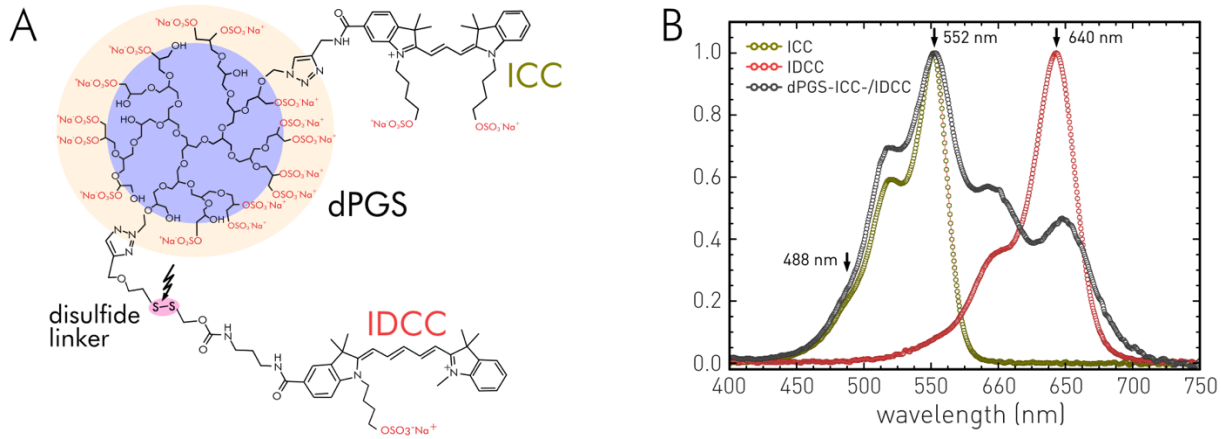

Figure 4.3.9: Disulfide-cleavable dPGS-ICC/(-SS-IDCC) nanocarrier obtained from Porf. Haag's group (Freie Universität Berlin, Germany). **A** Scheme of dPGS-ICC/(-SS-IDCC): the dendritic polyglycerol sulfate nanoparticle is equipped with the fluorescent molecular rotor tag ICC and cleavable IDCC fluorophore (disulfide-linker). **B** Absorption and fluorescence emission spectra of ICC, IDCC and dPGS-ICC/(-SS-IDCC).

The aim of my study is to investigate the extent to which the time-resolved fluorescence properties of the double-labeled dPGS polymer can be used to determine location, interaction and cleavage of the triggerable nanocarrier system in FLIM experiments. For that purpose, the time-resolved decay behavior of intact and cleaved dPGS-ICC/(-SS-IDCC) in solution was characterized in FLIM experiments using two spectral channels (IDCC-CH: λ_{ex} = 640 nm, λ_{em} > 650 nm, ICC-CH: λ_{ex} = 530 nm, λ_{em} > 545 – 600 nm, Figure 4.3.10). The cleavage of the disulfide bond was chemically induced by incubating the nanoparticle with dithiothreitol (DTT, 30 nM) and ethylenediaminetetraacetic acid (EDTA, 2 nM) for 2 days at 37°C.

Figure 4.3.10A compares FLIM images of the spectral IDCC channel showing dPGS-ICC/(-SS-IDCC) in its uncleaved and cleaved state to FLIM images of free IDCC. The FLIM images were analyzed by the tau-plot approach (Section 3.4.2) using a bi-exponential decay model. The resulting false-color FLIM images were parameterized by the mean fluorescence lifetime (Eq. 20), which ranges between 0.4 and 1.0 ns. The shown fluorescence lifetime distributions of all three samples (Figure 4.3.10, bottom) clearly show that the fluorescence decay characteristics of IDCC change drastically (0.8 ± 0.2 ns to 0.45 ± 0.01 ns) upon induced IDCC cleavage. The new fluorescence lifetime signature is very similar to free IDCC in solution (0.49 ± 0.01 ns). Individual decay traces of the three samples are shown in Figure 4.3.10B. From this strong change in the fluorescence decay of the dPGS conjugate, it can be concluded that it is possible to monitor the cleavage based on the fluorescence lifetime changes of IDCC. This conclusion can be theoretically supported by the following measures: As soon as the FMR IDCC is released from the disulfide linker, it can rotate intramolecularly with reduced or without external interference. This leads to faster fluorescence lifetimes.

The effect of IDCC cleavage on the dPGS-ICC-/ fluorescence characteristics in the spectral ICC channel is demonstrated in the tau-plot FLIM images shown in Figure 4.3.10C. Here, only a minimal change in dPGS-ICC-/'s fluorescence lifetime can be observed upon IDCC cleavage. Interestingly enough, the dPGS-ICC-/ has a different fluorescence decay signature than the standard dPGS-ICC, having no disulfide linker attached. This could indicate that the rotations of some ICC FMRs are hindered by neighboring disulfide linkers or linker fragments on the dPGS surface.

In principle, ICC and IDCC are an excellent FRET pair. This energy transfer could theoretically have an influence on the fluorescence lifetime of ICC (donor), especially with the small distances on the dPGS surface. However, due to the low labeling stoichiometry of 0.16 (IDCC) and 0.18 (ICC) molecules per dPGS nanoparticle, only 3% of dPGS conjugates will be equipped with both FMRs simultaneously. Therefore, the influence of FRET on the fluorescence lifetime is negligible.

Additional to the reduction in the fluorescence lifetime of IDCC, I observed increasing fluorescence intensities after the IDCC cleavage (Figure 4.3.10E,F). This indicates additional fluorescence quenching effects by the conjugation of IDCC to dPGS. The intensity increase upon cleavage is about a

factor of 4 to 5. Also, in the ICC channel, an increase in the fluorescence intensity was observed after the cleavage of IDCC.

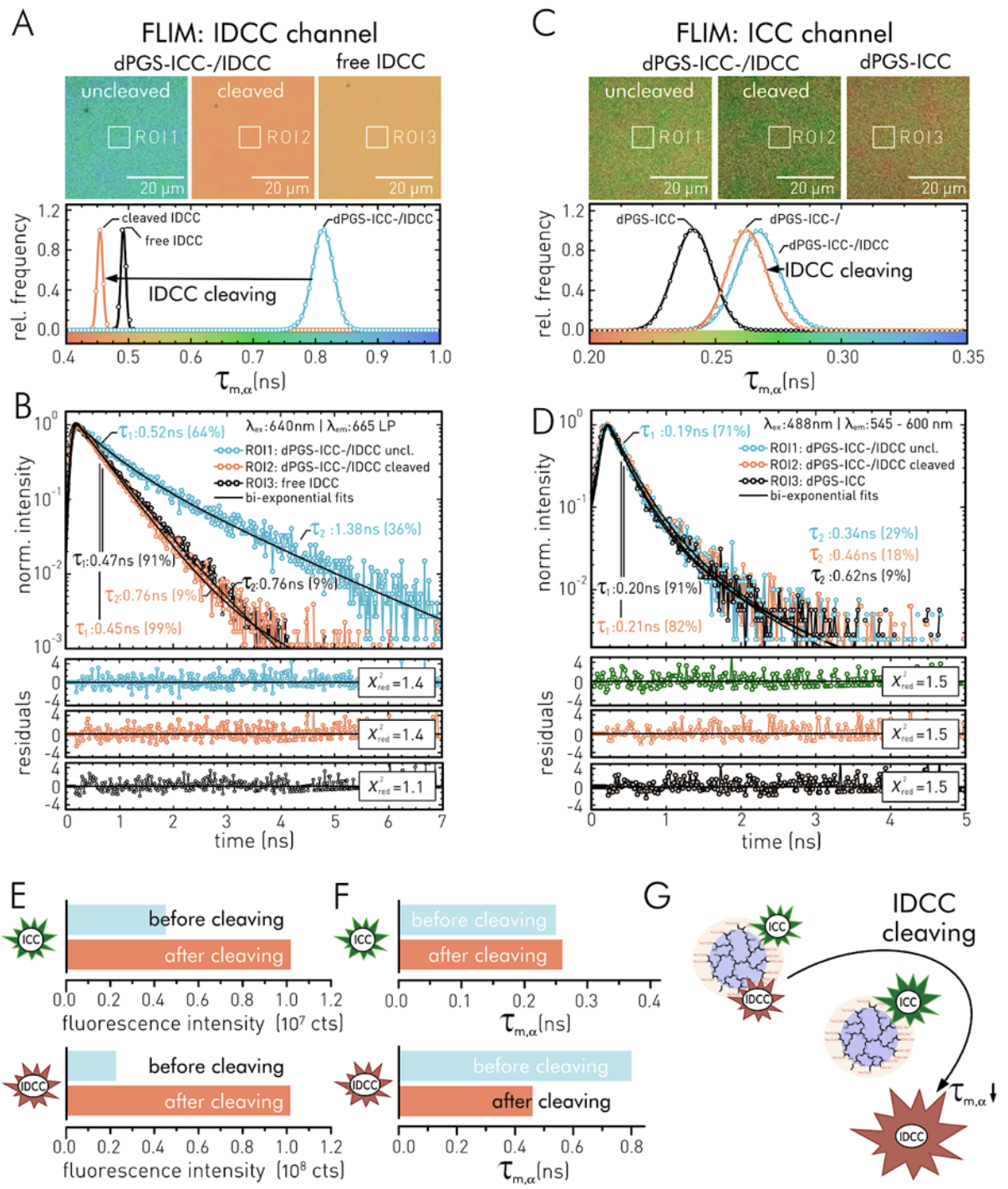

Figure 4.3.10: Monitoring disulfide-based cleavage of dPGS-ICC/(-SS-IDCC) by changes in IDCC's fluorescence lifetime characteristics. **A** dPGS-ICC/(-SS-IDCC) and IDCC in solution subjected to FLIM (IDCC channel). Top: Tau-plot FLIM images of dPGS-ICC/(-SS-IDCC) in solution (uncleaved, cleaved (DTT)) and of free IDCC. Bottom: Mean fluorescence lifetime distributions of the three compared samples. **B** Fluorescence decay traces present in the ROIs shown in A. **C** dPGS-ICC/(-SS-IDCC) and dPGS-ICC subjected to FLIM (channel). Top: Tau-plot FLIM images of dPGS-ICC/(-SS-IDCC) in solution (uncleaved, cleaved (DTT)) and of dPGS-ICC. Bottom: Mean fluorescence lifetime distributions of the three compared samples. **D** Fluorescence decay traces present in the ROIs shown in A. **E** Comparison of fluorescence intensity increase in both spectral channels before and after cleaving. **F** Comparison of mean fluorescence lifetime change in both spectral channels before and after cleaving. **G** Illustration: effects on fluorescence characteristics of dPGS-ICC/(-SS-IDCC) by IDCC cleaving.

The observed fluorescence decay characteristics promote the dual FMR equipped dPGS nanocarrier system for the use in cellular uptake experiments. The specific fluorescence lifetime features together with the fluorescence intensity enhancements after cleavage of the disulfide linker may allow to investigate in which cellular site an incorporated dPGS nanocarrier will release its cargo molecules. Moreover, it might even be possible to identify the positions of the triggered dPGS-ICC molecules via their altered fluorescence lifetime signatures at the same time.

4.3.2 Dendritic core multi-shell (CMS) nanocarrier

Fluorescence decay characterization of CMS-ICC

The fluorescence decay characteristics of CMS-ICC were first described by Alexiev and colleagues (Boreham et al., 2014, Ref. 258). The authors found changes in ICC's fluorescence lifetime upon conjugation with the CMS nanocarrier at its hyperbranched polyglycerol core. The CMS-ICC nanocarriers examined by the authors were obtained by the same source (Prof. Haag's group, Freie Universität Berlin, Germany) as the investigated nanocarriers in this thesis. The authors observed a characteristic fluorescence decay behavior of CMS-ICC in aqueous solutions, which was best described by three fluorescence decay components (τ_i (α_i), Eq. 19) of 0.16 ns (60 %), 0.5 ns (32 %), and 1.4 ns (8 %).[258]

The experiments of the following section investigating the CMS-ICC fluorescence decay characteristics were performed on suspensions of different lyophilized CMS-ICC stocks. To estimate the experimental precision of the determined fluorescence decay components and to compare my results to the earlier experiments mentioned above, I visualized the decay parameters obtained from CMS-ICC samples over a period of 3 years (Figure 4.3.11). All samples showed a fluorescence decay characteristic best fitted by a tri-exponential model function (Eq. 19, compare Figure 4.2.1/ 4.2.2). The values obtained are compatible with the results from Ref. 258 (see Table 4.3.3). The relative precision between the individual experiments vary between 3 % for slow (τ_3) and 7 % for the fast (τ_1) decay component. The corresponding decay amplitudes fluctuate between 5 % (α_1) and 18 % (α_3). A similar picture emerges for the calculated relative steady state fluorescence contributions and mean fluorescence lifetime (Figure 4.3.11A,C). The experimental precision has its origin in superimposed processes like the general sample handling, the suspension process of the lyophilized CMS-nanocarrier stock, the different CMS-ICC synthesis, the measurement uncertainties of the TCSPC-cuvette setup and the corresponding uncertainty of the decay analysis.

Table 4.3.3: Precision and fits accuracy in time-resolved fluorescence experiments of CMS-ICC. Tri-exponential decay fitting of seven independent time-resolved fluorescence experiments result in the indicated mean values of the individually determined fit parameters. The respective standard deviation is used as a measure of the general experimental precision (see Figure 4.3.11). Mean and standard deviation of the absolute and relative fit accuracy are determined by seven single confidence interval analyses (Section 3.4.1) of fluorescence decay traces from seven individual experiments.

fit parameter	mean	precision		fit accuracy	
		absolute	*relative*	*absolute*	*relative**
τ_1	0.14 ns	0.01 ns	7 %	0.005 ± 0.001ns	3.6 ± 0.7 %
τ_2	0.57 ns	0.02 ns	4 %	0.022 ± 0.008 ns	4 ± 1 %
τ_3	1.35 ns	0.04 ns	3 %	0.033 ± 0.007 ns	2.4 ± 0.5 %
α_1	56 %	3 %	5 %	1.0 ± 0.3 %	1.8 ± 0.5 %
α_2	33 %	2 %	6 %	0.9 ± 0.3 %	2.7 ± 0.9 %
α_3	11 %	2 %	18 %	0.8 ± 0.3 %	7 ± 3 %

* relative values refer to the given mean.

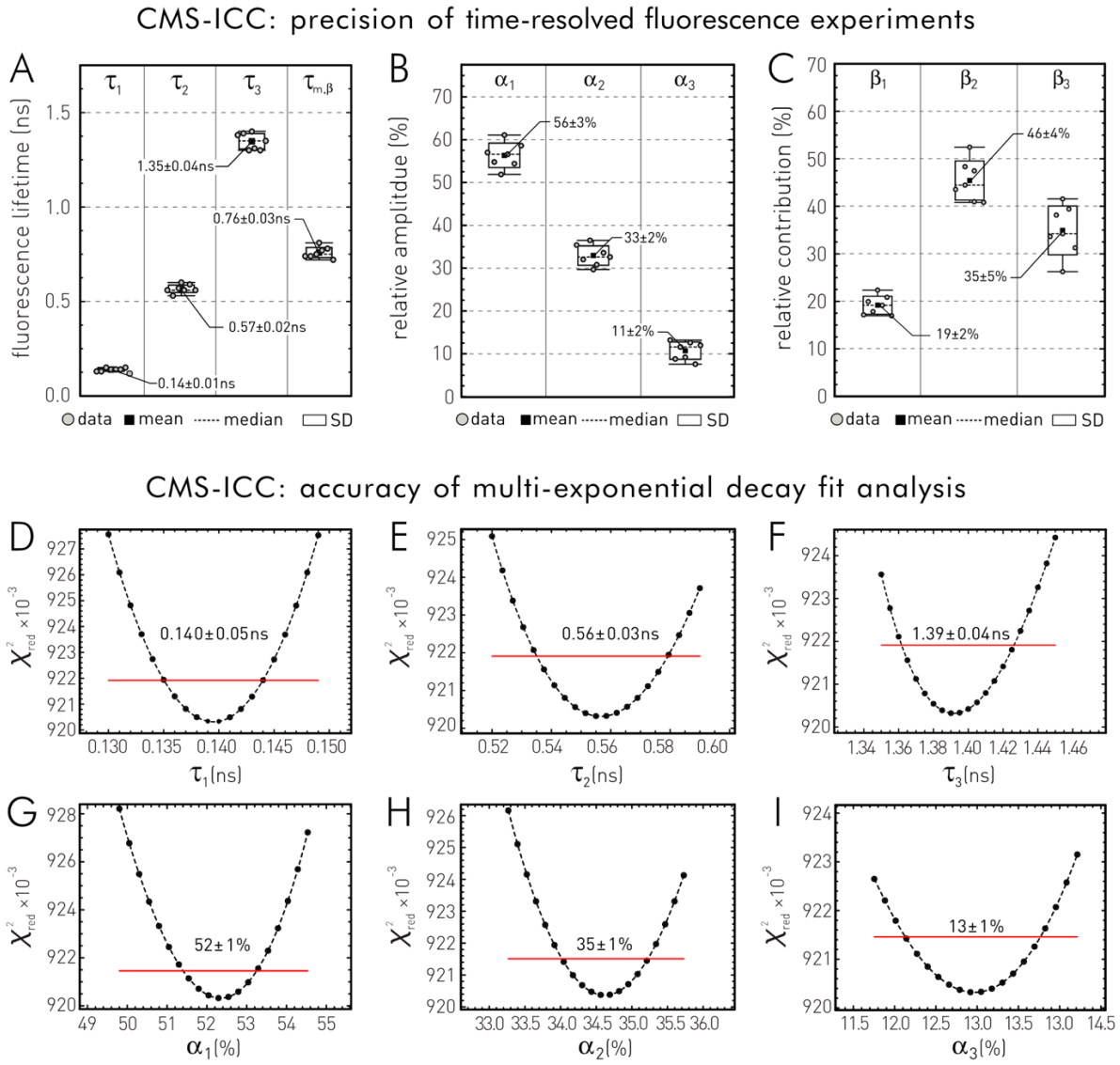

Figure 4.3.11: Precision and fit accuracy in the fluorescence decays measurements of CMS-ICC. Tri-exponential decay fitting of seven different TCSPC experiments on CMS-ICC in aqueous solutions originating from the same polymer syntheses but different production batches are compared. The experiments were conducted over a period of 3 years. **A** Fluorescence decay components and mean fluorescence lifetime. **B** Relative decay amplitudes. **C** Relative steady-state fluorescence contributions. Box plots show the individual fitting parameters as gray dots. **D-I** Exemplary determination of the accuracy of fit-parameters obtained by a confidence interval analysis according to Section 3.4.1. Black squares indicate the respective mean and the dashed black lines the median. The Box visualizes the standard deviation (SD). Whiskers show minimal and maximal values. Experimental conditions: TCSPC-cuvette setup (Section 3.3.3), T=20 °C, λ_{ex} = 488 nm, λ_{em} > 570 nm.

The uncertainty of the decay analyses was estimated by confidence interval analyses of the individual fit parameters according to Section 3.4.1. I applied this approach to the data files of seven CMS-ICC decay traces of seven independent experiments and calculated mean and standard deviation of this data set in order to assess the general fit uncertainties of the experiments. Table 4.3.3 compares them to the general experimental precision according to Figure 4.3.11. The displayed values should serve as a general measure for the accuracy of the decay fit analysis of CMS-ICC's time-resolved fluorescence behavior. The relative accuracy range between 2.4 ± 0.5 % for the slow (τ_3) and 4 ± 1 % for the intermediate (τ_2) decay component. The respective decay amplitudes vary

between 1.8 ± 0.5 % (α_1) and 7 ± 3 % (α_3). Similar relative fit accuracies in fluorescence decay analyses were observed for the dPGS-ICC sample (Section 4.3.1). Since the precision of the experiments is generally lower than the fit accuracy of the fit analysis, the relative precision is used in the following analyses as a measure for the experimental uncertainty of the individual fluorescence decay analyses.

CMS-ICC interactions with BSA

When macromolecular materials enter the bloodstream, absorption of proteins[280-281] can take place on their surfaces. In section 4.3.2, I describe this protein-corona effect in detail, which is mainly caused by *serum albumin* from the blood. Since the protein corona determines the further interaction in the organism, absorbed proteins on nanoparticle surfaces can change the recognizability or invisibility for certain cells (stealth effect).[281-282]

After investigating the interactions of the hyperbranched dPGS-ICC nanoparticles with HS and BSA in the previous section, I now repeat the fluorescence lifetime-based investigations with dendritic core multishell-nanocarriers (CMS-NC), using the same FMR probe ICC covalently attached to the hyperbranched polyglycerol core of the CMS-NC. I monitor the BSA binding affinity of CMS-ICC again by the fluorescence decays behavior of ICC. Figure 4.3.12A shows the respective fluorescence decay traces of 0.1 µM CMS-ICC interacting with BSA at different concentrations. The decay traces indicate that the fluorescence decay of CMS-ICC slows down with increasing BSA concentration, i.e., with higher probability of molecular interaction between both molecules. This process saturates for high BSA concentrations.

To compare the observed fluorescence decay behaviors more quantitively, I applied a decay analysis (see Sec. 3.4.1) to the recorded fluorescence decay traces of Figure 4.3.12A using a tri-exponential decay model (see Appendix, Table A14). Figure 4.3.12B shows in its upper segment the determined decay components τ_c as a function of BSA concentration. While the fastest decay component ($\tau_1 \sim 0.16 – 0.23$ ns) remains almost constant over the entire concentration range of BSA, the second and third decay component increases from 0.62 ± 0.02 ns to 1.00 ± 0.04 ns and from 1.46 ± 0.04 ns to 3.3 ± 0.1 ns, respectively. The corresponding decay amplitudes (α_c) shown in the middle segment of Figure 4.3.12B stays practically constant over the entire BSA concentration range: averaged over this range, α_1 shows a mean value of 57 ± 2 %, α_2 of 37 ± 2 %, and α_3 of 6 ± 2 %. To study the relative population of the individual fluorescence species, the relative-steady state contributions β_c of the three decay components were calculated. The results are shown in the lower segment of Figure 4.3.12B. But again, only marginal changes occur due to the BSA interaction. This behavior of CMS-ICC decay components is similar to the ones previous investigated for dPGS-ICC – BSA interactions. However, the concentration dependent progress of the relative amplitude α_c and contributions β_c differs by being constant. The change only occurs in the fluorescence decay components. By applying the fractional saturation method and using a fit to a Hill function (Eq. 58), I

determined apparent binding affinity K_{50} of 400 ± 200 µM BSA (Figure 4.3.12C). This corresponds to a K_{50} value of 4,000 ± 2,000 BSA molecules per CMS-ICC molecule (C = 0.1 µM, Figure 4.3.12C). The affinity of CMS molecules to bind to BSA is thus significantly reduced compared to the dPGS-nanoparticle (see Section 4.3.1). Furthermore, the fit yielded a cooperativity factor of 1.0 ± 0.3, indicating a non-cooperative binding. This means that if a CMS molecule bounds to a BSA protein, the affinity for other CMS – protein interactions are not altered.

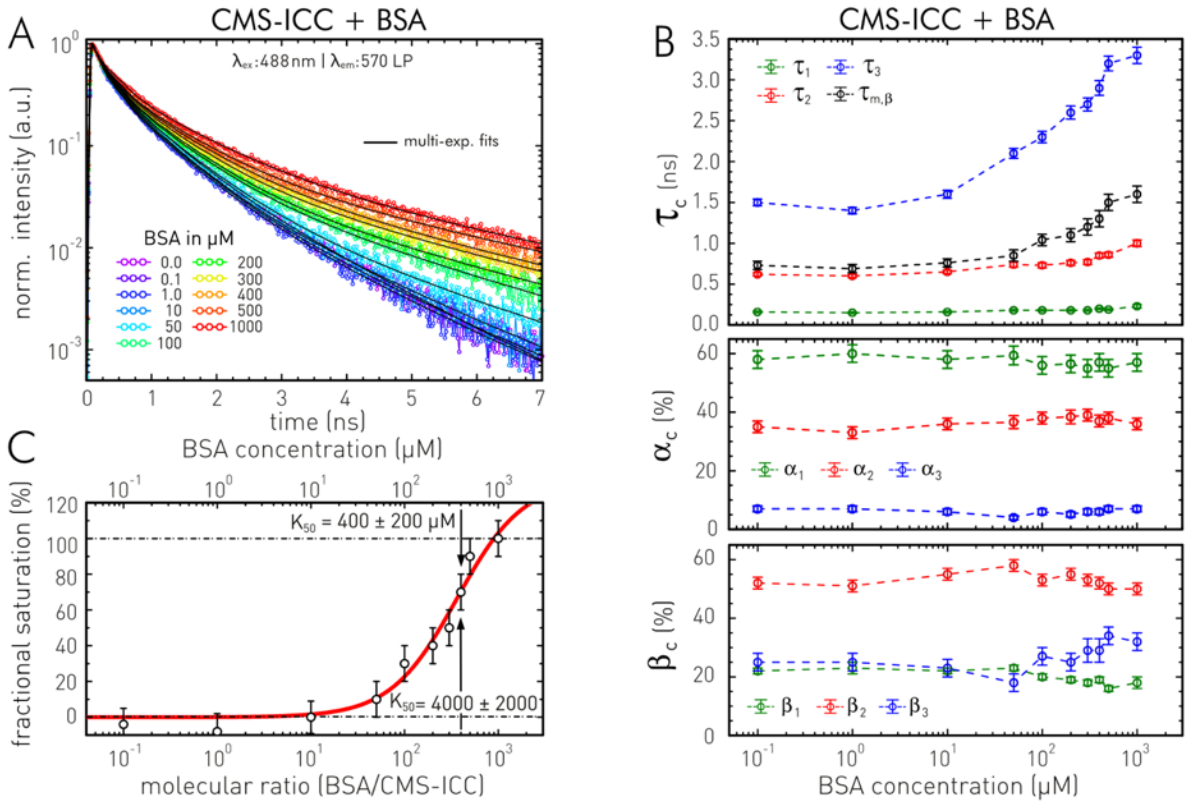

Figure 4.3.12: CMS-ICC interaction with bovine *serum albumin* (BSA). **A** fluorescence decay traces of 0.1 µM CMS-ICC in solutions of varying BSA concentration (rainbow colors), black solid lines display tri-exponential fits. T = 20 °C. **B** Fit results (see Table A14). Top: CMS-ICC's decay components and mean fluorescence lifetime versus BSA concentration (in log scale). Center: Relative decay amplitudes versus BSA concentration (in log scale). Bottom: Relative steady-state fluorescence contributions β_c versus BSA concentration (in log scale). **C** Fractional saturation (Eq. 57) of the binding of CMS-ICC to BSA molecules and fit to a Hill model (Eq. 58). K_{50} amounts to 400 ± 200 µM (≙ 4000 ± 2000 BSA/CMS-ICC molecules), g=1.0 ± 0.3. Experimental conditions: TCSPC-cuvette setup (Section 3.3.3), spectral parameters are indicated in A.

CMS-ICC sensitivity to local viscosity

In this section, the sensitivity of CMS-ICC's fluorescence lifetime to the prevalent local viscosity is investigated. Characterizing this dependency is especially important to the *in vitro* and *ex vivo* investigations of CMS-ICC's interactions with cellular constituents in Section 4.4 and with skin structures in Section 4.5. For these investigations, a reduced sensitivity to ambient viscosity is desirable in order to detect specific molecular or cellular interactions. This is important as intracellular viscosities are inhomogeneous and can change by orders of magnitude.[66] Equally variable is the viscosity of the

stratum corneum, the penetration barrier of the skin, which represents the first interaction layer when CMS-NC is topically applied on skin.[315]

The molecular rotor ICC applied here (see Section 2.1.2) shows a direct correlation of local viscosity and its fluorescence decays (Figure 4.2.3). Section 4.3.1 shows that if ICC is attached to the surface of the dendritic nanoparticle dPGS, its fluorescence decay becomes sensitive to different molecular nanoparticle interactions. Thus, when applying nanoparticle – ICC conjugates in *in vitro* live-cell experiments, fluorescence decay changes of ICC associated with viscosity would overlap with those specific for protein interactions. Here, I show that the attachment site of the fluorescent molecular rotor probe at the nanoparticle is crucial for distinguishing viscosity-based and biomolecular interaction-based changes in ICC's fluorescence lifetime (Figure 4.3.13). In the case of CMS-ICC, the ICC is bound to the hPG core of the CMS nanocarrier. So, it is shielded, to some extent, from the direct environment by the nanocarrier's inner and outer shell.

The general effect of solvent viscosity on CMS-ICC's fluorescence lifetime was investigated using different H_2O/sucrose mixtures of different molecular ratios generating viscosities between 1.01 cP and 1,170 cP.[316] Figure 4.3.13A shows the corresponding fluorescence decay traces of 0.1 µM CMS-ICC which display a viscosity dependency. However, compared to free ICC and dPGS-ICC, stronger changes occur only above 50 % (w/w) sucrose. To further investigate the fluorescence decay behavior (Figure 4.3.13A), I applied a multicomponent decay analysis (see section 3.4.1). For that purpose, CMS-ICC's time-resolved fluorescence traces were fitted to a tri-exponential decay model (see Appendix, Table A15). Figure 4.3.13B shows in its upper two segments the determined decay components τ_c as a function of the solvent viscosity, which was realized as a Förster-Hoffmann plot (Log-Log) and a Log-Lin plot. While the fastest and intermediate decay components change only marginally over the entire viscosity interval (τ_1 = 0.14 – 0.18 ns, τ_2 = 0.56 – 0.68 ns), the third decay component varies between 1.20 ± 0.04 ns and 1.71 ± 0.04 ns. The corresponding relative decay amplitudes (α_c) are shown in the middle segment of Figure 4.3.13B. The relative steady state contributions β_c were calculated to investigate the relative population of the individual fluorescence species. The results are shown in the lower segment of Figure 4.3.13B.

Interestingly enough, the general viscosity dependence of CMS-ICC's decay amplitudes and populations is more complex and less intense than for the surface-labelled dPGS-ICC. The complex viscosity dependency might indicate that the different solvent viscosities lead to conformational changes within the CMS-nanoparticle, with its flexible shells of octadecanoic acid and mPEG. In the viscosity range below 30 cP, the amplitudes and populations of the third decay component stay stable. Simultaneously, both parameters decease in the first decay component on cost of the second component in this viscosity range. Above 30 cP, another process sets in, leading to a decrease in amplitude and population of the second decay component and an increase in both parameters of the third component. The resulting oscillation pattern of the amplitudes was never observed for the free ICC or for surface-labelled dPGS-ICC. But in the case of latter, the effect of viscosity result in a

significantly larger change of the fluorescence lifetime (Figure 4.3.13C). Thus, in CMS-ICC, the ICC probe must be shielded to some extent from direct contact with the solvent.

For a lower viscosity range (~0 – 500 cP) CMS-ICC interactions with biomolecules like BSA has a much stronger influence on the fluorescence lifetime than the pure viscosity effect (see Figure 4.3.13C). Thus, the shielding of ICC by the CMS shells renders the molecular rotor probe inert to smaller changes in solvent viscosity, while at the same time its sensitivity to biomolecular interaction is retained. This observation is especially important for biomolecular interactions studies in the cytoplasm of living cells, where viscosities between a few and several hundred centipoises can be present, but also in dermal interaction studies upon dermal CMS-ICC penetration.

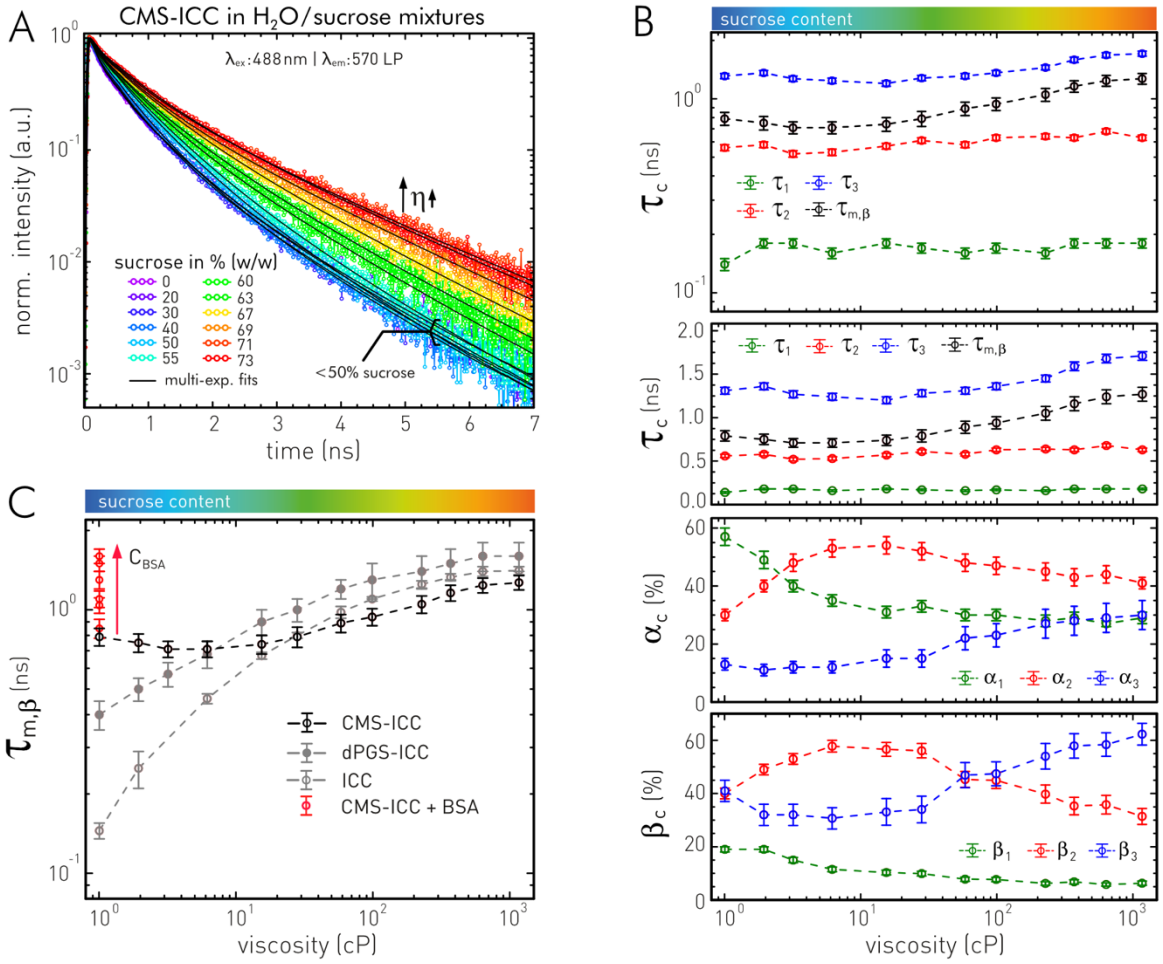

Figure 4.3.13: Fluorescence decay characteristics of 0.1 µM CMS-ICC at different viscosities generated by H_2O/Sucrose mixtures of varied molecular ratios. **A** Fluorescence decay traces of CMS-ICC dissolved in H_2O/sucrose mixtures of different ratios (rainbow colors), i.e., different viscosities at T=20 °C. Black solid lines display multi-exponential fits (see Table A15). **B** Fit results. Top: Förster-Hoffmann plot of CMS-ICC's decay components and mean fluorescence lifetime versus the respective viscosity. Center I: Same as data, decay components in linear scale. Center II: Relative decay amplitudes versus viscosity (log scale). Bottom: Relative steady-state fluorescence contributions β_c versus viscosity (log scale). **C** Comparison of mean fluorescence lifetimes – viscosity dependence for free ICC, dPGS-ICC and CMS-ICC. Experimental conditions: TCSPC-cuvette setup (Section 3.3.3), spectral parameters for both series in A and C: λ_{ex} = 488 nm, λ_{em} > 570 nm.

4.3.3 G5G2.5 core-shell tecto-dendrimers

Labeling stoichiometry affects the fluorescence properties of G5G2.5-MG-FITC

In this section, I would like to investigate potential pitfalls in the fluorescence detection of fluorescently labeled nanoparticles using the example of G5G2.5-MG-FITC (see Section 3.2.1). The megamer nanoparticle was synthesized and provided by Dr. Priscila Schilrreff (Prof. Romero's group, National University of Quilmes, Argentina / Prof. Schäfer-Korting's group, Freie Universität Berlin, Germany). In general, the electronic structure and state of fluorescent labels have an impact on the interpretation and evaluation of fluorescence-based analytical methods. Especially, in early phases of nanoparticle development, fluorophores are heavily used.[317] They are loaded as drug mimetics onto nanocarriers or are conjugated as labels to study nanoparticle uptake in cells and localization in tissue with the aim to characterize the underlying dynamic transports and target specificity.[318-319] In particular, investigations based on the fluorescence intensity by (wide-field and confocal) fluorescence microscopy approaches are widely used methods.[320-321] These methods can be susceptible for misinterpretations of the fluorescence read-out depending on the sensitivity of the used fluorophore and the prevailing physical-chemical boundary conditions. In addition to general occurring environmental factors in the different application scenarios, the degree of labeling, the fluorophore and nanoparticle concentration in particular can influence the interpretation of (confocal) microscopic fluorescence images. In the following investigation, fluorescein isothiocyanate (FITC) was selected as a fluorescent label for the tecto-dendrimeric nanocarrier G5G2.5-MG, since FITC has a wide range of applications in biomolecular and nanotechnological studies.[322-323] The data presented here was first published in Ann. N. Y. Acad. Sci. (Volz et al.,2017, Ref. 19). Hence, the next paragraph relies on my contributions to this paper.

First, I performed detailed characterization experiments on the fluorescence properties of G5G2.5-MG-FITC as a function of relative labeling stoichiometry and G5G2.5-MG concentration. For this characterization, I applied UV-Vis spectroscopy, stationary and time-resolved fluorescence spectroscopy. In order to achieve a high FITC labeling yield, FITC was added to the core-shell tecto-dendrimers in varying molar excess, resulting in label stoichiometries between 0.3 and ~40 FITC molecules per G5G2.5-MG molecule. The different labeling ratios unexpectedly led to the phenomenon, that at a certain point, a higher labeling ratio no longer leads to a higher fluorescence intensity when normalizing it to the intensity of free FITC (Figure 4.3.14A-D). This means that the rate of increase in fluorescence intensity decreases at higher labeling levels, with the consequence that more label per nanoparticle does not automatically lead to "brighter" nanoparticles. To quantify this effect, I determined the quenching factors by comparing the fluorescence intensities of the different G5G2.5-MG-FITC labeling samples with free FITC. Figure 4.3.14E shows the dependency of labeling ratio and quenching factor. While for low labeling ratios below 5 FITC molecules per G5G2.5-MG molecule the quenching factor is constant, it rises with higher labeling degree. For that reason, I sorted the G5G2.5-MG-FITC samples into two groups for further investigation. Low-labeled G5G2.5-MG-

FITC characterized by a labeling ratio of ~5 FITC molecules per nanoparticle and highly labeled G5G2.5-MG-FITC with ~20 – 40 FITC molecules per nanoparticle. When comparing the quenching parameters of both groups with regard to the emitting fluorescent FITC labels on an individual nanoparticle, one can estimate that for the low-labeled samples, on average, one emitting fluorophore per tecto-dendrimer exists (Figure 4.3.14C). On the contrary, only every second or third G5G2.5-MG-FITC nanoparticle of the highly labeled sample would fluoresce, based on a quenching factor of ~90 (Figure 4.3.14D). This observation has the consequence that a higher labeling ratio, in the present case, leads to a reduced fluorescence read-out and thus to a worse localization in fluorescence microscopic examinations.

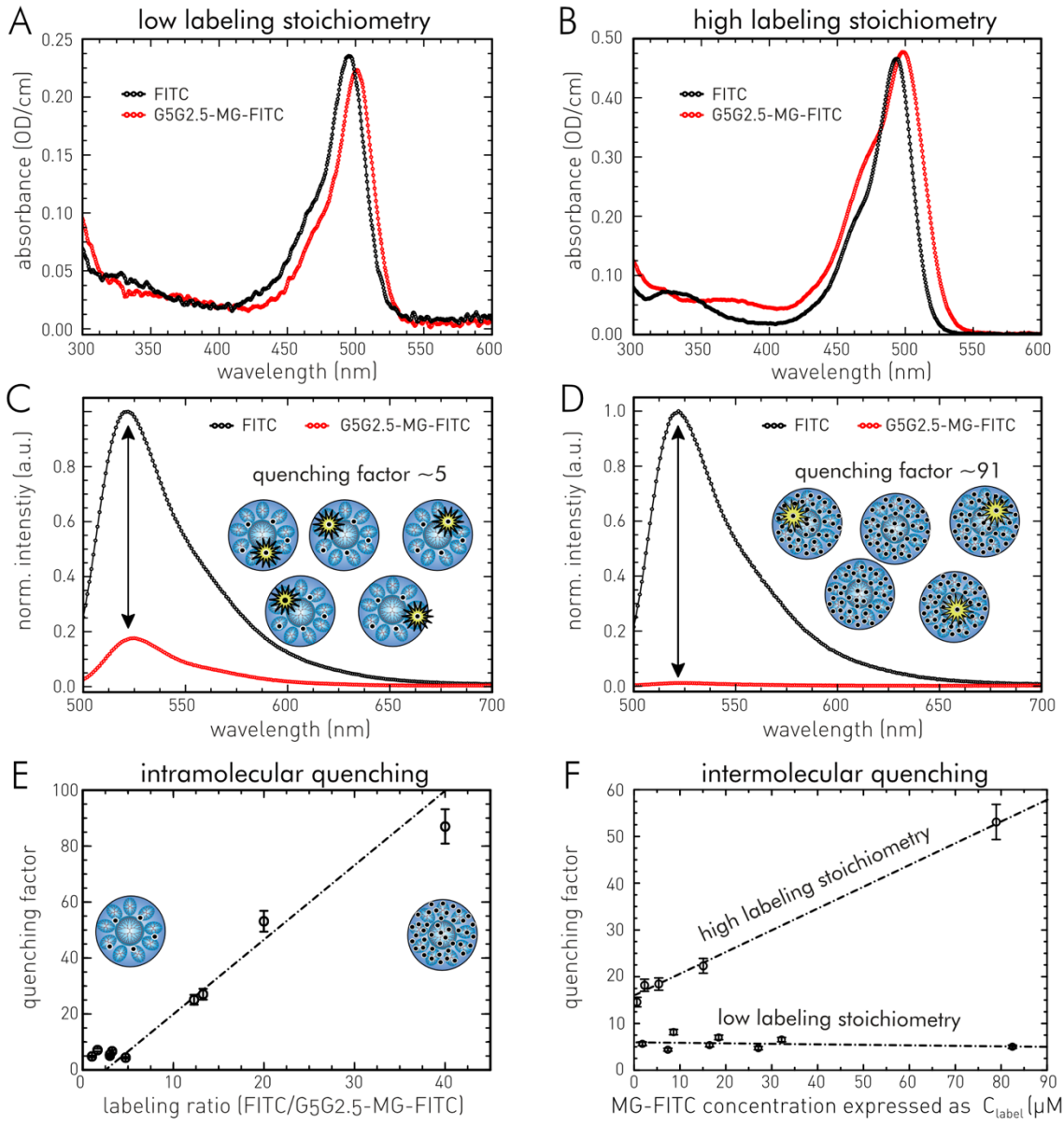

Figure 4.3.14: Labeling induced quenching effects on G5G2.5-MG-FITC'S steady-state fluorescence. **A,B** Absorbance of FITC (black) and G5G2.5-MG-FITC (red) for low (A) and high (B) labeling ratio (PBS pH 7.4). **C,D** Emission spectra and quenching factors of the FITC (black) and G5G2.5-FITC (red) samples shown in A and B. **E** Quenching factors of G5G2.5-MG-FITC in dependence on labeling ratio (FITC/MG). **F** Relationship of G5G2.5-MG-FITC concentration and quenching factor. Quenching factors shown here were determined from steady-state fluorescence intensities. A-F are reprints from Volz et al.,[19] Copyright 2017, with the kind permission of Ann. N.Y. Acad. Sci..

At the same time, it is to be expected that the physicochemical properties of the labeled G5G2.5-MG are altered by a high number of labels with a pH-sensitive (i.e. ionizable) fluorophore like FITC. The net charge of a FITC molecule varies depending on the present pH value. Consequently, the environment and the degree of labeling can influence the surface (ζ)-potential, the electrostatic interactions, and the conformation or aggregation of the megamer nanoparticle and thus also its mode of action. The ζ-potential of unlabeled G5G2.5-MG is slightly negative, with -4 – -9 mV.[161] The FITC-labeling should lead to an amplification of the negative potential. For that reason, pH titrations of G5G2.5-MG-FITC were performed by Jens Pikkemaat (Prof. Alexiev's group, Freie Universität Berlin to determine the pK_a value of nanoparticle bound FITC. The titration curves showed that the pK_a increases from ~6.5 for free FITC in 10 mM salt to a pK_a of ~7 for G5G2.5-MG-FITC with low labeling and to pK_a ~8 with high labeling stoichiometry. Such a shift to higher pK_a values indicates a more negative electrostatic potential.[324-325] This behavior can be explained by the higher number of negatively charged FITC molecules bound to the tecto-dendrimers.

Further factors that could reduce the detectable fluorescence intensity are re-absorption effects (inner filter effects), especially for fluorophores with small Stoke shifts like FITC (see Figure 2.1.2),[326-327] and static or dynamic quenching (see Section 2.1.2).[328] To address the latter, I recorded time-resolved fluorescence decay traces of highly and low labeled G5G2.5MG-FITC and of free FITC. The results of a subsequent decay analysis by (multi-)exponential decay fitting are shown in Figure 4.3.15E. The revealed decay parameters are used to calculate the mean fluorescence lifetime (Eq. 20) and the respective quenching factors.

In the case of dynamic quenching, a quencher molecule collides with the fluorophore in its excited state. Since this causes an energy transfer, an alternative depopulating pathway of the excited state becomes present which affects the rate of fluorescence transition and thus the observed fluorescence decay which becomes faster. In static quenching, a fluorophore and a quencher molecule form a ground-state complex with altered absorption/emission properties, often the complexes are non-fluorescent. Therefore, higher quencher concentrations lead to a higher number of these complexes, which is associated with a decrease in observable fluorescence intensities. Quenching caused by non-fluorescent complexes is called static. While it reduces the observed steady-state fluorescence quantum yield, it has no effect on the fluorescence decays (fluorescence lifetime) of the remaining non-complexed fluorophores. In the case of G5G2.5MG-FITC, one can consider the nanoparticle as a quencher which interacts with the labeled FITC molecules. This influences either the probability of static ground-state quenching, or the dynamic quenching, or both simultaneously.

Dynamic quenching occurs for both, the high and low labeled G5G2.5-MG-FITC nanoparticles. In both cases, the fluorescence decay of FTIC changes significantly upon labeling (Figure 4.3.15A,B). Since the fluorescence quenching determined by stationary fluorescence intensities yields much higher quenching factors, a general occurrence of ground state quenching is obvious for both labeling regimes. However, while the determined dynamic quenching factors differ only slightly between

these regimes (Figure 4.3.15C/D), I observed very different factors in the stationary fluorescence experiments. For that reason, I conclude that in the case of highly labeled G5G2.5-MG-FITC much stronger ground-state quenching occurs.

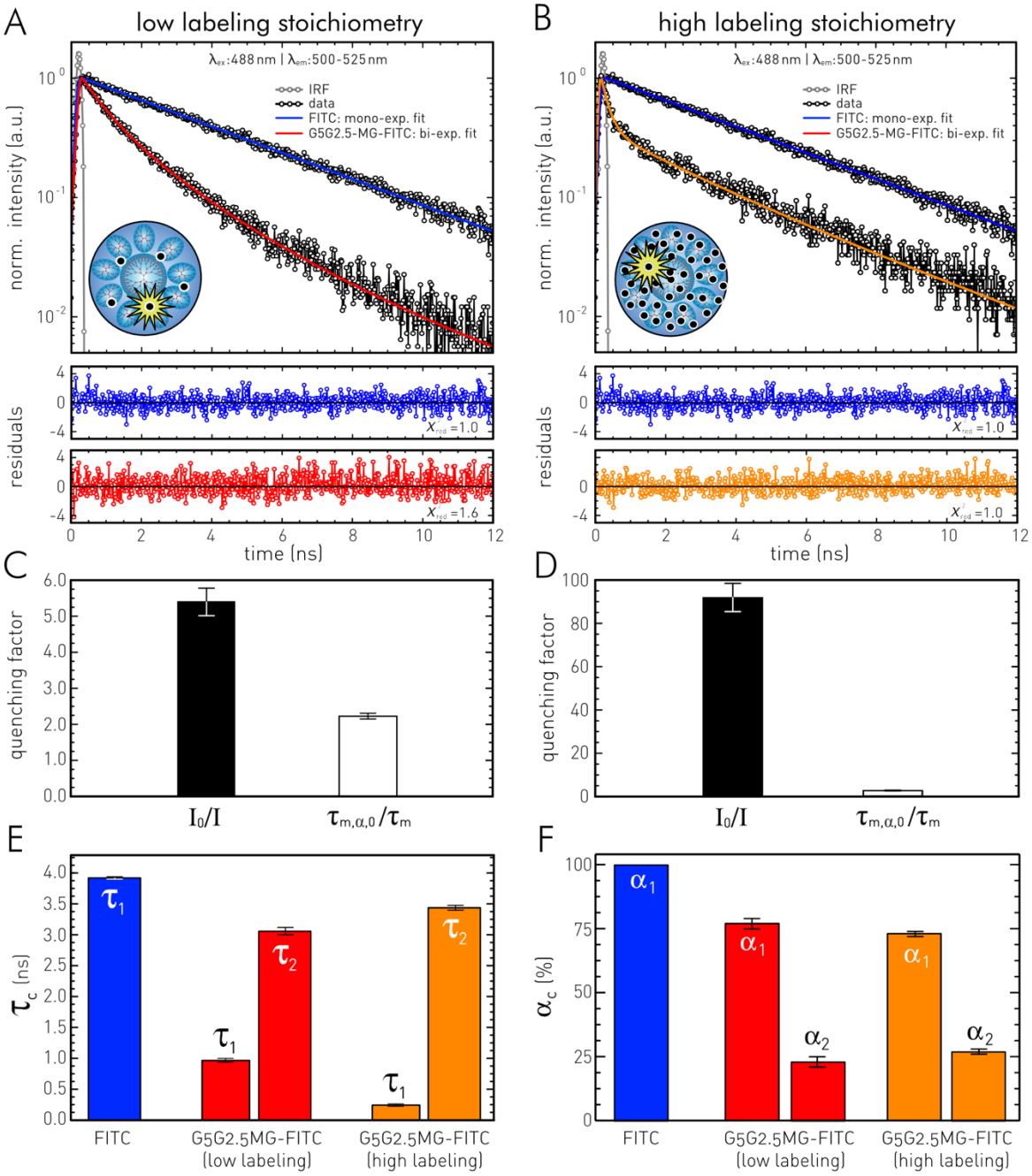

Figure 4.3.15: Labeling induced quenching effects on G5G2.5-MG-FITC's time-resolved fluorescence. **A,B** Fluorescence decay traces of FITC and low (A) and highly (B) labeled G5G2.5-MG-FIT, solid lines display (multi-)exponential fits. PBS at pH7.4; T = 20 °C. **C,D** Comparison of static and dynamic quenching for high (C) and low (D) labeling ratios, as revealed by steady-state (intensity (I)) and time-resolved fluorescence experiments (fluorescence lifetime ($\tau_{m,\alpha}$)). The values obtained for FITC ($I_0, \tau_{m,\alpha,0}$) are compared to those obtained from MG-FITC ($I, \tau_{m,\alpha}$). $\tau_{m,\alpha}$ were determined to be 3.95 ± 0.02 ns for FITC and 1.44 ± 0.03 ns (high labeling) and 1.77 ± 0.06 ns (low labeling) for G5G2.5-MG-FITC. Shown uncertainties of decay components and relative amplitudes are based on confidence interval analyses (Section 3.4.1). C&D are modified reprints from Volz et al.,[19] Copyright 2017, with the kind permission of Ann. N.Y. Acad. Sci..

As the formation of ground-state complexes only takes place when molecules are in close proximity (several Å), the question whether the formation is induced by the FITC – FITC or FITC – G5G2.5-MG interactions arises. If one considers the plots of intramolecular quenching in Figure 4.3.14E, a plateau in quenching becomes evident, below five FITC molecules per nanoparticle. This indicates that fluorescence quenching occurring in this labeling regime seems to be induced mainly by FITC – G5G2.5-MG interactions. So, in the case of higher labeling ratios, additional interactions between the individual FITC labels at the nanoparticle must occur, leading to the formation of inter-fluorophore ground-state complexes.

In addition to quenching effects that take place on individual nanoparticles, quenching effects between the individual G5G2.5-MG-FITC molecules were observed in the case of high labeling stoichiometries (Figure 4.3.14F). This intermolecular quenching effect has the consequence that at sites of higher nanoparticle concentrations fewer confocal fluorescence read-outs can be detected. Such a behavior renders a quantitative image analysis impossible. When extrapolating the plot for highly labeled G5G2.5-MG-FITC in Figure 4.3.14F to very low nanoparticle concentrations, the intersection with the y-axis yields a quenching factor of about 18, suggesting that one FITC per G5G2.5-MG fluoresces also for the highly labeled samples which is comparable to the low-labeled nanoparticles.

Although there are guidelines for standardized fluorescence measurements,[20] nanoparticles with fluorescence labels have to be characterized individually before their fluorescence read-out can be used. In most labeling procedures, fluorescent labels are added in excess to ensure high labeling yields. However, depending on the nanoparticle and the chosen label, this might lead to complications when aiming for (semi-) quantitative fluorescence evaluations, especially as high labeling degree does not automatically result in higher photon emission and thus higher detectability in fluorescence-based techniques like confocal imaging or fluorescence-activated cell sorting. For that reason, I determined an optimal labeling stoichiometry of five FITC labels per nanoparticle to ensure high detection rates and a low influence on the physicochemical characteristics of the G5G2.5-MG.

Environmental effects on fluorescence lifetime properties of G5G2.5-MG-FITC

In addition to labeling-related quenching effects, the complex environment in the biological target systems has a significant influence on the fluorescence properties of the labelled nanoparticles, too. Looking at the G5G2.5-MG core-shell nanoparticles and its possible use for topical skin application, the following question arise: How are the fluorescence properties of G5G2.5-MG-FITC affected when exposed to the various environmental parameters of the individual skin layers? On the one hand, the skin shows a depth-dependent pH profile. On the other hand, there are different polarity and viscosity regions due to the lipid matrix in the *stratum corneum* and hydrophilic regions in the viable epidermis, which could influence the fluorescence properties of the G5G2.5-MG-FITC.

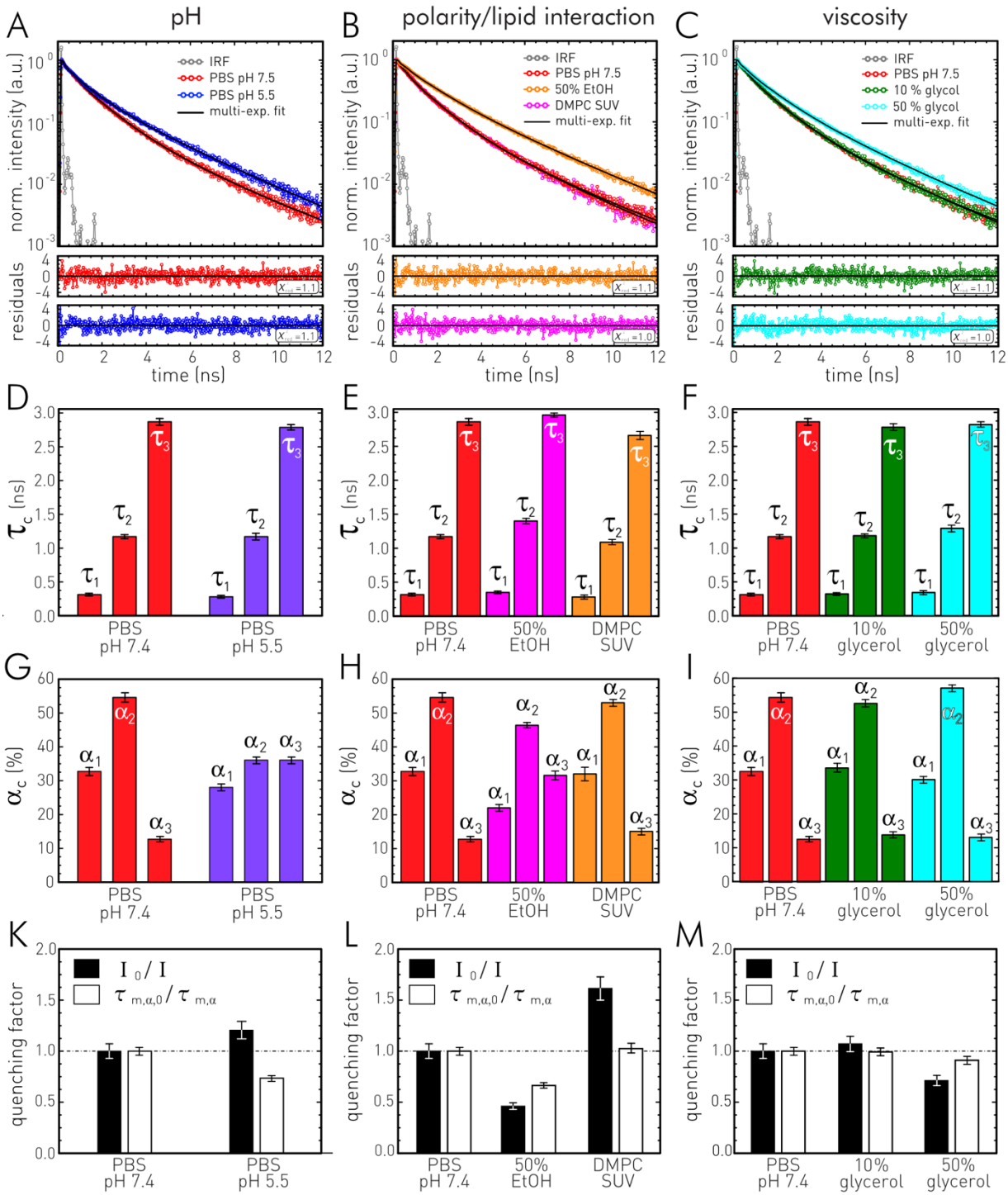

Figure 4.3.16: Environmental effects on G5G2.5-MG-FITC's time-resolved fluorescence. **A – C** Fluorescence decay traces of low-labeled G5G2.5-MG-FIT in different environments: (A) pH 5.5 vs. 7.5, (B) PBS vs. 50 % PBS/ethanol (EtOH) mixture vs. DMPC SUV solution, and (C) PBS/glycerol mixtures with 10 % and 50 % (w/w) glycerol. Solid lines indicate (multi-)exponential fits, T = 20 °C. The fluorescence decay trace of G5G2.5-MG-FITC in PBS (pH 7.4) is shown as reference. **D – F** Fluorescence decay components determined by multi-exponential decay fitting of time-resolved fluorescence traces in A-C. D shows comparison of different pH, E of differing polarities and F for different viscosities. **G – I** Respective decay amplitude of the decay components shown in D – F. **K – M** Comparison of static and dynamic quenching for the three different environmental parameters, calculated by stationary fluorescence intensities (intensity (I)) and by fluorescence lifetimes ($\tau_{m,\alpha}$)). The values obtained for G5G2.5-MG-FITC ($I_0, \tau_{m,\alpha,0}$) in PBS, pH 7.4 are compared to those obtained from G5G2.5-MG-FITC in the individual environment ($I, \tau_{m,\alpha}$). A-C & K-M are modified reprints from Volz et al.,[19] Copyright 2017, with the kind permission of Ann. N.Y. Acad. Sci.. Fluorescence decay traces were recorded in cooperation with Johannes Stellmacher (Prof. Alexiev's group, Freie Universität Berlin, Germany). Shown uncertainties of decay components and relative amplitudes are based on confidence interval analyses (Section 3.4.1).

Thus, I tested the effects of these parameters on the stationary and time-resolved fluorescence parameters of G5G2.5-MG-FITC in *in vitro* experiments. I compared environments of different pH values, different polarity, and different viscosity. In contrast to the quenching factors observed for the low and high labeling ratios discussed earlier (Figure 4.3.15C,D), these environmental effects only marginally influence the stationary fluorescence intensity, as indicated by relative quenching factors (in respect to the intensity of the low labeling G5G2.5-MG-FITC in aqueous solution at pH 7.4), ranging from 0.5 to 1.6 (Figure 4.3.16 K-M).

Figure 4.3.16 displays the fluorescence decay traces for a low-labeled G5G2.5-MG-FITC sample in different pH environments (Figure 4.3.16A), in solutions with different polarity (Figure 4.3.16B), and in solutions of different viscosity (Figure 4.3.16C). To compare the observed fluorescence decay behaviors more quantitively, I applied a decay analysis (see Sec. 3.4.1) to the recorded fluorescence decay traces shown in Figure 4.3.16A-C using a tri-exponential decay model (see Appendix, Table A16). The obtained decay components and respective amplitudes are visualized in Figure 4.3.16D-I. The data show that the investigated environmental effects only marginally influence the individual decay components (Figure 4.3.16D-F). A stronger effect can be observed in respect to the decay amplitudes (Figure 4.3.16G-I).

However, when comparing the dynamic quenching factors, it can be seen that these effects influence the mean fluorescence lifetime even less than the total fluorescence intensity. The strongest impact was observed for the reduced polarity environment of a 50 % EtOH/PBS mixture, followed by the low pH and high viscosity environments. However, these changes practically have only minor influences on the fluorescence read-out. The most important determinant for effective fluorescent labeling of G5G2.5-MG nanoparticles by FITC is appropriate label stoichiometry.

4.4 FLIM-based cellular interaction imaging of dendritic nanoparticles

4.4.1 CMS-NC uptake mechanism and cellular fate in human keratinocytes

In this section, I present a study on the interactions of a fluorescently tagged and loaded dendritic core-multishell (CMS) nanocarrier (NC) with cellular components during its cellular uptake in primary keratinocytes (Figure 4.4.1). As described in Section 2.3.2, the dendritic CMS-NC[132, 150] consists of a hyperbranched polyglycerol (hPG) core, and two spherical shells build up from octadecanoicdiacid and monomethyl polyethylene glycol (mPEG). The unimolecular nanoparticle mimics the polarity gradient of a liposome and have been successfully loaded with a wide range of hydrophobic and hydrophilic compounds, like cell-penetrating peptides, drugs, and fluorescent dye surrogates.[4, 150] In topical applications, CMS-nanocarriers seem to enhance the notoriously low skin penetration of drugs, and thus could pave the way for a reduction of severe systemic adverse effects in the treatment of skin diseases like atopic dermatitis or psoriasis.[4] Since it was shown that CMS-NC penetrate damaged and diseased skin,[170, 211] (see section 4.5) the probability is high that they interact with cutaneous cells like keratinocytes, dermal fibroblasts, dermal immune cells, and if used in the delivery of chemotherapeutic agents, also carcinoma cells.

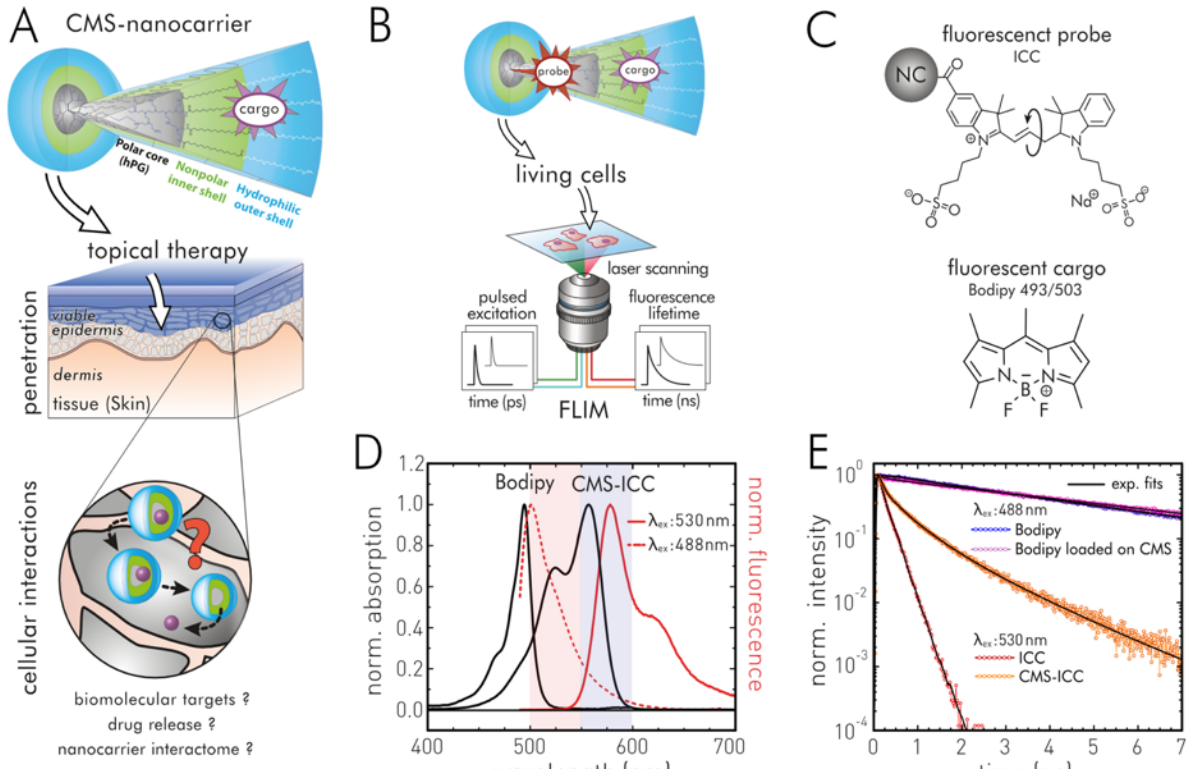

Figure 4.4.1 **A** Scheme of a cargo-loaded CMS-nanocarrier and its application in topical drug delivery. CMS-nanocarriers consists of a polar core (hyperbranched polyglycerol (hPG)), a nonpolar inner shell (octadecanoicdiacid), and hydrophilic outer shell (monomethyl poly(ethylene) glycol). **B** Experimental design of live-cell FLIM investigation of the cargo-loaded and fluorescently tagged CMS-NC. **C** Chemical structure of the interaction-sensitive molecular rotor tag indocarbocyanine (ICC) and the hydrophobic fluorescent drug mimetic bodipy. **D** Normalized absorption and fluorescence emission spectra of CMS-ICC and Bodipy. **E** Fluorescence decay traces and exponential fits of bodipy and ICC in aqueous solution, and loaded, or covalently labeled to the CMS-nanocarrier, respectively.

However, these interactions between the CMS-NC and living cells of the deeper cutaneous layers is only partially investigated.[151, 166, 174] As several drug targets are localized intracellularly, for example the lysosom or the nucleus, studying biomolecular interactions of a nanocarrier with cellular and subcellular structures, i.e., the celluar nanocarrier "interactome", may provide essential insights into their mechanism of drug delivery, potenitally revealing off-target effects. This knowledge is especially advantageous for the designing and success of diagnostic and therapeutic nanomedicine.[283]

For this study, I utilize a non-covalently loaded fluorescent cargo bodipy493/503 (bodipy, logP = 3.5, MW=262 Da)[102] as hydrophobic drug mimetic and the interaction-sensitive FMR ICC, covalently bound to the core of the CMS-nanocarrier for the sensitive detection of biomolecular interactions of the nanocarrier during its cellular uptake (Figure 4.4.1B,C, see Section 3.2.1). In the following, the loaded nanocarrier is termed as CMS-ICC/bodipy. While the conjugation of ICC to the nanocarrier prolongs its fluorescence lifetime as displayed in Figure 4.4.1E, bodipy shows no significant change between its loaded and unloaded state. Live-cell FLIM experiments were conducted, using the white-light supercontinuum laser system (see Section 3.3.4/4.1.1) as multicolor picosecond excitation source.[48] This setup allows to track multiple fluorophores, such as ICC and bodipy with excitation wavelengths of 530 nm and 488 nm, respectively (Figure 4.4.1D) and to correlate the fluorescence lifetime information with spatial location of the fluorescent probes (Figure 4.4.1E). Using the Cluster-FLIM approach to analyze the fluorescence lifetime data enables an all-optical dissection of cell targeting, as well as effects of protein corona formation on cell targeting. Furthermore, it makes it possible to reveal consecutive cellular uptake steps, to identify intracellular interactions of the CMS-ICC nanocarrier and to recognize and quantify membrane receptor binding, and intracellular cargo delivery. The data presented in the next section was partly published in Theranostics (Brodwolf et al., Ref. 44). Hence, the next paragraph relies on my contributions to this paper.

Cellular uptake of CMS-ICC/bodipy by NHK

First, I tested whether bodipy loaded CMS-ICC nanocarrier enters the NHK cells. For this purpose, NHKs were incubated for 270 min in whole-cell medium (KGM) containing 10 µg/ml CMS-ICC/bodipy, at 37 °C and 5 % CO_2. Confocal fluorescence microcopy of these incubated cells indicates that bodipy as well as CMS-ICC clearly locates in the cytosol of NHK after this time interval (Figure 4.4.2A). As spatial orientation markers, I stained cellular nuclei and plasma membranes with DAPI and CellMask, respectively. The merged imaged (optical overlay) displays an intracellular distribution of the nanocarrier. The hydrophobic cargo bodipy shows a different localization.

Next, I studied the time-dependent uptake of the nanocarrier by incubating the NHK for varying times (15 min to 270 min) at 37 °C and for 210 min at 4 °C. As at low temperatures, energy dependent uptake pathways are stalled. An initial tau-plot analysis of the FLIM data is displayed in

Figure 4.4.2B. For this analysis, the individual decay traces of all image pixels are fitted by tri-exponentials. In order to obtain enough photons for a proper fitting process, the decay histograms of 9 neighboring pixels were combined to a single histogram (pixel-binning). After calculating the amplitude-weighted mean fluorescence lifetimes, a pixel frequency distribution was calculated for each incubation time. Figure 4.4.2B shows the individual mean fluorescence lifetime distributions, next to the tau-plots (left). One can observe a clear shift to shorter mean fluorescence lifetimes with longer incubation times at 37 °C. The 4 °C experiment shows the slowest lifetime distribution.

Figure 4.4.2C shows the application of the Cluster-FLIM analysis to a FLIM time series of CMS-ICC/bodipy interactions with primary normal human keratinocytes (NHK). A global cluster analysis of all images obtained in the time series retrieves four distinct fluorescence lifetime signatures (FLSs), three for CMS-ICC and one for bodipy (Figure 4.4.2F). The autofluorescence background of the NHK cells make a negligible contribution to the observed fluorescence intensity. The FLS are color-coded: Magenta for bodipy, and cyan, yellow, and red for the different CMS-ICC interactions within the NHK cell. Thus, the Cluster-FLIM analysis is able to identify multiple fluorescent species of CMS-ICC appearing simultaneously and in close spatial distance within the single cells.

The nanocarrier-loaded bodipy penetrates the cytosol of NHK already after a 15-minute incubation, as the fluorescent drug mimetic accumulates intracellularly (Figure 4.4.2C, right, magenta-colored areas) between the cell membranes stained by CellMask (dark red). As the Cluster-FLIM analysis identifies only a single FLS for bodipy, it either locates in a homogenous intracellular microenvironment, or it possesses a generally weak sensitivity of its fluorescence lifetime to intracellular microenvironments. The uniform intracellular distribution of bodipy and the observation that no uptake into the nucleus occurs, in none of the incubation times, corresponds to previous studies on lipid droplets staining using the bodipy493/503 derivate.[102] While bodipy strongly enters the NHK cells after 15 min, the CMS-ICC nanocarrier is only interacting with the plasma membrane of cells. Also, after a 45-minute incubation, the CMS-ICC still interacts with the membranes. At prolonged incubation times (>90 min), the nanocarrier CMS-ICC than appears then intracellularly. And with further incubation time, more and more CMS-ICC are concentrated within the cells. Figure 4.4.2C indicates that multiple interactions occur upon the entry of the nanocarrier into the cell as indicated by the change from the cyan to the yellow and red FLS as a function of the incubation time.

To discriminate between passive and active processes in the cell entry and to obtain a "time zero"-image for active processes, I employ the FLIM image of the CMS-ICC interaction at 4 °C, as at this temperature all active endocytosis pathways are stalled (Figure 4.4.2C, Figure 4.4.3B). Lowering the temperature does not inhibit bodipy penetration into the cytosol (Figure 4.4.2C), indicating a passive uptake for the hydrophobic cargo. Contrary to this, low temperature strongly reduces the CMS-ICC uptake into NHK, however not its cell membrane interaction, pointing to the internalization of CMS-ICC into NHK via an active pathway. The assumption of an energy-dependent transport is supported by ATP-depletion experiments using azide (Figure 4.4.3D, Table 4.4.1).

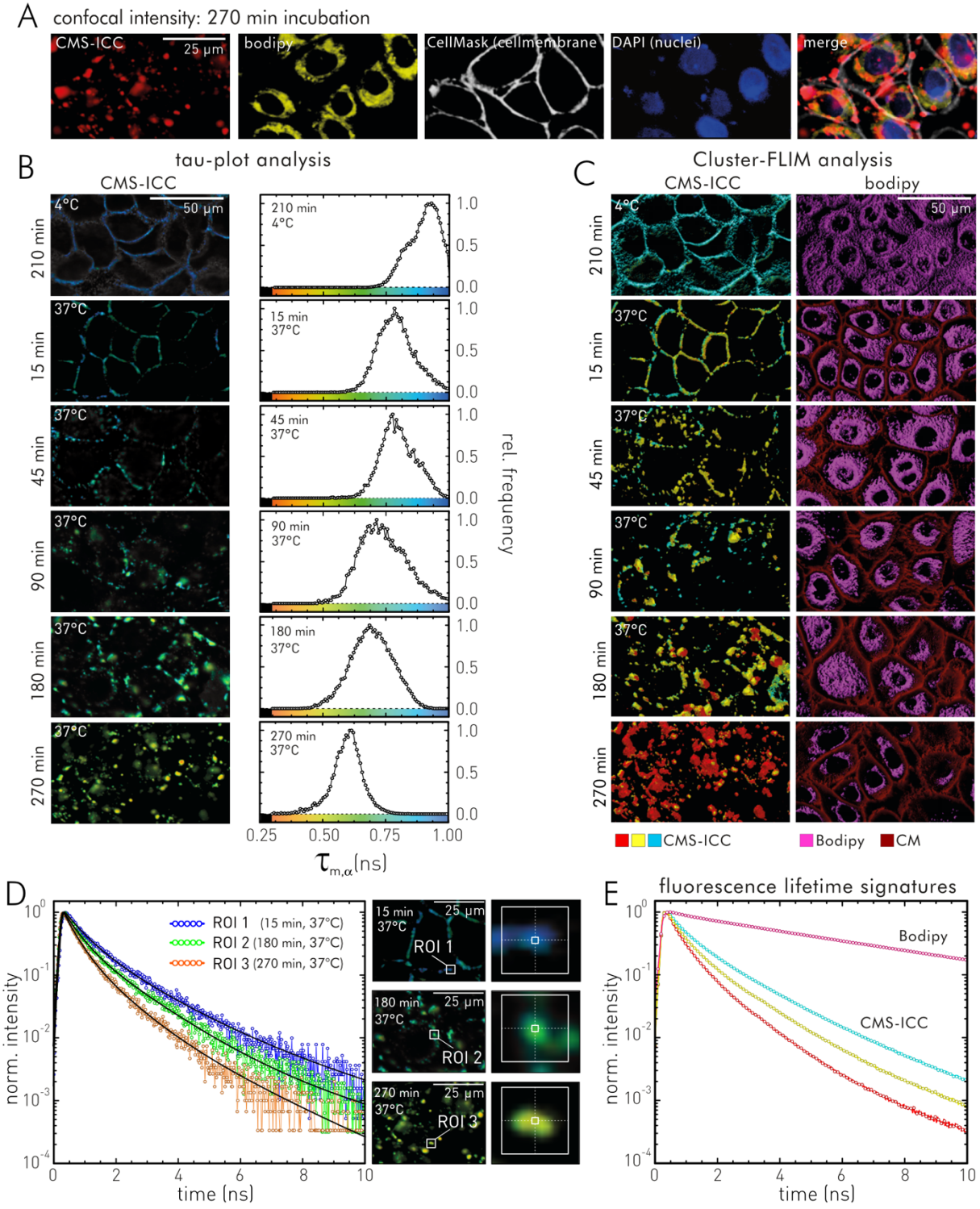

Figure 4.4.2 Cellular uptake and interaction of CMS-IC/bodipy. **A** multispectral confocal laser scanning microscopy of NHK cells after a 270-minute incubation with CMS-ICC/bodipy (10 µg/ml, in KGM) at 37 °C. False colored-coded intensity images: blue for DAPI, white for CellMask, red for CMS-ICC, and yellow for the bodipy channel. Cell nuclei stained by DAPI. Cell membrane stained by CellMask Deep Red. Merge: Digital overlay of the individual spectral channels. **B** Tau-plot analysis of CMS-ICC uptake dynamics in NHK at indicated temperature and incubation time. **C** Cluster-FLIM analysis of CMS-ICC (left) and cargo Bodipy (right) uptake dynamics in NHK. Cell membrane stained by CellMask false colored in dark red (C, right). **D** Characteristic fluorescence decays of CMS-ICC for different incubation times. Histograms are generated from indicated ROIs, black lines indicate tri-exponential fits. **E** Characteristic FLS for the CMS-ICC/bodipy nanocarrier interactions with NHK cells: bodipy (magenta) and CMS-ICC (cyan, yellow, red). Experimental conditions: DAPI with λ_{ex}=405 nm, λ_{em}=430 – 475 nm; bodipy with λ_{ex}=488 nm, λ_{em}=500 – 550 nm; CMS-ICC with λ_{ex}=530 nm, λ_{em} =545 – 600 nm; and CellMask with λ_{ex}=640 nm, λ_{em}>665nm; objective: 60X.

Identification and assignment of cellular CMS-ICC interactions

To dissect the active CMS-ICC entry steps into NHK and to identify the corresponding interaction partners, I calculated the relative amounts of the three CMS-ICC FLIM-clusters, based on their respective photon intensities spatially separated in the plasma membrane and within the cytoplasm (Figure 4.4.3B). At "time-zero", i.e., at 4 °C, one observes only the cyan FLS in the membrane, a result of a passive binding process (Figure 4.4.2C, Figure 4.4.3B). Since the same cyan FLIM-cluster appears also after the 15-minutes incubation time almost exclusively in the membrane, I conclude an affinity-based binding of CMS-ICC to the plasma membrane, e.g., to a membrane receptor. This binding can be regarded as the first uptake step (Figure 4.4.3B, Step 1 "initial membrane interaction"). To assign the cyan FLS to an interaction partner in this uptake step I apply further pharmacological inhibition experiments. I began with the inhibition of scavenger receptors (SRs), which belong to the cell-surface pattern-recognition receptors and bind a variety of ligands including nanocarriers.[329] Poly I and fucoidan, well-known SR ligands, in particular for SR class A, inhibit CMS-ICC uptake by more than 90 % and 99 %, respectively. Poly C, although having a similar structure to Poly I is not a ligand for SR[295] and shows no inhibition (Figure 4.4.3D). Next, I investigated the involvement of lipid binding using giant unilamellar vesicle (GUV) model systems. Beside monolipidic DMPC, I utilized lipid mixtures containing cholesterol because of the known dependence of SR-mediated endocytosis on membrane areas rich in cholesterol (lipid rafts).[330-331] Since CMS-ICC only shows a weak binding to the lipid systems and the fluorescence decay of GUV-bound CMS-ICC does not match the cyan FLS of CMS-ICC in NHK membranes, sole lipid binding then can be excluded (Figure 4.4.4A-C).

Further support for the assignment of the cyan FLS to receptor binding is provided by concentration dependent uptake experiments (Figure 4.4.4F). Uptake of CMS-ICC in NHK yields a saturation curve with increasing CMS-ICC concentrations, which is expected for receptor-mediated uptake.[208] Both CMS-ICC and the untagged CMS-nanocarrier bind to the same receptor as shown by inhibition and competition experiments (Figure 4.4.4D,E). Thus, one can assign the cyan FLS to the interaction of the CMS-nanocarrier with SR in the NHK membrane and conclude that the CMS-nanocarrier acts as a ligand for SR with an apparent binding constant of ~1 µM under live-cell conditions (Figure 4.4.4E,F).

The yellow FLS is intimately connected with molecular interaction and segregation processes in the membrane that facilitate the uptake of CMS-ICC into the cell as shown in Figure 4.4.3B, steps 2 – 4 (Step 2 "early membrane interactions, Step 3 "later membrane interactions: segregation and aggregation", Step 4 "uptake into near-membrane space"). At later times, the yellow FLS also appears within the cell in individual spike-like spots, probably CMS-ICC containing vesicles, mostly around the nucleus (Figure 4.4.3B, Step 5 "intracellular transport to perinuclear space").

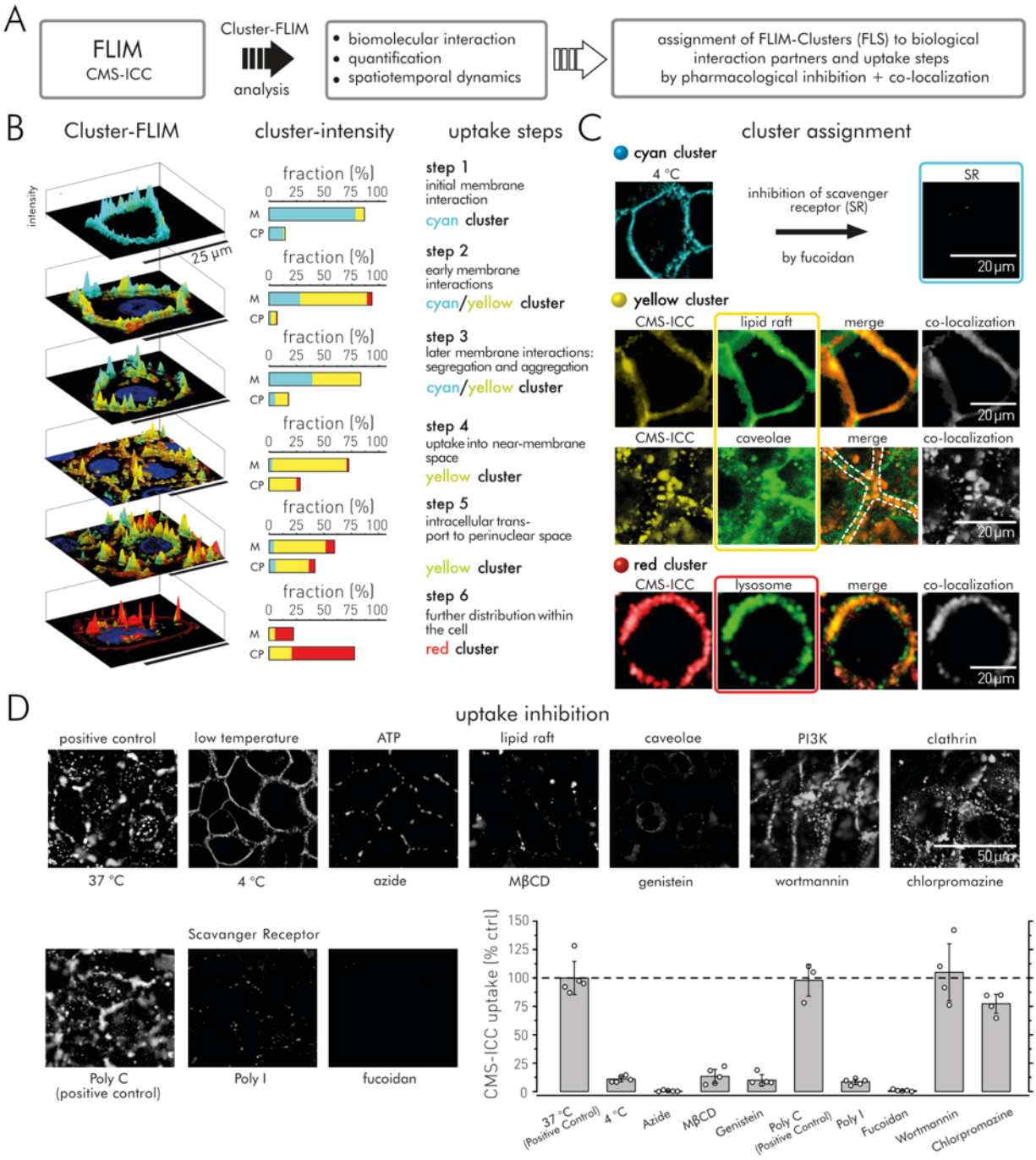

Figure 4.4.3. CMS-ICC uptake kinetics in living NHK cells. **A** Procedure of Cluster-FLIM based interaction analysis. (**B**) CMS-ICC uptake steps based on visual inspection of spatial organization in the Cluster-FLIM image and quantification of cluster intensities (bar graph with respect to total photon intensity in the cell, separated for cell membrane (M) and for cytoplasm (CP)). Cyan, yellow, and red indicate the different FLIM-clusters (see Figure 4.4.2E). The images are zooms from Figure 4.4.2C. Nuclei are stained by DAPI (blue), plasma membranes by CellMask (dark red). **C** Assignment of the cyan FLIM-cluster (FLS) to scavenger receptor (SR) binding. Co-localization of yellow FLIM-cluster with lipid rafts stained by CTB-A647 and with caveolae stained by a caveolin-1 antibody (Cav-1-A488). Co-localization of red FLIM-cluster with lysosomes stained by LysoTracker. **D** Inhibition of cellular uptake of CMS-ICC nanocarrier towards NHK after 180 min. Values are means ± SD (n=4-6). For details see Table 4.4.1. Modified reprints from Brodwolf et al., [44] Copyright 2020, with the kind permission of Theranostics.

In a successive step, I applied different inhibition and co-localization experiments to assign the yellow FLS to a biological structure after considering possible endocytotic pathways.[330, 332] The segregation/ aggregation process observed in step 3 (Figure 4.4.3B) and the binding of CMS-ICC to SR

points to the involvement of lipid rafts.[330-331] Cholesterol depletion by methyl-ß-cyclodextrin (MßCD) efficiently blocks CMS-ICC internalization (Figure 4.4.3D, Table 4.4.1), indicating a lipid raft/caveolae-mediated uptake mechanism.[333-334] The involvement of caveolae is supported by genistein inhibition,[335] blocking CMS-ICC uptake by about 90 % (Figure 4.4.3D, Table 4.4.1). While almost complete inhibition of CMS-ICC uptake is observed in the presence of MßCD and genistein, blocking of macropinocytosis via the phosphoinositide 3-kinase (PI3K) inhibitor wortmannin[336] and clathrin-mediated endocytosis by chlorpromazine[337] does not affect CMS-ICC uptake (Figure 4.4.3D, Table 4.4.1). As cholera toxin internalization is caveolae/lipid raft dependent,[329, 338] I conducted co-localization experiments of the yellow CMS-ICC FLIM-cluster with a fluorescently labeled cholera toxin B (CTB-A647) (Figure 4.4.3C, second row). The Manders' coefficients[206] $M_1 = 0.59$ and $M_2 = 0.53$, representing the overlapping fraction of CTB-A647 fluorescence and the yellow FLIM-cluster with respect to the other (M_1: yellow Cluster with CTB, M_2: CTB with yellow Cluster), indicate an interaction of CMS-ICC with structures of a caveolae/lipid raft dependent uptake pathway. To further specify the molecular interactions of CMS-ICC, I conducted a second co-localization experiment of the yellow CMS-ICC FLIM-cluster, this time, with a fluorescently tagged Caveolin-1 antibody. Here, a co-localization also takes place, in both the NHK cell membrane and in the lumen (Fig. 4c, third row) characterized by Manders' coefficients of $M_1 = 0.81$ and $M_2 = 0.64$. Summarized, the yellow FLS can be assigned to CMS-ICC interacting with constituents of caveolae, both in the cell membrane and upon release into the lumen of NHK cells.

The red FLS of CMS-ICC appears after 180 min (Figure 4.4.3C) and becomes the major interaction signature of CMS-ICC inside NHK cells with a fraction of > 70 % after 270 min of incubation (Figure 4.4.3B, Step 6 "further distribution within the cell"). Large accumulations of CMS-ICC near the nucleus are visible, shown by the red FLS (Figure 4.4.3B). To facilitate the assignment of the red FLS to a biological structure, the intracellular fate of CMS-ICC at these longer incubation times becomes important. A caveolae-mediated uptake may be associated with lysosomal escape or converge with the endolysosomal pathway.[339] For the latter I tested co-localization of the red FLIM-cluster with the fluorescent lysosomal marker LysoTracker after prolonged incubation times (Figure 4.4.3C, forth row). Manders' coefficients of $M_1 = 0.87$ and $M_2 = 0.79$ demonstrate a very high co-localization of CMS-ICC with LysoTracker. Thus, the red FLS appears while CMS-ICC localizes/interacts with lysosomal structures.

The Cluster-FLIM analysis and the respective FLS assignment of the CMS-ICC nanocarrier in the cellular uptake process by NHK can be summarized as follows: CMS-ICC experiences three distinctive biomolecular interaction modes, monitored by three distinctive lifetime signatures (Figure 4.4.2F). I identify the respective interaction partners responsible for these changes in the ICC's lifetime by pharmacological inhibition and co-localization experiments as a SR for the cyan FLS, constituents of caveolae for the yellow FLS, and lysosomal structures for the red FLS.

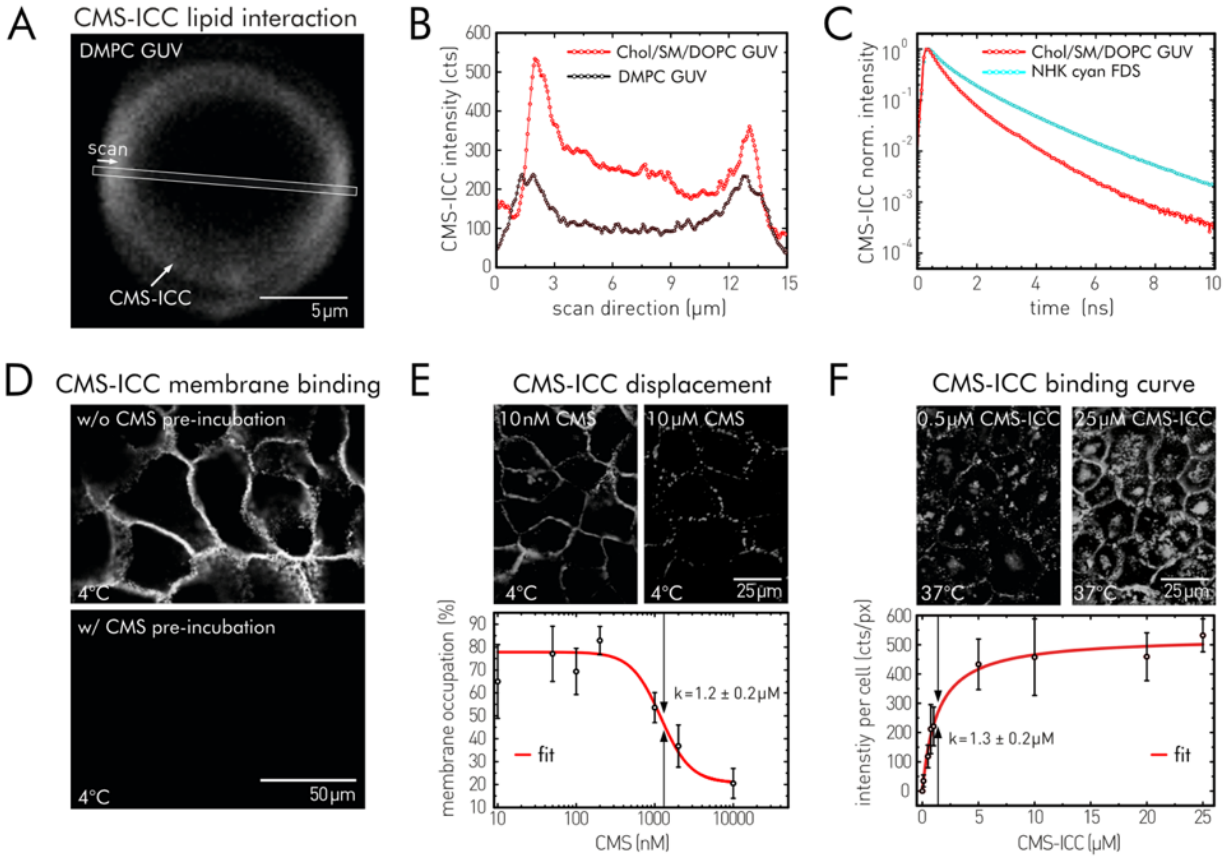

Figure 4.4.4: Reference experiments for lipid/receptor interaction and CMS-ICC uptake by other dermal cells. **A** fluorescence intensity image of CMS-ICC interacting with DMPC GUVs. **B** Intensity scans of DMPC and Chol/SM/DOPC GUVs. Scan for DMPC GUV is indicated in (A) by a white outlined bar. CMS-ICC intensity in Chol/SM/DOPC and DMPC GUVs is shown in red and black, respectively. **C** Comparison of the cyan colored CMS-ICC FLS found in the plasma membrane of NHK and the FLS observed of CMS-ICC interacting with Chol/SM/DOPC GUV membranes. DMPC:1,2-dimyristoyl-sn-glycero-3-phosphocholine, Chol: cholesterol, SM: sphingomyelin, DOPC: 1,2-dioleoyl-sn-glycero-3-phosphocholine. **D** competition experiments with unlabeled CMS-nanocarrier and normal human keratinocytes (NHK). Top: Interaction of CMS-ICC (10 µg/ml) with NHK cell membranes. Bottom: Inhibition of CMS-ICC (10 µg/ml) binding to NHK cell membranes when pre-incubated with 1000 µg/ml (~50 µM) unlabeled CMS nanocarrier. In both experiments NHK were incubated with CMS-ICC for 180 minutes at 4 °C in KGM. **E** Displacement of CMS-ICC from plasma membrane at 4 °C. CMS-ICC (10µg/ml, ~ 0.5 µM) was incubated in KGM at 4 °C for 1 h. Afterwards unlabeled CMS was added with concentrations ranging from 10 nM to 10 µM at 4 °C. Top: NHK cells after pre-incubation with CMS-ICC at 4 °C and addition of 10 nM and 10 µM unlabeled CMS. Bottom: plot of CMS-ICC membrane displacement versus CMS concentration. The displacement of CMS-ICC from the plasma membrane was observed by the fluorescence intensity of the area CMS-ICC is occupying in the plasma membrane. The decrease of occupied membrane areas with increasing CMS concentrations was fitted by a modified Hill function (red line, Eq. 62), yielding a half-maximum binding constant of 1.2 ± 0.2 µM CMS. **F** CMS-ICC uptake by NHK in KGM at 37°C for CMS-ICC concentrations varying between 0 and 25 µM. Top: NHK incubated with 0.5 µM CMS-ICC and 25 µM CMS-ICC. Bottom: Plot of cellular fluorescence intensity versus the CMS-ICC concentration. The saturation of the CMS-ICC uptake curve points to a receptor-limited up uptake mechanism, which is in agreement with the assignment of the initial membrane-binding step to scavenger receptor binding. The non-linear uptake behavior was fitted (red line) by Eq. 61, yielding a half-maximum uptake concentration (apparent receptor binding affinity) of 1.3 ± 0.2 µM CMS-ICC. Values are means ± SD (n=3-6). Experimental conditions: CMS-ICC with λ_{ex} = 530 nm, λ_{em} = 545 – 600 nm; objective: 60X.

Table 4.4.1: Inhibition of cellular uptake of CMS-ICC nanocarrier towards NHK after 180 min using low temperature, ATP and cholesterol depletion by azide and MßCD, respectively. Blocking of caveolin phosphorylation, macropinocytosis (PI3K activity), and clathrin mediated endocytosis was performed by addition of genistein, wortmannin, or chlorpromazine, respectively. Scavenger receptor class A ligands polyionosinic acid (poly I) and fucoidan were used to inhibit CMS-ICC binding to scavenger receptors. Polycytidylic acid (poly C) is not a ligand of scavenger receptor and serves as a positive control. CMS-ICC uptake at 37° C is used as reference and set to 100 %.

inhibitor	*concentration*	*CMS-ICC uptake (% of control ± SD)*
low temperature (4°C)	–	11 ± 2
azide	3 mg/ml	0.5 ± 0.5
MβCD	5 mg/ml	13 ± 6
genistein	27 µg/ml	10 ± 5
polyinosinic acid (Poly I)	50 µg/ml	8.6 ± 2.3
polycytidylic acid (PolyC, positive control)	50 µg/ml	98 ± 14
fucoidan	100 µg/ml	0.9 ± 0.7
wortmannin	150 ng/ml	105 ± 25
chlorpromazine	10 µg/ml	77 ± 8

Kinetic treatment of CMS-ICC uptake process

Based on the identified interactions of CMS-ICC with NHK cells using ICC's fluorescence lifetime sensitivity, one can conclude that the nanocarrier uptake into this cell type is mediated by a mechanism, that includes scavenger receptors located in lipid rafts/caveolae rich membrane regions and converges with an endolysosomal pathway. The spatial quantification of the nanocarrier interactions as a function of time based on fluorescence lifetime changes enables a direct kinetic treatment of the CMS-nanocarrier uptake process (Figure 4.4.5A). The applied kinetic model for CMS-nanocarrier internalization and intracellular transport bases on first order rate equations (see Section 3.2.2, Eq. 63 – 67) and yields the underlying time constants of the individual steps (Figure 4.4.5C). A fit of the fractional cluster intensities to this model supposes that the SR-bound CMS-nanocarrier at the cell surface is rapidly captured by caveolae in the cell membrane with a time constant of 8 ± 2 min. Slightly delayed with a time constant of 28 ± 11 min, a back-reaction occurs, resulting in a slower temporal decay of the cyan FLIM-cluster. The capture of the SR-CMS-nanocarrier complex by caveolae results in a CMS-nanocarrier internalization with a time constant of 88 ± 6 min. Finally, the entered CMS-nanocarrier accumulates in lysosomes with a time constant of 107 ± 9 min.

In opposite, the hydrophobic non-covalently loaded fluorescence cargo bodipy enters the cell significantly faster. CMS-nanocarriers release bodipy continuously upon its first interaction with the membrane-based SR (Figure 4.4.5B). This immediate release of bodipy from the nanocarrier is probably governed by conformational changes of CMS' shell branches when interacting at the cell membrane. Previous investigations on the molecular flexibility of this nanocarrier reveal a highly flexible and squeezable architecture, which changes its dimensions on surfaces.[170]

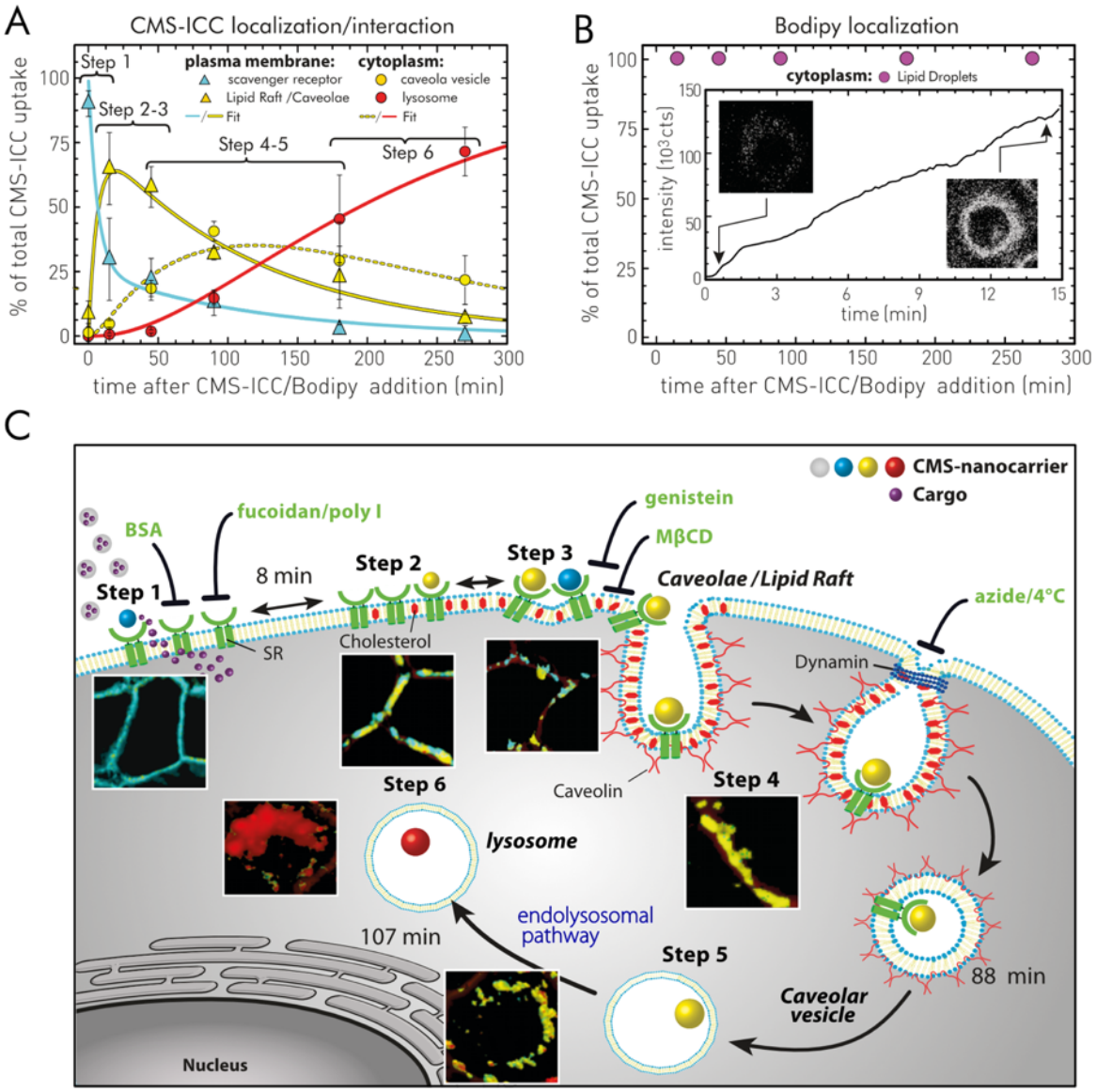

Figure 4.4.5: Spatiotemporal dynamics of the bodipy-loaded CMS-nanocarrier interactions in NHK cells: cellular binding, internalization, and intracellular transport. **A** Temporal development of the relative CMS-ICC FLIM-cluster intensities as a function of localization (plasma membrane and cytoplasm). Values are means ± SD (n=3 – 6). Fits of the CMS-ICC internalization and transport kinetics according to the model (Eq. 63 – 77) are shown. The fit reveals the time constants: τ_1 = 8 ± 2 min (SR-CMS-ICC complex → caveolae), τ_{-1} = 28 ± 11 min (back reaction of τ_1), τ_2 = 88 ± 6 min (internalization of SR-CMS-ICC complex by caveolae), τ_3 = 107 ± 9 min (transport to lysosome). **B** Kinetics of bodipy uptake (n = 44 cells). Inset: Bodipy uptake kinetics in the first 15 minutes after addition of CMS-ICC/bodipy. **C** Schematic showing the itinerary of CMS-nanocarrier from binding to the SR at the NHK surface via trafficking into the cell by caveolae until the nanocarriers eventually reach the lysosomes. Individual uptake steps and time constants from the kinetic model as well as the cargo release at the cell membrane are indicated. FLIM-images to highlight the specific cellular interaction are shown (zoom with respect to Figure 4.4.2C: step 1: 2.0, step 2: 2.4, step 3: 2.1, step 4: 3.2, step 5: 2.0, step 6: 2.1). Modified reprints from Brodwolf et al., [44] Copyright 2020, with the kind permission of Theranostics.

Furthermore, an increasing flexibility of the multi-shell design connected with an modified cargo distribution was observed at higher temperatures.[258] Subsequent to the conformational changes of the shell branches, hydrophobic forces between bodipy and the lipids of the cell membrane may explain its fast passive uptake into the NHK cytoplasm. The schematic of the predicted uptake pathway for the cargo-loaded nanocarrier in Figure 4.4.5C illustrates the apparent advantages of time-resolved fluorescence detection in living cells for an in-depth understanding of the occurring

biomolecular interactions: Cluster-FLIM in combination with a molecular rotor-based sensor design allows to identify biological interaction partners. Based on this information, it is also capable of identifying the nanocarrier uptake pathway and its kinetics.

Protein corona effect on cellular uptake

Non-specific protein adsorption in nanoparticulate drug delivery, also called protein corona formation, is a regularly observed phenomenon and commonly alters the transport capabilities and targeting specificity of nanocarrier systems.[281-283] For this reason, I investigated the interaction of CMS-ICC with *fetal bovine serum* (FBS) or *bovine serum albumin* (BSA) as the major serum protein might affect cellular uptake in NHK, in particular the binding to SR [300] According to Section 4.3.2 BSA binds with an apparent binding affinity of 400 ± 200 µM to CMS-ICC (Figure 4.3.12). Repeating the experiment in the FLIM setup (Figure 4.4.6A/B) reveals an apparent binding affinity of 310 ± 70 µM. Incubation of CMS-ICC with 7.5 % FBS (~ 25 – 40 µM BSA)[340] results in a change of the CMS-ICC fluorescence decay trace (Figure 4.4.6A), comparable to 100 µM BSA (displayed in Figure 4.4.6B). This change indicates that besides BSA, other serum constituents absorb to the CMS-nanocarrier.

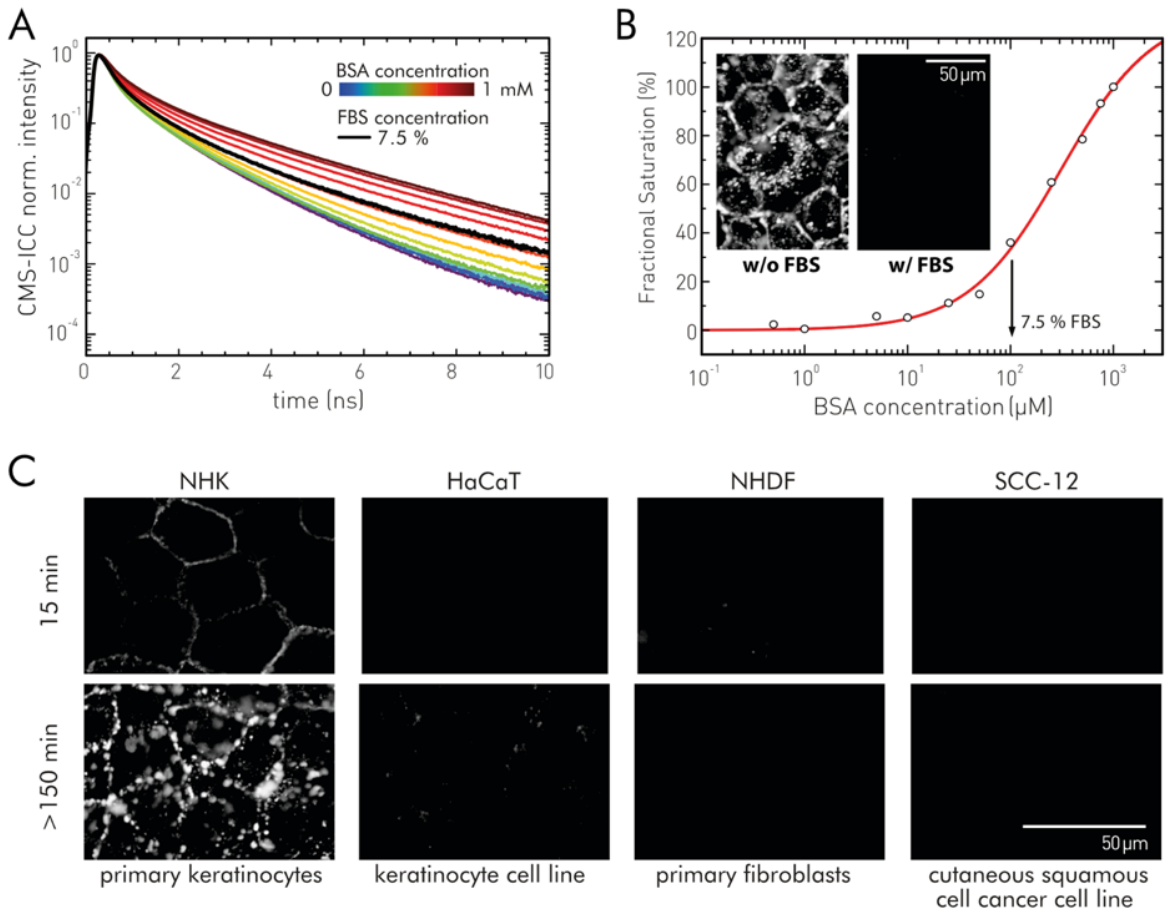

Figure 4.4.6: Protein corona effect on cellular uptake of CMS-ICC. **A** CMS-ICC fluorescence decay curves recorded by FLIM as function of BSA concentration and for 7.5 % FBS in PBS at 20 °C (left). BSA-binding to CMS-ICC (0.5 µM) as fractional saturation vs. BSA concentration (right). The half-maximum binding concentration was determined to be 310 ± 70 µM with n = 0.95 ± 0.09. Inset: comparison of CMS-ICC uptake by NHK cells after a 180-minute incubation with CMS-ICC at 37 °C in whole-cell medium

(KGM) w/o and w/ 7.5 % FBS. **B** Comparison of CMS-ICC uptake towards different cutaneous cell types. Intensity images are shown after 15 minutes and after 150 minutes incubation with CMS-ICC in the respective cell medium at 37 °C. From left to the right: Primary keratinocytes (NHK) w/o 7.5 % FBS, keratinocyte cell line (HaCaT) w/ 7.5 % FBS, primary normal human dermal fibroblasts (NHDF) w/ 7.5 % FBS, cutaneous squamous cell carcinoma cell line (SCC-12) w/ 7.5 % FBS. Experimental conditions: CMS-ICC with λ_{ex} = 530 nm, λ_{em} = 545 – 600 nm; objective: 60X.

The BSA corona formation has a direct impact on the CMS-ICC uptake behavior of NHK cells as addition of 7.5 % FBS to the cell medium inhibits the uptake (inlay, Figure 4.4.6B). The result is in line with previous uptake experiments of a CMS-ICC nanocarrier by HaCaT cells (immortalized human keratinocytes) showing only marginal uptake for CMS-ICC in the FBS-supplemented cell medium.[156] Like HaCaT cells, other cutaneous cells such as fibroblasts and cutaneous squamous cell carcinoma cells typically cultured in FBS-supplemented medium, likewise do not show any CMS-uptake (Figure 4.4.6C).

Comparison of CMS-ICC's FLS in NHK and SCC-25

To investigate the analytical potential of Cluster-FLIM in combination with the CMS-ICC molecular rotor sensor design, I quantified the differences between the interaction of CMS-ICC in NHK and human squamous cell carcinoma cells (SCC-25, originated from human tongue). To compare the cellular interactome of CMS-ICC, I recorded an incubation time series (15, 180, 270, 360 min, 37 °C) with SCC-25 cells and analyzed the FLIM data stack by Cluster-FLIM. Figure 4.4.7 visualizes the differences between both cell types. Fluorescence intensity images (Figure 4.4.7A) of both time series already show variations between the cellular nanocarrier localization in NHK and SCC-25 cells at all incubation times. Especially in the 15-minute incubation, the lack of strong membrane interaction, as observed for NHK, constitutes a major difference in the cellular uptake process of both cell types. By applying the Cluster-FLIM analysis and false-coloring, the FLIM images a substantially more detailed picture becomes visible (Figure 4.4.7B,C). Again, Cluster-FLIM can identify three different FLSs in the SCC-25 cells. For a direct comparison, I selected the same color code as for the NHKs analysis, that is, cyan for the fast, yellow for the intermediate and red for the slowest fluorescence lifetime signature (FLS, Figure 4.4.7D,E). The FLSs of CMS-ICC in SCC-25 are generally slower compared to NHKs, which indicates cell specific differences in the uptake mechanism and thus in the occurring interactions.

The SCC-25 tumor cell line displays two significant differences compared to NHK: First, as already seen in the intensity based monochromatic images, no early membrane interaction of the nanocarrier by the absence of a membrane localization and the missing membrane based cyan cluster (Figure 4.4.7B, 15 min), and, secondly, a missing lysosomal trapping defined by a single FLS as observed in NHK. In SCC-25, divergent cytoplasmic pathways seem to be present simultaneously characterized by different CMS interactions at longer incubation times. The different interactions of the CMS-nanocarrier can be directly quantified using the fractional cluster appearance in % (Figure 4.4.7D,E). A homogenous appearance of all three FLIM clusters to about 20 – 40 % characterize

the intracellular fate in the tumor cell line after 360 min incubation; in contrast to the 99 % appearance of the red cluster indicative for a lysosomal localization in NHK cells. The observed increase of the two slower FLS (cyan, yellow) at the expense of the red cluster suggests that lysosomal escape occurs related with an altered nanocarrier uptake, transport and intracellular localization.

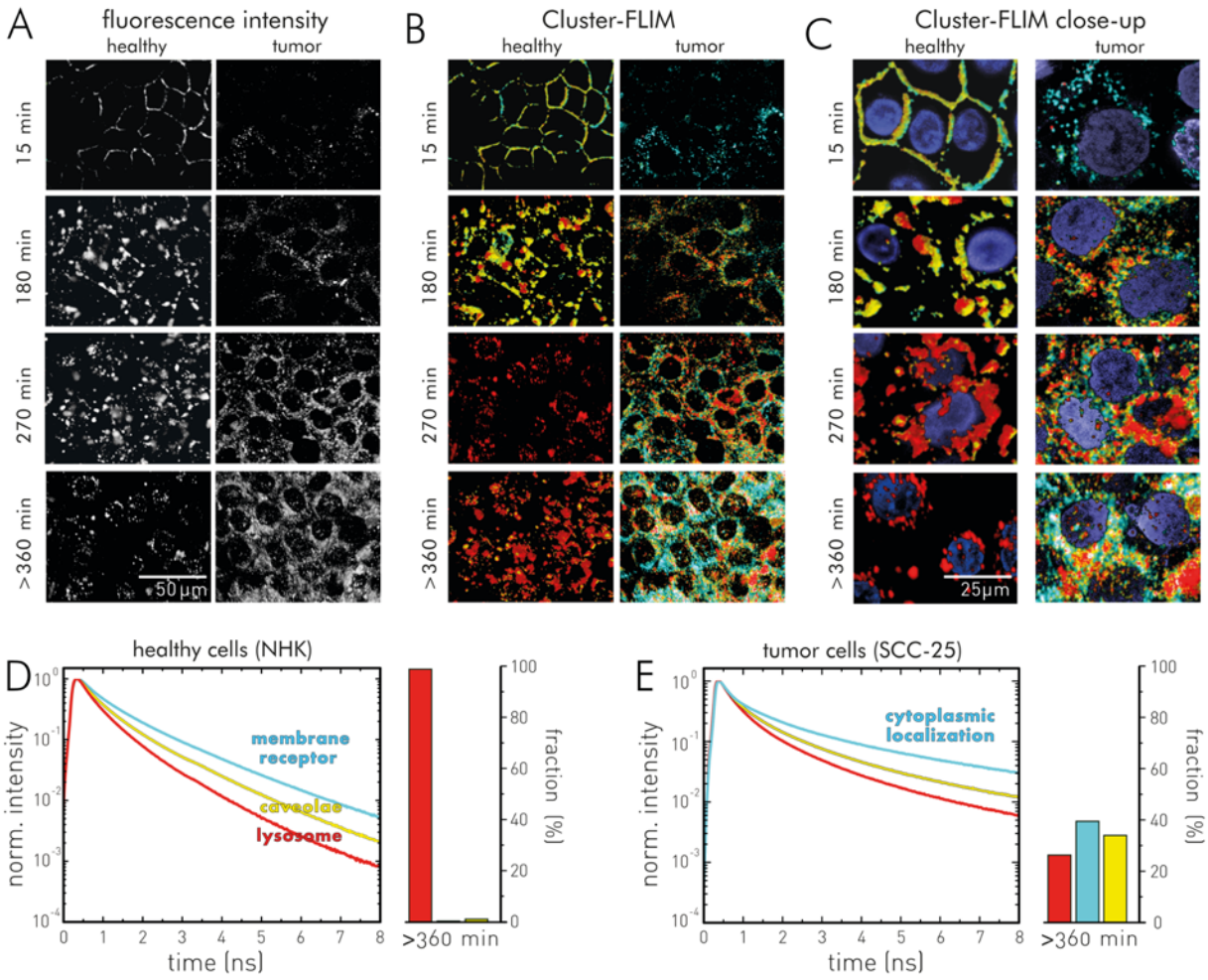

Figure 4.4.7: Cell specific uptake pathways of CMS nanocarrier into NHK (healthy) and SCC-25 (tumor) investigated by Cluster-FLIM. **A** Fluorescence intensity-based confocal microscopy images of CMS-ICC uptake into NHK and SCC25 cells after indicated incubation times (15 min, 180 min, 270 min and >360 min). **B** Correspondent Cluster-FLIM images of areas shown in (A). **C** Close up: subcellular resolution of the single cells shown in (B). FLIM images are merged with the DAPI channel, showing cell nuclei (blue). **D/E** Left: Identified fluorescence lifetime signatures of CMS-ICC nanocarrier uptake by NHK (D) and SCC-25 (E) cells. Right: Relative cluster appearance after 360 min for NHK (D) and SCC-25 (E). Modified reprints from Brodwolf et al., [44] Copyright 2020, with the kind permission of Theranostics.

Discussion

In this section, I reported on a new concept for the identification and visualization of (intra)cellular interactions of a fluorescently tagged CMS-nanocarrier by using an interaction-sensitive fluorescence lifetime probe and a cluster-based FLIM analysis approach. Cluster-FLIM identifies multiple fluorescence decays associated with unknown interactions of a fluorescently tagged molecule by using a multivariate clustering method to analyze and group the pixel-based decay traces into clusters. To use the capabilities of Cluster-FLIM a fluorescence probe with sensitive fluorescence lifetime is necessary. Here, the interaction-sensitive fluorescence lifetime probe ICC, an FMR, is attached to the dendritic core of the CMS-NC. This approach successfully identified and simultaneously visualized multiple interactions of the nanocarrier system with cellular constituents that are not known in advance. In contrast, the commonly available spectral and intensity fluorescence-based techniques, which investigate biomolecular interactions in living cells, are limited by monitoring only predetermined interactions of known interaction partners by tagging both partners fluorescently.[341]

Compared to these techniques, the advantage of (Cluster-)FLIM in combination with an application-specific fluorescence lifetime probe is the FLS-based identification of an interaction or environmental variation. The identification allows a direct tempo-spatial visualization of different and simultaneously occurring biomolecular interactions by false-color coding. As Cluster-FLIM uses no decay fitting algorithm, individual fluorescence decay curves, even complex multi-exponential fluorescence decays, often observed in live-cell experiments, become resolvable at low count rates. This allows the local identification and separation of the triggering interaction or altered environment that modifies the fluorescence lifetime.

Section 4.4.1 describes the investigation of intracellular interactions of a dendritic CMS-NC during its uptake into NHK cells. The interaction-sensitive fluorescence sensor design increases the sensitivity to biomolecular interactions. It suppresses the viscosity effects of the surrounding solutions to a FMR probe[66] by attaching the ICC probe to the dendritic core of the CMS-nanocarrier (see Section 4.2.3). The inner and outer shell branches shield ICC from the intracellular viscosity. At the same time they promote specificity and sensitivity to certain biomolecular interactions of the NP via triggering different steric restrictions to ICC's intramolecular twisting motion. This indirect mediation between the NP interaction and ICC's intramolecular rotation is probably caused by a compression or squeezing of the shell branches due to the biomolecular interaction.[25, 258] Utilizing this effect constitutes a novel implementation to existing fluorescent "molecular-rotor"-based approaches.[65, 342] For the case of CMS-nanocarriers and NHK cells, three distinct biomolecular interaction modes, defined by three FLSs of CMS-ICC, were obtained and assigned to the respective biological interaction with (I) scavenger receptors at the cell surface, (II) constituents of caveolae and caveolar vesicles in the cell membrane and lumen, and (III) constituents of lysosomes. The assignment was facilitated by a strategy (Figure 4.4.3A) that combined Cluster-FLIM with co-localization and pharmacological inhibition studies to identify the biomolecular interaction causing the FLS.

These new results on the biomolecular interactions of the CMS-NC in dermal NHK cells may lead to a more mechanistic model of the link between nanocarrier design and biological interactions which currently clearly limits the potential of targeting nanomedicine in topical and general applications.[283] Such advanced models are necessary to improve targeting nanomedicine in general by more rational nanocarrier designs either for targeting specific cellular pathways or specific cells. Without knowing the precise biological interactions of a nanocarrier system and its relevant uptake pathway, successful targeting can hardly be achieved.[283]

The benefit of applying the combination of the FMR-based fluorescence lifetime sensor design, Custer-FLIM, and the pharmacological/co-localization interaction assignment is not only the identification of different biomolecular interactions of the CMS-NC, but also the quantification of the relative frequency of these interactions in a spatiotemporal manner. With this approach, it is possible to characterize the cellular uptake path(s) of the dendritic nanocarrier at a level of detail that allows to resolve the uptake kinetics (Figure 4.4.5C). In the case of the uptake of CMS-nanocarrier by NHK cells, a SR- and lipid raft/caveolae-mediated uptake converging with the endolysosomal pathway was identified. The uptake of the CMS nanocarrier by only a single relevant cell pathway in NHK was a somewhat surprising observation,[174] but opens the rare opportunity to apply this CMS-nanocarrier architecture to specific targeting of keratinocytes via SR. The keratinocyte SR-A (MARCO) was recently found to be involved in epithelial absorption and infection of Herpes simplex virus type 1,[343] indicating a potential therapeutic target. Furthermore, the protein corona effect on SR-directed uptake, as observed in BSA and FBS containing media, will be most important in systemic applications of the CMS-nanocarrier, but less important in topical therapy of skin because of the absence of any vasculature and therefore the absence of serum proteins. The total loss of SR-specificity on CMS-nanocarrier uptake in serum is a good example of how a biological environment can alter or even abrogate specific targeting and, for the case at hand, even completely inhibit the uptake of a nanomedicine.

The ability to obtain detailed real-time kinetics of the caveolae-mediated uptake pathway with a cellular fate that exclusively leads to lysosomal localization may also pave the way for advanced targeted drug release, facilitated by pH-responsive CMS-architectures, allowing for a lysosomal-targeted drug delivery.[275, 344] However, a caveolae-mediated endocytosis is usually of special interest in drug delivery, because of its potential lysosomal escape facilitating a protective effect against lysosomal degradation.[345] The insights into the cellular uptake pathway of the dendritic CMS-nanocarrier into NHK expands the knowledge on nanoparticle uptake processes, which are heterogenous and not yet fully clarified.[346]

The novel experimental and analytical approach may provide more information on molecular details of a given cellular pathway, e.g., by using CMS-ICC as a nano-sized sensor for SR/caveolae-mediated transport. Caveolae-mediated uptake is a highly regulated process and involves complex cell signaling,[333, 347-348] resulting in relatively long uptake half-lives, like for the prototypical caveolae-

mediated uptake of the SV40 virus (90 min).[345] For CMS-ICC, I determined an internalization of CMS-ICC via a SR and lipid raft/caveolae-mediated pathway with a half-life of around 60 minutes. In addition to that, I was able to resolve the intermediate steps by applying a kinetic model. The steps are a fast capture ($\tau \sim 8$ min) of CMS-ICC by caveolae in the cell membrane from its SR-mediated localization in caveolae-devoid membrane areas, including a back-reaction with a time constant of about 30 minutes, and lysosomal uptake with a time constant of $\sim$ 107 min. With regard to targeted drug delivery, the non-covalently loaded hydrophobic fluorescent cargo bodipy, transported by the CMS-nanocarrier, enters the cells by an unspecific and energy-independent mechanism as soon as the nanocarrier interacts with the cell membrane.

By comparing the CMS-ICC uptake of NHK to SCC-25 tumor cells, I identified differences in the uptake characteristics and interaction modes. Most important is the homogenous occurrence of multiple interaction patterns of CMS-ICC at later incubation times in SCC-25. This is opposed to the single lysosomal interaction pattern observed for NHK. This result suggests that lysosomal escape occurs in the tumor cell line or that the lysosomal pathway is missing completely. The quantitative assessment of the intracellular fate of the CMS-NC as shown in Figure 4.4.7D,E is compatible with automated downstream data processing by bioinformatics tools[349] and can be potentially applied in FLIM-based high content screening. The observed distinct differences in cellular uptake between healthy and related tumor cells could be an important information for future nanocarrier designs aiming for cell specific action modes, trigger and drug release mechanisms.[32, 350]

4.4.2 CMS uptake and release mechanisms in dendritic Langerhans-like cells

Dendritic core-multishell nanocarriers (CMS-NCs) have a penetration-enhancing effect in cutaneous drug delivery. Topically administered drugs pass more efficiently through the dermal barrier into deeper layers of the viable epidermis (VE) when loaded onto CMS-NC. In contrast, the transporting nanocarrier accumulates in layers of the *stratum corneum* (SC), far above the VE and its dense tight junction barrier. This behavior has been demonstrated in numerous *in vitro* and *ex vivo* studies on human, murine, and reconstructed model skin.[151, 170, 173] A different behavior is observed in damaged and diseased skin, where the amount and penetration depth of CMS-NC into the VE is remarkably increased due to barrier damages in the SC.[130, 170, 211, 232] Interestingly enough, deeper penetration of CMS-NC into the VE was also observed after prolonged exposure[130, 170, 351] and selectively in healthy skin[352-353].

In a recent study on CMS-NC penetration behavior in human *ex-vivo* skin, a preferential accumulation of CMS-NC in CD1a positive cells (Langerhans cells (LC)) was observed.[169] The cellular uptake was only detectable to a small extent, but in a reproducible manner. CMS-NC uptake in CD1a positive cells was found especially in areas with focal aggregation of hair follicles and furrows. In this case, hair follicles play an important role as reservoir and interface for exchange between nanocarrier depots, the upper hair follicle compartments and associated immune cell populations[193, 354]. Thus, a probable scenario to explain these observations is the involvement of epidermal and dermal dendritic cells, that may interact with the CMS-NCs once they have manage to pass to the SC-VE interface; especially if one considers the ability of epidermal LCs to elongate their dendrites through the tight junction barrier in order to screen the external environment for antigens (Figure 4.4.8A).[355] First results of a cell culture study suggest that CMS-NC does not induce cytotoxicity, genotoxicity or increased ROS levels.[174] However, an precise understanding of the interaction between CMS-NC and components of the immune system is necessary and requires an in-depth investigation, especially with regard to biodistribution and biocompatibility of CMS nanocarriers *in vivo* and potentially induced, still unknown, immunological responses.

After having investigated the interaction of CMS-NC with NHK cells in the last section, I will now focus on the interaction with dendritic cells of the skin. The experiments were the result of a collaboration between the groups of Prof. Alexiev (Freie Universität Berlin, Germany), Prof. Vogt (Charité – Universitätsmedizin Berlin, Germany) and Prof. Kleuser (Universität Potsdam/Freie Universität Berlin, Germany). First investigations on the uptake behavior of CMS-ICC by a dendritic cell line have been conducted in my master's thesis (Volz, FU-Berlin, 2015). The results presented here were partly published in Biomolecules (Edlich et al., 2018, Ref. 174) and in the Journal of Controlled Release (Frombach et al., 2019, Ref. 169). A further manuscript on these experiments is in preparation. Hence, the next paragraph relies on my contribution to these papers.

The strategy for the following characterization of the interaction between CMS-NC and CD1a positive cells will be described first. To obtain a conclusive picture of the cellular internalization of CMS-NC by epidermal CD1a+ cells and possible interaction mechanisms, two experimental approaches are pursued and compared (Figure 4.4.8B). First, epidermal cells isolated after topical application of CMS-ICC to human skin explants are investigated (cf. Ref. 169). In this procedure, the identity of the isolated cells is ensured by additional CD1a-immunostaining. Cellular CMS-ICC uptake, distribution, and release into and from dendritic cells are demonstrated by live-cell experiments on the XS52 LC-like cell line. Both approaches use dual-color fluorescence lifetime imaging microscopy (Section 3.3.4) in combination with Cluster-FLIM (Section 3.4.2) to characterize and visualize the CMS-NC interaction and its spatial distribution on a single-cell level.

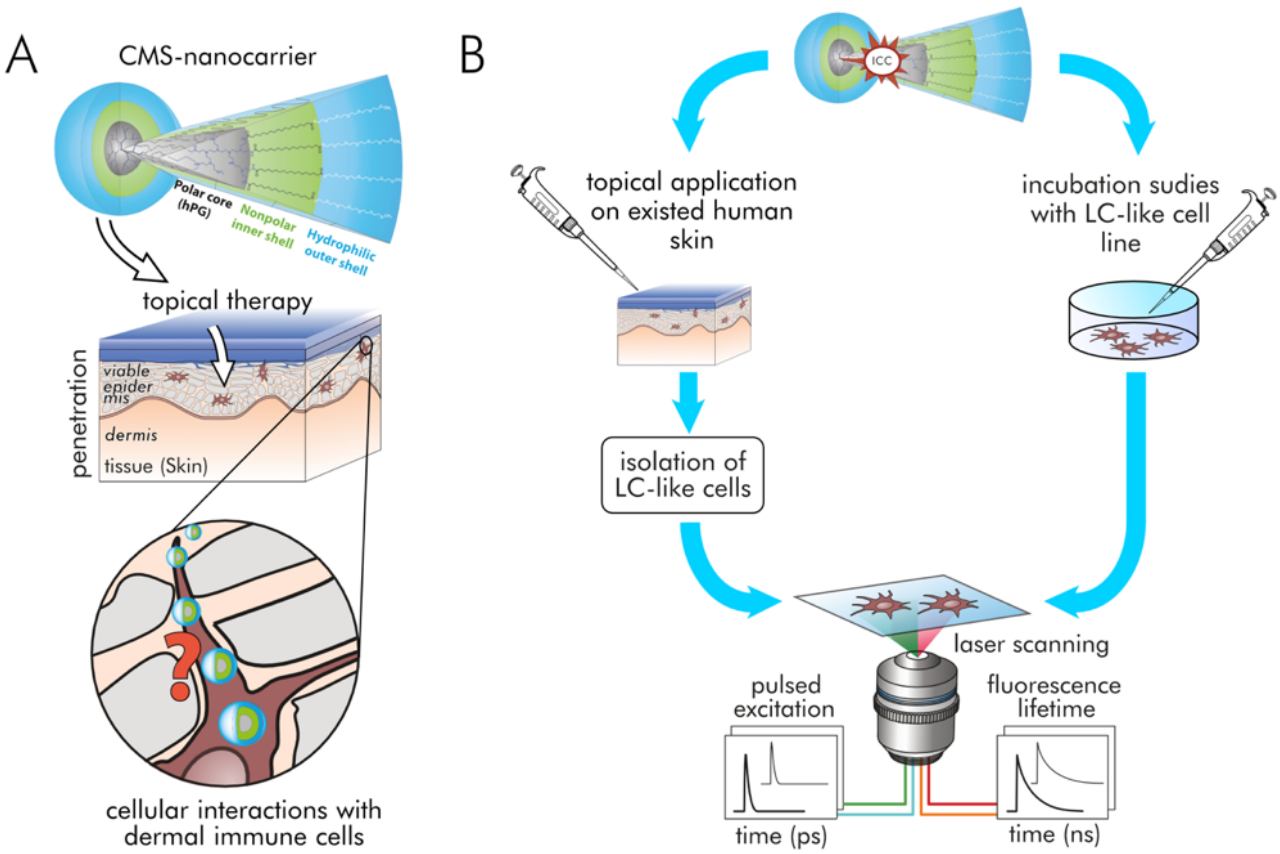

Figure 4.4.8: A Scheme of CMS-nanocarrier, its application in topical drug delivery, and possible uptake path by dermal immune cells. **B** Experimental designs for FLIM investigations: 1. LC-like immune cells originating from existed (*in-vivo*) human skin tissue after topical treatment with CMS-ICC. 2. *Ex-vivo* live-cell uptake studies in a LC-like XS52 cell line.

CMS-ICC uptake in human epidermal cells

First, the cellular uptake of CMS-ICC by epidermal cells after topical application will be investigated, which has already been observed by flow cytometry.[169] The flow cytometry experiments performed by Janna Frombach (Prof. Vogt's group, Charité – Universitätsmedizin Berlin, Germany) show that a small number of CD1a positive and negative cells take up the nanomaterial (Figure 4.4.9C). My goal now is a clear identification of CMS-ICC in these cells on a single cell level via the fluorescence lifetime signatures (FLSs) of the ICC FMR probe. For this purpose, CMS-ICC was applied topically for 16 h on healthy human full-thickness *ex-vivo* skin. Figure 4.4.9A shows a FLIM image of a corresponding cryosection of the treated tissue. The typical CMS-ICC distribution in the SC, characterized by two FLS (cyan & green), is clearly visible. In the VE, CD1a antibody staining visualizes LC cells (red). The CD1a$^+$ cells are also present in the border region of the SC-VE where a possible interaction with the CMS-ICC could take place. In order to study the VE cells dissociated from their cell network, they were isolated, fixated and subjected to FLIM.

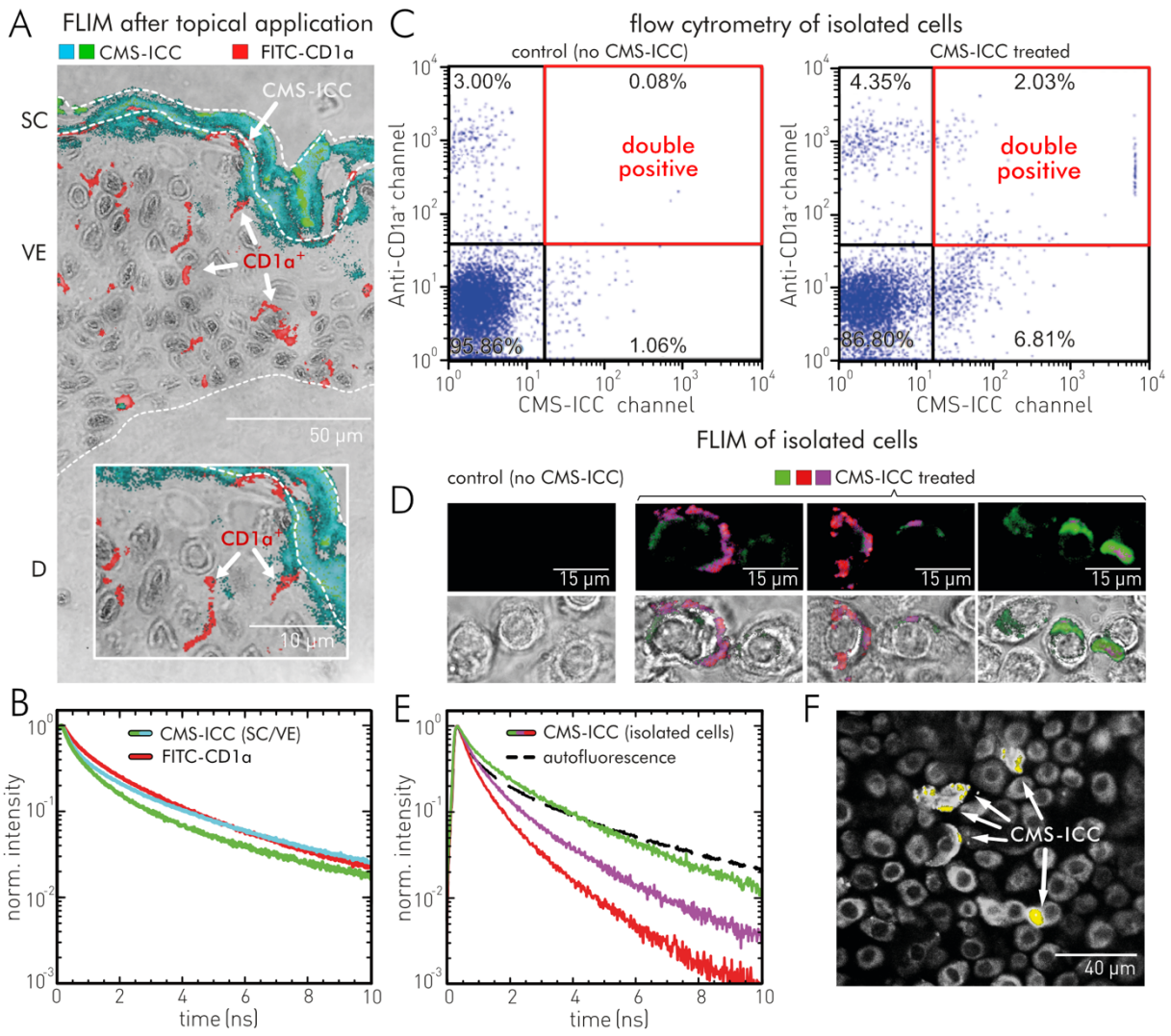

Figure 4.4.9: Identification of CMS-ICC in cells isolated from excised *ex-vivo* human skin after a topical treatment with CMS-ICC. **A** CD1a antibody-stained cryosections of excised human skin after topical application with CMS-ICC for 16 h. The shown picture is an overlay of a monochromatic bright-field image and Cluster-FLIM images of the CD1a-FITC (red) and CMS-ICC (green, cyan)

detection channels. The inlay shows a magnification to the interface between the *stratum corneum* (SC) and viable epidermis (VE). **B** Fluorescence lifetime signatures of CMS-ICC and CD1a-FITC. **C** Flow cytometry analyses of CMS-ICC and CD1a-APC detection channel. Left: isolated dermal cells originating from tissue topically treated with a CMS-ICC solution for 16h (right). Right: control experiment with topically applied PBS, pH 7.4 (left, control). Flow cytometry experiments were conducted by Janna Frombach. **D** Epidermal cells isolated from skin tissue after topical application with CMS-ICC (16 h incubation), containing CMS-ICC and control. Top: Cluster-FLIM images of CMS-ICC fluorescence, color code according to the three identified fluorescence lifetime signatures (red, magenta, green) with a threshold of 100 counts/pixel. Bottom: Overlay of bright-field and Cluster-FLIM-image. Negative control group shows no autofluorescence above the threshold of 100 counts/pixel. **E** Fluorescence lifetime signatures of CMS-ICC in isolated epidermal cells. **F** Confocal fluorescence intensity image of with no intensity threshold. All cells are visualized by their autofluorescence, CMS-ICC containing cells show intensities over 100 counts/pixel (yellow). Three independent experiments show that 4 – 8 % of the isolated cells are CMS-ICC positive. Experimental conditions: CMS-ICC excitation with λ_{ex} = 530 nm; λ_{em} > 575 nm; FITC-CD1a excitation with λ_{ex} = 488 nm, λ_{em} = 500 – 550 nm; objective: 60x.

The FLIM-images in Figure 4.4.9D shows that epidermal cells internalize CMS-ICC after previous topical application. A cluster FLIM analysis revealed three different interaction modes of CMS-ICC within the isolated cells, which are identified by their different FLS, color-coded in green, magenta, and red (Figure 4.4.9D,E). The cellular heterogeneity in the observation of the different CMS-ICC fluorescence lifetimes could be cell-specific or due to different intracellular localizations. Only relatively low intracellular autofluorescence intensities could be detected compared to intracellular CMS-ICC fluorescence (Figure 4.4.9D). The fluorescence decay characteristics of the autofluorescence differs from CMS-ICC (Figure 4.4.9E). These differences in the cellular autofluorescence can be utilized to visualize all isolated skin cells in the FOV (Figure 4.4.9F, white). This allows to quantify the proportion of cells that have internalized CMS-ICC. In three conducted FLIM experiments, the percentage of cellular CMS-NC uptake was between 4 and 8 %.

CMS-ICC identification in isolated epidermal CD1a$^+$-cells

Next, I set out to identify the LCs (CD1a$^+$ cells) among the epidermal cells that internalized the CMS-NC. To accomplish this goal, I utilized dual-color FLIM in order to simultaneously detect the fluorescence lifetime of CMS-ICC and of an APC-tagged secondary antibody for CD1a (APC-CD1a). Figure 4.4.10A,B show a dual-color FLIM experiment as an example for the presence and the absence of CMS-NC uptake by CD1a$^+$ cells. In the center of the image, I observed co-localization of CMS-ICC and APC-CD1a. Out of the three experiments, only one displayed CMS-ICC within CD1a$^+$ cells (4.2.10A,B), highlighting the low percentage of CMS-containing LCs among all cells. Based on the three experiments, the estimated percentage of double positive cells is less than 1 % of the total cell number in the FLIM images. Normalizing the value of about 1 % double positive cells to the number of all cells containing CMS-ICC would correspond to a presence of about 12 % LCs among the cells that have internalized CMS-ICC.

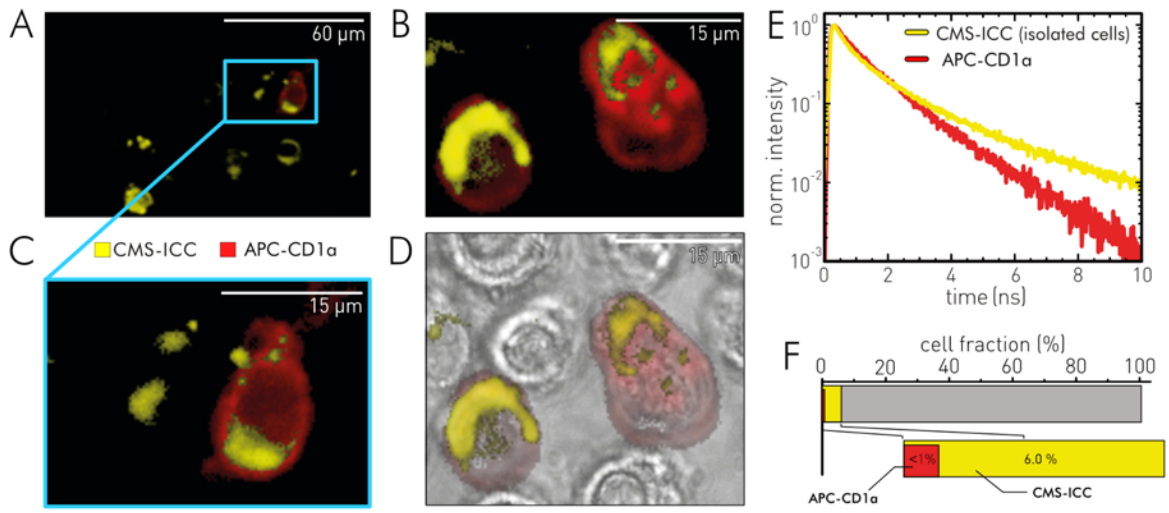

Figure 4.4.10: Identification of CMS-ICC in cells isolated from excised *ex-vivo* human skin after a topical treatment with CMS-ICC. **A,B,C** CD1a antibody-stained epidermal cells isolated from ex-vivo skin after topical application with CMS-ICC (16h incubation). double positive cells (red: APC-CD1a, yellow: CMS-ICC). **E** Fluorescence lifetime signatures of CMS-ICC and APC-CD1a antibody (APC-CD1a) observed in A,B. **D** Monochromatic bright-field overlay with fluorescence image in B. **F** Estimated percental fraction of CMS-ICC positive cells and of double positive cells (APC-CD1a and CMS-ICC). Experimental conditions: CMS-ICC excitation with λ_{ex} = 530 nm; λ_{em} > 575 nm; APC-CD1a excitation with λ_{ex} = 640 nm, λ_{em} > 665 nm; objective: 60x.

CMS-ICC uptake by a LC-like dendritic cells line XS52

After the uptake of CMS-ICC in epidermal LCs has been established, the uptake and release dynamics of CMS-ICC in the LC-like dendritic cell line XS52 (provided by Prof. Kleuser's lab, Universität Potsdam/Freie Universität Berlin, Germany) were investigated. Therefore, incubation series with the nanocarrier were conducted and recorded, using live-cell FLIM. I analyzed the distribution and local interactions of CMS-ICC during the cellular uptake process as a function of nanocarrier incubation time. For a direct comparison of the Cluster-FLIM analyses, all experiments were performed under the same experimental conditions. In contrast to my previous studies on the uptake of CMS-ICC - XS52, I have now quantified the uptake at the single cell level. For this purpose, each cell was identified by eye and a respective spatial pixel mask was generated to select all pixels belonging to an individual cell.

The analysis of the FLIM-images obtained in the time series (0.0, 0.5, 1.5, 3.0, and 5.0 h incubation at 37 °C) revealed four distinct fluorescence lifetimes signatures, three for CMS-ICC (colored magenta, yellow, red, Figure 4.4.11A,C) and one for the background autofluorescence (blue) and thus allowed a clear-cut discrimination between fluorescence lifetimes indicative for CMS-ICC fluorescence and cellular autofluorescence. An evaluation of the Cluster-FLIM results shows a substantial CMS-ICC internalization by XS52 cells already at 30 minutes incubation time (Figure 4.4.11A,B). At this time, only one CMS-ICC fluorescent species is present as evidenced by the homogeneous appearance of the magenta-colored fluorescence lifetime signature (~77 % of total fluorescence intensity). This observation indicates a homogeneous intracellular environment of CMS-ICC at this early stage of uptake (Figure 4.4.11B). Due to the general low CMS-ICC intensity at this stage, a high

fraction of autofluorescence (~23 % of total fluorescence intensity) can also be observed within the XS52 cells. Please note the magenta-colored fluorescence lifetime signature in XS52 cells matches the fluorescence lifetime of CMS-ICC in isolated epidermal LCs from skin tissue (dashed black line, Figure 4.4.11C).

With further incubation (1.5 h), a second fluorescence lifetime signature (yellow-colored) of CMS-ICC appears (Figure 4.4.11A). This CMS-ICC species exhibits a slower fluorescence decay (Figure 4.4.11C) compared to the magenta-colored FLS. I attribute this change in CMS-ICC's fluorescence lifetime to an altered intracellular environment of the nanocarrier, indicating a subsequent step in the CMS-ICC uptake pathway. For extended incubation times (3.0 h and 5.0 h), I observed another change of the CMS-ICC fluorescence lifetime, that leads to the appearance of a third FLS (red-colored, Figure 4.4.11A). This signature displays the fastest fluorescence decay observed for CMS-ICC in XS52 cells (Figure 4.4.11C). The contribution of this red FLS to the total fluorescence is about 9 %.

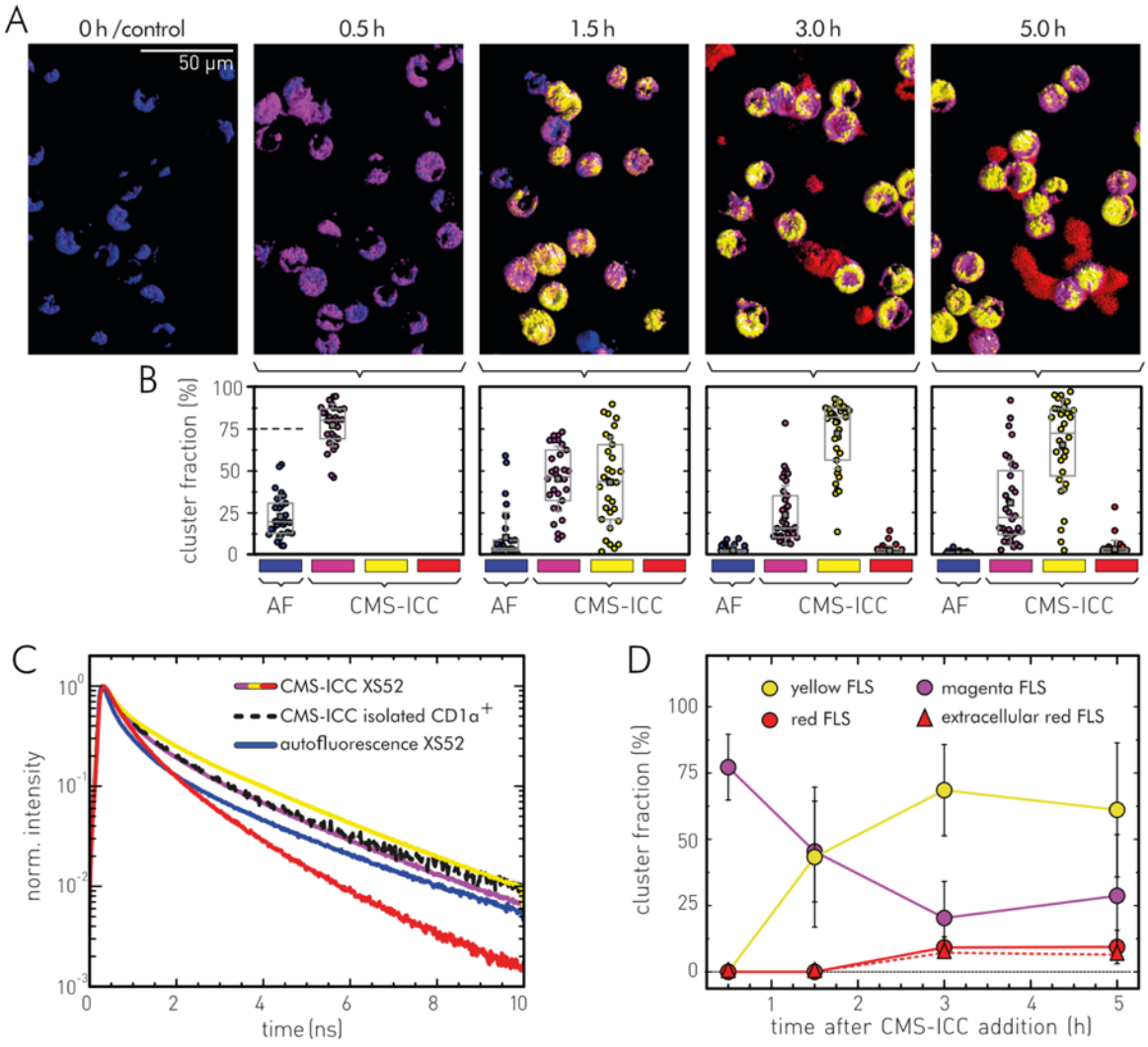

Figure 4.4.11: Time-dependent uptake of CMS-ICC by XS52 cells. **A** Cluster-FLIM images of time-dependent CMS-ICC uptake dynamics in XS52 after 0.0, 0.5, 1.5, 3, 5 hours incubation (50 µg/ml) at 37 °C in complete cell medium. Four different fluorescence lifetime signatures are identified, three for CMS-ICC (magenta, yellow, red) and one for the autofluorescence (AF, blue). **B** Single

cell analysis of the cluster fractions from the four clusters. Each data point indicates the relative cluster concentration in an individual cell. **C** Fluorescence lifetime signatures of the three clusters from CMS-ICC and the autofluorescence cluster in XS52 cells. For comparison, the CMS-ICC fluorescence lifetime signature in cutaneous LCs (see Figure 4.4.10E) is shown in black (dashed). **D** Cluster-resolved uptake kinetics of CMS-ICC in XS52 cells. The values reflect the mean relative cluster fraction obtained from (B), color coding according to the fluorescence lifetime decay (FLS) in (C). Experimental conditions: CMS-ICC excitation with λ_{ex} = 530 nm, λ_{em} > 575 nm; objective: 60x.

In addition to its intracellular occurrence, I detected the red FLS also extracellularly as cellular "foot-print"-like structures on the glass bottom surface of the culture dish (Figure 4.4.11A), suggesting that excreted CMS-ICC sticks to the surface beneath the cells. Moreover, this observation indicates a link between the red FLS that is observed within the XS52 cells to a potential cellular release of CMS-ICC. To obtain a more detailed insight into the uptake process, I further quantified the occurring FLSs as a function of time. The temporal change of the relative contributions of the three different CMS-ICC species with increasing incubation time indicates distinct intracellular processes. Figure 4.4.11D shows their temporal evolution: 1) the transition of the initial uptake state of CMS-ICC, characterized by the magenta-colored fluorescence lifetime, to a subsequent uptake stage characterized by the yellow-colored fluorescence lifetime, and 2) the appearance of a late intracellular stage characterized by the red-colored FLS of CMS-ICC.

CMS-ICC fate and release from the LC-like dendritic cells line XS52

A further experiment on the cellular uptake at a 10-fold CMS-ICC concentration (500 µg/ml) points to a correlation between the intracellular occurrence of the CMS-ICC species, defined by the red-colored FLS, and a potential CMS-ICC excretion (Figure 4.4.12A). The experiment shows that at this concentration, the red-colored FLS appeared at intracellular, high intensity spots already after 2 h incubation. The same FLS was observed predominantly as extracellular "foot-prints" of the CMS-ICC, in particular at longer incubation times with the 1-fold CMS-NC concentration (50 µg/ml, Figure 4.4.11A). These intracellular hot spot-like structures indicate the localization of CMS-ICC in distinct compartments in the cytoplasm.

For the 10-fold CMS-ICC concentration of 500 µg/ml, I observed an average red FLIM-cluster fraction of about 25 % (Figure 4.4.12A). However, there are also several cells with contributions above 30 % (dashed ellipsoid, Figure 4.4.12A) and some cells even exhibit relative contributions of more than 50 %. One can speculate that these hot spot-like structures indicate compartments from where a cellular release of the CMS-NC occurs. Importantly, I also observed the appearance of some "foot-print"-like structures (red-colored) in the extracellular space (Figure 4.4.12C) at this concentration. These look similar to the ones shown in Figure 4.4.11D (time series of CMS-NC uptake). For the reason of a better comparison, Figure 4.4.12B shows a magnification of these extracellular structures. The intracellular occurrence of the red-colored FLS seems to be an indicator of a pre-release state of the nanocarrier.

Before I continue with the cellular release of the CMS-NC by the XS52 cells, I will first describe its cellular fate. Having shown in section 4.3.1 that CMS-NC accumulates in the lysosomes of NHK cells, it is reasonable to assume that this behavior could also apply to the XS52 cell line. This hypothesis is also supported by numerous studies that have revealed intracellular accumulation of various nanoparticles in dendritic cells.[356-358] For this reason, I have performed, again, co-localization experiments between the internalized CMS-ICC and fluorescently stained lysosomes. Fast sequential confocal FLIM measurements of CMS-ICC and LysoTracker in the respective spectral windows clearly indicated a co-localization between lysosomal compartments and CMS-ICC (Figure 4.4.12C). I determined Manders' colocalization coefficients[206] M_1 and M_2 for both spectral channels (Lysotracker and CMS-ICC), quantifying the fraction of overlap of each channel in respect to the other. M_1 and M_2 can range from 0 (no overlap) to 1 (total overlap). Coefficients of $M_1 = 0.86$ and $M_2 = 0.92$ were determined, indicating high co-localization. This result is confirmed by the obtained Pearson's correlation coefficient of 0.70 (-1: anticorrelated, 1: correlated).[174]

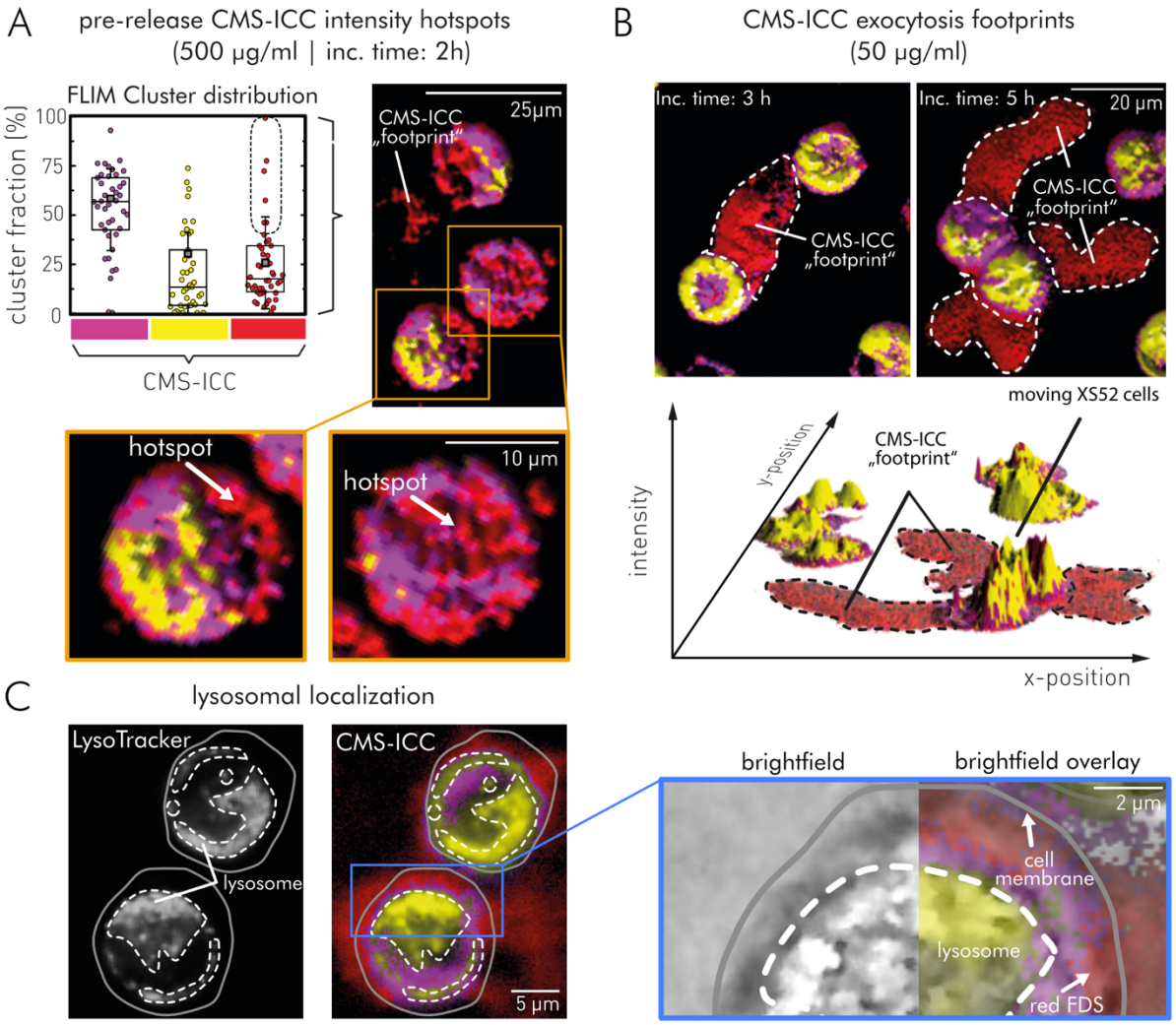

Figure 4.4.12: Correlation of FLS of CMS-ICC in XS52 cells to lysosomal localizations and events in exocytosis. **A** Cluster-FLIM analysis of nanocarrier uptake by XS52 at high CMS-ICC concentrations (10-fold, 500 µg/ml) after for 2 h at 37 ° C in complete cell medium. **B** Localization of released CMS-ICC from XS52 cells after 3h (left) and 5h (right) incubation and respective FLIM cluster assignment. Footprint-like CMS-ICC fluorescence traces (red-colored) of moving XS52 on the glass surface. Bottom: 3D visualization

(x,y: spatial coordinates, z: fluorescence intensity, color: based on FLS). **C** Comparison of LysoTracker and CMS-ICC localization after 3h incubation (50 µg/ml). Left: LysoTracker, Right: CMS-ICC. The area indicated with white hatched lines represents the localization of LysoTracker, which co-localizes with the yellow FLS of CMS-ICC. They gray lines indicates the cell membrane. Experimental conditions: CMS-ICC excitation with λ_{ex} = 530 nm; λ_{em} > 575 nm; LysoTracker excitation with λ_{ex} = 640 nm, λ_{em} > 665 nm; objective: 60x.

Since the different species of CMS-ICC revealed in the incubation series (Figure 4.4.11D) appear at different times, I compared the co-localization of LysoTracker with the appearance of the different FLIM-clusters. Figure 4.4.12C shows that co-localization with LysoTracker matches with the pixels assigned to the yellow-colored FLS, indicating that a lysosomal localization of CMS-ICC gives rise to the yellow-colored FLS.

To further investigate the already suspected cellular excretion of the incorporated CMS-ICC, I incubated XS52 cells with CMS-ICC for 5 h at a concentration of 50 µg/ml. After removal of the extracellular nanocarrier solution, the internalized CMS-ICC were monitored for 24 h using FLIM The Cluster-FLIM analysis of the second time series shows that the fraction of the three identified FLIM clusters do not remain constant of time (Figure 4.4.13A,B). The yellow-colored FLS of CMS-ICC (Figure 4.4.11C), which is characteristic of a lysosomal CMS-NC localization and dominant after 5 h of incubation, gradually decreases over a period of 24 h, after exchanging the nanocarrier solution to cell medium. In contrast, the magenta FLIM cluster, which is dominant for short incubation periods, increases again. Likewise, the proportion of areas with a red FLS increases as the time progresses. In addition to the changes in the FLIM cluster distribution, I also observed a decrease in fluorescence intensity within the cells, which supports the thesis of cellular released CMS-NC. This decrease in intensity was also observed in accompanying fluorescence-activated cell sorting (FACS) experiments by Dr. Alexander Edlich (Prof. Kleuser's group, Universität Potsdam/Freie Universität Berlin, Germany). In summary, the nanocarrier release pathway, characterized by the red FLS, seems to drain the accumulated nanocarriers from the lysosomes and release them from local spots on the cell surface.

As reference measurements and to exclude a possible acidic degradation of the nanocarrier in the lysosomes, I investigated the pH stability of CMS-ICC and compared the FLSs of CMS-ICC and ICC after a 24 h incubation at pH 4. Low pH does not affect the fluorescence lifetime neither of the free ICC FMR probe, nor of CMS-ICC in solution (Figure 4.4.13C). In a further reference experiment, I compared the fluorescence lifetime of CMS-ICC (and ICC) in solution and at the glass surface of the cell culture dish to the red-colored FLS of CMS-ICC observed in XS52 cells (Figure 4.4.12A). The experiment reveals that all FLSs (CMS-ICC in solution, CMS-ICC or ICC interacting with the glass surface, and excreted CMS-ICC interacting with the glass surface) clearly differ (Figure 4.4.12D).

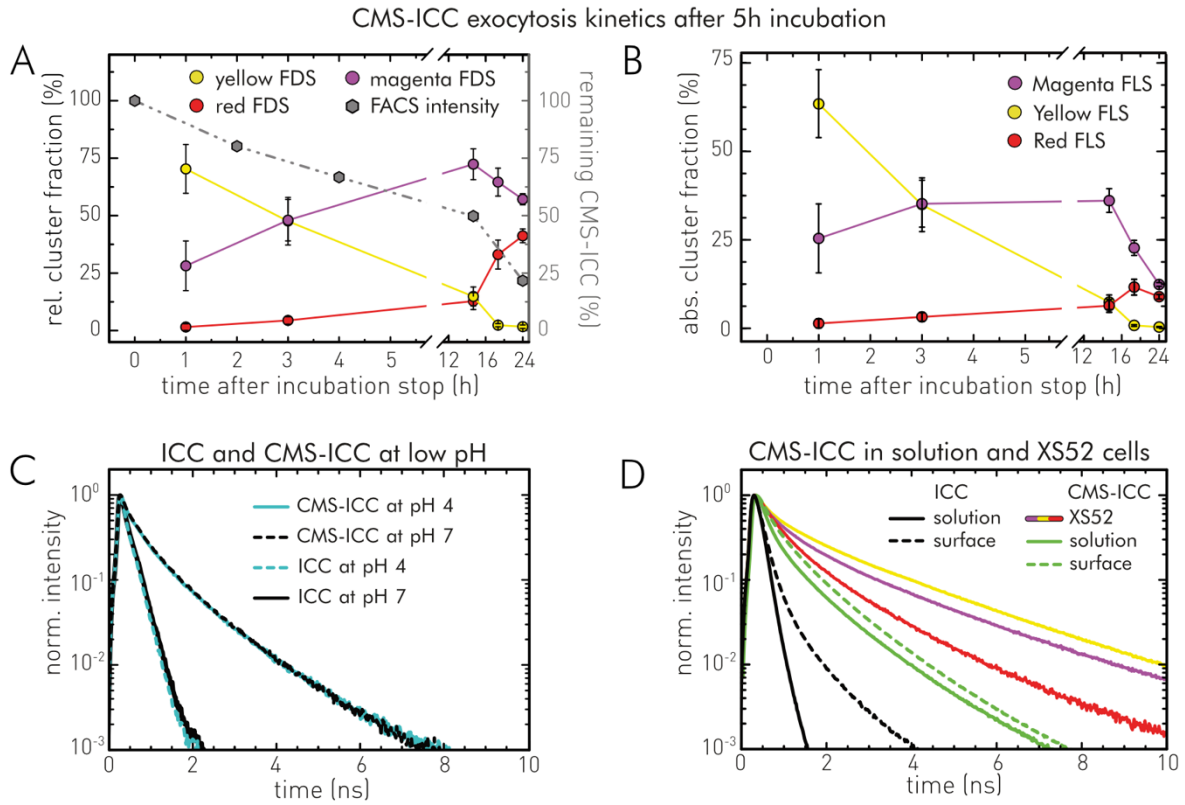

Figure 4.4.13: Intracellular fate of CMS-ICC in the XS52 cells and reference experiments. **A** Time-course of intracellular occurring CMS-ICC FLIM clusters fractions after removal of excess CMS-ICC nanocarriers in the medium. XS52 cells were previously exposed to 50 mg/ml of CMS-ICC for 5 h at 37 °C. For comparison FACS (fluorescence-activated cell sorting) intensities are displayed. **B** Absolute cluster fractions obtained by normalizing to the FACS intensities. **C** Comparison of low pH condition (pH 4) and pH 7 on ICC and CMS-ICC fluorescence lifetime after incubation for 24 h in the respective buffer. **D** Comparison of ICC and CMS-ICC fluorescence lifetime signatures in PBS pH 7.4 (focus into the solution and at the glass surface, respectively) with CMS-ICC internalized/released in/from XS52. Experimental conditions: CMS-ICC excitation with λ_{ex} = 530 nm; λ_{em} > 575 nm; LysoTracker excitation with λ_{ex} = 640 nm, λ_{em} > 665 nm; objective: 60x.

Discussion

In this section, a clear-cut proof for the preferential uptake of CMS-NC by LCs in skin tissue is provided using a FLIM-based approach for the first time. The applied Clusters-FLIM analysis of isolated epidermal cells from *ex vivo* full-thickness skin after a topical application of CMS-ICC did not only directly visualize the uptake of CMS-NC by epidermal cells, but also revealed different intracellular CMS-ICC species that are characterized by different FLSs (Figure 4.4.9). The simultaneous presence of different FLSs can be explained by occurring intracellular interactions, affecting the fluorescence lifetime of the covalently attached FMR probe ICC (see Section 4.2.1).

By applying dual-color FLIM, I identified LCs among the isolated epidermal cells and visualized cellular uptake and intracellular distribution of CMS-ICC at the single cell level. I further quantified the fraction of LCs among the CMS-NC positive cells to about 12 %, a much higher percentage than the natural abundance of LCs among skin cells with 2 – 5 %.[359-360] The result agrees with the flow cytometry data[169] of Frombach et al. and proves the preferential uptake of CMS-ICC by epidermal LCs after the topical application on *ex vivo* full-thickness skin. As discussed in Ref. 169, LCs populate

up to 20 – 25 % of the entire skin surface area and act as a second immunologic line of defense.[361-362] One can assume that the increased cellular uptake by LCs can be explained by this strategic localization within the epidermis. This observation could serve as a basis for future CMS-based immune cell targeting strategies for specific drug delivery and transcutaneous immunization.[354, 363-364]

For a detailed insight into the uptake and release mechanism of CMS-NC by LCs, I further analyzed the cellular uptake and distribution of the nanocarrier within the XS52 LC-like cell line. The experiments revealed three different intracellular interaction modes of CMS-ICC, characteristic for initial uptake, a subsequent intermediate step in endocytosis, and a precursor step for nanocarrier release (Figure 4.4.11/12). The magenta-colored FLS of CMS-ICC characteristic for initial uptake into the XS52 cells was found to be similar to the FLS of CMS-ICC observed in isolated $CD1a^+$ cells from skin tissue (Figure 4.4.11C). Even though the XS52 cell line originates from the epidermis of newborn BALB/c mice,[365] this finding indicates comparable uptake processes in LCs and XS52 cells and suggests that after 16 h topical application on skin tissue the CMS-NC become available to LCs.

The yellow-colored fluorescence lifetime signature (Figure 4.4.11C) characterizes the main intermediate step in the intracellular transport process and was identified as a lysosomal localization of CMS-ICC, in agreement with the finding that nanocarriers mainly accumulate in lysosomes of dendritic cells.[356-358] CMS-ICC containing lysosomes may merge with the cell membrane[366] and release of the nanocarrier into the extracellular space may occur from there. First evidence of an energy-dependent continuous release mechanism of CMS-ICC from XS52 cells was observed previously and attributed to lysosomal exocytosis.[174] Here, I identify the pathway that leads to CMS-ICC excretion (Figure 4.4.13A/B) by its characteristic FLS (red-colored). Such a CMS-nanocarrier release mechanism is in agreement with the hypothesis that lysosomes may undergo exocytosis and release their undigested content by fusion with the plasma membrane.[367-369] Lysosomal exocytosis is frequently found for nanoparticles.[370-371] At high nanocarrier concentrations (Figure 4.4.12A) and towards later stages of the release process (Figure 4.4.12C), the pre-release compartments containing the CMS-ICC species with the red FLS seem to accumulate and become detectable by FLIM. These pre-release compartments are non-acidic as evidenced by the absence of co-localization with LysoTracker (Figure 4.4.12C), which selectively accumulates in cellular compartments with low internal pH. Such a connection between the rise in lysosomal pH followed by a lysosomal secretion, is also described in literature.[372] Thus, based on the identification and assignment of the red-colored FLS of CMS-ICC in these fluorescent hot spots, it seems possible to observe intracellular sites in the XS52 immune cell (Figure 4.4.12A) which could be part of the exocytosis pathway. From these sites, cellular release of CMS-ICC may occur. This release process is further evidenced by extracellular "foot-print"-like structures and the decreasing intracellular CMS-ICC fluorescence intensities (Figure 4.4.13A/B).

An essential functional feature of dermal immune cells is their migration within the skin for antigen screening and their emigration into draining lymph nodes.[373] The capability of these cells to move at surfaces[374] seems to allow the observation of mentioned "foot-prints" indicating released CMS-

ICC on the microscope glass slide (Figure 4.4.12B). A general affinity of CMS-NCs to glass surfaces was seen in my previous experiments, but the formation of the observed traces (Figure 4.4.12B) requires substantial release of CMS-ICC from the immune cells. Interestingly enough, I observed clear differences in the FLS from freshly dissolved CMS-ICC interacting with the glass surface and from excreted CMS-ICC Figure 4.4.13D. Since an acidic degradation of CMS-ICC can be excluded (Figure 4.4.13C), it is obvious that CMS-ICC is released by the lysosomes into the extracellular space without decomposition. The change in FLS (yellow-colored to red-colored) can probably be attributed to an intracellularly formed protein corona (compare Section 4.3.2). Thus, a possible uptake of excreted CMS-NC by native keratinocytes in the viable epidermis may occur by different uptake pathways than those observed in *ex vivo* experiments (Section 4.4.1).

4.5 Localization and interactions of polymeric nanoparticles in tissue

4.5.1 G5G2.5-tecto-dendrimer interaction with the dermal penetration barrier

G5G2.5 core-shell tecto-dendrimers (G5G2.5-MG) were originally developed to overcome the limited tolerability of dendritic cationic polyamidoamine nanocarriers and to increase the transport capabilities by a higher number of drug cavities (for further details see Section 2.3.2).[19, 159] In Section 4.3.3, I presented an investigation on the optimal fluorescence labeling stoichiometry of a FITC tagged G5G2.5-tecto-dendrimer. On the one hand, the used procedure ensures a high detectability by fluorescence techniques. On the other hand, it reduces inter- and intramolecular quenching which disturbs a quantitative analysis. In contrast to the strong impact of the labeling stoichiometry on fluorescence quenching, changes in environmental parameters, such as pH or polarity, only marginally affect the fluorescence quenching factor when using a low-labeled G5G2.5-MG-FITC conjugate. In summary, only a careful preliminary analysis of the fluorescence properties of a fluorescently labeled nanoparticle enables quantitative evaluations of nanoparticle penetration behaviors. Otherwise, various quenching effects may mask the real localization and relative concentration of the nanoparticle within the tissue.

In this section, I will present a (semi-)quantitative evaluation of the G5G2.5-tecto-dendrimer penetration into skin, which was obtained in the context of a collaboration between Prof. Alexiev's group (Freie Universität Berlin, Germany), Dr. Christian Zoschke (Prof. Schäfer-Korting's group, Freie Universität Berlin, Germany) and Dr. Priscila Schilrreff (Prof. Romero's group, National University of Quilmes, Argentina). Fluorescence lifetime imaging microscopy (FLIM) is applied to distinguish the target fluorescence of G5G2.5-MG-FITC from skin autofluorescence. In order to achieve this, I parameterized the FLIM data obtained from the treated skin blocks after cryo-sectioning by the Cluster-FLIM algorithm (Section 4.3.2). This approach constitutes a highly sensitive tool for clear-cut localization of fluorescent targets by their fluorescence decay characteristics.[130] The generated Cluster-FLIM images reveal that the FITC-labeled tecto-dendrimers penetrate the *stratum corneum* (SC) of human skin *ex vivo* and reconstructed human skin (RHS), but do not cross the tight junction barrier of the viable epidermis (VE). RHS is a three-dimensional skin model, which consists of primary human cells. These models have shown to be useful in studies of skin absorption and local immunological effects of small molecules and are subject to validated test guidelines.[375-377] RHS models have promising advantages that go beyond the mere assessment of skin absorption, allowing the basic investigation of molecular mechanisms of skin permeation. RHS represents a metabolically active system[378], that replicates native fibroblast effects[379] on keratinocyte phenotypes and can be extended to more complex test systems, including disease models.[213, 380]

Besides the dermal penetration behavior of G5G2.5-MG, I study the cutaneous transport properties of the dendrimeric nanocarrier system in healthy and diseased skin models using RhoB as a fluorescent drug mimetic. For this purpose, RhoB (Section 2.1.3) dissolved in PBS (pH7.4) or loaded

to G5G2.5-tecto-dendrimers were topical applied on RHS models mimicking healthy (normal) skin and skin suffering from cutaneous squamous-cell carcinoma (cSCC). The RHS models were developed and provided by Dr. Christian Zoschke (Prof. Schäfer-Korting's group, Freie Universität Berlin, Germany). The data presented here was partly published in Ann. N. Y. Acad. Sci. (Volz et al.,2017, Ref. 19). Hence, the next paragraph relies on my contribution to this paper.

How background autofluorescence affects evaluation of skin penetration

Intensity-based fluorescence microscopy on labeled targets in biological tissue can be erroneous due to similar fluorescence properties of the labeled target and the tissue's autofluorescence. Especially similar spectral or changing fluorescence properties make it difficult to distinguish target fluorescence from background autofluorescence. Typically, in intensity-based fluorescence microscopy, target and autofluorescence are separated by spectral emission filters. If this is not possible, e.g., if both spectral emission ranges overlap, background thresholding is applied. Figure 4.5.1F shows an image of the autofluorescent background of an untreated human skin sample, generated by CLSM of cryosection. Figure 4.5.1G shows the corresponding CLSM image of a cryosection from excised skin tissue after topical application with G5G2.5MG-FITC *ex vivo*. In this case, the target fluorescence is superimposed with the autofluorescence signal. Background intensity subtraction most likely induces false-positive readings when the threshold intensity is assumed to be low, making a correct assessment of the penetration behavior difficult. In Figure 4.5.1H–J, different degrees of background thresholding are presented. The chosen background thresholding is based on the control sample in Figure 4.5.1F. To simulate different degrees of background, the threshold was gradually increased to more conservative values in the analysis (Figure 4.5.1H–J). Figure 4.5.1G and H show the intensity-based localizations of G5G2.5-MG-FITC in the SC and in lower VE layers. In contrast, more conservative background thresholding (Figure 4.5.1I,J) limits the localization solely to the upper SC.

The application of FLIM can avoid the search for an optimal background threshold. (Figure 4.5.1K–O). Since the fluorescence lifetime depends on the electronic structure of the fluorescing target molecule as well as on its environmental interactions, FLIM allows distinguishing background fluorescence from target fluorescence via the pixel-based fluorescence decay traces, enabling the decision whether a pixel of a microscopic image can be assigned to the target or autofluorescence. This approach, however, becomes more complicated if complex fluorescence lifetime decays are involved. To meet this challenge, I apply the cluster based multivariate FLIM analysis tool (Section 3.4.2), that allows the discrimination of background from target fluorescence despite complex fluorescence decays or multiple target fluorescence subspecies. Such subspecies can be induced by interactions in the complex and often unpredictable molecular environments in biological tissues. Cluster-FLIM recognizes the multi-exponential fluorescence lifetime signature (FLS) of the autofluorescence background (cyan) and of G5G2.5-MG-FITC (red) in the skin section (Figure 4.5.1P). Figure 4.5.1K–O show Cluster-FLIM images for different background thresholding levels displaying both background autofluorescence (cyan) and target fluorescence of G5G2.5-MG-FITC (red). G5G2.5-

MG-FITC can be clearly discriminated from autofluorescence, independently of the amount of thresholding. Figure 4.5.1Q and R show a higher magnification of the images in Figure 4.5.1D and L.

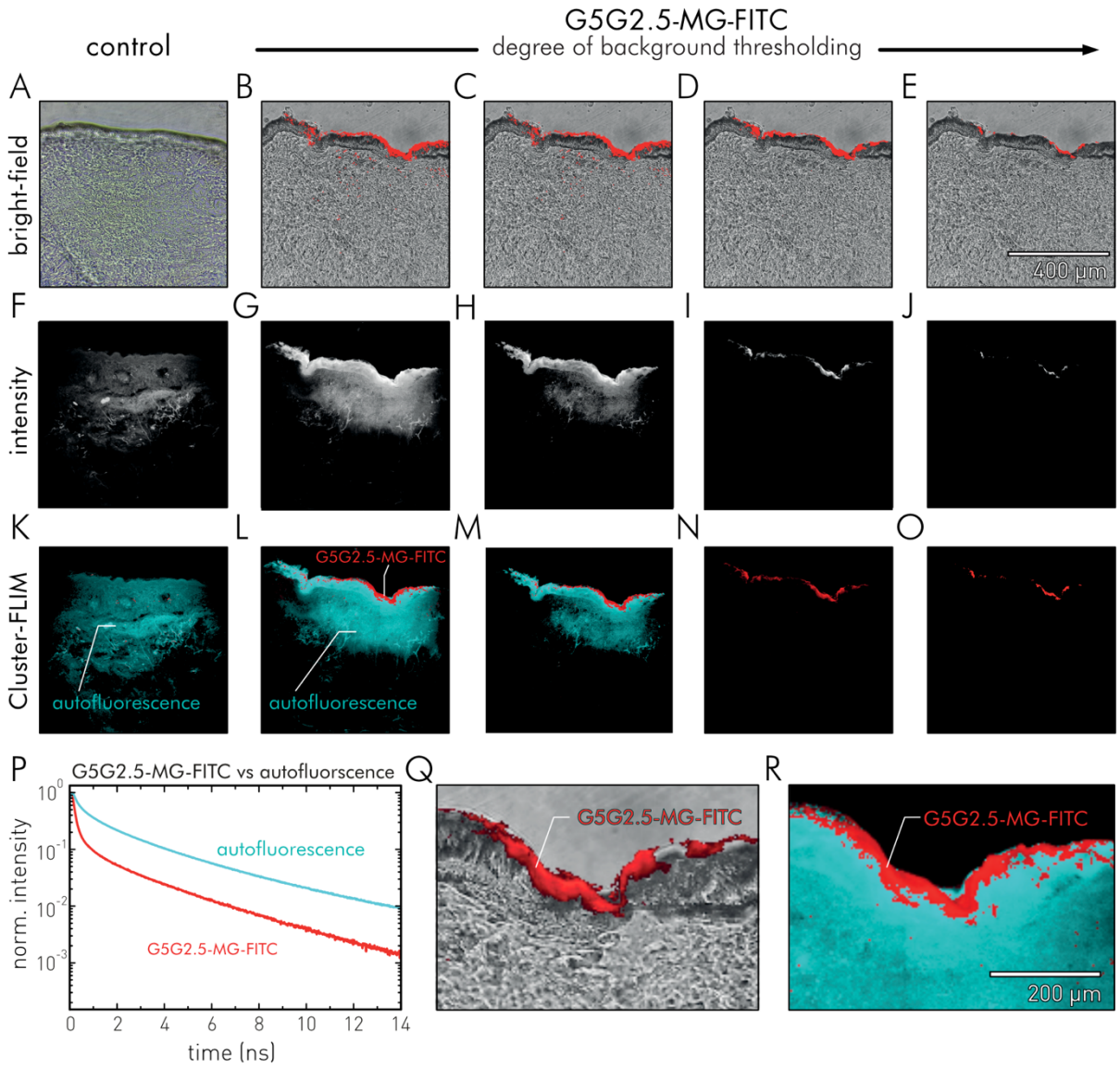

Figure 4.5.1: FLIM study of G5G2.5-MG-FITC penetration into excised human skin and the effect of background thresholding. **A–E** Bright-field image of untreated (A) and overlay of the bright-field images of G5G2.5-MG-FITC-treated (B–E) human skin with the G5G2.5-MG-FITC localizations from FLIM analysis as shown in L and M. G5G2.5-MG-FITC intensities are false-color coded in red on the basis of fluorescence lifetime cluster analysis. **F–J** Confocal intensities of G5G2.5-MG-FITC-treated skin with different background thresholds (G: 100 cts/px; H: 300 cts/px; I: 1200 cts/px; and J: 2500 cts/px). (F) Confocal intensity of untreated skin. **K–O** Cluster-FLIM : autofluorescence is colored in cyan, and G5G2.5-MG-FITC fluorescence is colored in red. **P** Normalized fluorescence decay traces (red: G5G2.5-MG-FITC; cyan: autofluorescence) as extracted with Cluster-FLIM from K–O. **Q, R** Magnification of D and L, respectively. Experimental conditions: Confocal FLIM; G5G2.5-MG-FITC excitation with λ_{ex}=488 nm; λ_{em} > 515 nm; objective: 40x. A-R are reprints from Volz et al.,[19] Copyright 2017, with the kind permission of Ann. N.Y. Acad. Sci..

Cluster-FLIM-based evaluation of G5G2.5-MG-FITC penetration into intact skin

As shown in the demonstration example on fluorescence target discrimination using Cluster-FLIM (Figure 4.5.1), G5G2.5-MG-FITC penetrates exclusively into the SC but not into VE layers of human skin. This behavior was observed for both experimental skin testing models, Human skin *ex vivo* as well as RHS (Figure 4.5.2A,C; red and green). In order to investigate if the tight junction barrier at

the interface between SC and VE causes this penetration stop,[381] I used immunostained *ex-vivo* human skin and RHS samples, which were provided by Christopher Wolff (Prof. Schäfer-Korting's group, Freie Universität Berlin, Germany). FLIM experiments visualized the successful immunofluorescence staining of the tight junction protein claudin-1 in both investigated skin models (Figure 4.5.2). The detected claudin-1 is located on keratinocyte membranes from the basal layer to the *stratum granulosum* (Figure 4.5.2B,D; yellow), which corresponds to the typical occurrence in native skin.[382] The immunostaining apparently has no influence on the detection of G5G2.5-MG-FITC, as can be seen from the comparable fluorescence lifetime signatures (FLSs) for immunostained and unstained excised human skin in Figures 4.5.1 and 4.5.2. Although the applied combination of confocal FLIM and Cluster-FLIM analysis can localize even small amounts of G5G2.5-MG-FITC with high precision and resolution, it did not detect G5G2.5-MG-FITC beyond the tight junction protein barrier in the *stratum granulosum* (dashed white lines). While two different FLSs of G5G2.5-MG-FITC in human skin *ex vivo* indicate heterogeneous interactions of the nanocarrier in the SC (Figure 4.5.2A,B; green vs. red FLS), Cluster-FLIM recognizes only a single FLS for G5G2.5-MG-FITC within RHS (Figure 4.5.2C,F).

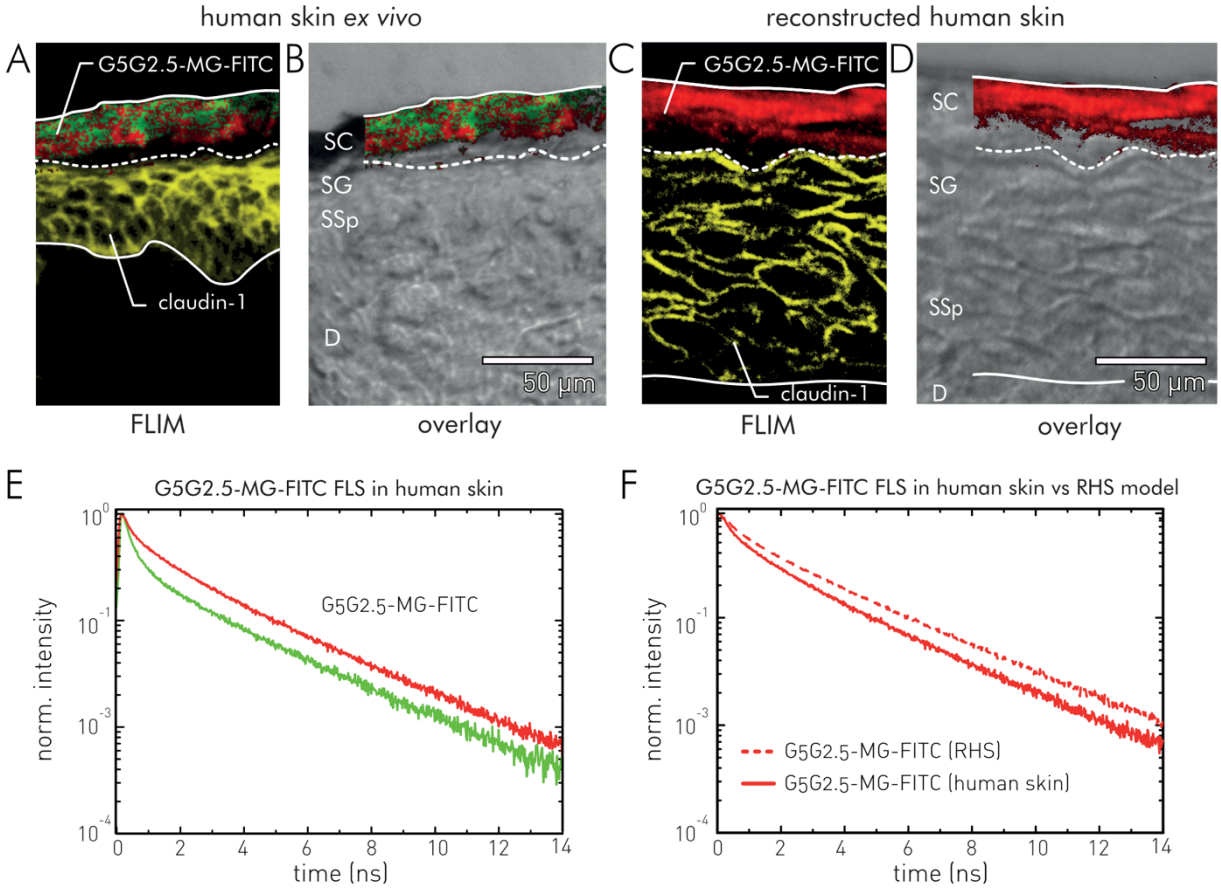

Figure 4.5.2: Comparison of G5G2.5-MG-FITC penetration and localization of the tight junction protein claudin-1in human epidermis. **A** False-color coded Cluster-FLIM image of G5G2.5-MG-FITC-treated human skin. White dashed line indicates the border (barrier layer) between the SC and viable epidermis. Claudin-1 immunostaining is shown in yellow; G5G2.5-MG-FITC FLSs are indicated green and red. **B** Brightfield overlay with Cluster-FLIM image shown in A. **C** False-color coded Cluster-FLIM image of G5G2.5-MG-FITC-treated RHS. Claudin-1 immunostaining is shown in yellow; G5G2.5-MG-FITC FLS is indicated red. **D** Brightfield

overlay with Cluster-FLIM image shown in C. **E** FLS of G5G2.5-MG-FITC as extracted with Cluster-FLIM from A. **F** Comparison of G5G2.5-MG-FITC FLS (red traces) in human skin (continues line) and RHS (extracted from E, dashed line). Abbreviations: SC: *stratum corneum*; SG: *stratum granulosum*; SSp: *stratum spinosum*; D: dermis; FLS: fluorescence lifetime signature. Experimental conditions: Confocal FLIM; G5G2.5-MG-FITC excitation with λ_{ex} = 488 nm; λ_{em} > 515 nm; Alexa-Fluor 594 excitation with λ_{ex} = 561 nm, λ_{em} > 575 nm; objective: 60x. A-F are reprints from Volz et al.,[19] Copyright 2017, with the kind permission of Ann. N.Y. Acad. Sci..

Cutaneous transport properties of G5G2.5-tecto-dendrimers carrying RhoB

After having demonstrated that topically applied G5G2.5-MG does not penetrate into the VE, but remains in the SC, I will investigate the dermal transport efficiency of the nanocarrier in healthy and diseased skin next. For this purpose, G5G2.5-MG was loaded non-covalently with the fluorescent drug mimetic rhodamine B (RhoB, m_w=479 Da, LogP=1.95, Section 2.1.3). Subsequently, G5G2.5-MG/RhoB was applied topically to the RHS models and incubated for 6 h. The resulting penetration behavior was investigated on cryosections cut horizontally to the skin surface by FLIM (from SC to dermis). The results are compared with the penetration behavior of an equally concentrated RhoB reference solution (PBS, pH 7.4) incubated under identical experimental conditions. As an organotypic skin disease model, RHS with cutaneous squamous cell carcinoma (cSCC) was investigated, showing a penetration barrier deficiency.

Figure 4.5.3A compares fluorescence intensity-based CLSM images of the RhoB fluorescence in normal RHS models after application of RhoB and G5G2.5-MG/RhoB. In both cases, there is a penetration of the RhoB up to the *stratum basale*, the lowest layer of the VE. The comparison of the fluorescence intensities clearly shows an increased intensity of RhoB once loaded on G5G2.5-MG. So, a nanocarrier-related increase in penetration efficiency can be deduced. Comparing the fluorescence intensities in the form of a depth profile (Figure 4.5.3B), an increase can be observed in all epidermal layers. The difference of the total fluorescence intensity accumulated over the entire depth profiles is a factor of ~4.3. This factor cannot be converted 1:1 into a concentration ratio (see Section 2.1.2), but it indicates a higher penetration efficiency of RhoB molecules when loaded on G5G2.5-MG.

In addition to this pure increase in intensity, the RhoB fluorescence emission also changes in its time-dependent behavior when loaded on the tectodendrimers. In order to quantify these changes, I conducted a fluorescence decay analysis of the FLIM images using a bi-exponential fit. The resulting mean fluorescence lifetimes range between 1.5 and 4.2 ns. Using this lifetime range, I generated the tau-plot FLIM images in Figure 4.5.3C. Here, one can see a clear difference in the spatial fluorescence lifetime distribution in the skin. This differs between RhoB applied in solution and RhoB that was transported in the tecto-dendrimers. In order to illustrate this change more detailed, I selected two ROIs from Figure 4.5.3C. The ROIs are characteristic of the fluorescence decay behavior because they match the distribution average of the respective mean fluorescence lifetimes (Figure 4.5.3E) in the RhoB and G5G2.5-MG/RhoB sample. Figure 4.5.3D shows the fluorescence decay traces that

appear there, as well as the decay traces of G5G2.5-MG/RhoB free in solution (PBS, pH 7.4). Additionally, the values of the individual determined decay components are indicated.

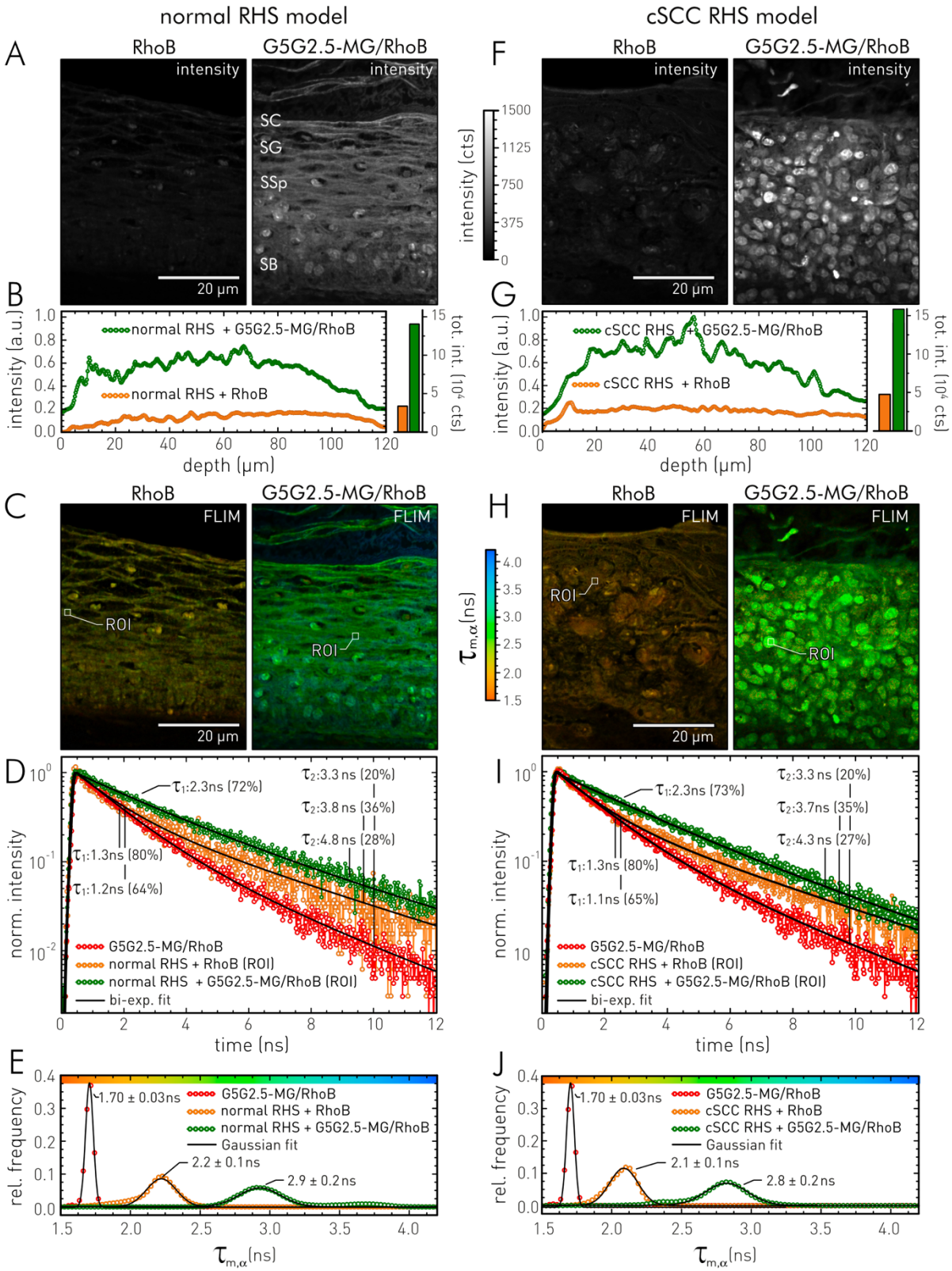

Figure 4.5.3: Cutaneous transport properties of G5G2.5-MG in normal and cSCC RHS model using RhoB as a fluorescent drug mimetic. **A** CLSM intensity images of RhoB (in PBS) and RhoB loaded on G5G2.5-MG penetrating a normal RHS model. **B** Dermal depth profiles of RhoB fluorescence intensities in normal RHS. **C** Tau-plot FLIM images of RhoB and G5G2.5-MG/RhoB topical applied to normal RHS models; same sites as in A. **D** Comparison of fluorescence decay traces of RhoB for G5G2.5-MG/RhoB, G5G2.5-MG/RhoB and RhoB topical applied to normal RHS. **E** Mean fluorescence lifetime distributions of the indicated samples.

The distributions are fitted to Gaussian functions, determined means and standard deviations are indicated. **F** CLSM intensity images of RhoB (in PBS) and RhoB loaded on G5G2.5-MG penetrating a cSCC RHS model. **G** Dermal depth profiles of RhoB fluorescence intensities in RHS with cSCC. **H** Tau-plot FLIM images of RhoB and G5G2.5-MG/RhoB topical applied to cSCC RHS models; same sites as in F. **I** Comparison of fluorescence decay traces of RhoB for G5G2.5-MG/RhoB, G5G2.5-MG/RhoB and RhoB in PBS topical applied to RHS with cSCC. **J** Mean fluorescence lifetime distributions. The distributions are fitted to Gaussian functions, determined means and standard deviations are indicated. Shown uncertainties of decay components and relative amplitudes are based on confidence interval analyses (Section 3.4.1). Experimental conditions: Confocal FLIM; RhoB excitation with λ_{ex} = 561 nm; λ_{em} > 575 nm; objective: 40x.

If one compares the fluorescence decay traces of G5G2.5-MG/RhoB free in solution with free RhoB that has penetrated the normal skin model (Figure 4.5.3D), it is noticeable that the fast decay component is approximately the same (1.2 vs. 1.3 ns). The difference is determined by the slow decay component (3.3 vs. 3.8 ns) and its higher relative amplitude. This leads to a prolonged fluorescence decay of RhoB in the skin (Figure 4.5.3D). Considering RhoB that penetrated the skin when loaded on G5G2.5-MG, the fluorescence decay slowed down further compared to the other two RhoB samples. This behavior is also illustrated in Figure 4.5.3E which compares the mean fluorescence lifetime distributions of all three RhoB samples. According to Gaussian fitting (Figure 4.5.3F), the mean distribution values (mean ± SD) are determined by 1.70 ± 0.01 ns (G5G2.5-MG/RhoB, H_2O), 2.2 ± 0.1 ns (RhoB, skin) and 2.9 ± 0.1 ns (G5G2.5-MG/RhoB, skin).

The general fluorescence lifetime shift between both application types is also visible within the FLIM images. While RhoB topically applied in solution occupies in the FLIM image the false color range between orange and green (2.0 – 2.5 ns), the nanoparticular transported RhoB occupies the color range from green to blue (2.5 – 4.0 ns). Interestingly enough, slower RhoB lifetimes are observed within the cytoplasm of RHS models treated with G5G2.5-MG/RhoB. In contrast, the free RhoB seems to accumulate in the membranes of the upper epidermal layers, while in the basal layer the entire cells are stained. In both samples the RhoB agglomerate in the cell nuclei. Here, it should be emphasized that especially the nuclei of the stratum basale are strongly stained in case of the tecto-dendrimeric transport.

The investigated organotypic disease model of cSCC skin shows very similar penetration properties of RhoB as the normal RHS model. Figure 4.5.3F compares fluorescence intensity-based CLSM images of the RhoB fluorescence in cSCC RHS models after application of RhoB and G5G2.5-MG/RhoB. The general picture which is shown here corresponds to that of healthy skin with the exception of the differences in tissue morphology caused by the disease model. Again, the comparison of the fluorescence intensities clearly shows an increased intensity of RhoB once loaded on G5G2.5-MG. Comparing the intensity-based depth profiles (Figure 4.5.3G), an increase in all epidermal layers is revealed. The difference of the total fluorescence intensity over the entire depth profiles amount to a factor of ~4. But the intensity distribution in the G5G2.5-MG/RhoB treated skin is less homogeneous, some nuclei have higher intensities which results in a wavier profile shape.

As in the experiments on normal skin, RhoB's time-resolved fluorescence also changes when loaded on the tectodendrimers. In order to quantify these changes, a fluorescence decay analysis

(tau-plot) was conducted, using a bi-exponential fit. Again, the resulting mean fluorescence lifetimes located between 1.5 and 4.2 ns. Using this lifetime range, the tau-plot FLIM images in Figure 4.5.3H were generated. Again, I have chosen ROIs to compare the two penetration scenarios. Figure 4.5.3I shows the corresponding fluorescence decay curves. Only marginal non-relevant differences to normal RHS can be found. Which suggests the same interaction pattern of the RhoB in both skin types. This becomes clear when looking at the histogram of the mean fluorescence lifetime distribution in Figure 4.5.3J. This diagram reproduces the results in normal RHS models, with the exception of the RhoB species which have a mean fluorescence lifetime of more than 3 ns. This species, occurring in the normal RHS model, mainly in the cytoplasm, is not present in the cSCC RHS model.

Discussion

Initial studies on nanoparticle-based drug delivery typically aim for the tracking of the nanoparticle or its cargo to the desired target site within the tissue.[4, 383] Here, I demonstrated the impact of advanced techniques like FLIM and the Cluster-FLIM analysis tool on the read-out of nanocarrier penetration into skin tissue with the aim to improve pre-clinical evaluation applied to novel concepts in dermal drug delivery. Apart from inter- and intramolecular quenching effects caused by the choice of the fluorescent label, the labelling site and stoichiometry (see Section 4.3.3), and unpredictable tissue-related quenching, strong autofluorescence in particular makes the localization of fluorescently labeled nanoparticles difficult.

Cutaneous autofluorescence in paraffin- or cryosections limits the sensitivity of intensity-based fluorescence techniques. Since cutaneous autofluorescence depends on serval parameters like skin color or body site,[384] the limit of detection varies from skin sample to skin sample. Moreover, snap freezing or paraffin embedding, both standard approaches in the analysis of tissue samples, induce additional variation. Tissue blocks are cut to slices of a few micrometers but cutting blocks into slices of exactly the same thickness requires a very well-maintained cryotome and years of experience in cutting. Variation in slice thickness can cause variation in the autofluorescence level even within the same sample. Finally, the determination of the threshold value of the fluorescence exposure time to exclude autofluorescence remains arbitrary and error prone. Depending on photo or chemical bleaching probabilities of the used fluorescent label, the fluorescence intensity can be changed which might lead to false-negative results. If the background autofluorescence is underestimated, as shown in Figure 4.5.1, false-positive results will occur. Using this example of FITC-labelled G5G2.5-tectodendrimers in human skin, I emphasize the importance of correct background subtraction, which is not always possible with purely intensity-based fluorescence microscopy. Cluster-FLIM provides a tool to overcome these challenges by enabling the differentiation of label fluorescence from tissue autofluorescence without intensity-based thresholding, as shown in Figure 4.5.1L – O.

Although FLIM is a highly specialized microscopic technique and not readily accessible, the number of publications using FLIM as an analytical tool is increasing, indicating the impact of this

technique in skin research.[130, 190, 248, 385] However, the technique also has its disadvantages. FLIM based on confocal time-correlated single photon counting requires longer exposure times than the stationary CLSM, since reduced excitation photon densities and fluorescence intensities are required in the single photon counting regime, simultaneously, FLIM data analyses require a higher total number of detected fluorescence photons per image pixel. New and advanced analysis tools, as shown here with the Cluster-FLIM method (Section 3.4.2 and 4.1.3), enable accurate fluorescence background subtraction, even at lower photon counts. Employing Cluster-FLIM, G5G2.5-MG-tecto-dendrimers were exclusively found within the SC of human skin *ex vivo* and RHS and not within viable layers. This result is consistent with the limited permeation of macromolecules through tight junction proteins.[381] The absence of tecto-dendrimers in viable epidermal layers limits their drug-like use as described for melanoma cells.[159] On the other hand, it reduces the toxicological concern of a topical nanocarrier application, since they access neither viable layers and the immune system, nor systemic circulation. However, diseases might change the skin barrier function, which could enable tecto-dendrimer penetration into viable layers and require further studies. Among other conditions, non-melanoma skin cancer alters the expression of tight junction proteins.[386]

Finally, a controlled interaction between tight junction proteins and nanocarrier would allow targeted delivery. FLIM analysis of fluorescent labels with adaptive fluorescent lifetimes can provide additional information on the microenvironment of a nanoparticle. Such insights into molecular interactions between cutaneous lipids/proteins with nanoparticles can be of great importance for adaptations in nanoparticle design. Concerning G5G2.5-MG-FITC, changes in the pH value or polarity alter the fluorescence lifetime, whereas a slightly increased viscosity has no effect (Section 4.3.3). This observation might further aid nanocarrier studies on cellular or direct protein interactions to investigate the above-mentioned opening mechanism for tight junctions.

The additional FLS in human skin *ex vivo* (Figure 4.5.2E) compared with RHS can be explained by differences in SC lipid composition or packing order in RHS. Nevertheless, RHS correctly predicted the penetration of tecto-dendrimers into the SC without penetration into the VE. To the best of my knowledge, this is the first study investigating the cutaneous uptake of tecto-dendrimers into RHS models. The predictive power of reconstructed human epidermis (RHE) models (skin constructs without a dermis) has already been validated for the absorption of small molecules.[377] In the future, these studies have to be expanded to RHS providing epidermal – dermal interactions.

Besides the dermal penetration behavior of G5G2.5-MG in normal RHS, I study the cutaneous transport properties of the dendrimeric nanocarrier system in healthy and cSCC diseased skin models, using RhoB as a fluorescent drug mimetic. The transport by the G5G2.5-MG nanocarrier increased the dermal penetration efficiency for RhoB in both skin types significantly. The total fluorescence signal intensity in both models increased by an average factor of ~4. Interestingly enough, the cell nuclei of the cSCC RHS model treated with G5G2.5-MG/RhoB have an increased fluorescence signal compared to the normal RHS model, indicating a different interaction mode in the

diseased state of the skin. This hypothesis is supported by the absence of a mean fluorescence lifetime species above 3.5 ns in the cSCC-RHS model. However, it must be mentioned that this species has a very low abundance in the normal RHS model, as can be seen in the fluorescence lifetime distribution in Figure 4.5.3E. Besides an actually low abundance, this can also be a result of artifacts in the analysis process. The low photon statistics of the recorded FLIM data limits the fit accuracy of the tau-plot analysis and thus the significance, especially with respect to the slow third decay component. This also has an impact on the calculated mean lifetimes in the fluorescence lifetime distributions 4.5.3E/J. It is possible that other analysis approaches not relying on mean fluorescence lifetimes (tau-plot analysis, Section 3.4.2) could reveal a stronger contrast of RhoB fluorescence lifetimes after topical application of G5G2.5-MG/RhoB between both RHS models.

However, the applied tau-plot analysis reveals clear differences in RhoB interactions for both skin models depending on whether RhoB was applied topically free in solution or on the G5G2.5-MG nanocarriers. The well-separated mean fluorescence lifetime distributions obtained by the tau-plot analyses indicate that the autofluorescent background in these samples was negligible and that the fluorescence in the four tissue samples originated mainly from RhoB. Therefore, the use of a Cluster-FLIM analysis was not necessary.

In summary, FLIM-based read-outs can improve the accuracy of nonclinical research during the early development of new nanoparticles and nanocarriers by providing molecular insights into nanocarrier – tissue interactions. With this study, I demonstrate that testing of nanocarrier systems with RHS can bridge the lack of excised human skin which promotes the replacement, reduction, and refinement (3Rs principle) of animal experiments.

4.5.2 FLIM-based interaction imaging of epidermal CMS-ICC penetration in model skin

Another nanoscale vehicle for transdermal transport of poorly penetrating therapeutics is the dendritic core-multishell nanocarrier system (CMS-NC) introduced in Section 2.3. Previous studies have shown that this polymer-based nanocarrier can penetrate into dermal layers and enables a penetration enhancement to its loaded cargo.[152, 170, 173] These findings speak in favor of applying CMS-NC in topical treatment of skin diseases, since a release of active agents in the immediate vicinity of potential targets in the viable epidermis (VE) or dermis is greatly desired.[4] In addition, once located there, the nanocarrier could increase the persistence of loaded drugs in the skin by acting as a local drug reservoir. The CMS-NC platform is able to solubilize various hydrophobic fluorophores and active agents for skin disease therapy, in aqueous solutions. Likewise, the nanocarrier release them again with high release rates.[149, 153, 387] Studies on human skin *ex vivo* using Franz diffusion cells and reconstructed human skin (RHS) models suggests that loaded cargo molecules are transported more efficiently into deeper compartments of the stratum corneum (SC) and even into the VE compared to conventional formulations.[152, 170] However, neither the molecular mechanisms, interactions, and penetration pathways are answered, nor the question whether CMS-NC can reach living epidermal

layers *in vivo* with the potential consequence of triggering immune responses. Cellular interactions such as the uptake of CMS-NC by keratinocytes and dermal CD1a-positive cells *in vitro* and *ex vivo* are investigated in Section 4.4. Although penetration studies on reconstructed skin and human skin *ex vivo* using Franz diffusion cells are highly standardized and adequate methods for comparing penetration rates, they also have disadvantages such as their tendency to hyperpermeability.[377, 388] In the case of RHS, the additional absence of immune cells and skin appendages reduces the ability to fully map *in-vivo* conditions. This difference is essential for a comprehensive penetration prediction *in vivo*, since these structures provide alternative transdermal penetration routes and present important structures for reservoir formation.[169]

The penetration and transport behavior of a nanocarrier system in diseased skin tissue makes the application of active substances necessary in the first place. It represents a central and important object of investigation and should be placed in the focus of penetration studies. Therefore, in this section the penetration and interaction behavior of CMS-NC will be examined in different *in vitro, in vivo* and *ex vivo* skin models using fluorescence lifetime imaging microscopy in combination with the fluorescent molecular rotor probe ICC (see Section 4.2.1).

In a first experiment, I will demonstrate that CMS-NC accumulates in skin furrows and skin appendages, like hair follicles, after being topically applied to human skin. For these experiments, I use excised full-thickness human skin *ex vivo* provided by the group of Prof. Vogt (Charité – Universitätsmedizin Berlin, Germany). Such local accumulations of nanocarriers are potential drug reservoirs. They could also enable the penetration of nanocarrier beyond the SC barrier by prolonged interaction times with components of the barrier. In further experiments, I will study the influences of skin diseases and related barrier damages on the penetration behavior. Here, I will use reconstructed human epidermal models mimicking epidermal aging *in vitro* provided by Prof. Schäfer-Korting's lab (Freie Universität Berlin, Germany) and animal *in-vivo* models provided by the group of Prof. Gruber (Freie Universität Berlin, Germany). The data and results presented were partly published in the following journals: J. Control. Release (Frombach et al., 2019, Ref. 169), Eur. J. Pharm. Biopharm. (Löwenau et al., 2017, Ref. 211), Nanomedicine (Pischon et al., 2017, Ref. 172), and Nanoscale Res. Lett. (Radbruch et al., 2017, Ref. 166). Hence, the next sections rely on my contributions to these papers.

CMS-ICC penetration and interactions in *ex-vivo* human skin

After topical application of CMS-ICC (5 g/L) on normal *ex-vivo* human skin, CMS-ICC fluorescence is almost exclusively observed in the SC, characterized by high fluorescence intensities in the spectral emission band of ICC (550 – 650 nm). This applies to short incubation periods of 4h, but also to longer periods such as 16 h. Figure 4.5.4A visualizes the CMS-ICC localization using a CLSM intensity image taken on a cryo-cross section (~5 µm) of excised human skin after 16 h incubation at 37 °C. Neither penetration of CMS-ICC into the VE, nor an autofluorescent background (reference

skin) was detected at the chosen excitation intensities. In addition to a flat SC, Figure 4.5.4A shows a skin furrow, which exhibits particularly high fluorescence intensities of CMS-ICC. Accumulations of CMS-ICC in these structures were regularly observed in different experiments involving human skin.[169] In addition to the fluorescence image, Figure 4.5.4A also shows a depth profile of the fluorescence intensity in the three indicated vertical areas (black: I, blue: II, red: III). The profiles (black and red) show that CMS-ICC can be detected down to a maximum depth of 20 – 30 µm relative to the flat skin surface. This penetration depth corresponds with the typical thickness of human SC. In areas with furrows, the nanocarrier can be detected up to a depth of 200 µm, but this does not mean that the skin barrier in the SC has been penetrated. Also, in this case the CMS-NC remains within the SC layers and the VE is free of the nanoparticle. Morphological structures like skin furrows or folds are possible source of errors in the interpretation of fluorescence based dermal penetration profiles generated for example by tape stripping methods.[389]

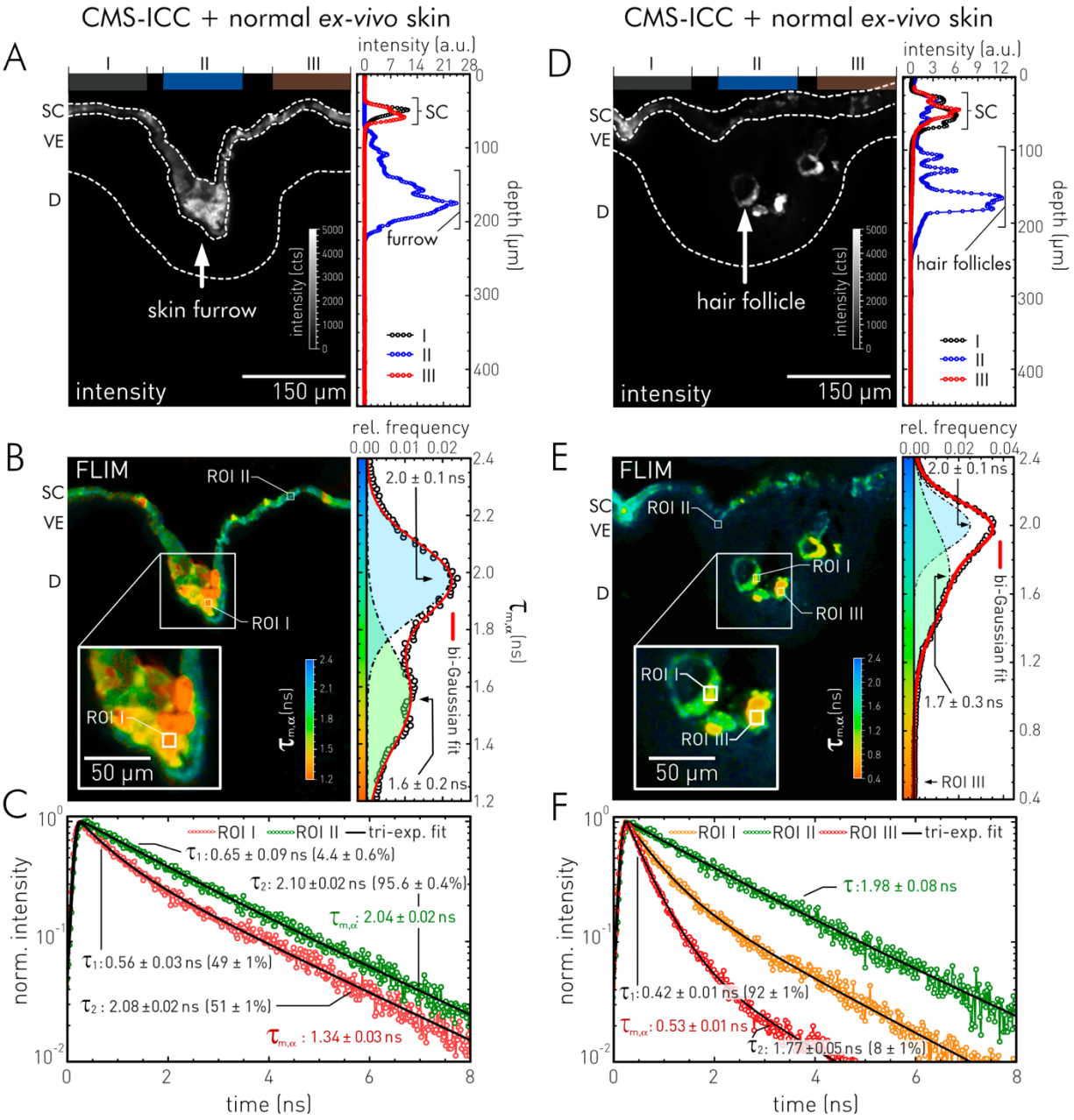

Figure 4.5.4: *Ex-vivo* penetration of CMS-ICC into excised human skin after topically application for 16 h. Fluorescence microscopic examinations performed on cryo-cut skin cross sections. **A** CLSM fluorescence intensity image of CMS-ICC located in the SC and skin furrows. Three vertical areas (black, I; blue, II; red, III) indicate regions, that are used for intensity depth profiles of the CMS-ICC fluorescence. Correspondent depth profiles are shown on the right side next to the CLSM image. **B** Tau-plot FLIM image of the same site as shown in A using the mean fluorescence lifetime for color parameterization. Mean fluorescence lifetime – Color legend is shown as an inlay. Frequency histogram and a bi-Gaussian fit of the occurring mean lifetimes are shown on the right hand side next to the FLIM image, populations are indicated by black dashed lines. Mean and standard deviation (Mean ± SD) of the single Gaussian fit functions are indicated. Zoom-in show the skin furrow on detail. **C** Comparison of fluorescence decay traces and multi-exponential model fits of CMS-ICC in both ROIs shown in B. **D** CLSM fluorescence intensity image of CMS-ICC located in the SC and hair follicles. Three vertical areas (black, I; blue, II; red, III) indicate regions, that are used for intensity depth profiles of the CMS-ICC fluorescence. Correspondent depth profiles are shown on the right side next to the CLSM image. **E** Tau-plot FLIM image of the same site as shown in A using the mean fluorescence lifetime for color parameterization. Mean fluorescence lifetime – Color legend is shown as an inlay. Frequency histogram and b-Gaussian fit of the occurring mean lifetimes are shown on the right side next to the FLIM image. Mean and standard deviation of the single Gaussian fit functions are indicated. Zoom-in show incised hair follicles on detail. **F** Comparison of fluorescence decay traces and multi-exponential model fits of CMS-ICC in both ROIs shown in B. Shown uncertainties of decay components and relative amplitudes are based on confidence interval analyses (Section 3.4.1). Abbreviation: ROI: region of interest. CMS-ICC incubation conditions: Topical application for 6 h, 37 °C, 100 % humidity. Experimental conditions: CMS-ICC excitation with λ_{ex} = 530 nm; λ_{em} > 575 nm; objective: 20x.

In a next step, I investigated the influenced of CMS-ICC penetration into the SC on the time-resolved fluorescence properties of the covalently attached ICC probe by FLIM. For this purpose, a confocal FLIM image of the same site as the intensity-based CLSM image in Figure 4.5.4A was analyzed by the tau-plot approach, using a tri-exponential decay model (compare Section 4.3.2). The resulting false-color FLIM image (Figure 4.5.4B) was parameterized by the mean fluorescence lifetime (Eq. 20) in a range between 1.2 and 2.4 ns. The respective frequency distribution histogram (Figure 4.5.4B, right) of the occurring mean fluorescence lifetimes indicates different CMS-ICC species. A simple bi-Gaussian fit model applied to the frequency distribution identified at least two populations. One population had a distribution center at 2.0 ± 0.1 ns (± SD). These CMS-ICC species where characteristic of SC regions of lower fluorescence intensities.

In regions of SC with higher CMS-ICC intensities, especially within the skin furrow (area: II), the second population was present, defined by faster fluorescence decays. These CMS-ICC species show a distribution maximum at 1.6 ± 0.2 ns. To illustrate this inhomogeneous behavior, the decay histograms within two ROIs have been integrated (see Figure 4.5.4B). The resulting cumulative decay histograms are shown in Figure 4.5.4C. A subsequent decay fit revealed varying numbers of decay components. The general differences of the fluorescence lifetime in both regions can be attributable to different CMS-ICC interactions, characterized in the selected ROIs by $\tau_{m,\alpha}$-values of 1.34 ± 0.03 ns and 2.04 ± 0.02 ns. The faster fluorescence decays in the regions of high intensities indicate a more efficient competing depopulation pathway of ICC's S_1 state compared to lower intensity regions (see Section 4.2.1). The observed decay traces are generally slower than for CMS-ICC in aqueous solution with a mean fluorescence lifetime of $\tau_{m,\alpha} = 0.41 \pm 0.03$ ns.

In some of the investigated cross sections I found hair follicles. Some of them were filled with accumulated CMS-ICC (Figure 4.5.4D). These sites had a similar high fluorescence intensity as previously observed in skin furrows (Figure 4.5.4A) and also here an associated decrease in CMS-ICC's fluorescence lifetime is observed. The corresponding tau-plot FLIM image shows an incised hair follicle filled with CMS-ICC (Figure 4.5.4E). Here, the respective mean fluorescence lifetime frequency distribution (Figure 4.5.4E, right) ranges between 0.4 and 2.4 ns. To illustrate the differences in fluorescence decay behavior, I again select characteristic ROIs. The decay traces detected therein are shown in Figure 4.5.4F. In the case of ROI III, an extremely fast fluorescence decay was detected ($\tau_{m,\alpha} = 0.53 \pm 0.01$ ns) which approaches almost to the fluorescence lifetime signature and mean fluorescence lifetime of CMS-ICC free in solution.

Since CMS-ICC located in a hair follicle represents a possible penetration route of the nanocarrier into the VE or dermis, further areas in the vicinity of hair follicles were examined under higher magnification. Since these areas had much lower fluorescence intensity levels than the SC or hair follicles penetrated by large concentrations of CMS-ICC, higher excitation intensities could be applied. This procedure leads to an increased sensitivity due to a higher fluorescence emission probability of CMS-ICC, but also to the generation of an autofluorescent background in the VE and dermis. Here, the

tau-plot analysis probably reaches its limits, as a necessary multi-exponential decay model and a broad autofluorescence lifetime distribution meet (see Section 3.4.2).[198] In order to verify if the observed fluorescence in the VE indeed originated from CMS-ICC or from autofluorescent species, I applied this time the Cluster-FLIM approach.[44] A global cluster analysis of FLIM images acquired from CMS-ICC treated skin (16 h) and untreated skin, acting as an autofluorescence reference, recognized three distinct fluorescence lifetime signatures (FLSs, Figure 4.5.5B). The obtained FLSs allow a clear-cut discrimination between tissue related autofluorescence (green) and the target fluorescence of CMS-ICC (cyan, red). In the SC and partly within the hair follicle, I observed a slower FLS of CMS-ICC (cyan, Figure 4.5.5A), while a fast FLS (red) was found in the center of the hair follicle. This result matches the tau-plot analysis in Figure 4.5.4E. Figure 4.5.5B compares the three fluorescence decay traces of Figure 4.4.5F to the FLSs obtained by the Cluster-FLIM analysis. While the slowest and the intermediate decay trace correspond very well with the cyan and red FLSs, the analysis could not resolve the fastest decay trace (ROI III) in a separate cluster. However, this decay behavior occurs only in a few pixels as the frequency distribution in Figure 4.5.4E shows.

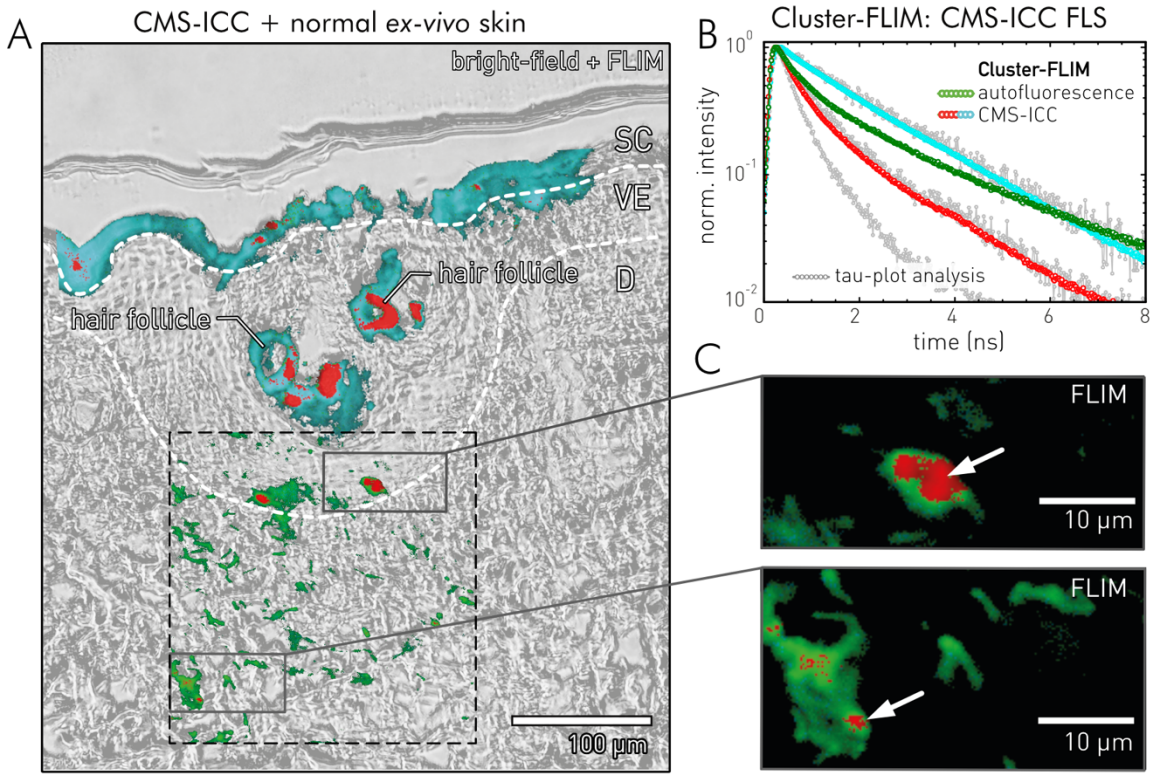

Figure 4.5.5: Cluster-FLIM analysis of *ex-vivo* penetration of CMS-ICC into excised human skin after topically application for 16 h. FLIM examinations performed on cryo-cut skin sections. Cluster-FLIM-bright-field overlay of CMS-ICC penetration into human skin. The site corresponds to the Tau-plot FLIM image of Figure 4.5.4D. The black dashed square indicates a second FLIM acquisition using a higher magnification level by changing to a higher magnifying microscope objective (40x). Cluster-FLIM globally analyzed both CMS-ICC FLIM images with a FLIM image of untreated reference sample for autofluorescence background determination. Three Clusters were recognized, they are colored cyan, red for CMS-ICC and green for autofluorescence. **B** Comparison of the three recognized FLSs and fluorescence decay traces (gray) of Figure 4.5.4F. **C** Image details of A. Arrows indicate CMS-ICC localization. Abbreviations: SC: *stratum corneum*; SG: *stratum granulosum*; SSp: *stratum spinosum*; D: dermis; FLS: fluorescence lifetime signature. CMS-ICC incubation conditions: Topical application for 16 h, 37 °C, 100 % humidity. Experimental conditions:

CMS-ICC excitation with λ_{ex} = 530 nm; λ_{em} > 575 nm; objective: 20x and 40x. Modified reprint from Frombach et al.[169], Copyright 2018, with the kind permission of J. Control. Release.

The area investigated on a higher magnification level and with higher excitation intensities exhibits the green-colored FLS representing the autofluorescent background, but also, occasionally, the red-colored FLS indicating small amounts of CMS-ICC within VE and dermis (Figure 4.5.5C). This means that the interaction mode of the nanocarrier in these spots is different from the one in the flat SC and from the CMS-ICC species at the high intensity sites in the hair follicle (Figure 4.5.4F, ROI III).

CMS-ICC *in-vivo* interactions with mouse models of psoriasis and atopic dermatitis

Inflammatory skin diseases such as atopic dermatitis or psoriasis present special therapeutic challenges due to their complex structural and functional changes to the skin barrier. This generally leads to the fact that various anti-inflammatory drugs do not reach the intended target sites in the VE and dermis.[166, 172] Therefore, the penetration behavior of CMS-NC after topical *in-vivo* administration in healthy mice, in mice with oxazolone-induced atopic dermatitis and mice with psoriasis-like dermatitis were investigated by FLIM and compared next. The samples were prepared and provided by the lab of Prof. Gruber (Freie Universität Berlin, Germany). The FLIM experiments described below compare mice from five groups. These groups consist of both dermatitis models treated with CMS-ICC (5 g/L), each with a negative control group treated with a 0.9 % sodium chloride (NaCl) solution, and another reference group which was injected subcutaneously with an aqueous CMS-ICC solution (5 g/L). The experimental sequence of topical CMS-ICC and NaCl applications over five days is shown in Figure 4.5.6A.

Confocal FLIM measurements were conducted on horizontal sections (<10 µm, SC to dermis) of formalin-fixed and paraffin-embedded skin. The skin sections prepared by this method showed high autofluorescent background levels in the SC and VE which made a clear-cut discrimination via the Cluster-FLIM analysis tool necessary. The FLIM data collected from all five investigated groups were evaluated in a global cluster analysis (Figure 4.5.6). Cluster-FLIM recognized two FLSs, which can be assigned to the topical applied CMS-ICC (red-colored) and to an autofluorescent background species (cyan-colored).

The topically applied CMS-ICC accumulate in high concentrations within SC layers, the site of application. The recognized FLSs show no significant differences between the healthy and inflamed skin models. An identification of the red-colored FLS in the negative control reference groups did not occur. In the second group of false-positive mice subcutaneously injected with the nanocarrier, the red FLS of CMS-ICC was detected in almost all pixels of both VE and SC.

Thus, CMS-ICC seems to accumulate throughout the SC after topical application with no differences between healthy, atopic dermatitis, and psoriatic mouse skin. A further penetration into VE does not occur significantly. In contrast to the penetration experiments on human skin *ex vivo*, CMS-ICC did not accumulate in murine hair follicles. Thus, Cluster-FLIM identifies the SC as the main

target structure of topically applied CMS-NC in healthy, psoriatic, and atopic dermatitis murine model skin.

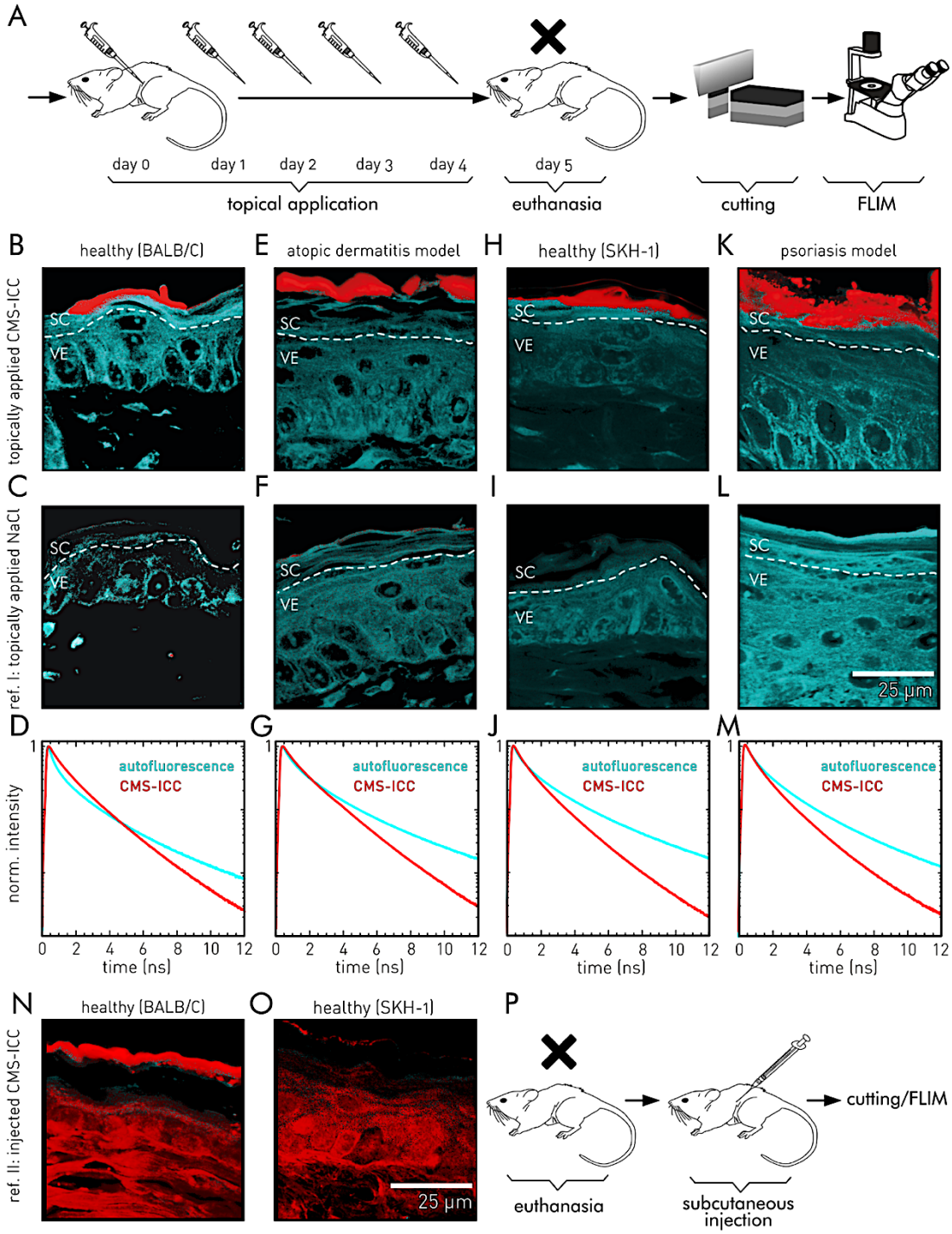

Figure 4.5.6: Cluster-FLIM analysis identifies the SC as the main target structure of topically applied CMS in healthy, psoriatic and atopic dermatitis murine model skin. **A** Topical application scheme of CMS-ICC on murine skin *in vivo* as performed in the lab of Prof. Gruber (Freie Universität Berlin, Germany). **B** Cluster-FLIM image of healthy murine skin (BALB/C mouse) after topical application of CMS-ICC. **C** Cluster-FLIM image of healthy murine skin after topical application of 0.9 % NaCl solution. **D** FLS from Cluster-FLIM analysis, generated by integrating over all pixels of a recognized cluster in images B, C and N. Red indicates CMS-ICC; cyan indicates dermal autofluorescence. **E** Cluster-FLIM image of murine atopic dermatitis model after topical application of CMS-ICC. **F** Cluster-FLIM image of murine atopic dermatitis model after topical application of 0.9 % NaCl solution. **G** FLS from Cluster-FLIM analysis, generated by integrating over all pixels of a cluster in images E, F and N. **H** Cluster-FLIM image of healthy murine skin (SKH-1 mouse) after topical application of CMS-ICC. **I** Cluster-FLIM image of healthy murine skin (SKH-1 mouse) after

topical application of 0.9 % NaCl solution. **J** FLS form Cluster-FLIM analysis, generated by integrating all pixels of a cluster in images H, I and O. **K** Cluster-FLIM image of murine psoriasis model after topical application of CMS-ICC. **L** Cluster-FLIM image of murine psoriasis model after topical application of 0.9 % NaCl solution. **M** FLS from Cluster-FLIM analysis, generated by integrating over all pixels of a cluster in images K, L and M. **N** Subcutaneous injection of CMS-ICC in healthy murine skin (BALB/C mouse). **O** Subcutaneous injection of CMS-ICC in healthy murine skin (SKH-1 mouse). **P** Injection scheme of CMS-ICC in euthanized mice. Experimental conditions: CMS-ICC excitation with λ_{ex} = 530 nm; λ_{em} > 545 nm; objective: 60x. B,E,C,F,D,G are modified reprints from Radbruch et al.[166], Copyright 2017, with the kind permission of Nanoscale Res. Lett.; H,K,I,L,J,M are modified reprints from Pischon et al.[172], Copyright 2017, with the kind permission of Nanomedicine.

CMS-ICC penetration into an epidermal aging model

Reduced barrier functions of aged skin might lead to increasing penetration rates of nanoparticles or nanocarriers like CMS-ICC. *In-vivo* studies on age-related barrier damage have to deal with overlapping effects of intrinsic and extrinsic skin ageing.[390] Thus, the exact influence of skin aging on the barrier function remains unclear. In this paragraph, I will investigate the influence of age-associated changes to the penetration probability of CMS-ICC by using reconstructed human epidermis (RHE) models, developed and provided by Prof. Schäfer-Korting's lab (Freie Universität Berlin, Germany), and FLIM-based CMS-ICC detection.

Normal RHE models from juvenile normal human keratinocytes (NHK) do not map aging effects like chronologically aging or extrinsic factors like sun light. However, UVB-irradiation of NHK cells in cell culture generates a higher activity of senescence associated β-galactosidase, less cell proliferation, and reduced viability. Using such UVB-irradiated keratinocytes to reconstruct human epidermis (UVB-RHE) produces an epidermal aging model that features hallmarks of aged skin. These are increased concentrations of β-galactosidase, higher release rates of interleukin-1α and -8 into the culture medium compared to normal RHE and an altered cell differentiation leading to a thinner SC. The morphological differences in the SC formation between normal RHE and UVB-RHE becomes evident by considering Figure 4.5.7A and B.

The FLIM experiments on CMS-ICC penetration described below compare RHE from three different groups. The first group consists of normal RHE models, the second, and third group of UVB-RHE models constructed from NHK treated with a low and high dose of UVB-irradiation (9.6 mJ/cm^2 vs. 25 mJ/cm^2). A CMS-ICC solution (5 g/L) or PBS (control) was applied topically to all RHE models for 6 hours at equivalent conditions. FLIM experiments were conducted on horizontal sections (<10 µm) of cryo-embedded RHE. A global Cluster-FLIM analysis of the FLIM data over all groups recognized two FLSs (Figure 4.5.7F), characterizing to species of CMS-ICC which are color-coded in cyan (slower fluorescence decay) and yellow (faster fluorescence decay). Autofluorescence did not contribute to the analyses due to its low intensity in the RHE models.

Despite a generally reduced barrier function of RHE models compared to human skin *in vivo*, only marginal amounts of CMS-ICC penetrate into the SC of normal RHE constructs (Figure 4.5.7B). Furthermore, no crossing of the SC barrier and penetration into the VE was observed for the nanocarrier. The latter observation is well in accordance with previous penetration studies on human skin *ex-*

vivo and animal models *in vitro* (see above). The detected cyan FLS can be attributed to penetrated CMS-ICC within the SC. Here, the slow decay is characteristic, as it was in the *ex-vivo* human skin penetration experiments shown above. The second FLS seems to originate mainly from CMS-ICC located and interacting with the cryo-medium above the SC. Leftovers of CMS-NC were found within the cryo-medium in all investigated constructs. However, it cannot be excluded that the faster FLS might originated from a CMS-ICC interaction with the upper layers of the SC. Faster fluorescence decays of CMS-ICC at stratum corneal sites with high CMS-ICC intensities were also observed in human skin *ex-vivo*.

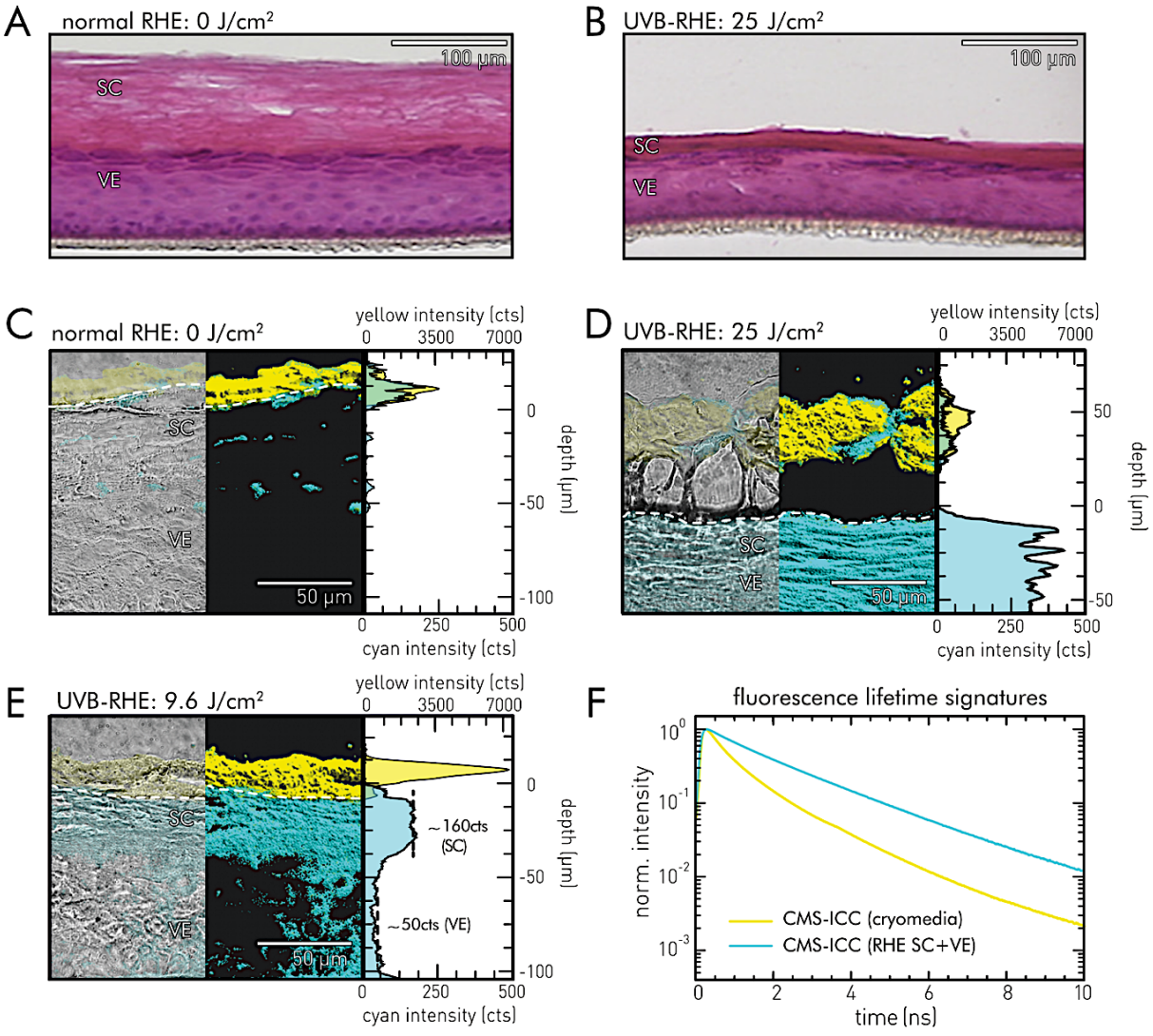

Figure 4.5.7: Penetration and interaction patterns of CMS-ICC into UVB-RHE. **A** HE-stained normal RHE; the construct shows a multilayered, fully stratified, orthokeratosis morphology (Images were obtained by Prof. Schäfer-Korting's group, Germany). **B** HE-Stained UVB-RHE (25 J/cm²) shows a reduced thickness of the SC, a hyperchromatic stratum granulosum, and slight acantholysis. **C-D** Representative overlays of bright field and false-color coded Cluster-FLIM images of cryo-sectioned RHE models as analyzed together with Robert Brodwolf (Prof. Alexiev's group, Freie Universität Berlin, Germany). Cluster-resolved fluorescence intensity profiles of CMS-ICC are shown next to FLIM images. Color coding according to the recognized FLS of CMS-ICC in the RHE models. **C** normal RHE; almost no penetration of CMS-ICC into the construct. **D** UVB-RHE (25 J/cm²); pronounced penetration of CMS-ICC into all epidermal layers of the UVB-RHE model. **E** UVB-RHE (9.6 J/cm2); increased penetration of CMS-ICC into SC and VE of UVB-RHE. **F** Comparison of the three recognized FLSs. Abbreviations: SC: *stratum corneum*; VE; viable epidermis; FLS: fluorescence lifetime signatures. CMS-ICC incubation conditions: Topical application for 6 h, 37 °C, 100 % humidity. Experimental conditions:

CMS-ICC excitation with λ_{ex} = 530 nm; λ_{em} > 545 nm; objective: 60x. Modified reprints from Löwenau et al.[211], Copyright 2017, with the kind permission of Eur. J. Pharm. Biopharm..

When applied to the UVB-RHE constructed from NHKs irradiated with 25 mJ/cm^2, CMS-ICC penetrated readily into the SC and into the VE, also indicated by the cyan colored FLS (Figure 4.5.7D). The second group of UVB-RHB models were constructed from NHK cells irradiated by a lower UVB dose of 9.6 mJ/cm^2. Also, in this FLIM image, Cluster-FLIM recognizes both FLSs and indicates that CMS-ICC penetrates into the SC and VE layers by the cyan colored FLS (Figure 4.5.7E). If one compares the CMS-ICC penetration profiles (Figure 4.5.7C and F) in RHE constructed from non-irradiated and low dose UVB-irradiated NHK (9.6 mJ/cm^2), the relative CMS-ICC intensities in the SC are increased by a factor of ~7. In the case of the high UVB dose, this factor is even further increased (~13-fold).

Discussion

The SC is the first layer of the skin interacting with topically applied CMS-NC. In all investigated skin models, CMS-ICC penetrated into the *stratum corneal* layers as shown by CLSM and FLIM experiments. In human skin *ex vivo*, accumulations of CMS-ICC were also found to be embedded in skin furrows and hair follicles (Figure 4.5.4). It can therefore be assumed that the increased local nanocarrier concentration in these structures may facilitate a translocation into the VE, where interactions with epidermal cells like keratinocytes or Langerhans cells can take place. Respective *in vitro* experiments on CMS-ICC uptake and intracellular interactions by these cell types are shown in Section 4.4. *In vivo*, an even higher accumulation rate and thus larger follicular reservoirs of CMS-NC can be assumed, since *ex-vivo* skin models show a significantly reduced follicular penetration capacity due to a contraction process of elastic fibers after excision.[391]

The application of FLIM using the interaction sensitive FMR probe ICC enables the detection of different interaction modes of CMS-ICC within the flat SC, SC that lines skin furrows and within hair follicles. Thus, various dermal interactions, together with possible effects by cryo-freezing and cutting alter the fluorescence lifetime of CMS-ICC in tissue sections. As Section 4.3.2 demonstrates, the CMS-ICC probe design can provide environmental shielding of its FMR-probe by the multi-shell system. Thereby, the nanocarrier structure inherently reduces the fluorescence lifetime sensitivity to changes in environmental viscosity, while it maintains the sensitivity to biomolecular interactions.

The detected correlation between the fast fluorescence lifetime (~0.5 ns vs ~ 2 ns) of the FMR probe at corneal areas with high CMS-ICC intensities allows the conclusion that the CMS-NCs at these sites are less interactive. This is an interesting observation as it contradicts the common intuition that higher intensities in a fluorescence microscopic image indicate areas of a high residence probability and thus stronger interaction modes. For extremely high fluorescence intensities, like within hair follicles, CMS-ICC's fluorescence decay traces even approach the FLS characteristic for CMS-ICC in solution, i.e., non-interacting CMS-NC. When comparing different fluorescence intensities of

CMS-ICC in steady-state fluorescence microscopy, this change in the decay behavior leads to a drastic underestimation of the CMS-NC concentrations in regions with high fluorescence intensity due to faster fluorescence lifetimes (reduced quantum yield) in these regions.

Additional to the general pitfalls in quantitative fluorescence experiments, such as the deviations from linearity between fluorescence intensity and fluorophore concentration for high fluorophore concentrations (Eq.13) and internal filter effects (re-absorption), this phenomenon leads to a reduced significance of fluorescence intensity images as quantitative indicators of local CMS-ICC distributions. CMS-ICC emitting with lower intensity shows slower fluorescence decay traces. This indicates a different mode of interaction and appears to lead to stronger intramolecular changes within the nanocarrier. This results in a reduced intramolecular rotation probability of the ICC probe and thus a slower fluorescence decay. CMS-ICC species characterized by the slower FLS are situated primarily in the flat SC (Figure 4.5.5).

Despite the detailed knowledge on the skin structure (see Section 2.4), specific and conclusive information on skin penetration and SC barrier crossing of larger molecules than urea, especially for macromolecules like nanoparticles, is still largely missing. In addition to the size-dependent penetration of topically applied nanomaterials, physicochemical properties such as deformability, flexibility[258] and elasticity play an important role in the penetration capacity and depths. It is known that PEG coatings, which are comparable to the outer shell of CMS-NC, can improve the penetration through biological barriers by reducing interactions with extracellular tissue matrices, cellular barriers, and biological fluids such as mucus, leading to improved delivery.[392] A recently published atomic force microscopy study of nanogels demonstrates that physicochemical stiffness can result in a reduced penetration capacity.[393] Morilla et al. concluded that the general deformability of a nanocarrier system is the decisive feature for an effective penetration into the skin without causing damage to the lipid barrier.[394]

For CMS-NC, it has been postulated that they may aggregate to form larger, sub-micron nanoparticle clusters.[150, 153] If this occurs, they have a high chance of entering the hair follicles *infundibulum* by the so-called ratchet effect.[194] This effect explains the higher follicular penetration rates of larger nanoparticles with a size of approximately 600 nm.[195] One can speculate that CMS-NC aggregates located deep within the follicles form nanocarrier depos, which can act as drug reservoirs. Furthermore, the nanoparticle clusters within these depos might disaggregate over time to single CMS-NC units and penetrate deeper into the follicle canal, from where they cross the skin barrier, until they reach living epidermal cells.[4] If and how the CMS-NC aggregates disintegrate and separate and if a translocation as individual particles occurs has not been answered yet.

Nevertheless the penetration of CMS-NC into the VE of intact human skin *ex vivo* happened only in a small number of cases, it took place and could therefore clearly be verified (see also Section 4.4.2). Cluster-FLIM allows to identify the epidermal fluorescence signal from CMS-ICC, as well

as a wider distribution of minute amounts of CMS-ICC within the perifollicular dermis. A recent study related the passage of hydrophilic molecules through the SC barrier to regions of poor intra- and intercellular lipid packing, which coincide with furrows on the skin's surface (intercellular "gorges").[395] These are structural changes representative of sites of low skin resistance. I observed CMS-ICC species within the skin furrows, characterized mainly by a reduced interaction mode (fast fluorescence decays). This could indicate conversely that the strong interaction mode (slow fluorescence decay) observed in the flat SC is generated by a specific interaction of CMS-ICC with SC lipids present in the usual SC package formation.

Only a few studies analyzed interactions between nanoparticles and the skin barrier on a molecular level. Most data available were obtained in skin penetration studies with vesicular nanocarrier systems. For example, hydrophobic fluorophores loaded on highly deformable lipid vesicles have been detected at depths of several microns below the skin surface, as well as traces of lipidic building blocks of the transporting vesicles.[396] In another study, nanogels were found to interact with the SC and induced a perturbation of lipid and protein organization as assessed by Raman Spectro microscopy.[397] From a therapeutic point of view, a CMS-NC reservoir within the SC and the hair follicles could be useful, if it led to increased concentrations or to longer exposure times with the loaded drugs.

The *in-vivo* application of CMS-ICC on murine disease models of atopic dermatitis and psoriasis showed a similar picture of the penetration behavior as the experiments on human skin *ex vivo* (Figure 4.5.6). The conducted FLIM experiments suggest that CMS-NC applied topically onto the skin of mice over five subsequent days accumulates in the SC (Figure 4.5.6B,E,H,K). A crossing of the SC barrier to the VE could neither be detected to a significant extent nor quantified. Cluster-FLIM recognized two FLSs, which were assigned to the topical applied CMS-ICC and to a strong autofluorescent background. Using the false-positive reference group of subcutaneously injected mice improved the outcome of a global Cluster-FLIM analysis by providing the FLS of CMS-ICC located within the VE. The clear-cut separation of CMS-ICC from other fluorescence species allows the local identification and the determination of the dermal penetration depth of the CMS-NC in the high autofluorescent tissue sections. The complex skin barrier changes associated with atopic dermatitis or psoriasis do neither appear to lead to an altered penetration behavior, nor to an otherwise changed distribution of CMS-NC within the SC.

These results, and the results on the dermal CMS-NC penetration in human skin described above are contrasting the previous *in-vitro* and *ex-vivo* studies on RHS models and excised human skin in Franz diffusion cells. Here, CMS-NC partially penetrated into both: into the VE layers of taped-stripped skin after 24 h and into the VE of RHS disease models after 6 h already.[170] However, these simulated barrier damages introduced by the use of Franz diffusion cells, tape stripping, or RHS design, differ structurally and physicochemically from barrier damages present in psoriatic or atopic dermatitis skin. This applies to the murine skin models, but also to native human skin *in vivo*.

Despite the assumption of an impaired barrier function in RHE models compared to human skin *ex vivo*,[377] CMS-ICC penetrates only marginally into the SC of the investigated normal RHE models after a 6 h-incubation. When applied to the UVB-RHE constructed from NHKs irradiated with 25 J/cm^2, CMS-ICC penetrated readily into the SC and into the VE (Figure 4.5.7D). The 25 J/cm^2 UVB dosage results in RHE models, which reproducibly generates hallmarks of (extrinsic) skin aging.[211] It is particularly interesting to see that the second group of UVB-RHE models consisting of NHK cells irradiated with a lower UVB dose of 9.6 mJ/cm^2 exhibits an increased CMS-ICC penetration, too. Conventional tests of this model neither show reduced NHK viability nor a slower cell cycle nor a reduced β-galactosidase activity. Despite this lack of biological markers of aging, Cluster-FLIM images (Figure 4.5.7E) were able to show that CMS-ICC penetrates into the SC and into the VE layers in these UVB-RHE constructs. The induced aging affects the barrier function drastically, constituting a new indicator for altered penetrations behavior of nanomaterials in aged skin.

4.5.3 mpFLIM-ROX for ROS detection in murine model skin

It is known that oxidative stress promotes inflammatory diseases of the skin as in the case of atopic dermatitis (AD) or psoriasis.[398-399] In skin of this state, inflammatory cells release free radicals when activated, thereby increasing the effect of oxidative stress.[398] In addition, inflammatory skin diseases such as psoriasis and atopic dermatitis alter the SC layers, which may result in a reduced barrier function. It was shown that atopic dermatitis-like skin lesions aggravate upon nanoparticle exposure.[400] In order to understand the consequences of nanoparticle interactions on cellular ROS production *in vivo*[401], it is desirable to extend the FLIM-ROX assay (see Section 4.2.3) from living cells to living tissue.

The FLIM-ROX experiments shown here were conducted together with Jens Balke and Robert Brodwolf (Prof. Alexiev's group, Freie Universität Berlin, Germany). I would like to use the FLIM data to demonstrate the capabilities of the mpFLIM setup, which I have built during my doctoral work (see Section 4.1.2) as well as the application of cluster-based mpFLIM-ROX to compare ROS levels in tissue (see Section 2.1.3). The investigated full-thickness biopsies of murine skin tissue of healthy and diseased state were provided by Prof. Gruber's lab (Freie Universität Berlin, Germany). The data presented here was first published in Small (Balke et al., 2018, Ref. 49).

mpFLIM measurements were performed together with Jens Balke on CellROX treated and untreated (control groups) excised murine skin of three different ROS states (normal healthy skin, UVB irradiated skin, and skin with induced atomic dermatitis). CellROX treated skin biopsies of healthy murine skin served as a negative ROS control. UVB irradiated (50 mJ/cm^2) murine skin was used as positive ROS control for the murine animal model of AD. The skin explants not treated with the CellROX reagent served as autofluorescence controls. mpFLIM images of all investigated groups were recorded 5 µm below the SC surface and were analyzed by a global Cluster-FLIM analysis. The Cluster-FLIM analysis performed by Robert Brodwolf recognized several CellROX species. Two major

FLS indicating regions of strong autofluorescence (green) and regions with high ROS levels by activated CellROX species (red) are shown in Figure 4.5.8G. Pixels of other colors are inactivated CellROX or further autofluorescence species.

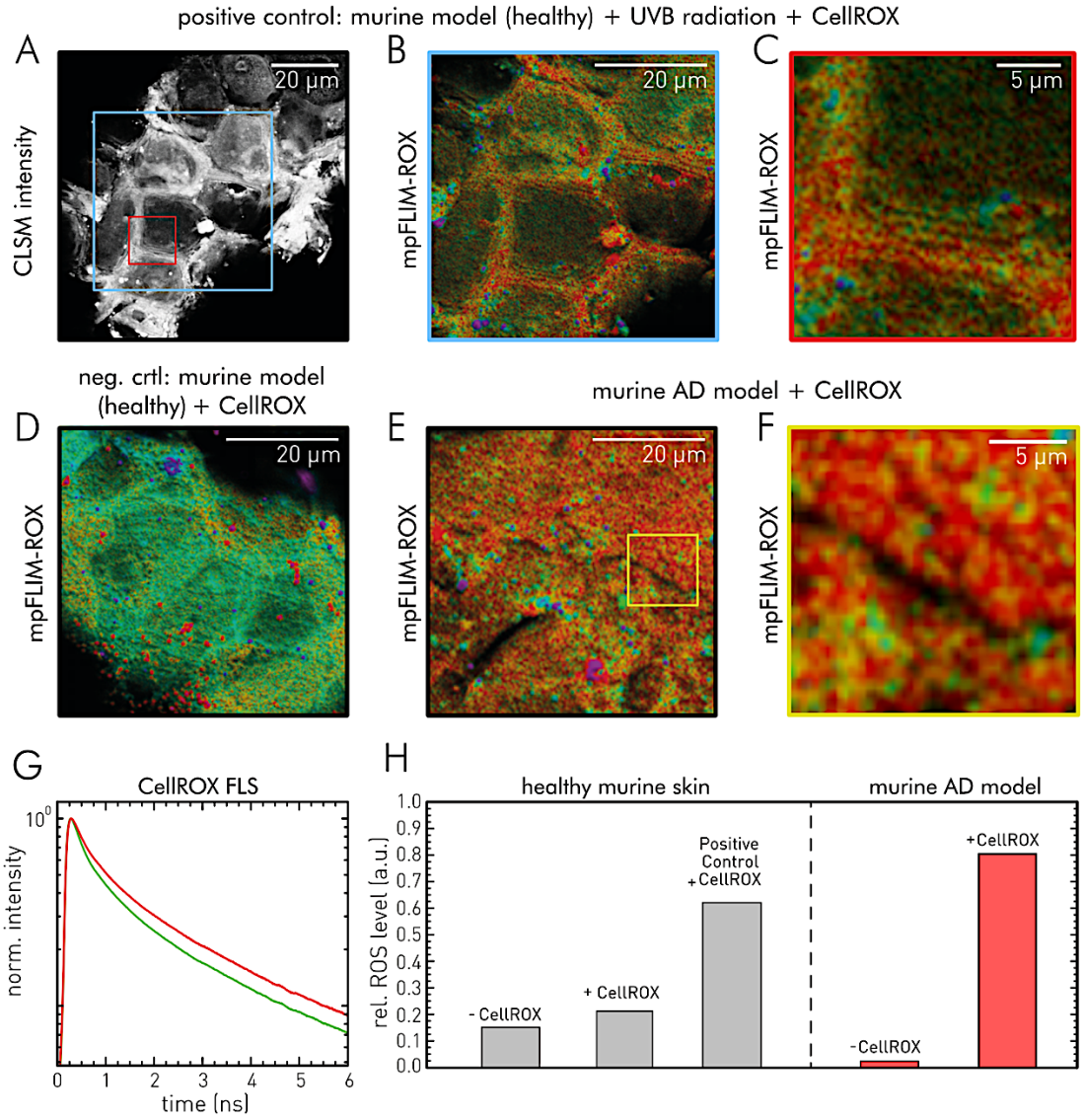

Figure 4.5.8: Quantification of ROS levels by mpFLIM-ROX in healthy and atopic dermatitis (AD) model skin, recorded in cooperation with Jens Balke and analyzed by Robert Brodwolf (Prof. Alexiev's group, Freie Universität Berlin, Germany). **A** Intensity-based CLSM image of SC (skin depth: 5 µm) of healthy murine skin after 15 min incubation with CellROX reagent and UVB irradiation (as positive control). **B** Cluster-FLIM image, color-coded according to the cluster-based FLIM analysis. Red-colored areas indicate the FLS of activated CellROX, and thus high ROS levels. **C** image detail of B. **D** Cluster-FLIM image of healthy murine skin with treated with CellROX (negative control). **E** Cluster-FLIM image of AD model skin with CellROX Green. **G** Main FLS from the global Cluster-FLIM analysis. The color-coding of the FLS correlates with the pseudo coloring of the Cluster-FLIM images, with the red-colored FLS representing activated CellROX and the green-colored FLS representing major autofluorescence component. **H** Relative ROS-levels based on the relative cluster intensities in healthy and AD-like murine skin. Experimental conditions: λ_{ex} = 800 nm, main beam splitter edge wavelength at 643 nm, single detector mode: λ_{em} = 500 – 550 nm (525/25BP + 745SP); objective: 60x. All images are modified reprints from Balke et al. (2018, Ref. 49), Copyright 2020, with the kind permission of Small.

Figure 4.5.8A shows a CLSM intensity image of typical corneocyte structures. Corneocytes are embedded in a lipid matrix consisting mainly of ceramides, free fatty acids, and cholesterol (see Section 2.4). Within the negative control group (Figure 4.5.8D), red areas are limited to a few small

cell compartments while the positive control (Figure 4.5.8B) is characterized predominantly by red areas, indicating increased oxidative stress due to extensive UVB irradiation.[402] Figure 4.5.8H compares the different FLIM-ROX intensities for healthy and AD model skin. In healthy murine skin, the addition of CellROX Green ("+CellROX", without activation) increases the CellROX fluorescence intensity by 36 % with respect to the autofluorescence background ("-CellROX"). Activation with UVB radiation induces oxidative stress and yields a fluorescence increase of 263 %.

While in AD murine skin autofluorescence background is reduced to a fraction (15 %) of the healthy murine skin, the intensity immediately increases after addition of CellROX Green to 3560 % over the autofluorescent baseline level, indicating significant ROS levels in the AD model skin compared to normal (healthy) murine skin. The multiphoton FLIM-ROX approach outperforms previously reported methods which are solely intensity based[402] by means of selectivity and signal artefact reduction. This novel approach allows for the precise assessment and monitoring of enhanced ROS levels in tissue. Among others, enhanced ROS levels can be utilized as triggers for controlled release of drugs from nanocarriers or activation of prodrugs.[403] Thus, the mpFLIM-ROX approach might also prove useful in the development of novel drug delivery systems.

4.5.4 mpFLIM-based tomographic interaction imaging of CMS-ICC penetration in RHS

In Section 4.5.2, specific interaction modes of CMS-NC were observed. The observation took place while the nanocarriers penetrated into the epidermal layers of different skin models. The interactions were studied via confocal FLIM, using the fluorescence lifetime of the environmentally sensitive FMR probe ICC attached to the core of the CMS-NC (Section 2.3.2). All experiments of Section 4.5.2 were based on skin tissue prepared as cryo or paraffin sections. An effect of these preparation methods on the detected fluorescence lifetimes cannot be excluded *per se*. Firstly, these methods could influence the molecular state of the nanocarrier or the state of the fluorescence lifetime probe itself. Secondly, analyzing and interpreting penetration into 3D structures, such as skin furrows in a horizontal 2D section, is difficult and prone to errors, even though 2D sectioning is the standard preparation method in microscopy-based skin penetration studies.

So, I expanded the scope of my nanocarrier-skin interaction studies by establishing and applying a mpFLIM setup for tomographic time-resolved fluorescence detection in two spectral detection channels. In Section 4.1.2, I give a detailed description of the setup and show a system characterization for live-tissue imaging as well as its capability to detect CMS-ICC and loaded bodipy in spectrally separated detection channels (CH). In the following section, I will use this mpFLIM setup to establish a tomographic live-tissue imaging approach and apply it to reconstructed human skin (RHS) topically treated with CMS-ICC or CMS-ICC/bodipy solutions. The investigated RHS models were developed and provided by Prof. Schäfer-Korting's lab (Freie Universität Berlin, Germany).

RHS represents a multilayer *in-vitro* test platform simulating human skin *in vivo*. These full-thickness skin models were developed to overcome the lack of human *ex-vivo* skin and to reduce the number of animal trials, which are scientifically and ethically questionable. RHS models are characterized by many *in vivo*-like properties. They have been proven useful in studies on dermal penetration and on local medical effects of small molecules, as validated test guidelines exist.[375-376] RHS models consist of a dermis, formed by a collagen matrix containing normal human fibroblast, a VE and a *SC* both formed via cell differentiation of primary keratinocytes (NHK).[19, 170, 213] The RHS models used here are metabolically active systems[378], which modulate native fibroblast influences on keratinocyte phenotypes.[379] In addition to normal healthy skin, complex disease states such as non-melanoma skin cancer (NMSC) can be modelled by RHS.[213, 380] Data and results presented in the next section were partly published in Theranostics (Brodwolf et al., 2020, Ref. 44). Hence, the next paragraph relies partially on my contribution to this paper.

mpFLIM-based detection of CMS-ICC interactions in the SC and VE of RHS models

The confocal FLIM experiments of Section 4.5.2 indicate CMS-NC interacting with *stratum corneal* layers and accumulating in skin furrows to a large extent after being topically applied. Both interaction states are characterized by specific fluorescence lifetime changes. Local CMS-NC accumulations represent an interesting observation as they point to the formation of potential nanoparticulate drug reservoirs in skin furrows. In the following, these structures will be investigated in detail using mpFLIM. For this purpose, FLIM images of the SC and VE layers were acquired in intact living RHS models in top view mode (x-y direction) using the z-scan feature of the mpFLIM setup (Section 4.1.2).

After topical application of CMS-ICC (5 g/L) on normal RHS models, live-tissue mpFLIM of the SC (depth: 0 – 15 µm) revealed some of the nanoparticle's interaction modes. Since the autofluorescence levels are an order of magnitude below the fluorescence intensity of CMS-ICC treated models, a significant autofluorescence contribution is neglected in the following tau-plot analysis. It is assumed that the determined fluorescence lifetimes originated primarily from ICC and thus indicate CMS-ICC interactions within the dermal layers. For the tau-plot analysis, I fitted the fluorescence decay histograms of the recoded FLIM data to a tri-exponential decay model (Eq.19).

Figure 4.5.9C displays a tau-plot FLIM image of CMS-ICC interacting with an intact living RHS model at a depth of 4 µm after a 6 h-incubation. The chosen mean lifetime parameterization ranges between 0.4 and 1.8 ns and is visualized by a rainbow color code (blue to red). The FLIM image shows a location of the SC which is marked by a skin furrow. Within the flat SC layer, mean fluorescence lifetimes of CMS-ICC were observed between 1.2 and 1.6 ns (orange – red color). Within the furrow, fluorescence lifetimes of CMS-ICC are faster (0.54 ± 0.05 ns, ± SD). These sites are additionally characterized by high fluorescence intensities.

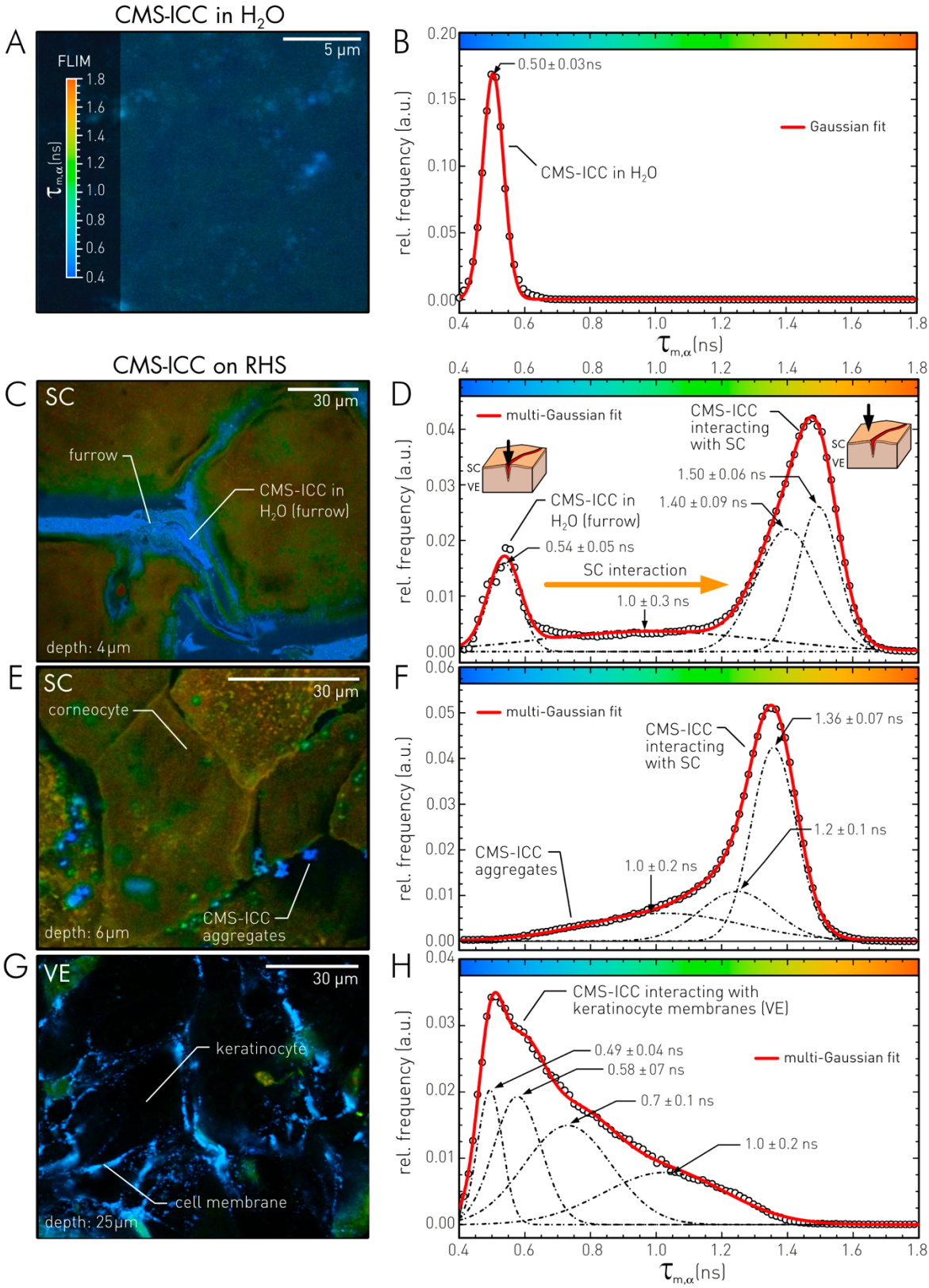

Figure 4.5.9: mpFLIM reveals different CMS-ICC interactions with epidermal structures in living RHS models. FLIM data is fitted by a tri-exponential decay model. All tau-plot images are false color-coded according to calculated mean fluorescence lifetime (0.4 – 1.8 ns). **A** Tau-plot image of CMS-ICC in aqueous solution. **B** Frequency histogram and a bi-Gaussian fit of the occurring mean lifetimes in A are shown on the right hand side next to the FLIM image, populations are indicated by black dashed lines. **C** Tau-plot image of CMS-ICC interacting with SC layer (depth: 4 µm) after 6 h topical incubation at 37 °C. **D** Frequency histogram of the occurring mean fluorescence lifetimes in C. **E** Tau-plot image of CMS-ICC interacting with corneocytes (depth: 6 µm) after 6 h topical incubation at 37 °C. **D** Frequency histogram of the occurring mean fluorescence lifetimes in E. **G** Tau-plot image of CMS-ICC interacting with VE layer (depth: 25 µm) after 6 h topical incubation at 37 °C. **H** Frequency histogram of the occurring mean

fluorescence lifetimes in G. **D,F,H** Multi-Gaussian fits to the respective fluorescence lifetime distributions, means and standard deviations (± SD) are indicated. Experimental conditions: λ_{ex} = 845 nm, main beam splitter edge wavelength at 705 nm, single detector mode: λ_{em} = 575 – 600 nm; objective: 60x.

By comparing the fluorescence lifetime distributions of CMS-ICC interacting with the SC layer shown in Figure 4.5.9D to non-interacting CMS-ICC free in aqueous solution (Figure 4.5.9A,B), it becomes immediately clear that CMS-ICC located within the furrow is not interacting as both fluorescence lifetimes are almost identical. This CMS-ICC species seems to remain in an aqueous environment. Once the nanocarrier interacts with the SC, a significant increase in CMS-ICC's fluorescence lifetime occurs (>1.2 ns), indicating a strong interaction due to changes in the nanocarrier's conformation (compare Section 4.3.2). A multi-Gaussian fit analysis of the mean fluorescence lifetime frequency distribution revealed at least four populations (Figure 4.5.9D). The analysis clearly identified the CMS-ICC species in the furrow (0.54 ± 0.05 ns) and two species with $\tau_{m,\alpha}$-values above 1 ns, characterized by distribution means (±SD) of 1.40 ± 0.09 ns and 1.50 ± 0.06 ns. Faster fluorescence decays below 0.8 ns were also observed between some "loose" corneocytes (Figure 4.5.9E, depth: 6 µm). In these cases, CMS-ICC was present in an aggregated supramolecular form. The individual aggregates typically had diameters between 0.5 and 3.0 µm and seemed to associate with the vertical corneocyte surfaces. Applying a multi-Gaussian fit analysis to the respective frequency distribution identified three CMS-ICC species. The analyses did not resolve the CMS-ICC aggregates, but only a fast population characterized by a distribution mean (±SD) of 1.0 ± 0.2 ns. Globally, however, and also in this case, the main interaction mode within the SC was characterized by mean fluorescence lifetimes above 1 ns, originating from two populations defined by 1.2 ± 0.1 ns and 1.36 ± 0.07 ns.

When examining deeper viable epidermal layers after 6 h incubation, a different picture occurs. In contrast to the experiments in Section 4.5.2, a regular penetration into the VE cannot be neglected (Figure 4.5.9G). In these epidermal layers, CMS-ICC is characterized by faster fluorescence lifetimes (Figure 4.5.9H). At a depth of 25 µm, the nanoparticle is mainly detected at the cell membranes of keratinocytes. A similar membrane localization was observed in the 2D cell model (Section 4.4.1). Applying a multi-Gaussian fit analysis to the frequency distribution recognized at least four populations of CMS-ICC, all belonging to the faster fluorescence lifetime spectrum (see Figure 4.5.9H). This indicates a change of the interaction mode once the CMS-ICC nanocarrier has passed the SC.

I will now focus on the CMS-ICC accumulations within the skin furrows, representing potential drug reservoirs again. The question of how loaded cargo molecules behave at these sites arises. To address this question, I expand my interaction study to loaded CMS-ICC nanocarriers. For that purpose, bodipy493/503 (bodipy, logP = 3.5, MW=262 Da)[102] was utilized as a non-covalently loaded fluorescent cargo (see Section 3.2.1). After topical application of CMS-ICC/bodipy (5 g/L) on normal RHS models for 6 h at 37 °C, live-tissue mpFLIM data were acquired in the SC and VE in two separated spectral detection channels (see Section 4.1.2). The resulting FLIM data of both channels were

analyzed by tri-exponential decay fitting and a mean fluorescence lifetime parameterization. Figure 4.5.10A and B show the respectively generated tau-plot FLIM images of CMS-ICC (A) and bodipy (B) located at the SC surface (depth: 0 µm) of an intact living RHS model. The selected site shows a corneocyte (center) with gaps to its neighboring corneocytes. Like the FLIM data shown in Figure 4.5.9, this FLIM image (Figure 4.5.10A) reveals that CMS-ICC is characterized by a mean fluorescence lifetime between 1.2 and 1.4 ns when interacting with corneocytes. This indicates a strong interaction. In addition to this strong interaction mode, CMS-ICC species with a faster decay time of less than 1 ns and a supramolecular appearance are present, again. The reduced lifetime indicates a reduced probability of interaction compared to the SC. As shown in Figure 4.5.9E, these CMS-ICC aggregates are located in the inter-corneocyte gaps.

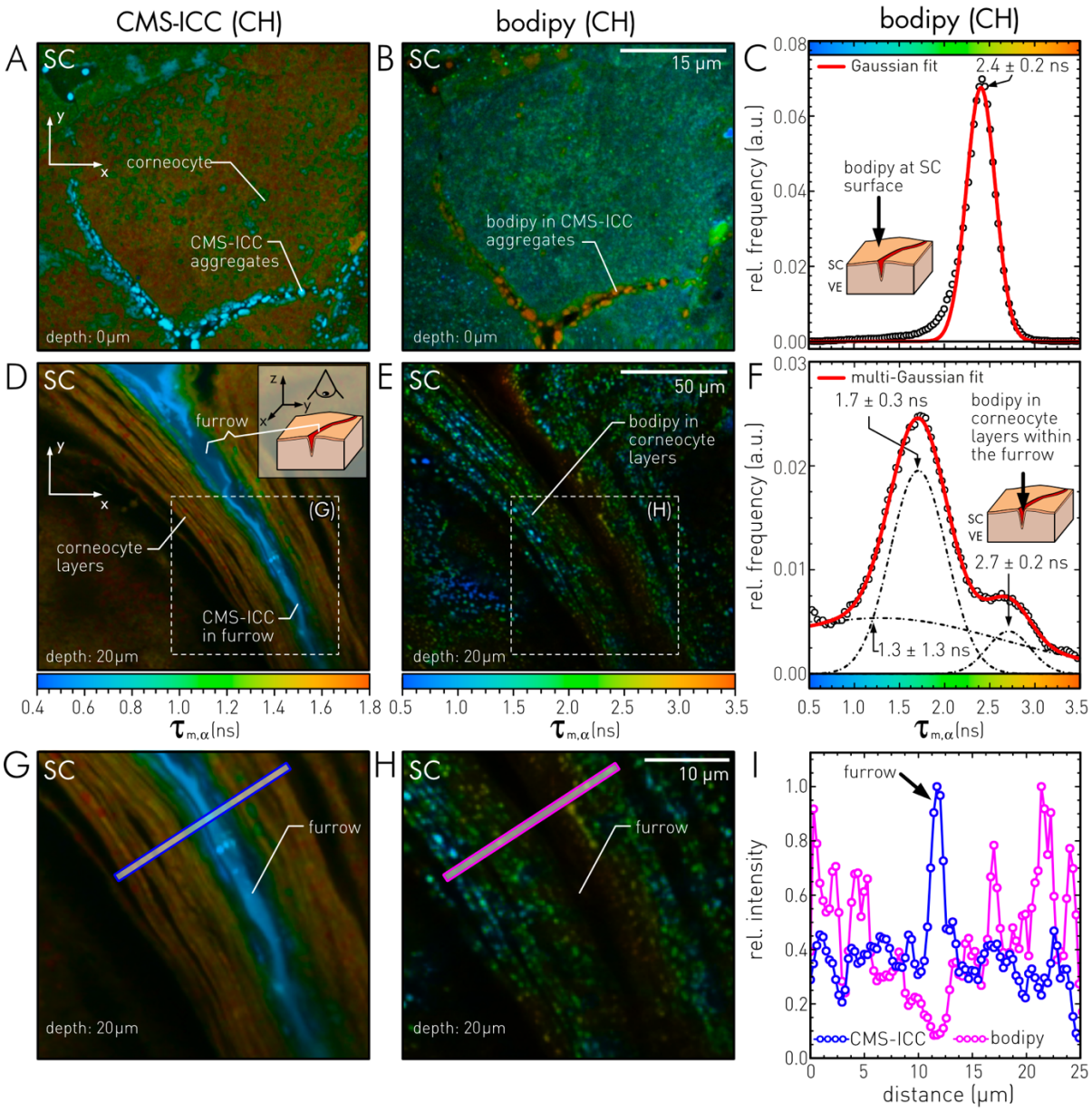

Figure 4.5.10: Two-color mpFLIM reveals CMS-ICC and bodipy locations and interactions in skin furrows of living RHS models after topical application with CMS-ICC/bodipy. FLIM data in both spectral detection channels are fitted by a tri-exponential decay model. Tau-plot images are false color-coded according to calculated mean fluorescence lifetime (CMS-ICC: 0.4 – 1.8 ns; bodipy: 0.5 – 3.5 ns). **A** Tau-plot image of CMS-ICC interacting with SC surface (depth: 0 µm), after 6 h topical incubation at 37 °C. **B** Tau-

plot image of bodipy channel at the same site as A. **C** Frequency distribution and respective Gaussian fit of the occurring mean fluorescence lifetimes in B, mean and standard deviation (± SD) are indicated. **D** Tau-plot image of CMS-ICC interacting with corneocyte layers which line a skin furrow (depth: 20 µm), after 6 h topical incubation at 37 °C. **E** Tau-plot image of bodipy channel at the same site as D. **F** Frequency histogram and respective multi-Gaussian fit of the occurring mean fluorescence lifetimes in E, means and standard deviations (± SD) are indicated. **G** CMS-ICC channel: Digital zoom into the area of the skin furrow (indicated in D). Blue-colored bar indicates position of a fluorescence intensity line scan. **H** bodipy channel: Digital zoom into the area of the skin furrow (indicated in E). Magenta-colored bar indicates position of a fluorescence intensity line scan. **I** Intensity profile along the line scans shown in G and H. Blue: CMS-ICC channel; magenta: bodipy channel. Experimental conditions: λ_{ex} = 845 nm, main beam splitter edge wavelength at 705 nm, two-color detector mode: CMS-ICC CH λ_{em} = 575 – 600 nm; bodipy CH λ_{em} = 460 – 500 nm; objective: 60x.

The FLIM image of the corresponding bodipy channel (Figure 4.5.10B) indicates bodipy still mainly being inside the nanocarrier. This becomes especially clear when looking at the inter-corneocyte aggregates. Here, the co-localization is particularly evident. The tau-plot FLIM images of the bodipy channel are parameterized by the mean fluorescence lifetime. The corresponding false-color scale ranges between 0.5 and 3.5 ns. Figure 4.5.10C shows the corresponding frequency distribution of the mean fluorescence lifetimes of bodipy at the surface. According to a Gaussian fit, the distribution maximum locates at 2.4 ± 0.2 ns. As soon as bodipy locates within the CMS-ICC aggregates, fluorescence lifetimes become slower (> 3.0 ns, orange areas in Figure 4.5.10B). So, while CMS-ICC in its aggregated form is characterized by faster fluorescence lifetimes, loaded bodipy in these nanocarrier aggregates is determined by slower fluorescence lifetimes, considered in relation to the lifetimes of CMS-ICC/bodipy on the corneocyte surfaces.

The distribution and interaction of bodipy changes when observing skin areas with furrows. Through these furrows, the SC sinks into the depths of the skin surface, sometimes up to several hundred micrometers.[404] Figure 4.5.10D shows the CMS-ICC localization within such a skin furrow at a depth of 20 µm. The interaction of CMS-NC with these structures can be divided into a weak interaction within the aqueous phase (blue, $\tau_{m,\alpha}$ ~0.5 ns) in the center of the furrow and a strong interaction (yellow to red, $\tau_{m,\alpha}$ =1.2 – 1.8 ns) with the corneocyte layer that lines the furrow. CMS-ICC completely penetrates these individual corneal layers in the furrow.

The localization of bodipy and CMS-ICC in the furrow region differs, suggesting the cargo is at least partially released. Especially in the aqueous phase in the center of the furrow, no bodipy was detected (Figure 4.5.10E). The bodipy signal originates solely from small spot-like structures in the corneal lining layers of the furrow. Bodipy at this location has an extended range in mean fluorescence lifetime compared to the SC surface (Figure 4.5.10F versus Figure 4.5.10C). This altered interaction mode of bodipy as well as its different localization compared to CMS-ICC indicate a change in the loading behavior of the CMS-NC within the furrow. In order to illustrate this effect on a semi-quantitative level, I compared the fluorescence intensity profiles from line scans through the skin furrow in both detection channels (Figure 4.5.10G & H). Figure 4.5.10I indicates a release of bodipy from CMS-ICC within the furrow, while in the corneocyte layers a correlation between cargo and nanocarrier positions still partially existed.

Differences of CMS-ICC interactions in 2D NHK monolayers and 3D RHS models

Detecting systematic discrepancies in different *in-vitro* test platforms simulating human tissues is an essential prerequisite for predictive preclinical studies. Therefore, I investigated and compared inherent variations in CMS-ICC interactions with normal human keratinocytes (NHK) located in 2D monolayers as they were used in Section 4.4.1 and in multilayered 3D RHS models consisting of SC, VE, and dermis. Both test platforms seem comparable at first sight as they are generated by patient-derived keratinocytes. While confocal FLIM easily detects CMS-ICC interactions in the 2D monolayer, it fails in deep tissue examinations below the SC. So, I applied multiphoton excitation (see Section 4.1.2) to get access to the NHK cells located in the VE of the full-thickness skin models (depth: 40 µm).

In order to compare both test platforms, 2D monolayers were incubated directly with CMS-ICC (10 mg/L) via the cell medium. RHS models were incubated by applying CMS-ICC (5 g/L) onto their SC simulating the scenario of a topical application. As shown above, mpFLIM is able to detect CMS-ICC within the VE of RHS models after a topical 6 h-application at this concentration. A concentration reduction of a factor of 500 between monolayer and RHS model seemed realistic, because most CMS-ICC remains in the SC and does not penetrate into the viable epidermis. To compensate for the necessary penetration time, I investigated cellular interactions in the 2D monolayer and 3D RHS models at different points in time.

After 6 h, I observed fluorescence signals from CMS-ICC interacting with epidermal NHK cells in a depth of 40 µm (Figure 4.5.11C). At this point in time, CMS-ICC was located mainly in cell membranes. This resembles the nanocarrier location of the initial membrane interactions after 15 min in the 2D monolayer experiment (Figure 4.5.11A, see also Section 4.4.1). In order to compare the fluorescence decay characteristics of CMS-ICC in both test platforms and to draw conclusions about the existing interaction modes of CMS-ICC, a comparative cluster-FLIM analysis was applied. Cluster-FLIM recognizes differences in the initial cellular interaction with NHK in the VE of the RHS models and in 2D monolayers by substantially altered FLSs (Figure 4.5.11F vs. G). Equally to NHK in the monolayered 2D model, the Cluster-FLIM analysis recognized three different fluorescence lifetime signatures of CMS-ICC in the 3D model which reflects different interaction patterns. The FLIM image in Figure 4.5.11C was false color-coded in the reverse order than in the 2D models, i.e., the fast FLS in cyan, the intermediate FLS in yellow, and the slow FLS in orange (Figure 4.5.11G). I chose this code, because the main FLS in the cell membrane had the fastest decay, opposing the observation in the 2D monolayer. Surprisingly, the yellow FLS in both model types shows a high similarity (dashed line in Figure 4.5.11G), leading to the interpretation that in the 3D model, too, caveolae are responsible for the CMS-ICC internalization (Figure 4.5.11A and C).

For prolonged application times (22 h), I observed a new FLS (orange), characterized by a slow fluorescence decay in addition to the cyan/yellow FLS, still located in vicinity of the cell membrane. This FLS seems indicative of the cellular fate of CMS-ICC in NHKs of the VE as it emerges

intracellularly. In contrast to the confocal live-cell FLIM studies of the 2D monolayer (Figure 4.5.11A,B), I localized the CMS-nanocarriers also in the nuclei of the NHK cells at this incubation time (Figure 4.5.11D). This observation is supported by horizontal cryosections produced from the 3D models (Figure 4.5.11E) and a subsequent DAPI staining of the nuclei. Figure 4.5.11E clearly shows CMS-ICC penetrating the SC and VE completely after such a long application time. This also includes the NHK nuclei.

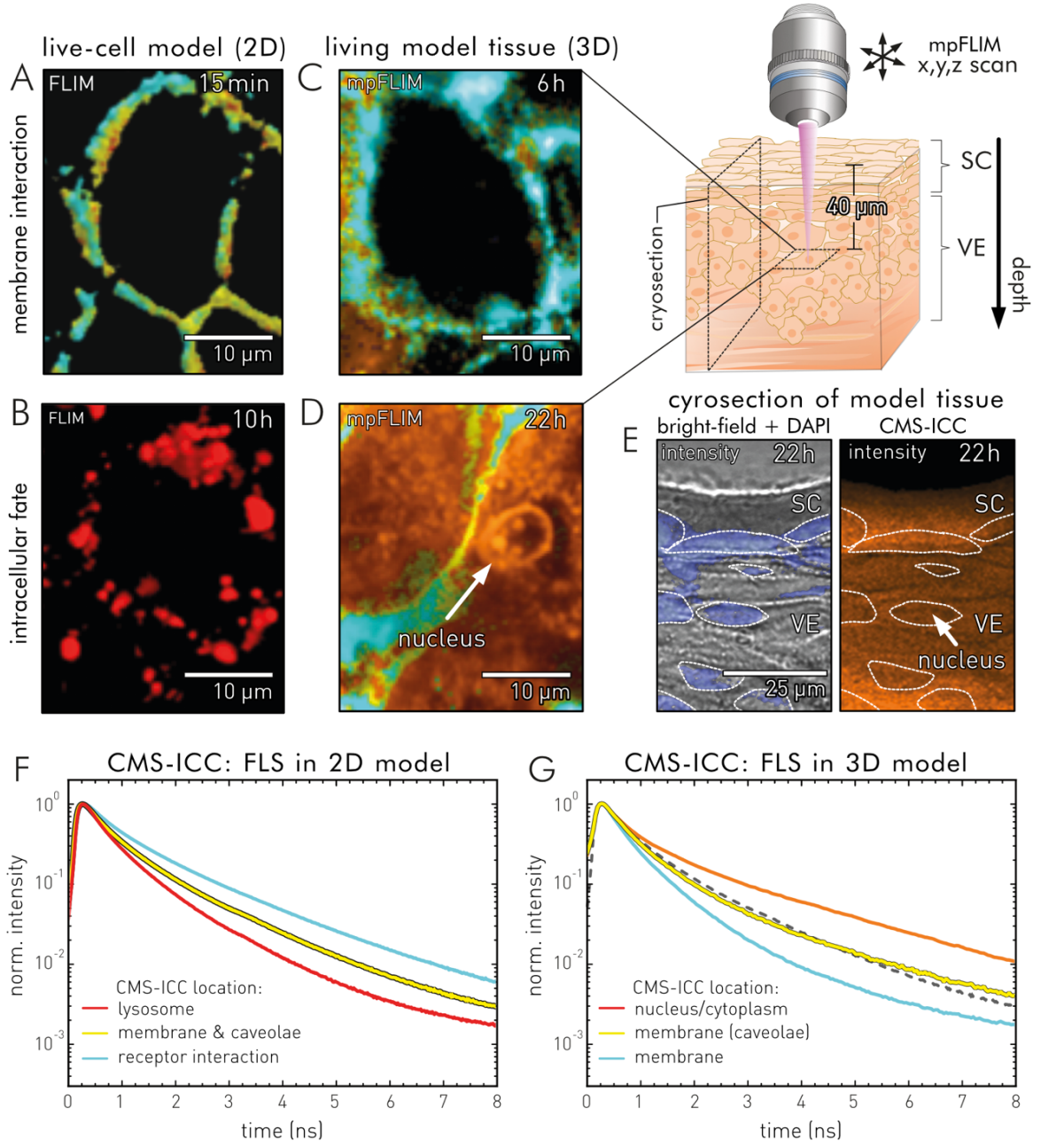

Figure 4.5.11: Comparison of CMS-ICC fluorescence decay characteristics in NHK obtained from monolayer 2D models via confocal FLIM and multilayer 3D tissue models via multiphoton excitation. **A** Cluster-FLIM image of an individual NHK cell in a monolayer after a 15 min CMS-ICC incubation. **B** Cluster-FLIM image of an individual NHK cell in a monolayer after a 600 min CMS-ICC incubation. Color coding according to a cluster analysis (F) of the confocal FLIM data recognizing three FLS. **C** Cluster-FLIM image of an individual NHK cell in 40 µm depth of an RHS tissue model obtained by multiphoton excitation after a 6 h-incubation with CMS-ICC. **D** Cluster-FLIM image of an individual NHK cell in 40 µm depth of an RHS tissue model obtained by multiphoton excitation after a 22 h-incubation with CMS-ICC. Color coding in accordance to a second Cluster-FLIM analysis recognizing shown in (G). **E** verification of CMS-ICC nuclei interaction after 22 h incubation via cryosectioning of the 3D tissue model. Left: Bright-field overlay with DAPI fluorescence intensity showing the nuclei. Right: Confocal intensity image (orange) of the same site, the nuclei are

indicated by white dashed lines. **F** FLS of CMS-ICC in NHK of a monolayer 2D model. The respective assignments of the FLS to environmental interactions are indicated. **G** FLS of CMS-ICC in NHK of a 3D tissue model. The respective assignments of the FLS to environmental interactions are indicated. FLS: fluorescence lifetime signatures. Experimental conditions mpFLIM: λ_{ex} = 845 nm, main beam splitter edge wavelength at 705 nm, single detector mode: λ_{em} = 575 – 600 nm; Experimental conditions confocal FLIM: CMS-ICC with λ_{ex}=530 nm, λ_{em} =545 – 600 nm; DAPI with λ_{ex}=405 nm, λ_{em}=430 – 475 nm; objective: 60x. Modified reprints from Brodwolf et al., [44] Copyright 2020, with the kind permission of Theranostics.

Tomographic interaction imaging of CMS-ICC in healthy and diseased RHS models

After establishing mpFLIM-based CMS-ICC detection and the corresponding interaction monitoring in single epidermal layers, I will extend the approach towards tomographic FLIM imaging of living tissue. As already described in section 4.1.2, tomographic images are acquired by scanning image planes along the z-axis (along the "skin" depth, Figure 4.5.12A). Here, successive FLIM data are recorded in different depths of the skin, parallel to the skin surface (see Figure 4.512A). Figure 4.5.11B shows the experimental procedure for CMS-ICC penetrations and interaction studies in multilayer RHS tissue models. At first, the topical application takes place on the surface (SC) of the RHS model. Subsequently, the model is positioned upside down in a glass bottom dish and subjected to mpFLIM. There, FLIM data is recorded at different depths by scanning the microscope objective in z-direction. The resulting FLIM data stacks are subsequently analyzed with Cluster-FLIM.

The Cluster-FLIM analysis tool reduces the computation time needed in FLIM data evaluation compared to conventional FLIM analysis techniques like the tau-plot approach by circumventing time-intensive pixel-based fitting procedures. This feature is particularly advantageous for high-throughput screenings or tomographic approaches as large amounts of FLIM data have to be analyzed.[44] For these applications, linear scalable computation times are also significant. In order to show the linear scalability of the cluster method, I globally analyzed up to 12 duplicates of the same FLIM-image (512×512 pixels, 1024 time bins), resulting in a linear increase of the required computation times (Figure 4.5.12B). This scaling behavior promotes the use of Cluster-FLIM as a valuable analysis tool for tomographic FLIM approaches as large numbers of individual FLIM images have to be analyzed in a reasonable time frame.

Figure 4.5.12C shows a FLIM image stack generated by taking images at different depths (step size: 2 µm) and a global Cluster-FLIM analysis of CMS-ICC's fluorescence decay characteristics integrating all FLIM images. The images show a location on an RHS model marked by a skin furrow (compare Figure 4.5.9C). The Cluster-FLIM analysis recognized five different FLS; the signatures are shown in Figure 4.5.12F. Using a standard image processing tool (3D volume viewer, ImageJ/FIJI),[207] the respectively false-color coded Cluster-FLIM images were transformed into tomographic 3D images (Figure 4.5.12D). Tomographic Cluster-FLIM live imaging provides a precise insight into the three-dimensional penetration and interaction process of CMS-ICC and potential cargos. The five identified FLS sorts the local interaction events into discrete interactions patterns indicated via the chosen color code, from cyan (fastest decay, lowest interaction) over green, yellow, orange to red (slowest decay, highest interaction). As already shown in Figure 4.5.9C using a

classical tau-plot analysis, the fastest fluorescence decays of the ICC probe can be found within the furrow. This indicates a weak CMS-ICC interaction. Within the SC, a slower FLS was found, resulting from a strong interaction between CMS-ICC and corneocytes or the surrounding lipid matrix (Section 2.4).

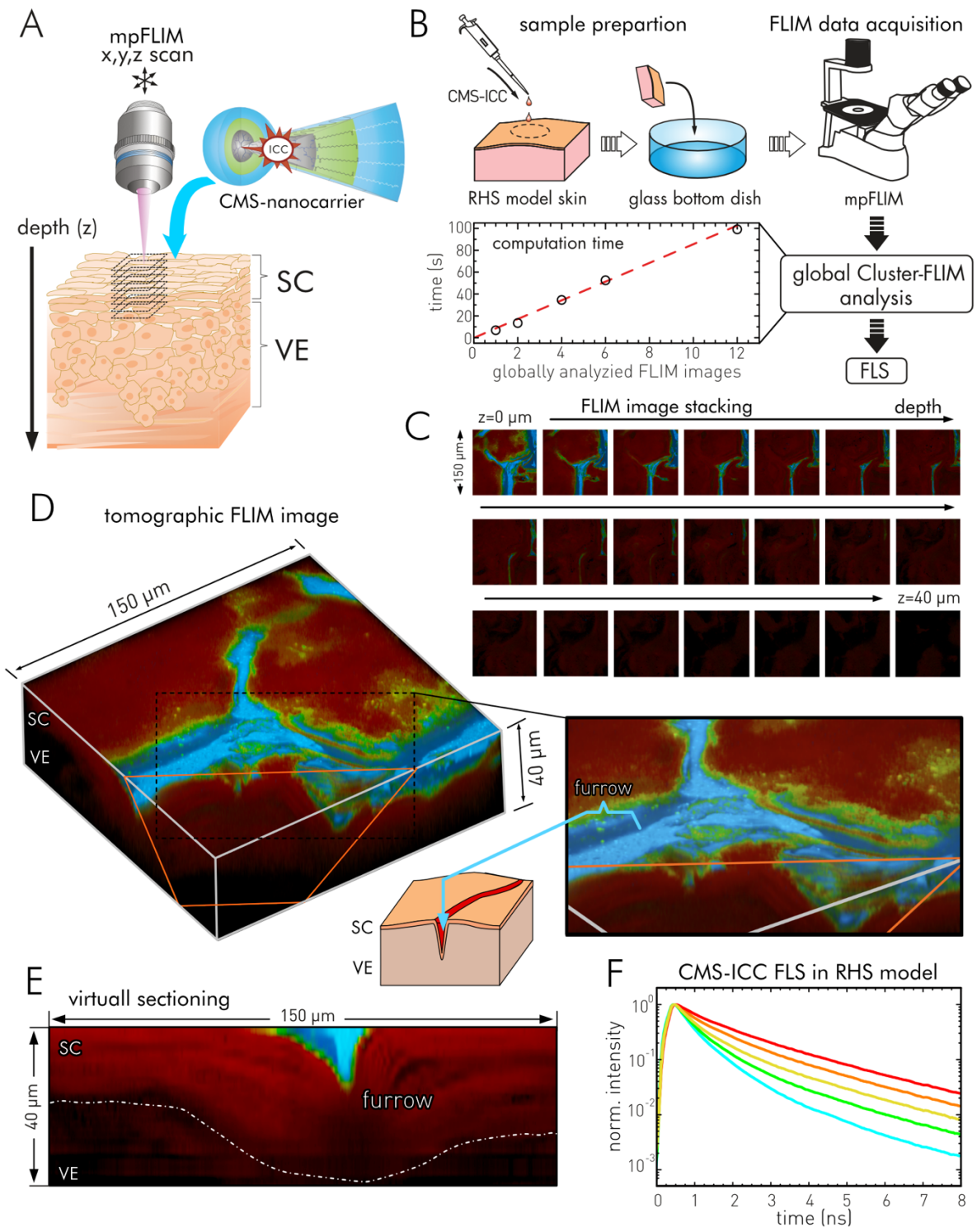

Figure 4.5.12: mpFLIM tomography for live-tissue interaction imaging. **A** Scanning principle for acquiring image stacks. **B** Experimental process: Topical application of CMS-ICC (nanocarrier) to the living RHS model; placing the living model into glass bottom dish; subjecting the dish to mpFLIM; analyzing the FLIM image stacks by Cluster-FLIM.**C** Cluster-FLIM image stack of CMS-ICC treated RHS models, site shows a skin furrow. Color code indicating different CMS-ICC interactions with epidermal structures in living RHS models. **D** Generated tomographic Cluster-FLIM image using the data set shown in C. **E** Virtual sectioning through the

skin furrow. **F** FLS of CMS-ICC in the investigated RHS model. Abbreviations: FLS: fluorescence lifetime signatures. Experimental conditions: λ_{ex} = 845 nm, main beam splitter wavelength at 705 nm, single detector mode: λ_{em} = 575 – 600 nm; objective: 60x.

Interestingly enough, tomographic Cluster-FLIM images identify intermediate forms of interaction (green, yellow, orange). These are found at the spatial transition areas between the furrows and the SC surface, signaling a gradual increase of the CMS-NC interaction. Tomography also allows virtual sectioning along the z-direction. Thus, the method enables the generation of penetration profiles and horizontal image sections. Figure 4.5.12E shows such a virtual sectioning of the skin furrow. The horizontal Cluster-FLIM image always shows an intermediate CMS-ICC species between the fast FLS (cyan) and the slow FLS (red). This indicates a transition process between CMS-ICC in the furrow, non-interactive within the aqueous solution and the CMS-ICC that strongly interacts with the corneal layers. Since the virtual section is an overlay of Cluster-FLIM and fluorescence intensity images, changes in the total fluorescence intensity become visible. As a result, one notices the vanishing fluorescence signal at the interface between SC and VE at this site of the RHS model. The penetration of CMS-ICC stops at this point.

After tomographic interaction imaging of CMS-ICC in RHS was demonstrated on normal (healthy) RHS models using the Cluster-FLIM analysis tool, I will now focus on differences in penetration and interaction of CMS-ICC/bodipy between healthy RHS and RHS showing non-melanoma-skin cancer (NMSC). NMSC is the most frequent cancer found in humans.[405] Here, the cutaneous squamous cell carcinoma (cSCC) type will be investigated, the most lethal tumor among the NMSC family.[405] Although several attempts have been made to treat cSCC lesions in their early stages (actinic keratosis), using anti-cancer drugs like 5-fluorouracil or ingenol mebutate,[406-407] a topical drug-based anti-cancer treatment of cSCC is still an unmet clinical challenge.[213] Previous studies on NMSC indicate an impaired barrier function.[408-410] A detailed characterization of organotypic RHS models showing NMSC also indicates an impaired skin barrier function which appears to be related to changes in lipid packing in SC and alterations in tight junctions. Furthermore, the investigated RHS models were able to simulate the ingenol mebutate effects previously observed in human skin.[213] To overcome the low success rates of drug-based cSCC treatment, nanoparticular drug delivery seems promising, especially since an increased penetration ability of CMS-ICC and a loaded fluorescent drug mimetic has already been observed for NMSC compared to normal RHS models by classical fluorescence microscopy of 2D sections.[170]

After topical application of CMS-ICC/bodipy (5 g/L) on normal RHS and NMSC models for 6 h, live-tissue mpFLIM was applied to record FLIM image stacks of both groups. The subsequent global Cluster-FLIM analysis of the CMS-ICC channels recognized five FLS. For reasons of clarity and comprehensibility, the three slowest FLSs, occurring at neighboring sites in the images, were combined to a single FLS (red) in the further analysis (Figure 4.5.13F). This results in a fast FLS color-coded in cyan, an intermediate FLS color-coded in green, and a slow FLS color-coded in red. The generated Cluster-FLIM images of the individual depths were used to generate tomographic Cluster-FLIM

representations. Figure 4.5.13A and G compare these spatial 3D FLIM images. The normal RHS is characterized by the red-colored FLS in the SC and the green and cyan FLS in the VE, a picture similar to that in Figure 4.5.12D. This indicates a strong CMS-ICC interaction in the SC and altered interaction mode of the nanocarrier when interacting with the viable keratinocytes in the VE. For a better comparison, the occurrence of all three FLS are shown individually in Figure 4.5.13C.

When comparing these interaction patterns with the NMSC model, a clear difference in their local distribution can be observed directly from the tomographic FLIM image (Figure 4.5.13G). The NMSC model shows a site characterized by a tumor nest in its center. The main interaction of CMS-ICC at the surface is determined by the intermediate interaction mode indicated by the green FLS. Furthermore, the NMSC modes generally show a stronger penetration into deeper levels, indicated by the absolute FLS-resolved fluorescence intensity depth profiles (compare Figure 4.513A and G, right). The penetration enhancement effect of CMS-ICC seems to be caused by the tumor nest. This is also shown by the comparative total fluorescence intensity line scans through the VE and the tumor nest (Figure 4.513A and G, center).

More than the absolute fluorescence (FLS-resolved) intensities (Figure 4.513A and G, right), the comparison of the depth-dependent FLS fractions (Figure 4.513B and H) is an indicative measure of the relative occurrence of different CMS-ICC interaction modes. The respective profiles show that in the healthy RHS model, the red color-coded FLS (slow decay) decreases with increasing depth in favor of the other two FLSs. In the NMSC model, a reverse behavior occurs. If one compares Figure 4.5.13C and 4.5.13I, one finds the source for this behavior: Whereas in the healthy RHS model (C) the slow FLS (red) occurs mainly in the SC, in the NMSC model (I) this interaction pattern occurs mainly in spherical structures distributed throughout the tumor nest.

To examine these structures in detail and compare them to the healthy RHS model, I juxtaposed characteristic FLIM images after 6 h topical application from the VE (depth 40 µm) of the healthy RHS model and the tumor nest (depth 10 µm) of the NMSC model. Figure 4.5.13D shows the typical interaction mode of CMS-ICC with plasma membranes of NHK cells in the VE, characterized by a fast FLS (cyan, membrane interaction) and the intermediate FLS (green, initial uptake). In the NMSC model, a different spatial distribution of the CMS-ICC interaction modes was observed. While in the tumor nest, the green and cyan FLS characterize the intra- and extracellular area, some of the tumor cells show the red FLS within their nuclei (Figure 4.5.13J and K). These nuclei are visible in the tomographic image as red stained spherical structures (Figure 4.5.13I, Figure A2). In normal keratinocytes (NHK) surrounding the tumor nest, the fast FLS (cyan) is found again in the cell membranes as shown in Figure 4.5.13L. For better orientation, the cell membrane is indicated by dashed white lines. Since the red FLS indicates a strong interaction of CMS-ICC with the nuclei, it seems that the tumor cell nuclei are a potential cellular target of the nanocarrier. A similar interaction between CMS-ICC and cell nuclei were observed in normal RHS models only for long topical incubations (>22 h, VE late uptake) as shown in Figure 4.5.13E.

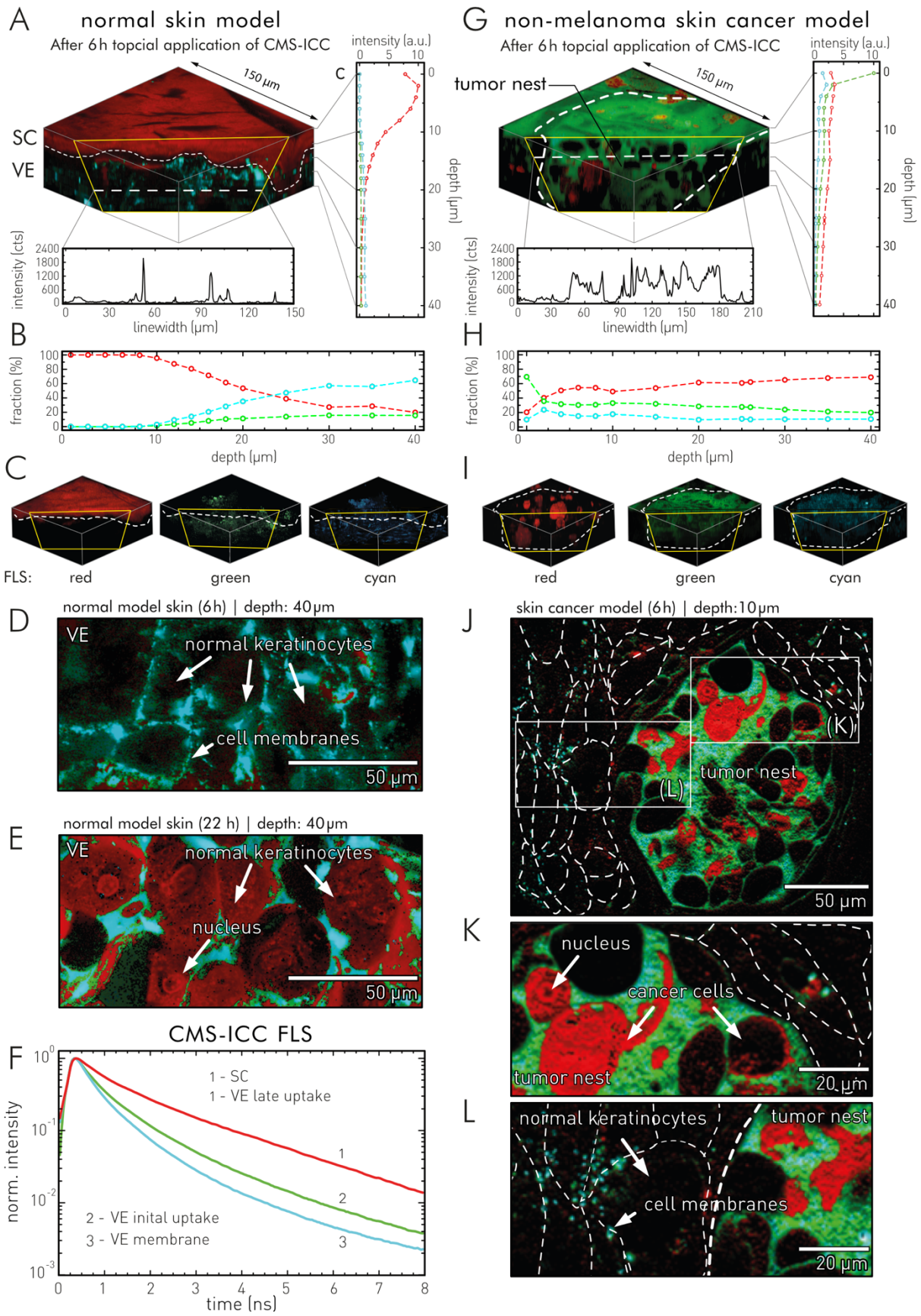

Figure 4.5.13: Live-tissue interaction imaging of CMS-ICC during its penetration into normal RHS and NMSC models using tomographic Cluster-FLIM images. **A** Tomographic Cluster-FLIM image of CMS-ICC in normal RHS models after 6h topical application of CMS-ICC/bodipy. Right: Total fluorescence intensity depth profile separated for the three FLS. Center: Total fluorescence Intensity

line scan through the VE. **B** Relative fractions of the three FLS in dependence of the RHS depth. **C** Tomographic Cluster-FLIM images, each image shows only one of the three FLS (detail view, see Appendix. Figure A2). **D** Cluster-FLIM image of CMS-ICC interacting with NHK cells in the VE (depth: 40 µm, after 6 h topical application). **E** Cluster-FLIM image of CMS-ICC interacting with NHK cells in the VE (depth: 40 µm, after 22 h topical application). **F** FLS of CMS-ICC in the investigated RHS model. **G** Tomographic Cluster-FLIM image of CMS-ICC in normal RHS models after 6h topical application. Right: Total fluorescence intensity depth profile separated for the three FLS. Center: Total fluorescence Intensity line scan through the central tumor nest. **H** Relative fractions of the three FLS in dependence of the RHS depth. **I** Tomographic Cluster-FLIM images, each image shows only one of the three FLS (detail view, see Appendix. Figure A2). **J** Cluster-FLIM image of CMS-ICC interacting with tumor cells in the tumor nest (depth: 20 µm, after 6 h topical application). Dashed lines indicate keratinocyte cell membranes. **K** Zoom into the tumor nest shown in the Cluster-FLIM in J. **L** Zoom into the interface of the tumor nest and sounding normal keratinocytes (NHK) shown in the Cluster-FLIM in J. Abbreviations: NHK: normal human keratinocytes; FLS: fluorescence lifetime signatures. Experimental conditions: λ_{ex} = 845 nm, main beam splitter edge wavelength at 705 nm, single detector mode: λ_{em} = 575 – 600 nm; objective: 60x.

Now, the spatial interaction behavior of the CMS-ICC nanocarriers in both skin models and the cellular distribution of loaded bodipy cargo will be investigated. Figure 4.5.14A shows the spectral CMS-ICC CH of a normal RHS model after 6h topical application with CMS-ICC at a depth of 40 µm (in the VE, the same Cluster-FLIM image as in Figure 4.5.13D). The simultaneously recorded bodipy CH provides the corresponding fluorescence intensity image (blue-colored) of the bodipy cargo (Figure 4.5.14B). The overlay of both channels is visualized in Figure 4.5.14C and indicates an intracellular point-like distribution of bodipy within the individual NHK cells. The distributions appear similar to the bodipy distributions within NHK cells observed in the 2D live-cell experiments of Section 4.4.1.

Within the NMSC model, bodipy distribution appears heterogeneous. The difference can be observed directly between the tumor cells in the tumor nest (Figure 4.5.14F) and the surrounding normal keratinocytes (NHK). Bodipy in normal NHK cells is located in punctiform structures in the cytoplasm and not in the cell nuclei. However, within the tumor nest, bodipy is localized within tumor cell nuclei as indicated by Figure 4.5.14F. This means both the CMS-ICC nanocarrier and its cargo end up in the tumor nuclei as shown in the overlay of CMS-ICC and bodipy channel in Figure 4.5.14G. Thus, the uptake process of CMS-ICC/bodipy in the tumor model seems to be fundamentally different from that in healthy NHK cells. The observed cellular fate of both nanocarrier and cargo indicate a potential tumor targeting mechanism of the nanocarrier system. This potential is underlined by the intensity plot in Figure 4.5.14G. Here, the relative fluorescence intensities of the CMS-ICC CH in the tumor nest were compared to the surrounding keratinocytes. CMS-ICC fluorescence intensities in the tumor nest were increased by a factor of ~4 (Figure 4.5.14H).

Finally, the CMS-ICC distribution on the skin surface of normal RHS models will be compared to NMSC models. Figure 4.5.14D shows the CMS-ICC distribution in the SC of a normal RHS model. One recognizes individual corneocytes. The CMS-ICC species is characterized by the typical slow FLS (red), indicating a strong corneal interaction. Reversely, Figure 4.5.14I shows a surface of an NMSC model (at lower magnification). In addition to typical skin furrows filled with CMS-ICC with a lower degree of interaction (see above), tumor nests can be seen which extend to the surface and thus break through the SC at some sites. Here, too, cell nuclei are characterized by a strong interaction with the nanocarrier, indicated by a slow FLS (red).

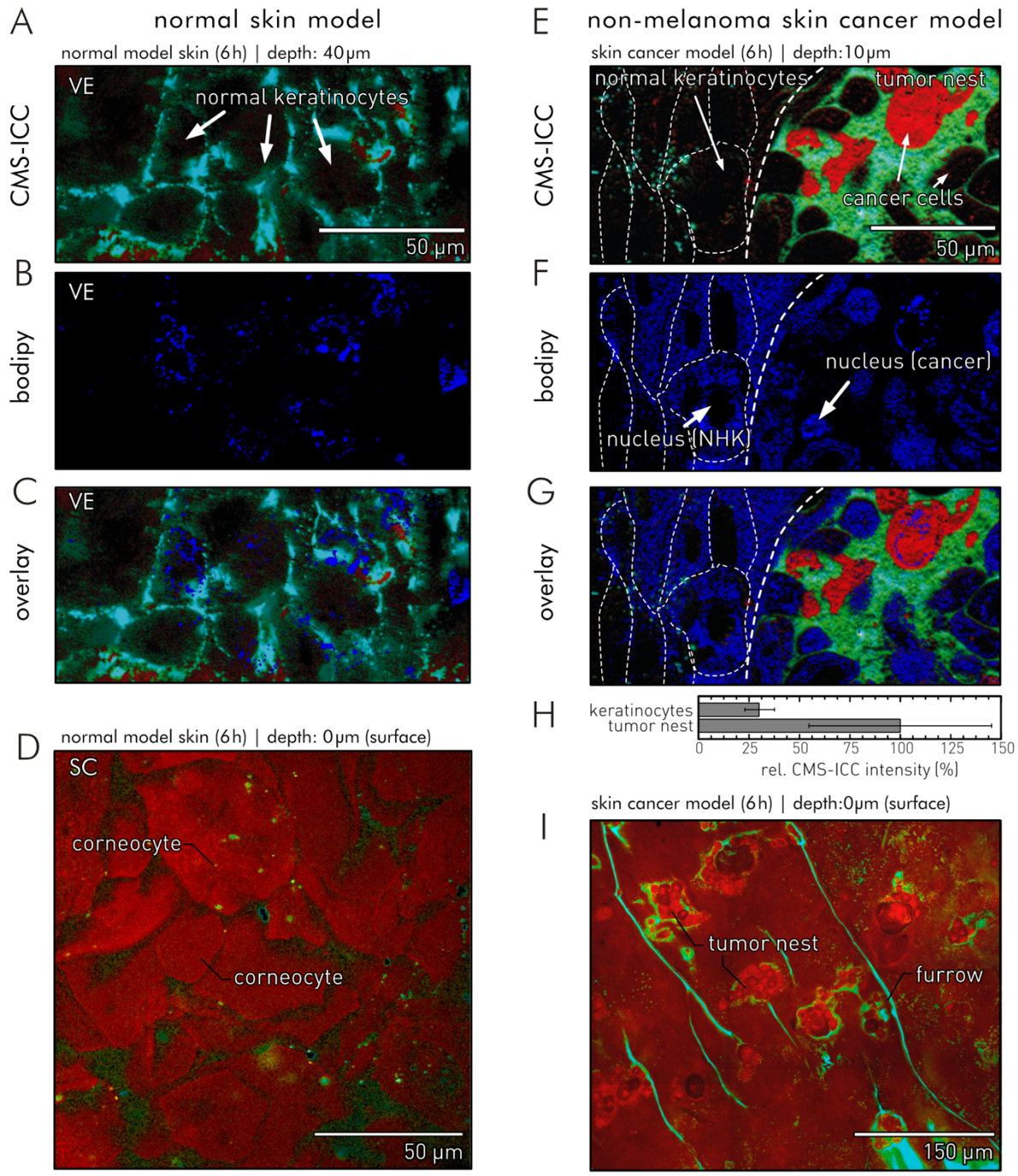

Figure 4.5.14: Live-tissue interaction imaging of CMS-ICC and locations of its cargo bodipy after penetration into normal RHS models and NMSC models. **A** CMS-ICC CH: Cluster-FLIM image of CMS-ICC interacting with NHK cells in the VE (normal RHS model, depth: 40 µm, after 6 h topical application). **B** Bodipy CH: Bodipy localization at the same site as A. **C** Digital overlay of A and B. **D** CMS-ICC CH: Surface of a healthy RHS model after 6 h of topical CMS-ICC/bodipy. **E** CMS-ICC CH: Cluster-FLIM image of CMS-ICC interacting with tumor cells (NMSC model, depth: 10 µm, after 6 h topical application). **F** Bodipy CH: Bodipy localization at the same site as E. **G** Digital overlay of E and F. **H** Relative CMS-ICC fluorescence intensities in keratinocytes and tumor nest, normalized to the latter. **I** CMS-ICC CH: Surface of a NMSC model after 6 h of topical CMS-ICC/bodipy. Experimental conditions: λ_{ex} = 845 nm, main beam splitter edge wavelength at 705 nm, CMS-ICC CH: λ_{em} = 575 – 600 nm; bodipy CH: λ_{em} = 460 – 500 nm; objective: 60x.

Discussion

Firstly, I will compare the results of the 3D live tissue examinations to the results obtained from confocal FLIM experiments of 2D sections (previous Section 4.5.3). The mpFLIM-based live-tissue examination supports the previous results: (I) After topical application, CMS-ICC shows a heterogeneous fluorescence lifetime distribution within the epidermal layers, caused by different interaction modes of the nanocarrier and the related effect on the rotational behavior of applied FMR probe.

(II) CMS-ICC shows strong interaction modes in the SC layers. The applied mpFLIM method allows the resolution of single corneocytes and the intercellular area around them by a top-view detection. In the false color-coded mpFLIM images, heterogeneous interactions of the nanocarrier at the corneocyte surfaces were observed. At some locations, CMS-ICC aggregates can be found between corneocytes. This CMS-ICC species are characterized by a faster FLS, indicating a different, reduced interaction mode in this state. Confocal FLIM images of 2D sections showed a similar heterogeneity in CMS-ICC's fluorescence lifetimes (Section 4.5.2). However, the high spatial fluorescence lifetime resolution of the applied mpFLIM, together with the examination of skin models in their original state, directly without further preparation steps, leads to a generally stronger significance of the gained information. In particular, 3D-resolved structures and associated nanocarrier interactions are easier to recognize and interpret.

(III) CMS-ICC incorporate in skin furrows and remain there in an aqueous environment. CMS-ICC penetrating into skin furrows is characterized by a fast FLS indicating reduced or no interaction with the skin model (Figure 4.5.9). At the interface with the SC, the FLS gradually decelerates, implying a gradual increase in interaction (Figure 4.5.12E). The aforementioned potential reservoir function of CMS-NC in the skin furrows is partially further supported by the live-tissue tomographic examination, since non-interacting CMS-NC implicates a sustained loading capacity for active ingredients. However, after 6 h topical application with CMS-ICC/bodipy, the drug mimetic bodipy was not detected within these furrows (Figure 4.5.10D and E), in contrast to the CMS-ICC nanocarrier. On the one hand, this could be explained by a cargo release. Bodipy leaves the CMS-NC and is translocated to the SC due to hydrophobic effects. On the other hand, this observation can be explained by the generally reduced probability of bodipy to fluoresce in the loaded state. The fluorescence probability becomes much higher as soon as bodipy locates in lipidic environments such as cellular lipid droplets, where its fluorescence quantum yield significantly increases. This would explain why within the SC lining layer of the furrow, I observed significantly increased and heterogeneous fluorescence intensities of bodipy. The fluorescence is also characterized by strongly heterogeneous fluorescence lifetimes. The incorporation of nanomaterial, like zinc oxide or poly(lactic-co-glycolic acid) nanoparticles in skin furrows after topical application has also been observed in other studies based on tomographic fluorescence methods.[383, 411] However, the study presented here goes beyond the previous investigations as the fluorescence lifetime variations of the FMR probe can directly be related to the interaction strength allowing to make mechanistic predictions.

Furthermore, the applied mpFLIM-based live-tissue approach reveals significant differences between the cellular uptake and the fate of CMS-ICC in keratinocytes (NHK) in a simple 2D monolayer live-cell test platform and a more complex multi-layered 3D tissue mimicking skin model (RHS). Model-dependent differences in the cellular uptake of drugs and nanocarriers via FLIM were reported earlier, e.g., for doxorubicin delivery systems.[21, 34] However, these studies investigated simpler multicellular 3D models like tumor spheroids. The skin models investigated here are more complex. They contain different cell types with related cell proliferation and differentiation steps. This leads to a multilayered structure (SC, VE and dermis), very similar to native tissue. Many of the biochemical parameters resemble *the in vivo*-like behavior.[213]

FLIM data of CMS-ICC interacting with NHK cells were analyzed for both test platforms by Cluster-FLIM, which recognized three FLS. Although an initial CMS-ICC interaction with the cell membranes of keratinocytes was observed in both test platforms, the FLIM based investigation reveals significant differences between the interaction modes. The characteristic FLS recognized in the NHK membranes in the RHS models suggests a much stronger interaction than their counterparts in the monolayer since the FLS describes a significantly slower fluorescence decay of the ICC FMR probe. It can be assumed that this discrepancy is attributable to differences in the extracellular matrix of both test platforms, leading to a changed membrane interaction of the CMS-ICC nanocarrier.[412]

In contrast to the FLSs indicative for the early membrane interactions, which differ in both test platforms, an intermediate FLS shows a high similarity between both models, suggesting an internalization of the dendritic CMS-NC via caveolae. As shown in the 2D monolayer test platform in Section 4.4.1, visual inspection of keratinocytes in the 3D model after 22h of topical application revealed an accumulation of the nanocarrier in cytoplasm and cell nuclei as the major site of intracellular fate. This means that no lysosomal trapping of CMS-ICC occurs in keratinocytes located in the VE of the RHS model. This principal distinction, revealed by the Cluster-FLIM approach, indicates fundamentally different interaction modes in NHKs in 2D monolayers. A general need for the application of more complex tissue models in preclinical trails can be derived from this observation. Often, monolayers cannot mirror the complex intercellular functions and interactions occurring in 3D multicellular tissue models, not to mention genuine tissue.[413-415] I therefore conclude that new types of reconstructed skin models together with advanced imaging techniques like the tomographic mpFLIM approach will produce more realistic predictions in preclinical studies and will increase the chance of successful clinical trials.[19, 213, 412]

Finally, Cluster-based mpFLIM tomography was used to investigate differences in CMS-ICC penetration and interaction behavior between normal skin and NMSC using organotypic RHS models. NMSC, especially the common cSCC type used in this study, is a deadly threat due to high metastasis rates.[416] Before metastasizing, carcinoma grow within the viable epidermis, which is, in this state, referred to as actinic keratosis.[213] Clinically, both hyperkeratosis and epidermal atrophy are characteristics of skin suffering from NMSC.[417] The investigated organotypic NMSC models showed no

hyperkeratosis, but a reduced barrier function in accordance with the clinical signs of early actinic keratosis.[418]

The mpFLIM live-tissue tomographic images revealed strong differences between the penetration behavior of the CMS-ICC nanocarrier and the loaded fluorescent drug mimetic bodipy. This result is consistent with a fluorescence-based microscopy study that examined the penetration of CMS-ICC and Nile red loaded on CMS-NC using 2D sections.[170] In this study, an increased penetration of both molecules was detected in NMSC constructs. With the results shown here, tumor nests, which cross the VE and reach the upper SC layers, can be identified as the causative factor for the impaired barrier function (Figure 4.5.13). Within the tumor nest, different fluorescence lifetime signatures of CMS-ICC were observed, indicating varying interactions modes of the penetrating dendritic nanoparticle. Increased penetration through this structure changed the classical interaction distribution found in normal healthy skin. The comparison of the relative fractions of the individual interaction modes along the depth axes showed that in NMSC a different interaction between CMS-ICC and the tumor cells occurs (Figure 4.5.13B and H).

Furthermore, live-cell FLIM studies of the tumor cell line SCC-25 in 2D monolayers (Section 4.4.1) revealed an altered interaction pattern different to the one in the NHK cells. The tumor cells in the NMSC model had incorporated CMS-ICC within their nucleus already after 6h topical incubation time. This significantly altered intracellular fate promotes the assumption that CMS-ICC targets the tumor nuclei. CMS-ICC was also observed within nuclei of NHK cells, but after a considerably longer incubation time of 22 h. Besides finding CMS-NC in tumor cell nuclei, one also finds its loaded cargo bodipy there. This is a significant contrast to healthy keratinocytes. They only show bodipy localizations in the cytoplasm, but not in the cell nucleus. Such striking differences in cellular uptake between healthy cells and tumor cells are fundamental for the understanding to tumor cell-specific modes of action, trigger and drug release mechanisms.[32, 350]

The accumulation of bodipy in the nucleus suggests to conduct future studies on the nuclear uptake of hydrophobic anticancer drugs by CMS-NC. Nanoparticulate targeted drug delivery to tumor tissue and cells is discussed in literature, especially for the fluorescent chemotherapeutic agent doxorubicin.[31, 34, 419] Once this drug enters the cell nuclei, it changes its fluorescence lifetime after interactions and activation.[21] While doxorubicin is regularly translocated to the nuclei after entering the cells by different nanocarrier systems, a simultaneous nuclear position of the used nanocarrier system is rarely observed.[24] Most nanocarriers release doxorubicin in the cytoplasm, e.g., through pH-dependent cleavage in the lysosome. The drug subsequently enters the cell nucleus alone. As the CMS-ICC nanocarrier enters the nuclei, it may lead to additional damage to the nuclear structures and acts as a tumor drug itself. To test this hypothesis, it is advisable to conduct future cell activity assays comparing active ingredients, CMS-NC solely and CMS-NC loaded with active ingredients.

Chapter 5: Conclusion

This doctoral thesis investigated the application of fluorescence lifetime probes in order to identify and explore interactions between dendritic nanoparticles and biological matter. The general conclusion of the thesis is that changes in the fluorescence decay behavior are excellently suited to monitoring and interpreting nanoparticulate interactions with biological systems on different complexity levels under the condition of an initial characterization of the fluorescence lifetime dependencies of the applied probe. Correlations between detected lifetime changes and interactions of a tagged nanoparticles were made on the basis of known and unknown biological interaction partners. This enabled me to investigate specific biomolecular, cellular and tissue-related interaction modes. Two major advantages over steady-state fluorescence approaches were identified for the investigated application scenarios. Firstly, changes in the probe's fluorescence lifetime can be very sensitive and specific to parameters of the local molecular environment of a nanoparticle. Secondly, the common independency of the fluorescence decay from probe concentrations, detection efficiencies, and fluorescence intensities enables qualitative investigations in complex biological and highly autofluorescent environments such as cells or tissue.

For time-resolved fluorescence detection, I applied, established, and developed different spectroscopic and microscopic approaches as well as respective analyses and software tools. Custom-built FLIM setups (Section 4.1) allowed me to precisely detect and determine time-resolved fluorescence decays and the corresponding fluorescence lifetimes spatially resolved in living cells or tissues. For this purpose, I adapted these setups specifically for the applied fluorescence probes and the biological test platforms. TCSPC-FLIM with spectrally selected SWL excitation enabled me to investigate several fluorescent probes or labels within the same optical setting. This made live-cell imaging of multiple spectrally separated fluorescent species faster and less prone to errors. Using a single SWL source, I was able to detect up two four different fluorophores intracellularly (Section 4.4). The application of mpFLIM using femtosecond excitation increased the deep tissue sensitivity enormously. Fluorescence decay signals of skin layers up to a depth of 250 µm were detected and resolved. For this thesis, I analyzed the generated highly multi-dimensional FLIM data by a new cluster-based approach which reduces the data's dimensionality while retaining the essential information of the fluorescence lifetime characteristic (Brodwolf et al., Ref. 44). Before I applied Cluster-FLIM, I evaluated the analysis tool in test experiments (Section 4.1.3).

For successful fluorescence lifetime sensing, it is particularly necessary to understand the exact dependency between fluorescence lifetime and the investigated parameter. I characterized different fluorescent lifetime probes in order to investigate interactions, environmental parameters, or metabolic states. The investigated Pac-SNARF fluoroprobe proved to be a precise tool for the determination of pH values by specific changes in its fluorescence lifetime (Section 4.2). Its cellular application allowed the determination of local intracellular pH environments as demonstrated by primary

keratinocytes. This is particularly useful in experiments on mechanisms and modes of action of nanoparticles or nanocarriers that have lysosome targets or pH-triggered release mechanisms. Future nanomedical concepts relying on pH-triggers can be carried out passively via co-localization studies between fluorescently tagged nanomaterials and freely added PAc-SNARF, but also directly by tagging the nanoparticles via SNARF.

The fluorescent ROS probe CellROX Green shows a strong fluorescence lifetime increase after its activation by intracellular ROS. The presented fluorescence lifetime characterization in HeLa cells was used to investigate intracellular probe locations and to demonstrate a specific ROS concentration dependence of CellROX Green's fluorescence lifetime change. This characterization was the rationale for the presented scatterplot method for FLIM-based intracellular ROS determination. Furthermore, I was able to establish mpFLIM-based detection of ROS in murine skin models, constituting a first step towards ROS detection in tissue structures. This is particularly interesting for toxicological studies of nanoparticle interactions and complements the widely used mpFLIM-readout for metabolic activity states in tissue via autofluorescent nicotinamide adenine dinucleotide (NADH).

Beside fluorescence lifetime probes, the thesis also investigated the fluorescein-based label FITC, which is often applied in fluorescent tagging or antibody-based fluorescence staining. Since FITC's steady-state and time-resolved fluorescence properties depend on environmental parameters, it can render a consistent fluorescence analysis impossible, for example in microscopic penetrations studies. A major pitfall is choosing the wrong labeling parameters. In order to avoid this, I characterized FITC's fluorescence properties after the attachment to a dendrimer (G5G2.5-MG-FITC) as a function of relative labeling stoichiometry and G5G2.5-MG concentration. Hereinafter, I compared the dynamic quenching factors of G5G2.5-MG-FITC, introduced by different environmental parameters. I conclude that the major determinate for a predictive fluorescence detection of the FITC label is a low labeling stoichiometry of the nanomaterial. According to this labelling strategy, it was possible to investigate the skin penetration of G5G2.5-MG-FITC. This was characterized by a penetration of SC. A penetration into the viable epidermal layer was not observed, presumably due to the dermal TJ-barrier.

The fluorescent molecular rotor indocarbocyanine was characterized with the aim to establish a fluorescence lifetime-based interaction probe for dendritic nanoparticle architectures like dPGS and CMS nanocarriers. The initial characterization of ICC revealed a strong fluorescence lifetime sensitivity to changes in solvent viscosity and steric restrictions. This observation is in accordance with the FMR theory, in which these changes are explained by competing electronic transitions mediated by the efficiency of the intramolecular rotation. Additionally, polarity affects ICC's fluorescence lifetime, but only to a minor extent. Section 4.3 showed that ICC attached to dPGS surfaces allowed for a monitoring of binding interactions with serval biomolecules like a surface receptor (MSR), serum protein (SA) and lipids (DPPC and DMPC).

The established interaction sensing enabled me to monitor the protein corona formation on dPGS-ICC and CMS-ICC directly via ICC's fluorescence lifetime changes. This study can be expanded to systematic investigations on corona formation under various *in vitro* conditions in a simple and effective way. This helps to minimize the common problem of a protein corona-related loss of medical efficacy after systemic application of nanomedicine.

Furthermore, it was possible to investigate the binding interaction between dPGS-NP and CMS-NC and to quantify the respective binding parameters. Since fluorescence lifetime changes of FMRs are correlated to prevailing local viscosities, I applied a viscosity – lifetime calibration to dPGS-ICC interacting with MLVs and CMS-NC. The resulting experimental data revealed phase transitions comparable to common literature values. Attaching ICC to the core of a CMS-NC shields the FMR probe from solvent viscosity. However, ICC's sensitivity to biomolecular interactions of the nanocarrier remains, despite the shielded location. This observation motivated the application of CMS-ICC to biomolecular interactions studies in the cytoplasm of living cells, where heterogenous viscosities levels are ranging from a few to several hundred centipoises. The same holds true for the tissue environment the nanoparticle faces in dermal interaction studies. Finally, it was possible to track the cleavage of the FMR IDCC attached to modified dPGS nanoparticle's surface by a disulfide linker.

FLIM-based live-cell interaction monitoring of CMS-ICC in primary NHK, SCC tumor cells, and Langerhans-like dendritic cells demonstrated a new concept for the identification and visualization of nanoparticulate (intra)cellular interactions using an interaction-sensitive FMR probe and a cluster-based FLIM analysis approach (Section 4.4). I characterized the uptake of CMS-nanocarrier by NHK cells by identifying a SR- and lipid raft/Caveolae-mediated uptake converging with the endolysosomal pathway. The uptake of the CMS nanocarrier by only a single relevant cell pathway in NHK is a somewhat surprising result, but opens the opportunity to apply this CMS-nanocarrier architecture for a specific targeting of keratinocytes via SR. The ability to obtain detailed real-time kinetics of the caveolae-mediated uptake pathway with a cellular fate that exclusively leads to lysosomal localization may also pave the way to advanced targeted drug release facilitated by pH-responsive CMS-architectures, allowing for a lysosomal-targeted drug delivery. The study furthermore showed strong differences between the CMS-ICC interaction in all three cell types, underscoring the plethora of cellular interaction modes of nanoparticles and the need for cell specific investigations.

The number of interactions even rises when nanomaterials encounter tissue. I applied confocal and multiphoton excitation FLIM to study such interactions between CMS-ICC and skin tissue (Section 4.5). The SC is the first layer of the skin that will interact with topically applied nanoparticles. Using FLIM and the interaction sensitive FMR probe ICC enabled me to detect different nanoparticulate interaction modes of CMS-ICC within the flat SC, SC that lines skin furrows and within hair follicles. I applied the toolbox of FLIM-based interaction sensing to different skin models including diseased skin. In most skin models, no penetration of CMS-ICC into the VE was detected. Exceptions are the investigated RHS models, which were examined in their native state using mpFLIM, and RHE

aging models with a damaged penetration barrier. The thesis shows that FLIM-based read-outs can improve the results of nonclinical research during the process of nanoparticle and nanocarrier development by providing mechanistic insights into nanocarrier – tissue interactions. Furthermore, I demonstrate that testing of nanocarrier systems with RHS can substitute excised human skin. This promotes the replacement, reduction, and refinement (3Rs principle) of animal experiments.

There have been many potential applications for mpFLIM-based tomographic imaging in the literature on nanoparticulated dermal drug delivery, including investigations of the metabolic activity state by NADH and the localization/penetration of fluorescently tagged nanomaterials.[238, 250] My investigations on dendritic nanoparticle penetration using an interaction sensitive FMR probe add another parameter to the available analysis spectrum. Future penetration studies using mpFLIM technology and a sufficient analysis tool (e.g. Cluster-FLIM) can simultaneously address localization, interaction strength and influence of metabolic activity in the biological test platform.

In conclusion, the results of this thesis expand the scope of fluorescence readouts for nonclinical research during the early stage of nanoparticle and nanocarrier development. Future investigation might provide new molecular insights into biomolecular interactions and lead to a better use of nanomedicine's potential.

References

1. Mirza, A. Z.; Siddiqui, F. A., Nanomedicine and drug delivery: a mini review. Int. Nano Lett. 2014, 4 (1).
2. Martinelli, C.; Pucci, C.; Ciofani, G., Nanostructured carriers as innovative tools for cancer diagnosis and therapy. APL Bioeng. 2019, 3 (1), 011502.
3. Rizzo, L. Y.; Theek, B.; Storm, G.; Kiessling, F.; Lammers, T., Recent progress in nanomedicine: therapeutic, diagnostic and theranostic applications. Curr. Opin. Biotechnol. 2013, 24 (6), 1159-1166.
4. Vogt, A.; Wischke, C.; Neffe, A. T.; Ma, N.; Alexiev, U.; Lendlein, A., Nanocarriers for drug delivery into and through the skin - do existing technologies match clinical challenges? J. Control. Release 2016, 242, 3-15.
5. Duncan, R.; Gaspar, R., Nanomedicine(s) under the Microscope. Mol. Pharmaceut. 2011, 8 (6), 2101-2141.
6. Sanhai, W. R.; Sakamoto, J. H.; Canady, R.; Ferrari, M., Seven challenges for nanomedicine. Nat. Nanotechnol. 2008, 3 (5), 242-244.
7. Ioannidis, J. P. A.; Kim, B. Y. S.; Trounson, A., How to design preclinical studies in nanomedicine and cell therapy to maximize the prospects of clinical translation. Nat. Biomed. Eng. 2018, 2 (11), 797-809.
8. Greish, K.; Mathur, A.; Bakhiet, M.; Taurin, S., Nanomedicine: is it lost in translation? Ther. Deliv. 2018, 9 (4), 269-285.
9. Wilhelm, S.; Tavares, A. J.; Dai, Q.; Ohta, S.; Audet, J.; Dvorak, H. F.; Chan, W. C. W., Analysis of nanoparticle delivery to tumours. Nat. Rev. Mater. 2016, 1 (5).
10. Veiseh, O.; Tang, B. C.; Whitehead, K. A.; Anderson, D. G.; Langer, R., Managing diabetes with nanomedicine: challenges and opportunities. Nat. Rev. Drug Discov. 2015, 14 (1), 45-57.
11. Cooke, J. P.; Ferrari, M., Inflammation-targeted vascular nanomedicine. Nat. Biomed. Eng. 2018, 2 (5), 269-270.
12. Hausmann, N.; Prendergast, A. L.; Lemonis, A.; Zech, J.; Roberts, P.; Siozos, P.; Anglos, D., Extensive elemental mapping unlocks Mg/Ca ratios as climate proxy in seasonal records of Mediterranean limpets. Sci. Rep. 2019, 9 (1), 3698.
13. Nirmalanandhan, V. S.; Duren, A.; Hendricks, P.; Vielhauer, G.; Sittampalam, G. S., Activity of anticancer agents in a three-dimensional cell culture model. Assay Drug. Dev. Technol. 2010, 8 (5), 581-590.
14. Bailey, J.; Thew, M.; Balls, M., An Analysis of the Use of Animal Models in Predicting Human Toxicology and Drug Safety. Altern. Lab. Anim. 2014, 42 (3), 181-199.
15. Seok, J.; Warren, H. S.; Cuenca, A. G.; Mindrinos, M. N.; Baker, H. V.; Xu, W.; Richards, D. R.; McDonald-Smith, G. P.; Gao, H.; Hennessy, L.; Finnerty, C. C.; Lopez, C. M.; Honari, S.; Moore, E. E.; Minei, J. P.; Cuschieri, J.; Bankey, P. E.; Johnson, J. L.; Sperry, J.; Nathens, A. B.; Billiar, T. R.; West, M. A.; Jeschke, M. G.; Klein, M. B.; Gamelli, R. L.; Gibran, N. S.; Brownstein, B. H.; Miller-Graziano, C.; Calvano, S. E.; Mason, P. H.; Cobb, J. P.; Rahme, L. G.; Lowry, S. F.; Maier, R. V.; Moldawer, L. L.; Herndon, D. N.; Davis, R. W.; Xiao, W.; Tompkins, R. G.; Inflammation; Host Response to Injury, L. S. C. R. P., Genomic responses in mouse models poorly mimic human inflammatory diseases. Proc. Natl. Acad. Sci. U. S. A. 2013, 110 (9), 3507-3512.
16. Cassidy, J. W.; Caldas, C.; Bruna, A., Maintaining Tumor Heterogeneity in Patient-Derived Tumor Xenografts. Cancer Res. 2015, 75 (15), 2963-2968.
17. Dutta, D.; Heo, I.; Clevers, H., Disease Modeling in Stem Cell-Derived 3D Organoid Systems. Trends Mol. Med. 2017, 23 (5), 393-410.
18. Lancaster, M. A.; Knoblich, J. A., Organogenesis in a dish: modeling development and disease using organoid technologies. Science 2014, 345 (6194), 1247125.
19. Volz, P.; Schilrreff, P.; Brodwolf, R.; Wolff, C.; Stellmacher, J.; Balke, J.; Morilla, M. J.; Zoschke, C.; Schäfer-Korting, M.; Alexiev, U., Pitfalls in using fluorescence tagging of nanomaterials: tecto-dendrimers in skin tissue as investigated by Cluster-FLIM. Ann. N. Y. Acad. Sci. 2017, 1405 (1), 202-214.
20. Resch-Genger, U.; Hoffmann, K.; Hoffmann, A., Standardization of Fluorescence Measurements: Criteria for the Choice of Suitable Standards and Approaches to Fit-for-Purpose Calibration Tools. Ann. N. Y. Acad. Sci. 2008, 1130 (1), 35-43.
21. Basuki, J. S.; Duong, H. T. T.; Macmillan, A.; Erlich, R. B.; Esser, L.; Akerfeldt, M. C.; Whan, R. M.; Kavallaris, M.; Boyer, C.; Davis, T. P., Using Fluorescence Lifetime Imaging Microscopy to Monitor Theranostic Nanoparticle Uptake and Intracellular Doxorubicin Release. ACS Nano 2013, 7 (11), 10175-10189.
22. Conroy, J.; Byrne, S. J.; Gun'ko, Y. K.; Rakovich, Y. P.; Donegan, J. F.; Davies, A.; Kelleher, D.; Volkov, Y., CdTe nanoparticles display tropism to core histones and histone-rich cell organelles. Small 2008, 4 (11), 2006-2015.
23. Xu, Y.; He, R.; Lin, D.; Ji, M.; Chen, J., Laser beam controlled drug release from Ce6-gold nanorod composites in living cells: a FLIM study. Nanoscale 2015, 7 (6), 2433-2441.
24. Zhang, X.; Shastry, S.; Bradforth, S. E.; Nadeau, J. L., Nuclear uptake of ultrasmall gold-doxorubicin conjugates imaged by fluorescence lifetime imaging microscopy (FLIM) and electron microscopy. Nanoscale 2015, 7 (1), 240-251.
25. Boreham, A.; Pikkemaat, J.; Volz, P.; Brodwolf, R.; Kuehne, C.; Licha, K.; Haag, R.; Dernedde, J.; Alexiev, U., Detecting and Quantifying Biomolecular Interactions of a Dendritic Polyglycerol Sulfate Nanoparticle Using Fluorescence Lifetime Measurements. Molecules 2015, 21 (1), e22.
26. Dziuba, D.; Jurkiewicz, P.; Cebecauer, M.; Hof, M.; Hocek, M., A Rotational BODIPY Nucleotide: An Environment-Sensitive Fluorescence-Lifetime Probe for DNA Interactions and Applications in Live-Cell Microscopy. Angew. Chem. Int. Ed. Engl. 2016, 55 (1), 174-178.
27. Okabe, K.; Inada, N.; Gota, C.; Harada, Y.; Funatsu, T.; Uchiyama, S., Intracellular temperature mapping with a fluorescent polymeric thermometer and fluorescence lifetime imaging microscopy. Nat. Commun. 2012, 3, 705.
28. Shivalingam, A.; Izquierdo, M. A.; Le Marois, A.; Vysniauskas, A.; Suhling, K.; Kuimova, M. K.; Vilar, R., The interactions between a small molecule and G-quadruplexes are visualized by fluorescence lifetime imaging microscopy. Nat. Commun. 2015, 6, 8178.
29. Saari, H.; Lisitsyna, E.; Rautaniemi, K.; Rojalin, T.; Niemi, L.; Nivaro, O.; Laaksonen, T.; Yliperttula, M.; Vuorimaa-Laukkanen, E., FLIM reveals alternative EV-mediated cellular up-take pathways of paclitaxel. J. Control. Release 2018, 284, 133-143.
30. Zhou, T.; Luo, T.; Song, J.; Qu, J., Phasor-Fluorescence Lifetime Imaging Microscopy Analysis to Monitor Intercellular Drug Release from a pH-Sensitive Polymeric Nanocarrier. Anal. Chem. 2018, 90 (3), 2170-2177.
31. Tawagi, E.; Massmann, C.; Chibli, H.; Nadeau, J. L., Differential toxicity of gold-doxorubicin in cancer cells vs. cardiomyocytes as measured by real-time growth assays and fluorescence lifetime imaging microscopy (FLIM). Analyst 2015, 140 (16), 5732-5741.

32. Chen, X.; Soeriyadi, A. H.; Lu, X.; Sagnella, S. M.; Kavallaris, M.; Gooding, J. J., Dual Bioresponsive Mesoporous Silica Nanocarrier as an "AND" Logic Gate for Targeted Drug Delivery Cancer Cells. Adv. Funct. Mater. 2014, 24 (44), 6999-7006.
33. Li, Y.; Duong, H. T.; Laurent, S.; MacMillan, A.; Whan, R. M.; Elst, L. V.; Muller, R. N.; Hu, J.; Lowe, A.; Boyer, C.; Davis, T. P., Nanoparticles based on star polymers as theranostic vectors: endosomal-triggered drug release combined with MRI sensitivity. Adv. Healthc. Mater. 2015, 4 (1), 148-156.
34. Sagnella, S. M.; Duong, H.; MacMillan, A.; Boyer, C.; Whan, R.; McCarroll, J. A.; Davis, T. P.; Kavallaris, M., Dextran-based doxorubicin nanocarriers with improved tumor penetration. Biomacromolecules 2014, 15 (1), 262-275.
35. Zhang, S.; Gao, H.; Bao, G., Physical Principles of Nanoparticle Cellular Endocytosis. ACS Nano 2015, 9 (9), 8655-8671.
36. Köllner, M.; Wolfrum, J., How Many Photons Are Necessary for Fluorescence-Lifetime Measurements. Chem. Phys. Lett. 1992, 200 (1-2), 199-204.
37. Rowley, M. I.; Barber, P. R.; Coolen, A. C. C.; Vojnovic, B., Bayesian analysis of fluorescence lifetime imaging data. Proc. Spie. 2011, 7903, 790325.
38. Schleifenbaum, F.; Elgass, K.; Sackrow, M.; Caesar, K.; Berendzen, K.; Meixner, A. J.; Harter, K., Fluorescence intensity decay shape analysis microscopy (FIDSAM) for quantitative and sensitive live-cell imaging: a novel technique for fluorescence microscopy of endogenously expressed fusion-proteins. Mol. Plant. 2010, 3 (3), 555-562.
39. Warren, S. C.; Margineanu, A.; Alibhai, D.; Kelly, D. J.; Talbot, C.; Alexandrov, Y.; Munro, I.; Katan, M.; Dunsby, C.; French, P. M., Rapid global fitting of large fluorescence lifetime imaging microscopy datasets. PLoS One 2013, 8 (8), e70687.
40. Niehörster, T.; Löschberger, A.; Gregor, I.; Krämer, B.; Rahn, H. J.; Patting, M.; Koberling, F.; Enderlein, J.; Sauer, M., Multi-target spectrally resolved fluorescence lifetime imaging microscopy. Nat. Methods 2016, 13 (3), 257-262.
41. Digman, M. A.; Caiolfa, V. R.; Zamai, M.; Gratton, E., The phasor approach to fluorescence lifetime imaging analysis. Biophys. J. 2008, 94 (2), L14-16.
42. Kaye, B.; Foster, P. J.; Yoo, T. Y.; Needleman, D. J., Developing and Testing a Bayesian Analysis of Fluorescence Lifetime Measurements. PLoS One 2017, 12 (1), e0169337.
43. Gregor, I.; Patting, M., Pattern-based linear unmixing for efficient and reliable analysis of multicomponent TCSPC data. In Advanced Photon Counting, Springer: 2014; pp 241-263.
44. Brodwolf, R.; Volz-Rakebrand, P.; Stellmacher, J.; Wolff, C.; Unbehauen, M.; Haag, R.; Schäfer-Korting, M.; Zoschke, C.; Alexiev, U., Faster, sharper, more precise: Automated Cluster-FLIM in preclinical testing directly identifies the intracellular fate of theranostics in live cells and tissue. Theranostics 2020, 10 (14), 6322-6336.
45. Jeon, I. Y.; Noh, H. J.; Baek, J. B., Hyperbranched Macromolecules: From Synthesis to Applications. Molecules 2018, 23 (3).
46. Higashihara, T.; Segawa, Y.; Sinananwanich, W.; Ueda, M., Synthesis of hyperbranched polymers with controlled degree of branching. Polym. J. 2011, 44 (1), 14-29.
47. King Spencer, B., Angioplasty From Bench to Bedside to Bench. Circulation 1996, 93 (9), 1621-1629.
48. Volz, P.; Brodwolf, R.; Zoschke, C.; Haag, R.; Schäfer-Korting, M.; Alexiev, U., White-Light Supercontinuum Laser-Based Multiple Wavelength Excitation for TCSPC-FLIM of Cutaneous Nanocarrier Uptake. Z. Phys. Chem 2018, 232 (5-6), 671-688.
49. Balke, J.; Volz, P.; Neumann, F.; Brodwolf, R.; Wolf, A.; Pischon, H.; Radbruch, M.; Mundhenk, L.; Gruber, A. D.; Ma, N.; Alexiev, U., Visualizing Oxidative Cellular Stress Induced by Nanoparticles in the Subcytotoxic Range Using Fluorescence Lifetime Imaging. Small 2018, 14 (23), e1800310.
50. Herschel, J. F. W., Αμο'ρφωτα No. I. On a case of superficial colour presented by a homogeneous liquid internally colourless. Philos. Trans. R. Soc. Lond. 1845, 135, 143-145.
51. Valeur, B.; Berberan-Santos, M. N., Molecular fluorescence: principles and applications. John Wiley & Sons: 2012.
52. Kasha, M., Characterization of electronic transitions in complex molecules. Discuss. Faraday Soc. 1950, 9 (0), 14-19.
53. Williams, R. M.; Verhoeven, J. W., On the applicability of the Kasha – Vavilov rule to C60. Spectrochim. Acta Part A 1994, 50 (2), 251-254.
54. He, G. S.; Tan, L. S.; Zheng, Q.; Prasad, P. N., Multiphoton absorbing materials: Molecular designs, characterizations, and applications. Chem. Rev. 2008, 108 (4), 1245-1330.
55. Rumi, M.; Barlow, S.; Wang, J.; Perry, J. W.; Marder, S. R., Two-Photon Absorbing Materials and Two-Photon-Induced Chemistry. In Photoresponsive Polymers I, 2008; Chapter 133, pp 1-95.
56. Sillen, A.; Engelborghs, Y., The Correct Use of "Average" Fluorescence Parameters. Photochem. Photobiol. 1998, 67 (5), 475-486.
57. Fiserova, E.; Kubala, M., Mean fluorescence lifetime and its error. J. Lumin. 2012, 132 (8), 2059-2064.
58. Förster, T., Zwischenmolekulare Energiewanderung und Fluoreszenz. Ann. Phys. 1948, 437 (1-2), 55-75.
59. Gehlen, M. H., The centenary of the Stern-Volmer equation of fluorescence quenching: From the single line plot to the SV quenching map. J. Photochem. Photobiol. C 2020, 42.
60. Castanho, M. A. R. B.; Prieto, M. J. E., Fluorescence quenching data interpretation in biological systems: The use of microscopic models for data analysis and interpretation of complex systems. Biochim. Biophys. Acta - Biomembranes 1998, 1373 (1), 1-16.
61. Haidekker, M. A.; Theodorakis, E. A., Environment-sensitive behavior of fluorescent molecular rotors. J. Biol. Eng. 2010, 4, 11.
62. Åkesson, E.; Sundstrom, V.; Gillbro, T., Solvent-Dependent Barrier Heights of Excited-State Photoisomerization Reactions. Chem. Phys. Lett. 1985, 121 (6), 513-522.
63. Grabowski, Z. R.; Rotkiewicz, K.; Rettig, W., Structural changes accompanying intramolecular electron transfer: focus on twisted intramolecular charge-transfer states and structures. Chem. Rev. 2003, 103 (10), 3899-4032.
64. Förster, T.; Hoffmann, G., Die Viskositätsabhängigkeit der Fluoreszenzquantenausbeuten einiger Farbstoffsysteme. Z. Phys. Chem. 1971, 75 (1-2), 63-76.
65. Shimolina, L. E.; Izquierdo, M. A.; Lopez-Duarte, I.; Bull, J. A.; Shirmanova, M. V.; Klapshina, L. G.; Zagaynova, E. V.; Kuimova, M. K., Imaging tumor microscopic viscosity in vivo using molecular rotors. Sci. Rep. 2017, 7, 41097.
66. Kuimova, M. K.; Yahioglu, G.; Levitt, J. A.; Suhling, K., Molecular rotor measures viscosity of live cells via fluorescence lifetime imaging. J. Am. Chem. Soc. 2008, 130 (21), 6672-6673.
67. Bagchi, B., Isomerization Dynamics in Solution. Int. Rev. Phys Chem. 1987, 6 (1), 1-33.

68. Loutfy, R. O.; Arnold, B. A., Effect of Viscosity and Temperature on Torsional Relaxation of Molecular Rotors. J. Phys. Chem. 1982, 86 (21), 4205-4211.
69. Vysniauskas , A.; Lopez-Duarte, I.; Duchemin, N.; Vu, T. T.; Wu, Y.; Budynina, E. M.; Volkova, Y. A.; Pena Cabrera, E.; Ramirez-Ornelas, D. E.; Kuimova, M. K., Exploring viscosity, polarity and temperature sensitivity of BODIPY-based molecular rotors. Phys. Chem. Chem. Phys. 2017, 19 (37), 25252-25259.
70. Åkesson, E.; Sundstrom, V.; Gillbro, T., Isomerization Dynamics in Solution Described by Kramers Theory with a Solvent-Dependent Activation-Energy. Chem. Phys. 1986, 106 (2), 269-280.
71. Velsko, S. P.; Fleming, G. R., Solvent Influence on Photochemical Isomerizations - Photophysics of Dodci. Chem. Phys. 1982, 65 (1), 59-70.
72. Doolittle, A. K., Studies in Newtonian Flow .2. The Dependence of the Viscosity of Liquids on Free-Space. J. Appl. Phys. 1951, 22 (12), 1471-1475.
73. Zeglinski, D. M.; Waldeck, D. H., Evidence for Dynamical Solvent Effects on the Photoisomerization of 4,4'-Dimethoxystilbene. J. Phys. Chem. 1988, 92 (3), 692-701.
74. Murarka, R. K.; Bhattacharyya, S.; Biswas, R.; Bagchi, B., Isomerization dynamics in viscous liquids: Microscopic investigation of the coupling and decoupling of the rate to and from solvent viscosity and dependence on the intermolecular potential. J. Chem. Phys. 1999, 110 (15), 7365-7375.
75. Cao, J.; Wu, T.; Hu, C.; Liu, T.; Sun, W.; Fan, J.; Peng, X., The nature of the different environmental sensitivity of symmetrical and unsymmetrical cyanine dyes: an experimental and theoretical study. Phys. Chem. Chem. Phys. 2012, 14 (39), 13702-13708.
76. Levitus, M.; Ranjit, S., Cyanine dyes in biophysical research: the photophysics of polymethine fluorescent dyes in biomolecular environments. Q. Rev. Biophys. 2011, 44 (1), 123-151.
77. Harvey, B. J.; Perez, C.; Levitus, M., DNA sequence-dependent enhancement of Cy3 fluorescence. Photochem. Photobiol. Sci. 2009, 8 (8), 1105-1110.
78. Peng, X.; Yang, Z.; Wang, J.; Fan, J.; He, Y.; Song, F.; Wang, B.; Sun, S.; Qu, J.; Qi, J.; Yan, M., Fluorescence ratiometry and fluorescence lifetime imaging: using a single molecular sensor for dual mode imaging of cellular viscosity. J. Am. Chem. Soc. 2011, 133 (17), 6626-6635.
79. Gatzogiannis, E.; Chen, Z.; Wei, L.; Wombacher, R.; Kao, Y. T.; Yefremov, G.; Cornish, V. W.; Min, W., Mapping protein-specific micro-environments in live cells by fluorescence lifetime imaging of a hybrid genetic-chemical molecular rotor tag. Chem. Commun. 2012, 48 (69), 8694-8696.
80. Thompson, A. J.; Herling, T. W.; Kubankova, M.; Vysniauskas, A.; Knowles, T. P.; Kuimova, M. K., Molecular Rotors Provide Insights into Microscopic Structural Changes During Protein Aggregation. J. Phys. Chem. B 2015, 119 (32), 10170-10179.
81. Sawangsang, P.; Buranachai, C.; Punwong, C., Excited state free energy calculations of Cy3 in different environments. J. Phys. D Appl. Phys. 2015, 48 (20).
82. Aramendia, P. F.; Negri, R. M.; Roman, E. S., Temperature Dependence of Fluorescence and Photoisomerization in Symmetric Carbocyanines.Influence of Medium Viscosity and Molecular Structure. J. Phys. Chem. 1994, 98 (12), 3165-3173.
83. Humphry-Baker, R.; Graetzel, M.; Steiger, R., Drastic fluorescence enhancement and photochemical stabilization of cyanine dyes through micellar systems. J. Am. Chem. Soc. 1980, 102 (2), 847-848.
84. Luby-Phelps, K.; Mujumdar, S.; Mujumdar, R. B.; Ernst, L. A.; Galbraith, W.; Waggoner, A. S., A novel fluorescence ratiometric method confirms the low solvent viscosity of the cytoplasm. Biophys. J. 1993, 65 (1), 236-242.
85. Hosny, N. A.; Fitzgerald, C.; Tong, C.; Kalberer, M.; Kuimova, M. K.; Pope, F. D., Fluorescent lifetime imaging of atmospheric aerosols: a direct probe of aerosol viscosity. Faraday Discuss. 2013, 165, 343.
86. Vyšniauskas, A.; Kuimova, M. K., A twisted tale: measuring viscosity and temperature of microenvironments using molecular rotors. Int. Rev. Phys. Chem. 2018, 37 (2), 259-285.
87. Jiang, N.; Fan, J.; Zhang, S.; Wu, T.; Wang, J.; Gao, P.; Qu, J.; Zhou, F.; Peng, X., Dual mode monitoring probe for mitochondrial viscosity in single cell. Sens. Actuators B Chem. 2014, 190, 685-693.
88. Ober, K.; Volz-Rakebrand, P.; Stellmacher, J.; Brodwolf, R.; Licha, K.; Haag, R.; Alexiev, U., Expanding the Scope of Reporting Nanoparticles: Sensing of Lipid Phase Transitions and Nanoviscosities in Lipid Membranes. Langmuir 2019, 35, 11422-11434.
89. Kung, C. E.; Reed, J. K., Microviscosity Measurements of Phospholipid-Bilayers Using Fluorescent Dyes That Undergo Torsional Relaxation. Biochemistry 1986, 25 (20), 6114-6121.
90. Zhang, X. F.; Zhang, J.; Liu, L., Fluorescence properties of twenty fluorescein derivatives: lifetime, quantum yield, absorption and emission spectra. J. Fluoresc. 2014, 24 (3), 819-826.
91. Zhang, X.-F.; Zhang, Y.; Liu, L., Fluorescence lifetimes and quantum yields of ten rhodamine derivatives: Structural effect on emission mechanism in different solvents. J. Lumin. 2014, 145, 448-453.
92. Richter, C.; Schneider, C.; Quick, M. T.; Volz, P.; Mahrwald, R.; Hughes, J.; Dick, B.; Alexiev, U.; Ernsting, N. P., Dual-fluorescence pH probe for bio-labelling. Phys. Chem. Chem. Phys. 2015, 17 (45), 30590-30597.
93. Klonis, N.; Sawyer, W. H., Spectral properties of the prototropic forms of fluorescein in aqueous solution. J. Fluoresc. 1996, 6 (3), 147-157.
94. pH indicators. In Molecular Probes Handbook: A Guide to Fluorescent Probes and Labeling Technologies, 11th Edition ed.; Johnson, I.; Spence, M. (Eds.) Life Technologies Corporation: 2010; Chapter 20, pp 885-902.
95. Han, J.; Burgess, K., Fluorescent indicators for intracellular pH. Chem. Rev. 2010, 110 (5), 2709-28.
96. Kvach, M. V.; Tsybulsky, D. A.; Ustinov, A. V.; Stepanova, I. A.; Bondarev, S. L.; Gontarev, S. V.; Korshun, V. A.; Shmanai, V. V., 5(6)-Carboxyfluorescein Revisited: New Protecting Group, Separation of Isomers, and their Spectral Properties on Oligonucleotides. Bioconjug. Chem. 2007, 18 (5), 1691-1696.
97. Nakata, E.; Yukimachi, Y.; Nazumi, Y.; Uwate, M.; Maseda, H.; Uto, Y.; Hashimoto, T.; Okamoto, Y.; Hori, H.; Morii, T., A novel strategy to design latent ratiometric fluorescent pH probes based on self-assembled SNARF derivatives. RSC Adv. 2014, 4 (1), 348-357.
98. de Rezende, L. C.; da Silva Emery, F., A Review of the Synthetic Strategies for the Development of BODIPY Dyes for Conjugation with Proteins. Orbital Elec. J. Chem. 2013, 5 (1), 62-88.

99. Kaur, P.; Singh, K., Recent advances in the application of BODIPY in bioimaging and chemosensing. J. Mater. Chem. C 2019, 7 (37), 11361-11405.
100. Boens, N.; Leen, V.; Dehaen, W., Fluorescent indicators based on BODIPY. Chem. Soc. Rev. 2012, 41 (3), 1130-1172.
101. Su, D.; Teoh, C. L.; Gao, N.; Xu, Q. H.; Chang, Y. T., A Simple BODIPY-Based Viscosity Probe for Imaging of Cellular Viscosity in Live Cells. Sensors 2016, 16 (9), 1397.
102. Spandl, J.; White, D. J.; Peychl, J.; Thiele, C., Live Cell Multicolor Imaging of Lipid Droplets with a New Dye, LD540. Traffic 2009, 10 (11), 1579-1584.
103. Ranall, M. V.; Gabrielli, B. G.; Gonda, T. J., High-content imaging of neutral lipid droplets with 1,6-diphenylhexatriene. Biotechniques 2011, 51 (1), 35-6, 38-42.
104. Molecular Probes, I. Certificate of analysis: BODIPY® 493/503. https://assets.thermofisher.com/TFS-Assets/LSG/certificate/ Certificates%20of%20Analysis/1158013_D3922.pdf (accessed 01.04.2020).
105. Hayyan, M.; Hashim, M. A.; AlNashef, I. M., Superoxide Ion: Generation and Chemical Implications. Chem. Rev. 2016, 116 (5), 3029-3085.
106. Bergamini, C. M.; Gambetti, S.; Dondi, A.; Cervellati, C., Oxygen, reactive oxygen species and tissue damage. Curr. Pharm. Des. 2004, 10 (14), 1611-1626.
107. Brieger, K.; Schiavone, S.; Miller, F. J.; Krause, K. H., Reactive oxygen species: from health to disease. Swiss Med. Wkly. 2012, 142, w13659.
108. Sarker, U.; Oba, S., Catalase, superoxide dismutase and ascorbate-glutathione cycle enzymes confer drought tolerance of Amaranthus tricolor. Sci Sci. Rep. 2018, 8 (1), 16496.
109. Schafer, F. Q.; Buettner, G. R., Redox environment of the cell as viewed through the redox state of the glutathione disulfide/glutathione couple. Free Radic. Biol. Med. 2001, 30 (11), 1191-1212.
110. Liu, S.; Oshita, S.; Kawabata, S.; Makino, Y.; Yoshimoto, T., Identification of ROS Produced by Nanobubbles and Their Positive and Negative Effects on Vegetable Seed Germination. Langmuir 2016, 32 (43), 11295-11302.
111. Napierska, D.; Rabolli, V.; Thomassen, L. C.; Dinsdale, D.; Princen, C.; Gonzalez, L.; Poels, K. L.; Kirsch-Volders, M.; Lison, D.; Martens, J. A.; Hoet, P. H., Oxidative stress induced by pure and iron-doped amorphous silica nanoparticles in subtoxic conditions. Chem. Res. Toxicol. 2012, 25 (4), 828-837.
112. Khalili Fard, J.; Jafari, S.; Eghbal, M. A., A Review of Molecular Mechanisms Involved in Toxicity of Nanoparticles. Adv. Pharm. Bull. 2015, 5 (4), 447-454.
113. Pujalté, I.; Passagne, I.; Brouillaud, B.; Tréguer, M.; Durand, E.; Ohayon-Courtès, C.; L'Azou, B., Cytotoxicity and oxidative stress induced by different metallic nanoparticles on human kidney cells. Part. Fibre Toxicol. 2011, 8 (1), 10.
114. Jomova, K.; Baros, S.; Valko, M., Redox active metal-induced oxidative stress in biological systems. Transit. Met. Chem. 2012, 37 (2), 127-134.
115. Soenen, S. J.; Rivera-Gil, P.; Montenegro, J.-M.; Parak, W. J.; De Smedt, S. C.; Braeckmans, K., Cellular toxicity of inorganic nanoparticles: Common aspects and guidelines for improved nanotoxicity evaluation. Nano Today 2011, 6 (5), 446-465.
116. Tada, D. B.; Baptista, M. S., Photosensitizing nanoparticles and the modulation of ROS generation. Front. Chem. 2015, 3, 33.
117. Lavado, A. S.; Chauhan, V. M.; Zen, A. A.; Giuntini, F.; Jones, D. R.; Boyle, R. W.; Beeby, A.; Chan, W. C.; Aylott, J. W., Controlled intracellular generation of reactive oxygen species in human mesenchymal stem cells using porphyrin conjugated nanoparticles. Nanoscale 2015, 7 (34), 14525-14531.
118. Prasad, A.; Pospisil, P.; Tada, M., Editorial: Reactive Oxygen Species (ROS) Detection Methods in Biological System. Front. Physiol. 2019, 10, 1316.
119. Gomes, A.; Fernandes, E.; Lima, J. L. F. C., Fluorescence probes used for detection of reactive oxygen species. J. Biochem. Biophys. Methods 2005, 65 (2), 45-80.
120. Molecular Probes, I. CellROX Oxidative Stress Reagents. https://assets.thermofisher.com/TFS-Assets/LSG/manuals/mp10422.pdf (accessed 01.04.2020).
121. Chosrowjan, H.; Taniguchi, S.; Tanaka, F., Ultrafast fluorescence upconversion technique and its applications to proteins. FEBS J. 2015, 282 (16), 3003-3015.
122. Hirvonen, L. M.; Suhling, K., Wide-field TCSPC: methods and applications. Meas. Sci. Technol. 2017, 28 (1).
123. Borst, J. W.; Visser, A. J. W. G., Fluorescence lifetime imaging microscopy in life sciences. Meas. Sci. Technol. 2010, 21 (10).
124. Boens, N.; Qin, W. W.; Basaric, N.; Hofkens, J.; Ameloot, M.; Pouget, J.; Lefevre, J. P.; Valeur, B.; Gratton, E.; Vandeven, M.; Silva, N. D.; Engelborghs, Y.; Willaert, K.; Sillen, A.; Rumbles, G.; Phillips, D.; Visser, A. J. W. G.; van Hoek, A.; Lakowicz, J. R.; Malak, H.; Gryczynski, I.; Szabo, A. G.; Krajcarski, D. T.; Tamai, N.; Miura, A., Fluorescence lifetime standards for time and frequency domain fluorescence spectroscopy. Anal. Chem. 2007, 79 (5), 2137-2149.
125. Berezin, M. Y.; Achilefu, S., Fluorescence lifetime measurements and biological imaging. Chem. Rev. 2010, 110 (5), 2641-2684.
126. Wei, L.; Yan, W.; Ho, D., Recent Advances in Fluorescence Lifetime Analytical Microsystems: Contact Optics and CMOS Time-Resolved Electronics. Sensors 2017, 17 (12), 2800.
127. Weber, J. P., Resolution of the individual steps in the reaction of lysozyme with the trimer and hexamer of N-acetyl-D-glucosamine at subzero temperatures. Biochemistry 1980, 19 (4), 811-820.
128. Becker, W.; Bergmann, A.; Kacprzak, M.; Liebert, A. In Advanced time-correlated single photon counting technique for spectroscopy and imaging of biological systems, Fourth International Conference on Photonics and Imaging in Biology and Medicine, International Society for Optics and Photonics: 2006; 604714.
129. Alexiev, U.; Rimke, I.; Pohlmann, T., Elucidation of the nature of the conformational changes of the EF-interhelical loop in bacteriorhodopsin and of the helix VIII on the cytoplasmic surface of bovine rhodopsin: a time-resolved fluorescence depolarization study. J. Mol. Biol. 2003, 328 (3), 705-719.
130. Alexiev, U.; Volz, P.; Boreham, A.; Brodwolf, R., Time-resolved fluorescence microscopy (FLIM) as an analytical tool in skin nanomedicine. Eur. J. Pharm. Biopharm. 2017, 116, 111-124.
131. Pearson, R. M.; Sunoqrot, S.; Hsu, H. J.; Bae, J. W.; Hong, S., Dendritic nanoparticles: the next generation of nanocarriers? Ther. Deliv. 2012, 3 (8), 941-959.

132. Kurniasih, I. N.; Keilitz, J.; Haag, R., Dendritic nanocarriers based on hyperbranched polymers. Chem. Soc. Rev. 2015, 44 (12), 4145-4164.
133. Kavand, A.; Anton, N.; Vandamme, T.; Serra, C. A.; Chan-Seng, D., Synthesis and functionalization of hyperbranched polymers for targeted drug delivery. J. Control. Release 2020, 321, 285-311.
134. Buhleier, E.; Wehner, W.; Vögtle, F., " Cascade"- and "Nonskid-Chain-like" Synthesis of Molecular Cavity Topologies. Synthesis 1978, 2, 155–158.
135. Carlmark, A.; Hawker, C.; Hult, A.; Malkoch, M., New methodologies in the construction of dendritic materials. Chem. Soc. Rev. 2009, 38 (2), 352-362.
136. Kannan, R. M.; Nance, E.; Kannan, S.; Tomalia, D. A., Emerging concepts in dendrimer-based nanomedicine: from design principles to clinical applications. J. Intern. Med. 2014, 276 (6), 579-617.
137. Zheng, Y.; Li, S.; Weng, Z.; Gao, C., Hyperbranched polymers: advances from synthesis to applications. Chem. Soc. Rev. 2015, 44 (12), 4091-4130.
138. Jiang, G.; Chen, W.; Xia, W., Environmental-Sensitive Hyperbranched Polymers as Drug Carriers. Des. Monomers. Polym. 2012, 11 (2), 105-122.
139. Khandare, J.; Calderon, M.; Dagia, N. M.; Haag, R., Multifunctional dendritic polymers in nanomedicine: opportunities and challenges. Chem. Soc. Rev. 2012, 41 (7), 2824-2848.
140. Türk, H.; Haag, R.; Alban, S., Dendritic polyglycerol sulfates as new heparin analogues and potent inhibitors of the complement system. Bioconjug. Chem. 2004, 15 (1), 162-167.
141. Ran, Q.; Xu, X.; Dey, P.; Yu, S.; Lu, Y.; Dzubiella, J.; Haag, R.; Ballauff, M., Interaction of human serum albumin with dendritic polyglycerol sulfate: Rationalizing the thermodynamics of binding. J. Chem. Phys. 2018, 149 (16), 163324.
142. Rades, N.; Licha, K.; Haag, R., Dendritic Polyglycerol Sulfate for Therapy and Diagnostics. Polymers 2018, 10 (6), 595.
143. Frey, H.; Haag, R., Dendritic polyglycerol: a new versatile biocompatible material. J. Biotechnol. 2002, 90 (3-4), 257-267.
144. Khandare, J.; Mohr, A.; Calderon, M.; Welker, P.; Licha, K.; Haag, R., Structure-biocompatibility relationship of dendritic polyglycerol derivatives. Biomaterials 2010, 31 (15), 4268-4277.
145. Weinhart, M.; Gröger, D.; Enders, S.; Riese, S. B.; Dernedde, J.; Kainthan, R. K.; Brooks, D. E.; Haag, R., The Role of Dimension in Multivalent Binding Events: Structure–Activity Relationship of Dendritic Polyglycerol Sulfate Binding to L-Selectin in Correlation with Size and Surface Charge Density. Macromol. Biosci. 2011, 11 (8), 1088-1098.
146. Paulus, F.; Schulze, R.; Steinhilber, D.; Zieringer, M.; Steinke, I.; Welker, P.; Licha, K.; Wedepohl, S.; Dernedde, J.; Haag, R., The effect of polyglycerol sulfate branching on inflammatory processes. Macromol. Biosci. 2014, 14 (5), 643-654.
147. Dernedde, J.; Rausch, A.; Weinhart, M.; Enders, S.; Tauber, R.; Licha, K.; Schirner, M.; Zugel, U.; von Bonin, A.; Haag, R., Dendritic polyglycerol sulfates as multivalent inhibitors of inflammation. Proc. Natl. Acad. Sci. U.S.A. 2010, 107 (46), 19679-19684.
148. Lukowiak, M. C.; Thota, B. N. S.; Haag, R., Dendritic core–shell systems as soft drug delivery nanocarriers. Biotechnol. Adv. 2015, 33 (6, Part 3), 1327-1341.
149. Quadir, M. A.; Radowski, M. R.; Kratz, F.; Licha, K.; Hauff, P.; Haag, R., Dendritic multishell architectures for drug and dye transport. J. Control. Release 2008, 132 (3), 289-294.
150. Radowski, M. R.; Shukla, A.; von Berlepsch, H.; Bottcher, C.; Pickaert, G.; Rehage, H.; Haag, R., Supramolecular aggregates of dendritic multishell architectures as universal nanocarriers. Angew. Chem. Int. Ed. Engl. 2007, 46 (8), 1265-1269.
151. Do, N.; Weindl, G.; Fleige, E.; Salwiczek, M.; Koksch, B.; Haag, R.; Schäfer-Korting, M., Core-multishell nanotransporters enhance skin penetration of the cell-penetrating peptide low molecular weight protamine. Polym. Adv. Technol. 2014, 25 (11), 1337-1341.
152. Küchler, S.; Radowski, M. R.; Blaschke, T.; Dathe, M.; Plendl, J.; Haag, R.; Schäfer-Korting, M.; Kramer, K. D., Nanoparticles for skin penetration enhancement - A comparison of a dendritic core-multishell-nanotransporter and solid lipid nanoparticles. Eur. J. Pharm. Biopharm. 2009, 71 (2), 243-250.
153. Fleige, E.; Ziem, B.; Grabolle, M.; Haag, R.; Resch-Genger, U., Aggregation Phenomena of Host and Guest upon the Loading of Dendritic Core-Multishell Nanoparticles with Solvatochromic Dyes. Macromolecules 2012, 45 (23), 9452-9459.
154. Walker, K.; Stumbé, J.-F.; Haag, R., Polyester-Based, Biodegradable Core-Multishell Nanocarriers for the Transport of Hydrophobic Drugs. Polymers 2016, 8 (5), 192.
155. Unbehauen, M.; Fleige, E.; Paulus, F.; Schemmer, B.; Mecking, S.; Moré, S.; Haag, R., Biodegradable Core–Multishell Nanocarriers: Influence of Inner Shell Structure on the Encapsulation Behavior of Dexamethasone and Tacrolimus. Polymers 2017, 9 (12), 316.
156. Du, F.; Hönzke, S.; Neumann, F.; Keilitz, J.; Chen, W.; Ma, N.; Hedtrich, S.; Haag, R., Development of biodegradable hyperbranched core-multishell nanocarriers for efficient topical drug delivery. J. Control. Release 2016, 242, 42-49.
157. Fleige, E.; Achazi, K.; Schaletzki, K.; Triemer, T.; Haag, R., pH-responsive dendritic core-multishell nanocarriers. J. Control. Release 2014, 185, 99-108.
158. Tomalia, D. A.; Uppuluri, S.; Swanson, D. R.; Li, J., Dendrimers as reactive modules for the synthesis of new structure-controlled, higher-complexity megamers. Pure Appl. Chem. 2000, 72 (12), 2343-2358.
159. Schilrreff, P.; Mundina-Weilenmann, C.; Romero, E. L.; Morilla, M. J., Selective cytotoxicity of PAMAM G5 core--PAMAM G2.5 shell tecto-dendrimers on melanoma cells. Int. J. Nanomedicine 2012, 7, 4121-4133.
160. Uppuluri, S.; Swanson, D. R.; Piehler, L. T.; Li, J.; Hagnauer, G. L.; Tomalia, D. A., Core-shell tecto(dendrimers): I. Synthesis and characterization of saturated shell models. Adv. Mater. 2000, 12 (11), 796-800.
161. Murta, V.; Schilrreff, P.; Rosciszewski, G.; Morilla, M. J.; Ramos, A. J., G5G2.5 core-shell tecto-dendrimer specifically targets reactive glia in brain ischemia. J. Neurochem. 2018, 144 (6), 748-760.
162. Schilrreff, P.; Cervini, G.; Romero, E. L.; Morilla, M. J., Enhanced antimelanoma activity of methotrexate and zoledronic acid within polymeric sandwiches. Colloids Surf. B. Biointerfaces 2014, 122, 19-29.
163. Silberreis, K.; Niesler, N.; Rades, N.; Haag, R.; Dernedde, J., Sulfated Dendritic Polyglycerol Is a Potent Complement Inhibitor. Biomacromolecules 2019, 20 (10), 3809-3818.
164. Zhong, Y.; Dimde, M.; Stobener, D.; Meng, F.; Deng, C.; Zhong, Z.; Haag, R., Micelles with Sheddable Dendritic Polyglycerol Sulfate Shells Show Extraordinary Tumor Targetability and Chemotherapy in Vivo. ACS Appl. Mater. Interfaces 2016, 8 (41), 27530-27538.

165. Sousa-Herves, A.; Wurfel, P.; Wegner, N.; Khandare, J.; Licha, K.; Haag, R.; Welker, P.; Calderon, M., Dendritic polyglycerol sulfate as a novel platform for paclitaxel delivery: pitfalls of ester linkage. Nanoscale 2015, 7 (9), 3923-3932.
166. Radbruch, M.; Pischon, H.; Ostrowski, A.; Volz, P.; Brodwolf, R.; Neumann, F.; Unbehauen, M.; Kleuser, B.; Haag, R.; Ma, N.; Alexiev, U.; Mundhenk, L.; Gruber, A. D., Dendritic Core-Multishell Nanocarriers in Murine Models of Healthy and Atopic Skin. Nanoscale Res. Lett. 2017, 12 (1), 64.
167. Rabe, C.; Fleige, E.; Vogtt, K.; Szekely, N.; Lindner, P.; Burchard, W.; Haag, R.; Ballauff, M., The multi-domain nanoparticle structure of a universal core-multi-shell nanocarrier. Polymer 2014, 55 (26), 6735-6742.
168. Karande, P.; Jain, A.; Ergun, K.; Kispersky, V.; Mitragotri, S., Design principles of chemical penetration enhancers for transdermal drug delivery. Proc. Natl. Acad. Sci. U. S. A. 2005, 102 (13), 4688-4693.
169. Frombach, J.; Unbehauen, M.; Kurniasih, I. N.; Schumacher, F.; Volz, P.; Hadam, S.; Rancan, F.; Blume-Peytavi, U.; Kleuser, B.; Haag, R.; Alexiev, U.; Vogt, A., Core-multishell nanocarriers enhance drug penetration and reach keratinocytes and antigen-presenting cells in intact human skin. J. Control. Release 2019, 299, 138-148.
170. Alnasif, N.; Zoschke, C.; Fleige, E.; Brodwolf, R.; Boreham, A.; Rühl, E.; Eckl, K. M.; Merk, H. F.; Hennies, H. C.; Alexiev, U.; Haag, R.; Küchler, S.; Schäfer-Korting, M., Penetration of normal, damaged and diseased skin--an in vitro study on dendritic core-multishell nanotransporters. J. Control. Release 2014, 185, 45-50.
171. Küchler, S.; Abdel-Mottaleb, M.; Lamprecht, A.; Radowski, M. R.; Haag, R.; Schäfer-Korting, M., Influence of nanocarrier type and size on skin delivery of hydrophilic agents. Eur. J. Pharm. Biopharm. 2009, 377 (1-2), 169-172.
172. Pischon, H.; Radbruch, M.; Ostrowski, A.; Volz, P.; Gerecke, C.; Unbehauen, M.; Honzke, S.; Hedtrich, S.; Fluhr, J. W.; Haag, R.; Kleuser, B.; Alexiev, U.; Gruber, A. D.; Mundhenk, L., Stratum corneum targeting by dendritic core-multishell-nanocarriers in a mouse model of psoriasis. Nanomedicine 2017, 13 (1), 317-327.
173. Yamamoto, K.; Klossek, A.; Flesch, R.; Ohigashi, T.; Fleige, E.; Rancan, F.; Frombach, J.; Vogt, A.; Blume-Peytavi, U.; Schrade, P.; Bachmann, S.; Haag, R.; Hedtrich, S.; Schäfer-Korting, M.; Kosugi, N.; Rühl, E., Core-multishell nanocarriers: Transport and release of dexamethasone probed by soft X-ray spectromicroscopy. J. Control. Release 2016, 242, 64-70.
174. Edlich, A.; Volz, P.; Brodwolf, R.; Unbehauen, M.; Mundhenk, L.; Gruber, A. D.; Hedtrich, S.; Haag, R.; Alexiev, U.; Kleuser, B., Crosstalk between core-multishell nanocarriers for cutaneous drug delivery and antigen-presenting cells of the skin. Biomaterials 2018, 162, 60-70.
175. Jepps, O. G.; Dancik, Y.; Anissimov, Y. G.; Roberts, M. S., Modeling the human skin barrier--towards a better understanding of dermal absorption. Adv. Drug Deliv. Rev. 2013, 65 (2), 152-168.
176. McGrath, J.; Eady, R.; Pope, F., Anatomy and organization of human skin. In Rook's textbook of dermatology, 2004; Chapter 3.
177. Lemos, C. N.; Pereira, F.; Dalmolin, L. F.; Cubayachi, C.; Ramos, D. N.; Lopez, R. F. V., Nanoparticles influence in skin penetration of drugs. In Nanostructures for the Engineering of Cells, Tissues and Organs, 2018; pp 187-248.
178. Kabashima, K.; Honda, T.; Ginhoux, F.; Egawa, G., The immunological anatomy of the skin. Nat. Rev. Immunol. 2019, 19 (1), 19-30.
179. Sandby-Moller, J.; Poulsen, T.; Wulf, H. C., Epidermal thickness at different body sites: relationship to age, gender, pigmentation, blood content, skin type and smoking habits. Acta Derm. Venereol. 2003, 83 (6), 410-413.
180. Turcan, I.; Jonkman, M. F., Blistering disease: insight from the hemidesmosome and other components of the dermal-epidermal junction. Cell Tissue Res. 2015, 360 (3), 545-569.
181. Baroli, B., Penetration of nanoparticles and nanomaterials in the skin: Fiction or reality? J. Pharm. Sci. 2010, 99 (1), 21-50.
182. Yokouchi, M.; Atsugi, T.; Logtestijn, M. V.; Tanaka, R. J.; Kajimura, M.; Suematsu, M.; Furuse, M.; Amagai, M.; Kubo, A., Epidermal cell turnover across tight junctions based on Kelvin's tetrakaidecahedron cell shape. Elife 2016, 5.
183. Brandner, J. M.; Zorn-Kruppa, M.; Yoshida, T.; Moll, I.; Beck, L. A.; De Benedetto, A., Epidermal tight junctions in health and disease. Tissue Barriers 2015, 3 (1-2), e974451.
184. Joshi, R., Learning from eponyms: George F. Odland and Odland bodies. Indian Dermatol. Online J. 2014, 5 (3), 334-338.
185. Elias, P. M.; Menon, G. K., Structural and Lipid Biochemical Correlates of the Epidermal Permeability Barrier. In Adv. Lipid Res., Elias, P. M. (Ed.) Elsevier: 1991, 24, 1-26.
186. Feingold, K. R., Thematic review series: skin lipids. The role of epidermal lipids in cutaneous permeability barrier homeostasis. J. Lipid Res. 2007, 48 (12), 2531-2546.
187. Eichner, A.; Sonnenberger, S.; Dobner, B.; Hauss, T.; Schroeter, A.; Neubert, R. H. H., Localization of methyl-branched ceramide [EOS] species within the long-periodicity phase in stratum corneum lipid model membranes: A neutron diffraction study. Biochim. Biophys. Acta 2016, 1858 (11), 2911-2922.
188. Schroter, A.; Kessner, D.; Kiselev, M. A.; Hauss, T.; Dante, S.; Neubert, R. H., Basic nanostructure of stratum corneum lipid matrices based on ceramides [EOS] and [AP]: a neutron diffraction study. Biophys. J. 2009, 97 (4), 1104-1114.
189. Bolzinger, M.-A.; Briançon, S.; Pelletier, J.; Chevalier, Y., Penetration of drugs through skin, a complex rate-controlling membrane. Curr. Opin. Colloid Interface Sci. 2012, 17 (3), 156-165.
190. Xiao Wen, L.; Zhi Ping, X.; Jeffrey, G.; Andrei, V. Z.; Michael, S. R.; Xin, L., Penetration of Nanoparticles into Human Skin. Curr. Pharm. Des. 2013, 19 (35), 6353-6366.
191. Bos, J. D.; Meinardi, M. M. H. M., The 500 Dalton rule for the skin penetration of chemical compounds and drugs. Exp. Dermatol. 2000, 9 (3), 165-169.
192. Gupta, M.; Agrawal, U.; Vyas, S. P., Nanocarrier-based topical drug delivery for the treatment of skin diseases. Expert. Opin. Drug Deliv. 2012, 9 (7), 783-804.
193. Vogt, A.; Combadiere, B.; Hadam, S.; Stieler, K. M.; Lademann, J.; Schaefer, H.; Autran, B.; Sterry, W.; Blume-Peytavi, U., 40 nm, but not 750 or 1,500 nm, nanoparticles enter epidermal CD1a+ cells after transcutaneous application on human skin. J. Invest. Dermatol. 2006, 126 (6), 1316-1322.
194. Radtke, M.; Patzelt, A.; Knorr, F.; Lademann, J.; Netz, R. R., Ratchet effect for nanoparticle transport in hair follicles. Eur. J. Pharm. Biopharm. 2017, 116, 125-130.
195. Lademann, J.; Knorr, F.; Richter, H.; Jung, S.; Meinke, M.; Rühl, E.; Alexiev, U.; Calderón, M.; Patzelt, A., Hair follicles as a target structure for nanoparticles. J. Innov. Opt. Health Sci. 2015, 8 (04), 1530004.
196. Boreham, A.; Kim, T. Y.; Spahn, V.; Stein, C.; Mundhenk, L.; Gruber, A. D.; Haag, R.; Welker, P.; Licha, K.; Alexiev, U., Exploiting Fluorescence Lifetime Plasticity in FLIM: Target Molecule Localization in Cells and Tissues. ACS Med. Chem. Lett. 2011, 2 (10), 724-728.

197. Licha, K.; Welker, P.; Weinhart, M.; Wegner, N.; Kern, S.; Reichert, S.; Gemeinhardt, I.; Weissbach, C.; Ebert, B.; Haag, R.; Schirner, M., Fluorescence imaging with multifunctional polyglycerol sulfates: novel polymeric near-IR probes targeting inflammation. Bioconjug. Chem. 2011, 22 (12), 2453-2460.
198. Boreham, A.; Brodwolf, R.; Pfaff, M.; Kim, T.-Y.; Schlieter, T.; Mundhenk, L.; Gruber, A. D.; Gröger, D.; Licha, K.; Haag, R.; Alexiev, U., Temperature and environment dependent dynamic properties of a dendritic polyglycerol sulfate. Polym. Adv. Technol. 2014, 25 (11), 1329-1336.
199. Wycisk, V.; Achazi, K.; Hirsch, O.; Kuehne, C.; Dernedde, J.; Haag, R.; Licha, K., Heterobifunctional Dyes: Highly Fluorescent Linkers Based on Cyanine Dyes. ChemistryOpen 2017, 6 (3), 437-446.
200. Rades, N.; Achazi, K.; Qiu, M.; Deng, C.; Haag, R.; Zhong, Z.; Licha, K., Reductively cleavable polymer-drug conjugates based on dendritic polyglycerol sulfate and monomethyl auristatin E as anticancer drugs. J. Control. Release 2019, 300, 13-21.
201. Molecular Probes, I. Certificate of analysis: fluorescein-5-isothiocyanate https://tools.thermofisher.com/content/sfs/COAPDFs/2014/1541999_F143.pdf (accessed 01.05.2017).
202. Jiang, Y. W.; Guo, H. Y.; Chen, Z.; Yu, Z. W.; Wang, Z.; Wu, F. G., In Situ Visualization of Lipid Raft Domains by Fluorescent Glycol Chitosan Derivatives. Langmuir 2016, 32 (26), 6739-6745.
203. Parasassi, T.; De Stasio, G.; Dubaldo, A.; Gratton, E., Phase Fluctuation in Phospholipid-Membranes Revealed by Laurdan Fluorescence. Biophys. J. 1990, 57 (6), 1179-1186.
204. Edlich, A.; Gerecke, C.; Giulbudagian, M.; Neumann, F.; Hedtrich, S.; Schäfer-Korting, M.; Ma, N.; Calderon, M.; Kleuser, B., Specific uptake mechanisms of well-tolerated thermoresponsive polyglycerol-based nanogels in antigen-presenting cells of the skin. Eur. J. Pharm. Biopharm. 2017, 116, 155-163.
205. Japtok, L.; Schaper, K.; Baumer, W.; Radeke, H. H.; Jeong, S. K.; Kleuser, B., Sphingosine 1-phosphate modulates antigen capture by murine Langerhans cells via the S1P2 receptor subtype. PLoS One 2012, 7 (11), e49427.
206. Costes, S. V.; Daelemans, D.; Cho, E. H.; Dobbin, Z.; Pavlakis, G.; Lockett, S., Automatic and quantitative measurement of protein-protein colocalization in live cells. Biophys. J. 2004, 86 (6), 3993-4003.
207. Schindelin, J.; Arganda-Carreras, I.; Frise, E.; Kaynig, V.; Longair, M.; Pietzsch, T.; Preibisch, S.; Rueden, C.; Saalfeld, S.; Schmid, B.; Tinevez, J. Y.; White, D. J.; Hartenstein, V.; Eliceiri, K.; Tomancak, P.; Cardona, A., Fiji: an open-source platform for biological-image analysis. Nat. Methods 2012, 9 (7), 676-682.
208. Heinrich, R.; Neel, B. G.; Rapoport, T. A., Mathematical models of protein kinase signal transduction. Mol. Cell 2002, 9 (5), 957-970.
209. Pople, P. V.; Singh, K. K., Targeting tacrolimus to deeper layers of skin with improved safety for treatment of atopic dermatitis—Part II: In vivo assessment of dermatopharmacokinetics, biodistribution and efficacy. Int. J. Pharm. 2012, 434 (1), 70-79.
210. Man, M.-Q.; Hatano, Y.; Lee, S. H.; Man, M.; Chang, S.; Feingold, K. R.; Leung, D. Y. M.; Holleran, W.; Uchida, Y.; Elias, P. M., Characterization of a Hapten-Induced, Murine Model with Multiple Features of Atopic Dermatitis: Structural, Immunologic, and Biochemical Changes following Single Versus Multiple Oxazolone Challenges. J. Invest. Dermatol. 2008, 128 (1), 79-86.
211. Löwenau, L. J.; Zoschke, C.; Brodwolf, R.; Volz, P.; Hausmann, C.; Wattanapitayakul, S.; Boreham, A.; Alexiev, U.; Schäfer-Korting, M., Increased permeability of reconstructed human epidermis from UVB-irradiated keratinocytes. Eur. J. Pharm. Biopharm. 2017, 116, 149-154.
212. Netzlaff, F.; Kaca, M.; Bock, U.; Haltner-Ukomadu, E.; Meiers, P.; Lehr, C.-M.; Schaefer, U. F., Permeability of the reconstructed human epidermis model Episkin® in comparison to various human skin preparations. Eur. J. Pharm. Biopharm. 2007, 66 (1), 127-134.
213. Zoschke, C.; Ulrich, M.; Sochorova, M.; Wolff, C.; Vavrova, K.; Ma, N.; Ulrich, C.; Brandner, J. M.; Schafer-Korting, M., The barrier function of organotypic non-melanoma skin cancer models. J. Control. Release 2016, 233, 10-18.
214. Becker, W.; Bergmann, A. Detectors for High-Speed Photon Counting. https://www.becker-hickl.com/wp-content/uploads/2018/12/spcdetect-v01.pdf (accessed 04.04.2020).
215. Kim, T.-Y. Time-resolved fluorescence spectroscopic studies at the cytoplasmic surface of rhodopsin. Dissertation, Freie Universität Berlin, 2013.
216. Press, W. H.; Teukolsky, S. A.; Vetterling, W. T.; Flannery, B. P., Numerical Recipes: The Art of Scientific Computing. 3rd Edition ed.; Cambridge University Press: New York, NY, United States of America, 2007; 810 – 816
217. Weber, G., Resolution of the fluorescence lifetimes in a heterogeneous system by phase and modulation measurements. J. Phys. Chem. 1981, 85 (8), 949-953.
218. Wu, G.; Nowotny, T.; Zhang, Y.; Yu, H. Q.; Li, D. D., Artificial neural network approaches for fluorescence lifetime imaging techniques. Opt. Lett. 2016, 41 (11), 2561-2564.
219. Jameson, D. M.; Gratton, E.; Hall, R. D., The Measurement and Analysis of Heterogeneous Emissions by Multifrequency Phase and Modulation Fluorometry. Appl. Spectrosc. Rev. 1984, 20 (1), 55-106.
220. Ranjit, S.; Malacrida, L.; Jameson, D. M.; Gratton, E., Fit-free analysis of fluorescence lifetime imaging data using the phasor approach. Nat. Protoc. 2018, 13 (9), 1979-2004.
221. Hartigan, J. A.; Wong, M. A., Algorithm AS 136: A K-Means Clustering Algorithm. J. R. Stat. Soc. Ser. C Appl. Stat. 1979, 28 (1), 100-108.
222. Betz, T.; Teipel, J.; Koch, D.; Hartig, W.; Guck, J.; Kas, J.; Giessen, H., Excitation beyond the monochromatic laser limit: simultaneous 3-D confocal and multiphoton microscopy with a tapered fiber as white-light laser source. J. Biomed. Opt. 2005, 10 (5), 054009.
223. Chiu, L. D.; Su, L.; Reichelt, S.; Amos, W. B., Use of a white light supercontinuum laser for confocal interference-reflection microscopy. J. Microsc. 2012, 246 (2), 153-159.
224. Dunsby, C.; Lanigan, P. M. P.; McGinty, J.; Elson, D. S.; Requejo-Isidro, J.; Munro, I.; Galletly, N.; McCann, F.; Treanor, B.; Onfelt, B.; Davis, D. M.; Neil, M. A. A.; French, P. M. W., An electronically tunable ultrafast laser source applied to fluorescence imaging and fluorescence lifetime imaging microscopy. J. Phys. D Appl. Phys. 2004, 37 (23), 3296-3303.
225. Frank, J. H.; Elder, A. D.; Swartling, J.; Venkitaraman, A. R.; Jeyasekharan, A. D.; Kaminski, C. F., A white light confocal microscope for spectrally resolved multidimensional imaging. J. Microsc. 2007, 227 (3), 203-215.
226. Girkin, J. M.; McConnell, G., Advances in laser sources for confocal and multiphoton microscopy. Microsc. Res. Tech. 2005, 67 (1), 8-14.

227. McConnell, G.; Girkin, J. M.; Ameer-Beg, S. M.; Barber, P. R.; Vojnovic, B.; Ng, T.; Banerjee, A.; Watson, T. F.; Cook, R. J., Time-correlated single-photon counting fluorescence lifetime confocal imaging of decayed and sound dental structures with a white-light supercontinuum source. J. Microsc. 2007, 225 (2), 126-136.
228. Ye, J. Y.; Divin, C. J.; Baker, J. R.; Norris, T. B., Whole spectrum fluorescence detection with ultrafast white light excitation. Opt. Express 2007, 15 (16), 10439-10445.
229. NKT Photonics A/S (Denmark) - Application Note: Supercontinuum Generation in Photonics Crystal Fibers. http://www.nktphotonics.com/wp-content/uploads/sites/3/2015/02/Application_note_-_Supercontinuum-General.pdf (accessed 08.12.2017).
230. GmbH, B. H. The HPM-100-40 Hybrid Detector. https://www.becker-hickl.com/wp-content/uploads/2018/12/hpm-appnote-v03.pdf (accessed 04.04.2020).
231. Kim, T. Y.; Winkler, K.; Alexiev, U., Picosecond multidimensional fluorescence spectroscopy: a tool to measure real-time protein dynamics during function. Photochem. Photobiol. 2007, 83 (2), 378-384.
232. Boreham, A.; Brodwolf, R.; Walker, K.; Haag, R.; Alexiev, U., Time-Resolved Fluorescence Spectroscopy and Fluorescence Lifetime Imaging Microscopy for Characterization of Dendritic Polymer Nanoparticles and Applications in Nanomedicine. Molecules 2016, 22 (1), e17.
233. Kirchberg, K.; Kim, T. Y.; Moller, M.; Skegro, D.; Dasara Raju, G.; Granzin, J.; Buldt, G.; Schlesinger, R.; Alexiev, U., Conformational dynamics of helix 8 in the GPCR rhodopsin controls arrestin activation in the desensitization process. Proc. Natl. Acad. Sci. U.S.A. 2011, 108 (46), 18690-18695.
234. Hoover, E. E.; Squier, J. A., Advances in multiphoton microscopy technology. Nat. Photonics 2013, 7 (2), 93-101.
235. Helmchen, F.; Denk, W., Deep tissue two-photon microscopy. Nat. Methods 2005, 2 (12), 932-940.
236. Lefort, C., A review of biomedical multiphoton microscopy and its laser sources. J. Phys. D Appl. Phys. 2017, 50 (42).
237. Zipfel, W. R.; Williams, R. M.; Webb, W. W., Nonlinear magic: multiphoton microscopy in the biosciences. Nat. Biotechnol. 2003, 21 (11), 1369-1377.
238. Huck, V.; Gorzelanny, C.; Thomas, K.; Getova, V.; Niemeyer, V.; Zens, K.; Unnerstall, T. R.; Feger, J. S.; Fallah, M. A.; Metze, D.; Stander, S.; Luger, T. A.; Koenig, K.; Mess, C.; Schneider, S. W., From morphology to biochemical state - intravital multiphoton fluorescence lifetime imaging of inflamed human skin. Sci. Rep. 2016, 6, 22789.
239. Denk, W.; Strickler, J. H.; Webb, W. W., Two-photon laser scanning fluorescence microscopy. Science 1990, 248 (4951), 73.
240. Wang, S.; Li, L.; Zhu, X.; Zheng, L.; Zhuo, S.; Chen, J., Applications of multiphoton microscopy in the field of colorectal cancer. Laser Phys. 2018, 28 (6).
241. Lin, H.; Fan, T.; Sui, J.; Wang, G.; Chen, J.; Zhuo, S.; Zhang, H., Recent advances in multiphoton microscopy combined with nanomaterials in the field of disease evolution and clinical applications to liver cancer. Nanoscale 2019, 11 (42), 19619-19635.
242. Kantelhardt, S. R.; Kalasauskas, D.; Konig, K.; Kim, E.; Weinigel, M.; Uchugonova, A.; Giese, A., In vivo multiphoton tomography and fluorescence lifetime imaging of human brain tumor tissue. J. Neurooncol. 2016, 127 (3), 473-482.
243. Svoboda, K.; Yasuda, R., Principles of two-photon excitation microscopy and its applications to neuroscience. Neuron 2006, 50 (6), 823-839.
244. Yaseen, M. A.; Sutin, J.; Wu, W.; Fu, B.; Uhlirova, H.; Devor, A.; Boas, D. A.; Sakadzic, S., Fluorescence lifetime microscopy of NADH distinguishes alterations in cerebral metabolism in vivo. Biomed. Opt. Express 2017, 8 (5), 2368-2385.
245. Sun, T. Y.; Haberman, A. M.; Greco, V., Preclinical Advances with Multiphoton Microscopy in Live Imaging of Skin Cancers. J. Invest. Dermatol. 2017, 137 (2), 282-287.
246. Yew, E.; Rowlands, C.; So, P. T., Application of Multiphoton Microscopy in Dermatological Studies: a Mini-Review. J. Innov. Opt. Health Sci. 2014, 7 (5), 1330010.
247. Patalay, R.; Talbot, C.; Alexandrov, Y.; Lenz, M. O.; Kumar, S.; Warren, S.; Munro, I.; Neil, M. A.; Konig, K.; French, P. M.; Chu, A.; Stamp, G. W.; Dunsby, C., Multiphoton multispectral fluorescence lifetime tomography for the evaluation of basal cell carcinomas. PLoS One 2012, 7 (9), e43460.
248. Pastore, M. N.; Studier, H.; Bonder, C. S.; Roberts, M. S., Non-invasive metabolic imaging of melanoma progression. Exp. Dermatol. 2017, 26 (7), 607-614.
249. Schaefer, P. M.; Kalinina, S.; Rueck, A.; von Arnim, C. A. F.; von Einem, B., NADH Autofluorescence-A Marker on its Way to Boost Bioenergetic Research. Cytometry A 2019, 95 (1), 34-46.
250. Holmes, A. M.; Lim, J.; Studier, H.; Roberts, M. S., Varying the morphology of silver nanoparticles results in differential toxicity against micro-organisms, HaCaT keratinocytes and affects skin deposition. Nanotoxicology 2016, 10 (10), 1503-1514.
251. Robertson, T. A.; Bunel, F.; Roberts, M. S., Fluorescein derivatives in intravital fluorescence imaging. Cells 2013, 2 (3), 591-606.
252. Niesner, R.; Gericke, K.-H., Fluorescence lifetime imaging in biosciences: technologies and applications. Front. Phys. China 2008, 3 (1), 88-104.
253. Hanson, K. M.; Behne, M. J.; Barry, N. P.; Mauro, T. M.; Gratton, E.; Clegg, R. M., Two-photon fluorescence lifetime imaging of the skin stratum corneum pH gradient. Biophys. J. 2002, 83 (3), 1682-1690.
254. Martin, M. M.; Lindqvist, L., The pH dependence of fluorescein fluorescence. J. Lumin. 1975, 10 (6), 381-390.
255. Schulz, R.; Yamamoto, K.; Klossek, A.; Flesch, R.; Honzke, S.; Rancan, F.; Vogt, A.; Blume-Peytavi, U.; Hedtrich, S.; Schafer-Korting, M.; Ruhl, E.; Netz, R. R., Data-based modeling of drug penetration relates human skin barrier function to the interplay of diffusivity and free-energy profiles. Proc. Natl. Acad. Sci. U. S. A. 2017, 114 (14), 3631-3636.
256. Kalwarczyk, T.; Ziebacz, N.; Bielejewska, A.; Zaboklicka, E.; Koynov, K.; Szymanski, J.; Wilk, A.; Patkowski, A.; Gapinski, J.; Butt, H. J.; Holyst, R., Comparative analysis of viscosity of complex liquids and cytoplasm of mammalian cells at the nanoscale. Nano. Lett. 2011, 11 (5), 2157-2163.
257. Sluch, M. I.; Somoza, M. M.; Berg, M. A., Friction on Small Objects and the Breakdown of Hydrodynamics in Solution: Rotation of Anthracene in Poly(isobutylene) from the Small-Molecule to Polymer Limits. J. Phys. Chem. B 2002, 106 (29), 7385-7397.
258. Boreham, A.; Pfaff, M.; Fleige, E.; Haag, R.; Alexiev, U., Nanodynamics of dendritic core-multishell nanocarriers. Langmuir 2014, 30 (6), 1686-1695.
259. González, B.; Calvar, N.; Gómez, E.; Domínguez, Á., Density, dynamic viscosity, and derived properties of binary mixtures of methanol or ethanol with water, ethyl acetate, and methyl acetate at T=(293.15, 298.15, and 303.15)K. J. Chem. Thermodyn. 2007, 39 (12), 1578-1588.

260. Physical Properties of Glycerine and Its Solutions. New York: Glycerine Producers' Association: 1963.
261. Vyšniauskas , A.; Qurashi, M.; Gallop, N.; Balaz, M.; Anderson, H. L.; Kuimova, M. K., Unravelling the effect of temperature on viscosity-sensitive fluorescent molecular rotors. Chem. Sci. 2015, 6 (10), 5773-5778.
262. Sanborn, M. E.; Connolly, B. K.; Gurunathan, K.; Levitus, M., Fluorescence Properties and Photophysics of the Sulfoindocyanine Cy3 Linked Covalently to DNA. J. Phys. Chem. B 2007, 111 (37), 11064-11074.
263. Haidekker, M. A.; Brady, T. P.; Lichlyter, D.; Theodorakis, E. A., Effects of solvent polarity and solvent viscosity on the fluorescent properties of molecular rotors and related probes. Bioorg. Chem. 2005, 33 (6), 415-425.
264. Wyman, J., The Dielectric Constant of Mixtures of Ethyl Alcohol and Water from -5 to 40°. J. Am. Chem. Soc. 1931, 53 (9), 3292-3301.
265. Wessendorf, M. W.; Brelje, T. C., Which fluorophore is brightest? A comparison of the staining obtained using fluorescein, tetramethylrhodamine, lissamine rhodamine, Texas red, and cyanine 3.18. Histochemistry 1992, 98 (2), 81-85.
266. Mujumdar, R. B.; Ernst, L. A.; Mujumdar, S. R.; Lewis, C. J.; Waggoner, A. S., Cyanine dye labeling reagents: sulfoindocyanine succinimidyl esters. Bioconjug. Chem. 1993, 4 (2), 105-111.
267. Wäldchen, S.; Lehmann, J.; Klein, T.; van de Linde, S.; Sauer, M., Light-induced cell damage in live-cell super-resolution microscopy. Sci. Rep. 2015, 5, 15348.
268. van Erp, P. E.; Jansen, M. J.; de Jongh, G. J.; Boezeman, J. B.; Schalkwijk, J., Ratiometric measurement of intracellular pH in cultured human keratinocytes using carboxy-SNARF-1 and flow cytometry. Cytometry 1991, 12 (2), 127-132.
269. Madshus, I. H., Regulation of intracellular pH in eukaryotic cells. Biochem. J. 1988, 250 (1), 1-8.
270. Hou, H.; Zhao, Y.; Li, C.; Wang, M.; Xu, X.; Jin, Y., Single-cell pH imaging and detection for pH profiling and label-free rapid identification of cancer-cells. Sci. Rep. 2017, 7 (1), 1759.
271. Seksek, O.; Bolard, J., Nuclear pH gradient in mammalian cells revealed by laser microspectrofluorimetry. J. Cell Sci. 1996, 109 (1), 257-262.
272. Asokan, A.; Cho, M. J., Exploitation of Intracellular pH Gradients in the Cellular Delivery of Macromolecules. J. Pharm. Sci. 2002, 91 (4), 903-913.
273. Ning, Y.; Cheng, S.; Wang, J. X.; Liu, Y. W.; Feng, W.; Li, F.; Zhang, J. L., Fluorescence lifetime imaging of upper gastrointestinal pH in vivo with a lanthanide based near-infrared tau probe. Chem. Sci. 2019, 10 (15), 4227-4235.
274. Battisti, A.; Digman, M. A.; Gratton, E.; Storti, B.; Beltram, F.; Bizzarri, R., Intracellular pH measurements made simple by fluorescent protein probes and the phasor approach to fluorescence lifetime imaging. Chem. Commun. 2012, 48 (42), 5127-5129.
275. Krüger, H. R.; Schutz, I.; Justies, A.; Licha, K.; Welker, P.; Haucke, V.; Calderon, M., Imaging of doxorubicin release from theranostic macromolecular prodrugs via fluorescence resonance energy transfer. J. Control. Release 2014, 194, 189-196.
276. Gao, W.; Chan, J. M.; Farokhzad, O. C., pH-Responsive Nanoparticles for Drug Delivery. Mol. Pharm. 2010, 7 (6), 1913-1920.
277. Singh, A. V.; Laux, P.; Luch, A.; Sudrik, C.; Wiehr, S.; Wild, A. M.; Santomauro, G.; Bill, J.; Sitti, M., Review of emerging concepts in nanotoxicology: opportunities and challenges for safer nanomaterial design. Toxicol. Mech. Methods 2019, 29 (5), 378-387.
278. Biancardi, A.; Biver, T.; Secco, F.; Mennucci, B., An investigation of the photophysical properties of minor groove bound and intercalated DAPI through quantum-mechanical and spectroscopic tools. Phys. Chem. Chem. Phys. 2013, 15 (13), 4596-4603.
279. Volz, P.; Krause, N.; Balke, J.; Schneider, C.; Walter, M.; Schneider, F.; Schlesinger, R.; Alexiev, U., Light and pH-induced Changes in Structure and Accessibility of Transmembrane Helix B and Its Immediate Environment in Channelrhodopsin-2. J. Biol. Chem. 2016, 291 (33), 17382-17393.
280. Cedervall, T.; Lynch, I.; Lindman, S.; Berggard, T.; Thulin, E.; Nilsson, H.; Dawson, K. A.; Linse, S., Understanding the nanoparticle-protein corona using methods to quantify exchange rates and affinities of proteins for nanoparticles. Proc. Natl. Acad. Sci. U. S. A. 2007, 104 (7), 2050-2055.
281. Monopoli, M. P.; Aberg, C.; Salvati, A.; Dawson, K. A., Biomolecular coronas provide the biological identity of nanosized materials. Nat. Nanotechnol. 2012, 7 (12), 779-786.
282. Schottler, S.; Becker, G.; Winzen, S.; Steinbach, T.; Mohr, K.; Landfester, K.; Mailander, V.; Wurm, F. R., Protein adsorption is required for stealth effect of poly(ethylene glycol)- and poly(phosphoester)-coated nanocarriers. Nat. Nanotechnol. 2016, 11 (4), 372-377.
283. Salvati, A.; Pitek, A. S.; Monopoli, M. P.; Prapainop, K.; Bombelli, F. B.; Hristov, D. R.; Kelly, P. M.; Aberg, C.; Mahon, E.; Dawson, K. A., Transferrin-functionalized nanoparticles lose their targeting capabilities when a biomolecule corona adsorbs on the surface. Nat. Nanotechnol. 2013, 8 (2), 137-143.
284. Hadjidemetriou, M.; Kostarelos, K., Nanomedicine: Evolution of the nanoparticle corona. Nat. Nanotechnol. 2017, 12 (4), 288-290.
285. Gornall, A. G.; Bardawill, C. J.; David, M. M., Determination of serum proteins by means of the biuret reaction. J. Biol. Chem. 1949, 177 (2), 751-766.
286. Kragh-Hansen, U., Molecular aspects of ligand binding to serum albumin. Pharmacol. Rev. 1981, 33 (1), 17-53.
287. He, X. M.; Carter, D. C., Atomic structure and chemistry of human serum albumin. Nature 1992, 358 (6383), 209-215.
288. Klajnert, B.; Stanislawska, L.; Bryszewska, M.; Palecz, B., Interactions between PAMAM dendrimers and bovine serum albumin. Biochim. Biophys. Acta 2003, 1648 (1-2), 115-26.
289. De, M.; Rana, S.; Akpinar, H.; Miranda, O. R.; Arvizo, R. R.; Bunz, U. H. F.; Rotello, V. M., Sensing of proteins in human serum using conjugates of nanoparticles and green fluorescent protein. Nat. Chem. 2009, 1 (6), 461-465.
290. Lee, S.; Sung, D.-B.; Kang, S.; Parameswaran, S.; Choi, J.-H.; Lee, J. S.; Han, M. S., Development of Human Serum Albumin Selective Fluorescent Probe Using Thieno[3,2-b]pyridine-5(4H)-one Fluorophore Derivatives. Sensors 2019, 19 (23), 5298.
291. Ravindran, A.; Singh, A.; Raichur, A. M.; Chandrasekaran, N.; Mukherjee, A., Studies on interaction of colloidal Ag nanoparticles with bovine serum albumin (BSA). Colloids Surf. B. Biointerfaces 2010, 76 (1), 32-37.
292. Shcharbin, D.; Ottaviani, M. F.; Cangiotti, M.; Przybyszewska, M.; Zaborski, M.; Bryszewska, M., Impact of PAMAM G2 and G6 dendrimers on bovine serum albumin (fatty acids free and loaded with different fatty acids). Colloids Surf. B. Biointerfaces 2008, 63 (1), 27-33.
293. Fleischer, C. C.; Payne, C. K., Nanoparticle-cell interactions: molecular structure of the protein corona and cellular outcomes. Acc. Chem. Res. 2014, 47 (8), 2651-2659.
294. Yu, X.; Guo, C.; Fisher, P. B.; Subjeck, J. R.; Wang, X.-Y., Scavenger Receptors: Emerging Roles in Cancer Biology and Immunology. Adv. Cancer Res. 2015, 128, 309-364.

295. Platt, N.; Gordon, S., Scavenger receptors: diverse activities and promiscuous binding of polyanionic ligands. Chem. Biol. 1998, 5 (8), 193-203.
296. Krieger, M.; Herz, J., Structures and Functions of Multiligand Lipoprotein Receptors - Macrophage Scavenger Receptors and Ldl Receptor-Related Protein (Lrp). Annu. Rev. Biochem. 1994, 63, 601-637.
297. Pluddemann, A.; Neyen, C.; Gordon, S., Macrophage scavenger receptors and host-derived ligands. Methods 2007, 43 (3), 207-217.
298. Kanno, S.; Furuyama, A.; Hirano, S., A murine scavenger receptor MARCO recognizes polystyrene nanoparticles. Toxicol. Sci. 2007, 97 (2), 398-406.
299. Orr, G. A.; Chrisler, W. B.; Cassens, K. J.; Tan, R.; Tarasevich, B. J.; Markillie, L. M.; Zangar, R. C.; Thrall, B. D., Cellular recognition and trafficking of amorphous silica nanoparticles by macrophage scavenger receptor A. Nanotoxicology 2011, 5 (3), 296-311.
300. Patel, P. C.; Giljohann, D. A.; Daniel, W. L.; Zheng, D.; Prigodich, A. E.; Mirkin, C. A., Scavenger receptors mediate cellular uptake of polyvalent oligonucleotide-functionalized gold nanoparticles. Bioconjug. Chem. 2010, 21 (12), 2250-2256.
301. Singh, R. P.; Ramarao, P., Cellular uptake, intracellular trafficking and cytotoxicity of silver nanoparticles. Toxicol. Lett. 2012, 213 (2), 249-259.
302. Wang, H.; Wu, L.; Reinhard, B. M., Scavenger Receptor Mediated Endocytosis of Silver Nanoparticles into J774A.1 Macrophages Is Heterogeneous. ACS Nano 2012, 6 (8), 7122-7132.
303. Anachi, R. B.; Siegel, D. L.; Baum, J.; Brodsky, B., Acid Destabilization of a Triple-Helical Peptide Model of the Macrophage Scavenger Receptor. FEBS Lett. 1995, 368 (3), 551-555.
304. Tang, T.; Tu, C.; Chow, S. Y.; Leung, K. H.; Du, S.; Louie, A. Y., Quantitative assessment of binding affinities for nanoparticles targeted to vulnerable plaque. Bioconjug. Chem. 2015, 26 (6), 1086-1094.
305. Hsu, H.-Y.; Hajjar, D. P.; Khan, K. F.; Falcone, D. J., Ligand binding to macrophage scavenger receptor-A induces urokinase-type plasminogen activator expression by a protein kinase-dependent signaling pathway. J. Biol. Chem. 1998, 273 (2), 1240-1246.
306. Jin, J.-O.; Park, H.-Y.; Xu, Q.; Park, J.-I.; Zvyagintseva, T.; Stonik, V. A.; Kwak, J.-Y., Ligand of scavenger receptor class A indirectly induces maturation of human blood dendritic cells via production of tumor necrosis factor-α. Blood 2009, 113 (23), 5839-5847.
307. Berteau, O.; Mulloy, B., Sulfated fucans, fresh perspectives: structures, functions, and biological properties of sulfated fucans and an overview of enzymes active toward this class of polysaccharide. Glycobiology 2003, 13 (6), 29-40.
308. Peng, A.; Pisal, D. S.; Doty, A.; Balu-Iyer, S. V., Phosphatidylinositol induces fluid phase formation and packing defects in phosphatidylcholine model membranes. Chem. Phys. Lipids 2012, 165 (1), 15-22.
309. Heimburg, T., A model for the lipid pretransition: coupling of ripple formation with the chain-melting transition. Biophys. J. 2000, 78 (3), 1154-1165.
310. Nagle, J. F.; Tristram-Nagle, S., Structure of lipid bilayers. Biochim. Biophys. Acta - Reviews on Biomembranes 2000, 1469 (3), 159-195.
311. Mittal, N. K.; Mandal, B.; Balabathula, P.; Setua, S.; Janagam, D. R.; Lothstein, L.; Thoma, L. A.; Wood, G. C., Formulation, Development, and In Vitro Evaluation of a CD22 Targeted Liposomal System Containing a Non-Cardiotoxic Anthracycline for B Cell Malignancies. Pharmaceutics 2018, 10 (2).
312. Riske, K. A.; Barroso, R. P.; Vequi-Suplicy, C. C.; Germano, R.; Henriques, V. B.; Lamy, M. T., Lipid bilayer pre-transition as the beginning of the melting process. Biochim. Biophys. Acta 2009, 1788 (5), 954-963.
313. Wu, Y.; Stefl, M.; Olzynska, A.; Hof, M.; Yahioglu, G.; Yip, P.; Casey, D. R.; Ces, O.; Humpolickova, J.; Kuimova, M. K., Molecular rheometry: direct determination of viscosity in Lo and Ld lipid phases via fluorescence lifetime imaging. Phys. Chem. Chem. Phys. 2013, 15 (36), 14986-14893.
314. Nojima, Y.; Iwata, K., Viscosity heterogeneity inside lipid bilayers of single-component phosphatidylcholine liposomes observed with picosecond time-resolved fluorescence spectroscopy. J. Phys. Chem. B 2014, 118 (29), 8631-8641.
315. Christensen, M. S.; Hargens, C. W.; Nacht, S.; Gans, E. H., Viscoelastic Properties of Intact Human Skin: Intrumentation, Hydration Effects, and the Contribution of the Stratum Corneum. J. Invest. Dermatol. 1977, 69 (3), 282-286.
316. Swindells, J. F.; Synder, C. F.; Hardy, R. C.; Golden, P. E., Viscosities of Sucrose Solutions at Varoius Temperatures: Tables of Recalculated Values. Nat. Bur. Stand. Circular No. 440, suppl., U.S. Government Printing Office: Washington, 1958.
317. Murray, R. A.; Escobar, A.; Bastús, N. G.; Andreozzi, P.; Puntes, V.; Moya, S. E., Fluorescently labelled nanomaterials in nanosafety research: Practical advice to avoid artefacts and trace unbound dye. NanoImpact 2018, 9, 102-113.
318. Sokolova, V.; Epple, M., Synthetic pathways to make nanoparticles fluorescent. Nanoscale 2011, 3 (5), 1957-1962.
319. Behzadi, S.; Serpooshan, V.; Tao, W.; Hamaly, M. A.; Alkawareek, M. Y.; Dreaden, E. C.; Brown, D.; Alkilany, A. M.; Farokhzad, O. C.; Mahmoudi, M., Cellular uptake of nanoparticles: journey inside the cell. Chem. Soc. Rev. 2017, 46 (14), 4218-4244.
320. Cutrona, M. B.; Simpson, J. C., A High-Throughput Automated Confocal Microscopy Platform for Quantitative Phenotyping of Nanoparticle Uptake and Transport in Spheroids. Small 2019, 15 (37), e1902033.
321. Abdel-Hafez, S. M.; Hathout, R. M.; Sammour, O. A., Tracking the transdermal penetration pathways of optimized curcumin-loaded chitosan nanoparticles via confocal laser scanning microscopy. Int. J. Biol. Macromol. 2018, 108, 753-764.
322. Lin, C.-Y.; Liu, C.-H.; Tseng, W.-L., Fluorescein isothiocyanate-capped gold nanoparticles for fluorescent detection of reactive oxygen species based on thiol oxidation and their application for sensing glucose in serum. Anal. Methods 2010, 2 (11).
323. Jacob, D.; Joan Taylor, M.; Tomlins, P.; Sahota, T. S., Synthesis and Identification of FITC-Insulin Conjugates Produced Using Human Insulin and Insulin Analogues for Biomedical Applications. J. Fluoresc. 2016, 26 (2), 617-629.
324. Möller, M.; Alexiev, U., Surface charge changes upon formation of the signaling state in visual rhodopsin. Photochem. Photobiol. 2009, 85 (2), 501-508.
325. Alexiev, U.; Scherrer, P.; Marti, T.; Khorana, H. G.; Heyn, M. P., Time-resolved surface charge change on the cytoplasmic side of bacteriorhodopsin. FEBS Lett. 1995, 373 (1), 81-84.
326. Fonin, A. V.; Sulatskaya, A. I.; Kuznetsova, I. M.; Turoverov, K. K., Fluorescence of dyes in solutions with high absorbance. Inner filter effect correction. PLoS One 2014, 9 (7), e103878.
327. Cao, J.; Fan, J.; Sun, W.; Guo, Y.; Wu, H.; Peng, X., The photoprocess effects of an amino group located at different positions along the polymethine chain in indodicarbocyanine dyes. RSC Adv. 2017, 7 (49), 30740-30746.
328. Seidel, C. A. M.; Schulz, A.; Sauer, M. H. M., Nucleobase-Specific Quenching of Fluorescent Dyes. 1. Nucleobase One-Electron Redox Potentials and Their Correlation with Static and Dynamic Quenching Efficiencies. J. Phys. Chem. B 1996, 100 (13), 5541-5553.

329. Choi, C. H.; Hao, L.; Narayan, S. P.; Auyeung, E.; Mirkin, C. A., Mechanism for the endocytosis of spherical nucleic acid nanoparticle conjugates. Proc. Natl. Acad. Sci. U. S. A. 2013, 110 (19), 7625-7630.
330. Amiel, E.; Nicholson-Dykstra, S.; Walters, J. J.; Higgs, H.; Berwin, B., Scavenger receptor-A functions in phagocytosis of E. coli by bone marrow dendritic cells. Exp. Cell Res. 2007, 313 (7), 1438-1448.
331. Zhu, X. D.; Zhuang, Y.; Ben, J. J.; Qian, L. L.; Huang, H. P.; Bai, H.; Sha, J. H.; He, Z. G.; Chen, Q., Caveolae-dependent endocytosis is required for class A macrophage scavenger receptor-mediated apoptosis in macrophages. J. Biol. Chem. 2011, 286 (10), 8231-8239.
332. Sahay, G.; Alakhova, D. Y.; Kabanov, A. V., Endocytosis of nanomedicines. J. Control. Release 2010, 145 (3), 182-195.
333. Parton, R. G.; del Pozo, M. A., Caveolae as plasma membrane sensors, protectors and organizers. Nat. Rev. Mol. Cell. Bio. 2013, 14 (2), 98-112.
334. Zidovetzki, R.; Levitan, I., Use of cyclodextrins to manipulate plasma membrane cholesterol content: evidence, misconceptions and control strategies. Biochim. Biophys. Acta 2007, 1768 (6), 1311-1324.
335. Aoki, T.; Nomura, R.; Fujimoto, T., Tyrosine phosphorylation of caveolin-1 in the endothelium. Exp. Cell Res. 1999, 253 (2), 629-636.
336. Araki, N.; Johnson, M. T.; Swanson, J. A., A role for phosphoinositide 3-kinase in the completion of macropinocytosis and phagocytosis by macrophages. J. Cell Biol. 1996, 135 (5), 1249-1260.
337. Stuart, A. D.; Brown, T. D., Entry of feline calicivirus is dependent on clathrin-mediated endocytosis and acidification in endosomes. J. Virol. 2006, 80 (15), 7500-7509.
338. Doherty, G. J.; McMahon, H. T., Mechanisms of Endocytosis. Annu. Rev. Biochem. 2009, 78, 857-902.
339. Paillard, A.; Hindré, F.; Vignes-Colombeix, C.; Benoit, J.-P.; Garcion, E., The importance of endo-lysosomal escape with lipid nanocapsules for drug subcellular bioavailability. Biomaterials 2010, 31 (29), 7542-7554.
340. Price, P. J.; Gregory, E. A., Relationship between in vitro growth promotion and biophysical and biochemical properties of the serum supplement. In Vitro 1982, 18 (6), 576-584.
341. Buntru, A.; Trepte, P.; Klockmeier, K.; Schnoegl, S.; Wanker, E. E., Current Approaches Toward Quantitative Mapping of the Interactome. Front. Genet. 2016, 7, 74.
342. Kubankova, M.; Lopez-Duarte, I.; Bull, J. A.; Vadukul, D. M.; Serpell, L. C.; de Saint Victor, M.; Stride, E.; Kuimova, M. K., Probing supramolecular protein assembly using covalently attached fluorescent molecular rotors. Biomaterials 2017, 139, 195-201.
343. MacLeod, D. T.; Nakatsuji, T.; Yamasaki, K.; Kobzik, L.; Gallo, R. L., HSV-1 exploits the innate immune scavenger receptor MARCO to enhance epithelial adsorption and infection. Nat. Commun. 2013, 4, 963.
344. Zhou, K.; Wang, Y.; Huang, X.; Luby-Phelps, K.; Sumer, B. D.; Gao, J., Tunable, ultrasensitive pH-responsive nanoparticles targeting specific endocytic organelles in living cells. Angew. Chem. Int. Ed. Engl. 2011, 50 (27), 6109-6114.
345. Pelkmans, L.; Helenius, A., Endocytosis via caveolae. Traffic 2002, 3 (5), 311-320.
346. Iversen, T.-G.; Skotland, T.; Sandvig, K., Endocytosis and intracellular transport of nanoparticles: Present knowledge and need for future studies. Nano Today 2011, 6 (2), 176-185.
347. Pelkmans, L.; Kartenbeck, J.; Helenius, A., Caveolar endocytosis of simian virus 40 reveals a new two-step vesicular-transport pathway to the ER. Nat. Cell Biol. 2001, 3 (5), 473-483.
348. Pelkmans, L., Secrets of caveolae- and lipid raft-mediated endocytosis revealed by mammalian viruses. Biochim. Biophys. Acta 2005, 1746 (3), 295-304.
349. Menshykau, D., Emerging technologies for prediction of drug candidate efficacy in the preclinical pipeline. Drug Discov. Today 2017, 22 (11), 1598-1603.
350. Jäger, E.; Hocherl, A.; Janouskova, O.; Jager, A.; Hruby, M.; Konefal, R.; Netopilik, M.; Panek, J.; Slouf, M.; Ulbrich, K.; Stepanek, P., Fluorescent boronate-based polymer nanoparticles with reactive oxygen species (ROS)-triggered cargo release for drug-delivery applications. Nanoscale 2016, 8 (13), 6958-6963.
351. Witting, M.; Boreham, A.; Brodwolf, R.; Vavrova, K.; Alexiev, U.; Friess, W.; Hedtrich, S., Interactions of hyaluronic Acid with the skin and implications for the dermal delivery of biomacromolecules. Mol. Pharm. 2015, 12 (5), 1391-1401.
352. Döge, N.; Hadam, S.; Volz, P.; Wolf, A.; Schönborn, K. H.; Blume-Peytavi, U.; Alexiev, U.; Vogt, A., Identification of polystyrene nanoparticle penetration across intact skin barrier as rare event at sites of focal particle aggregations. J. Biophotonics 2018, 11 (4), e201700169.
353. Volz, P.; Boreham, A.; Wolf, A.; Kim, T. Y.; Balke, J.; Frombach, J.; Hadam, S.; Afraz, Z.; Rancan, F.; Blume-Peytavi, U.; Vogt, A.; Alexiev, U., Application of single molecule fluorescence microscopy to characterize the penetration of a large amphiphilic molecule in the stratum corneum of human skin. Int. J. Mol. Sci. 2015, 16 (4), 6960-6977.
354. Vogt, A.; Hadam, S.; Deckert, I.; Schmidt, J.; Stroux, A.; Afraz, Z.; Rancan, F.; Lademann, J.; Combadiere, B.; Blume-Peytavi, U., Hair follicle targeting, penetration enhancement and Langerhans cell activation make cyanoacrylate skin surface stripping a promising delivery technique for transcutaneous immunization with large molecules and particle-based vaccines. Exp. Dermatol. 2015, 24 (1), 73-75.
355. Kubo, A.; Nagao, K.; Yokouchi, M.; Sasaki, H.; Amagai, M., External antigen uptake by Langerhans cells with reorganization of epidermal tight junction barriers. J. Exp. Med. 2009, 206 (13), 2937-2946.
356. Coester, C.; Nayyar, P.; Samuel, J., In vitro uptake of gelatin nanoparticles by murine dendritic cells and their intracellular localisation. Eur. J. Pharm. Biopharm. 2006, 62 (3), 306-314.
357. Ribeiro-Viana, R.; Garcia-Vallejo, J. J.; Collado, D.; Perez-Inestrosa, E.; Bloem, K.; van Kooyk, Y.; Rojo, J., BODIPY-labeled DC-SIGN-targeting glycodendrons efficiently internalize and route to lysosomes in human dendritic cells. Biomacromolecules 2012, 13 (10), 3209-3219.
358. Seydoux, E.; Rothen-Rutishauser, B.; Nita, I. M.; Balog, S.; Gazdhar, A.; Stumbles, P. A.; Petri-Fink, A.; Blank, F.; von Garnier, C., Size-dependent accumulation of particles in lysosomes modulates dendritic cell function through impaired antigen degradation. Int. J. Nanomedicine 2014, 9, 3885-3902.
359. Vaigot, P.; Czernielewski, J.; Prunieras, M., Detection of Distinct Subpopulations of Langerhans Cells by Flow-Cytometry and Sorting. Cytometry 1985, 6 (5), 422-427.
360. Merad, M.; Ginhoux, F.; Collin, M., Origin, homeostasis and function of Langerhans cells and other langerin-expressing dendritic cells. Nat. Rev. Immunol. 2008, 8 (12), 935-947.
361. Yu, R. C.; Abrams, D. C.; Alaibac, M.; Chu, A. C., Morphological and Quantitative-Analyses of Normal Epidermal Langerhans Cells Using Confocal Scanning Laser Microscopy. Brit. J. Dermatol. 1994, 131 (6), 843-848.

362. Hansen, S.; Lehr, C. M., Nanoparticles for transcutaneous vaccination. Microb. Biotechnol. 2012, 5 (2), 156-167.
363. Kolonics, A.; Csiszovszki, Z.; Toke, E. R.; Lorincz, O.; Haluszka, D.; Szipocs, R., In vivo study of targeted nanomedicine delivery into Langerhans cells by multiphoton laser scanning microscopy. Exp. Dermatol. 2014, 23 (8), 596-605.
364. Silva, J. M.; Videira, M.; Gaspar, R.; Preat, V.; Florindo, H. F., Immune system targeting by biodegradable nanoparticles for cancer vaccines. J. Control. Release 2013, 168 (2), 179-199.
365. Yamada, N.; Katz, S. I., Generation of mature dendritic cells from a CD14(+) cell line (XS52) by IL-4, TNF-alpha, IL-1 beta, and agonistic anti-CD40 monoclonal antibody. J. Immunol. 1999, 163 (10), 5331-5337.
366. Medina, D. L.; Fraldi, A.; Bouche, V.; Annunziata, F.; Mansueto, G.; Spampanato, C.; Puri, C.; Pignata, A.; Martina, J. A.; Sardiello, M.; Palmieri, M.; Polishchuk, R.; Puertollano, R.; Ballabio, A., Transcriptional activation of lysosomal exocytosis promotes cellular clearance. Dev. Cell 2011, 21 (3), 421-430.
367. Machado, E.; White-Gilbertson, S.; van de Vlekkert, D.; Janke, L.; Moshiach, S.; Campos, Y.; Finkelstein, D.; Gomero, E.; Mosca, R.; Qiu, X. H.; Morton, C. L.; Annunziata, I.; d'Azzo, A., Regulated lysosomal exocytosis mediates cancer progression. Sci. Adv. 2015, 1 (11), e1500603.
368. Sakhtianchi, R.; Minchin, R. F.; Lee, K. B.; Alkilany, A. M.; Serpooshan, V.; Mahmoudi, M., Exocytosis of nanoparticles from cells: role in cellular retention and toxicity. Adv. Colloid. Interface Sci. 2013, 201-202, 18-29.
369. Settembre, C.; Fraldi, A.; Medina, D. L.; Ballabio, A., Signals from the lysosome: a control centre for cellular clearance and energy metabolism. Nat. Rev. Mol. Cell Biol. 2013, 14 (5), 283-296.
370. Fröhlich, E., Cellular elimination of nanoparticles. Environ. Toxicol. Phar. 2016, 46, 90-94.
371. Yanes, R. E.; Tarn, D.; Hwang, A. A.; Ferris, D. P.; Sherman, S. P.; Thomas, C. R.; Lu, J.; Pyle, A. D.; Zink, J. I.; Tamanoi, F., Involvement of lysosomal exocytosis in the excretion of mesoporous silica nanoparticles and enhancement of the drug delivery effect by exocytosis inhibition. Small 2013, 9 (5), 697-704.
372. Sundler, R., Lysosomal and cytosolic pH as regulators of exocytosis in mouse macrophages. Acta Physiol. Scand. 1997, 161 (4), 553-556.
373. Roediger, B.; Ng, L. G.; Smith, A. L.; Fazekas de St Groth, B.; Weninger, W., Visualizing dendritic cell migration within the skin. Histochem. Cell Biol. 2008, 130 (6), 1131-1146.
374. Lämmermann, T.; Bader, B. L.; Monkley, S. J.; Worbs, T.; Wedlich-Soldner, R.; Hirsch, K.; Keller, M.; Forster, R.; Critchley, D. R.; Fassler, R.; Sixt, M., Rapid leukocyte migration by integrin-independent flowing and squeezing. Nature 2008, 453 (7191), 51-55.
375. Test No. 428: Skin absorption: in vitro method. In OECD Guidelines for the Testing of Chemicals, Section 4: Health Effects , Available from: http://dx.doi.org/10.1787/9789264071087-en 2004. (accessed 17.07.2017)
376. Test No. 439: In vitro skin irritation. In OECD Guidelines for the testing of chemicals, section 4: Health effects, Available from: http://dx.doi.org/10.1787/9789264242845-en 2015. (accessed 17.07.2017)
377. Schäfer-Korting, M.; Bock, U.; Diembeck, W.; Dusing, H. J.; Gamer, A.; Haltner-Ukomadu, E.; Hoffmann, C.; Kaca, M.; Kamp, H.; Kersen, S.; Kietzmann, M.; Korting, H. C.; Krächter, H. U.; Lehr, C. M.; Liebsch, M.; Mehling, A.; Müller-Goymann, C.; Netzlaff, F.; Niedorf, F.; Rübbelke, M. K.; Schäfer, U.; Schmidt, E.; Schreiber, S.; Spielmann, H.; Vuia, A.; Weimer, M., The use of reconstructed human epidermis for skin absorption testing: Results of the validation study. Altern. Lab. Anim. 2008, 36 (2), 161-187.
378. Bätz, F. M.; Klipper, W.; Korting, H. C.; Henkler, F.; Landsiedel, R.; Luch, A.; von Fritschen, U.; Weindl, G.; Schäfer-Korting, M., Esterase activity in excised and reconstructed human skin--biotransformation of prednicarbate and the model dye fluorescein diacetate. Eur. J. Pharm. Biopharm. 2013, 84 (2), 374-385.
379. Berroth, A.; Kuhnl, J.; Kurschat, N.; Schwarz, A.; Stab, F.; Schwarz, T.; Wenck, H.; Folster-Holst, R.; Neufang, G., Role of fibroblasts in the pathogenesis of atopic dermatitis. J. Allergy Clin. Immun. 2013, 131 (6), 1547-1554.
380. Hönzke, S.; Gerecke, C.; Elpelt, A.; Zhang, N.; Unbehauen, M.; Kral, V.; Fleige, E.; Paulus, F.; Haag, R.; Schafer-Korting, M.; Kleuser, B.; Hedtrich, S., Tailored dendritic core-multishell nanocarriers for efficient dermal drug delivery: A systematic top-down approach from synthesis to preclinical testing. J. Control. Release 2016, 242, 50-63.
381. Kirschner, N.; Brandner, J. M., Barriers and more: functions of tight junction proteins in the skin. Ann. N. Y. Acad. Sci. 2012, 1257, 158-166.
382. Brandner, J. M.; Kief, S.; Grund, C.; Rendl, M.; Houdek, P.; Kuhn, C.; Tschachler, E.; Franke, W. W.; Moll, I., Organization and formation of the tight junction system in human epidermis and cultured keratinocytes. Eur. J. Cell Biol. 2002, 81 (5), 253-263.
383. Roberts, M. S.; Mohammed, Y.; Pastore, M. N.; Namjoshi, S.; Yousef, S.; Alinaghi, A.; Haridass, I. N.; Abd, E.; Leite-Silva, V. R.; Benson, H.; Grice, J. E., Topical and cutaneous delivery using nanosystems. J. Control. Release 2017, 247, 86-105.
384. Czekalla, C.; Schönborn, K. H.; Döge, N.; Jung, S.; Darvin, M. E.; Lademann, J.; Meinke, M. C., Body regions have an impact on the collagen/elastin index of the skin measured by non-invasive in vivo vertical two photon microscopy. Exp. Dermatol. 2017, doi: 10.1111/exd.13283.
385. Jeong, S.; Hermsmeier, M.; Osseiran, S.; Yamamoto, A.; Nagavarapu, U.; Chan, K. F.; Evans, C. L., Visualization of drug distribution of a topical minocycline gel in human facial skin. Biomed. Opt. Express 2018, 9 (7), 3434-3448.
386. Rachow, S.; Zorn-Kruppa, M.; Ohnemus, U.; Kirschner, N.; Vidal-y-Sy, S.; von den Driesch, P.; Bornchen, C.; Eberle, J.; Mildner, M.; Vettorazzi, E.; Rosenthal, R.; Moll, I.; Brandner, J. M., Occludin is involved in adhesion, apoptosis, differentiation and Ca2+-homeostasis of human keratinocytes: implications for tumorigenesis. PLoS One 2013, 8 (2), e55116.
387. Schwarzl, R.; Du, F.; Haag, R.; Netz, R. R., General method for the quantification of drug loading and release kinetics of nanocarriers. Eur. J. Pharm. Biopharm. 2017, 116, 131-137.
388. Schäfer-Korting, M.; Bock, U.; Gamer, A.; Haberland, A.; Haltner-Ukomadu, E.; Kaca, M.; Kamp, H.; Kietzmann, M.; Korting, H. C.; Krächter, H.-U.; Lehr, C.-M.; Liebsch, M.; Mehling, A.; Netzlaff, F.; Niedorf, F.; Rübbelke, M. K.; Schäfer, U.; Schmidt, E.; Schreiber, S.; Schröder, K.-R.; Spielmann, H.; Vuia, A., Reconstructed Human Epidermis for Skin Absorption Testing: Results of the German Prevalidation Study. Altern. Lab. Anim. 2006, 34 (3), 283-294.
389. Alsheddi, L.; Ananthapadmanabhan, K.; Li, S. K., Influence of skin furrows on tape stripping in characterizing the depth of skin penetration. Int. J. Pharm. 2020, 576, 118903.
390. Elias, P. M.; Ghadially, R., The Aged Epidermal Permeability Barrier: Basis for Functional Abnormalities. Clin. Geriatr. Med. 2002, 18 (1), 103-120.

391. Patzelt, A.; Richter, H.; Buettemeyer, R.; Huber, H. J. R.; Blume-Peytavi, U.; Sterry, W.; Lademann, J., Differential stripping demonstrates a significant reduction of the hair follicle reservoir in vitro compared to in vivo. Eur. J. Pharm. Biopharm. 2008, 70 (1), 234-238.
392. Suk, J. S.; Xu, Q.; Kim, N.; Hanes, J.; Ensign, L. M., PEGylation as a strategy for improving nanoparticle-based drug and gene delivery. Adv. Drug Deliv. Rev. 2016, 99, 28-51.
393. Rancan, F.; Asadian-Birjand, M.; Dogan, S.; Graf, C.; Cuellar, L.; Lommatzsch, S.; Blume-Peytavi, U.; Calderón, M.; Vogt, A., Effects of thermoresponsivity and softness on skin penetration and cellular uptake of polyglycerol-based nanogels. J. Control. Release 2016, 228, 159-169.
394. Morilla, M. J.; Romero, E. L., Carrier Deformability in Drug Delivery. Curr. Pharm. Des. 2016, 22 (9), 1118-1134.
395. Cevc, G.; Vierl, U., Nanotechnology and the transdermal route: A state of the art review and critical appraisal. J. Control. Release 2010, 141 (3), 277-299.
396. Romero, E. L.; Morilla, M. J., Ultradeformable phospholipid vesicles as a drug delivery system: a review. Res. Rep. Transderm. Drug Deliv. 2015, 4.
397. Giulbudagian, M.; Rancan, F.; Klossek, A.; Yamamoto, K.; Jurisch, J.; Neto, V. C.; Schrade, P.; Bachmann, S.; Rühl, E.; Blume-Peytavi, U.; Vogt, A.; Calderón, M., Correlation between the chemical composition of thermoresponsive nanogels and their interaction with the skin barrier. J. Control. Release 2016, 243, 323-332.
398. Ji, H.; Li, X. K., Oxidative Stress in Atopic Dermatitis. Oxid. Med. Cell Longev. 2016, 2016, 2721469.
399. Khmaladze, I.; Nandakumar, K. S.; Holmdahl, R., Reactive Oxygen Species in Psoriasis and Psoriasis Arthritis: Relevance to Human Disease. Int. Arch. Allergy Immunol. 2015, 166 (2), 135-149.
400. Yanagisawa, R.; Takano, H.; Inoue, K.; Koike, E.; Kamachi, T.; Sadakane, K.; Ichinose, T., Titanium dioxide nanoparticles aggravate atopic dermatitis-like skin lesions in NC/Nga mice. Exp. Biol. Med. (Maywood) 2009, 234 (3), 314-322.
401. Fischer, H. C.; Chan, W. C., Nanotoxicity: the growing need for in vivo study. Curr. Opin. Biotechnol. 2007, 18 (6), 565-571.
402. Hanson, K. M.; Clegg, R. M., Observation and quantification of ultraviolet-induced reactive oxygen species in ex vivo human skin. Photochem. Photobiol. 2002, 76 (1), 57-63.
403. Daum, S.; Reshetnikov, M. S. V.; Sisa, M.; Dumych, T.; Lootsik, M. D.; Bilyy, R.; Bila, E.; Janko, C.; Alexiou, C.; Herrmann, M.; Sellner, L.; Mokhir, A., Lysosome-Targeting Amplifiers of Reactive Oxygen Species as Anticancer Prodrugs. Angew. Chem. Int. Ed. Engl. 2017, 56 (49), 15545-15549.
404. Tring, F. C.; Murgatroyd, L. B., Surface Microtopography of Normal Human Skin. Arch. Dermatol. 1974, 109 (2), 223-226.
405. Alam, M.; Ratner, D., Cutaneous squamous-cell carcinoma. N. Engl. J. Med. 2001, 344 (13), 975-983.
406. Askew, D. A.; Mickan, S. M.; Soyer, H. P.; Wilkinson, D., Effectiveness of 5-fluorouracil treatment for actinic keratosis--a systematic review of randomized controlled trials. Int. J. Dermatol. 2009, 48 (5), 453-463.
407. Lebwohl, M.; Swanson, N.; Anderson, L. L.; Melgaard, A.; Xu, Z.; Berman, B., Ingenol mebutate gel for actinic keratosis. N. Engl. J. Med. 2012, 366 (11), 1010-1019.
408. Wennberg, A. M.; Larkö, O.; Lönnroth, P.; Larson, G.; Krogstad, A. L., Delta-aminolevulinic acid in superficial basal cell carcinomas and normal skin-a microdialysis and perfusion study. Clin. Exp. Dermatol. 2000, 25 (4), 317-322.
409. Kuzmina, N.; Talme, T.; Lapins, J.; Emtestam, L., Non-invasive preoperative assessment of basal cell carcinoma of nodular and superficial types. Skin Res. Technol. 2005, 11 (3), 196-200.
410. González Ochoa, A.; ortega Herrera, E., [Percutaneous absorption of 5-fluorouracil]. Int. J. Dermatol. 1971, 10 (2), 139-144.
411. Schneider, M.; Stracke, F.; Hansen, S.; Schaefer, U. F., Nanoparticles and their interactions with the dermal barrier. Dermatoendocrinol. 2009, 1 (4), 197-206.
412. Langhans, S. A., Three-Dimensional in Vitro Cell Culture Models in Drug Discovery and Drug Repositioning. Front. Pharmacol. 2018, 9, 6.
413. Rimann, M.; Graf-Hausner, U., Synthetic 3D multicellular systems for drug development. Curr. Opin. Biotechnol. 2012, 23 (5), 803-9.
414. Montanez-Sauri, S. I.; Beebe, D. J.; Sung, K. E., Microscale screening systems for 3D cellular microenvironments: platforms, advances, and challenges. Cell Mol. Life Sci. 2015, 72 (2), 237-249.
415. Ryan, S. L.; Baird, A. M.; Vaz, G.; Urquhart, A. J.; Senge, M.; Richard, D. J.; O'Byrne, K. J.; Davies, A. M., Drug Discovery Approaches Utilizing Three-Dimensional Cell Culture. Assay Drug. Dev. Technol. 2016, 14 (1), 19-28.
416. Barton, V.; Armeson, K.; Hampras, S.; Ferris, L. K.; Visvanathan, K.; Rollison, D.; Alberg, A. J., Nonmelanoma skin cancer and risk of all-cause and cancer-related mortality: a systematic review. Arch. Dermatol. Res. 2017, 309 (4), 243-251.
417. Schmitt, J. V.; Miot, H. A., Actinic keratosis: a clinical and epidemiological revision. An. Bras. Dermatol. 2012, 87 (3), 425-434.
418. Braun-Falco, O.; Plewig, G.; Wolff, H., Dermatologie undVenerologie. Springer: 1996.
419. Suarasan, S.; Craciun, A. M.; Licarete, E.; Focsan, M.; Magyari, K.; Astilean, S., Intracellular Dynamic Disentangling of Doxorubicin Release from Luminescent Nanogold Carriers by Fluorescence Lifetime Imaging Microscopy (FLIM) under Two-Photon Excitation. ACS Appl. Mater. Interfaces 2019, 11 (8), 7812-7822.
420. Levitt, J. A.; Chung, P. H.; Kuimova, M. K.; Yahioglu, G.; Wang, Y.; Qu, J.; Suhling, K., Fluorescence anisotropy of molecular rotors. Chemphyschem 2011, 12 (3), 662-672.
421. Malmberg, C. G.; Maryott, A. A., Dielecttric Constants of Aqueous Solutions of Dextrose and Sucrose. J. Res. Natl. Bur. Stand. 1950, 45 (4), 299-303.

Acknowledgements

First and foremost, I would like to thank my supervisor Prof. Dr. Ulrike Alexiev for giving me the opportunity to pursue a Ph.D. and to conduct the research that led to this thesis in her lab. I am grateful not only for getting to know and applying a wide range of experimental techniques, but also for deepening my ability to think scientifically. Her lab's many collaborations offered me the chance to gain an insight into a multitude of different scientific fields – joint forces my work greatly benefited from.

I would also like to thank Prof. Dr. Karsten Heyne for agreeing to be my second adviser and for discussing my results with me and his group.

Furthermore, I would like to thank the aforementioned cooperation partners I was given the opportunity to collaborate with on different research projects: Prof. Dr. Monika Schäfer-Korting and her lab, namely Dr. Christian Zoschke, Dr. Lilian Löwenau, Dr. Priscila Schilrreff and Christopher Wolff, Leonie Gronbach, Prof. Dr. Rainer Haag and his lab, especially Dr. Michael Unbehauen and Dr. Nadine Rades, Prof. Dr. Annika Vogt and her group, especially Dr. Janna Frombach, Prof. Dr. Burkhard Kleuser and his group, namely Dr. Alexander Edlich, Prof. Dr. Achim Gruber and his lab, especially Dr. Hannah Pischon and Moritz Radbruch. Prof. Dr. Nikolaus P. Ernsting and his group, especially Dr. Celin Richter. Each and every one of them contributed to my progress significantly, either with knowledge and advice, by letting me join in the valuable group discussions or by preparing and proving biological samples, probes, or nanomaterials in long lab and office hours.

I would like to extend my thanks to Prof. Dr. Roland Netz and Prof. Dr. Robert Bittl for lending an ear to me when I needed one.

Moreover, I would like to acknowledge the funding I received from the collaborative research centers 1078 and 1112 of the Deutsche Forschungsgemeinschaft.

Special thanks goes to my coworkers from the group. Apart from their intellectual input and assistance, which cannot be overstated, I would like to thank them on a more personal note: Dr. des. Alexander Wolf for his reassurance, Jens Balke for his unceasing willingness to help, Juliane Wonneberg for her reliability and Robert Brodwolf for his alternative take on the world. Johannes Stellmacher's morale has often lightened my spirits and Katja Ober has been a pillar of strength to all of us. I would like to thank Maryam Sadeghi, Victor Cruz, Constantin Schneider and Dr. Alexander Boreham for being there for me.

Finally, I would like to thank my family and friends for providing a compass when I was going astray. Sometimes, they even lovingly pulled my sleeve.

List of acronyms

Abbreviation	Meaning
2D	Two-dimensional
2PA	Two Photon Absorption
3D	One-dimensional
AD	Atopic Dermatitis
AF	Autofluorescence
AO	Atomic Orbitals
AOTF	Acousto-optical Tunable Filter
APC	Allophycocyanine
APD	Avalanche Photo Diodes
ATP	Adenosine Triphosphate
BCECF	2′,7′-Bis(CarboxyEthyl)-5′(or 6′)-Carboxy-Fluorescein
BP	Binding Partner or Band-pass filter
BS	Beam Splitter
BSA	Bovine Serum Albumin
CD1a	Cluster of Differentiation 1a (Protein)
CFDA	5(or 6)-Carboxy-Fluorescein Diacetate
CMS	Core Multi-shell
CMS-ICC	Core Multi-shell Nanocarrier - Indocarbocyanine Conjugate
CMS-ICC/bodipy	CMS-ICC with loaded bodipy
CS	Core-shell
CTB	Cholera Toxin B
DAPI	4′,6-diamidino-2-phenylindole
DCF	Dichlorodihydrofluorescein
DFR	Double Fresnel Rhomb
DL	Dispersing Lens
DLS	Dynamic Light Scattering
DMPC	Dimyristoylphosphatidylcholine
DMSO	Dimethyl Sulfoxide
dPG	Dendritic Polyglycerol
dPGS	Dendritic Polyglycerol Sulfate
DPPC	Dipalmitoylphosphatidylcholine
DPSSL	Diode Pumped Solid State Laser
dsDNA	Double-stranded Deoxyribonucleic Acid
DTT	Dithiothreitol
EDTA	Ethylenediaminetetraacetic Acid
EPR	Enhanced Permeability and Retention
EtOH	Ethanol
FACS	Fluorescence-activated Cell Sorting
FBS	Fetal Bovine Serum
FDA	Fluorescein Diacetate
FLS	Fluorescence Lifetime Signature
FIFO	First-In-First-Out
FITC	fluorescein Isothiocyanate
FLIM	Fluorescence Lifetime Microscopy
FluNa	Fluorescein Sodium Salt
FLUPS	Fluorescence Up-Conversion Spectroscopy
FMR	Fluorescent Molecular Rotor
FOV	Field of View
FRET	Förster Resonance Energy Transfer
fs	Femtosecond
FWHM	Full Width at Half Maximum
GaAsP	Gallium Arsenide Phosphide
GS	Ground State
GTP	Glan-Thompson Polarizer
GUV	Giant Unilamellar Vesicle
HaCaT	Spontaneously transformed aneuploid immortal keratinocyte cell line
HOMO	Highest Occupied Molecular Orbital
hPG	Hyperbranched Polyglycerol
HSA	Human Serum Albumin
HS	Human Serum
ICC	Indocarbocyanine

Abbreviation	Meaning
IDCC	Indodicarbocyanine
IRF	Instrument Response Function
KGM	Keratinocyte Growth Medium
LACO	Linear Combinations of Atomic Orbitals
LC	Langerhans Cells
LD	Lipid Droplets
LDL	Low-density Lipoprotein
LE	Locally Excited
LP	Long-pass Filter
LUMO	Lowest Unoccupied Molecular Orbital
MCP	Micro-channel plates
MeOH	Methanol
MLV	Multilamellar Vesicles
MO	Molecular Orbital
MOI	Molecule of Interest
mPEG	Monomethyl Polyethylene Glycol
mpFE	Multiphoton Fluorescence Excitation
mpFLIM	Multiphoton FLIM
mpLSM	Multiphoton Laser Scanning Microscopy
MßCD	Methyl-ß-cyclodextrin
MSR	Macrophage Scavenger Receptor
NA	Numerical Aperture
NaCl	Sodium Chloride
NADH	Nicotinamide Adenine Dinucleotides Hybrid
NaOH	Sodium hydroxide
NC	Nanocarrier
ND	Neutral Density
NHDF	Normal Human Dermal Fibroblasts
NHK	Normal Human Keratinocytes
NMSC	Non-melanoma Skin Cancer
NP	Nanoparticle
PA	Photon Absorption
PAc	Propionic Acid
PBS	Phosphate-buffered Saline
PC	Polymethine Carbocyanines
PCF	Photonic Crystal Fiber
PI3K	Phosphoinositide 3-kinase
PMT	Photo Multiplier Tubes
poly C	Polycytidylic Acid
poly I	Polyionosinic Acid
RHC	Refrigerated/Heating Circulator
RHE	Reconstructed Human Epidermis
RhoB	Rhodamine B
RHS	Reconstructed Human Skin
ROI	Region of Interest
ROS	Reactive Oxygen Species
SC	Stratum Corneum
SCC-12	Human Cutaneous Squamous Cell Cancer Cell Line
SCC-25	Human (Oral Tongue) Squamous Cell Carcinoma Cell Line
SD	Standard Deviation
SNARF	Seminapthorhodafluor
SNR	Signal to Noise Ratio
SP	Short-pass Filter
SPC	Single Photon Counting
SR	Scavenger Receptor
SUV	Small Unilamellar Vesicle
SWL	Supercontinuum White Light
TCSPC	Time Correlated Single Photon Counting
Ti:Sa	Titanium:Sapphire
TICT	Twisted Intramolecular Charge Transfer
UV-Vis	Ultraviolet to Visible
VE	Viable Epidermis

Publications and conferences

Publications *(underscores indicate equally contributing authors; * indicate publications relevant to this dissertation)*

2020 R. Brodwolf, **P. Volz-Rakebrand***, J Stellmacher, C. Wolff, M. Unbehauen, R. Haag, M. Schäfer-Korting, C. Zoschke, U. Alexiev. Faster, sharper, more precise: Automated Cluster-FLIM in preclinical testing directly identifies the intracellular fate of theranostics in live cells and tissue. Theranostics, 10(14), 6322-6336, 2020, doi: doi:10.7150/thno.42581

2019 K. Ober, **P. Volz-Rakebrand***, J. Stellmacher, R. Brodwolf, K. Licha, R. Haag, U. Alexiev. Expanding the scope of reporting nanoparticles to sensing of lipid phase transitions and nanoviscosities in living cells. Langmuir, 35, 11422-11434, 2019, doi: 10.1021/acs.langmuir.9b01372

J. Frombach, M. Unbehauen, I.N. Kurniasih, F. Schumacher, **P. Volz***, S. Hadam, F. Rancan, U. Blume-Peytavi, B. Kleuser, R. Haag, U. Alexiev, A. Vogt. Core-multishell nanocarriers enhance drug penetration and reach keratinocytes and antigen-presenting cells in intact human skin. J. Control. Release 299, 138-148, 2019, doi: 10.1016/j.jconrel.2019.02.028

2018 **P. Volz***, R. Brodwolf, C. Zoschke, R. Haag, M. Schäfer-Korting, U. Alexiev. White-Light Supercontinuum Laser-Based Multiple Wavelength Excitation for TCSPC-FLIM of Cutaneous Nanocarrier Uptake. Z. Phys. Chem., 232 (5-6), 671-688, 2018, doi: 10.1515/zpch-2017-1050

J. Balke, **P. Volz***, F. Neumann, R. Brodwolf, A. Wolf, H. Pischon, M. Radbruch, L. Mundhenk, A.D. Gruber, N. Ma, U. Alexiev. Visualizing Oxidative Cellular Stress Induced by Nanoparticles in the Subcytotoxic Range using Fluorescence Lifetime Imaging. Small 14(23), 1800310, 2018, doi: 10.1002/smll.201800310

A. Edlich, **P. Volz***, R. Brodwolf, M. Unbehauen, L. Mundhenk, A. Gruber, S. Hedrich, R. Haag, U. Alexiev, B. Kleuser. Crosstalk between core-multishell nanocarriers for cutaneous drug delivery and antigen-presenting cells of the skin. Biomaterials 162, 60-70, 2018, doi: 10.1016/j.biomaterials.2018.01.058

N. Döge, S. Hadam, **P. Volz**, K.H. Schönborn, U. Blume-Peytavi, U. Alexiev, A. Vogt. Identification of polystyrene nanoparticle penetration across intact skin barrier as rare event at sites of focal particle aggregations. J. Biophotonics 11(4), e201700169, 2018 doi:10.1002/jbio.201700169

2017 H. Pischon, M. Radbruch, A. Ostrowski, **P. Volz***, C. Gerecke, M. Unbehauen, S. Hönzke, S. Hedtrich, J. Fluhr, R. Haag, B. Kleuser, U. Alexiev, A. Gruber, L. Mundhenk. Stratum corneum targeting by dendritic core-multishell-nanocarriers in a mouse model of psoriasis. Nanomedicine 13(1), 317-327, 2017. doi: 10.1016/j.nano.2016.09.004

A. Boreham, **P. Volz**, D. Peters, C. Keck, U. Alexiev. Determination of nanostructures and drug distribution in lipid nanoparticles by single molecule microscopy. Eur. J. Pharm. Biopharm. 110, 31-38, 2017. doi: 10.1016/j.ejpb.2016.10.020

L. Löwenau, C. Zoschk, R. Brodwolf, **P. Volz***, C. Hausmann, S. Wattanapitayakul, A. Boreham, U. Alexiev, M. Schäfer-Korting. Increased permeability of reconstructed human epidermis from UVB-irradiated keratinocytes. Eur. J. Pharm. Biopharm. 116, 149-154, 2017. doi: 10.1016/j.ejpb.2016.12.017

U. Alexiev, **P. Volz***, R. Brodwolf, A. Boreham. Time-resolved fluorescence microscopy (FLIM) as an analytical tool in skin nanomedicine. Eur. J. Pharm. Biopharm. 116, 111-124, 2017. doi: 10.1016/j.ejpb.2017.01.005

M. Radbruch, H. Pischon, A. Ostrowski, **P. Volz***, R. Brodwolf, F. Neumann, M. Unbehauen, B. Kleuser, R. Haag, N. Ma, U. Alexiev, L. Mundhenk, A. Gruber. Dendritic Core-Multishell Nanocarriers in Murine Models of Healthy and Atopic Skin. Nanoscale Res. Lett. 12(1), 64, 2017. doi: 10.1186/s11671-017-1835-0

P. Volz*, P. Schilrreff, R. Brodwolf, C. Wolff, J. Stellmacher, J. Balke, M. Morilla, C. Zoschke, M. Schäfer-Korting, U. Alexiev. Pitfalls in using fluorescence tagging of nanomaterials: tecto-dendrimers in skin tissue as investigated by Cluster-FLIM. Ann. N.Y. Acad. Sci., 1405, 202-214, 2017. DOI: 10.1111/nyas.13473

2016 A. Boreham, J. Pikkemaat, **P. Volz***, R. Brodwolf, C. Kuehne, K. Licha, R. Haag, J. Dernedde, U. Alexiev. Detecting and Quantifying Biomolecular Interactions of a Dendritic Polyglycerol Sulfate Nanoparticle Using Fluorescence Lifetime Measurements. Molecules 21(1), 22, 2016. doi:10.3390/molecules21010022

A. Wolf, C. Schneider, T.-Y. Kim, K. Kirchberg, **P. Volz**, U. Alexiev. A simulation-guided fluorescence correlation spectroscopy tool to investigate to protonation dynamics of cytrochrome c oxidase. Phys. Chem. Chem. Phys. 18, 12877-12885, 2016. doi: 10.1039/c5cp07925j.

P. Volz, N. Krause, J. Balke, C. Schneider, M. Walter, F. Schneider, R. Schlesinger, U. Alexiev. Light and pH-induced changes in structure and accessibility of transmembrane helix B and its immediate environment in Channelrhodopsin-2. J. Biol. Chem. 291(33), 17382-17393, 2016. doi: 10.1074/jbc.M115.711200

N. Zhang, A. Said, C. Wischke, V. Kral, R. Brodwolf, **P. Volz**, A. Boreham, C. Gerecke, W. Li, A. Neffe, B. Kleuser, U. Alexiev, A. Lendlein, M. Schäfer-Korting. Poly[acrylonitrile-co-(N-vinyl pyrrolidone)] nanoparticles -composition-dependent skin penetration enhancement of a dye probe andbiocompatibility. Eur. J. Pharm. Biopharm. 2016. doi: 10.1016/j.ejpb.2016.10.019

G. Zoubari, S. Staufenbiel, **P. Volz**, U. Alexiev, R. Bodmeier. Effect of drug solubility and lipid carrier on drug release from lipid nanoparticles for dermal delivery. Eur. J. Pharm. Biopharm. 110, 39–46. 2016. doi: 10.1016/j.ejpb.2016.10.021

2015 **P. Volz**, A. Boreham, A. Wolf, T.-Y. Kim, J. Balke, J. Frombach, S. Hadam, Z. Afraz, F. Rancan, U. Blume-Peytavi, A. Vogt, U. Alexiev. Application of Single Molecule Fluorescence Microscopy to Characterize the Penetration of a Large Amphiphilic Molecule in the Stratum Conerum of Human Skin. Int. J. Mol. Sci. 16(4), 6960-77. 2015. doi:10.3390/ijms16046960

C. Richter, C. Schneider, M.T. Quick, **P. Volz***, R. Mahrwald, J. Hughes, B. Dick, U. Alexiev, N.P. Ernsting. Dual-fluorescence pH probe for bio-labelling. Phys. Chem. Chem. Phys. 17(45), 30590-30597. 2015. doi: 10.1039/c5cp05454k

Talks and poster presentations at conferences

2018 DGFB – Membrane Section Meeting 2018. Drübeck, Germany. 05.03-07.03.2018

Poster presentation: Cluster-FLIM as a tool to analyze membrane interactions of nanocarriers in vitro and vivo

Biobarriers 2018. Saarbrücken, Germany. 27.08-29.08.2018

Talk & poster presentation: Cluster Fluorescence Lifetime Imaging as a tool to detect oxidative stress and visualize nanocarriers interacting with the skin barrier

2017 15th Conference on Methods and Applications in Fluorescence. Brügge, Belgium. 10.09 - 13.09.2017

Poster presentation I: A tracking free diffusivity and population distribution analysis for localization based single molecule microscopy.

Poster presentation II: Quantitative multiphoton FLIM of living cells and whole tissue samples

2016 60th Annual Meeting of the Biophysical Society. Los Angeles, USA. 27.02-02.03.2015

Poster presentation: Extending the potential of pH-sensitive dyes by new dual-fluorescence SNARF Probes and FLIM.

International Conference on Dermal Drug Delivery by Nanocarriers. Berlin, Germany. 14.03 - 16.03.2016

Poster presentation: Live-Cell imaging using FLIM to reveal the cellular uptake and fate of a core-multishell CMS Nanocarrier

Talk: Application of single molecule fluorescence microscopy to characterize the penetration of a large amphipilic molecule in the Stratum corneum of human skin.

Förster Resonance Energy Transfer in life sciences: FRET 2. Göttingen, Germany. 03.04 - 06.04.2016

Poster presentation: Investigation of a FRET-based theranostic macromolecular prodrug in live-cell experiments using time-resolved fluorescence microscopy

5th Galenus Workshop "The Advanced Use of Nanocarriers in Future Skin Drug Delivery". Berlin, Germany. 16.11 - 18.11.2016

Poster presentation: Single molecule fluorescence microscopy as a tool to characterize the diffusion of a large amphiplilic molecule in the Stratum corneum of human skin and within nanostructured lipid carriers

2015 10th European Biophysics Congress. Dresden, Germany. 18.07 - 22.07.2015

Poster presentation: Single molecule fluorescence microscopy of a large molecule penetrating into the human skin

PicoQuant Single Molecule Workshop. Berlin, Germany. 02.09 - 04.09.2015

Poster presentation: Application of single molecule fluorescence microscopy to characterize the penetration of a large amphipilic molecule in the Stratum corneum of human skin.

2014 XVI. Linz Winterworkshop Advances in Single-Molecule Research for Biology & Nanoscience. Linz, Austria. 31.01 - 03.02.2014

Poster presentation: Total internal reflection fluorescence (TIRF) based single molecule microscopy studies of fluorescent molecules and particles penetrating the human skin.

Appendix

Table A1: Fluorescence decay analysis of ICC in different molecular environments. (Multi-)exponential curve-fitting of ICC's fluorescence decay traces (Figure 4.2.2) to Eq.19 yield the following decay parameters. For assessing a prober number of decay components (n) the analysis was performed for $n = 1 - 3$. Reduced chi squares (χ^2_{red}) show the goodness of the respective fit. Relative amplitudes α_c and fluorescence lifetime components τ_c are displayed as well as calculated relative steady-state fluorescence contributions β_c and population-weighted mean fluorescence lifetimes $\tau_{m,\beta}$ (Eq. 21). Spectral condition as indicated in Figure 4.2.2. Indicated uncertainties are based on confidence interval analyses of each fit parameter (Section 3.4.1).

environment	n	α_1 (%)	α_2 (%)	α_3 (%)	β_1 (%)	β_2 (%)	β_3 (%)	τ_1 (ns)	τ_2 (ns)	τ_3 (ns)	$\tau_{m,\beta}$ (ns)	χ^2_{red}
H_2O	1	100			100			0.16			0.16	1.6
	2	60 (± 11)	40 (± 13)		50 (± 10)	50 (± 10)		0.127 (± 0.008)	0.19 (± 0.01)		0.16 (± 0.03)	0.9
	3	40.5	32.5	27	44.9	55.0	0.1	0.12	0.19	$2x10^{-4}$	0.16	0.9
MeOH	1	100			100			0.22			0.23	2.0
	2	58 (± 4)	42 (± 4)		42 (± 4)	58 (±4)		0.145 (± 0.008)	0.283 (± 0.008)		0.23 (± 0.03)	0.8
	3	54.0	38.4	7.6	41.7	57.3	1.0	0.15	0.28	0.03	0.23	0.8
glycerol	**1**	100			100			2.180 (± 0.003)			2.180 (± 0.003)	1.1
	2	87.8	12.2		88.2	11.8		2.2	2.1		2.2	1.1
	3	83.6	7.3	9.1	84.1	7.1	9.8	2.2	2.1	2.1	2.2	1.1
EtOH	1	100			100			0.22			0.22	13
	2	98.9	1.1		94.6	5.4		0.43	2.3		0.53	2.0
	3	47.01 (± 6.33)	52.43 (± 7.23)	0.56 (0.05)	33 (± 5)	63 (± 5)	3.9 (± 0.6)	0.30 (± 0.02)	0.52 (± 0.02)	3.0 (± 0.1)	0.54 (± 0.04)	1.2
dPGS-ICC	1	100			100			0.40			0.40	18
	2	76.3	23.7		43.2	56.8		0.16	0.68		0.45	1.8
	3	55 (± 2)	38 (± 2)	7 (± 1)	25 (± 2)	50 (± 3)	25 (± 3)	0.133 (± 0.007)	0.39 (± 0.02)	1.01 (± 0.02)	0.48 (± 0.04)	0.9
CMS-ICC	1	100			100			0.71			0.71	36
	2	72.2	27.8		36.9	63.1		0.26	1.1		0.81	2.1
	3	52 (± 1)	35 (± 1)	13 (± 1)	16 (± 1)	43 (± 3)	41 (± 4)	0.140 (± 0.005)	0.56 (± 0.03)	1.39 (± 0.04)	0.83 (± 0.04)	0.9

Table A2: Fluorescence decay analysis of ICC dissolved in glycerol at various temperatures. Mono-exponential curve-fitting of the fluorescence decay traces shown in Figure 4.2.3E to Eq.19 reveals the fluorescence lifetime τ. Spectral condition: λ_{ex} = 488 nm, λ_{em} > 570 nm. Uncertainty of temperature amounts to ± 0.1°C/K. Viscosity values from Ref. 260. Indicated uncertainties are based on confidence interval analyses of each fit parameter (Section 3.4.1).

T (°C)	T (K)	viscosity (cP)	τ (ns)	χ^2_{red}
0	273.15	12100	2.536 ± 0.004	1.0
5	278.15	6647	2.474 ± 0.003	1.0
10	283.15	3817	2.391 ± 0.003	1.1
15	288.15	2281	2.299 ± 0.003	1.0
20	293.15	1412	2.180 ± 0.003	1.3
25	298.15	905.7	2.045 ± 0.003	1.1
30	303.15	597.9	1.895 ± 0.003	1.1
35	308.15	405.8	1.736 ± 0.003	1.0
40	313.15	282.4	1.558 ± 0.002	1.1
45	318.15	201.2	1.372 ± 0.002	1.2
50	323.15	146.5	1.220 ± 0.002	1.3
55	328.15	108.7	1.058 ± 0.002	1.3
60	333.15	82.2	0.931 ± 0.002	1.2
65	338.15	63.2	0.804 ± 0.002	1.1
70	343.15	49.4	0.706 ± 0.002	1.1

Table A3: Fluorescence decay analysis of ICC dissolved in MeOH/glycerol mixtures at 25°C. Bi-exponential curve-fitting of the fluorescence decay traces of Figure 4.2.4A by a global fitting procedure to Eq. 19 with the condition of a shared first decay component. The table summarizes relative amplitudes α_c, fluorescence lifetime components τ_c, and calculated relative steady-state fluorescence populations β_c and population-weighted mean lifetimes $\tau_{m,\beta}$ (Eq. 21). Spectral condition: λ_{ex} = 488 nm, λ_{em} > 570 nm. Values for viscosities (η) and dielectric constants (ε) taken from Ref. 420. Indicated uncertainties are based on confidence interval analyses of each fit parameter (Section 3.4.1). The given digits of α_c and β_c are chosen so that the individual values add up to 100 %. The respective uncertainties are indicated by the same number of digits.

glycerol (% v/v)	η (cP)	ε	α_1 (%)	α_2 (%)	β_1 (%)	β_2 (%)	τ_1 (ns)	τ_2 (ns)	$\tau_{m,\beta}$ (ns)	χ^2_{red}
0	0.6	33.0	64 (± 2)	36 (± 1)	47.3 (± 1.6)	52.7 (± 0.8)	0.147 (± 0.008)	0.291 (± 0.004)	0.223 (± 0.005)	0.8
10	1.8	33.7	52 (± 2)	48 (± 1)	32.8 (± 1.5)	67.2 (± 0.6)	0.147 (± 0.008)	0.327 (± 0.003)	0.268 (± 0.004)	1.2
15	2.8	34.4	49 (±2)	51 (± 1)	28.2 (± 1.4)	71.8 (± 0.6)	0.147 (± 0.008)	0.36 (± 0.003)	0.300 (± 0.004)	0.8
25	6.0	36.1	43.9 (± 1.1)	56.1 (± 0.7)	21.7 (± 1.0)	78.3 (± 0.4)	0.147 (± 0.008)	0.414 (± 0.003)	0.356 (± 0.004)	1.2
35	10	37.1	36.3 (± 1.3)	63.7 (± 0.8)	14.2 (± 0.8)	85.8 (± 0.3)	0.147 (± 0.008)	0.508 (± 0.003)	0.457 (± 0.003)	1.1
45	18	38.1	27.6 (± 1.1)	72.4 (± 0.4)	8.3 (± 0.5)	91.7 (± 0.3)	0.147 (± 0.008)	0.621 (± 0.003)	0.582 (± 0.003)	1.1
55	36	38.6	31.9 (± 1.3)	68.1 (± 0.4)	7.3 (± 0.5)	92.7 (± 0.3)	0.147 (± 0.008)	0.871 (± 0.004)	0.818 (± 0.005)	0.9
60	58	39.3	29.9 (± 1.4)	70.1 (± 0.4)	6.2 (± 0.4)	93.8 (± 0.3)	0.147 (± 0.008)	0.946 (± 0.004)	0.896 (± 0.005)	1.1
65	70	39.7	32.7 (± 1.1)	67.3 (± 0.4)	6.5 (± 0.4)	93.5 (± 0.3)	0.147 (± 0.008)	1.03 (± 0.005)	0.973 (± 0.006)	0.9
70	130	40.1	29.1 (± 1.8)	70.9 (± 0.4)	4.7 (± 0.4)	95.3 (± 0.3)	0.147 (± 0.008)	1.226 (± 0.005)	1.175 (± 0.006)	0.9
75	170	40.4	29.0 (± 2.0)	71.0 (± 0.4)	4.5 (± 0.4)	95.5 (± 0.4)	0.147 (± 0.008)	1.28 (± 0.005)	1.229 (± 0.007)	0.8
80	250	40.8	28.8 (± 1.6)	71.2 (± 0.3)	4.1 (± 0.3)	95.9 (± 0.3)	0.147 (± 0.008)	1.408 (± 0.004)	1.356 (± 0.006)	1.0
85	350	41.1	27.6 (± 1.6)	72.4 (± 0.3)	3.5 (± 0.3)	96.5 (± 0.3)	0.147 (± 0.008)	1.528 (± 0.005)	1.480 (± 0.007)	1.0
90	630	41.4	30.6 (± 1.4)	69.4 (± 0.3)	3.8 (± 0.3)	96.2 (± 0.3)	0.147 (± 0.008)	1.642 (± 0.005)	1.585 (± 0.007)	1.1
95	950	–	28.4 (± 1.4)	71.6 (± 0.3)	3.3 (± 0.2)	96.7 (± 0.3)	0.147 (± 0.008)	1.686 (± 0.004)	1.635 (± 0.006)	1.3

Table A4: Fluorescence decay analysis of ICC dissolved in sucrose/H_2O mixtures at 20°C. Tri-exponential curve-fitting of the fluorescence decay traces of Figure 4.2.4C by a global fitting procedure to Eq. 19 with the condition of a shared first decay component. The table summarizes relative amplitudes α_c, fluorescence lifetime components τ_c, and calculated relative steady-state fluorescence populations β_c and population-weighted mean lifetimes $\tau_{m,\beta}$ (Eq. 21). Spectral condition: λ_{ex} = 488 nm, λ_{em} > 570 nm. Values for viscosities (η) and dielectric constants (ε) taken from Ref. 316 and 421. Indicated uncertainties are based on confidence interval analyses of each fit parameter (Section 3.4.1). The given digits of α_c and β_c are chosen so that the individual values add up to 100 %. The respective uncertainties are indicated by the same number of digits.

sucrose (% w/w)	η (cP)	ε	α_1 (%)	α_2 (%)	α_3 (%)	β_1 (%)	β_2 (%)	β_3 (%)	τ_1 (ns)	τ_2 (ns)	τ_3 (ns)	$\tau_{m,\beta}$ (ns)	χ^2_{red}
0	1.01	80.4	61 (± 2)	39 (± 1)		46 (± 2)	54 (± 1)		0.100 (± 0.007)	0.183 (± 0.002)		0.145 (± 0.004)	1.1
20	1.95	75.5	23 (± 6)	60 (± 4)	17 (± 6)	11 (± 3)	58 (± 3)	31 (± 8)	0.100 (± 0.007)	0.21 (± 0.02)	0.39 (± 0.03)	0.25 (± 0.04)	1.0
40	6.17	69.5	15 (± 1)	67 (± 1)	18 (± 2)	4.0 (± 0.4)	62.1 (± 1.1)	33.9 (± 2.6)	0.100 (± 0.007)	0.350 (± 0.008)	0.71 (± 0.02)	0.46 (± 0.02)	1.1
50	15.4	65.9	12.8 (± 0.8)	63.4 (± 1.3)	23.8 (± 1.5)	2.4 (± 0.2)	55.6 (± 1.1)	42.0 (± 1.7)	0.100 (± 0.007)	0.477 (± 0.008)	0.96 (± 0.02)	0.67 (± 0.02)	1.1
55	28.1	–	12 (± 1)	61 (± 1)	27 (± 2)	1.8 (± 0.2)	52.3 (± 1.3)	45.9 (± 1.9)	0.100 (± 0.007)	0.56 (± 0.01)	1.11 (± 0.02)	0.80 (± 0.03)	1.0
60	58.5	61.8	11 (± 2)	62 (± 3)	27 (± 3)	1.4 (± 0.3)	52.7 (± 2.6)	45.9 (± 3.1)	0.100 (± 0.007)	0.68 (± 0.02)	1.36 (± 0.04)	0.98 (± 0.05)	1.1
63	99.1	–	8.7 (± 0.9)	51.5 (± 1.5)	39.8 (± 1.5)	0.9 (± 0.1)	39.6 (± 1.3)	59.5 (± 1.3)	0.100 (± 0.007)	0.71 (± 0.02)	1.38 (± 0.02)	1.10 (± 0.02)	1.1
67	228	–	9 (± 1)	45 (± 2)	46 (± 3)	0.8 (± 0.1)	34.3 (± 2.0)	64.9 (± 2.0)	0.100 (± 0.007)	0.81 (± 0.03)	1.50 (± 0.02)	1.25 (± 0.04)	1.0
69	370	–	8 (± 1)	43 (± 2)	49 (± 3)	0.7 (± 0.1)	31.7 (± 2.0)	67.6 (± 2.0)	0.100 (± 0.007)	0.84 (± 0.03)	1.57 (± 0.02)	1.33 (± 0.04)	1.1
71	636	–	13.3 (± 0.8)	42.4 (± 3.9)	44.3 (± 3.9)	1.2 (± 0.1)	33.7 (± 3.1)	65.1 (± 3.2)	0.100 (± 0.007)	0.91 (± 0.03)	1.68 (± 0.03)	1.40 (± 0.06)	1.1
73	1170	–	14.0 (± 0.7)	43.0 (± 0.7)	43.0 (± 0.7)	1.2 (± 0.1)	34.9 (± 2.5)	63.9 (± 2.6)	0.100 (± 0.007)	0.93 (± 0.03)	1.70 (± 0.03)	1.41 (± 0.06)	1.2

Table A5: Fluorescence decay analysis of ICC dissolved in EtOH/H_2O mixtures at 20 °C. Multi-exponential curve-fitting of the fluorescence decay traces of Figure 4.2.5D by a global fitting procedure to Eq. 19 with the condition of a shared first decay component. The table summarizes relative amplitudes α_c, fluorescence lifetime components τ_c, and calculated relative steady-state fluorescence populations β_c and population-weighted mean lifetimes $\tau_{m,\beta}$ (Eq. 21). Spectral condition: λ_{ex} = 488 nm, λ_{em} > 570 nm. Dielectric constants (ε) are taken from Ref. 264. Indicated uncertainties are based on confidence interval analyses of each fit parameter (Section 3.4.1). The given digits of α_c and β_c are chosen so that the individual values add up to 100 %. The respective uncertainties are indicated by the same number of digits.

EtOH (% w/w)	ε	α_1 (%)	α_2 (%)	α_3 (%)	β_1 (%)	β_2 (%)	β_3 (%)	τ_1 (ns)	τ_2 (ns)	τ_3 (ns)	$\tau_{m,\beta}$ (ns)	χ^2_{red}
0.0	80.4	55.5 (± 0.2)	44.5 (± 0.1)		45.0 (± 3.8)	55.5 (± 0.7)		0.13 (± 0.02)	0.202 (± 0.002)		0.17 (± 0.01)	1.1
8.0	75.7	27.2 (± 0.2)	72.8 (± 0.2)		16.3 (± 2.1)	83.5 (± 0.5)		0.13 (± 0.02)	0.250 (± 0.002)		0.230 (± 0.005)	1.0
16.2	71.7	22.2 (± 0.4)	77.8 (± 0.4)		11.3 (± 1.6)	88.7 (± 0.4)		0.13 (± 0.02)	0.290 (± 0.002)		0.272 (± 0.04)	1.1
24.6	66.2	15.1 (± 0.7)	84.9 (± 0.4)		5.9 (± 0.9)	94.1 (± 0.3)		0.13 (± 0.02)	0.371 (± 0.002)		0.358 (± 0.003)	1.1
33.3	60.9	16.0 (± 0.4)	82.3 (± 0.4)	1.7 (± 0.2)	5.7 (± 0.8)	90.9 (± 0.3)	3.4 (± 0.4)	0.13 (± 0.02)	0.406 (± 0.002)	0.74 (± 0.02)	0.402 (± 0.004)	1.0
52.1	49.1	12.20 (± 0.60)	87.42 (± 0.34)	0.38 (± 0.06)	3.7 (± 0.6)	94.8 (± 0.3)	1.5 (± 0.2)	0.13 (± 0.02)	0.463 (± 0.002)	1.65 (± 0.02)	0.468 (± 0.005)	1.1
62.0	43.0	14.69 (± 0.51)	84.97 (± 0.34)	0.34 (± 0.02)	4.5 (± 0.7)	93.6 (± 0.3)	1.9 (± 0.1)	0.13 (± 0.02)	0.471 (± 0.002)	2.35 (± 0.04)	0.486 (± 0.004)	1.1
73.5	36.8	13.90 (± 0.71)	85.64 (± 0.40)	0.46 (± 0.03)	4.2 (± 0.6)	93.3 (± 0.3)	2.5 (± 0.2)	0.13 (± 0.02)	0.458 (± 0.002)	2.32 (± 0.03)	0.503 (± 0.005)	1.0
85.7	30.9	15.01 (± 0.80)	84.36 (± 0.44)	0.63 (± 0.04)	4.6 (± 0.7)	91.9 (± 0.3)	3.5 (± 0.2)	0.13 (± 0.02)	0.450 (± 0.002)	2.28 (± 0.05)	0.507 (± 0.006)	1.1
100	25.1	18.46 (± 0.80)	80.90 (± 0.56)	0.64 (± 0.04)	5.9 (± 0.9)	89.8 (± 0.4)	4.3 (± 0.4)	0.13 (± 0.02)	0.91 (± 0.03)	2.7 (± 0.2)	0.53 (± 0.01)	1.1

Table A6: Fluorescence decay analysis of PAc-SNARF at various pH level and spectral windows. Bi-exponential curve-fitting of the fluorescence decay traces shown in Figure 4.2.8A to Eq.19 reveals relative amplitudes α_c and fluorescence lifetime components τ_c. A global fitting procedure was applied to the data set with the spectral condition: $\lambda_{ex} = 526$ nm, $\lambda_{em} > 545$ nm, where the fast lifetime component (protonated) was linked between the individual decay traces. Fluorescence decay traces excited at λ_{ex}=488 nm, where fitted individually. Relative steady-state fluorescence populations β_c and amplitude-weighted mean lifetimes $\tau_{m,\alpha}$ are calculated using Eq. 20 & 21. Experimental conditions: 2.5 µM in 10 mM Tris-citrate buffer, 190 mM NaCl, and 5% DMSO at various pH values. Uncertainty of pH-values amounts to ± 0.1. Indicated uncertainties are based on confidence interval analyses of each fit parameter (Section 3.4.1). The given digits of α_c and β_c are chosen so that the individual values add up to 100 %. The respective uncertainties are indicated by the same number of digits.

pH	λ_{ex}	λ_{em} (nm)	α_1 (%)	α_2 (%)	β_1 (%)	β_2 (%)	τ_1 (ns)	τ_2 (ns)	$\tau_{m,\alpha}$ (ns)	χ^2_{red}
5.2	526	545 LP	97.19 (± 0.20)	2.81 (± 0.04)	81 (± 2)	19 (± 1)	0.49 (± 0.07)	3.99 (± 0.03)	0.59 (± 0.07)	1.1
5.8			95.80 (± 0.23)	4.20 (± 0.05)	77 (± 3)	23 (± 2)	0.49 (± 0.07)	3.41 (± 0.02)	0.62 (± 0.07)	0.9
6.4			91.72 (± 0.17)	8.28 (± 0.04)	66 (± 3)	34 (± 2)	0.49 (± 0.07)	2.861 (± 0.008)	0.69 (± 0.06)	1.3
7.1			69.96 (± 0.23)	30.04 (± 0.09)	33 (± 3)	67 (± 3)	0.49 (± 0.07)	2.367 (± 0.004)	1.06 (± 0.05)	1.1
7.6			50.2 (± 0.4)	49.8 (± 0.1)	18 (± 2)	82 (± 3)	0.49 (± 0.07)	2.283 (± 0.003)	1.38 (± 0.04)	1.1
8.0			30.2 (± 0.4)	69.8 (± 0.1)	9 (± 1)	91 (± 2)	0.49 (± 0.07)	2.258 (± 0.003)	1.72 (± 0.02)	1.1
8.3			20.6 (± 0.4)	79.4 (± 0.09)	5.4 (± 0.7)	96.6 (± 1.4)	0.49 (± 0.07)	2.231 (± 0.002)	1.87 (± 0.01)	1.1
8.7			10.8 (± 0.4)	89.2 (± 0.05)	2.6 (± 0.4)	97.4 (± 0.8)	0.49 (± 0.07)	2.221 (± 0.003)	2.034 (± 0.008)	1.1
9.2			6.0 (± 0.4)	94.0 (± 0.05)	1.4 (± 0.2)	98.6 (± 0.5)	0.49 (± 0.07)	2.216 (± 0.002)	2.114 (± 0.005)	1.0
10.2			3.3 (± 0.4)	96.7 (± 0.04)	0.7 (± 0.1)	99.3 (± 0.3)	0.49 (± 0.07)	2.214 (± 0.002)	2.161 (± 0.006)	1.1
5.0	488	525 BP	74.0 (± 0.5)	26.0 (± 0.2)	25.6 (± 0.3)	74.4 (± 0.4)	0.477 (± 0.005)	3.95 (± 0.02)	1.38 (± 0.01)	1.0
5.1		580 BP	97.8 (± 0.3)	2.2 (± 0.1)	87.6 (± 0.2)	12.4 (± 0.4)	0.505 (± 0.002)	3.22 (± 0.05)	0.564 (± 0.003)	1.1
5.0		630 BP	97.9 (± 0.4)	2.1 (± 0.1)	88.3 (± 0.3)	11.7 (± 0.5)	0.509 (± 0.003)	3.13 (± 0.07)	0.56 (± 0.01)	1.0
5.0		715 LP	97.8 (± 0.5)	2.2 (± 0.1)	89.7 (± 0.3)	10.3 (± 0.5)	0.497 (± 0.003)	2.51 (± 0.07)	0.54 (± 0.01)	1.1
9.7			5.2 (± 0.8)	94.8 (± 0.3)	1.1 (± 0.2)	98.9 (± 0.5)	0.46 (± 0.07)	2.232 (± 0.003)	2.14 (± 0.01)	1.1

Table A7: Fluorescence decay analysis of dPGS-ICC interacting with human serum (HS) at different concentrations. T = 20 °C. Tri-exponential curve-fitting of the fluorescence decay traces of Figure 4.3.2A by a global fitting procedure to Eq. 19 with the condition of a shared first decay component. The table summarizes relative amplitudes α_c, fluorescence lifetime components τ_c, and calculated relative steady-state fluorescence populations β_c and population-weighted mean lifetimes $\tau_{m,\beta}$ (Eq. 21). Spectral conditions: λ_{ex} = 530 nm, λ_{em} > 570 nm. Indicated uncertainties are based on relative precision, see Table 4.3.1. The given digits of α_c and β_c are chosen so that the individual values add up to 100 %. The respective uncertainties are indicated by the same number of digits.

HS (%V/V)	α_1 (%)	α_2 (%)	α_3 (%)	β_1 (%)	β_2 (%)	β_3 (%)	τ_1 (ns)	τ_2 (ns)	τ_3 (ns)	$\tau_{m,\beta}$ (ns)	χ^2_{red}
0.001	60 (± 5)	34 (± 4)	6 (± 1)	30 (± 3)	48 (± 4)	22 (± 3)	0.16 (± 0.02)	0.46 (± 0.06)	1.2 (± 0.1)	0.53 (± 0.05)	1.1
0.01	59 (± 5)	35 (± 4)	6 (± 1)	29 (± 3)	49 (± 4)	22 (± 3)	0.16 (± 0.02)	0.46 (± 0.06)	1.2 (± 0.1)	0.54 (± 0.06)	1.0
0.05	60 (± 5)	34 (± 4)	6 (± 1)	26 (± 3)	48 (± 5)	26 (± 4)	0.16 (± 0.02)	0.53 (± 0.07)	1.6 (± 0.1)	0.71 (± 0.07)	1.1
0.1	57 (± 5)	34 (± 4)	9 (± 2)	21 (± 3)	42 (± 5)	37 (± 6)	0.16 (± 0.02)	0.55 (± 0.07)	1.8 (± 0.2)	0.9 (± 0.1)	1.1
0.2	52 (± 4)	36 (± 4)	12 (± 2)	16 (± 2)	40 (± 4)	44 (± 5)	0.16 (± 0.02)	0.59 (± 0.07)	1.9 (± 0.2)	1.1 (± 0.1)	1.0
0.5	46 (± 4)	36 (± 4)	18 (± 3)	11 (± 2)	35 (± 5)	54 (± 5)	0.16 (± 0.02)	0.65 (± 0.08)	2.0 (± 0.2)	1.3 (± 0.2)	1.1
1	37 (± 3)	39 (± 5)	24 (± 4)	7 (± 1)	34 (± 5)	59 (± 6)	0.16 (± 0.02)	0.70 (± 0.09)	2.0 (± 0.2)	1.4 (± 0.2)	1.1
3	30 (± 2)	38 (± 5)	32 (± 5)	4.8 (± 0.9)	28.3 (± 5.0)	66.9 (± 5.3)	0.16 (± 0.02)	0.75 (± 0.09)	2.1 (± 0.2)	1.6 (± 0.2)	1.0
5	28 (± 2)	38 (± 5)	34 (± 6)	4.2 (± 0.9)	28.6 (± 5.3)	67.2 (± 5.8)	0.16 (± 0.02)	0.8 (± 0.1)	2.1 (± 0.2)	1.6 (± 0.2)	1.0
10	21 (± 2)	38 (± 5)	41 (± 7)	2.7 (± 0.6)	24.5 (± 5.4)	72.8 (± 5.6)	0.16 (± 0.02)	0.8 (± 0.1)	2.2 (± 0.2)	1.8 (± 0.2)	0.9
30	21 (± 2)	37 (± 4)	42 (± 7)	2.7 (± 0.6)	23.6 (± 5.1)	73.7 (± 5.2)	0.16 (± 0.02)	0.9 (± 0.1)	2.2 (± 0.2)	1.8 (± 0.2)	1.0
40	22 (± 2)	35 (± 4)	43 (± 7)	2.6 (± 0.6)	23.5 (± 5.2)	73.9 (± 5.2)	0.16 (± 0.02)	0.9 (± 0.1)	2.3 (± 0.2)	1.9 (± 0.2)	1.0
50	23 (± 2)	35% (± 5)	42 (± 7)	2.9 (± 0.6)	24.7 (± 5.3)	72.4 (± 5.3)	0.16 (± 0.02)	0.9 (± 0.1)	2.2 (± 0.2)	1.8 (± 0.2)	1.0
70	26 (± 2)	35% (± 4)	39 (± 7)	3.3 (± 0.8)	25.1 (± 5.4)	71.6 (± 5.4)	0.16 (± 0.02)	0.9 (± 0.1)	2.3 (± 0.2)	1.9 (± 0.2)	1.0

Table A8: Fluorescence decay analysis of dPGS-ICC interacting with bovine serum albumin (BSA) at different concentrations. T = 20 °C. Tri-exponential curve-fitting of the fluorescence decay traces of Figure 4.3.2D by a global fitting procedure to Eq.19 with the condition of a shared first decay component. The table summarizes relative amplitudes α_c, fluorescence lifetime components τ_c, and calculated relative steady-state fluorescence populations β_c and population-weighted mean lifetimes $\tau_{m,\beta}$ (Eq. 21). Spectral conditions: λ_{ex} = 488 nm, λ_{em} > 570 nm. Indicated uncertainties are based on relative precision, see Table 4.3.1. The given digits of α_c and β_c are chosen so that the individual values add up to 100 %. The respective uncertainties are indicated by the same number of digits.

BSA (μM)	α_1 (%)	α_2 (%)	α_3 (%)	β_1 (%)	β_2 (%)	β_3 (%)	τ_1 (ns)	τ_2 (ns)	τ_3 (ns)	$\tau_{m,\beta}$ (ns)	χ^2_{red}
0.01	64.6 (± 4.9)	30.0 (± 3.6)	5.4 (± 0.9)	34 (± 3)	46 (± 4)	20 (± 3)	0.16 (± 0.02)	0.46 (± 0.06)	1.1 (± 0.1)	0.49 (± 0.05)	1.0
0.10	64.0 (± 5.0)	30.6 (± 3.7)	5.4 (± 0.9)	34 (± 3)	46 (± 5)	20 (± 3)	0.16 (± 0.02)	0.45 (± 0.06)	1.1 (± 0.1)	0.48 (± 0.05)	1.1
0.20	64.8 (± 5.3)	30.5 (± 3.7)	4.7 (± 0.8)	30 (± 3)	47 (± 5)	23 (± 4)	0.16 (± 0.02)	0.52 (± 0.07)	1.7 (± 0.2)	0.68 (± 0.08)	1.1
0.50	61 (± 5)	30 (± 4)	9 (± 2)	22 (± 3)	40 (± 4)	38 (± 6)	0.16 (± 0.02)	0.58 (± 0.07)	1.9 (± 0.2)	1.0 (± 0.1)	1.2
1.00	56 (± 5)	32 (± 4)	12 (± 2)	17 (± 2)	37 (± 4)	46 (± 5)	0.16 (± 0.02)	0.59 (± 0.07)	2.0 (± 0.2)	1.2 (± 0.1)	1.0
10.0	42 (± 3)	36 (± 4)	22 (± 4)	8 (± 1)	32 (± 5)	60 (± 6)	0.16 (± 0.02)	0.72 (± 0.09)	2.2 (± 0.2)	1.6 (± 0.2)	1.2
1000	26.9 (± 2)	44 (± 5)	29 (± 5)	3.8 (± 0.8)	34.9 (± 5.9)	61.3 (± 6.0)	0.16 (± 0.02)	0.9 (± 0.1)	2.4 (± 0.2)	1.8 (± 0.2)	1.0

Table A9: Fluorescence decay analysis of dPGS-ICC interacting with the triple helical model peptide MSR-1 at different concentrations and upon addition of fucoidan. T = 20 °C. Tri-exponential curve-fitting of the fluorescence decay traces of Figure 4.3.3A and D by a global fitting procedure to Eq.19 with the condition of a shared first decay component. The table summarizes relative amplitudes α_c, fluorescence lifetime components τ_c, and calculated relative steady-state fluorescence populations β_c and population-weighted mean lifetimes $\tau_{m,\beta}$ (Eq. 21). Spectral conditions: λ_{ex} = 488 nm, λ_{em} > 570 nm. Indicated uncertainties are based on relative precision, see Table 4.3.1. The given digits of α_c and β_c are chosen so that the individual values add up to 100 %. The respective uncertainties are indicated by the same number of digits.

MSR-1 (μM)	fucoidan (mg/ml)	α_1 (%)	α_2 (%)	α_3 (%)	β_1 (%)	β_2 (%)	β_3 (%)	τ_1 (ns)	τ_2 (ns)	τ_3 (ns)	$\tau_{m,\beta}$ (ns)	χ^2_{red}
0.001	0	67 (± 5)	27 (± 3)	6 (± 1)	38 (± 4)	39 (± 4)	23 (± 3)	0.16 (± 0.02)	0.41 (± 0.05)	1.1 (± 0.1)	0.47 (± 0.05)	1.0
0.01	0	64.7 (± 5.3)	29.7 (± 3.6)	5.6 (± 0.9)	36 (± 4)	42 (± 4)	22 (± 3)	0.16 (± 0.02)	0.40 (± 0.05)	1.1 (± 0.1)	0.47 (± 0.05)	1.1
0.1	0	64 (± 5)	30 (± 4)	6 (± 1)	36 (± 4)	41 (± 5)	23 (± 3)	0.16 (± 0.02)	0.39 (± 0.05)	1.1 (± 0.1)	0.47 (± 0.05)	1.1
1.0	0	61 (± 5)	32 (± 4)	7 (± 1)	32 (± 3)	42 (± 4)	26 (± 3)	0.16 (± 0.02)	0.39 (± 0.05)	1.1 (± 0.1)	0.50 (± 0.05)	1.2
1.5	0	60 (± 5)	33 (± 4)	7 (± 1)	30 (± 3)	44 (± 4)	26 (± 3)	0.16 (± 0.02)	0.43 (± 0.05)	1.2 (± 0.1)	0.55 (± 0.05)	1.1
3.0	0	58 (± 5)	35 (± 4)	7 (± 1)	25 (± 3)	48 (± 4)	27 (± 3)	0.16 (± 0.02)	0.51 (± 0.06)	1.4 (± 0.1)	0.66 (± 0.06)	1.1
10	0	50 (± 4)	40 (± 5)	10 (± 2)	18 (± 2)	50 (± 5)	32 (± 5)	0.16 (± 0.02)	0.54 (± 0.07)	1.4 (± 0.1)	0.75 (± 0.07)	1.1
100	0	38 (± 3)	48 (± 6)	14 (± 3)	11 (± 2)	50 (± 5)	39 (± 4)	0.16 (± 0.02)	0.57 (± 0.07)	1.5 (± 0.1)	0.89 (± 0.08)	1.2
222	0	38 (± 3)	46 (± 6)	16 (± 3)	11 (± 2)	47 (± 5)	42 (± 5)	0.16 (± 0.02)	0.58 (± 0.07)	1.5 (± 0.1)	0.9 (± 0.1)	1.0
222	30	40 (± 3)	44 (± 5)	16 (± 3)	11 (± 2)	46 (± 5)	43 (± 5)	0.16 (± 0.02)	0.61 (± 0.08)	1.6 (± 0.1)	1.0 (± 0.1)	1.0
222	160	42 (± 3)	43 (± 5)	15 (± 3)	12 (± 2)	46 (± 4)	42 (± 5)	0.16 (± 0.02)	0.57 (± 0.07)	1.5 (± 0.1)	0.9 (± 0.1)	1.1
222	400	49 (± 4)	41 (± 5)	10 (± 2)	17 (± 2)	50 (± 4)	33 (± 5)	0.16 (± 0.02)	0.56 (± 0.07)	1.5 (± 0.1)	0.80 (± 0.09)	1.1
222	800	52 (± 4)	39 (± 5)	9 (± 2)	22 (± 3)	48 (± 5)	30 (± 5)	0.16 (± 0.02)	0.48 (± 0.06)	1.3 (± 0.1)	0.66 (± 0.08)	0.9
222	1200	56 (± 5)	36 (± 4)	8 (± 1)	25 (± 3)	46 (± 4)	29 (± 3)	0.16 (± 0.02)	0.46 (± 0.06)	1.3 (± 0.1)	0.63 (± 0.06)	0.9
222	1600	54 (± 4)	36 (± 4)	10 (± 2)	24 (± 3)	42 (± 4)	34 (± 5)	0.16 (± 0.02)	0.42 (± 0.05)	1.2 (± 0.1)	0.62 (± 0.07)	0.9

Table A10: Fluorescence decay analysis of dPGS-ICC interacting with DMPC SUVs at different lipid concentrations and at T = 5 and 20 °C. Tri-exponential curve-fitting of the fluorescence decay traces of Figure 4.3.5A and D by a global fitting procedure to Eq. 19 with the condition of a shared first decay component. The table summarizes relative amplitudes α_c, fluorescence lifetime components τ_c, and calculated relative steady-state fluorescence populations β_c and population-weighted mean lifetimes $\tau_{m,\beta}$ (Eq. 21). Spectral conditions: $\lambda_{ex} = 488$ nm, $\lambda_{em} > 570$ nm. Indicated uncertainties are based on relative precision, see Table 4.3.1. The given digits of α_c and β_c are chosen so that the individual values add up to 100 %. The respective uncertainties are indicated by the same number of digits.

DMPC (µM)	temp. (°C)	α_1 (%)	α_2 (%)	α_3 (%)	β_1 (%)	β_2 (%)	β_3 (%)	τ_1 (ns)	τ_2 (ns)	τ_3 (ns)	$\tau_{m,\beta}$ (ns)	χ^2_{red}
0.01	5	49 (± 4)	42 (± 5)	9 (± 2)	19 (± 3)	52 (± 5)	29 (± 5)	0.19 (± 0.03)	0.62 (± 0.08)	1.6 (± 0.1)	0.8 (± 0.1)	1.0
0.1		46 (± 4)	44 (± 5)	10 (± 2)	17 (± 3)	52 (± 5)	31 (± 5)	0.19 (± 0.03)	0.60 (± 0.08)	1.6 (± 0.1)	0.8 (± 0.1)	1.2
1.0		46 (± 4)	43 (± 5)	11 (± 2)	17 (± 3)	49 (± 5)	34 (± 5)	0.19 (± 0.03)	0.59 (± 0.07)	1.6 (± 0.1)	0.90 (± 0.1)	1.0
10		40 (± 3)	46 (± 6)	14 (± 2)	13 (± 2)	48 (± 5)	39 (± 4)	0.19 (± 0.03)	0.59 (± 0.07)	1.6 (± 0.1)	0.93 (± 0.09)	1.0
50		29 (± 2)	43 (± 5)	28 (± 5)	7 (± 1)	35 (± 5)	58 (± 5)	0.19 (± 0.03)	0.63 (± 0.08)	1.6 (± 0.1)	1.2 (± 0.1)	1.0
100		26 (± 2)	44 (± 5)	30 (± 5)	6 (± 1)	35 (± 5)	59 (± 6)	0.19 (± 0.03)	0.70 (± 0.09)	1.7 (± 0.2)	1.3 (± 0.2)	1.2
200		23 (± 2)	40 (± 5)	37 (± 6)	4 (± 1)	31 (± 6)	65 (± 6)	0.19 (± 0.03)	0.8 (± 0.1)	1.8 (± 0.2)	1.4 (± 0.2)	1.1
300		20 (± 2)	40 (± 5)	40 (± 7)	3.5 (± 0.8)	29.7 (± 5.8)	66.8 (± 6.0)	0.19 (± 0.03)	0.8 (± 0.1)	1.8 (± 0.2)	1.4 (± 0.2)	1.1
500		15 (± 1)	39 (± 5)	46 (± 8)	2.4 (± 0.6)	26.7 (± 5.8)	70.9 (± 5.8)	0.19 (± 0.03)	0.8 (± 0.1)	1.8 (± 0.2)	1.5 (± 0.2)	1.1
1000		13 (± 1)	36 (± 4)	51 (± 9)	1.9 (± 0.5)	22.5 (± 5.3)	75.6 (± 5.3)	0.19 (± 0.03)	0.8 (± 0.1)	1.9 (± 0.2)	1.6 (± 0.2)	1.2
4000		8.5 (± 0.7)	35 (± 4.2)	56.5 (± 9.4)	1.2 (± 0.3)	22.4 (± 5.5)	76.4 (± 5.3)	0.19 (± 0.03)	0.9 (± 0.1)	1.9 (± 0.2)	1.7 (± 0.2)	1.2
0.01	20	64.3 (± 5.3)	30.7 (± 3.7)	5.0 (± 0.8)	32 (± 3)	49 (± 4)	19 (± 2)	0.16 (± 0.03)	0.51 (± 0.06)	1.2 (± 0.1)	0.53 (± 0.05)	0.9
0.1		63.1 (± 5.2)	31.6 (± 3.8)	5.3 (± 0.9)	31 (± 3)	49 (± 4)	20 (± 3)	0.16 (± 0.03)	0.50 (± 0.06)	1.2 (± 0.1)	0.53 (± 0.05)	0.9
1.0		60 (± 5)	34 (± 4)	6 (± 1)	29 (± 3)	49 (± 4)	22 (± 3)	0.16 (± 0.03)	0.48 (± 0.06)	1.2 (± 0.1)	0.55 (± 0.06)	0.8
10		61 (± 5)	33 (± 4)	6 (± 1)	29 (± 3)	48 (± 4)	22 (± 3)	0.16 (± 0.03)	0.48 (± 0.06)	1.2 (± 0.1)	0.54 (± 0.06)	0.8
50		60 (± 5)	34 (± 4)	7 (± 1)	29 (± 3)	49 (± 4)	22 (± 3)	0.16 (± 0.03)	0.47 (± 0.06)	1.2 (± 0.1)	0.54 (± 0.06)	0.8
100		58 (± 5)	35 (± 4)	7 (± 1)	27 (± 3)	48 (± 5)	25 (± 3)	0.16 (± 0.03)	0.47 (± 0.06)	1.2 (± 0.1)	0.57 (± 0.06)	0.9
200		58 (± 5)	35 (± 4)	7 (± 1)	27 (± 3)	49 (± 4)	25 (± 3)	0.16 (± 0.03)	0.47 (± 0.06)	1.2 (± 0.1)	0.57 (± 0.06)	0.8
300		57 (± 5)	36 (± 4)	7 (± 1)	27 (± 3)	49 (± 4)	24 (± 3)	0.16 (± 0.03)	0.47 (± 0.06)	1.2 (± 0.1)	0.56 (± 0.06)	1.1
500		58 (± 5)	35 (± 4)	7 (± 1)	27 (± 3)	49 (± 4)	24 (± 3)	0.16 (± 0.03)	0.48 (± 0.06)	1.2 (± 0.1)	0.57 (± 0.06)	0.8
1000		58 (± 5)	35 (± 4)	7 (± 1)	26 (± 3)	50 (± 4)	24 (± 3)	0.16 (± 0.03)	0.50 (± 0.06)	1.2 (± 0.1)	0.58 (± 0.06)	0.8
4000		54 (± 4)	39 (± 5)	7 (± 1)	22 (± 3)	55 (± 4)	23 (± 3)	0.16 (± 0.03)	0.56 (± 0.07)	1.3 (± 0.1)	0.64 (± 0.07)	1.1

Table A11: Fluorescence decay analysis of dPGS-ICC interacting with DMPC and DPPC SUVs. Tri-exponential curve-fitting of the fluorescence decay traces of Figure 4.3.6A and B by a global fitting procedure to Eq. 19 with the condition of a shared first decay component. The table summarizes relative amplitudes α_c, fluorescence lifetime components τ_c, and calculated relative steady-state fluorescence populations β_c and population-weighted mean lifetimes $\tau_{m,\beta}$ (Eq. 21). Spectral conditions: λ_{ex} = 488 nm, λ_{em} > 570 nm. Indicated uncertainties are based on relative precision, see Table 4.3.1. The given digits of α_c and β_c are chosen so that the individual values add up to 100 %. The respective uncertainties are indicated by the same number of digits.

temp. (°C)	lipid	α_1 (%)	α_2 (%)	α_3 (%)	β_1 (%)	β_2 (%)	β_3 (%)	τ_1 (ns)	τ_2 (ns)	τ_3 (ns)	$\tau_{m,\beta}$ (ns)	χ^2_{red}
5	w/o	44 (± 4)	46 (± 6)	10 (± 2)	16 (± 3)	53 (± 5)	31 (± 5)	0.19 (± 0.03)	0.60 (± 0.08)	1.6 (± 1.2)	0.8 (± 0.1)	1.1
	DMPC	8.5 (± 0.7)	35.0 (± 4.2)	56.5 (± 9.0)	1.2 (± 0.3)	22.6 (± 5.4)	76.2 (± 5.2)	0.19 (± 0.03)	0.9 (± 0.1)	1.9 (± 0.2)	1.7 (± 0.2)	1.0
	DPPC	13 (± 1)	31 (± 4)	56 (± 9)	1.6 (± 0.5)	18.2 (± 4.8)	80.2 (± 4.8)	0.19 (± 0.03)	0.9 (± 0.1)	2.2 (± 0.2)	1.9 (± 0.2)	1.0
20	w/o	58 (± 5)	35 (± 4)	7 (± 1)	27 (± 3)	48 (± 4)	25 (± 3)	0.16 (± 0.02)	0.46 (± 0.06)	1.2 (± 0.1)	0.56 (± 0.06)	1.1
	DMPC	54 (± 4)	39 (± 5)	7 (± 1)	22 (± 3)	55 (± 5)	23 (± 3)	0.16 (± 0.02)	0.56 (± 0.07)	1.3 (± 0.1)	0.64 (± 0.07)	1.0
	DPPC	43 (± 4)	35 (± 4)	22 (± 4)	12 (± 3)	36 (± 5)	52 (± 5)	0.16 (± 0.02)	0.60 (± 0.08)	1.4 (± 0.1)	1.0 (± 0.1)	1.1
30	w/o	65.9 (± 5.4)	29.2 (± 3.5)	4.9 (± 0.8)	35 (± 4)	46 (± 4)	19 (± 3)	0.13 (± 0.02)	0.39 (± 0.05)	0.96 (± 0.09)	0.41 (± 0.04)	1.0
	DMPC	68.0 (± 5.6)	29.1 (± 3.5)	2.9 (± 0.5)	35 (± 4)	51 (± 5)	14 (± 2)	0.13 (± 0.02)	0.44 (± 0.06)	1.2 (± 0.1)	0.44 (± 0.05)	1.1
	DPPC	64.9 (± 5.3)	30.5 (± 3.7)	4.6 (± 0.8)	32 (± 4)	49 (± 4)	19 (± 3)	0.13 (± 0.02)	0.43 (± 0.05)	1.1 (± 0.1)	0.46 (± 0.05)	1.0
45	w/o	77.5 (± 6.5)	21.5 (± 2.6)	1.0 (± 0.2)	50 (± 5)	43 (± 4)	7 (± 1)	0.11 (± 0.02)	0.34 (± 0.04)	1.1 (± 0.1)	0.28 (± 0.03)	1.1
	DMPC	76.8 (± 6.3)	22.0 (± 2.7)	1.2 (± 0.2)	49 (± 5)	44 (± 4)	7 (± 1)	0.11 (± 0.02)	0.34 (± 0.04)	1.02 (± 0.09)	0.27 (± 0.03)	0.9
	DPPC	77.2 (± 6.3)	21.1 (± 2.6)	1.7 (± 0.3)	50 (± 5)	41 (± 4)	9 (± 1)	0.11 (± 0.02)	0.33 (± 0.04)	0.88 (± 0.08)	0.27 (± 0.03)	0.1

Table A12: Fluorescence decay analysis of dPGS-ICC interacting with CMS nanoparticles (NP) at different CMS-NP concentrations at 20 °C. Tri-exponential curve-fitting of the fluorescence decay traces of Figure 4.3.8A by a global fitting procedure to Eq. 19 with the condition of a shared first decay component. The table summarizes relative amplitudes α_c, fluorescence lifetime components τ_c, and calculated relative steady-state fluorescence populations β_c and population-weighted mean lifetimes $\tau_{m,\beta}$ (Eq. 21). Spectral conditions: $\lambda_{ex} = 488$ nm, $\lambda_{em} > 570$ nm. Indicated uncertainties are based on relative precision, see Table 4.3.1. The given digits of α_c and β_c are chosen so that the individual values add up to 100 %. The respective uncertainties are indicated by the same number of digits.

CMS (μM)	α_1 (%)	α_2 (%)	α_3 (%)	β_1 (%)	β_2 (%)	β_3 (%)	τ_1 (ns)	τ_2 (ns)	τ_3 (ns)	$\tau_{m,\beta}$ (ns)	χ^2_{red}
0.01	68.5 (± 5.6)	27.3 (± 3.3)	4.2 (± 0.7)	40 (± 4)	43 (± 5)	17 (± 3)	0.16 (± 0.02)	0.44 (± 0.06)	1.1 (± 0.1)	0.44 (± 0.05)	0.9
0.05	67.5 (± 5.5)	28.5 (± 3.5)	4.0 (± 0.7)	37 (± 4)	45 (± 4)	18 (± 3)	0.16 (± 0.02)	0.47 (± 0.06)	1.3 (± 0.1)	0.50 (± 0.05)	0.9
0.08	68.1 (± 5.6)	27.7 (± 3.4)	4.2 (± 0.7)	36 (± 4)	44 (± 4)	20 (± 3)	0.16 (± 0.02)	0.48 (± 0.06)	1.4 (± 0.1)	0.55 (± 0.06)	0.9
0.10	67.2 (± 5.5)	28.4 (± 3.4)	4.4 (± 0.7)	34 (± 3)	45 (± 4)	21 (± 3)	0.16 (± 0.02)	0.49 (± 0.06)	1.5 (± 0.1)	0.59 (± 0.06)	1.0
0.26	64 (± 5)	29 (± 4)	7 (± 1)	29 (± 3)	40 (± 4)	32 (± 3)	0.16 (± 0.02)	0.50 (± 0.06)	1.6 (± 0.1)	0.74 (± 0.07)	1.1
0.50	59 (± 5)	30 (± 4)	11 (± 2)	21 (± 3)	37 (± 5)	42 (± 5)	0.16 (± 0.02)	0.55 (± 0.07)	1.7 (± 0.2)	1.0 (± 0.1)	1.1
0.77	52 (± 4)	31 (± 4)	17 (± 3)	14 (± 2)	34 (± 5)	52 (± 5)	0.16 (± 0.02)	0.64 (± 0.08)	1.8 (± 0.2)	1.2 (± 0.1)	1.1
1.0	50 (± 4)	31 (± 4)	19 (± 3)	13 (± 2)	33 (± 5)	54 (± 5)	0.16 (± 0.02)	0.67 (± 0.08)	1.8 (± 0.2)	1.2 (± 0.1)	1.0
2.5	20 (± 2)	44 (± 5)	36 (± 6)	2.8 (± 0.6)	34.5 (± 6.0)	62.7 (± 6.0)	0.16 (± 0.02)	0.9 (± 0.1)	2.0 (± 0.2)	1.6 (± 0.2)	1.2
5.0	14 (± 1)	44 (± 5)	42 (± 7)	1.8 (± 0.4)	31.5 (± 6.2)	66.8 (± 6.0)	0.16 (± 0.02)	0.9 (± 0.1)	2.0 (± 0.2)	1.6 (± 0.2)	1.0
10	9.5 (± 0.8)	45.5 (± 5.5)	45.0 (± 7.5)	1.1 (± 0.3)	32.1 (± 6.8)	66.8 (± 6.4)	0.16 (± 0.02)	1.0 (± 0.1)	2.1 (± 0.2)	1.7 (± 0.2)	1.0
15	10.6 (± 0.9)	47.7 (± 5.8)	41.7 (± 7.0)	1.2 (± 0.3)	33.8 (± 6.9)	65.0 (± 6.5)	0.16 (± 0.02)	1.0 (± 0.1)	2.2 (± 0.2)	1.8 (± 0.2)	1.1

Table A13: Fluorescence decay analysis of dPGS-ICC interacting with CMS nanoparticles (2.5 µM) as a function of temperature. in solution of 2.5 µM CMS-NP as function of temperature. Tri-exponential curve-fitting of the fluorescence decay traces of Figure 4.3.8D by a global fitting procedure to Eq. 19 with the condition of a shared first decay component. The table summarizes relative amplitudes α_c, fluorescence lifetime components τ_c, and calculated relative steady-state fluorescence populations β_c and population-weighted mean lifetimes $\tau_{m,\beta}$ (Eq. 21). Spectral conditions: $\lambda_{ex} = 488$ nm, $\lambda_{em} > 570$ nm. Indicated uncertainties are based on relative precision, see Table 4.3.1. The given digits of α_c and β_c are chosen so that the individual values add up to 100 %. The respective uncertainties are indicated by the same number of digits.

Temp. (°C)	α_1 (%)	α_2 (%)	α_3 (%)	β_1 (%)	β_2 (%)	β_3 (%)	τ_1 (ns)	τ_2 (ns)	τ_3 (ns)	$\tau_{m,\beta}$ (ns)	χ^2_{red}
9.6	12 (± 1)	35 (± 4)	53 (± 9)	1.3 (± 0.4)	21.8 (± 5.4)	76.9 (± 5.2)	0.16 (± 0.02)	0.90 (± 0.1)	2.1 (± 0.2)	1.8 (± 0.2)	1.0
15.1	16 (± 1)	40 (± 5)	44 (± 7)	2.0 (± 0.5)	28.5 (± 5.8)	69.5 (± 5.8)	0.16 (± 0.02)	0.9 (± 0.1)	2.0 (± 0.2)	1.6 (± 0.2)	1.1
19.6	18 (± 1)	44 (± 5)	38 (± 6)	2.4 (± 0.5)	33.4 (± 5.9)	64.2 (± 5.9)	0.16 (± 0.02)	0.9 (± 0.1)	2.0 (± 0.2)	1.6 (± 0.2)	1.3
24.9	23 (± 2)	47 (± 6)	30 (± 5)	3.7 (± 0.7)	38.3 (± 6.0)	58.0 (± 6.2)	0.16 (± 0.02)	0.8 (± 0.1)	1.9 (± 0.2)	1.4 (± 0.2)	1.1
30.1	28 (± 2)	48 (± 6)	24 (± 4)	5.2 (± 0.9)	44.6 (± 5.8)	50.2 (± 6.1)	0.16 (± 0.02)	0.8 (± 0.1)	1.8 (± 0.2)	1.3 (± 0.2)	1.2
38.6	32 (± 3)	49 (± 6)	19 (± 3)	7 (± 1)	49 (± 5)	44 (± 6)	0.16 (± 0.02)	0.72 (± 0.09)	1.7 (± 0.2)	1.1 (± 0.1)	1.1
45.5	39 (± 3)	47 (± 6)	14 (± 2)	10 (± 2)	52 (± 5)	38 (± 5)	0.16 (± 0.02)	0.70 (± 0.09)	1.7 (± 0.2)	1.0 (± 0.1)	1.0
54.0	42 (± 3)	47 (± 6)	11 (± 2)	13 (± 2)	54 (± 5)	33 (± 5)	0.16 (± 0.02)	0.62 (± 0.08)	1.6 (± 0.1)	0.9 (± 0.1)	1.2

Table A14: Fluorescence decay analysis of CMS-ICC interacting with *bovine serum albumin* (BSA) at different concentrations. T = 20 °C. Tri-exponential curve-fitting of the fluorescence decay traces of Figure 4.2.12A by a global fitting procedure to Eq.19. The table summarizes relative amplitudes α_c, fluorescence lifetime components τ_c, and calculated relative steady-state fluorescence populations β_c and population-weighted mean lifetimes $\tau_{m,\beta}$ (Eq. 21). Spectral conditions: λ_{ex} = 488 nm, λ_{em} > 570 nm. Indicated uncertainties are based on relative precision, see Table 4.3.3. The given digits of α_c and β_c are chosen so that the individual values add up to 100 %. The respective uncertainties are indicated by the same number of digits.

BSA (μM)	α_1 (%)	α_2 (%)	α_3 (%)	β_1 (%)	β_2 (%)	β_3 (%)	τ_1 (ns)	τ_2 (ns)	τ_3 (ns)	$\tau_{m,\beta}$ (ns)	χ^2_{red}
0.1	58 (± 3)	35 (± 2)	7 (± 1)	22 (± 1)	53 (± 2)	25 (± 3)	0.16 (± 0.01)	0.62 (± 0.02)	1.46 (± 0.04)	0.73 (± 0.05)	1.0
1.0	60 (± 3)	33 (± 2)	7 (± 1)	23 (± 2)	51 (± 2)	26 (± 3)	0.15 (± 0.01)	0.60 (± 0.02)	1.40 (± 0.04)	0.70 (± 0.05)	0.9
10	58 (± 3)	36 (± 2)	6 (± 1)	22 (± 1)	55 (± 2)	23 (± 3)	0.16 (± 0.01)	0.65 (± 0.02)	1.61 (± 0.05)	0.76 (± 0.05)	1.2
50	59 (± 3)	37 (± 2)	4 (± 1)	23 (± 1)	59 (± 2)	18 (± 3)	0.18 (± 0.01)	0.74 (± 0.03)	2.08 (± 0.06)	0.85 (± 0.05)	1.2
100	56 (± 3)	38 (± 2)	6 (± 1)	20 (± 1)	54 (± 2)	26 (± 3)	0.18 (± 0.01)	0.73 (± 0.03)	2.27 (± 0.07)	1.02 (± 0.07)	1.2
200	57 (± 3)	38 (± 2)	5 (± 1)	19 (± 1)	56 (± 2)	25 (± 3)	0.18 (± 0.01)	0.76 (± 0.03)	2.59 (± 0.08)	1.11 (± 0.08)	1.2
300	55 (± 3)	39 (± 2)	6 (± 1)	18 (± 1)	53 (± 2)	29 (± 4)	0.18 (± 0.01)	0.77 (± 0.03)	2.70 (± 0.08)	1.2 (± 0.1)	1.2
400	57 (± 3)	37 (± 2)	6 (± 1)	19 (± 1)	52 (± 2)	29 (± 4)	0.20 (± 0.01)	0.85 (± 0.03)	2.88 (± 0.09)	1.3 (± 0.1)	1.1
500	55 (± 3)	38 (± 2)	7 (± 1)	16 (± 1)	50 (± 2)	34 (± 3)	0.19 (± 0.01)	0.86 (± 0.03)	3.15 (± 0.09)	1.5 (± 0.1)	1.2
1000	57 (± 3)	36 (± 2)	7 (± 1)	18 (± 2)	50 (± 2)	32 (± 3)	0.23 (± 0.02)	1.00 (± 0.04)	3.3 (± 0.1)	1.6 (± 0.1)	1.1

Table A15: Fluorescence decay analysis of CMS-ICC in H_2O/sucrose mixtures of different viscosities. T = 20 °C. Tri-exponential curve-fitting of the fluorescence decay traces of Figure 4.3.13A by a global fitting procedure to Eq.19. The table summarizes relative amplitudes α_c, fluorescence lifetime components τ_c, and calculated relative steady-state fluorescence populations β_c and population-weighted mean lifetimes $\tau_{m,\beta}$ (Eq. 21). Spectral condition: λ_{ex} = 488 nm, λ_{em} > 570 nm. Values for viscosities (η) are taken from Ref. 316. The given digits of α_c and β_c are chosen so that the individual values add up to 100 %. The respective uncertainties are indicated by the same number of digits.

sucrose (% w/w)	η (cP)	α_1 (%)	α_2 (%)	α_3 (%)	β_1 (%)	β_2 (%)	β_3 (%)	τ_1 (ns)	τ_2 (ns)	τ_3 (ns)	$\tau_{m,\beta}$ (ns)	χ^2_{red}
0	1.01	57 (± 3)	30 (± 2)	13 (± 2)	19 (± 1)	40 (± 2)	41 (± 4)	0.14 (± 0.01)	0.56 (± 0.02)	1.31 (± 0.04)	0.79 (± 0.06)	1.1
20	1.95	49 (± 3)	40 (± 2)	11 (± 2)	19 (± 1)	49 (± 2)	32 (± 4)	0.18 (± 0.01)	0.58 (± 0.02)	1.36 (± 0.04)	0.75 (± 0.06)	1.1
30	3.19	40 (± 2)	48 (± 3)	12 (± 2)	15 (± 1)	53 (± 2)	32 (± 4)	0.18 (± 0.01)	0.52 (± 0.02)	1.27 (± 0.04)	0.71 (± 0.05)	1.1
40	6.17	35 (± 2)	53 (± 3)	12 (± 2)	11.5 (± 0.9)	57.8 (± 2.2)	30.7 (± 3.7)	0.16 (± 0.01)	0.53 (± 0.02)	1.24 (± 0.04)	0.71 (± 0.05)	1.1
50	15.4	31 (± 2)	54 (± 3)	15 (± 3)	10.3 (± 0.9)	56.6 (± 2.6)	33.1 (± 4.5)	0.18 (± 0.01)	0.57 (± 0.02)	1.20 (± 0.04)	0.74 (± 0.06)	1.1
55	28.1	33 (± 2)	52 (± 3)	15 (± 3)	9.9 (± 0.9)	56.1 (± 2.7)	34.0 (± 4.6)	0.17 (± 0.01)	0.61 (± 0.02)	1.28 (± 0.04)	0.79 (± 0.06)	1.0
60	58.5	30 (± 2)	48 (± 3)	22 (± 5)	7.8 (± 0.8)	45.3 (± 3.0)	46.9 (± 4.7)	0.16 (± 0.01)	0.58 (± 0.02)	1.31 (± 0.04)	0.89 (± 0.07)	1.0
63	99.1	30 (± 2)	47 (± 3)	23 (± 4)	7.7 (± 0.9)	44.9 (± 3.1)	47.4 (± 4.5)	0.17 (± 0.01)	0.63 (± 0.02)	1.36 (± 0.04)	0.94 (± 0.07)	1.0
67	228	28 (± 2)	45 (± 3)	27 (± 5)	6.2 (± 0.7)	39.8 (± 3.4)	54.0 (± 4.8)	0.16 (± 0.01)	0.64 (± 0.02)	1.45 (± 0.04)	1.05 (± 0.08)	1.1
69	370	29 (± 2)	43 (± 3)	28 (± 5)	6.8 (± 0.8)	35.3 (± 3.3)	57.9 (± 4.6)	0.18 (± 0.01)	0.63 (± 0.02)	1.59 (± 0.05)	1.16 (± 0.08)	1.1
71	636	27 (± 1)	44 (± 3)	29 (± 5)	5.8 (± 0.6)	35.8 (± 3.5)	58.4 (± 4.4)	0.18 (± 0.01)	0.68 (± 0.02)	1.68 (± 0.04)	1.24 (± 0.08)	1.0
73	1,170	29 (± 2)	41 (± 2)	30 (± 5)	6.3 (± 0.8)	31.4 (± 3.0)	62.3 (± 4.1)	0.18 (± 0.01)	0.63 (± 0.02)	1.71 (± 0.04)	1.27 (± 0.08)	1.0

Table A16: Fluorescence decay analysis of G5G2.5-MG-FITC's time-resolved fluorescence traces when facing different environments, T = 20 °C. Tri-exponential curve-fitting of the fluorescence decay traces of Figure 4.3.17A-C by a global fitting procedure to Eq.19. The table summarizes relative amplitudes α_c, fluorescence lifetime components τ_c, and calculated relative steady-state fluorescence populations β_c and amplitude-weighted mean lifetimes $\tau_{m,\alpha}$ (Eq. 20 & 21). Spectral conditions: λ_{ex} = 488 nm, λ_{em} > 515 nm. Indicated uncertainties are based on confidence interval analyses of each fit parameter (Section 3.4.1). The given digits of α_c and β_c are chosen so that the individual values add up to 100 %. The respective uncertainties are indicated by the same number of digits.

environment	α_1 (%)	α_2 (%)	α_3 (%)	β_1 (%)	β_2 (%)	β_3 (%)	τ_1 (ns)	τ_2 (ns)	τ_3 (ns)	$\tau_{m,\alpha}$ (ns)	χ^2_{red}
PBS pH 7.4	32.7 (± 1.2)	54.6 (± 1.4)	12.7 (± 0.8)	9.2 (± 0.7)	57.8 (± 1.7)	33.0 (± 1.7)	0.31 (± 0.02)	1.17 (± 0.03)	2.87 (± 0.05)	1.11 (± 0.03)	1.1
PBS pH 5.5	28 (± 1)	36 (± 1)	36 (± 1)	5.2 (± 0.4)	28.0 (± 1.4)	66.8 (± 1.6)	0.28 (± 0.02)	1.17 (± 0.05)	2.79 (± 0.04)	1.50 (± 0.05)	1.1
50 % (v/v) EtOH	22.0 (± 1.0)	46.4 (± 0.8)	31.6 (± 1.3)	4.6 (± 0.4)	39.1 (± 1.8)	56.3 (± 1.6)	0.35 (± 0.02)	1.40 (± 0.04)	2.96 (± 0.03)	1.66 (± 0.05)	1.1
DMPC SUV	32 (± 2)	53 (± 1)	15 (± 1)	8 (± 1)	54 (± 2)	38 (± 2)	0.28 (± 0.03)	1.09 (± 0.04)	2.66 (± 0.06)	1.07 (± 0.04)	1.0
10% (w/w) glycerol	33.6 (± 1.3)	52.6 (± 1.1)	13.8 (± 0.9)	9.6 (± 0.7)	55.8 (± 1.7)	34.6 (± 1.7)	0.32 (± 0.02)	1.18 (± 0.03)	2.79 (± 0.05)	1.11 (± 0.03)	1.1
50% (w/w) glycerol	30 (± 1)	57 (± 1)	13 (± 1)	8.5 (± 0.8)	61.0 (± 2.1)	30.5 (± 6)	0.34 (± 0.03)	1.29 (± 0.05)	2.83 (± 0.04)	1.21 (± 0.04)	1.0

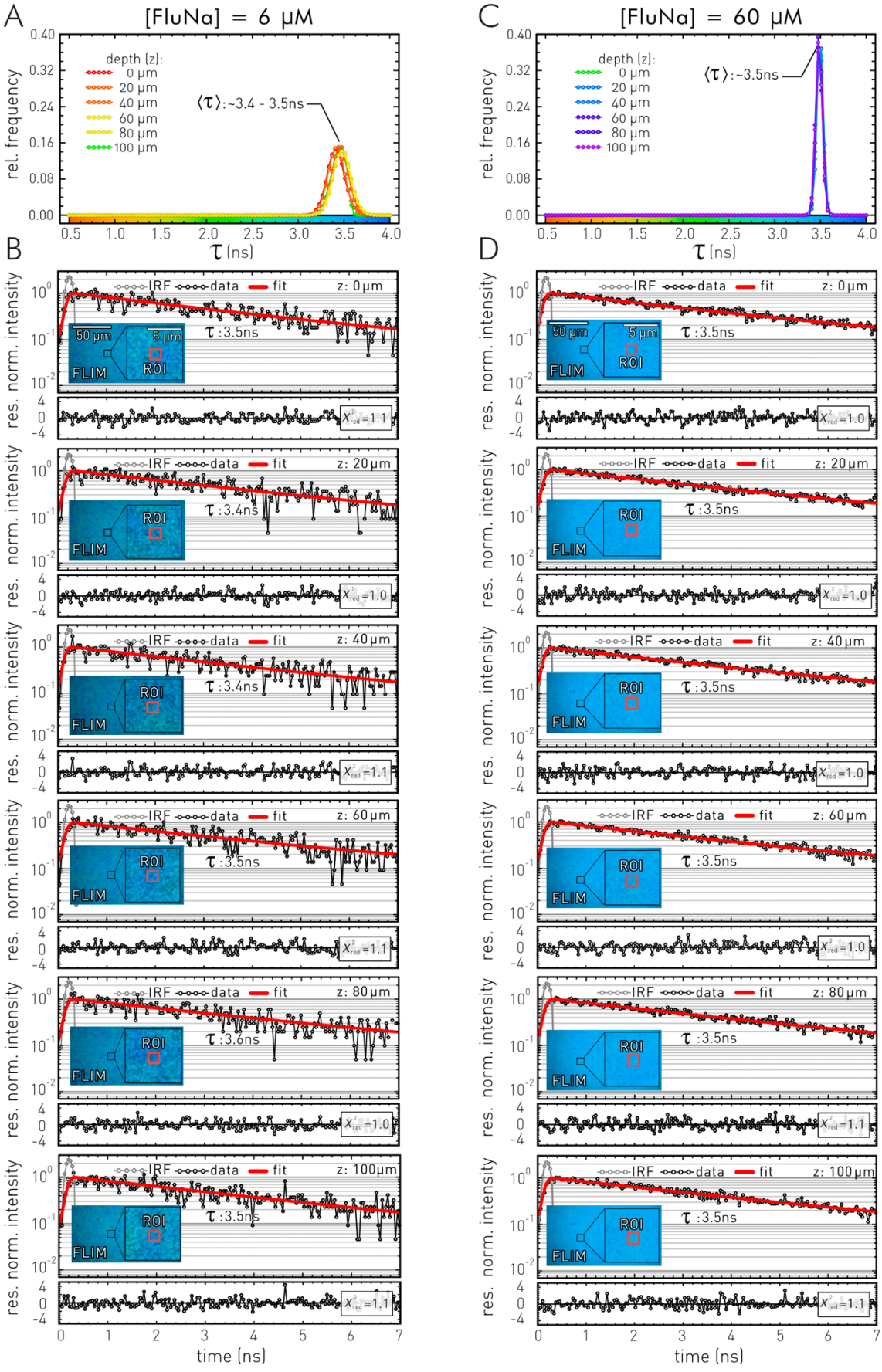

Figure A1: Exemplary fluorescence decay traces of fluorescein in agarose blocks (1.5%, pH 8) generated from the tau-plot analysis shown in Figure 4.1.5. Tau-plot analyses were performed with a local pixel-binning of 5 x 5 pixels. **A** Depth-dependent fluorescence lifetime distributions of fluorescein in agarose (6 µM FluNa). Distribution center: $\langle\tau\rangle$=~3.4–3.5 ns; distribution width: σ<0.1 ns.

B Exemplary depth-dependent fluorescence decay traces and fits to a mono-exponential decay model, recorded in the 6 µM FluNa agarose sample. Gaussian modeled instrument response function (IRF), fit, determined fluorescence lifetime, fit residuals and χ^2_{red} are indicated for the sample depths: 0, 20, 40, 60, 80, 100 µm. The displayed FLIM images show the respective regions of interest (ROI, 5 x 5 pixels) used to generate the shown fluorescence decay trace which is attributed to central pixel of the ROI. **C** Depth-dependent fluorescence lifetime distributions of fluorescein in agarose (60 µM FluNa). Distribution center: $\langle\tau\rangle$=~3.5 ns; distribution width: σ<0.05 ns. **D** Exemplary depth-dependent fluorescence decay traces and fits to a mono-exponential decay model, recorded in 60 µM FluNa agarose sample. Gaussian modeled instrument response function (IRF), fit, determined fluorescence lifetime, fit residuals and χ^2_{red} are indicated for the sample depths: 0, 20, 40, 60, 80, 100 µm. The displayed FLIM images show the respective ROIs (5 x 5 pixels) used to generate the shown fluorescence decay trace. Experimental conditions: λ_{ex} = 845 nm, main beam splitter edge wavelength at 705 nm, single detector mode: λ_{em} = 500 – 550 nm (525/50BP).

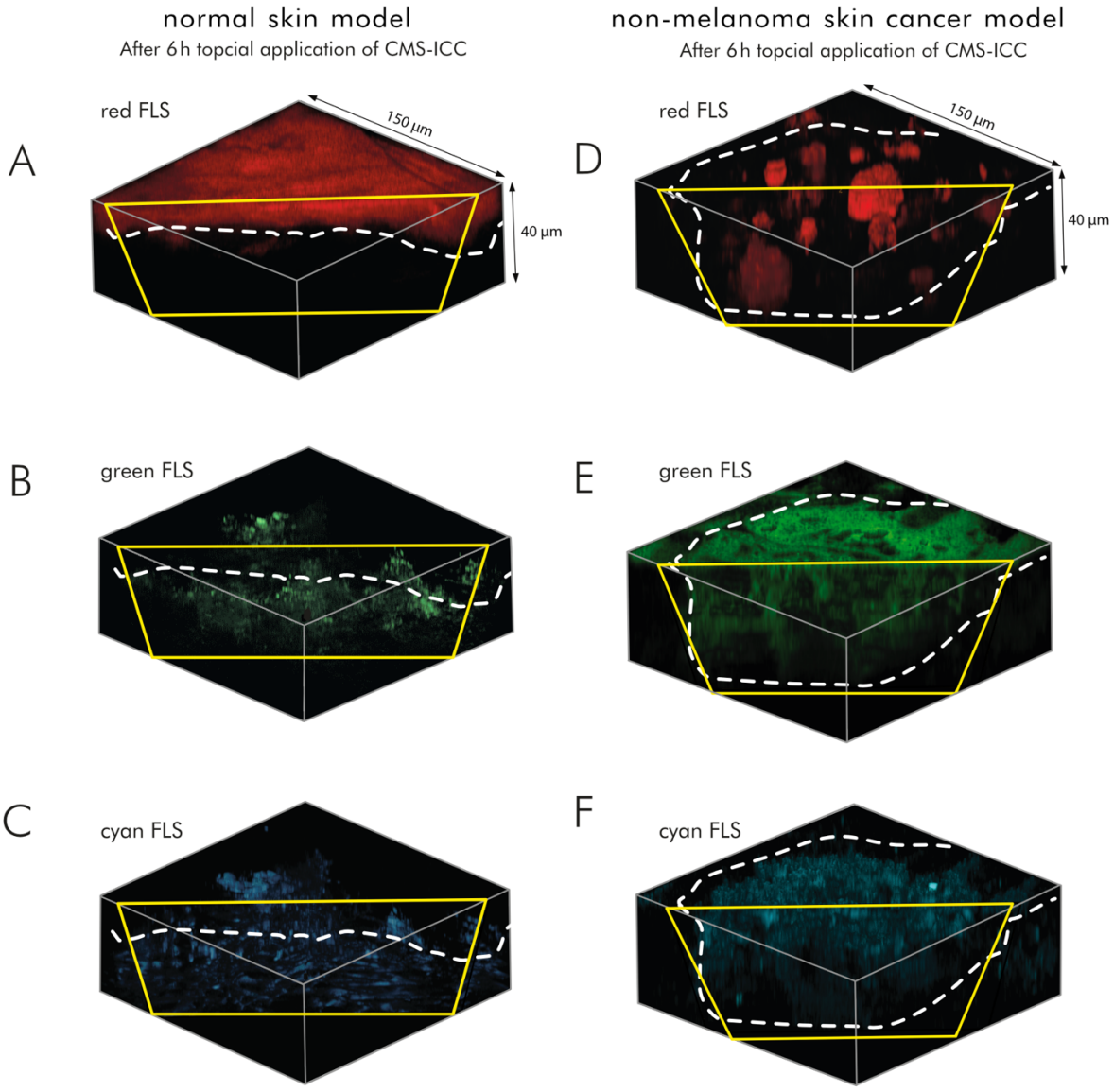

Figure A2: Live-tissue interaction imaging of CMS-ICC during its penetration into normal RHS and NMSC models using tomographic Cluster-FLIM images (detail view of Figure 4.5.13C&I). **A-C** Tomographic Cluster-FLIM image of CMS-ICC in normal RHS models after 6h topical application of CMS-ICC/bodipy resolved for the three determined FLS (red, green, cyan). **D-E** Tomographic Cluster-FLIM image of CMS-ICC in NMSC models after 6h topical application of CMS-ICC/bodipy resolved for the three determined FLS resolved for the three determined FLS (red, green, cyan).